Modelling single cavitation bubble dynamics near compliant surfaces using OpenFOAM

Thesis

for the degree of

doctor rerum naturalium (Dr. rer. nat.)

approved by the Faculty of Natural Sciences of
Otto-von-Guericke-University Magdeburg

by M. Sc. Hendrik Reese

born on 31.10.1998 in Stendal

Examiners: Prof. Dr. rer. nat. Claus-Dieter Ohl

Prof. Dr. Ing. Bettar Ould el Moctar

submitted on: 22.08.2023

defended on: 19.12.2023

Abstract

Cavitation bubbles are known to explosively expand and collapse, creating high-velocity liquid jets onto a nearby solid boundary and inducing strong shear flows and vortices along the boundary. Allowing the boundary to deform can significantly change the bubble and jetting dynamics and give rise to interesting flow phenomena. A viscous, compressible volume of fluid model for simulating a single bubble at a large seeding pressure in OpenFOAM is used to study its interaction with various boundaries. Three different computational solvers are developed to study the behaviour of the bubble near a perforated rigid boundary, a fluid-fluid interface, and an elastic solid boundary, respectively.
The use of a bubble-induced jet as a microfluidic pump through a perforation in a rigid solid wall is investigated. The observed dynamics are categorised into three types of jetting regimes as a function of the stand-off distance and the wall thickness.
Near a free boundary connected to a gaseous or liquid domain, a bubble may cause a breakup of the interface and spray/droplet formation, as well as a jet away from or towards the boundary, depending on the properties of both fluids on either side of the interface. In the case of a liquid-liquid interface, this is an underlying mechanism of bubble-based emulsification techniques. Water-in-oil emulsification mechanisms are investigated by creating a bubble in silicone oil near a similarly-sized water droplet. As a function of the stand-off distance and the viscosity ratio of the two liquids, two regimes of interface breakup are identified. A bubble created very close to a liquid-gas interface is studied, and a new type of liquid jet is observed that can pierce deep into the liquid bulk, the so-called "bullet jet". A similar bubble is also placed inside a falling liquid droplet, where the same type of jet is found, along with secondary cavitation bubbles created by the reflection of the shock wave on the free boundary.
The fluid solver is coupled to a finite volume solver for a linear elastic solid, which is used to model the stresses produced in the elastic solid by the jet and shock waves produced by a nearby collapsing bubble. The induced wall shear stress is investigated as a function of the stand-off distance, both for a planar and a ring-shaped wall geometry. A cavitation bubble confined between two elastic plates induces a surface acoustic wave, preceding the shock wave in the liquid and causing a tension region. This mechanism is used to investigate the role of local gas supersaturation caused by localised heating as cavitation bubble nuclei. With the same method, surface defects in glass are also found to be cavitation nuclei, making surface wave-created bubbles a viable method for surface damage detection and for creating bubbles with a controlled lifetime of less than 10 ns. Furthermore, it is found that the waves created by a shaped cavitation bubble can cause controlled surface damage. The role of the different waves in damage creation is evaluated by varying the time delay between the creation of two concentric circular wave sources. Finally, an ellipsoidal wave source is shown to create a surface crack along its minor semi-axis, while a point source can circularly extend the crack, thus enhancing the control over the length and the direction of the damage.

Kurzzusammenfassung

Es ist bekannt, dass Kavitationsblasen explosionsartig expandieren und kollabieren, dabei Flüssigkeitsjets mit hoher Geschwindigkeit auf naheliegende feste Oberflächen sowie starke Scher- und Wirbelströme entlang der Wand erzeugen. Ist es der Oberfläche erlaubt zu deformieren, so ändert sich die Blasen- und Jetbildungsdynamik und interessante Strömungsphänomene können auftreten. Ein viskoses, kompressibles Volume-of-Fluid-Modell für die Simulation einzelner Kavitationsblasen mit einem hohen Anfangsdruck in OpenFOAM wird verwendet, um die Wechselwirkung einer solchen Blase mit verschiedenen Oberflächen zu untersuchen. Drei verschiedene numerische Löser werden entwickelt, um das Verhalten der Blase in der Nähe einer perforierten festen Oberfläche, einer Fluid-Fluid-Oberfläche, und der Oberfläche eines elastischen Feststoffs zu untersuchen.
Die Anwendung eines durch eine Blase erzeugten Jets als mikrofluidische Flüssigkeitspumpe durch eine perforierte Wand wird untersucht. Die beobachteten Dynamiken werden in Abhängigkeit des Blasenabstands und der Wanddicke in drei Jet-Regime kategorisiert.
Nahe einer freien Oberfläche zu einem Gas oder einer Flüssigkeit kann eine Blase zu einem Aufbruch der Oberfläche und zur Spray-/Tropfenerzeugung führen, sowie, abhängig von den Eigenschaften der Fluide auf beiden Seiten der Oberfläche, einen Jet in Richtung oder entgegen der Oberfläche erzeugen. Im Fall einer Oberfläche zwischen zwei Flüssigkeiten ist dies ein unterliegender Mechanismus für blasenbasierte Emulsifikationstechniken. Mechanismen der Wasser-in-Öl-Emulsifikation werden untersucht, indem eine Blase in Silikonöl nahe eines Wassertropfens ähnlicher Größe erzeugt wird. In Abhängigkeit des Blasenabstandes und dem Verhältnis der Viskositäten beider Flüssigkeiten werden zwei Regime des Oberflächenaufbruchs identifiziert. Bei einer Blase nahe einer freien Oberfläche wird ein neuartiger Jet beobachtet, der tief in die Flüssigkeitsdomäne eindringen kann, der sogenannte Bullet-Jet. Eine ähnliche Blase wird auch in einem fallenden Flüssigkeitstropfen initiiert, wo ein gleichartiger Jet beobachtet wird, zusammen mit sekundären Kavitationsblasen, die durch die an der freien Oberfläche reflektierten Stoßwelle erzeugt werden.
Der Fluidlöser wird an einen finite-Volumen-Löser für einen linear-elastischen Feststoff gekoppelt. Dieser wird zur Modellierung der Spannungen verwendet, die durch den Jet und die Stoßwellen einer kollabierenden Blase in einem elastischen Feststoff erzeugt werden. Die erzeugte Wandschubspannung wird in Abhängigkeit des Blasenabstandes untersucht, sowohl für eine planare, als auch für eine ringförmige Wandgeometrie. Eine zwischen zwei elastischen Platten eingeschlossene Kavitationsblase erzeugt eine akustische Oberflächenwelle, die sich schneller als die Stoßwelle in der Flüssigkeit fortpflanzt und eine Region negativen Drucks hervorruft. Dieser Mechanismus wird genutzt, um zu untersuchen, ob eine durch lokales Heizen erzeugte lokale Gasübersättigung als Blasenkeim fungieren kann. Mit der gleichen Methode wird beobachtet, dass auch Oberflächendefekte als Blasenkeime dienen können, weshalb Oberflächenwellen eine Methode zur Detektion von Oberflächenschäden und zur kontrollierten Erzeugung von Blasen mit einer Lebenszeit von unter 10 ns darstellen. Des Weiteren wird gezeigt, dass eine geformte Kavitationsblase kontrolliert Oberflächenschäden verursachen kann. Die Rolle der verschiedenen Wellen bei der Schadenserzeugung wird durch die Variation des Zeitversatzes zwischen der Erzeugung zweier konzentrischer ringförmiger Wellenquellen untersucht. Schließlich wird gezeigt, dass eine elliptische Wellenquelle einen Oberflächenriss entlang ihrer kleinen Halbachse erzeugt, während eine Punktquelle einen Riss kreisförmig fortsetzen kann, womit die Kontrolle über die Länge und die Richtung des Schadens verbessert wird.

Contents

1 Introduction

Bubbles are ubiquitous. They are found in carbonated drinks, where solved carbon dioxide agglomerates, in boiling liquids, where they are created from the liquid through a phase transition, or in sloshing liquids like seawater, where they are mechanically introduced into the liquid bulk and rise to the surface due to gravity. Generally, larger bubbles quickly rise to the surface of the liquid and are hence removed from the liquid, while smaller bubbles are of a longer lifetime, allowing them to interact with their surroundings for a longer time. At the same time, nano-sized bubbles are difficult to observe and are due to large surface tension forces and gas diffusion inherently unstable. The ability to neglect the influence of gravity and the potential use in microfluidic and minimally invasive medical applications are reasons why micro-sized bubbles are of scientific interest. When perturbed, bubbles volumetrically oscillate around their equilibrium size, at which the internal gas pressure is balanced by the external pressure and surface tension. The interplay between inertia and compressibility gives rise to complex dynamics rich with interesting phenomena.

Bubbles gained attention in modern science after D. Silberrad [1] reported erosive damage on the propellers of the passenger ships “Lusitania” and “Mauretania” in 1912. Because of the importance of long-distance ship transport, research on its origin has intensified. The origin of this erosion was then to be found and suppressed. In 1917, Lord Rayleigh [2] proposed cavitation bubbles as a cause for the observed propeller erosion. Rayleigh found that the collapse of a spherical cavity can lead to localised high pressures. The collapse behaviour of bubbles near a rigid boundary was modelled numerically by Hickling and Plesset [3]. Plesset and Chapman [4], Blake and Gibson [5], and Best and Kucera [6] showed that such bubbles move towards the boundary. When a bubble collapses near a solid boundary or is subjected to another source of anisotropy, it commonly develops a jet that pierces the bubble. If this jet impacts on a nearby solid boundary, it induces large water hammer pressures and turns into a radial flow spreading across the boundary, creating large wall shear stresses. When bubbles collapse, they emit strong shock waves, which can then be reflected or refracted at nearby boundaries to another solid, liquid, or gaseous medium, causing different phenomena in each case. For instance, when a shock wave is reflected from a free boundary, it is turned into a rarefaction wave. Its energy can be transformed into other kinds of waves, such as elastic waves, or into other forms of energy, such as kinetic energy that translates, compresses, or expands another nearby bubble or causes the formation of liquid jets. The coupling between bubbles, waves, and other media can cause complex dynamics to arise from even rather simple geometries [7]. Today, it is known that cavitation bubbles can damage even the hardest materials available to mankind [8]. In the case of ship propellers or industrial flows, cavitation is an undesirable phenomenon that is to be avoided.

Nevertheless, controlled cavitation also has applications. Many small bubbles are used in ultrasound baths to clean jewellery, optical components, lab equipment, or medical tools [9]. There, the otherwise destructive pressures and shear forces are utilised to remove the dirt from surfaces. This is especially useful for small structures that are difficult to clean conventionally. Acoustically driven bubbles are also potentially useful as contrast agents for ultrasound imaging [10]. In medicine, acoustically induced cavitation is used to destroy unwanted tissue such as kidney stones (lithotripsy), fat cells, cancer cells and tumours (histotripsy). Drug-carrying bubbles may also be destroyed to release medicine

once they have reached a desired position. Laser-induced cavitation is also used in a controlled manner in laser eye surgery [11].
The use of bubbles to create high-speed liquid jets in air for the purpose of needle-free injection is currently under investigation [12–14]. The strong flows induced by cavitation bubbles are also used for the mixing of immiscible fluids [15]. Since an acoustically driven bubble collapse can lead to very high gas pressures and temperatures, bubbles can be used to induce a chemical reaction in the context of sonochemistry [16], or potentially even to ignite nuclear fusion, called nuclear confinement fusion [17, 18].
To further our understanding of the behaviour of bubbles, both for the sake of avoiding their destructive character and for applications as listed above, research on the behaviour of single cavitation bubbles is required. The experimental investigation of cavitation bubbles proved difficult since they are often small ($\lesssim 1$ mm) and their dynamics happen on short time scales ($\lesssim 1$ ms). Thus, instruments operating at high temporal and spatial resolutions are required. Even today, the behaviour of bubbles is only partly understood and is still a subject of ongoing research. Typically, high-speed cameras are used to capture the dynamics of the flow and the behaviour of the bubble. Early photographic studies of the dynamics of a bubble in the vicinity of a rigid boundary were carried out by Shutler and Mesler [19], as well as Benjamin and Ellis [20]. To measure the pressure at a specific position over time at high temporal resolution, hydrophones are used. There are a multitude of methods to induce cavitation in an experimental setting. Yet, the use of a focused laser pulse stands out due to its precise control and reproducibility [21].
Another point of scientific interest is the mechanism behind cavitation on the nanoscale. While it is known that the presence of nucleation sites in the liquid greatly aids the creation of cavitation bubbles, the precise nature of such nuclei is not fully understood. A specifically simple geometry is that of a thin liquid layer sandwiched between two solid plates [7], as this allows for optical observation of the entire region of interest while eliminating the limitation caused by the depth of field. The same advantage holds for the nucleation of bubbles through focused laser energy deposition. Additionally, the low Reynolds number of this confined geometry typically enforces laminar, predictable flows.
Besides experimental investigations, numerical simulations are typically used as a way to indirectly compare the experimental results with theoretical models. To study bubbles, the Boundary Element Method (BEM) was widely used, which offers a computationally efficient way to simulate two-phase flows in extended fluid domains. A more sophisticated, but computationally intensive approach is the Volume of Fluid (VoF) method, which allows one to account for viscosity, wave propagation, and surface tension. In recent years, VoF simulations have got increasingly more viable with advances achieved in computer technology. OpenFOAM is a highly versatile numerical framework based on the VoF method. It offers a multitude of numerical solvers for different aspects of fluid dynamics and allows for modifications of their code to suit the needs of a specific problem. Once a numerical solver is verified by experimental observations, it offers a powerful tool that allows one to inspect aspects of the flow of interest that are difficult to measure in experiments, such as the full pressure and velocity fields in the simulated fluids.

The present work is a cumulative dissertation, containing nine publications made over the course of the author's work at the department "Soft Matter" of the institute of physics in the faculty of natural sciences, at the Otto-von-Guericke-University (OvGU) in Magdeburg, Germany. All publications have been made in cooperation with fellow researchers from within the group and from other universities. Three of them list the present work's author as the first or a main author, and the remaining six as one of the co-authors. In all of these works, the author's contribution consists of the numerical simulations made in OpenFOAM, as well as taking part in the paper structuring, writing, and proofreading. Each chapter from chapter 4 to chapter 12 contains the work from one of these papers, including the full reference to the published version and published follow-up work, an abstract, an introduction, experimental and numerical methods, results, and conclusions. They can also be found in the list of references under [22–30]. Since the contributing authors and the publishing journals vary, the writing styles slightly differ between the papers. The author apologises for any perceived inconsistencies in the writing style throughout the present work, as well as repetitions in the numerical methods sections due to similarities between the papers.

Chapter 2 gives an introduction to fluid dynamics, linear elasticity, cavitation, and computational physics, and is aimed at beginners in the field. Derivations of the flow equations are largely taken from Batchelor [31]. For an introduction to elasticity theory, the author recommends the book by Landau and Lifschitz [32]. On bubble dynamics, there are books by Delale [33], Brennen [34], and Koukouvinis and Gavaises [35]. More references to cavitation and bubble dynamics are given in section 2.5. That being said, the present work merely provides the theoretical basics needed for modelling a single bubble interacting with boundaries of varying kinds. It does not cover acoustically driven bubbles and bubble clouds, an excellent review of which is given by Lauterborn and Kurz [36]. For an introduction to computational fluid dynamics, the author recommends the books by Darwish and Moukalled [37], Höpken and Mooney [38], and Tryggvason et al. [39], as well as the doctoral thesis of Prof. Jasak [40].

The software used for the CFD simulations is described in chapter 3. It describes three finite volume solvers within the OpenFOAM framework. CavBubbleFoam [41] is used in chapter 4 to model a cavitation bubble near a perforated rigid plate. It models two compressible, viscous, and immiscible fluids while neglecting mass and heat transfer. Since MultiphaseCavBubbleFoam [42] can model more than two fluid components, it was used to simulate a bubble interacting with a liquid-liquid interface in chapter 5, and with a free boundary in chapters 6 and 7. Fluid-structure interaction is modelled in chapter 8 by CavBubbleFsiFoam [43], where an expanding and collapsing bubble is coupled to a nearby linear elastic solid. This fluid-structure interaction solver is also used in the four following chapters, in which a bubble between two glass plates is simulated, where it excites Rayleigh waves that travel ahead of the shock waves emitted in the fluid, causing a tension region to form. This is used to show that localised gas supersaturation can act as a cavitation nucleus in chapter 9. In chapter 10 it is shown that nanoscopic cracks in the glass surface can do the same. In chapter 11, damage to the surface caused by two bubbles in the shape of concentric circles is studied in dependence of the time delay between their creation. Finally, in chapter 12 the generation of damage by an elliptical bubble as well as the effect of such a bubble on a pre-existing surface defect is investigated.

The work is concluded in chapter 13. The references from all chapters, including the published papers, are listed at the end of the present manuscript, just before the declaration of honour.

Acknowledgements

This work has been made possible by the unwavering love and support of my family as well as my partner, Yatha Sharma. I especially thank my parents, who always come to my aid, no matter what issues I face.
I also greatly appreciate the support of my friends and my co-students: Molly, Maarten, Rasmus, Gabriel, Guillo, Isabelle, Bailee, Raelynne, Theresa, Robin, Florian, Dominik, Kevin, Henning, Jonas, Saber, Fan, Anna, Hengzhu, Mingyuan, and Zeinab.
Whenever I lost sight of my scientific path, I could always count on my supervisor Claus-Dieter Ohl as a source of guidance and motivation.
The success of my work was enabled by the vivid collaboration with my co-authors: Robin Schädel, Fabian Reuter, Juan Manuel Rosselló, Ashoke Raman Kuppa, Patricia Pfeiffer, Julian Eisener, Mingbo Li, Xiaotong Ma, Chao Sun, Ulisses Gutiérrez-Hernández, Pedro Quinto-Su, Siew-Wan Ohl, and Claus-Dieter Ohl.
I wish to especially emphasise Juan Manuel Rosselló and Ulisses Gutiérrez-Hernández. Their moral values, hard work, and attention to detail make them great scientists and a joy to work with.
I thank Qingyun Zeng, Christiane Lechner, Max Koch, and Fabian Denner for helpful discussions about the numerical methods.
I also thank Derek Muller, Gavin Free, and Daniel Gruchy for consistently fueling my love for physics, as well as my school physics teachers: Iris Haberland, Sabrina Spieler, and Andrej Wölfer.
I gratefully acknowledge the financial support from the German Research Foundation (Deutsche Forschungsgemeinschaft, DFG, grant number OH75/4-1).

2 Theoretical basics

2.1 List of physical quantities and operators

The following table gives an overview of the quantities (quant.) used in chapter 2 and chapter 3. It includes variable and constant quantities in scalar, vectorial, and tensorial form as well as operators, along with their corresponding units. A unit of "1" signifies that the quantity is dimensionless.

Table 2.1: List of quantities and operators, along with their units and their meaning

quant.	unit	meaning	quant.	unit	meaning
t, τ	s	time	ζ	$\mathrm{kg{\cdot}m^{-1}{\cdot}s^{-1}}$	volume viscosity
m	kg	mass	κ	$\mathrm{m{\cdot}s^{2}{\cdot}kg^{-1}}$	compressibility
ρ	$\mathrm{kg{\cdot}m^{-3}}$	mass density	$c, c_\mathrm{l}, c_\mathrm{t}$	$\mathrm{m{\cdot}s^{-1}}$	wave velocity
$\vec{j}$	$\mathrm{kg{\cdot}m^{-2}{\cdot}s^{-1}}$	mass flux density	D	$\mathrm{m^2{\cdot}s^{-1}}$	diffusion coeff.
$\vec{x}$	m	location	T	K	temperature
l, L	m	length	λ	$\mathrm{kg{\cdot}m{\cdot}s^{-3}{\cdot}K^{-1}}$	heat conduction coeff.
r, R	m	radius	c_p, c_V	$\mathrm{m^2{\cdot}s^{-2}{\cdot}K^{-1}}$	specific heat capacity
$\vec{u}, \vec{v}, U$	$\mathrm{m{\cdot}s^{-1}}$	velocity	γ	1	adiabatic coeff.
$\vec{a}$	$\mathrm{m{\cdot}s^{-2}}$	acceleration	σ	$\mathrm{kg{\cdot}s^{-2}}$	surface tension coeff.
A	$\mathrm{m^2}$	surface area	Re	1	Reynolds number
∂A	m	circumference of ΔA	We	1	Weber number
$\vec{n}$	1	unit normal vector	Fr	1	Froude number
V	$\mathrm{m^3}$	volume	Ca	1	cavitation number
∂V	$\mathrm{m^2}$	surface of ΔV	d	1	stand-off distance
E	$\mathrm{kg{\cdot}m^2{\cdot}s^{-2}}$	energy	γ	1	stand-off parameter
w	$\mathrm{kg{\cdot}m^{-1}{\cdot}s^{-2}}$	energy density	$\vec{D}$	m	displacement
W	$\mathrm{kg{\cdot}m^2{\cdot}s^{-2}}$	work	$\overleftrightarrow{\varepsilon}$	1	strain tensor
F	$\mathrm{kg{\cdot}m^2{\cdot}s^{-2}}$	free energy density	K	$\mathrm{kg{\cdot}m^{-1}{\cdot}s^{-2}}$	bulk modulus
$\vec{F}$	$\mathrm{kg{\cdot}m{\cdot}s^{-2}}$	force	λ, G	$\mathrm{kg{\cdot}m^{-1}{\cdot}s^{-2}}$	Lamé parameters
$\vec{p}$	$\mathrm{kg{\cdot}m{\cdot}s^{-1}}$	momentum	E	$\mathrm{kg{\cdot}m^{-1}{\cdot}s^{-2}}$	elastic modulus
$\vec{f}_A, \vec{f}_V$	$\mathrm{kg{\cdot}m^{-2}{\cdot}s^{-2}}$	force density	v	1	Poisson's ratio
$\vec{M}$	$\mathrm{kg{\cdot}m^2{\cdot}s^{-2}}$	rotational moment	h, k	1	step size
$\vec{L}$	$\mathrm{kg{\cdot}m^2{\cdot}s^{-1}}$	angular momentum	Co	1	Courant number
p	$\mathrm{kg{\cdot}m^{-1}{\cdot}s^{-2}}$	pressure	ω	1	relaxation parameter
$\overleftrightarrow{\sigma}$	$\mathrm{kg{\cdot}m^{-1}{\cdot}s^{-2}}$	stress tensor	Γ	1	Gamma function
$\overleftrightarrow{s}$	$\mathrm{kg{\cdot}m^{-1}{\cdot}s^{-2}}$	deviatoric stress tensor	$\mathbb{1}$	1	unity matrix
N	$\mathrm{m^{-3}}$	number density	δ_{ik}	1	Kronecker delta
c_N	1	concentration	ϵ_{ijk}	1	Levi-Civita tensor
η	$\mathrm{kg{\cdot}m^{-1}{\cdot}s^{-1}}$	dynamic viscosity	∇	1	Nabla operator
ν	$\mathrm{m^2{\cdot}s^{-1}}$	kinematic viscosity	Δ	1	Laplace operator

2.2 Fluids

The branch of physics describing the properties of fluids is called fluid mechanics, or flow mechanics. The time-dependent behaviour of fluids is described by fluid dynamics, also called flow dynamics.
The defining property of fluids lies in their deformability under shear forces. The elements that make up the fluid can be rearranged freely without changing the macroscopic state of the fluid, as long as this rearrangement does not change its density ρ, which is a macroscopic quantity. A fluid subjected to a finite shear force $\vec{F}$ will continuously deform for as long as that force is applied. To be more precise, the fluid may offer some resistance to a shear force acting on it (e.g. viscous or inertial forces), but it will not be able to fully prevent the continuous rearrangement of its elements. This stands in contrast to the properties of a solid. If it is in equilibrium with its environment, the elements of a solid are arranged in a specific shape, which only changes if the environmental properties change.
This definition of a fluid encompasses especially liquids and gases, but also plasmas, solutions, foams, emulsions, suspensions, and aerosols. A plasma is a mixture of particles, a significant number of which are free, charged particles (electrons and ions). Such a plasma can be created through ionisation of a gas. A solution is a homogeneous mixture of two substances. The rest of the examples given above are heterogeneous mixtures of at least two substances, namely:

- foam: a gas in a liquid (or a solid)
- emulsion: a liquid in a liquid
- suspension: a solid in a liquid
- aerosol: a liquid or a solid in a gas (fog and smoke, respectively)

The categorisation between fluids and solids is not always clear. Some substances behave partly like a fluid and partly like a solid. Examples of this are viscoelastic materials like gelatine, non-Newtonian fluids like certain polymer solutions, liquid crystals, thixotropic substances like gels, paint, or quicksand, as well as high viscosity liquids like pitch.
The focus in the following work will lie on Newtonian fluids, or more precisely, compressible, isotropic liquids and gases that exhibit none of the above-listed properties of solids and a linear relationship between the local strain rate and the resulting viscous stress. One may refer to such a fluid as a "simple" fluid.

2.2.1 Molecular properties

To distinguish between a liquid and a gas, we will consider the molecular interactions taking place between the elements that make up the fluid. In the following, the word "particle" is representative of either atoms or molecules, which typically make up the fluids of interest. Figure 2.1 shows the force between two non-reactive neutral particles as a function of their distance d, as derived from the widely known Lennard-Jones potential [44]. This force is strongly repulsive for small distances of the order 10^{-10} m, since for sufficient proximity the particle's electrons are partly forced to move to higher energy states (Pauli repulsion). For larger distances, F is dominated by an electrostatic attraction (van-der-Waals force) between the particles, which stems from the particles being polarised in the electrostatic field of the other. This attractive force strongly diminishes

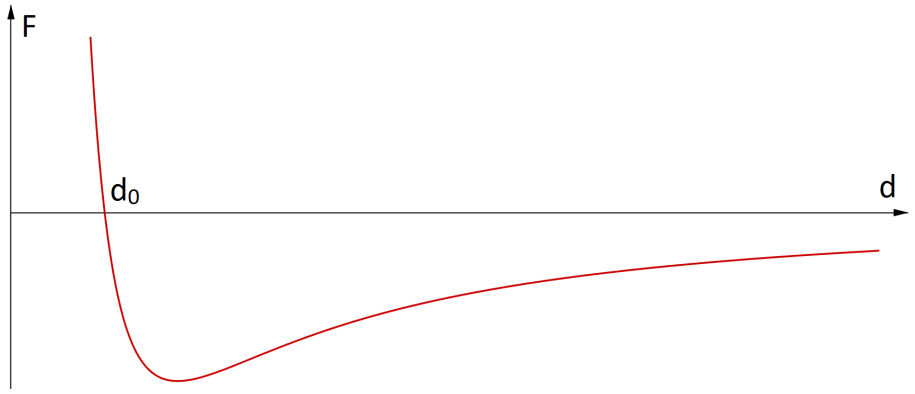

Figure 2.1: Force F between two simplified neutral particles as a function of their distance d. d_0 is usually of the order $3 \dots 4 \cdot 10^{-10}$ m.

as $\sim d^{-8}$ for $d \gg d_0$, and can thus be neglected for large d.
One may argue that a liquid is typically of much higher density than a gas. While this is an insufficient criterion to distinguish between liquids and gases, it is related to the distance between neighbouring fluid particles. For gases, the average distance between a particle and its nearest neighbour is much larger than their interaction cross-section diameter (at least of the order $10\,d_0$), and thus the intermolecular forces can be neglected most of the time. When two particles do come close to each other, their interaction can be approximated by a collision with an instantaneous transfer of energy and momentum. The particle interaction is thus approximated via a hard-core interaction potential.
In the case of liquids and solids, each particle is in the vicinity of multiple neighbours, and their attractive interaction is thus no longer negligible. In solids, the atomic grid typically stays constant or only changes slowly over time and is often even periodic in space, i.e. crystalline. Small groups of the particles of a liquid may temporarily arrange into a crystalline structure, which can then move as a whole, split into multiple groups or merge with others. It is remarkable that the density of a substance in a solid and a liquid state only differs by a few %, yet they still exhibit such fundamentally different properties.

2.2.2 The continuum hypothesis

Fluid mechanics is a branch of continuum mechanics, which describes substances as a continuous medium in space. It uses field quantities like density ρ and temperature T, which are continuous functions of space which change slowly on the scale of single particles. However, the mass distribution of a real fluid consisting of particles is far from such a continuous function. The mass of a particle is mostly concentrated in its core, which is much smaller than the particle itself. As a first approximation, the mass distribution of particles making up a fluid can be described as a sum of mass points, which is strongly discontinuous.
Despite this, continuum mechanics describes substances in macroscopic systems which are much larger than the intermolecular distances. Thus the basic assumption of continuum mechanics is made:

Substances macroscopically behave as if they were perfectly continuous.

So instead of describing discrete particles using physical quantities like mass m_i and velocity $\vec{v}_i$, in the region of space (domain) occupied by the substance, field quantities like the mass density ρ and the velocity field $\vec{u}$ are used. Those field quantities are macroscopic and can be measured as a function of space and time. They can be defined using a volume element ΔV, which is much smaller than the important length scales of the described macroscopic system. Thus, all partial volumes considered in the system should be larger than ΔV. The number of particles ΔN encompassed by the volume element ΔV, and thus also the value of a field quantity, then depends on the choice of the volume element's shape. For a small ΔN, this field value would then also strongly vary over time because of statistical fluctuations. Thus, ΔV should also be much larger than the intermolecular distance d, such that it contains a large number of particles, $\Delta N \gg 1$. This diminishes the statistical fluctuations of the field values (both in time and space) to the point that they can be neglected.
Under these conditions, the density field $\rho(\vec{x}, t)$ and the velocity field $\vec{u}(\vec{x}, t)$ can be defined as follows:

$$\rho(\vec{x}, t) = \frac{1}{\Delta V} \sum_{i=1}^{\Delta N} m_i = \frac{\Delta m}{\Delta V} \ , \tag{2.1}$$

$$\vec{u}(\vec{x}, t) = \frac{1}{\Delta N} \sum_{i=1}^{\Delta N} \vec{v}_i(t) = \langle \vec{v}_i \rangle \ . \tag{2.2}$$

The position $\vec{x}$ denotes the position of the volume element and can be taken as an arbitrary point within ΔV. In the following, the functional dependence $(\vec{x}, t)$ is omitted for simplicity. Also, the word "field" is omitted when regarding the field quantities.

2.2.3 Volume forces and surface forces

The forces acting on a fluid element can be categorised into two groups.
Long-range forces like gravity act on macroscopic regions of the fluid. Such forces are called volume forces. They typically change only slowly with the distance from their source. Thus within a fluid element, they can be taken to be spatially independent. The total volume force $\vec{F}_V$ acting on the fluid element is thus proportional to its mass Δm. Since the scale of the volume element is chosen such that density variations can be neglected and thus ρ can be taken to be constant within the fluid element, its mass and thus also $\vec{F}_V$ is proportional to its volume:

$$\vec{F}_V = \int_{\Delta V} \vec{f}_V \, dV \approx \vec{f}_V \, \Delta V \ , \tag{2.3}$$

where the volume force density $\vec{f}_V$ does not depend on the choice of ΔV.
The gravitational force density is

$$\vec{f}_V = \rho \, \vec{g} \ . \tag{2.4}$$

A commonly considered case is a homogeneous, time-independent gravitational field, which is a good approximation for the gravitational field in a stationary laboratory on earth. Then, the gravitational acceleration is given by $\vec{g} = -g \, \vec{e}_z = \text{const.}$, where $\vec{e}_z$ is the unit vector in the vertical axis.
The second group consists of short-range forces that quickly diminish with the distance from their source. Thus, as a first approximation, they only act on the surface of a fluid element. These surface forces may occur at the interface between any two neighbouring

fluid elements or at the interface between a fluid and another medium.
In gases, the main source of surface forces is the momentum transport through a given surface by particles passing through that surface, i.e. pressure. In liquids, an additional force occurs due to the attraction of neighbouring fluid particles, i.e. viscosity.
To describe surface forces, one may consider a planar surface element ΔA, which shall be much larger than the range of intermolecular forces, but much smaller than the length scale on which macroscopic quantities vary significantly. Thus, in the vicinity of ΔA the field quantities can be taken to be constant. The surface force acting on the surface element must then also be constant everywhere on ΔA, and it follows that the total force acting on the surface element is proportional to its area,

$$\vec{F}_A = \int_{\Delta A} \vec{f}_A \, dA \approx \vec{f}_A(\vec{n}) \, \Delta A \ . \tag{2.5}$$

The surface force density $\vec{f}_A$ here depends on the orientation of ΔA, given by the unit normal vector $\vec{n}$. If $\vec{n}$ points from fluid element A to fluid element B, $\vec{f}_A$ gives the surface force density that is acted on fluid element A by fluid element B at their interface ΔA. If the sign (i.e. the direction) of $\vec{n}$ is flipped, then the sign of $\vec{f}_A$ must also be flipped, i.e., $\vec{f}_A(\vec{n}) = -\vec{f}_A(-\vec{n})$. In other words, $\vec{f}_A$ is an odd function of $\vec{n}$.

The stress tensor

To examine the form of the surface force density $\vec{f}_A$, one can consider a triangular surface element ΔA as shown in figure 2.2. ΔA is chosen such that each of its sides lies in one of the three coordinate planes y-z, x-z, and x-y. The projection of ΔA on each of these planes results in the triangular surface elements ΔA_x, ΔA_y, and ΔA_z, respectively. These four surface elements with the unit normal vectors $\vec{n}$, $\vec{e}_x$, $\vec{e}_y$, and $\vec{e}_z$ form an irregular tetrahedron. The total surface force $\vec{F}_A$ acting on this tetrahedron can thus be written as

$$\vec{F}_A = \vec{f}_A(\vec{n}) \, \Delta A + \vec{f}_A(-\vec{e}_x) \, \Delta A_x + \vec{f}_A(-\vec{e}_y) \, \Delta A_y + \vec{f}_A(-\vec{e}_z) \, \Delta A_z \ . \tag{2.6}$$

The projections of ΔA can be expressed by ΔA itself,

$$\Delta A_x = \vec{e}_x \cdot \vec{n} \ \Delta A = n_x \, \Delta A; \ \Delta A_y = n_y \, \Delta A; \ \Delta A_z = n_z \, \Delta A \ . \tag{2.7}$$

Combining the equations (2.6) and (2.7) gives

$$\vec{F}_A = \left(\vec{f}_A(\vec{n}) - \left(n_x \, \vec{f}_A(\vec{e}_x) + n_y \, \vec{f}_A(\vec{e}_y) + n_z \, \vec{f}_A(\vec{e}_z) \right) \right) \Delta A \ . \tag{2.8}$$

Newton's second law relates the force acting on the fluid element with the rate of change of its momentum,

$$\begin{aligned} \vec{F} = \dot{p} &= \frac{d(\Delta m \, \vec{v})}{dt} = \frac{d(\rho \, \Delta V \, \vec{v})}{dt} = \frac{d(\rho \, \vec{v})}{dt} \Delta V \\ &= \vec{F}_V + \vec{F}_A = \vec{f}_V \, \Delta V + \left(\vec{f}_A(\vec{n}) - \left(n_x \, \vec{f}_A(\vec{e}_x) + n_y \, \vec{f}_A(\vec{e}_y) + n_z \, \vec{f}_A(\vec{e}_z) \right) \right) \Delta A \ . \end{aligned} \tag{2.9}$$

For the last step in the first line, the volume element was chosen to be stationary and of a constant size.
Rearranging equation (2.9) gives

$$\left(\vec{f}_A(\vec{n}) - \left(n_x \, \vec{f}_A(\vec{e}_x) + n_y \, \vec{f}_A(\vec{e}_y) + n_z \, \vec{f}_A(\vec{e}_z) \right) \right) = \left(\frac{d(\rho \, \vec{v})}{dt} - \vec{f}_V \right) \frac{\Delta V}{\Delta A} \ . \tag{2.10}$$

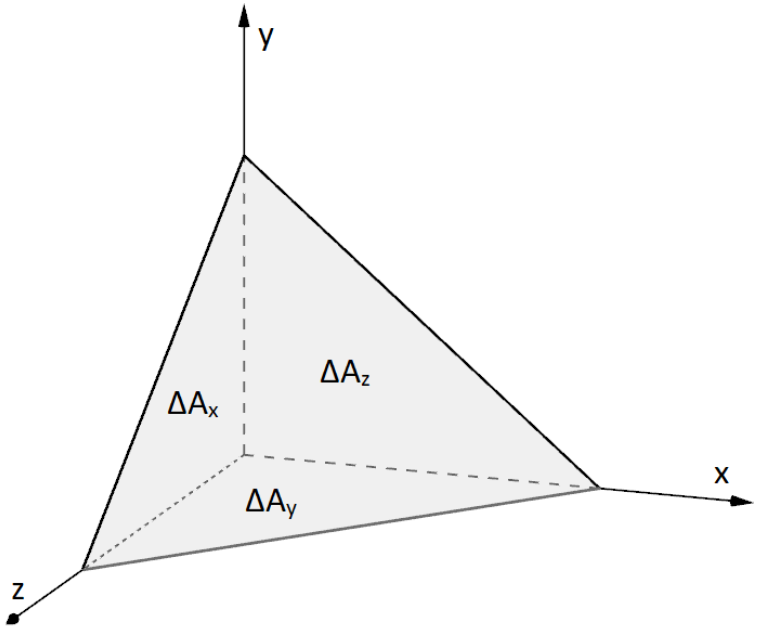

Figure 2.2: Irregular tetrahedron made up of the surface element ΔA and its projections on the coordinate planes ΔA_x, ΔA_y, and ΔA_z.

In the limit of a very small volume element, the right side of equation (2.10) vanishes, such that

$$\vec{f}_A(\vec{n}) = n_x\,\vec{f}_A(\vec{e}_x) + n_y\,\vec{f}_A(\vec{e}_y) + n_z\,\vec{f}_A(\vec{e}_z)\ . \tag{2.11}$$

The three vectors $\vec{f}_A(\vec{e}_x)$, $\vec{f}_A(\vec{e}_y)$, and $\vec{f}_A(\vec{e}_z)$ can now be interpreted as the columns of a tensorial quantity $\overleftrightarrow{\sigma}$ that is independent of $\vec{n}$,

$$\vec{f}_A = \overleftrightarrow{\sigma}\cdot\vec{n} \ \Leftrightarrow\ f_{A,i} = \sigma_{ij}\,n_j\ . \tag{2.12}$$

The right side of equation (2.12) uses index notation and Einstein's summation convention, i.e., for a term with a multiply occurring index variable, a sum of that term is taken over all available indices.
This newly introduced tensorial quantity $\overleftrightarrow{\sigma}$ is called the stress tensor. Its components σ_{ij} give the i-th component of the force that acts onto a surface with its normal vector in the j-direction.
To investigate the properties of the stress tensor, the rotational moment applied to a fluid element by volume forces and surface forces is considered,

$$\begin{aligned}
\vec{M} &\overset{(2.3),(2.5),(2.12)}{=} \int_{\Delta V} \vec{x}\times\vec{f}_V\,dV + \int_{\Delta A}\vec{x}\times(\overleftrightarrow{\sigma}\cdot\vec{n})\,dA \\
&\widehat{=} \int_{\Delta V}\epsilon_{ijk}\,x_j\,f_{V,k}\,dV + \int_{\Delta A}\epsilon_{ijk}\,x_j\,\sigma_{kl}\,n_l\,dA \\
&= \int_{\Delta V}\epsilon_{ijk}\,x_j\,f_{V,k}\,dV + \int_{\Delta V}\epsilon_{ijk}\,\frac{\partial(x_j\,\sigma_{kl})}{\partial x_l}\,dV \\
&\overset{\frac{\partial x_i}{\partial x_j}=\delta_{ij}}{=} \int_{\Delta V}\epsilon_{ijk}\,x_j\,f_{V,k} + \epsilon_{ijk}\left(\sigma_{kj} + x_j\,\frac{\partial\sigma_{kl}}{\partial x_l}\right)dV\ .
\end{aligned} \tag{2.13}$$

In the second step, the Levi-Civita tensor ϵ_{ijk} is introduced along with index notation ($\vec{a}\times\vec{b} = \epsilon_{ijk}a_jb_k$). Its components are 1 (-1), if i,j,k is an even (odd) permutation of

1,2,3, and 0 otherwise. In the third step, Gauss's theorem is used to replace the surface integral with a volume integral.
The equation for rotation analogous to Newton's second law relates the rotational moment to the rate of change of angular momentum and gives

$$\begin{aligned}\vec{M} = \dot{\vec{L}} &= \frac{d(\vec{x}\times\vec{p})}{dt} = \frac{d}{dt}\int_{\Delta m}\vec{x}\times\vec{v}\;dm = \frac{d}{dt}\int_{\Delta V}\vec{x}\times\vec{v}\;\rho\,dV \\ &\widehat{=}\;\frac{d}{dt}\int_{\Delta V}\epsilon_{ijk}\,x_j\,v_k\;\rho\,dV \overset{(2.13)}{=} \int_{\Delta V}\epsilon_{ijk}\,x_j\,f_{V,k} + \epsilon_{ijk}\left(\sigma_{kj} + x_j\,\frac{\partial\sigma_{kl}}{\partial x_l}\right)dV\;.\end{aligned} \tag{2.14}$$

In the limit of $\Delta V \to 0$, if the coordinates are chosen such that $\vec{x}$ stays within ΔV, $|\vec{x}|$ also approaches 0. Then in that limit, the left side of (2.14) as well as the first and third terms on the right side are proportional to $|\vec{x}|\,\Delta V$, while the second term on the right side is only proportional to ΔV. This term must thus be 0 for any choice of ΔV,

$$\int_{\Delta V}\epsilon_{ijk}\,\sigma_{kj}\,dV = 0 \;\Leftrightarrow\; \epsilon_{ijk}\,\sigma_{kj} = 0 \;\Leftrightarrow\; \sigma_{ij} = \sigma_{ji}\;. \tag{2.15}$$

The last step in equation (2.15) is done by executing the sum over j and k for all choices of i.
$\overset{\leftrightarrow}{\sigma}$ is thus symmetrical and only has six independent elements. The role of each element of the stress tensor in two dimensions is illustrated in figure 2.3 (a). The diagonal elements of $\overset{\leftrightarrow}{\sigma}$ are normal stresses in the sense that they represent the normal forces that act on a surface element that is parallel to one of the coordinate planes. They tend to squish or stretch a volume element along a coordinate axis. The non-diagonal elements meanwhile are tangential stresses, also called shear stresses, since they stand for the tangential forces acting on such a surface element. They tend to parallelly displace neighbouring layers of the medium.
It is always possible to choose the coordinate system such that the non-diagonal elements of a symmetrical tensor locally vanish. After such a main axis transformation, the diagonal elements of the stress tensors are called the main stresses. The trace of a tensor ($\mathrm{tr}(\overset{\leftrightarrow}{\sigma}) = \sum_i \sigma_{ii} = \sigma_{ii}$) is unchanged in a coordinate transformation. The stress tensor can thus be split into two summands such that one of them is traceless,

$$\overset{\leftrightarrow}{\sigma} = \frac{1}{3}\sigma_{ii}\,\mathbb{1} + \begin{pmatrix}\sigma_{11} - \frac{1}{3}\sigma_{ii} & 0 & 0\\ 0 & \sigma_{22} - \frac{1}{3}\sigma_{ii} & 0\\ 0 & 0 & \sigma_{33} - \frac{1}{3}\sigma_{ii}\end{pmatrix}\;. \tag{2.16}$$

The first term on the right side of equation (2.16) is the isotropic component of $\overset{\leftrightarrow}{\sigma}$ and represents an isotropic compression or expansion (see figure 2.3 (b)). The pressure p is thus defined as

$$p = -\frac{1}{3}\sigma_{ii}\;. \tag{2.17}$$

The second term represents a compression in one axis, an expansion in another and either a compression or an expansion in the third axis (see figure 2.3 (c)). Since the sum of these three elements is 0, this term tends to deform the volume element without changing its volume. In the case of a fluid, which is not able to prevent a rearrangement of its particles, this term leads to an acceleration of parts of the fluid. Thus, in a fluid at rest, only the first term is non-zero.

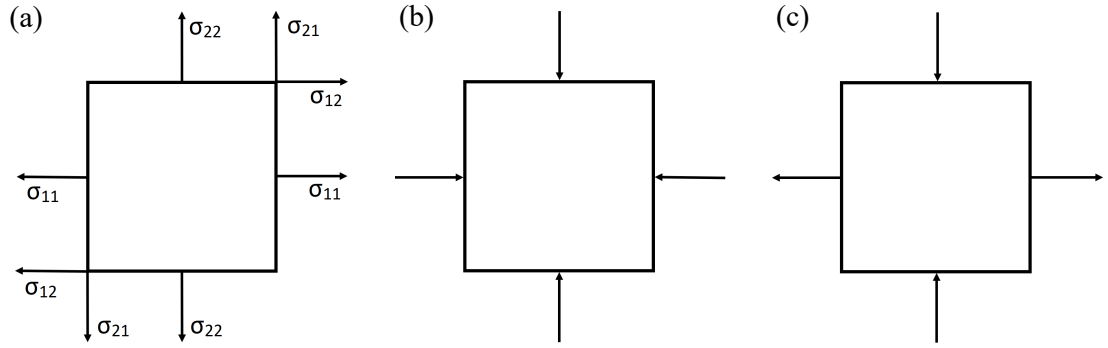

Figure 2.3: Role of the stress tensor $\overleftrightarrow{\sigma}$ in two dimensions. Left: directions, in which the components of the stress tensor $\overleftrightarrow{\sigma}$ act upon a fluid element. Centre: isotropic part of the stress tensor. Right: Anisotropic part of the stress tensor.

2.2.4 Transport phenomena

The equilibrium state of a fluid is a state in which specific quantities are spatially constant within the fluid. Such quantities are the temperature T, the velocity $\vec{u}$, and if the fluid consists of multiple different kinds of particles, the particle concentration c_N. If one of these quantities is not spatially constant, the system tends to smooth out non-uniformities via an exchange of heat, momentum, and particles, respectively.

Diffusion

If a fluid consists of multiple components, the concentration of each component may be non-uniform. Since a particle in a fluid frequently collides with other particles, its motion is effectively a random walk. This is also called Brownian motion [45].
One can consider only the particles of one of the components of the fluid. If the concentrations $c_N = \frac{\Delta N}{\Delta V}$ on the two sides of a surface element ΔA are not equal, the random motion of the particles will likely lead to a finite mass flux j_A across ΔA to the side of lower c_N. This phenomenon is called diffusion of the considered particles. j_A can be expressed by a particle flux vector $\vec{j}$ that is independent of the choice of orientation of ΔA, which is given by its normal unit vector $\vec{n}$,

$$j_A = \vec{j} \cdot \vec{n} \; \Delta A \; . \tag{2.18}$$

To find a relation between $\vec{j}$ and c_N, the assumption is made that c_N only varies slowly in space, such that near a surface element it may be approximated by a linear function. Then, $\vec{j}$ should only depend on the local properties of the fluid and the first-order spatial derivatives of c_N. The simplest form for $\vec{j}$ is then:

$$\vec{j} = \overleftrightarrow{k} \nabla c_N \; . \tag{2.19}$$

The tensorial quantity $\overleftrightarrow{k}$ is called the transport coefficient. This term can be used for any transport phenomenon, not just for diffusion. $\overleftrightarrow{k}$ can depend on the local properties of the fluid, and thus also on space and time, and possibly also on c_N. For isotropic media, like the fluids considered here, the transport coefficient can be described by a

scalar quantity, $\overleftrightarrow{k} = -k\,\mathbb{1}$. The negative sign was chosen so that $\vec{j}$ points in the direction of lower concentration c_N. k is then positive and equation (2.19) becomes

$$\vec{j} = -k\,\nabla c_N \ . \tag{2.20}$$

In practice, equation (2.20) holds well for a large range of ∇c_N. The mass flux of the considered particles out of a volume element ΔV is

$$\oint_{\partial V} \vec{j}\cdot d\vec{A} = -\oint_{\partial V} k\,\nabla c_N \cdot \vec{n}\,dA \overset{\text{Gauss's theorem}}{=} -\int_{\Delta V} \nabla\cdot(k\,\nabla c_N)\,dV \ , \tag{2.21}$$

where ∂V is the surface of ΔV.
Since the total number of particles is conserved, the mass flux out of ΔV must be related to a change in the particle number density in ΔV,

$$\begin{aligned}\oint_{\partial V} \vec{j}\cdot d\vec{A} \overset{\text{Gauss's theorem}}{=} -\frac{\partial}{\partial t}\int_{\Delta V} c_N\,m\,dV \overset{(2.21)}{=} -\int_{\Delta V}\nabla\cdot(k\,\nabla c_N)\,dV \\ \Leftrightarrow \quad \int_{\Delta V} m\,\frac{\partial c_N}{\partial t} - \nabla\cdot(k\,\nabla c_N)\,dV = 0 \ .\end{aligned} \tag{2.22}$$

Here, m stands for the mass of a considered particle, which was taken to be constant.
Since equation (2.22) should hold for any choice of ΔV, the integrand must vanish everywhere in the fluid. With the assumption that k does not vary in space, it follows that

$$\frac{\partial c_N}{\partial t} = D\,\Delta c_N \ . \tag{2.23}$$

Here, Δ is the Laplace operator. The newly introduced quantity $D = \frac{k}{m}$ is called the diffusion coefficient.
Equation (2.23) is the diffusion equation. It is one of the most important partial differential equations and its analytical and numerical solutions are well understood.

Heat conduction

Along with the migration of particles through a surface element ΔA, the kinetic energy they carry is transported. Additionally, through intermolecular forces kinetic energy is exchanged between neighbouring particles. These processes cause an energy flux, i.e. a heat flux, that tends to smooth out spatial temperature variations. Analogously to the arguments in the previous section, a heat flux caused by a local temperature gradient ∇T is related to a change in the local energy density $w = \frac{\Delta E}{\Delta V}$,

$$\frac{\partial w}{\partial t} = \nabla\cdot(\lambda\,\nabla T) \overset{\lambda=\text{const.}}{=} \lambda\,\Delta T \ . \tag{2.24}$$

The associated coefficient λ is called the heat conduction coefficient.
At constant pressure, a change in the energy density w leads to a change in the temperature T,

$$\frac{\partial w}{\partial t} = \rho\,c_p\,\frac{\partial T}{\partial t} = \nabla\cdot(\lambda\,\nabla T) \overset{\lambda=\text{const.}}{\Leftrightarrow} \frac{\partial T}{\partial t} = \frac{\lambda}{\rho\,c_p}\Delta T \ . \tag{2.25}$$

This is the heat conduction equation, where c_p is the specific heat capacity at a constant pressure p.

Momentum transport

Just like their kinetic energy, the momentum of the particles is transported through their migration and through particle interactions. But unlike the previous transported scalar quantities, the momentum $\vec{p}$ is a vectorial quantity, and thus needs to be treated differently.
Consider the case of a simple shear flow, where only the x-component of the velocity is non-zero. The velocity should also only depend on y, so $\vec{u}(y) = u_x(y)\,\vec{e}_x$. The inhomogeneity in $\vec{u}$ leads to tangential stress that tends to counteract this velocity gradient. Again a simple, linear form for the dependence on the gradient is assumed,

$$\sigma_{xy} = \mu \frac{du_x}{dy} \ , \tag{2.26}$$

where μ is the dynamic viscosity. It is interpreted as a measure of the inner friction forces in the fluid. It is thus a measure of the resistance of the fluid against the rearrangement of its particles and for the dissipation of macroscopic (or ordered) kinetic energy. This energy typically gets transformed into unordered kinetic energy, i.e. heat. Thus, to describe an energy dissipation, μ is necessarily positive. Often the kinematic viscosity is used, which is defined as $\nu = \frac{\mu}{\rho}$. The effect of the stress tensor $\overleftrightarrow{\sigma}$ on the velocity of the fluid is examined in greater detail in section 2.3.3.

2.2.5 Surface tension

Interfaces between media are of special interest since they determine the boundary conditions of the fluid and special phenomena occur at the boundary between different media. As is known in thermodynamics, two media that are in contact tend towards an equilibrium state, which is given by a constant temperature across both media. If there is a temperature difference between the two media, a heat flux across the interface of the two media towards the lower temperature occurs. Thus, the temperature must be continuous across their boundary, since a hypothetical jump in the temperature would cause an infinite heat flux. The heat fluxes on both sides of the interface must also be equal,

$$(\lambda\,\vec{n}\cdot\nabla T)_{\text{medium 1}} = (\lambda\,\vec{n}\cdot\nabla T)_{\text{medium 2}} \ . \tag{2.27}$$

This means that, if the heat conduction coefficients of the two media are not equal, the temperature gradient exhibits a jump at the boundary.
As long as the interface between the media stays intact, the velocity component normal to the interface must be continuous as well.
Often, a mass flux across the interface does not occur, e.g. between a fluid and a solid (if the solid is not porous or soluble), or between two immiscible fluids, so long as no phase transitions occur.
Small liquid droplets in a gas or small gas bubbles in a liquid often take an approximately spherical shape. For larger droplets and bubbles, gravitational effects become important and they are forced to take a different shape. This behaviour can be explained by a form of energy that is proportional to the surface of a fluid, $E = \sigma A$ since a sphere is the body of minimal surface area (and thus minimal surface energy E) for a given volume. The proportionality factor σ depends on the combination of the two media that form the interface. It has the form of a specific energy per unit area, but can also be interpreted as a line stress that tends to minimise the fluid surface, which is why it is referred to as

the surface tension coefficient.
The origin of surface tension lies in the attractive forces of the particles that make up the fluid. If the cohesive forces between the particles of one medium are larger than the adhesive forces between different particles of the two media, a particle near the interface experiences a non-zero force towards the fluid of its own kind, and the surface between the media is stable. In the opposite case, a particle near the interface between the two media gets pulled out of its own medium into the other. This corresponds to a negative value of σ and thus the medium tends to maximise its surface area. This is achieved when every particle of the medium is surrounded by particles of the other medium, if possible. Thus, in that case, the two media are miscible and any interface between them is unstable.
σ typically decreases with increasing temperature, and can also heavily depend on the presence of further components, like e.g. tensides, which decrease σ and can sometimes even make immiscible fluids miscible. A common example of tensides is soaps, which are used to decrease the surface tension of water with other media to improve the wettability of surfaces so that unwanted contaminants can be removed more easily from those surfaces.

Equilibrium shape between two fluids

The shape of the interface between two fluids can change freely, as opposed to the interface between a fluid and a rigid solid boundary. Consider two fluids in mechanical and thermodynamic equilibrium. σ is then constant along their interface.
It is apparent from observations that surface tension tends to flatten out curved surfaces. At a point P on an interface between two fluids, the coordinate system can be chosen such that P is at the coordinate origin and the x-y plane is the tangential plane on the surface at point P. Then, the shape of the surface near P can locally be described by a function $z = f(x, y)$, where the first-order spatial derivatives of f are zero. Near P, the normal unit vector can be approximated by $\vec{n} \approx (-\frac{\partial f}{\partial x}, -\frac{\partial f}{\partial y}, 1)$. Then, the surface tension force acting on an element ΔA of the interface can be calculated as

$$\begin{aligned} \Delta\vec{F} = -\sigma \oint_{\partial A} \vec{n} \times d\vec{x} = -\sigma\, \vec{e}_z \oint_{\partial A} -\frac{\partial f}{\partial x}\, dy + \frac{\partial f}{\partial y}\, dx = \sigma\, \vec{e}_z \left(\frac{\partial^2 f}{\partial x^2} + \frac{\partial^2 f}{\partial y^2}\right)_P \Delta A \\ \Rightarrow\ \Delta p = \sigma\, \Delta f\ . \end{aligned} \tag{2.28}$$

In the second step, Stokes' theorem was used and the second-order spatial derivatives were assumed to be constant near P. The surface tension force is thus inversely proportional to the local curvature of the interface.
The surface tension force generally causes a pressure jump Δp at the interface,

$$\frac{\Delta F}{\Delta A} = \Delta p = \sigma\, \Delta f \ \Rightarrow\ \overleftrightarrow{\sigma}_1 - \overleftrightarrow{\sigma}_2 = \Delta p\, \mathbb{1}\ . \tag{2.29}$$

The pressure is larger on the concave side of the interface. The pressure difference can be expressed as a jump in the stress tensor $\overleftrightarrow{\sigma}$ at the interface according to the right side of equation (2.29).

2.3 Fluid dynamics

In this section, the temporal evolution of the flow field is considered, with the goal of deriving the flow equations for simple fluids.
The flow field is typically described in one of two different ways. The Euler representation $\vec{u}(\vec{x},t)$ gives the average velocity of the fluid particles near $\vec{x}$ at time t. In the case of $\vec{u}$ being time-independent, the flow is called a stationary flow. In the Lagrange representation, $\vec{x}(\vec{x}_0,t_0)$ gives the trajectory of a fluid element that was at the position $\vec{x}_0$ at time t_0. $\vec{x}_0$ can be defined, for instance, as the geometric centre of ΔV. ΔV is assumed to be small enough so that even after any deformation by the flow field, it can be considered point-like at any relevant time t. In the preceding chapters, the Eulerian representation has been used, and it will also be used in the following calculations.
A curve that is tangential to $\vec{u}$ everywhere at a given time t is called a streamline. Streamlines are helpful for visualising the flow field at a specific time t. Streamlines are solutions of the following relation:

$$\frac{dx}{du_x} = \frac{dy}{du_y} = \frac{dz}{du_z} \ . \tag{2.30}$$

A line made up of the points visited by a fluid element is called a path line. It shows the trajectory taken by the fluid element and is a solution of the following differential equation,

$$\frac{d\vec{x}}{dt} = \vec{u}(\vec{x},t), \ \ \vec{x}(t_0) = \vec{x}_0 \ . \tag{2.31}$$

Another useful definition is that of a streak line, which consists of the positions at time t of all fluid elements that visit the position $\vec{x}_0$ at any time t'. Streak lines can be visualised in practice through continuous injection of ink at $\vec{x}_0$, so long as that does not disturb the flow field. An example of a streak line is the line made of smoke leaving a chimney. The points of a streak line are obtained by integrating equation (2.31) from each starting time t' to a specific time t, where $\vec{x}(t') = \vec{x}_0$. In a stationary flow, streamlines, path lines, and streak lines coincide.
In a stationary flow, $\frac{d\vec{u}}{dt} = 0$. Nonetheless, a fluid element experiences an acceleration $\frac{d\vec{v}}{dt}$ if it moves along a path on which $\vec{u}$ is not constant everywhere. Since the fluid element moves by $d\vec{x} = \vec{u}\,dt$ in time dt, its acceleration is given by

$$\frac{d\vec{v}}{dt} = \frac{\vec{u}(\vec{x}+\vec{u}\,dt, t+dt) - \vec{u}(\vec{x},t)}{dt} = \frac{\partial \vec{u}}{\partial t} + (\vec{u}\cdot\nabla)\,\vec{u} = \frac{D\vec{u}}{Dt} \ . \tag{2.32}$$

In the last step, the material derivative $\frac{D}{Dt} = \frac{\partial}{\partial t} + \vec{u}\cdot\nabla$ was introduced. A field quantity X attributed to the fluid element, like temperature T, density ρ, or momentum $\vec{p}$, changes on one hand because of its local rate of change $\frac{\partial X}{\partial t}$, but on the other also because the fluid element can move to another location where X takes a different value, $\vec{u}\cdot\nabla X$. Thus, the total rate of change of X for a given fluid element is given by $\frac{DX}{Dt}$. The temporal evolution of a surface defined by $X(\vec{x},t) = \text{const.}$ is given by $\frac{DX}{Dt} = 0$.

2.3.1 The continuity equation

If the mass of a fluid is conserved, then the mass flux $\vec{j}$ out of a volume element ΔV must be related to the rate of change of the density ρ,

$$\begin{aligned} \frac{d}{dt}\int_{\Delta V}\rho\,dV = -\int_{\partial V}\vec{j}\cdot d\vec{A} = -\int_{\partial V}\rho\,\vec{u}\cdot\vec{n}\,dA \overset{\text{Gauss theorem}}{=} -\int_{\Delta V}\nabla\cdot(\rho\vec{u})\,dV \\ \Leftrightarrow \int_{\Delta V}\frac{\partial\rho}{\partial t}+\nabla\cdot(\rho\vec{u})\,dV = 0\ . \end{aligned} \tag{2.33}$$

Since this must be true for any choice of ΔV, the integrand in equation (2.33) must vanish everywhere,

$$\frac{\partial\rho}{\partial t}+\nabla\cdot(\rho\vec{u}) = 0\ . \tag{2.34}$$

This is called the continuity equation. It is one of the fundamental equations of flow dynamics.
By factoring out the parentheses in equation (2.34), it can be written in a different form:

$$\frac{\partial\rho}{\partial t}+\vec{u}\cdot\nabla\rho+\rho\,\nabla\cdot\vec{u} = 0 \ \Leftrightarrow\ \frac{1}{\rho}\frac{D\rho}{Dt}+\nabla\cdot\vec{u} = 0\ . \tag{2.35}$$

The first term in equation (2.35) can be interpreted as a relative rate of change of the density ρ in a fluid element. The second term represents the expansion of the fluid caused by the divergence of the velocity field. Thus, $\nabla\cdot\vec{u}$ can be called the local expansion rate of the fluid.
In the special case of an incompressible fluid, which is often a good approximation for liquids, the density of the fluid stays constant everywhere in the fluid. It follows that $\nabla\cdot\vec{u} = 0$, as a special simple form of the continuity equation. In this case, since the divergence of the vector field $\vec{u}$ vanishes, $\vec{u}$ is called a source-free vector field.

2.3.2 Material integrals

To derive the equations of motion for a fluid, the integral form of conservation equations in a moving fluid is needed. Consider the time-dependent volume $\Delta V_\mathrm{F}(t)$ of a fluid element in motion. The rate of change of ΔV_F is given by equation (2.35) as

$$\frac{d\Delta V_\mathrm{F}}{dt} = \int_{\Delta V_\mathrm{F}}\nabla\cdot\vec{u}\,dV = \nabla\cdot\vec{u}\,\Delta V_\mathrm{F}+\mathcal{O}(\Delta V_\mathrm{F}^2)\ . \tag{2.36}$$

The rate of change of a line element in motion $\Delta\vec{x}_\mathrm{F}$ is given by the difference of the velocities of the two sides of the length element,

$$\frac{d\Delta\vec{x}_\mathrm{F}}{dt} = (\Delta\vec{x}_\mathrm{F}\cdot\nabla)\,\vec{u}+\mathcal{O}({\Delta\vec{x}_\mathrm{F}}^2)\ , \tag{2.37}$$

under the assumption that the line element stays approximately straight.
To calculate the rate of change of a surface element in motion $\Delta\vec{A}_\mathrm{F}$, one can consider a cylindrical volume element,

$$\Delta V_\mathrm{F} = \Delta\vec{A}_\mathrm{F}\cdot\Delta\vec{x}_\mathrm{F}\ , \tag{2.38}$$

with the base $\Delta\vec{A}_\mathrm{F}$ and the height $\Delta\vec{x}_\mathrm{F}$. Combining the equations (2.36)-(2.38) gives

$$\begin{aligned} &\frac{d\Delta V_\mathrm{F}}{dt} = \nabla\cdot\vec{u}\,\Delta\vec{A}_\mathrm{F}\cdot\Delta\vec{x}_\mathrm{F} = \frac{d\Delta\vec{A}_\mathrm{F}}{dt}\cdot\Delta\vec{x}_\mathrm{F}+\Delta\vec{A}_\mathrm{F}\cdot(\Delta\vec{x}_\mathrm{F}\cdot\nabla)\,\vec{u}+\mathcal{O}(\Delta V_\mathrm{F}^2) \\ \Leftrightarrow\ &\Delta x_{\mathrm{F},i}\left(\frac{d\Delta A_{\mathrm{F},i}}{dt}+\Delta A_{\mathrm{F},j}\frac{\partial u_j}{\partial x_i}-\Delta A_{\mathrm{F},i}\frac{\partial u_j}{\partial x_j}\right) = \mathcal{O}(\Delta V_\mathrm{F}^2)\ . \end{aligned} \tag{2.39}$$

Since equation (2.39) should hold for any choice of $\Delta\vec{x}_\mathrm{F}$, the expression in the parentheses should be small,

$$\frac{d\Delta A_{\mathrm{F},i}}{dt} = \Delta A_{\mathrm{F},i}\,\frac{\partial u_j}{\partial x_j} - \Delta A_{\mathrm{F},j}\,\frac{\partial u_j}{\partial x_i} + \mathcal{O}(\Delta\vec{A}_\mathrm{F}^{\,2}) \ . \tag{2.40}$$

Now consider a quantity X attributed to the medium. The line integral $\int_P^Q X\,d\vec{x}_\mathrm{F}$ only depends on time and changes because of the local change of X and the change of the length and shape of the curve $\vec{x}_\mathrm{F}$ from P to Q. To determine the time dependence of that integral, it is written in sum notation,

$$\frac{d}{dt}\int_P^Q X\,d\vec{x}_\mathrm{F} = \frac{d}{dt}\Big(\lim_{n\to\infty}\sum_n X_n\,\Delta\vec{x}_{\mathrm{F},n}\Big) \ . \tag{2.41}$$

The length elements $\Delta\vec{x}_{\mathrm{F},n}$ are time-dependent, but should stay small under the assumption that $\nabla\cdot\vec{u}$ is not very large.
The values X_n change because of a local change of X and because of the translation of the length elements, according to the material derivative $\frac{D}{Dt}$. The change of the length and orientation of $\Delta\vec{x}_{\mathrm{F},n}$ is given by equation (2.37). Thus, equation (2.41) becomes

$$\begin{aligned}\frac{d}{dt}\int_P^Q X\,d\vec{x}_\mathrm{F} &= \lim_{n\to\infty}\sum_n \frac{DX_n}{Dt}\,\Delta\vec{x}_{\mathrm{F},n} + X_n\,(\Delta\vec{x}_{\mathrm{F},n}\cdot\nabla)\,\vec{u} \\ &= \int_P^Q \frac{DX}{Dt}\,d\vec{x}_\mathrm{F} + \int_P^Q X\,(d\vec{x}_\mathrm{F}\cdot\nabla)\,\vec{u} \ .\end{aligned} \tag{2.42}$$

The derivations for the material surface integral and the volume integral are analogous, with the use of equation (2.39) and equation (2.36), respectively:

$$\frac{d}{dt}\int X\,dA_{\mathrm{F},i} = \int \frac{DX}{Dt} + X\,\frac{\partial u_j}{\partial x_j}\,dA_{\mathrm{F},i} - \int X\,\frac{\partial u_j}{\partial x_i}\,dA_{\mathrm{F},j} \ , \tag{2.43}$$

$$\frac{d}{dt}\int X\,dV_\mathrm{F} = \int \frac{DX}{Dt} + X\,\nabla\cdot\vec{u}\,dV_\mathrm{F} \ . \tag{2.44}$$

2.3.3 The Navier-Stokes equations

An equation of motion is acquired by applying Newton's second law, $\vec{F} = \dot{\vec{p}}$, on a system or a class of systems. In the following, it is applied to the class of simple fluids. Using $\rho\,\vec{u}$ for X and equation (2.35) in equation (2.44) gives

$$\vec{F} = \frac{d\vec{p}}{dt} = \frac{d}{dt}\int_{\Delta V_\mathrm{F}} \rho\,\vec{u}\,dV_\mathrm{F} = \int_{\Delta V_\mathrm{F}} \rho\,\frac{D\vec{u}}{Dt}\,dV_\mathrm{F} \ . \tag{2.45}$$

In section 2.2.3, the force $\vec{F}$ acting on a fluid element was categorised into volume forces and surface forces. Combining the equations (2.3), (2.5), and (2.12) gives

$$F_i = \int_{\Delta V_\mathrm{F}} f_{V,i}\,dV_\mathrm{F} + \int_{\partial V_\mathrm{F}} \sigma_{ij}\,n_j\,dA_\mathrm{F} = \int_{\Delta V_\mathrm{F}} f_{V,i} + \frac{\partial\sigma_{ij}}{\partial x_j}\,dV_\mathrm{F} \ . \tag{2.46}$$

The equations (2.45) and (2.46) must hold for any choice of ΔV_F. Thus, their integrands must be equal everywhere in the fluid,

$$\rho\,\frac{Du_i}{Dt} = f_{V,i} + \frac{\partial\sigma_{ij}}{\partial x_j} \ . \tag{2.47}$$

The volume forces typically only consist of the gravitational force, $\vec{f}_V = \rho\,\vec{g}$, and even that can often be neglected on microfluidic scales.
In section 2.2.3 it was also shown that in a fluid at rest, the stress tensor is described by an isotropic pressure, $\overleftrightarrow{\sigma} = -p\,\mathbb{1}$. Even in a fluid in motion, the pressure was defined as $p = -\frac{1}{3}\sigma_{ii}$ such that it describes the isotropic component of the stress tensor. The anisotropic, trace-less component of $\overleftrightarrow{\sigma}$ is called the deviatoric stress tensor $\overleftrightarrow{s}$,

$$\overleftrightarrow{\sigma} = \overleftrightarrow{s} - p\,\mathbb{1}\ . \tag{2.48}$$

Since $\overleftrightarrow{\sigma}$ is a surface force density, $\overleftrightarrow{s}$ should only depend on the local state and properties of the fluid. Furthermore, if $\overleftrightarrow{s}$ was a function of $\vec{u}$, it would depend on the choice of frame of reference. The flow fields developed in the different reference frames would lead to a contradiction. Thus, under the assumption that the flow field varies slowly on the scale of the considered volume elements, $\overleftrightarrow{s}$ can be taken to be linear in the first-order spatial derivatives of $\vec{u}$. The general form of $\overleftrightarrow{s}$ is then

$$s_{ij} = A_{ijkl}\,\frac{\partial u_k}{\partial x_l}\ . \tag{2.49}$$

The fourth-order tensor A_{ijkl} depends on the local properties of the fluid, but not on the flow field. Also, just like $\overleftrightarrow{s}$, it should be symmetric in the indices i, j. All isotropic tensors of an even order can be written via scalar coefficients and Kronecker deltas as follows:

$$A_{ijkl} = \mu\,\delta_{ik}\,\delta_{jl} + \mu'\,\delta_{il}\,\delta_{jk} + \mu''\,\delta_{ij}\,\delta_{kl}\ . \tag{2.50}$$

From the symmetry condition, it follows that $\mu' = \mu$.
Inserting equation (2.50) into equation (2.49) gives

$$s_{ij} = \mu\left(\frac{\partial u_i}{\partial x_j} + \frac{\partial u_j}{\partial x_i}\right) + \mu''\ \nabla\cdot\vec{u}\ \delta_{ij}\ . \tag{2.51}$$

Since $\overleftrightarrow{s}$ is trace-less by definition, taking its trace gives a further condition:

$$s_{ii} = (2\mu + 3\mu'')\ \nabla\cdot\vec{u} = 0\ \Rightarrow\ 2\mu + 3\mu'' = 0\ . \tag{2.52}$$

Then, only one independent coefficient remains:

$$s_{ij} = \mu\left(\frac{\partial u_i}{\partial x_j} + \frac{\partial u_j}{\partial x_i} - \frac{2}{3}\nabla\cdot\vec{u}\ \delta_{ij}\right)\ . \tag{2.53}$$

To obtain a comparison with equation (2.26), just like in section 2.2.4 the case of a simple shear flow is considered, where $\frac{\partial u_x}{\partial y}$ is the only non-zero first-order spatial derivative of the flow field. Then, the only non-zero elements of $\overleftrightarrow{s}$ are:

$$s_{xy} = s_{yx} = \mu\,\frac{\partial u_x}{\partial y} \tag{2.54}$$

Thus the coefficient μ introduced in equation (2.50) is the kinematic viscosity introduced in equation (2.26). Inserting the equations (2.48) and (2.53) into equation (2.47) gives the equation of motion for simple fluids,

$$\rho\,\frac{Du_i}{Dt} = f_{V,i} - \frac{\partial p}{\partial x_i} + \frac{\partial}{\partial x_j}\,\mu\left(\frac{\partial u_i}{\partial x_j} + \frac{\partial u_j}{\partial x_i} - \frac{2}{3}\,\nabla\cdot\vec{u}\ \delta_{ij}\right)\ , \tag{2.55}$$

the vectorial form of which is given by

$$\rho\frac{D\vec{u}}{Dt} = \vec{f_V} - \nabla p + \nabla\cdot\left(\mu\left(\nabla\circ\vec{u} + (\nabla\circ\vec{u})^{\mathrm{T}} - \frac{2}{3}\nabla\cdot\vec{u}\;\mathbb{1}\right)\right) . \tag{2.56}$$

These are the Navier-Stokes equations.
For many fluids, μ is mostly dependent on the temperature. If temperature variations are sufficiently small, μ can be taken to be spatially independent, and equation (2.3.3) becomes

$$\begin{aligned}\rho\,\frac{Du_i}{Dt} &= f_{V,i} - \frac{\partial p}{\partial x_i} + \mu\left(\frac{\partial^2 u_i}{\partial x_j^2} + \frac{\partial^2 u_j}{\partial x_j \partial x_i} - \frac{2}{3}\,\frac{\partial}{\partial x_i}\nabla\cdot\vec{u}\right)\\ &= f_{V,i} - \frac{\partial p}{\partial x_i} + \mu\left(\frac{\partial^2 u_i}{\partial x_j^2} + \frac{1}{3}\,\frac{\partial}{\partial x_i}\nabla\cdot\vec{u}\right) ,\end{aligned} \tag{2.57}$$

the vectorial form of which is given by

$$\rho\,\frac{D\vec{u}}{Dt} = \vec{f_V} - \nabla p + \mu\,(\Delta\vec{u} + \frac{1}{3}\,\nabla(\nabla\cdot\vec{u})) . \tag{2.58}$$

The coefficient in front of $\nabla(\nabla\cdot\vec{u})$ is referred to as the volume viscosity $\zeta = \frac{\mu}{3}$.
A special case commonly considered for liquids is that of an incompressible fluid, where $\nabla\cdot\vec{u} = 0$. Then, equation (2.58) becomes

$$\rho\,\frac{D\vec{u}}{Dt} = \vec{f_V} - \nabla p + \mu\,\Delta\vec{u} . \tag{2.59}$$

Boundary conditions

As stated in section 2.2.5, the normal component of the flow velocity must be continuous at an interface between two immiscible media. This should also be true for the tangential components since a jump in the tangential velocity would lead to an infinite stress on the interface according to equation (2.53). Even for fluids that can intrinsically be described as approximately inviscid, viscosity still plays a role near boundaries. The region near the boundary in which viscosity is important is called the boundary layer.
In the case of an interface between a fluid and a solid, it immediately follows that the velocity of the fluid at the interface must be equal to that of the solid. Thus at the surface of a solid wall at rest, it follows that $\vec{u} = 0$. This is the so-called no-slip boundary condition. It describes the property of fluids to stay on a solid boundary rather than sliding freely across it.
Another boundary condition is required for the stress tensor $\overleftrightarrow{\sigma}$. According to equation (2.28), surface tension causes a finite pressure difference between both sides of a boundary. The deviatoric stress tensor $\overleftrightarrow{s}$ is required to be continuous at the fluid surface.

2.3.4 Equation of state

The continuity equation (2.34) and the Navier-Stokes equations (2.58) are four equations for the five fields $\vec{u}$, ρ, and p. Thus, to solve the system of equations, another equation is necessary. The equation of choice is typically of thermodynamic origin. It describes the state of the considered medium by locally relating its properties to the pressure field. In general, such an equation of state can be written as

$$\rho = \rho(p) . \tag{2.60}$$

An especially simple equation of state is that of an isothermal ideal gas, $\rho = \text{const.} \cdot p$, or that of an incompressible liquid, $\rho = \text{const.}$ To describe weakly compressible liquids, e.g. water, a commonly used equation is the Tait equation of state [46],

$$p = (p_0 + B)\left(\frac{\rho}{\rho_0}\right)^{\gamma} - B \ , \tag{2.61}$$

where p_0 and ρ_0 is a reference pair of values for the pressure and the density. B is a fitting parameter that can be obtained experimentally for the fluid considered. A positive value of B allows the pressure to be negative for positive densities, which is not possible for an ideal gas. For $B = 0$, equation (2.61) becomes the equation of state for an adiabatic ideal gas. γ is the exponent that describes the functional dependence between p and ρ. For an ideal gas, it has the meaning of the adiabatic exponent $\gamma = \frac{c_p}{c_V}$, which is the ratio of specific heats at constant pressure and a constant volume, respectively.
To describe the rate at which the volume V of a fluid changes with varying pressure p, the compressibility κ is defined as follows:

$$\kappa = -\frac{1}{V}\left(\frac{\partial V}{\partial p}\right) = \frac{1}{\rho}\left(\frac{\partial \rho}{\partial p}\right) \ . \tag{2.62}$$

To also describe the temporal evolution of the temperature T, one more equation is necessary, which is typically the heat conduction equation (2.25). In that case, the temperature dependence also needs to be included in the equation of state.

2.3.5 The Reynolds number

Consider the case of an incompressible flow without regarding any volume forces, $\vec{f}_V = 0$, which is described by equation (2.59) and $\nabla \cdot \vec{u} = 0$,

$$\rho\left(\frac{\partial \vec{u}}{\partial t} + (\vec{u} \cdot \nabla)\,\vec{u}\right) = -\nabla p + \mu\,\Delta\vec{u},\ \nabla \cdot \vec{u} = 0 \ . \tag{2.63}$$

It is useful to express equation (2.63) using dimensionless quantities. For this, a characteristic length L and a characteristic velocity U that describe the system are chosen. Dimensionless quantities are introduced as

$$\vec{u}' = \frac{\vec{u}}{U},\ t' = \frac{U\,t}{L},\ \vec{x}' = \frac{\vec{x}}{L},\ p' = \frac{p}{\rho\,U^2} \ . \tag{2.64}$$

Then, equation (2.63) becomes

$$\frac{\partial \vec{u}'}{\partial t'} + (\vec{u}' \cdot \nabla')\,\vec{u}' = -\nabla'\vec{u}' + \frac{1}{Re}\Delta'\vec{u}',\ \nabla' \cdot \vec{u}' = 0 \ , \tag{2.65}$$

where ∇' and Δ' denote derivatives by the primed coordinates $\vec{x}'$ and the newly introduced quantity $Re = \frac{\rho L U}{\mu}$ is called the Reynolds number.
Equation (2.65) is analogous to the Navier-Stokes equations for incompressible fluids (2.63), but it now only depends on the geometry, the initial conditions, and the boundary conditions in the primed coordinates, as well as the independent variables $\vec{x}'(t')$ and t' and the dimensionless parameter Re.
This form of the Navier-Stokes equations gives two significant insights. If the flow field of a specific system is known, its non-dimensional form can be applied to the triple-infinite family of systems with the same Reynolds number. Systems that may differ in

the parameters ρ, L, U, and μ, but not in the Reynolds number, are called dynamically similar.
The second insight is that, by calculating the Reynolds number of a specific system, one can estimate the importance of the viscous term in equation (2.65) for that system. One can thus categorise flow systems by the value of Re. In systems with a very low Reynolds number, $Re \ll 1$, the inner friction of the fluid is largely responsible for the structure of the flow field. Typically, so-called laminar flows are created, in which the fluid flows in layers that stay adjacent to each other. In the case of a large Reynolds number, $Re \gg 1$, the viscous properties of the fluid should only play a minor role. Such flows are often chaotic, in the sense that small variations in the initial conditions grow exponentially in time. Such flows are called turbulent. This is the reason why weather predictions are very mathematically challenging, since the inaccuracies in the measured weather conditions at a certain time limit how far into the future the air flows can be predicted.
The nature of the whole flow field often cannot be described by a single number. In most cases, there are multiple ways to define L and dependent on space and time. For instance, even for flows with arbitrarily large Reynolds numbers, the no-slip boundary condition causes a boundary layer near the boundaries of the fluid, in which the viscosity plays an important role. Still, this approach is useful to make qualitative statements about the nature of a flow, and especially for comparing similar systems in which the characteristic length and velocity scales are similarly defined. Also, dynamic similarity allows one to examine a large-scale flow system via a down-scaled physical model.
There are other non-dimensional quantities useful in fluid mechanics, such as the Weber number $We = \frac{\rho U^2 L}{\sigma}$, which compares the influence of inertial effects to those of surface tension σ. A large Weber number corresponds to a higher likeliness of a breakup of bubbles or droplets. The Froude number $Fr = \frac{U}{\sqrt{|\vec{g}|L}}$ compares the influence of inertial effects to those of gravity or buoyancy, and in the present work is commonly of the order of 10^3 or higher, such that gravitational effects can be neglected. The Mach number $Ma = \frac{U}{c}$ relates the flow velocity U to the fluid's speed of sound c. For small Mach numbers, energy dissipation due to acoustic wave radiation may be neglected. The cavitation number $Ca = \frac{p - p_\mathrm{v}}{\frac{1}{2}\rho U^2}$ characterises the likeliness of cavitation occurring in a liquid, where p_v is the vapour pressure of the liquid. To describe a specific experimental configuration, non-dimensional length and time scales are often introduced, such as the non-dimensional stand-off distance $\gamma = \frac{d}{R_\mathrm{max}}$ between a cavitation bubble and a wall, where d denotes the distance between the wall and the centre of the bubble upon the bubble's creation, and R_max the bubble's maximum radius.

2.3.6 Pressure waves

With the Ansatz of a planar wave, $\vec{u} = u_x(x,t)\,\vec{e}_x \approx 0,\ p = p(x,t)$, and neglecting volume forces and viscosity, equation (2.59) becomes

$$\rho \frac{Du_x}{Dt} \approx \rho \frac{du_x}{dt} = -\frac{dp}{dx} \ \Leftrightarrow\ dp = -\rho \frac{dx}{dt}\, du_x = -\rho\, u_x\, du_x \ . \tag{2.66}$$

Also, assuming that the wave is of small amplitude, the density field $\rho(x)$ stays approximately constant, and equation (2.34) becomes

$$u_x \frac{d\rho}{dx} + \rho \frac{du_x}{dx} \approx 0 \ \Leftrightarrow\ \ -\rho\, du_x = u_x\, d\rho \ . \tag{2.67}$$

Using this, equation (2.66) gives

$$dp = u_x^2\, d\rho \ \Leftrightarrow\ u_x = c = \sqrt{\frac{dp}{d\rho}} \overset{(2.62)}{=} \sqrt{\frac{1}{\kappa\rho}} \ . \tag{2.68}$$

This is the speed of sound in a simple fluid with a compressibility κ and a density ρ. Evaluating this for the Tait equation of state (2.61) gives

$$c = \sqrt{\gamma \frac{p_0 + B}{\rho} \left(\frac{\rho}{\rho_0}\right)^{\gamma}} \tag{2.69}$$

In the context of a wave that lasts for many oscillation cycles, such a pressure wave is called a sound wave. If it lasts for only one or a few cycles, it is typically referred to as a shock wave. The low-pressure part of a wave is called a rarefaction wave. If the amplitude exceeds the ambient pressure, such that negative pressures are achieved by a rarefaction wave, it is referred to as a tension wave.

2.4 Linear elasticity

Elasticity theory describes deformable solids in the scope of continuum mechanics. The continuum hypothesis postulated in section 2.2.2 is thus also applied to elastic solids. In contrast to simple fluids, a finite force on an elastic solid will lead to a finite deformation, i.e. a rearrangement of the particles that make up the solid. This is due to inner elastic stress forces counteracting external forces, thus allowing for an equilibrium state to be established between them. The solids considered in the following are idealised. Non-isotropic effects due to an inner crystalline structure, as well as viscoelasticity and heat conduction are neglected.
Every point in a solid can be defined via its coordinates $\vec{x}_0$ at some time t_0. Its displacement from these original coordinates can then be defined as

$$\vec{D}(\vec{x}_0, t) = \vec{x}(t) - \vec{x}_0 \ . \tag{2.70}$$

In the discussions of fluids, the Eulerian description was used, with a fixed coordinate system that the fluid moves in. Here the Lagrangian description is used, where the movement of mass elements is followed via its coordinates $\vec{x}(t)$.
While the displacement field $\vec{D}$ depends on the choice of the coordinate system and may also include translation and rotation of the solid, all physical quantities related to the elastic behaviour of the solid depend on derivatives of $\vec{D}$ that describe the local deformation or strain of the solid and are thus coordinate system invariant.
A choice can be made here. Since the coordinates $\vec{x}(t)$ and $\vec{x}_0$ describe the same element of the solid, they are related via a diffeomorphism $\vec{x}(\vec{x}_0, t) = \vec{x}_0(\vec{x}, t)^{-1}$, where the superscript denotes an inverse function. Thus, $\vec{D}$ can be chosen to be written either in terms of the original positions of its elements $\vec{x}_0$, or equivalently, in terms of their positions $\vec{x}$ at time t. The latter may be a more intuitive choice, since then $\vec{D}$ is defined at the current positions of its elements, and in that way follows the motion of the solid. On the other hand, the updated coordinates of the solid elements are already given by $\vec{x}_0 + \vec{D}$ and do not need to be updated explicitly. Thus, to reduce redundancy the former option is chosen in the numerical implementation discussed in chapter 3.
The distance vector between two infinitesimally neighbouring points that are at the positions $\vec{x}_0$, $\vec{x}_0'$ at time t_0 can be written as $d\vec{l_0} = \vec{x}_0' - \vec{x}_0$. At a later time t, the distance between them is given by

$$d\vec{l}(t) = \vec{x}'(t) - \vec{x}(t) \overset{(2.70)}{=} \vec{x}_0' + \vec{D}(\vec{x}_0', t) - \vec{x}_0 - \vec{D}(\vec{x}_0, t) := d\vec{l_0} + d\vec{D}(t) \ . \tag{2.71}$$

Using index notation with Einstein's summation convention gives

$$dl_i^2 = (dl_{i,0} + dD_i)^2 = (dl_{i,0} + \frac{\partial D_i}{\partial x_j}\, dx_j)^2 = dl_{i,0}^2 + 2\,\frac{\partial D_i}{\partial x_j}\, dx_j\, dx_i + \frac{\partial D_i}{\partial x_j}\,\frac{\partial D_i}{\partial x_k}\, dx_j\, dx_k \ . \tag{2.72}$$

By switching the indices i and j in half of the second term and i and k in the third term, the right side of equation (2.72) becomes

$$dl_i^2 = dl_{i,0}^2 + 2\,\varepsilon_{ij}\, dx_j\, dx_i, \ \varepsilon_{ij} = \frac{1}{2}\Big(\frac{\partial D_i}{\partial x_j} + \frac{\partial D_j}{\partial x_i} + \frac{\partial D_k}{\partial x_i}\,\frac{\partial D_k}{\partial x_j}\Big) \ . \tag{2.73}$$

The newly introduced quantity is the strain tensor $\overset{\leftrightarrow}{\varepsilon}$. It is symmetric from its definition, $\varepsilon_{ji} = \varepsilon_{ij}$. For small strains, the second-order derivative may be neglected and the strain tensor becomes

$$\varepsilon_{ij} = \frac{1}{2}\Big(\frac{\partial D_i}{\partial x_j} + \frac{\partial D_j}{\partial x_i}\Big) \mathrel{\widehat{=}} \frac{1}{2}\Big(\nabla \circ \vec{D} + (\nabla \circ \vec{D})^{\mathrm{T}}\Big) \tag{2.74}$$

Since ε_{ij} is symmetric, it is diagonalisable. In the principle coordinates of ε_{ij}, equation (2.73) becomes

$$dl_i^2 = dx_i^2 \overset{dl_{i,0}^2 = dx_{i,0}^2}{=} dx_{i,0}^2 + 2\,\varepsilon_{ij}\,dx_{j,0}\,dx_{i,0} = (\delta_{ij} + 2\,\varepsilon_{ij})\,dx_{j,0}\,dx_{i,0} = (1 + 2\,\varepsilon_{ii})\,dx_{i,0}^2 \ , \quad (2.75)$$

where ε_{11}, ε_{22}, ε_{33} are the Eigenvalues of ε_{ij}. The deformation now consists of three independent terms that can be considered as simple rarefaction or compression deformations in the three principle axes of ε, $dx_1 = \sqrt{1 + 2\,\varepsilon_{11}}\,dx_{1,0}$. The relative length difference is then given by $\frac{(dx_1 - dx_{1,0})}{dx_{1,0}} = \sqrt{1 + 2\,\varepsilon_{11}} - 1 \approx \varepsilon_{11}$. In the last step, a Taylor expansion around $\varepsilon_{11} = 0$ was applied. Equivalent expressions hold for the coordinates x_2 and x_3. The cubic volume element $dV_0 = dx_{1,0}\,dx_{2,0}\,dx_{3,0}$ thus gets transformed by ε_{ij} into

$$dV = dx_1\,dx_2\,dx_3 = (1 + \varepsilon_{11})\,(1 + \varepsilon_{22})\,(1 + \varepsilon_{33})\,dx_{1,0}\,dx_{2,0}\,dx_{3,0} \approx (1 + \varepsilon_{ii})\,dV_0 \ . \quad (2.76)$$

In the last step, second-order terms such as $\varepsilon_{11}\,\varepsilon_{22}$ were neglected. Thus, for a small strain the relative volume change is given by $\frac{(dV - dV_0)}{dV_0} \approx \varepsilon_{ii} = \varepsilon_{11} + \varepsilon_{22} + \varepsilon_{33}$.
The discussion of volume and surface forces in section 2.2.3 and the equation of motion (2.46) derived in section 2.3.3 hold for solids as well. It is important to note that the material derivative of the velocity field uses the Eulerian description, and is here replaced by a partial derivative of the movement velocity $\dot{\vec{D}}$ of the solid elements,

$$\rho\,\frac{\partial^2 D_i}{\partial t^2} = \rho f_{V,i} + \frac{\partial \sigma_{ij}}{\partial x_j} \ . \quad (2.77)$$

The work done on an elastic solid against its internal stresses is

$$\begin{aligned} W &= \int_V \frac{\Delta W}{\Delta V}\,dV = \int_{V,\vec{D}} \frac{\Delta \vec{F}}{\Delta V} \cdot d\vec{D}\,dV = \int_{V,\vec{D}} \vec{f} \cdot d\vec{D}\,dV \\ &\widehat{=} \int_{V,D_i} f_i\,dD_i\,dV \overset{(2.46)}{=} \int_{V,D_i} \frac{\partial \sigma_{ij}}{\partial x_j}\,dD_i\,dV \ , \end{aligned} \quad (2.78)$$

where volume forces were disregarded.
A partial integration along with Gauss's theorem gives

$$W = \int_{\partial V} \sigma_{ij}\,dD_i\,dA_j - \int_{V,D_i} \sigma_{ij}\,\frac{\partial\,dD_i}{\partial x_j}\,dV \ . \quad (2.79)$$

For an infinitely extended solid which is not deformed at infinity, $\sigma_{ij} = 0$ on its surface, and thus the first integral in equation (2.79) vanishes. By using the symmetry of the stress tensor, $\sigma_{ji} = \sigma_{ij}$, the second integral can be written in the following way:

$$\begin{aligned} W &= -\frac{1}{2} \int_{V,D_i} \sigma_{ij} \Big(\frac{\partial\,dD_i}{dx_j} + \frac{\partial\,dD_j}{dx_i} \Big)\,dV \\ &= -\frac{1}{2} \int_{V,D_i} \sigma_{ij}\,d\Big(\frac{\partial D_i}{dx_j} + \frac{\partial D_j}{dx_i} \Big)\,dV \overset{(2.73)}{=} -\int_{V,\varepsilon_{ij}} \sigma_{ij}\,d\varepsilon_{ij}\,dV \ . \end{aligned} \quad (2.80)$$

Thus, the free mechanical energy satisfies

$$dF = \sigma_{ij}\,d\varepsilon_{ij}\,dV \ , \quad (2.81)$$

where F is the free energy density of the elastic solid.

2.4.1 Hooke's law

For a small strain, the free energy density can be developed about the non-deformed state, $\varepsilon_{ij} = 0$, $F = F_0 := 0$. This is a local minimum in the free energy since work must be done to achieve any strain of the solid. Hence, the terms linear in ε_{ij} must vanish. Since F is a scalar, the higher-order terms must also be a scalar. A general Ansatz for the second-order terms is given by

$$F = \frac{\lambda}{2}\,\varepsilon_{ii}^2 + G\,\varepsilon_{ij}^2 \ . \tag{2.82}$$

λ and G are the so-called Lamé coefficients.
Analogously to equation (2.16), equation (2.82) can be expressed using the traceless component and the trace of ε_{ij},

$$F = \frac{K}{2}\,\varepsilon_{kk}^2 + G\left(\varepsilon_{ij} - \frac{1}{3}\,\varepsilon_{kk}\,\delta_{ij}\right)^2,\ K = \lambda + \frac{2}{3}\,G \ . \tag{2.83}$$

As is visualised in figure 2.3, the tensor is now split into its compressive and shear components, which is why the coefficients K and G are called the bulk modulus and the shear modulus, respectively. If only the diagonal elements of ε_{ij} are non-zero, the deformation is a pure compression or expansion. If ε_{ij} is traceless, a pure shear deformation is achieved. In both of these cases, the corresponding terms in equation (2.83) must be positive to ensure the stability of the equilibrium state $\varepsilon_{ij} = 0$. Thus, both coefficients must be positive, $K, G > 0$.
To calculate the stress tensor σ_{ij}, the differential of equation (2.83) is taken,

$$\begin{aligned} dF &= K\,\varepsilon_{kk}\,d\varepsilon_{kk} + 2\,G\left(\varepsilon_{ij} - \frac{1}{3}\,\varepsilon_{kk}\,\delta_{ij}\right) d\Big(\varepsilon_{ij} - \frac{1}{3}\,\varepsilon_{kk}\,\delta_{ij}\Big) \\ &= K\,\varepsilon_{kk}\,d\varepsilon_{kk} + 2\,G\left(\varepsilon_{ij} - \frac{1}{3}\,\varepsilon_{kk}\,\delta_{ij}\right) d\varepsilon_{ij} \\ &= \left(K\,\varepsilon_{kk}\,\delta_{ij} + 2\,G\left(\varepsilon_{ij} - \frac{1}{3}\varepsilon_{kk}\,\delta_{ij}\right)\right) d\varepsilon_{ij} \ . \end{aligned} \tag{2.84}$$

Comparing this with equation (2.81) yields

$$\sigma_{ij} = K\,\varepsilon_{kk}\,\delta_{ij} + 2\,G\left(\varepsilon_{ij} - \frac{1}{3}\,\varepsilon_{kk}\,\delta_{ij}\right) \overset{(2.83)}{=} \lambda\,\varepsilon_{kk}\,\delta_{ij} + 2\,G\,\varepsilon_{ij} \ . \tag{2.85}$$

This is Hooke's law. It states that the stress and the strain of an elastic solid are proportional to each other for small strains. This approximation is also called linear elasticity.
Writing equation (2.85) for the trace of σ_{ij} and for off-diagonal elements yields

$$\sigma_{ii} = 3\,K\,\varepsilon_{ii},\ \sigma_{xy} = 2\,G\,\varepsilon_{xy} \ . \tag{2.86}$$

Using this, equation (2.85) can be written as

$$\begin{aligned} \varepsilon_{ij} &= \frac{1}{2G}\left(\sigma_{ij} - K\,\varepsilon_{kk}\,\delta_{ij}\right) + \frac{1}{3}\,\varepsilon_{kk}\,\delta_{ij} \\ &= \frac{1}{2G}\left(\sigma_{ij} - \frac{1}{3}\,\sigma_{kk}\,\delta_{ij}\right) + \frac{1}{9K}\,\sigma_{kk}\,\delta_{ij} = \frac{1}{2G}\,\sigma_{ij} + \left(\frac{1}{9K} - \frac{1}{6G}\right)\sigma_{kk}\,\delta_{ij} \ . \end{aligned} \tag{2.87}$$

Writing this for the diagonal elements yields

$$\begin{aligned} \varepsilon_{xx} &= \left(\frac{1}{9K} + \frac{1}{3G}\right)\sigma_{xx} + \left(\frac{1}{9K} - \frac{1}{6G}\right)(\sigma_{yy} + \sigma_{zz}) \\ &= \frac{1}{E}(\sigma_{xx} - v\,(\sigma_{yy} + \sigma_{zz})),\ E = \frac{9KG}{3K+G},\ v = \frac{1}{2} - \frac{E}{6K} \ . \end{aligned} \tag{2.88}$$

The newly introduced variables are Young's modulus E, which is also called the elastic modulus, and Poisson's ratio v. The elastic modulus E relates a linear strain to the stress in the same direction. v is a number which typically lies between 0 and 0.5. It gives the amount by which an elastic solid contracts in the directions normal to the direction in which it is being stretched.

2.4.2 Equation of motion

Combining the equations (2.77), (2.85), and (2.74) yields equations of motion for linear elastic solids:

$$\rho \frac{\partial^2 D_i}{\partial t^2} = \rho f_{V,i} + \frac{\partial}{\partial x_j}\left(G\left(\frac{\partial D_i}{\partial x_j} + \frac{\partial D_j}{\partial x_i}\right) + \lambda \frac{\partial D_k}{\partial x_k}\delta_{ij}\right) . \tag{2.89}$$

Converting this into vector notation gives

$$\rho \frac{\partial^2 \vec{D}}{\partial t^2} = \rho \vec{f}_V + \nabla \cdot \left(G\left(\nabla \circ \vec{D}\right) + G\left(\nabla \circ \vec{D}\right)^{\mathrm{T}} + \lambda \nabla \cdot \vec{D}\, \overleftrightarrow{1}\right) . \tag{2.90}$$

An alternative version of the equation of motion is acquired by factoring out the parentheses in equation (2.89) and rearranging the terms to

$$\rho \frac{\partial^2 D_i}{\partial t^2} = \rho f_{V,i} + G \frac{\partial^2 D_i}{\partial x_j^2} + (\lambda + G) \frac{\partial^2 D_j}{\partial x_i \, \partial x_j} . \tag{2.91}$$

Converting this version into vector notation then gives

$$\rho \frac{\partial^2 \vec{D}}{\partial t^2} = \rho \vec{f}_V + G \, \Delta \vec{D} + (\lambda + G) \, \nabla(\nabla \cdot \vec{D}) . \tag{2.92}$$

To solve these equations, a continuity equation that relates the density ρ to the deformation $\vec{D}$ of the solid is needed. For a hydrostatic compression, $\sigma_{ii} = -3\,p$, just as in equation (2.17). Then, equation (2.86) becomes

$$\varepsilon_{ii} = -\frac{p}{K} \overset{(2.74)}{=} \nabla \cdot \vec{D} \overset{(2.76)}{=} \frac{V - V_0}{V_0} = \frac{\rho_0 - \rho}{\rho},\ \rho_0 = \frac{m}{V_0},\ \rho = \frac{m}{V} \ \Rightarrow\ \rho = \frac{\rho_0}{1 + \nabla \cdot \vec{D}} . \tag{2.93}$$

The definition of the compressibility κ then yields

$$\kappa = -\frac{1}{V}\frac{\partial V}{\partial p} = \frac{1}{\rho}\frac{\partial \rho}{\partial p} = \frac{1}{K} . \tag{2.94}$$

This is why the bulk modulus K is also referred to as the compressive modulus.

2.4.3 Elastic waves

Bulk waves

Using the Ansatz of a plane wave, $\vec{D} = \vec{D}(x,t)$, in equation (2.90) and neglecting volume forces gives

$$\begin{aligned} \frac{\partial^2 D_x}{\partial t^2} &= c_{\mathrm{l}}^2 \frac{\partial^2 D_x}{\partial x^2},\ c_{\mathrm{l}} = \sqrt{\frac{\lambda + 2\,G}{\rho}}, \\ \frac{\partial^2 D_y}{\partial t^2} &= c_{\mathrm{t}}^2 \frac{\partial^2 D_y}{\partial x^2},\ c_{\mathrm{t}} = \sqrt{\frac{G}{\rho}} . \end{aligned} \tag{2.95}$$

This corresponds to a longitudinal elastic wave, also called a bulk wave, propagating at a velocity of c_l, as well as a transversal elastic wave, also called a shear wave, propagating at a velocity of c_t. These wave modes are shown in figure 2.4 (a) and (b), respectively. For D_z, an equivalent transversal mode can be written. If λ and G are positive, it necessarily follows that $c_\mathrm{l} > \sqrt{2}\, c_\mathrm{t}$.
Using these definitions in equation (2.92) while still neglecting volume forces gives

$$\frac{\partial^2 \vec{D}}{\partial t^2} = c_\mathrm{t}^2\, \Delta \vec{D} + (c_\mathrm{l}^2 - c_\mathrm{t}^2)\, \nabla(\nabla \cdot \vec{D}) \ . \tag{2.96}$$

Even in the general case of non-planar waves, the deformation field can be decomposed into a longitudinal and a transversal component, $\vec{D} = \vec{D}_\mathrm{l} + \vec{D}_\mathrm{t}$, that satisfy the conditions $\nabla \times \vec{D}_\mathrm{l} = 0$ and $\nabla \cdot \vec{D}_\mathrm{t} = 0$. The divergence of equation (2.96) then gives

$$\begin{aligned} &\nabla \cdot \Big(\frac{\partial^2 \vec{D}}{\partial t^2} - c_\mathrm{t}^2\, \Delta \vec{D} - (c_\mathrm{l}^2 - c_\mathrm{t}^2)\, \nabla(\nabla \cdot \vec{D}) \Big) \\ &= \frac{\partial^2 (\nabla \cdot \vec{D}_\mathrm{l})}{\partial t^2} - c_\mathrm{t}^2\, \Delta(\nabla \cdot \vec{D}_\mathrm{l}) - (c_\mathrm{l}^2 - c_\mathrm{t}^2)\, \nabla \cdot (\nabla(\nabla \cdot \vec{D}_\mathrm{l})) \\ &= \nabla \cdot \Big(\frac{\partial^2 \vec{D}_\mathrm{l}}{\partial t^2} - c_\mathrm{t}^2\ \Delta \vec{D}_\mathrm{l} - (c_\mathrm{l}^2 - c_\mathrm{t}^2)\, \Delta \vec{D}_\mathrm{l} \Big) = \nabla \cdot \Big(\frac{\partial^2 \vec{D}_\mathrm{l}}{\partial t^2} - c_\mathrm{l}^2\, \Delta \vec{D}_\mathrm{l} \Big) = 0 \ , \end{aligned} \tag{2.97}$$

where the identity $\nabla(\nabla \cdot \vec{D}) = \Delta \vec{D} + \nabla \times (\nabla \times \vec{D})$ was used.
Analogously, the curl of equation (2.96) gives

$$\begin{aligned} &\nabla \times \Big(\frac{\partial^2 \vec{D}}{\partial t^2} - c_\mathrm{t}^2\, \Delta \vec{D} - (c_\mathrm{l}^2 - c_\mathrm{t}^2)\, \nabla(\nabla \cdot \vec{D}) \Big) \\ &= \frac{\partial^2 (\nabla \times \vec{D}_\mathrm{t})}{\partial t^2} - c_\mathrm{t}^2\, \Delta(\nabla \times \vec{D}_\mathrm{t}) = \nabla \times \Big(\frac{\partial^2 \vec{D}_\mathrm{t}}{\partial t^2} - c_\mathrm{t}^2\, \Delta \vec{D}_\mathrm{t} \Big) = 0 \ , \end{aligned} \tag{2.98}$$

where the identity $\nabla \times (\nabla(\nabla \cdot \vec{D})) = 0$ was used. Since for both equations (2.97) and (2.98), the divergence and the curl of the expression in the parentheses vanish, those expressions must be zero everywhere, and the following wave equations are obtained:

$$\frac{\partial^2 \vec{D}_\mathrm{l}}{\partial t^2} = c_\mathrm{l}^2\, \Delta \vec{D}_\mathrm{l}, \ \frac{\partial^2 \vec{D}_\mathrm{t}}{\partial t^2} = c_\mathrm{t}^2\, \Delta \vec{D}_\mathrm{t} \ . \tag{2.99}$$

Each component of $\vec{D}_\mathrm{l}$ and $\vec{D}_\mathrm{t}$ satisfies a wave equation of the form $\frac{\partial^2 D}{\partial t^2} - c^2\, \Delta D = 0$.

Surface waves

A special kind of elastic wave is found near a free surface of an elastic solid. Consider the example of an elastic solid occupying the infinite half-space defined by $z < 0$, and a wave propagating near $z = 0$ in the x-direction according to the Ansatz $D \sim e^{i(kx - \omega t)} f(z)$. Inserting this into the wave equation gives $f''(z) = a^2\, f(z)$, with $a^2 = k^2 - \frac{\omega^2}{c^2}$. It thus follows that $f(z) = e^{az}$. For $a^2 < 0$, the case of a planar wave is recovered. For $a^2 > 0$ and $a < 0$,

$$D = D_0\, e^{i(kx - \omega t) + az}, \ a = -\sqrt{k^2 - \frac{\omega^2}{c^2}} \tag{2.100}$$

describes a wave propagating in the x-direction with an amplitude that decays exponentially with decreasing z, i.e. with increasing depth in the elastic solid. This is a so-called

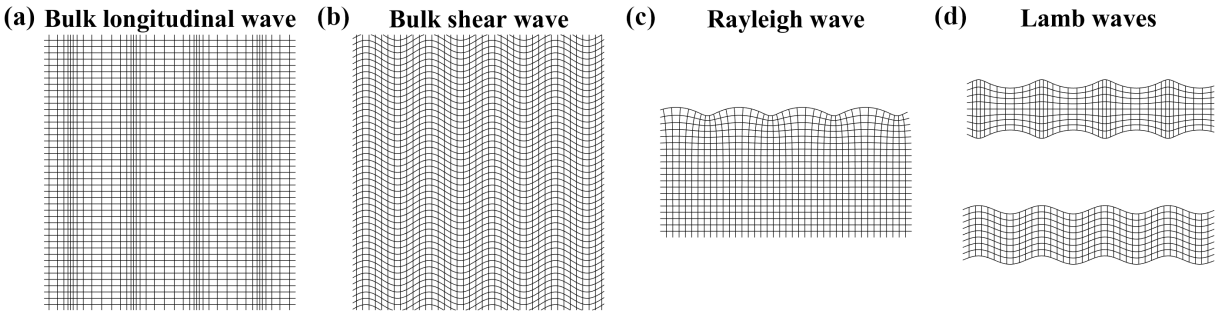

Figure 2.4: Schematic showing the longitudinal and transversal bulk wave modes, the Rayleigh wave, and the Lamb wave.

Rayleigh wave, as first described by Rayleigh [47]. The full deformation field $\vec{D}$ is obtained via a linear combination

$$\vec{D} = \vec{D}_\mathrm{l} + \vec{D}_\mathrm{t},\ \vec{D}_\mathrm{l} = \vec{D}_{\mathrm{l},0}\, e^{i(kx-\omega t)+a_\mathrm{l} z},\ \vec{D}_\mathrm{t} = \vec{D}_{\mathrm{t},0}\, e^{i(kx-\omega t)+a_\mathrm{t} z}\ , \tag{2.101}$$

which must satisfy the boundary condition of a free surface, $\overleftrightarrow{\sigma} \cdot \vec{n} = 0$. Since in this case $\vec{n} = \vec{e}_z$, it follows that $\sigma_{xz} = \sigma_{yz} = \sigma_{zz} = 0$. With equation (2.85) it then follows that

$$\varepsilon_{xz} = 0,\ \varepsilon_{yz} = 0,\ \lambda\,(\varepsilon_{xx} + \varepsilon_{yy}) + (\lambda + 2\,G)\,\varepsilon_{zz} = 0\ . \tag{2.102}$$

Using equation (2.74) and the definitions of c_l and c_t then gives

$$\frac{\partial D_x}{\partial z} + \frac{\partial D_z}{\partial x} = 0,\ D_y = 0,\ (c_\mathrm{l}^2 - 2\,c_\mathrm{t}^2)\,\frac{\partial D_x}{\partial x} + c_\mathrm{l}^2\,\frac{\partial D_z}{\partial z} = 0\ . \tag{2.103}$$

In the third equation, $D_y = 0$ was used. $D_y = 0$ means that the wave propagates in the x-z plane. From the conditions that the curl of the longitudinal component and the divergence of the transversal component of the wave vanish, it follows that

$$\frac{\partial D_{\mathrm{l},x}}{\partial z} - \frac{\partial D_{\mathrm{l},z}}{\partial x} = 0,\ \frac{\partial D_{\mathrm{t},x}}{\partial x} + \frac{\partial D_{\mathrm{t},z}}{\partial z} = 0\ . \tag{2.104}$$

With the Ansatz in equation (2.100), this leads to conditions for the wave coefficients:

$$\begin{aligned} &a_\mathrm{l}\,D_{\mathrm{l},x} - i\,k\,D_{\mathrm{l},z} = 0,\ i\,k\,D_{\mathrm{t},x} + a_\mathrm{t}\,D_{\mathrm{t},z} = 0 \\ \Rightarrow\ &\vec{D}_{\mathrm{l},0} = \begin{pmatrix} k\,b_\mathrm{l} \\ 0 \\ -i\,a_\mathrm{l}\,b_\mathrm{l} \end{pmatrix},\ \vec{D}_{\mathrm{t},0} = \begin{pmatrix} a_\mathrm{t}\,b_\mathrm{t} \\ 0 \\ -i\,k\,b_\mathrm{t} \end{pmatrix}\ . \end{aligned} \tag{2.105}$$

Using this, evaluating the first and third equations (2.103) at $z = 0$ yields

$$2\,k\,a_\mathrm{l}\,b_\mathrm{l} + (k^2 + a_\mathrm{t}^2)\,b_\mathrm{t} = 0,\ c_\mathrm{l}^2\,(a_\mathrm{l}^2 - k^2)\,b_\mathrm{l} + 2\,c_\mathrm{t}^2\,k^2\,b_\mathrm{l} + 2\,c_\mathrm{t}^2\,k\,a_\mathrm{t}\,b_\mathrm{t} = 0\ . \tag{2.106}$$

Dividing the second equation by c_t^2 and inserting $a_\mathrm{l}^2 - k^2 = -\frac{\omega^2}{c_\mathrm{l}^2} = (a_\mathrm{t}^2 - k^2)\,\frac{c_\mathrm{t}^2}{c_\mathrm{l}^2}$ gives

$$(k^2 + a_\mathrm{t}^2)\,b_\mathrm{l} + 2\,k\,a_\mathrm{t}\,b_\mathrm{t} = 0\ . \tag{2.107}$$

By isolating the parentheses in this and the first equation (2.106) and multiplying both equations, one obtains

$$(k^2 + a_\mathrm{t}^2)^2 = 4\,k^2\,a_\mathrm{l}\,a_\mathrm{t}\ . \tag{2.108}$$

Taking the square and using $a_\mathrm{l}^2 = k^2 - \frac{\omega^2}{c_\mathrm{l}^2}$, $a_\mathrm{t}^2 = k^2 - \frac{\omega^2}{c_\mathrm{t}^2}$ results in

$$\left(2\,k^2 - \frac{\omega^2}{c_\mathrm{t}^2}\right)^4 = 16\,k^4 \left(k^2 - \frac{\omega^2}{c_\mathrm{l}^2}\right)\left(k^2 - \frac{\omega^2}{c_\mathrm{t}^2}\right) . \tag{2.109}$$

This equation is fulfilled for the dispersion relation $\omega = d\,c_\mathrm{t}\,k$. $d\,c_\mathrm{t}$ is thus the propagation speed of the Rayleigh wave. After factoring out the parentheses, this substitution turns equation (2.109) into

$$d^6 - 8\,d^4 + 8\left(3 - 2\,\frac{c_\mathrm{t}^2}{c_\mathrm{l}^2}\right) d^2 - 16\left(1 - \frac{c_\mathrm{t}^2}{c_\mathrm{l}^2}\right) = 0 . \tag{2.110}$$

d thus only depends on the constant $\frac{c_\mathrm{t}}{c_\mathrm{l}} = \sqrt{\frac{G}{\lambda+2G}} = \sqrt{\frac{1-2v}{2-2v}}$. d must be real and positive. Furthermore, it must be smaller than 1 to ensure that a_t is real and positive. For any given v, equation (2.110) has only one solution that fulfils these conditions, which can be calculated numerically. For most materials, $0 \leq v \leq 0.5$. In this range, d increases monotonically from $d \approx 0.874$ for $v = 0$ to $d \approx 0.955$ for $v = 0.5$. The Rayleigh wave thus propagates slightly slower than the shear waves in the bulk of the solid. The Rayleigh wave is shown schematically in figure 2.4 (c). If the elastic solid is not bound by a free surface, but a fluid, it will emit pressure waves into the fluid from its position. Then, the Rayleigh wave is called a leaky Rayleigh wave.

Plate waves

Another special geometry of interest is that of an infinitely extended elastic solid plate that is much thinner than the wavelength of elastic waves. For the general case of a bent plate, one can choose an arbitrary point on the plate and define it as the coordinate origin, with the centre of the plate in the x-y plane. One side of a thin bent plate must be convex, on which it is stretched, while the opposite side is concave and the solid is compressed. Then, in the centre of the plate, these strains must vanish. Just like in the last section, from the boundary conditions at the free surface, it follows that $\sigma_{xz} = \sigma_{yz} = \sigma_{zz} = 0$. These stresses can then also be neglected throughout the plate. Equation (2.85) then gives

$$\varepsilon_{xz} = 0,\ \varepsilon_{yz} = 0,\ \lambda\,(\varepsilon_{xx}+\varepsilon_{yy}+\varepsilon_{zz})+2\,G\,\varepsilon_{zz} = 0 \ \Leftrightarrow\ \varepsilon_{zz} = -\frac{\lambda}{\lambda+2G}\,(\varepsilon_{xx}+\varepsilon_{yy}) . \tag{2.111}$$

This can be expressed by spatial derivatives of the deformation $\vec{D}$ using equation (2.74). With the Ansatz of a planar wave propagating in the x-direction, the derivatives by y are taken to be zero, which results in

$$\begin{aligned} &\varepsilon_{xx} = \frac{\partial D_x}{\partial x},\ \varepsilon_{yy} = 0,\ \varepsilon_{xy} = \frac{1}{2}\,\frac{\partial D_y}{\partial x}\ \Rightarrow\ \varepsilon_{zz} = -\frac{\lambda}{\lambda+2G}\,\frac{\partial D_x}{\partial x}, \\ &\varepsilon_{xz} = \frac{\partial D_x}{\partial z} + \frac{\partial D_z}{\partial x} = 0,\ \varepsilon_{yz} = \frac{\partial D_y}{\partial z} = 0 . \end{aligned} \tag{2.112}$$

By eliminating either the deformation normal to the plate D_z or the deformations within the plate, D_x and D_y, one can derive the waves oscillating within the plate and its bending waves, respectively.

The former is done by taking $D_z = 0$ and calculating the components of the two-dimensional stress tensor, by inserting the first line of equation (2.112) into Hooke's law (2.85),

$$\sigma_{xx} = 4\,G\,\frac{\lambda+G}{\lambda+2G}\,\frac{\partial D_x}{\partial x},\ \sigma_{yy} = \frac{2\lambda G}{\lambda+2G}\,\frac{\partial D_x}{\partial x},\ \sigma_{xy} = G\,\frac{\partial D_y}{\partial x}\ . \tag{2.113}$$

Combining this with equation (2.77) and neglecting external forces gives equations of motion of the plate,

$$\rho\,\frac{\partial^2 D_x}{\partial t^2} = 4\,G\,\frac{\lambda+G}{\lambda+2G}\,\frac{\partial^2 D_x}{\partial x^2},\ \rho\,\frac{\partial^2 D_y}{\partial t^2} = G\,\frac{\partial^2 D_y}{\partial x^2}\ . \tag{2.114}$$

This corresponds to a longitudinal wave with $c_\mathrm{l} = \sqrt{\frac{4G}{\rho}\,\frac{\lambda+G}{\lambda+2G}}$ and a transversal wave with $c_\mathrm{t} = \sqrt{\frac{G}{\rho}}$. The transversal wave thus propagates with the same speed as in an infinitely extended elastic solid. It corresponds to the schematic of the bulk shear wave shown in figure 2.4 (b) if that is taken to be a top view of the plate. The longitudinal wave is also called a symmetric mode Lamb wave and is shown on top in figure 2.4 (d). Its speed differs from that of its bulk wave counterpart. This makes sense when comparing both waves in figure 2.4. Because of the symmetry with respect to translation in the vertical direction, the longitudinal bulk wave forces the solid to undergo rather strong density variations, while in the case of a thin plate, the solid can partly avoid its compression by extending in the z-direction, changing the nature of the wave and subsequently also its propagation speed. Lamb waves were first described by Lamb [48].
Next, the bend waves of the plate are derived. The first line of equation (2.112) can be integrated to

$$D_x = -z\,\frac{\partial D_z}{\partial x},\ D_y = 0\ . \tag{2.115}$$

The integration constants were taken to be zero to fulfil $D_x = 0,\ D_y = 0$ at $z = 0$. With this, the non-zero components of the strain tensor can be written as

$$\varepsilon_{xx} = -z\,\frac{\partial^2 D_z}{\partial x^2},\ \varepsilon_{zz} = \frac{\lambda}{\lambda+2G}\,z\,\frac{\partial^2 D_z}{\partial x^2}\ . \tag{2.116}$$

Neglecting any deformation in the x- and y-directions, the only degree of freedom of each volume element of the plate is D_z. A decrease of the free energy density in this degree of freedom $-\frac{dF}{dD_z}$ causes a positive local volume force $\vec{f}_V$ in the plate. According to Newton's second law, this causes a local acceleration of the plate,

$$\rho\,\frac{\partial^2 D_z}{\partial t^2} = -\frac{dF}{dD_z}\ . \tag{2.117}$$

Multiplying by dD_z and integrating over the volume of the plate gives

$$\int \rho\,\frac{\partial^2 D_z}{\partial t^2}\,dD_z\,dV + \int dF\,dV = 0\ . \tag{2.118}$$

Executing the first integral in the z-direction turns this equation into

$$\int \rho\,h\left(\frac{\partial^2 D_z}{\partial t^2}\,dD_z\right)dA + d\int F\,dV = 0\ . \tag{2.119}$$

With equation (2.82), the free energy density of the plate is

$$F = 2\,z^2\,G\,\frac{\lambda+G}{\lambda+2G}\left(\frac{\partial^2 D_z}{\partial x^2}\right)^2 . \tag{2.120}$$

The total free energy of the plate is then given by the volume integral

$$\int F\,dV = \int_{-\frac{h}{2}}^{\frac{h}{2}} \int F\,dA\,dz = \frac{h^3 G}{6}\,\frac{\lambda+G}{\lambda+2G}\int \left(\frac{\partial^2 D_z}{\partial x^2}\right)^2 dA\ . \tag{2.121}$$

The variation of this integral can be evaluated by using partial integrations and Stokes' theorem,

$$\begin{aligned} d\int F\,dV &= \frac{h^3 G}{3}\,\frac{\lambda+G}{\lambda+2G}\int \frac{\partial^2 D_z}{\partial x^2}\,\frac{\partial^2\,dD_z}{\partial x^2}\,dA \\ &= \frac{h^3 G}{3}\,\frac{\lambda+G}{\lambda+2G}\int \frac{\partial}{\partial x}\Big(\frac{\partial^2 D_z}{\partial x^2}\,\frac{\partial\,dD_z}{\partial x}\Big) - \frac{\partial^3 D_z}{\partial x^3}\,\frac{\partial\,dD_z}{\partial x}\,dA \\ &= \frac{h^3 G}{3}\,\frac{\lambda+G}{\lambda+2G}\int \frac{\partial}{\partial x}\Big(\frac{\partial^2 D_z}{\partial x^2}\,\frac{\partial\,dD_z}{\partial x}\Big) - \frac{\partial}{\partial x}\Big(\frac{\partial^3 D_z}{\partial x^3}\,dD_z\Big) + \frac{\partial^4 D_z}{\partial x^4}\,dD_z\,dA \\ &= \frac{h^3 G}{3}\,\frac{\lambda+G}{\lambda+2G}\Big(\oint_{\partial A}\frac{\partial^2 D_z}{\partial x^2}\,\frac{\partial\,dD_z}{\partial x} - \frac{\partial^3 D_z}{\partial x^3}\,dD_z\,n_x\,dl + \int \frac{\partial^4 D_z}{\partial x^4}\,dD_z\,dA\Big)\ . \end{aligned} \tag{2.122}$$

For an infinitely extended plate, D_z and its derivatives can be taken to be zero, in which case the line integrals vanish. Then, only the surface integrals remain and equation (2.119) becomes

$$\int \Big(\rho\,h\,\frac{\partial^2 D_z}{\partial t^2} + \frac{h^3 G}{3}\,\frac{\lambda+G}{\lambda+2G}\,\frac{\partial^4 D_z}{\partial x^4}\Big)\,dD_z\,dA = 0\ . \tag{2.123}$$

This is true if

$$\rho\,h\,\frac{\partial^2 D_z}{\partial t^2} + \frac{h^3 G}{3}\,\frac{\lambda+G}{\lambda+2G}\,\frac{\partial^4 D_z}{\partial x^4} = 0\ . \tag{2.124}$$

With the Ansatz $D_z = A\,e^{i(kx-\omega t)}$, one obtains a dispersion relation

$$\omega = \sqrt{\frac{h^2 G}{3\rho}\,\frac{\lambda+G}{\lambda+2G}}\,k^2 \ \Leftrightarrow\ c = \frac{\partial\omega}{\partial k} = \sqrt{\frac{4h^2 G}{3\rho}\,\frac{\lambda+G}{\lambda+2G}}\,k\ . \tag{2.125}$$

This bend wave is called an asymmetric mode Lamb wave and is schematically shown at the bottom of figure 2.4 (d). Its nature is different from all other waves discussed so far, as its propagation speed is inversely proportional to its wavelength.

2.5 Cavitation

The phase diagram of water is illustrated schematically in figure 2.5. The phase transition from a liquid to a gas, also known as boiling, can occur either by increasing the temperature T or by decreasing the pressure p of the liquid. However, such a phase diagram is only valid if the substance of interest undergoes a series of quasi-stationary phase changes between equilibrium states. The term "cavitation" is used for highly dynamic, and thus non-equilibrium events in which one or more cavities are formed in a liquid that is not necessarily close to the boiling line. This is achieved either by a local heat deposition, thereby increasing the temperature T of the liquid above the boiling temperature, or by locally decreasing the pressure p of the liquid below the vapour pressure. The resulting gas- or vapour-filled cavities are called cavitation bubbles.
Regarding the first case, the sudden local admission of heat at a high heat density can be done in multiple ways, including the following examples, namely via dielectric breakdown (spark-generated cavitation [49]), by irradiating a region in the liquid with a high-intensity light source, typically a laser (laser-induced cavitation, [21, 50–52]), via plasmonic resonance [53–55], or via explosive combustion [56].
When a simple fluid is expanded, its inner pressure p decreases. For a gas, the pressure stays positive for an arbitrary amount of expansion. This is not the case for liquids. The density of a liquid is only weakly dependent on the pressure. In turn, a small expansion of the liquid leads to a strong pressure drop, where the resulting pressure can even be negative. In cases of sufficient symmetry without any exceptional points, the liquid can withstand such inner tensions and remain in an unstable state of tension, thus again not conforming to the phase diagram shown in figure 2.5. The strongest tension a liquid can withstand is called the cavitation threshold [57]. The value of the cavitation threshold varies strongly with the measurement method and is typically found at much smaller tension values than predicted by the theoretical limit [58], and is an ongoing point of discussion. The cavitation resistance of a liquid is strongly influenced by the presence of so-called cavitation nuclei, from which cavitation bubbles can be more easily expanded than from a point in the liquid bulk. The identification of cavitation nuclei is also a point of ongoing research. One might think that cavitation bubbles may simply originate from micro- or nano-sized bubbles that can then be expanded to a visible size. However, this idea is flawed. Larger bubbles in a gravitational field would rise to the top of the liquid in a rather short amount of time. For the remaining smaller bubbles, surface tension becomes more and more relevant, since the surface tension force is directly proportional to the curvature of its interface, and thus inversely proportional to the radius of the bubble. This causes an overpressure on the gas contents of the bubble, the so-called Laplace pressure, which increases with decreasing bubble size. This overpressure would induce the gas to dissolve into the surrounding liquid, or for sufficiently large pressure even condense. This means that such small bubbles are inherently unstable, and can thus after a short time be discarded as a candidate for cavitation nuclei in water. Additionally, expanding these bubbles to a visible size would require an underpressure strong enough to overcome the Laplace pressure. This pressure threshold for significantly expanding a small bubble is called the Blake threshold. A widely spread hypothesis for cavitation nuclei is that small solid particles may exhibit crevices in which gas could be trapped, which could then expand with little resistance, lowering the cavitation threshold significantly. Even without trapped gas, solid particles may act as cavitation nuclei. Recently, even small amounts of dissolved gas in the liquid bulk [59] and in liquid droplets [60] have been suggested to act as cavitation nuclei. In cases with exceptional points that break the symmetry, at such

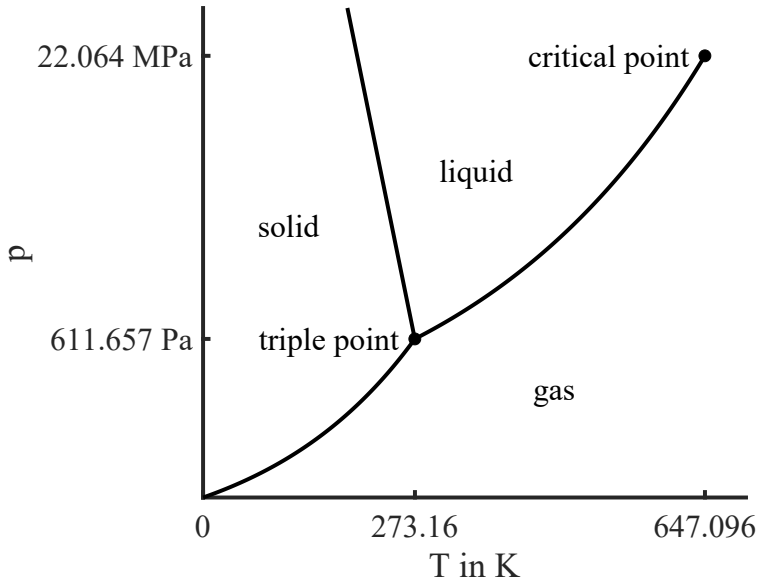

Figure 2.5: Schematic of the phase diagram of water.

points cavities form that relaxate the tension and expand with little resistance, achieving the required volume increase without a need for the pressure to drop further. Such points may be given by the presence of cavitation nuclei as discussed above, or by the pressure field being sufficiently inhomogeneous, such that cavities are created at preferred positions. Such pressure variations can be induced by diverging flows such as the flow caused by a rotation propeller, a hydrofoil, or by pressure waves. Underpressures can also be induced by surface waves on an elastic solid [7, 61].

2.5.1 Bubble dynamics

If gravity and gas diffusion can be neglected, a gas bubble at rest tends to take a spherical, stable equilibrium shape. Its equilibrium radius is given by the total mass of the gas contents of the bubble, the equation of state of the gas, and the condition that the internal pressure is balanced by the external pressure and the Laplace pressure induced by surface tension. If the bubble is compressed from this equilibrium state, its internal pressure will increase and counteract the compression. If it is expanded from the equilibrium size, its internal pressure decreases and the external pressure will counteract the bubble's expansion. Thus, the bubble is a volumetric oscillator. It will become evident in section 2.5.1 that the oscillation is non-linear, but like all classical oscillations it can be linearised for small oscillation amplitudes. As cavitation bubbles are created from a very small initial size, they typically expand past their equilibrium size and subsequently collapse again to a small size. An excellent review article about bubble oscillations is given by Lauterborn and Kurz [36]. If a bubble is driven to undergo a sufficiently strong collapse, the temperature of its gas contents may get high enough for it to emit visible light. This phenomenon is called sonoluminescence [62]. In the context of sonochemistry, these high temperatures are used to trigger chemical reactions in the bubble [16]. For even stronger collapses, the temperatures reached may be sufficient to ignite a nuclear fusion reaction. This approach is called inertial confinement fusion [17, 18].

The Rayleigh collapse time

Consider an infinitely extended, homogeneous, incompressible liquid. It shall be at rest and at an equilibrium state, at a homogeneous pressure p_0. At time t_0, a spherical volume of radius R_0 shall suddenly disappear, leaving an empty spherical cavity. The centre of the cavity is chosen as the coordinate origin. The liquid will then take some time τ to fill the cavity.
Since the considered problem is spherically symmetric and the liquid is incompressible, the volume flux of the liquid through any spherical shell outside the cavity and centred at the origin should be the same,

$$\int_{V(r)} \vec{u} \cdot d\vec{A} = 4\,\pi\,r^2\,u = \text{const.} \;\Rightarrow\; \frac{u}{\dot{R}} = \frac{R^2}{r^2}\;, \tag{2.126}$$

where $\dot{R}$ is the velocity at the surface of the cavity.
Using $dm = \rho\,dV = \rho\,4\,\pi\,r^2\,dr$, the kinetic energy of the liquid can be calculated as:

$$E = \frac{\rho}{2}\int_R^\infty u^2\,4\,\pi\,r^2\,dr = \frac{\rho}{2}\int_R^\infty \dot{R}^2\,4\,\pi\,\frac{R^4}{r^2}\,dr = 2\,\pi\,\rho\,\dot{R}^2\,R^3\;. \tag{2.127}$$

The mechanical work done by the liquid on the cavity since time t_0 is

$$W = \int_{R_0}^R \vec{F}\cdot d\vec{r} = \int_{R_0}^R p_0\,4\,\pi\,r^2\,dr = \frac{4}{3}\,\pi\,(R^3 - R_0^3)\,p_0\;. \tag{2.128}$$

Since equation (2.127) and equation (2.128) must be equal, it follows that

$$E = W \;\Leftrightarrow\; \dot{R}^2 = \frac{2p_0}{3\rho}\left(\frac{R_0^3}{R^3} - 1\right)\;. \tag{2.129}$$

This ordinary differential equation can be rewritten in an integral form,

$$\frac{dR}{dt} = -\sqrt{\frac{2p_0}{3\rho}\left(\frac{R_0^3}{R^3} - 1\right)} \;\Leftrightarrow\; t = \int_0^t dt = \sqrt{\frac{3\rho}{2p_0}}\int_R^{R_0} \frac{1}{\sqrt{\frac{R_0^3}{R^3} - 1}}\,dR\;. \tag{2.130}$$

Note that for a shrinking cavity, $\dot{R}$ is negative.
The integral in equation (2.130) can be solved by substituting R by the dimensionless quantity $\alpha = \frac{R^3}{R_0^3}$:

$$\begin{aligned}\tau &= \sqrt{\frac{3\rho}{2p_0}}\int_0^{R_0}\sqrt{\frac{\frac{R^3}{R_0^3}}{1-\frac{R^3}{R_0^3}}}\,dR = \sqrt{\frac{3\rho}{2p_0}}\,\frac{R_0}{3}\int_0^1 \alpha^{-\frac{1}{6}}\,(1-\alpha)^{-\frac{1}{2}}\,d\alpha \\ &= R_0\sqrt{\frac{\rho}{p_0}}\,\frac{\Gamma(\frac{5}{6})\,\Gamma(\frac{1}{2})}{\sqrt{6}\,\Gamma(\frac{4}{3})} \approx 0.91468\,R_0\sqrt{\frac{\rho}{p_0}}\;.\end{aligned} \tag{2.131}$$

The dimensionless integral was expressed by the Gamma function $\Gamma(z) = \int_0^\infty x^{z-1}\,e^{-x}\,dx$.
τ is called the Rayleigh collapse time. It is the time it takes for the cavity to shrink from $R(t=0) = R_0$ to $R(t=\tau) = 0$ [2].
In most cases, a real cavity contains at least a small amount of gas, which may be an incondensable gas, a vapour, or a mixture of both. Such a cavity exhibits an internal

pressure, which will sharply rise as the cavity shrinks and counteract the collapse. It can then only fully collapse if its contents fully transition to a liquid state. Otherwise, this bubble will reach a finite minimum volume and then re-expand. This was neglected in the derivation of equation (2.131). Thus, it can only be applied to cases in which the influence of the cavity contents is negligible. The presence of any anisotropies like the boundaries of the liquid, as well as liquid viscosity and liquid compressibility, influence the collapse time of a real bubble and must be negligible for equation (2.131) to be a good approximation.

The Keller-Miksis equation

To study the dynamics of cavitation bubbles, there have been several attempts to derive a model for spherically symmetric bubbles that also holds for large oscillation amplitudes. To derive a simple equation of motion, the incompressible Navier-Stokes equations (2.59) are used. Since the model shall be spherically symmetric, only the radial coordinate needs to be considered. Again, equation (2.126) applies. Viscous effects shall only be considered at the boundary of the bubble, and hence the viscous term in equation (2.59) is neglected. Equation (2.59) then turns into

$$\frac{Du}{Dt} = \frac{\partial u}{\partial t} + u\,\frac{\partial u}{\partial r} = \frac{\partial u}{\partial t} + \frac{1}{2}\,\frac{\partial}{\partial r}u^2 = -\frac{1}{\rho}\,\frac{\partial p}{\partial r}\ . \tag{2.132}$$

Introducing the flow potential $u := \nabla\Phi \ \Rightarrow\ \Phi = -\frac{R^2\dot{R}}{r}$ and integrating over r gives

$$\begin{aligned} &\frac{\partial^2\Phi}{\partial t\,\partial r} + \frac{1}{2}\,\frac{\partial}{\partial r}\Big(\frac{\partial\Phi}{\partial r}\Big)^2 + \frac{1}{\rho}\,\frac{\partial p}{\partial r} = 0 \\ \Rightarrow\ &\int_R^\infty \frac{\partial^2\Phi}{\partial t\,\partial r} + \frac{1}{2}\,\frac{\partial}{\partial r}\Big(\frac{\partial\Phi}{\partial r}\Big)^2 + \frac{1}{\rho}\,\frac{\partial p}{\partial r}\,dr = 0 \\ \Rightarrow\ &\frac{\partial\Phi}{\partial t} + \frac{1}{2}\Big(\frac{\partial\Phi}{\partial r}\Big)^2\Big|_R = \frac{\Delta p}{\rho} = \frac{p_0 + p_\mu + p_\sigma - p_\mathrm{g}}{\rho}\ , \end{aligned} \tag{2.133}$$

where p_0 denotes the ambient liquid pressure at infinity, p_σ and p_μ are the pressure contributions caused by surface tension and viscosity, respectively, and p_g is the gas pressure inside the bubble, which is assumed to be homogeneous within the bubble.
The first-order derivatives of $\Phi = -\frac{R^2\dot{R}}{r}$ at $r = R$ are

$$\frac{\partial\Phi}{\partial t}\Big|_R = -\frac{R^2\ddot{R} + 2R\dot{R}^2}{r}\Big|_R = -R\,\ddot{R} - 2\,\dot{R}^2,\ \frac{\partial\Phi}{\partial r}\Big|_R = \frac{R^2\dot{R}}{r^2}\Big|_R = \dot{R}\ . \tag{2.134}$$

From equation (2.28) it follows that $p_\sigma = \frac{2\sigma}{R}$, since the radius of the bubble is also the radius of curvature of its surface. The viscous term $\mu\,\Delta\vec{u}$, which was neglected in the liquid bulk, now causes a pressure p_μ at the bubble interface. If the viscosity of the bubble gas can be neglected, μ is the viscosity of the liquid. p_μ can be obtained from equation (2.55) by only considering the radial component of the velocity u_r and using $\nabla\cdot\vec{u} = 0$,

$$p_\mu = \int_R^\infty \frac{\partial}{\partial r}\,\mu\Big(\frac{\partial u}{\partial r} + \frac{\partial u}{\partial r}\Big)\,dr = -2\,\mu\,\frac{\partial u}{\partial r}\Big|_R = \frac{4\mu\dot{R}}{R}\ . \tag{2.135}$$

Equation (2.133) then turns into

$$R\,\ddot{R} + \frac{3}{2}\,\dot{R}^2 + \frac{4\nu\dot{R}}{R} + \frac{2\sigma}{\rho R} + \frac{p_0 - p_\mathrm{g}}{\rho} = 0\ . \tag{2.136}$$

This is the Rayleigh-Plesset equation [63]. To solve it, an equation of state $\rho(p_\mathrm{b})$ for the bubble contents needs to be chosen, to express p_b by the volume and thereby by the radius of the bubble.
Since the liquid was taken to be incompressible, the Rayleigh-Plesset equation does not describe the energy loss of the bubble due to the radiation of acoustic waves. To include acoustic wave radiation, the flow potential is written as a retarded potential $\Phi = \frac{1}{r} f(t - \frac{r}{c}) \approx \frac{1}{r} f(t) - \frac{\dot{f}(t)}{c}$, where c is the speed of sound in the liquid. It was assumed that $c \gg \dot{R}$. For $c \to \infty$ the incompressible case, $\Phi = -\frac{R^2 \dot{R}}{r}$, must be recovered. It thus follows that $f(t) = R^2 \dot{R}$. Using the retarded potential in equation (2.133) results in an additional term $-\frac{1}{c} \frac{d^2}{dt^2} (R^2 \dot{R}) = -\frac{1}{c} \left(R^2 \dddot{R} + 6 R \dot{R} \ddot{R} + 2 \dot{R}^3 \right)$ on the left side of equation (2.136). The Rayleigh-Plesset equation then turns into a third-order differential equation. At a glance this may seem strange since the initial conditions for R and $\dot{R}$ are specified, but not the one for $\ddot{R}$. This modified Rayleigh-Plesset equation features an unphysical solution that grows exponentially. This unstable solution can be suppressed by choosing an appropriate initial condition for $\ddot{R}$. But this method is impractical since any small numerical error excites the unstable solution. To circumvent this issue, the new term is calculated by multiplying the Rayleigh-Plesset equation (2.136) by R and differentiating by t,

$$R^2 \dddot{R} + 5 R \dot{R} \ddot{R} + \frac{3}{2} \dot{R}^3 + 4 \nu \ddot{R} + \dot{R} \frac{p_0 - p_\mathrm{g}}{\rho} - \frac{R \dot{p}_\mathrm{g}}{\rho} = 0 \; . \tag{2.137}$$

By inserting equation (2.137) into the additional term, the third-order time derivative can be eliminated,

$$R \ddot{R} + \frac{3}{2} \dot{R}^2 + \frac{4\nu \dot{R}}{R} + \frac{2\sigma}{\rho R} + \frac{p_0 - p_\mathrm{g}}{\rho} = \frac{1}{c} \left(R \dot{R} \ddot{R} + \frac{1}{2} \dot{R}^3 - 4 \nu \ddot{R} - \dot{R} \frac{p_0 - p_\mathrm{g}}{\rho} + \frac{R \dot{p}_\mathrm{g}}{\rho} \right) . \tag{2.138}$$

With the assumption $\frac{\dot{R}}{R} \gg \frac{\ddot{R}}{c}$ or $\frac{\dot{R}}{\ddot{R}} \frac{c}{R} \approx \frac{\tau c}{R} \gg 1$, the term $\frac{4\nu \ddot{R}}{c}$ in equation (2.138) can be neglected. Here, τ is a characteristic time scale of the bubble dynamics, e.g. the bubble collapse time. Values for $\frac{\tau c}{R}$ are typically in the range of $100 \ldots 1000$, e.g. for cavitation bubbles in water.
Equation (2.138) then turns into the Keller-Miksis-equation [64]:

$$R \ddot{R} \left(1 - \frac{\dot{R}}{c} \right) + \frac{3}{2} \dot{R}^2 \left(1 - \frac{\dot{R}}{3c} \right) + \frac{4\nu \dot{R}}{R} + \frac{2\sigma}{\rho R} + \frac{p_0 - p_\mathrm{g}}{\rho} \left(1 + \frac{\dot{R}}{c} \right) - \frac{R \dot{p}_\mathrm{g}}{\rho c} = 0 \; . \tag{2.139}$$

The differences between these models are illustrated in figure 2.6. While the Rayleigh collapse models an empty cavity collapsing to $R = 0$, the Rayleigh-Plesset equation takes the gas content of the cavity, the liquid viscosity, and surface tension into account, causing the bubble to rebound as an anharmonic oscillator, later regaining its initial radius. The Keller-Miksis equation also takes into account the compressibility of the liquid, and thus the bubble's energy loss due to the radiation of pressure waves, causing the bubble to reach a maximum radius smaller than $R(0)$ after its rebound.
These are not the only useful models for spherical bubble dynamics. The mass loss of a bubble due to gas diffusion was modelled by Epstein [65]. An alternative to the Keller-Miksis model is given by the Gilmore model [66, 67]. Church [68] derived a model for a bubble that is surrounded by an elastic shell in a viscous fluid. Adversely, Vincent and Marmottant [69] modelled a bubble in a viscous fluid that is confined in an elastic solid. Recently, Zhang [70] derived an ambitious model that unifies the Rayleigh-Plesset model, the Gilmore model, and the Keller-Miksis model, and further takes into account the effects of various non-spherical phenomena like the presence of boundaries, gravity, and flow fields.

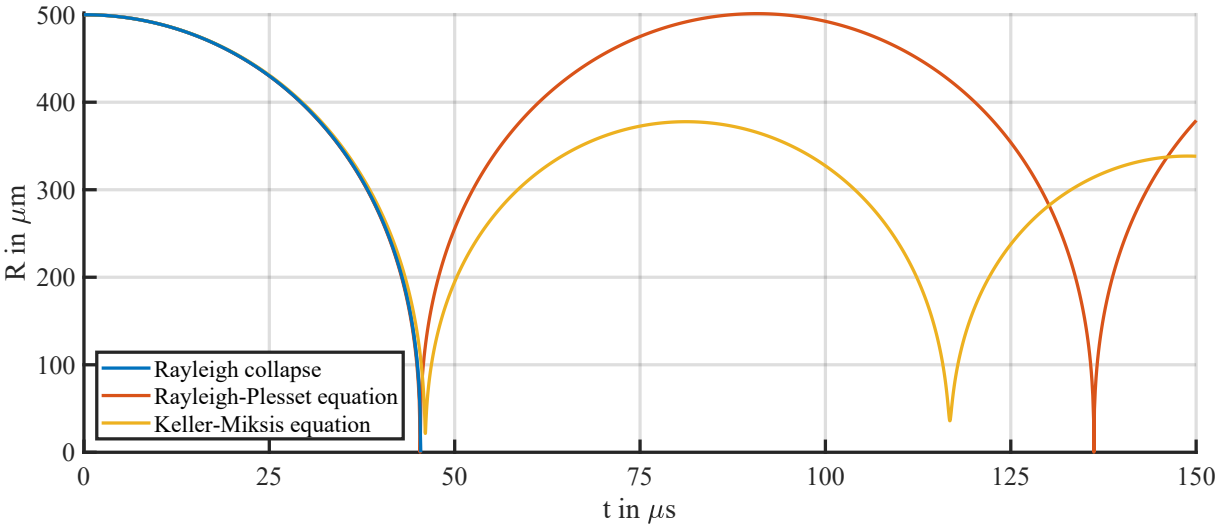

Figure 2.6: Cavity radius over time $R(t)$ showing the Rayleigh collapse of a cavity, as well as solutions of the Rayleigh-Plesset equation and Keller-Miksis equation for a bubble with $R(0) = 500\,\mu\text{m}$ and $p(0) = 1\,\text{kPa}$.

Jet formation

The bubble models derived above assume spherical symmetry of the conditions around the bubble, specifically homogeneity of the pressure field p. In the general case, the liquid pressure is a function of $\vec{x}$. If p varies slowly on the relevant length scales, e.g. the maximum bubble size, the variations can be approximated by a linear function, $p(\vec{x}) \approx p_0 + \nabla p \cdot \vec{x}$. The coordinate system can then be chosen such that the z axis points in the direction of ∇p, i.e., $p(\vec{x}) = p(z) = p_0 + \frac{dp}{dz}\, z$. Consider an initially spherical bubble with its centre on the z-axis. The system is then independent of the choice of direction of x and y, and is thus axisymmetric with respect to the z-axis. A rather simple case is that of a collapsing empty cavity, which is shown in figure 2.7 (a) at $t = 0$. If the liquid viscosity ν, surface tension σ, compressibility, and the effect of non-radial liquid flow are neglected, each point on the bubble surface evolves individually according to equation (2.130). Naturally, parts of the bubble wall that experience a larger external pressure are accelerated more strongly and thus reach the centre of the initial cavity sooner and with a higher velocity. Thus, a one-sided liquid jet is created in the opposite direction of the external pressure gradient. This is a well-known phenomenon in bubble physics. A bubble collapsing in a sufficiently strong pressure gradient develops a liquid jet that pierces the bubble and thus turns it into a toroidal shape. Such pressure gradients can be created by gravity [71], the flow field [72], or a pressure wave [73]. During jet formation, the liquid and the gas that make up the bubble gain a net momentum, which is also referred to as the Kelvin impulse [74]. The force accelerating the bubble caused by the pressure gradient is called the primary Bjerknes force [75]. It is typically used in the context of a bubble moving in a sound field. Momentum conservation still holds, but the opposite counterpart of the Kelvin impulse is transferred to the bulk of the liquid and the container holding it, and its effects can be neglected.

Generally, convergent flows lead to an acceleration of the fluid, and commonly to jet formation. In the context of a collapsing cavity, this can also happen if the pressure on two poles of the cavity is lower than in the radial directions, as shown in figure 2.7 (b). In this

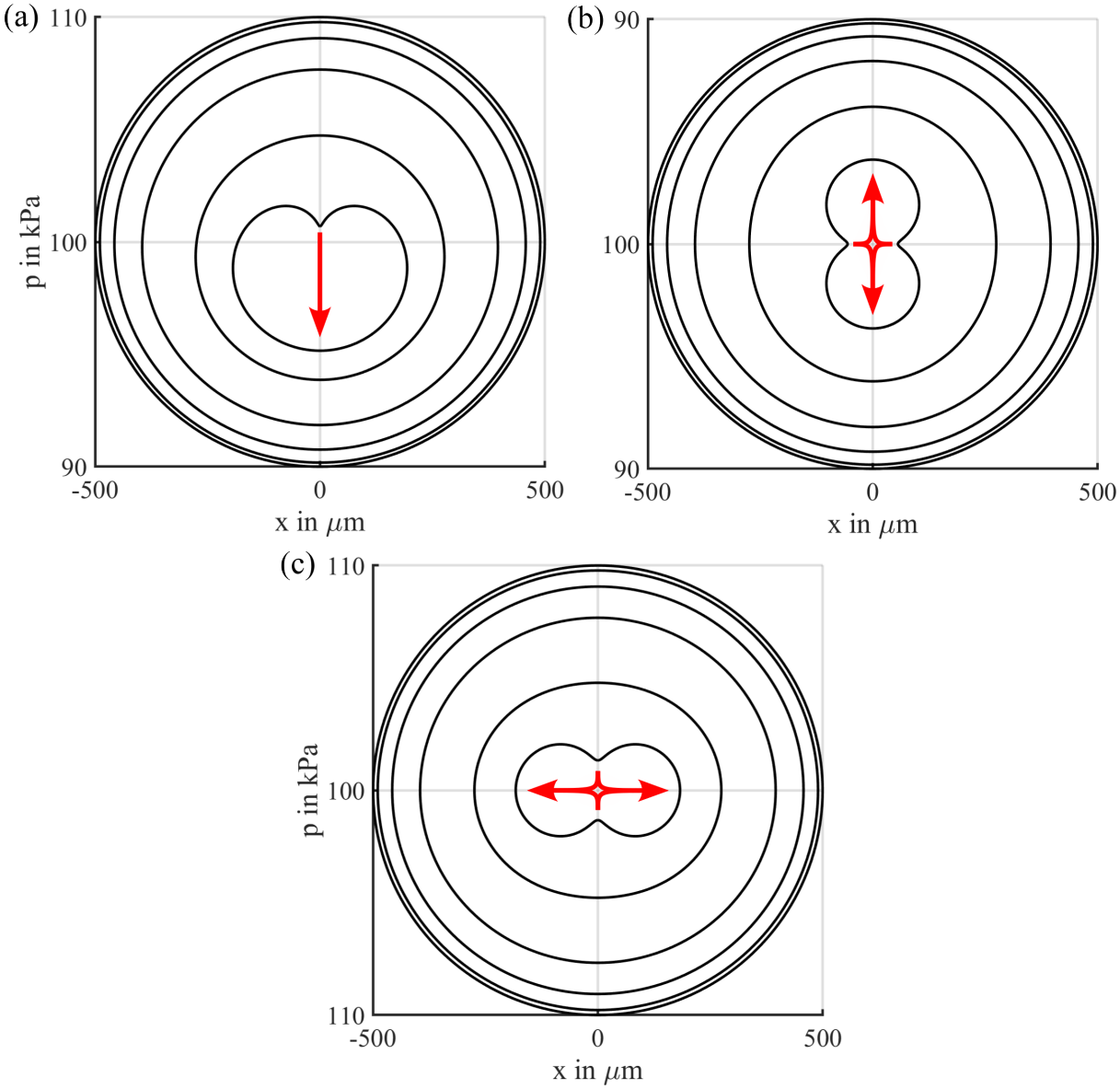

Figure 2.7: Jet formation from a cavity collapse in a pressure field. Jetting directions are denoted by red arrows. (a) Cavity collapsing in a pressure gradient. Contours are shown at $t = 0, 10, 20, 30, 40, 43.7\,\mu s$, from outside to inside. (b) Cavity collapsing in a parabolic pressure profile near the pressure maximum. Contours are shown at $t = 0, 10, 20, 30, 40, 45.7\,\mu s$, from outside to inside. (c) Cavity collapsing in a parabolic pressure profile near the pressure minimum. Contours are shown at $t = 0, 10, 20, 30, 40, 43.7\,\mu s$, from outside to inside.

special case, the parts of the cavity moving in from the radial directions reach its centre first and impact onto each other. This causes two jets to be developed along the axis of symmetry. A superposition of this phenomenon and the jet formation shown in figure 2.7 may result in either two jets, out of which one is stronger than the other, or only one especially strong jet. The inverse effect may occur if the pressure on two poles of the cavity is higher than in the radial directions, as shown in figure 2.7 (b), which would cause two jets to emerge which then collide within the cavity. For two jets of equal strength, this could result in a planar radially diverging flow, while jets of different strength result

in a single, weaker jet. Even in a homogeneous pressure field, similar types of jets as shown in figure 2.7 may form if the initial cavity is not spherical, as some parts of the cavity wall would reach its centre before others.
The pressure gradient may also be induced by the interaction between the collapsing bubble and a nearby interface. The geometry is typically classified using a non-dimensionalised stand-off parameter $\gamma = \frac{d}{R_{\max}}$, where d is the distance between the centre of the bubble and the boundary, and $R_{\max}$ is the maximum bubble radius. Since the bubble may be deformed from a spherical shape, the radius of the bubble is no longer well-defined. Since the part of the bubble furthest from the boundary may still be approximately spherical, often the distance between the position of bubble creation and the point furthest from the boundary is used. Another approach is to use the so-called unbound maximum bubble radius of a bubble far from the boundary with the same amount of energy.
A well-studied case is that of a bubble collapsing near a rigid solid boundary [76, 77]. A rigid boundary resists the acceleration of the nearest part of the bubble, which causes a prolongation of the bubble's collapse time [78], as well as a jet to be developed from the opposite side towards the solid. The jet then impinges onto the solid wall and develops into a vortex, causing large water-hammer pressures and shear stresses on the boundary. This is used for ultrasonic cleaning [9, 79–81]. The leftover bubble commonly fragments into a ring-shaped cloud of bubbles, which rebound and then collapse a second time. In specific cases, the slightly asynchronous collapse of these bubbles causes a shock wave focusing, resulting in surface stresses large enough to damage even very hard solids [82]. The destructive property of bubbles is to be avoided in most cases but also found application in medicine, e.g. in lithotripsy [11]. If a bubble is created very close to the rigid boundary, it expands into a hemispherical shape. During its subsequent collapse it develops a planar radial inflow which self-impacts on the axis of symmetry and creates a so-called "needle jet" or "fast jet" [83–86].
For more complex geometries, the bubble may still exhibit a singular jet, like in the case of a bubble collapsing near a corner [87]. For such cases, the jet direction and strength can be determined by an anisotropy parameter [88, 89]. In cases where boundaries are on opposite sides of the bubble, their competing effects may cause complex bubble dynamics, which can result in a jet in one or the other direction, or two jets and a splitting of the bubble [90–92]. Further, more complex cases are that of a granular boundary [93], a needle jet on a solid pillar [94], and a sheet jet on a fibre [95]. If a bubble collapses near a free boundary, this boundary offers a lower resistance against the bubble's collapse than the liquid bulk, which results in the formation of a jet directed away from the boundary [96, 97]. By incorporating free boundaries into a solid wall, the bubble may be forced to jet away from the boundary, effectively protecting the wall against cavitation erosion [98, 99].
An elastic solid offers an intermediate case between that of a rigid and that of a free boundary, and gives rise to complex flow phenomena during bubble collapse [100–103].
A bubble created near a liquid-liquid interface may also develop a jet, depending on the properties of both liquids involved [104].
Bubbles also interact with other bubbles. This behaviour is highly dynamic and complex, and the jetting direction depends on the sizes and oscillation phases of both bubbles [105]. The force acting between oscillating bubbles is called the secondary Bjerknes force [75].

2.6 Numerical mathematics

Numerical mathematics is a branch of mathematics that focuses on computing solutions to mathematical problems with numbers of finite precision. Numerical simulations can approximately describe many physical models and laws without the need for a physical experimental setup, only requiring a computer. Though it is immensely powerful and an important supplement to experimental research, it also has some severe limitations. Just like for analytical calculations, an appropriate model needs to be chosen for the considered problem, and all assumptions and conditions for approximations made in the model need to hold. The computer used for the simulations is also limited in its accuracy and speed. Inaccuracies due to rounding of numbers and discretisation of time and spatial dimensions are often unavoidable. This may also introduce instabilities of the mathematical solution, in which the computed result diverges exponentially from the exact solution. A solution with the desired accuracy is not always achievable in a reasonable computation time.

2.6.1 Numerical methods for ordinary differential equations

A first-order ordinary differential equation can be written in the following form:

$$\frac{d\vec{x}}{dt} = \vec{f}(t, \vec{x}) \ . \tag{2.140}$$

Since any N^{th}-order ordinary differential equation can be written as a system of N first-order ordinary differential equations, it can then also be written in the form of equation (2.140).
Equation (2.140) consists of an independent variable t, which is often time or a spatial coordinate, and an unknown variable $\vec{x}$. Combined with an initial condition it makes up an initial value problem,

$$\begin{aligned} \frac{d\vec{x}}{dt} &= \vec{f}(t, \vec{x}), \ t \in [t_0, t_0 + \alpha] \\ \vec{x}(t_0) &= \vec{x}_0 \in \mathbb{R}^N, t_0 \in \mathbb{R}, \alpha > 0 \ . \end{aligned} \tag{2.141}$$

To solve such a problem numerically, all derivatives, i.e. differential quotients, are replaced by difference quotients, since computers can only store a finite number of values for $\vec{x}$ and t. This method is called the finite difference method. There are multiple ways to approximate a first-order derivative by a difference quotient. A few examples of these are the forward difference $\frac{d\vec{x}}{dt} \approx \frac{\vec{x}(t+h)-\vec{x}(t)}{h}$, the backward difference $\frac{d\vec{x}}{dt} \approx \frac{\vec{x}(t)-\vec{x}(t-h)}{h}$, and the central difference $\frac{d\vec{x}}{dt} \approx \frac{\vec{x}(t+h)-\vec{x}(t-h)}{2h}$. h denotes a step size in t. Since these difference quotients are approximations, their accuracy and their dependence on h are of interest. For instance, for small step sizes the error made by the forward and backward differences is proportional to h, while the error of the central difference is proportional to h^2. They are said to have an order of convergence of 1 and 2, respectively.
When such a finite difference method is applied to the initial value problem, equation (2.140), a solution method is obtained. Using the forward difference results in the explicit Euler method $\vec{x}_{n+1} = \vec{x}_n + h\,\vec{f}_n$, the backward difference in the implicit Euler method $\vec{x}_{n+1} = \vec{x}_n + h\,\vec{f}_{n+1}$, and the central difference in the leap-frog method $\vec{x}_{n+1} = \vec{x}_{n-1} + 2\,h\,\vec{f}_n$. Here, the abbreviations $f_n = f(t_n, \vec{x}_n)$, $\vec{x}_n = \vec{x}(t_n)$, $t_{n+1} - t_n = h$ are used. For explicit methods, the right side only depends on $\vec{x}_n$, $\vec{x}_{n-1}$, +..., but not on $\vec{x}_{n+1}$. Otherwise, the method is called implicit. Thus, the leap-frog method is an explicit two-step method, since the terms are at most two steps apart in t. An explicit N-step method can be written in the form $x_{n+1} = x_n + h \sum_{j=0}^{N-1} c_j\, f_{n-j}$, with N coefficients c_j.

The Runge-Kutta method

Further single-step methods can be derived by writing equation (2.140) in the following form:

$$\vec{x}_{n+1} = \vec{x}_n + \int_{t_n}^{t_{n+1}} \vec{f}(t, \vec{x}(t))\, dt \ . \tag{2.142}$$

Any approximation of the integral in equation (2.142) will result in a solution method for ordinary differential equations. The simplest approximations for this integral are $h\, f_n$ and $h\, f_{n+1}$, which are called the left and the right rectangular approximation methods, respectively. They result in the explicit and the implicit Euler methods, respectively. Further integral approximation methods are the midpoint rule $\int_{t_n}^{t_{n+1}} \vec{f}\, dt \approx h\, \vec{f}_{n+\frac{1}{2}}$ and Kepler's barrel rule $\int_{t_n}^{t_{n+1}} \vec{f}\, dt \approx \frac{h}{6}\,(\vec{f}_n + 4\,\vec{f}_{n+\frac{1}{2}} + \vec{f}_{n+1})$. Since the values of $\vec{f}_{n+\frac{1}{2}}$ and $\vec{f}_{n+1}$ at $t_{n+\frac{1}{2}}$ and t_{n+1} are not known, they need to be approximated as well. To turn Kepler's barrel rule into a solution method for ordinary differential equations, $\vec{f}_n$ is renamed as

$$\vec{f}_n := \vec{k}_{1,n} \ . \tag{2.143}$$

Applying the explicit and the implicit Euler methods with step size $\frac{h}{2}$ gives

$$\vec{f}_{n+\frac{1}{2}} \approx \vec{f}(t_n + \frac{h}{2}\,,\, \vec{x}_n + \frac{h}{2}\,\vec{f}_n) = \vec{f}(t_n + \frac{h}{2}\,,\, \vec{x}_n + \frac{h}{2}\,\vec{k}_{1,n}) := \vec{k}_{2,n} \ , \tag{2.144}$$

$$\vec{f}_{n+\frac{1}{2}} \approx \vec{f}(t_n + \frac{h}{2}\,,\, \vec{x}_n + \frac{h}{2}\,\vec{f}_{n+\frac{1}{2}}) \approx \vec{f}(t_n + \frac{h}{2}\,,\, \vec{x}_n + \frac{h}{2}\,\vec{k}_{2,n}) := \vec{k}_{3,n} \ . \tag{2.145}$$

Finally, the central difference with step size $\frac{h}{2}$ gives

$$\vec{f}_{n+1} \approx \vec{f}(t_n + h, \vec{x}_n + h\,\vec{f}_{n+\frac{1}{2}}) \approx \vec{f}(t_n + h, \vec{x}_n + h\,\vec{k}_{3,n}) = \vec{k}_{4,n} \ . \tag{2.146}$$

By combining the equations (2.142)-(2.146), Kepler's barrel rule turns into

$$\vec{x}_{n+1} = \vec{x}_n + \frac{h}{6}\left(\vec{k}_{1,n} + 2\,\vec{k}_{2,n} + 2\,\vec{k}_{3,n} + \vec{k}_{4,n}\right) \ . \tag{2.147}$$

This is the so-called classic Runge-Kutta method, also referred to as *the* Runge-Kutta method.
The generic form of the class of Runge-Kutta methods is as follows:

$$\begin{aligned} \vec{k}_{i,n} &= \vec{f}(t_n + h\,c_i\,,\, \vec{x}_n + h \sum_m a_{im}\,\vec{k}_{m,n}) \ , \\ \vec{x}_{n+1} &= \vec{x}_n + h \sum_i b_i\,\vec{k}_{i,n} \ . \end{aligned} \tag{2.148}$$

Typically, the coefficients a_{im}, b_i, and c_i, that define a specific Runge-Kutta method, are written in the form of a so-called Butcher-tableau:

$$\begin{array}{c|c} \vec{c} & \overleftrightarrow{a} \\ \hline & \vec{b} \end{array} \qquad \begin{array}{c|c} 0 & \\ \hline & 1 \end{array} \qquad \begin{array}{c|c} 1 & 1 \\ \hline & 1 \end{array} \qquad \begin{array}{c|cccc} 0 & & & & \\ \frac{1}{2} & \frac{1}{2} & & & \\ \frac{1}{2} & 0 & \frac{1}{2} & & \\ 1 & 0 & 0 & 1 & \\ \hline & \frac{1}{6} & \frac{1}{3} & \frac{1}{3} & \frac{1}{6} \end{array} \tag{2.149}$$

The first tableau represents the generic form of the Runge-Kutta method. $\vec{c}$ is written as a column vector and $\vec{b}$ as a row vector. The second and third tableaus represent the explicit and the implicit Euler methods, respectively. The fourth tableau represents the classic Runge-Kutta method. For explicit methods, $\overleftrightarrow{a}$ is a strict lower triangle matrix, meaning that the diagonal elements and the upper triangle elements are 0. Hence, those elements are often omitted in tableaus for explicit methods. If $\overleftrightarrow{a}$ is a $s \times s$-matrix, the method is said to be of order s. To have an order of convergence of s, a Runge-Kutta method needs to be at least of order s. The classic Runge-Kutta method is of order 4, and its order of convergence is also 4. Thus, for small h the error in every step is proportional to h^4.

2.6.2 Numerical methods for partial differential equations

Partial differential equations (PDEs) contain derivatives of the unknown variable by at least two independent variables. Often, these include temporal and spatial derivatives. An example of such a differential equation are the Navier-Stokes equations. Similar to the methods described in section 2.6.1, for numerical computation the derivatives are replaced by difference quotients, and thus the independent variables are discretised.

The advection equation

A particularly simple partial differential equation is the linear advection equation,

$$\frac{\partial \vec{u}}{\partial t} + (\vec{a} \cdot \nabla)\, \vec{u} = 0 \tag{2.150}$$

It is used in mathematics as an example equation, on which the properties of different discretisation methods or schemes can be examined. The advection equation describes the propagation of a wave at a constant velocity $\vec{a}$. The wave is solitary, i.e., its shape does not change over time.
To solve this equation, a finite number of points in time and space need to be defined. An especially simple choice is a cubic spatial lattice with a grid parameter of $\Delta x_i = k$ and a constant time step size $\Delta t = h$.
Consider the one-dimensional case. One possible choice for the discretisation is a forward difference for the time derivative and a backward difference for the spatial derivative,

$$\frac{\partial u}{\partial t} + a\,\frac{\partial u}{\partial x} \;\rightarrow\; \frac{u_i^{n+1} - u_i^n}{h} + a\,\frac{u_i^n - u_{i-1}^n}{k} \;\Leftrightarrow\; u_i^{n+1} = u_i^n - a\,\frac{h}{k}\,(u_i^n - u_{i-1}^n)\ . \tag{2.151}$$

For $a > 0$, this is called the upwind scheme. The coefficient $Co = |a|\,\frac{h}{k}$ is called the Courant-Friedrichs-Lewy number, or for short CFL number or Courant number.
Figure 2.8 shows the behaviour of the solution of the advection equation when using the upwind scheme, with different values of the Courant number Co. The solution turns out to be exact for $Co = 1$. For $Co < 1$, numerical errors occur that tend to smooth out the solution compared to the exact solution. Because of its similarity with diffusion, this phenomenon is called numerical diffusion. For $Co > 1$ the solution is unstable, i.e., the occurring numerical errors grow exponentially in time t. Thus, a stability condition, also called CFL condition, can be formulated:

$$Co = |a|\,\frac{h}{k} \leq 1\ . \tag{2.152}$$

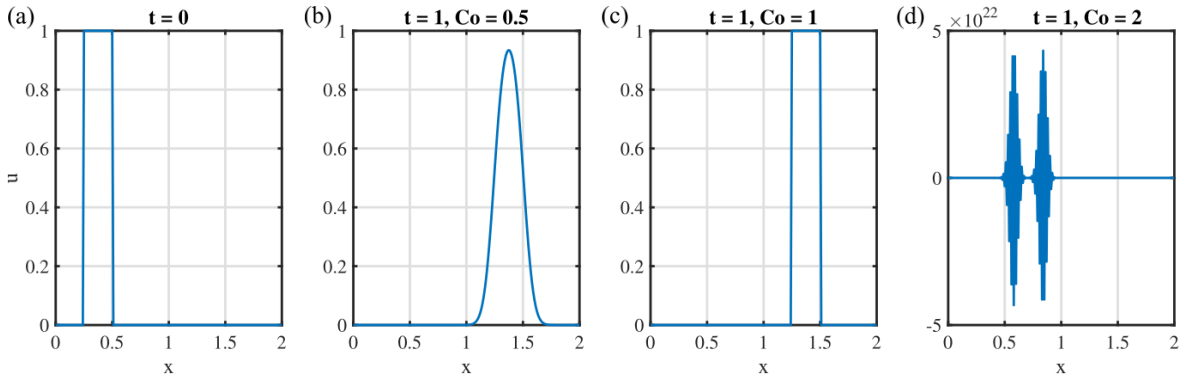

Figure 2.8: Numerical solution of the advection equation with $a = 1$, $k = 0.01$ using the upwind scheme. (a) Initial conditions. (b)-(d) Solutions at $t = 1$ for different Courant numbers $Co = |a|\frac{h}{k} = 100\,h$.

If $\vec{a}$ is replaced by $\vec{u}$, equation (2.150) turns into the non-linear advection equation, which corresponds to the left side of the Navier-Stokes equations (2.58),

$$\frac{\partial \vec{u}}{\partial t} + (\vec{u} \cdot \nabla)\,\vec{u} = \frac{D\vec{u}}{Dt} = 0\ . \tag{2.153}$$

Then, the CFL condition (2.152) becomes

$$Co = |\vec{u}|\,\frac{h}{k} \leq 1\ . \tag{2.154}$$

Here, even for constant step sizes h and k the Courant number is a function of space and time. For other grids, k is generally also not a constant. To ensure the stability of the solution, equation (2.154) must be fulfilled everywhere. Thus, the time step size h needs to be chosen according to the largest value of $\frac{|\vec{u}|}{k}$.

The diffusion equation

Another term in the Navier-Stokes equations (2.58) is described by the diffusion equation,

$$\frac{\partial \vec{u}}{\partial t} = \nu\,\Delta\vec{u}\ . \tag{2.155}$$

The diffusion equation features second-order partial derivatives in space. Once again, consider the one-dimensional case. Combining the forward difference and the backward difference results in a central difference for a second-order derivative,

$$\frac{\partial^2 u}{\partial x^2} \approx \frac{\partial}{\partial x}\,\frac{u_{i+1} - u_i}{k} \approx \frac{\frac{1}{k}\,(u_{i+1} - u_i) - \frac{1}{k}\,(u_i - u_{i-1})}{k} = \frac{u_{i+1} - 2u_i + u_{i-1}}{k^2}\ . \tag{2.156}$$

With this and a forward difference for the time derivative, equation (2.155) turns into

$$u_i^{n+1} = u_i^n + \nu\,\frac{h}{k^2}\,(u_{i+1}^n - 2\,u_i^n + u_{i-1}^n)\ . \tag{2.157}$$

Equation (2.157) also features a dimensionless coefficient, $C_\nu = \nu\,\frac{h}{k^2}$.

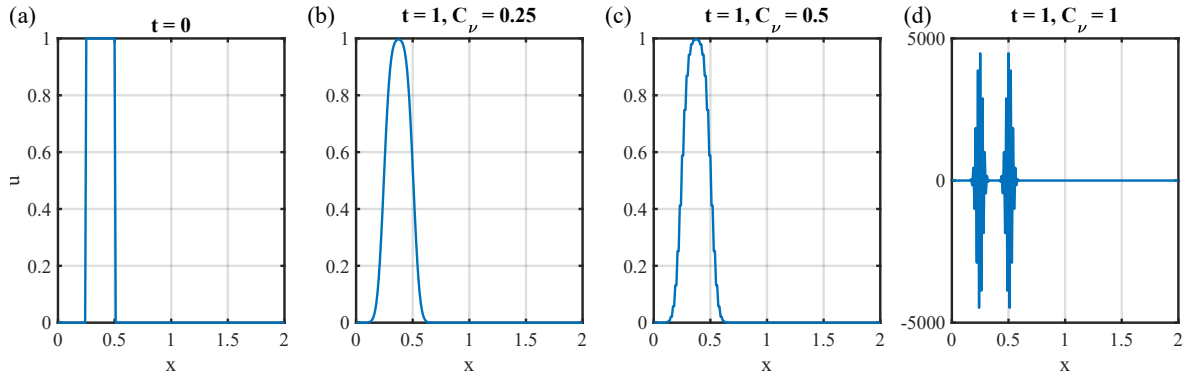

Figure 2.9: Numerical solution of the diffusion equation with $\nu = 0.001$, $k = 0.01$ using the discretisation scheme in equation (2.157). (a) Initial conditions. (b)-(d) Solutions at $t = 1$ for different $C_\nu = \nu \frac{h}{k}^2 = 10\,h$.

Solutions of the diffusion equation using the discretisation scheme in equation (2.157) are shown in figure 2.9. The most accurate solution is found for $C_\nu = 0.5$. For larger C_ν the solution is unstable. Thus, the stability condition in this case is given by:

$$C_\nu = \nu \frac{h}{k^2} \leq 0.5 \ . \tag{2.158}$$

Combining the equations (2.153) and (2.155) gives the so-called Burgers equation,

$$\frac{\partial \vec{u}}{\partial t} + (\vec{u} \cdot \nabla)\, \vec{u} = \nu\, \Delta \vec{u} \ . \tag{2.159}$$

The other terms of the Navier-Stokes equations (2.58) can be discretised in a similar fashion as the terms discussed so far.

The Poisson equation

Some differential equations do not feature time as an independent variable. Such an equation, along with the boundary conditions required to define the problem, is called a boundary value problem. A prominent example occurring in physics is the Poisson equation,

$$\Delta \phi = f(\vec{x}) \ , \tag{2.160}$$

where ϕ is an unknown, and f a known field. For $f(\vec{x}) = 0$, equation (2.160) turns into the Laplace equation, $\Delta \phi = 0$.
Consider the two-dimensional case, $\frac{\partial^2 \phi}{\partial x^2} + \frac{\partial^2 \phi}{\partial y^2} = f(x, y)$. One can make an arbitrary initial guess for the solution ϕ on the points (x_i, y_j), which shall lie on a square lattice with the grid parameter k. Discretising equation (2.160) with the central difference (2.156) gives

$$\begin{aligned} &\frac{1}{k^2} \left(\phi_{i+1,j} - 2\,\phi_{i,j} + \phi_{i-1,j} + \phi_{i,j+1} - 2\,\phi_{i,j} + \phi_{i,j-1}\right) = f(x_i, y_j) \\ \rightarrow \quad &\phi_{i,j}^{n+1} = \frac{\omega}{4} \left(\phi_{i+1,j}^n + \phi_{i-1,j}^n + \phi_{i,j+1}^n + \phi_{i,j-1}^n\right) + (1-\omega)\, \phi_{i,j}^n - \frac{k^2}{4} f(x_i, y_j)) \ . \end{aligned} \tag{2.161}$$

In the second line, an iterative method for computing the solution ϕ was defined. For an adequate choice of the newly introduced parameter ω, the computed field $\phi_{i,j}^n$ converges

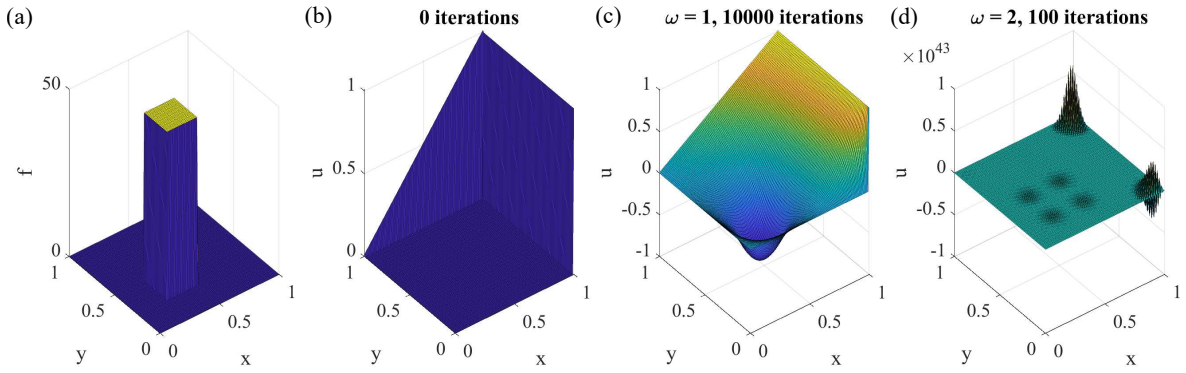

Figure 2.10: Numerical solution of the Poisson equation with $k = 0.01$ using the iterative method in equation (2.161). (a) $f(x_i, y_j)$. (b) Boundary conditions. (c) Converged solution for $\omega = 1$. (d) Unstable solution for $\omega = 2$.

towards the solution $\phi_{i,j}$ with subsequent iterations n. It is important to note that here, n does not denote a number of time steps, but a number of iterations, which does not have a physical meaning. ω is called the relaxation parameter of the iterative method. For $\omega = 1$, equation (2.161) corresponds to the discretised Poisson equation. Increasing ω can lead to a quicker convergence, but may also make the solution method unstable. This is called over-relaxation. Likewise, decreasing ω (under-relaxation) results in a more stable method with slower convergence. Optimal values for ω often lie between 1 and 2. Figure 2.10 shows an example for a numerical solution of the Poisson equation for $f(x_i, y_j)$ shown in figure 2.10 (a) and the boundary condition in figure 2.10 (b). Figure 2.10 (c) shows the converged solution for $\omega = 1$, while in figure 2.10 (d) a larger value of $\omega = 2$ was chosen, which led to an unstable solution.

2.6.3 Computational physics

Applying the Finite Difference Method (FDM) introduced above to solve PDEs in three dimensions requires a discretisation of the computational domain into a computational mesh, i.e., in three dimensions the volumetric domain of interest is divided into volumetric cells, which is why this method is then called the Finite Volume Method (FVM). By combining the terms of the PDEs above, one can solve the Navier-Stokes equations. Since this method is computationally intensive, it is gaining popularity as the advances in computational technology make it more accessible. Some popular software programs for Computational Fluid Dynamics (CFD) are COMSOL [106], ANSYS [107], and OpenFOAM, which is the software used for the present work. More details on OpenFOAM are given in chapter 3

There are other methods to solve the flow equations, each of them having different advantages and shortcomings compared to the VoF method. For the Boundary Integral Method (BIM), also called the Boundary Element Method (BEM), the flow equations are rewritten into integral equations [108]. The integral equation is then solved for the discretised boundary of the computational domain. This reduces the dimensionality by one, which can save valuable computation time. The BEM is especially suited for problems with open boundaries. However, it can only be applied to linear PDEs of which fundamental solutions are known.

The Finite Element Method (FEM) requires a computational mesh similar to the FVM [109]. But instead of using the FVM to evolve the field values at each computational cell to the next time step, a test function is chosen for each computational cell, resulting in a linear equation system, which can be solved using matrix algebra. The FEM may be harder to implement than the FVM, but it is more adaptable to complex geometries and the approximation quality is higher in many cases.
Multiphase flows that contain multiple immiscible fluids can be modelled by explicitly tracking the position of the fluid interfaces, or by using phase fraction fields α_i, which for each computational cell gives the fraction of the cell volume occupied by the i-th fluid.
To model an elastic material, typically the FEM is used, though the FVM method can also be employed. Since the components of the deformation $\vec{D}$ are coupled, an iterative solution of the linear elastic equation of motion (2.90) is required. There are multiple ways to couple a fluid to an elastic solid structure. In such Fluid-Structure Interaction (FSI) methods, one differentiates between weak coupling, in which the fluid acts upon the solid via surface stresses at the fluid-structure interface, but the deformation of the solid is negligible, and strong coupling, in which the deformation of the solid is imposed onto the fluid boundary. To model FSI with strong coupling, generally a dynamic mesh is required. OpenFOAM provides solvers for elastic solids as well as FSI using the FVM, more details on which are given in chapter 3.

The finite volume method

Take a three-dimensional volume of interest, in which a set of partial differential equations is to be solved. In the context of the finite volume method, this volume is divided into N cells. These cells are usually regular or irregular polyhedra, but can also have curved faces. Take the i-th cell, which has F faces, L edges, and X vertices, each of which is known and well-defined. Each of the cell's faces is either shared with one or more neighbouring cells or lies at the outer boundary of the volume of interest. A sketch of such a cell is shown in figure 2.11 (a).
The length of each edge is given by

$$l = \lim_{n\to\infty} \sum_{j=1}^{n} |\vec{f}(t_j) - \vec{f}(t_{j-1})| = \lim_{n\to\infty} \sum_{j=1}^{n} \left| \frac{\vec{f}(t_j) - \vec{f}(t_{j-1})}{\Delta t} \right| \Delta t = \int_a^b \left| \frac{\vec{f}(t)}{dt} \right| dt \ , \quad (2.162)$$

with its end points $\vec{x}_0 = \vec{f}(a)$ and $\vec{x}_1 = \vec{f}(b)$ coinciding with two of the cell's vertices. For a straight edge, $\vec{f}(t) = (\vec{x}_1 - \vec{x}_0)\, t + \vec{x}_0,\ a = 0,\ b = 1$, its length is simply $l = |\vec{l}| = |\vec{x}_1 - \vec{x}_0|$. Similarly, the surface area of each face is given by $A = \int dA$. The evaluation of this integral is non-trivial for an arbitrary curved surface, especially if it cannot easily be parametrised. For the case of a planar surface, the surface area can be calculated using Stokes's theorem,

$$A_\mathrm{f} = \int_{A_\mathrm{f}} \vec{n} \cdot d\vec{A} = \int_{A_\mathrm{f}} (\nabla \times \vec{B}) \cdot d\vec{A} = \oint_{\partial A_\mathrm{f}} \vec{B} \cdot d\vec{l},\ \nabla \times \vec{B} = \vec{n} \ . \quad (2.163)$$

It can be shown that the last condition is fulfilled by $\vec{B} = \frac{1}{2}\, \vec{n} \times \vec{x}$, with which the formula becomes

$$A_\mathrm{f} = \frac{1}{2} \oint_{\partial A_\mathrm{f}} (\vec{n} \times \vec{x}) \cdot d\vec{l} = \sum_{\text{edges}} \frac{1}{2} \int_{\vec{x}_0}^{\vec{x}_1} (\vec{n} \times \vec{x}) \cdot d\vec{l} \ . \quad (2.164)$$

The starting point $\vec{x}_0$ of each edge must be chosen to be an endpoint $\vec{x}_1$ of the neighbouring edge, such that a closed integral loop is formed. In the case of straight edges, this further simplifies to

$$A_\mathrm{f} = \sum_\mathrm{edges} (\vec{n} \times (\vec{x}_1 + \vec{x}_0)) \cdot (\vec{x}_1 - \vec{x}_0) \ , \tag{2.165}$$

where $(\vec{x}_1 + \vec{x}_0)/2$ is the midpoint of each edge $\vec{l}$. The normal vector $\vec{n}$ can be calculated from two of the face's non-parallel edges as $\vec{n} = \frac{\vec{l}_1 \times \vec{l}_2}{|\vec{l}_1 \times \vec{l}_2|}$. Similarly, the volume of the cell can be calculated using Gauss' theorem,

$$V = \int dV = \int \nabla \cdot \frac{\vec{x}}{3} \, dV = \oint_{\partial V} \frac{1}{3} \, \vec{x} \cdot \vec{n} \, dA = \frac{1}{3} \sum_\mathrm{faces} \oint_{A_\mathrm{f}} \vec{x} \cdot \vec{n} \, dA \ . \tag{2.166}$$

For flat edges, this simplifies to

$$V = \frac{1}{3} \sum_\mathrm{faces} \vec{x}_\mathrm{f} \cdot \vec{n} \, A_\mathrm{f} \ . \tag{2.167}$$

The face centres $\vec{x}_\mathrm{f}$ can be calculated component-wise as

$$\begin{aligned} x_{\mathrm{f},i} &= \frac{\int_{A_\mathrm{f}} x_i \, \vec{n} \cdot d\vec{A}}{\int_{A_\mathrm{f}} \vec{n} \cdot d\vec{A}} = \frac{1}{A_\mathrm{f}} \int_{A_\mathrm{f}} x_i \, \vec{n} \cdot d\vec{A} = \frac{1}{A_\mathrm{f}} \int_{A_\mathrm{f}} (\nabla \times \vec{B}) \cdot d\vec{A} = \frac{1}{A_\mathrm{f}} \oint_{\partial A_\mathrm{f}} \vec{B} \cdot d\vec{l} \\ &= \frac{1}{A_\mathrm{f}} \sum_\mathrm{edges} \int_{\vec{x}_0}^{\vec{x}_1} \vec{B} \cdot d\vec{l}, \ \nabla \times \vec{B} = x_i \, \vec{n} \ \Rightarrow \ \vec{B} = \frac{1}{2} \int x_i \, \vec{n} \times d\vec{x} \ . \end{aligned} \tag{2.168}$$

Note that $\vec{B}$ differs for each component of $\vec{x}_\mathrm{f}$, but is easily calculated in each case.
For straight edges, a similar simplification as above can be applied.
The centroid of the cell $\vec{x}_V$ can be calculated as

$$x_{V,i} = \frac{\int x_i \, dV}{\int dV} = \frac{1}{V} \int \nabla \cdot \frac{x_i \vec{x}}{4} \, dV = \frac{1}{V} \oint_{\partial V} \frac{x_i}{4} \, \vec{x} \cdot \vec{n} \, dA = \frac{1}{4V} \sum_\mathrm{faces} \oint_{A_\mathrm{f}} x_i \, \vec{x} \cdot \vec{n} \, dA \ . \tag{2.169}$$

For flat faces, this becomes

$$\vec{x}_V = \frac{1}{4V} \sum_\mathrm{faces} \vec{x}_\mathrm{f} \, (\vec{x}_\mathrm{f} \cdot \vec{n}) \, A_\mathrm{f} \ . \tag{2.170}$$

The partial differential equations are discretised by integrating them over the cell volume. The goal is to bring the considered equations into the form of an eigenvalue problem, $\overleftrightarrow{M} \, \vec{u} = \vec{b}$, with the $N \times N \times 3$-dimensional coefficient tensor $\overleftrightarrow{M}$, the unknown velocity field $\vec{u}$, and the source term $\vec{b}$, since well-known and efficient solution algorithms for such problems are available. The field values are stored at the cell centroid $\vec{x}_V$. Dividing equation (2.58) by ρ and integrating it over the cell volume gives

$$\int_V \frac{D\vec{u}}{Dt} \, dV = \int_V \frac{1}{\rho} \, \vec{f}_V - \frac{1}{\rho} \, \nabla p + \frac{1}{\rho} \, \nabla \cdot \left(\mu \left(\nabla \circ \vec{u} + (\nabla \circ \vec{u})^\mathrm{T} - \frac{2}{3} \, \nabla \cdot \vec{u} \ \mathbb{1} \right) \right) dV \ . \tag{2.171}$$

Each of these terms is then evaluated individually.

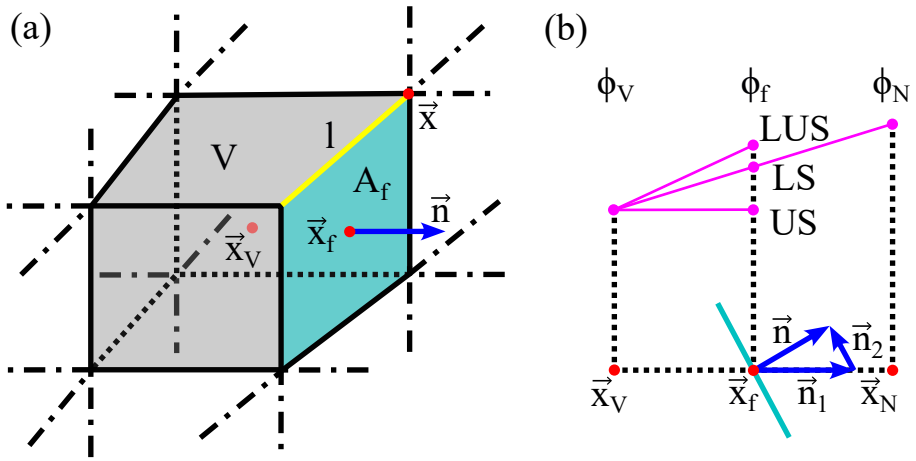

Figure 2.11: (a) Schematic example of a computational cell. A cell vertex $\vec{x}$ (red), edge l (yellow), face A_f (cyan), face normal $\vec{n}$ (blue), face centroid $\vec{x}_\mathrm{f}$ (red), volume V (grey), and volume centroid $\vec{x}_V$ (red) are highlighted. The neighbouring edges of its neighbour cells are indicated by dash-dotted lines. (b) Top: Schematic comparison between interpolation schemes, including the linear scheme (LS), upwind scheme (US), and linear upwind scheme (LUS) indicated in purple; bottom: normal vector decomposition $\vec{n} = \vec{n}_1 + \vec{n}_2$ for a non-orthogonal correction using the over-relaxed approach $\vec{n} \perp \vec{n}_2$ is shown.

Source terms that do not depend on $\vec{u}$, like $\frac{1}{\rho}\,\vec{f}_V$ and $-\frac{1}{\rho}\,\nabla p$, are approximated as varying linearly on the scale of the cell size, corresponding to second-order accuracy, which results in

$$\int_V \vec{a}_V \, dV = V \, \vec{a}_V \ . \tag{2.172}$$

For the case of the i-th cell, this term then gets added to $\vec{b}(i)$.
Source terms proportional to $\vec{u}$ yield

$$\int_V a\,\vec{u}\,dV = a_V \int_V \vec{u}\,dV = a_V \int_V (\vec{u}_V + (\vec{x} - \vec{x}_V)\,\nabla\cdot\vec{u})\,dV = a_V\,\vec{u}_V\,V \ . \tag{2.173}$$

Since $\vec{x}_V$ is the cell centroid, the second integral vanishes. This term can then either be treated explicitly by adding it to $\vec{b}(i)$, or implicitly by adding its negative, $-a_V\,V$, to $\overleftrightarrow{M}(i,i)$. The former is done if $a_V\,\vec{u}_V\,V < 0$, and the latter otherwise. This is because a positive contribution to the diagonal elements of $\overleftrightarrow{M}$ increases its stability.
Higher-order source terms can be linearised by using the values of $\vec{u}$ from the previous iteration, $a\,\vec{u}^{\,p} \ \rightarrow \ a\,\vec{u}_{j-1}^{\,p-1}\,\vec{u}$.
The time derivative is discretised using a discretisation method as discussed in section 2.6.1, typically the explicit Euler method. The resulting terms are either independent of or linear in the unknown velocity $\vec{u}$, and can thus be treated like the terms discussed above.
The advection term $\vec{u}\,\nabla\cdot\vec{u}$ is evaluated using Gauss' theorem,

$$\int_V \vec{u}\,\nabla\cdot\vec{u}\,dV = \int_{\partial V} \vec{u}\,(\vec{u}\cdot\vec{n})\,dA = \sum_{\text{faces}} \int_{A_\mathrm{f}} \vec{u}\,(\vec{u}\cdot\vec{n})\,dA = \sum_{\text{faces}} \vec{u}_\mathrm{f}\,(\vec{u}_\mathrm{f}\cdot\vec{n})\,A_\mathrm{f} \ . \tag{2.174}$$

Here, the interpolated velocity $\vec{u}_\mathrm{f}$ on the cell face centres $\vec{x}_\mathrm{f}$ is required. If the field values of other cells (typically the cell's face-sharing neighbours) are used for this interpolation, non-

diagonal terms in $\overleftrightarrow{M}$ are introduced. The number and values of the diagonal terms depend on the chosen interpolation scheme, the most simple examples of which are explained in the following.
Take the centre of the shared face $\vec{x}_\mathrm{f}$ between the cell of interest with centroid $\vec{x}_V$ and a neighbour cell with centroid $\vec{x}_\mathrm{N}$, as indicated at the bottom of figure 2.11 (b). The value of the field ϕ is known at the cell centroids and is to be interpolated on $\vec{x}_\mathrm{f}$. The linear (also called central) interpolation scheme simply assumes a linear variation of $\vec{u}$ between $\vec{x}_V$ and $\vec{x}_\mathrm{N}$, as indicated by a purple line in figure 2.11 (b),

$$\phi_\mathrm{f} = a\,\phi_\mathrm{N} + (1-a)\,\phi_V,\ a = \frac{|\vec{x}_\mathrm{f} - \vec{x}_V|}{|\vec{x}_\mathrm{N} - \vec{x}_V|}\ . \tag{2.175}$$

Due to this scheme being linear, it is second-order accurate. It is also unbounded and prone to numerical oscillations. Due to its high accuracy but lack of stability, it is typically used for the viscous term (which is discussed below), but often not for the advection term.
The linear upwind scheme calculates ϕ_f using ϕ and $\nabla\phi$ at only one of the cell centroids, the choice of which depends on the flow direction through the shared face,

$$\phi_\mathrm{f} = \begin{cases} \phi_V + a\,(\nabla\phi)_V \cdot (\vec{x}_\mathrm{f} - \vec{x}_V), & \vec{u}\cdot\vec{n} > 0 \text{ (mass flow out)} \\ \phi_\mathrm{N} + a\,(\nabla\phi)_\mathrm{N} \cdot (\vec{x}_\mathrm{f} - \vec{x}_\mathrm{N}), & \vec{u}\cdot\vec{n} < 0 \text{ (mass flow in)} \end{cases}\ . \tag{2.176}$$

This scheme is second-order accurate, and somewhat unstable since ϕ_f can be greater than both ϕ_V and ϕ_N, which is unphysical. To counteract this, the introduced parameter a, which should lie in the range from 0 to 1, can be chosen to ensure that ϕ_f lies between ϕ_V and ϕ_N. This scheme is typically only used for advective terms.
The trade-off between the accuracy and the stability of the different interpolation schemes means that the scheme should be chosen in accordance with the specific problem to be modelled. The linear and upwind schemes can also be combined using a weighted average, where the weights can also vary over the computational grid. Examples of such methods are TVD (total variation diminishing) schemes and the gamma differencing scheme.
If the cell face is part of the boundary of the computational domain, the value of $\vec{u}_\mathrm{f}$ is determined using the specified boundary condition.
Diffusive terms like the viscous term are treated in a similar fashion as the advective term,

$$\int_V \nabla\cdot\vec{f}(\vec{u}')\,dV = \int_{\partial V} \vec{f}(u')\cdot\vec{n}\,dA = \sum_\mathrm{faces}\int_{A_\mathrm{f}} \vec{f}(u')\cdot\vec{n}\,dA = \sum_\mathrm{faces} \vec{f}(u')|_\mathrm{f}\cdot\vec{n}\,A_\mathrm{f}\ , \tag{2.177}$$

where $\vec{f}(u')$ is a function of the first-order spatial derivatives of $\vec{u}$.
Since the connection vector between both cell centroids may not be perpendicular to the shared face, a non-orthogonal correction is required. For this, the normal vector is decomposed into a component along the centroid connection vector and a residual component, $\vec{n} = \vec{n}_1 + \vec{n}_2,\ \vec{n}_1 \,||\, \vec{x}_\mathrm{N} - \vec{x}_V$. This results in

$$\int_V \nabla\cdot\vec{f}(\vec{u}')\,dV = \sum_\mathrm{faces} \vec{f}(u')|_\mathrm{f}\cdot\vec{n}_1\,A_\mathrm{f} + \vec{f}(u')|_{\mathrm{f},j-1}\cdot\vec{n}_2\,A_\mathrm{f}\ . \tag{2.178}$$

The second term is treated explicitly by using the value of $u_{\mathrm{f},j-1}$ from the previous iteration and added to $\vec{b}(i)$ as a source term. The length of $\vec{n}_1$ is a degree of freedom. Typically, the condition $\vec{n}_2 \perp \vec{n}$ is chosen. This approach is generally more stable and converges quicker than other choices, even for a relatively large skew angle between $\vec{n}$ and $\vec{n}_1$. For strongly skewed cells, the explicit term may be limited or omitted to achieve a stable, although inaccurate solution.

3 Software

OpenFOAM is an open-source framework of simulation software based on the finite volume method. Here, "FOAM" stands for "Field Operation And Manipulation". It is written in C++ for Linux. It does not feature a user interface and is thus entirely text-based. Simulation properties are specified in text files and simulations are run using Linux terminal commands. The present work features three newly developed solvers using the OpenFOAM framework: `CavBubbleFoam` [41], `MultiphaseCavBubbleFoam` [42], and `CavBubbleFsiFoam` [43]. These solvers are described in the following sections.
The simulations were carried out on two workstations, with the following system specifications:

specification	work station 1	work station 2
processor	2 × AMD Epyc 7351	AMD Ryzen Threadripper 1900X
number of cores	2 × 16	8
processor clock speed	2.4 GHz	3.8 GHz
RAM	64 GB	64 GB
RAM clock speed	2933 MHz	2133 MHz
graphics card	Nvidia RTX 2060 Super	Nvidia GTX 1060
SSD storage capacity	1 TB	1 TB
HDD storage capacity	8 TB	10 TB
operating system	Ubuntu 20.04 LTS	Ubuntu 16.04 LTS

Table 3.1: Work station system specifications.

Workstation 2 was used for the OpenFOAM simulations for chapter 4. For the chapters 5-12, work station 1 was used.
For post-processing simulation data, ParaView [110] and Matlab [111] were used. Matlab was also used for plots and Rayleigh-Plesset-type models. For image processing, mainly ImageJ [112], InkScape [113], and GIMP [114] were used.

3.1 compressibleInterFoam

OpenFOAM contains different solvers for different classes of problems. For example, `compressibleInterFoam` is a solver for two compressible, non-isothermal, immiscible fluids. In the solvers used in the present work, heat conduction will be disregarded. It will thus not be discussed here, despite being modelled in `compressibleInterFoam`.
Instead of using the equation of state in its explicit form, $\rho = \rho(p)$, the compressibility of the fluid κ is used to calculate density changes of the modelled fluids. κ can be calculated according to equation (2.62) from the equation of state of choice (2.61),

$$\kappa = -\frac{1}{V}\left(\frac{\partial V}{\partial p}\right)_T = \frac{1}{\rho}\left(\frac{\partial \rho}{\partial p}\right)_T = \frac{1}{\rho\left(\frac{\partial p}{\partial \rho}\right)_T} = \frac{1}{\gamma\left(p_0 + B\right)\left(\frac{\rho}{\rho_0}\right)^{\gamma}} = \frac{1}{\gamma\left(p + B\right)} \ . \tag{3.1}$$

In `compressibleInterFoam`, the compressibility is described by the quantity $\psi = \kappa\,\rho = \frac{d\rho}{dp}$. It is calculated as a separate field quantity for each fluid at the start of the simulation and is then assumed to be constant over time.

To describe a system with two fluid components, a dimensionless field α is introduced, which is the volume fraction (or phase fraction) of a computational cell occupied by one of the components. For a given cell, $\alpha = 0$ and $\alpha = 1$ stand for the cell being fully occupied by one of the fluid components or the other. For $0 < \alpha < 1$, both components are present in the cell. It thus also contains a part of the interface between both fluids. In `compressibleInterFoam`, the notation $\alpha_1 = \alpha$ and $\alpha_2 = 1 - \alpha$ is used, from which it follows that $\alpha_1 + \alpha_2 = 1$. This method to describe the two components is called a "phase-fraction based interface capturing approach" in OpenFOAM.
The density fields ρ_1 and ρ_2, which each only describes one of the components, are calculated from the equation of state (2.61) using the pressure field p and the respective fluid parameters,

$$\rho_j = \rho_{0j} \left(\frac{p + B_j}{p_{0,j} + B_j} \right)^{\frac{1}{\gamma_j}} , \tag{3.2}$$

where the index $j = 1, 2$ stands for the two fluid components. The density field ρ can be constructed from these component density fields as $\rho = \alpha_1 \rho_1 + \alpha_2 \rho_2$. The fluid components individually fulfil a continuity equation,

$$\frac{\partial(\alpha_j \rho_j)}{\partial t} + \vec{u} \cdot \nabla(\alpha_j \rho_j) + \alpha_j \rho_j \nabla \cdot \vec{u} = \frac{\partial(\alpha_j \rho_j)}{\partial t} + \nabla \cdot (\alpha_j \rho_j \vec{u}) = 0 . \tag{3.3}$$

From this, it follows that ρ also obeys the continuity equation (2.34). Though, this equation is posed locally for continuous fields. When implemented for computational cells of finite size, the first term of equation (3.3) describes the rate of change of the density ρ_j in the cell volume, while the second term describes the mass flux of this fluid component through the surface of the cell. If the fields ρ_j and $\vec{u}$ are defined in the geometric centre of each cell, their values on the cell faces are to be acquired via interpolation. The interpolated values of the velocity field $\vec{u}$ on the cell faces are called $\vec{\phi}$ in `compressibleInterFoam`. With this, equation (2.34) and equation (3.3) turn into

$$\frac{\partial \rho}{\partial t} + \nabla \cdot (\rho \vec{\phi}) = 0 . \tag{3.4}$$

$$\frac{\partial(\alpha_j \rho_j)}{\partial t} + \nabla \cdot (\alpha_j \rho_j \vec{\phi}) = 0 . \tag{3.5}$$

The rate of change of ρ_j caused by pressure variations dp is given by

$$d\rho_j = \frac{d\rho_j}{dp} dp = \psi_j \, dp . \tag{3.6}$$

In a time step, first the phase fraction field α_1 is updated. From equation (3.6) it follows that $\frac{D\rho_j}{Dt} = \psi_j \frac{Dp}{Dt}$. With this and $j = 1$, equation (3.5) turns into

$$\frac{\partial \alpha_1}{\partial t} + \frac{\alpha_1}{\rho_1} \frac{\partial \rho_1}{\partial t} + \nabla \cdot (\alpha_1 \vec{\phi}) + \frac{\alpha_1}{\rho_1} \vec{\phi} \cdot \nabla \rho_1 = \frac{\partial \alpha_1}{\partial t} + \nabla \cdot (\alpha_1 \vec{\phi}) + \frac{\alpha_1}{\rho_1} \frac{D\rho_1}{Dt} = 0 \tag{3.7}$$

$$\rightarrow \frac{\partial \alpha_1}{\partial t} + \nabla \cdot (\alpha_1 \vec{\phi}) + \frac{\alpha_1}{\rho_1} \psi_1 \frac{Dp}{Dt} + \nabla \cdot (\alpha_1 \alpha_2 \vec{\phi}_r) = 0 \tag{3.8}$$

The discretisation methods used for the derivatives are specified in the simulation case files, as explained in section 3.2.1. The last term in equation (3.8) was added as a correction to counteract numerical diffusion, where $\vec{\phi}_r$ is defined as

$$\vec{\phi}_r = c_\alpha \sum_i \frac{|\phi_i|}{|\vec{A}_i|} \frac{\nabla \alpha}{|\nabla \alpha|} , \tag{3.9}$$

with a parameter $c_\alpha \leq 1$ and the cell faces $\vec{A}_i$.
Next, α_2 is updated according to $\alpha_2 = 1 - \alpha_1$, and ρ according to equation (3.4).
In the following step, the equation of motion, i.e. the Navier-Stokes equation (2.58), is used to update the velocity field $\vec{u}$. Afterwards, the pressure field p is updated. For this, the equation of motion is written in the form

$$\overleftrightarrow{M}\,\vec{u} = -\nabla p \ , \tag{3.10}$$

where the tensor $\overleftrightarrow{M}$ is known. The partial tensor of $\overleftrightarrow{M}$ that contains only its diagonal elements is named $\overleftrightarrow{A}$. Since $\overleftrightarrow{A}$ is a diagonal matrix, it can easily be inverted. Additionally, a further quantity $\vec{H}$ describing the non-diagonal elements of $\overleftrightarrow{M}$ is introduced as

$$\vec{H} = (\overleftrightarrow{M} - \overleftrightarrow{A})\,\vec{u} \ . \tag{3.11}$$

With this, equation (3.10) turns into

$$\begin{aligned} \overleftrightarrow{A}\,\vec{u} - \vec{H} = \overleftrightarrow{M}\,\vec{u} = -\nabla p \ \Leftrightarrow \ \vec{u} = \overleftrightarrow{A}^{-1}\,\vec{H} - \overleftrightarrow{A}^{-1}\,\nabla p \\ \Leftrightarrow \ \nabla\big(-\overleftrightarrow{A}^{-1}\,\nabla p\big) = \overleftrightarrow{A}^{-1}\,\vec{H} - \nabla\cdot\vec{u} \ . \end{aligned} \tag{3.12}$$

This scalar equation can be used to update the pressure field p.
With this, the density fields ρ_j can be updated according to equation (3.6), and the velocity field $\vec{u}$ according to equation (2.58).
The time step size h can be chosen to be constant, but in many cases it is advisable to use an adjustable time step size to decrease the computation time. For this, a maximum CFL number $Co_{\max}$ is chosen, that shall not be exceeded. Then after every time step, the current largest CFL number Co is calculated. Then, the time step size h is multiplied by the factor $\min(\frac{Co_{\max}}{Co}\ , 1 + 0.1\,\frac{Co_{\max}}{Co}\ , 1.2)$.

3.1.1 The Pimple algorithm

OpenFOAM includes three solution algorithms that solve the equations discussed in the previous section in different ways.
The so-called simple algorithm stands for "semi-implicit method for pressure-linked equations". It iterates over the steps discussed in the last section, i.e., it updates α and ρ according to the continuity equation (3.8,3.4), $\vec{u}$ according to the equation of motion (2.58) and p according to the pressure correction equation (3.12), followed by correcting ρ and $\vec{u}$ according to equation (3.6) and equation (2.58), respectively, until the solution is sufficiently converged or a specified number of iterations is reached. This algorithm is especially useful for stationary flows since over many iterations it can reach a high precision. For dynamic flows, in which many time steps need to be carried out, it is too computationally expensive, meaning that it is too time intensive as compared to the following algorithm.
The piso algorithm stands for "pressure-implicit with splitting of operators". It is used for transient, i.e. time-dependent flows. It also contains a loop, though in contrast to the simple-loop it only contains the solution of the pressure correction equation and the subsequent correction of ρ and $\vec{u}$. To achieve numerical stability, the CFL condition must be fulfilled, i.e., for a given cell size and velocity field $\vec{u}$, the time step size may not exceed a certain limit.

The pimple algorithm is a combination of the two aforementioned algorithms and contains both loops described above. Like the piso algorithm, it is suitable for transient flows. The flow equations are solved iteratively in every time step according to the simple algorithm. This leads to larger computation times for each time step, though a sufficient number of iterations may inhibit instabilities, such that larger time steps can be used, even if the CFL condition is not fulfilled. `compressibleInterFoam` uses the pimple algorithm, though for the simulations carried out in the present work, the number of iterations of the outer loop was set to 1, such that effectively the piso algorithm was used. Thus, the CFL condition had to be fulfilled.

3.2 CavBubbleFoam

OpenFOAM has been used by Max Koch and Christiane Lechner to model the expansion and collapse dynamics of a single bubble using a solver based on `compressibleInterFoam`, [83–85, 115–117]. It was later also used by Qingyun Zeng [118, 119], who kindly provided the solver called `CavBubbleFoam`, which the solvers described in the following are based on. `CavBubbleFoam` has recently been used successfully by Wang et al. [120].
This solver was attained via modifications on the base solver `compressibleInterFoam`. Firstly, it is assumed that all changes of state of each fluid are adiabatic, and thus all heat conduction effects are neglected, and consequently disabled in the solver. This assumption is supported by [121].
Furthermore, the fluid compressibility is taken to be constant in `compressibleInterFoam`. This is an unacceptable simplification for the application of a strongly oscillating bubble, and thus the compressibility is updated in every time step in `CavBubbleFoam`.
A further modification of the solver made by the author is that `CavBubbleFoam` exports useful information in a file called `info.csv` where in every time step, the time t and three further quantities $\sum_i V_i\,\alpha_{2i}$, $\sum_i V_i\,\alpha_{2i}\,p_i / \sum_i V_i\,\alpha_{2i}$, and $\sum_i V_i\,\alpha_{2i}\,\rho_i$ are written, each of which is calculated by summing over all computational cells. Each of these quantities is proportional to the volume V, the average pressure p and the mass m of the bubble.
To model an oscillating bubble more accurately, several corrections were implemented. Despite the absence of a phase transition model, m varies over time due to numerical inaccuracies. This is corrected in every time step by multiplying the density field by the factor $\frac{m_0}{m}$, such that the bubble mass stays constant over time. In reality, a laser-induced cavitation bubble loses mass over time due to condensation. This process is accounted for by a simple correction, in which the pressure field is multiplied by a numerical factor f_p when the bubble shrinks in volume for the first time. Since in the initial time steps, the smeared interface of the bubble contracts, this correction may be wrongly applied by the solver there, which is why the condensation correction is only applied if $t > 1\,\mu s$.
Lastly, numerical errors may lower the phase fraction field α slightly below 1, even in the liquid bulk far from the main bubble. These small gaseous regions can expand upon the occurrence of an under-pressure. To counteract this, in every time step α is set to exactly 1 in cells in which it exceeds a specified threshold, $\alpha > 1 - \alpha_{\text{limit}}$. This has the negative side effect that cells near a slowly advancing bubble surface, that only change to a value slightly below $\alpha = 1$ in every time step, are forcefully kept at $\alpha = 1$, which effectively locks the bubble wall in place. To avoid this undesirable effect, α_{limit} must be well chosen according to the configuration to be simulated. The inaccuracies of the underlying model as well as of the numerical implementation are discussed in chapter 13
`CavBubbleFoam` uses the version OpenFOAM 4.0 [122]. It is available in the supplemen-

tary material of [22], as well as on GitHub [41].

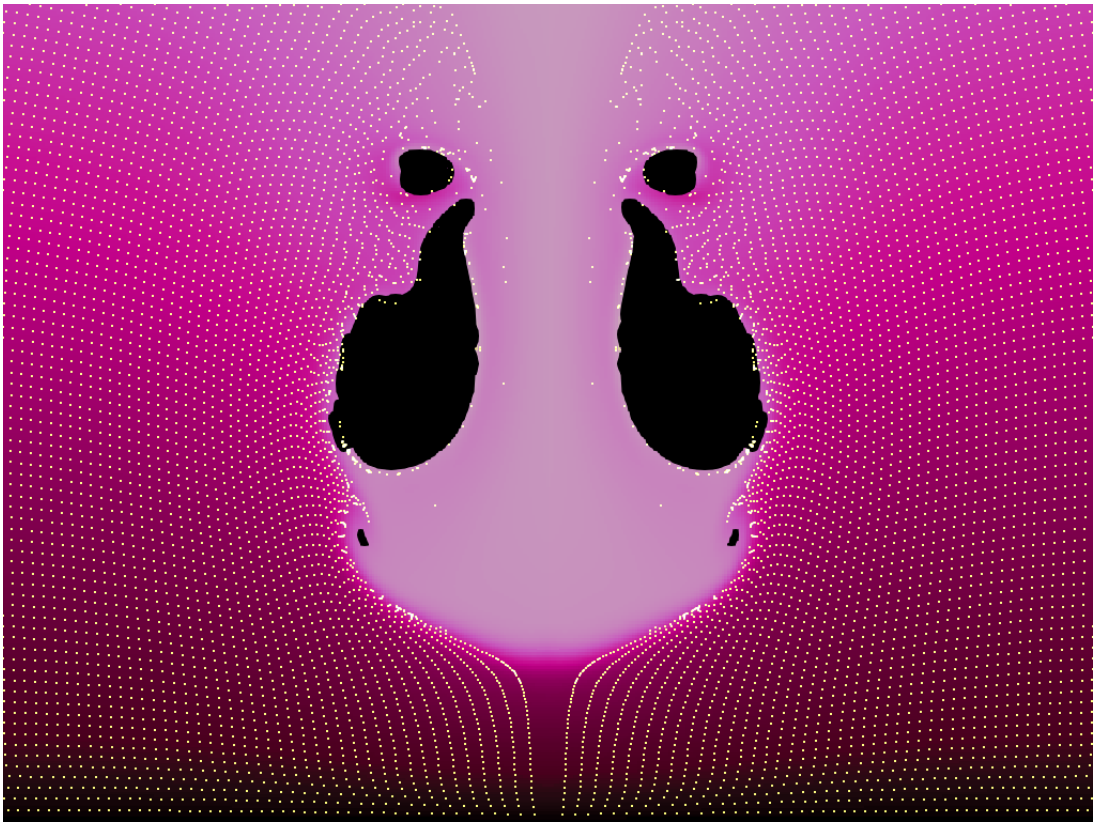

Figure 3.1: Example of y_{ink} and particles for a bubble, initiated at a stand-off $d = 1\,\text{mm}$, jetting towards a rigid wall (bottom). The frame width is 1 mm. The particles were initiated up to 1 mm from the wall. The ink map is scaled from $y = 0$ (black) to $y = 1.2\,\text{mm}$ (light magenta).

Two additional features were implemented into the solver for better data visualisation during post-processing. The first is a Lagrangian ink map, which is initialised as $\vec{x}_{\text{ink}}(t = 0) = \vec{x} - \vec{x}_0$, where $\vec{x}_0$ is the initial position of the bubble. It then obeys an advection equation,

$$\frac{\partial(\vec{x}_{\text{ink}})}{\partial t} + \nabla \cdot (\vec{x}_{\text{ink}}\,\vec{\phi}) = 0\ . \tag{3.13}$$

Then for an incompressible fluid, at a time t the ink map $\vec{x}_{\text{ink}}(\vec{x}, t)$ gives the approximate initial position of the fluid element found at the location $\vec{x}$. This breaks down for compressible fluids since an expansion or compression of the fluid also changes the value of $\vec{x}_{\text{ink}}$, but it can still be used approximately for liquids since they are only weakly compressible.
Additionally, Lagrangian particles that follow the velocity field $\vec{u}$ in a similar way to the ink map are modelled. This so-called `kinematicCloud` is a feature of OpenFOAM, the code of which was simply implemented into `CavBubbleFoam`. They are implemented as passive particles that follow the flow field without affecting it and are thus only to be used for visualisation purposes. They ended up not being used in the present work but were kept in the published version of the solver for potential future applications.
An example of the Lagrangian ink map and particles is shown in figure 3.1.

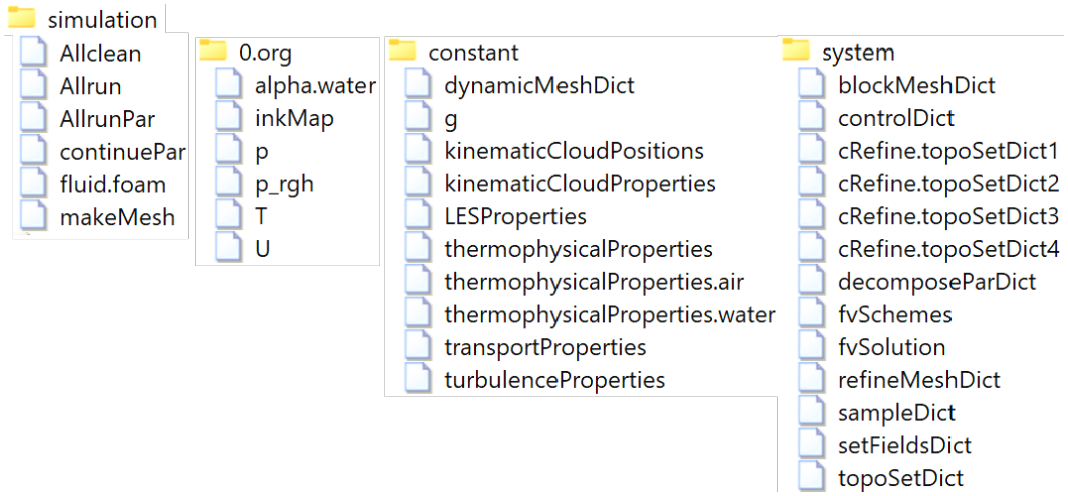

Figure 3.2: Tree view of the file structure of an example simulation case for `CavBubbleFoam`.

3.2.1 Case structure

Each simulation is contained in a separate folder. An example of the file structure of a simulation in its initial state is given in figure 3.2. Example cases are given along with each solver in their respective GitHub repositories [41–43]. The folder `0.org` contains the initial conditions and the boundary conditions for the considered fields α (`alpha.water`), T (unused), $\vec{u}$ (`U`) and p. `p_rgh` corresponds to the non-gravitational pressure field $p - \rho\, g\, z$. Since gravity is neglected in the present work, this is equal to the pressure p. While the simulation is running, at specified times t a folder with a name corresponding to t is created, containing numerical data for the respective fields.
To apply physical models, relevant physical constants need to be provided. These are given in the folder `constant` in the files `transportProperties` and `thermophysicalProperties` and listed in table 3.2:

quantity	symbol	value for water	value for vapour
density	ρ_0	1000 $\frac{\text{kg}}{\text{m}^3}$	1 $\frac{\text{kg}}{\text{m}^3}$
adiabatic exponent	γ	7.15	1.33
pressure	p_0	101325 Pa	10320 Pa
	B	303.6 MPa	0
dynamic viscosity	ν	10^{-3} $\frac{\text{kg}}{\text{ms}}$	$1.84 \cdot 10^{-5}$ $\frac{\text{kg}}{\text{ms}}$
surface tension coefficient	σ	0.07 $\frac{\text{kg}}{\text{m}^2}$	

Table 3.2: List of relevant physical constants.

The pressure factor f_p for the mass correction accounting for condensation is also given in `transportProperties`.
In the folder `system`, numerical parameters are specified. For instance, in `controlDict` the name of the solver to be used is specified, as well as the initial time step size, the field output time intervals, and the end time of the simulation. If an automatic time step adjustment is used, the maximum acceptable Courant number $Co_{\max}$ is also to be given there. In `fvSchemes`, discretisation schemes to be used for any occurring differentiations

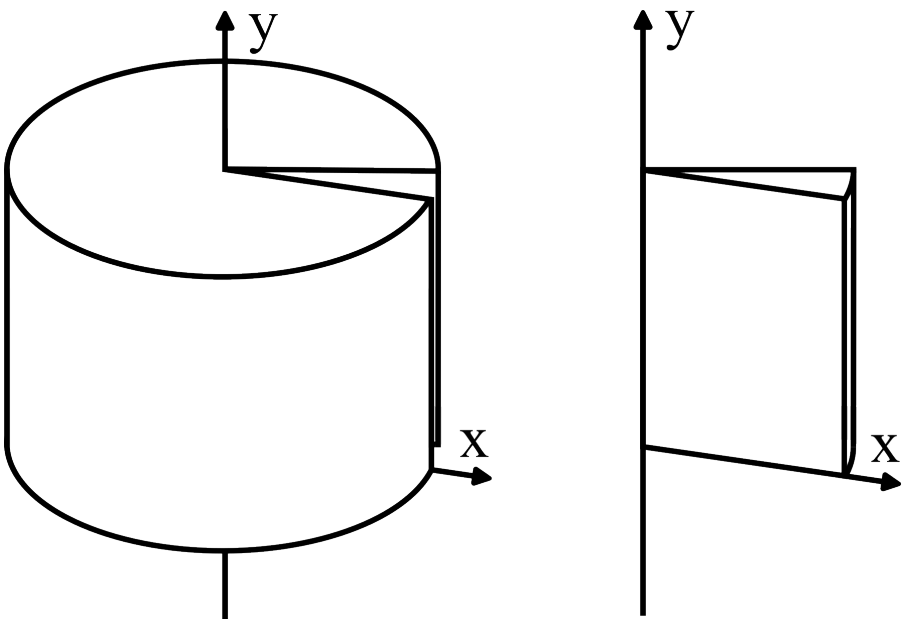

Figure 3.3: Underlying geometry of an axisymmetric simulation. A thin slice with circular boundary conditions between the front and back planes is modelled, representing the full cylindrical domain.

are specified, e.g. the upwind scheme for divergences. `fvSolution` contains further parameters of the solution algorithm, like residual error tolerances and maximum iteration numbers, as well as correction values like α_{limit}.
To run the simulation, `Allrun` is executed, which contains commands for a series of preparation steps and for subsequently carrying out the simulation as a serial computation. Alternatively, `AllrunPar` may be executed to carry out the simulation as a parallel computation. Before the simulation can be run, the geometry of the domain to be simulated as well as the computational mesh must be defined and turned into the format used by OpenFOAM. This is further explained in section 3.2.2. The corresponding files will then be located in a folder named `polyMesh`, which will be created within the folder `constant`. At this point, if parallel computation is to be used, the mesh is decomposed into chunks, each of which is designated to one processor core. Then, the fields are written corresponding to the specified initial state of the bubble. Finally, the simulation is carried out using the solver and the number of cores specified in the simulation files.
`foam.foam` is an empty file. It may be opened using ParaView to view the simulation data for post-processing.

3.2.2 Geometry and mesh

Symmetries are very useful for computational mathematics, as the associated redundancy allows for solving the equations of motion in only a partial domain that contains all the information characterising the full domain.
Axisymmetric problems are particularly useful, as any radial cross-section of the domain characterises the entire fields, and thus the dimensionality of the simulation is reduced by 1. Then, only a thin wedge of a cylindrical domain must be explicitly modelled, as shown in figure 3.3.

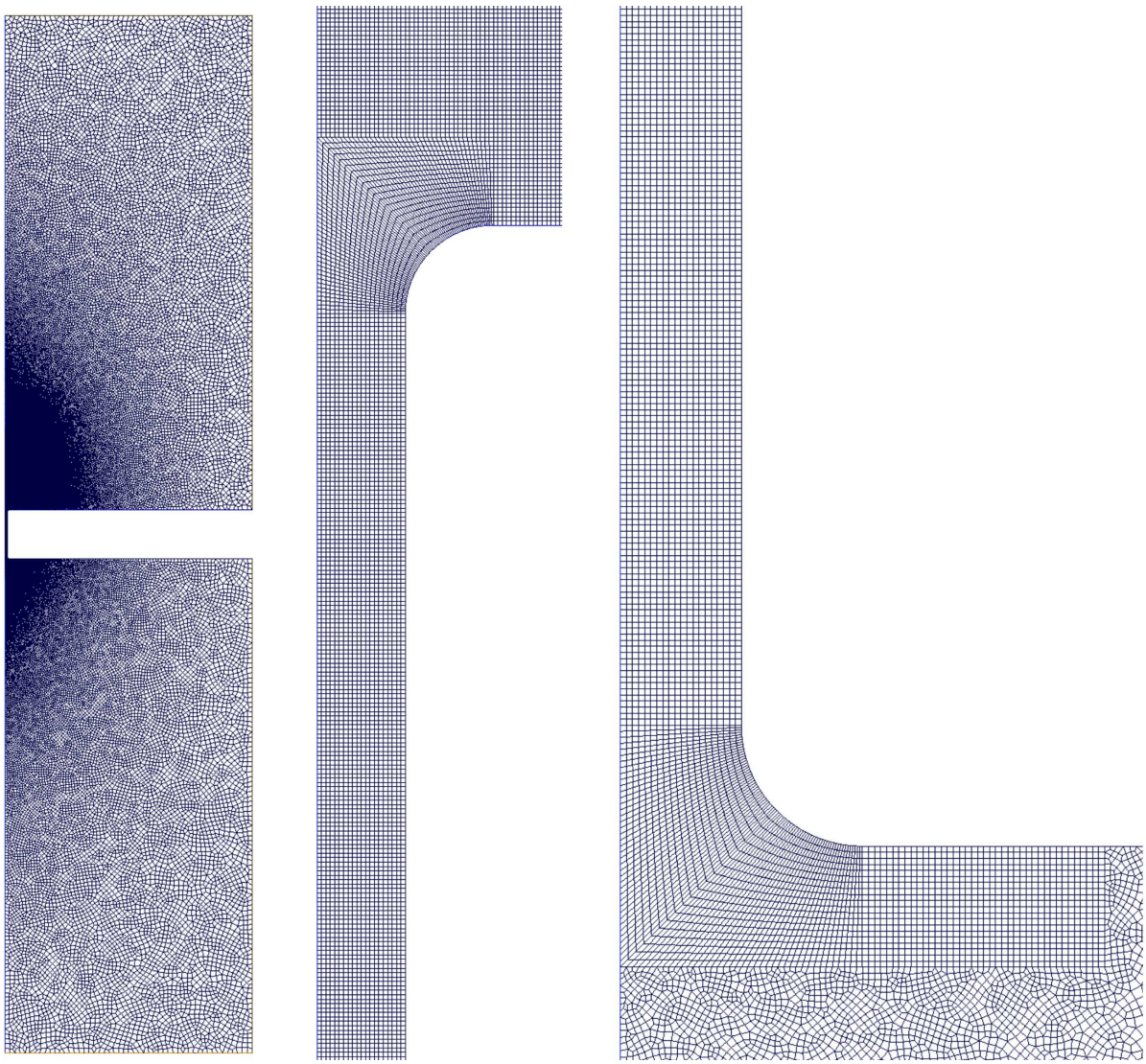

Figure 3.4: Example of a partly unstructured and partly structured mesh made with Gmsh. The mesh represents two cylindrical fluid domains that are connected via a cylindrical channel. The top and bottom ends of the channel are shown using zoomed-in images in the middle and on the right, respectively.

Gmsh

Gmsh [123] is a tool for creating three-dimensional geometries and computational meshes. In the present work it was only used for chapter 4, where the version Gmsh 4.4.1 was used.
Scripts for the creation of a geometry and the corresponding mesh are written in a .geo file. The mesh is then generated using Gmsh and exported as a .msh file. An example simulation case using a mesh made by Gmsh is shown in figure 3.4 and given in the supplementary material of [22] as well as on GitHub [41], along with the corresponding .geo and .msh files. In that case, two cylindrical fluid domains are connected by a filleted channel along the axis of symmetry.
To create this mesh using Gmsh, first the front surface of a wedge as shown in figure 3.3 is defined. For this, numerical parameters characterising the geometry and the mesh are

defined. Next, relevant points are defined using three-dimensional coordinates. Those points are subsequently used to define straight lines (made of their two endpoints) or circle segments (defined by their two endpoints and a third point along its path). The lines are segmented as transfinite curves, giving the boundary conditions for the later-created mesh. Using these lines, closed curve loops are defined that enclose each relevant surface of the geometry. Note that the order and direction of the lines must be given such that the curve loop is continuously followed, with the start and end points coinciding. Those surfaces can be denoted as transfinite surfaces if they are to be discretised using a structured mesh. Otherwise, an algorithmically generated unstructured mesh will be used. Once the entire surface is created, it is extruded by rotation about an axis near the axis of symmetry. The slight offset of this axis is used such that the left side of the domain is represented by a finitely sized surface, which is necessary for usage in OpenFOAM. Finally, the physical boundaries and the simulation domain are defined using the surfaces and their extrusions, respectively.
The .geo file is then loaded using Gmsh and the meshing process is carried out. The created mesh can then be exported as a .msh file for usage in OpenFOAM. Note that Version 2 ASCII must be used for OpenFOAM to be able to interpret the mesh data. With the command `gmshToFoam`, the .msh file is converted into OpenFOAM's internal mesh format.

BlockMesh

Instead of using an external mesh creation tool, the internal functions `blockMesh` or `snappyHexMesh` may be used, only the former of which will be discussed here.
The mesh is defined in `system/blockMeshDict`. Note that in some versions of OpenFOAM, this file is instead found in `constant/polyMesh`, where other files related to the computational mesh are also located. Similarly to Gmsh, first useful numerical parameters are defined, and subsequently relevant vertices are defined using three coordinates each. Then, hexahedra called blocks are defined using 8 vertices. Note that a specific order of the vertices must be used, first following the circumference of one side of the hexahedral, and then the circumference of its opposite side. The number of cells along each axis of the hexahedron is defined alongside it, with the option of making the cells denser on one side or the other. If circle segments are to be used for curved edges, they are subsequently defined using their two endpoints and a third point along their path. Finally, physical boundaries of the domain are defined as patches from curve loops around the circumference of a surface, that consist of 4 vertices each. The mesh is then created using the command `blockMesh`.
The mesh may subsequently be refined by splitting cells into two in every direction specified in `system/refineMeshDict`. For axisymmetric simulations, it is reasonable to refine the mesh in the radial and axial directions, and not in the azimuthal direction. To refine the mesh, the region to be refined is defined using simple shapes like cuboids or cylinders in `system/topoSetDict` and applied using the command `topoSet`. The mesh is then refined via the command `refineMesh`.
Figure 3.5 shows an example of a mesh defined using `blockMesh` and refined four times using `refineMesh`.

Mesh decomposition

For parallel computation, the computational domain is decomposed into regions that are

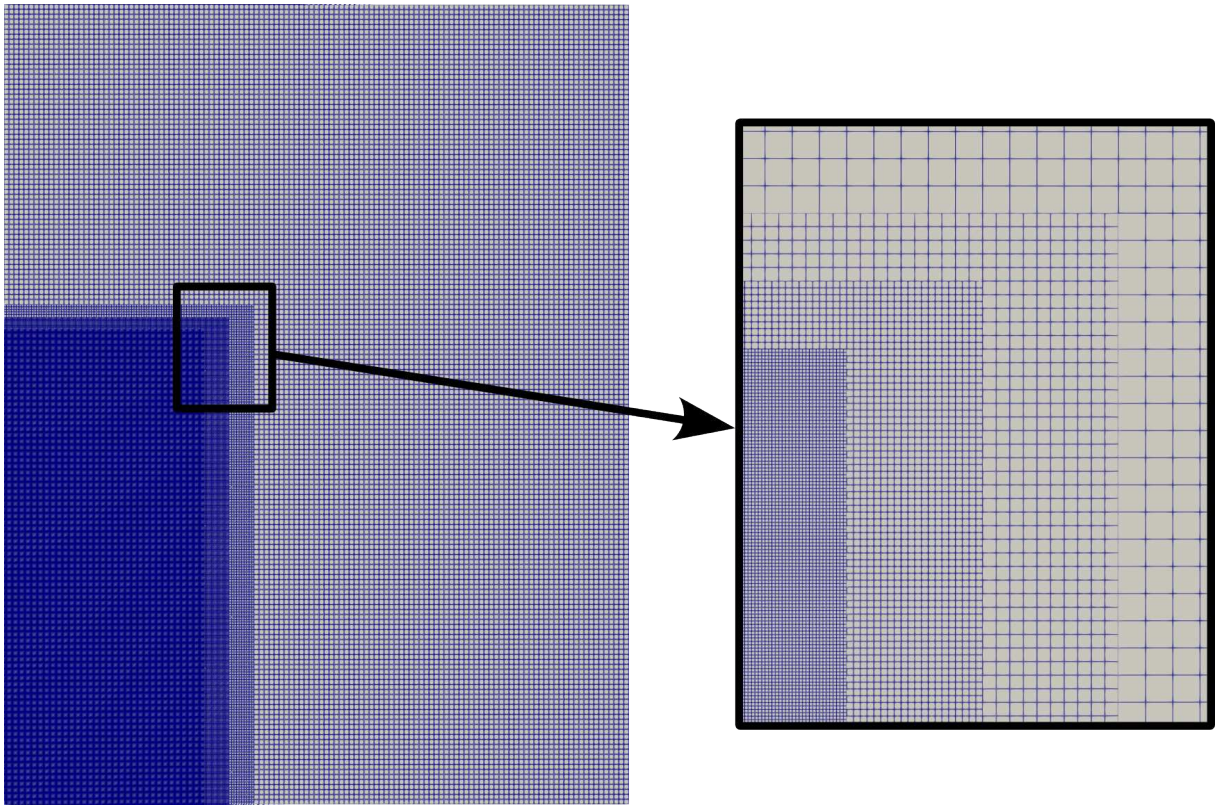

Figure 3.5: Example of a structured mesh made with blockMesh. A wedge representing a cylindrical fluid domain was successively refined four times in the region of interest.

assigned to different processor cores. Information of cells near the border between two regions must be exchanged between cores, which is slower than computation within a single core. Because of this, it is advisable to choose regions with rather small borders. How the decomposition is carried out thus affects the effectiveness of the parallel computation. The decomposition method is specified in `system/decomposeParDict`. The decomposition method `simple` divides the domain into regions of equal length in the directions specified. For an inhomogeneous cell distribution, this may cause the created regions to contain vastly different numbers of cells, in which case the parallel computation may not be significantly faster than its serial counterpart. For this reason, the decomposition method `scotch` is used, which is an algorithm that decomposes the computational domain into regions with similar cell numbers while minimising the number of cells at the border between regions. A similar alternative is the decomposition method `metis`, which uses a different algorithm but achieves a similar result. The decomposition is carried out using the command `decomposePar`.

3.2.3 Boundary conditions

For each field in `0.org`, boundary conditions must be defined for all boundaries of the computational domain. Take the example of a cylinder slice-shaped domain presented in 3.3. For the large front and back faces of the slice, the boundary condition `wedge` is used for all fields, which is a circular boundary condition between both faces and in this case represents the cylindrical symmetry. On the left side, the domain meets the axis. In OpenFOAM, it is represented by a very thin face imbued with the boundary condition

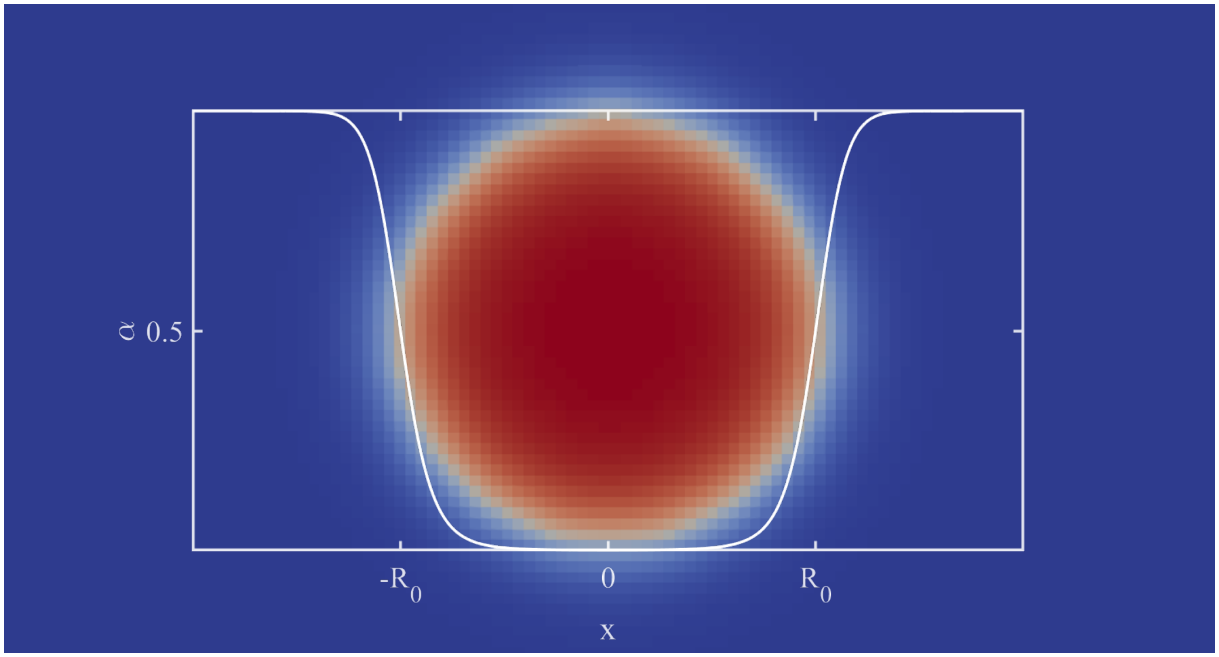

Figure 3.6: Initial condition for a bubble. The colour scheme ranges from blue ($\alpha = 1$, $p = 101325\,\mathrm{Pa}$) to red ($\alpha = 0$, $p = 1.69\,\mathrm{GPa}$). Superimposed is a plot of α as a function of x along a line through the centre of the bubble.

`symmetryPlane`. This means that the normal component of any vectorial quantity vanishes, $\vec{u} \cdot \vec{n} = 0$, as well as the normal component of the gradient of any scalar quantity, $\nabla\alpha \cdot \vec{n} = 0$.
Each of the three boundaries at the top, right, and bottom are chosen to represent either a rigid or an open boundary.
A rigid wall is represented by the boundary condition `noSlip` for the velocity, which means that $\vec{u} = \vec{u}_{\mathrm{boundary}}$. For scalar quantities, typically the `zeroGradient` boundary condition is used, i.e., $\nabla\alpha \cdot \vec{n} = 0$. Since the entire field `p` is calculated from `p_rgh`, the boundary condition used is simply `calculated`. Reuter and Kaiser [124] showed that cavitation bubbles created near a wall typically do not make direct contact with the wall. In the simulation, this is enforced by setting the phase fraction field on the wall to $\alpha = 1$ by using the boundary condition `fixedValue`.
Often, the simulated fluid domain is supposed to represent a large fluid domain, in which case open boundary conditions are used. To avoid wave reflections on those boundaries, the condition `waveTransmissive` is used for $\vec{u}$, which determines the boundary value according to an advection equation, $\frac{\partial\phi_n}{\partial t} + (\vec{u}_n + c) \cdot (\nabla \cdot \vec{n})\,\phi_n = 0$, with the speed of sound $c = \sqrt{\frac{\gamma}{\kappa}}$ and the normal components of the velocity u_n and the interpolated velocity at the cell faces ϕ_n. The boundary condition `zeroGradient` is used for α, and `fixedFluxPressure` for the pressure field `p_rgh`, which adjusts the pressure gradient according to the mass flux through the boundary.

3.2.4 Initial conditions

For a bubble initiated by a sufficiently short laser pulse, one can make the assumption that the laser energy deposition is much faster than any signification expansion of the bubble contents. Then, the density field must be approximately unperturbed, and thus

the initial density of the bubble contents is equal to that of the surrounding liquid. With this assumption and the parameters given in table 3.2, equation (2.61) gives an initial pressure of $p_\mathrm{b} = 1.69\,\mathrm{GPa}$. This value is used throughout most of the present work.
First, all fields are initialised as homogeneous, with $\vec{u} = 0$, $p_\mathrm{l} = 101325\,\mathrm{Pa}$, and $\alpha = 1$.
Then the script `initBubble` is executed to insert the bubble in its initial state. The required information about the initial conditions is given in the file `transportProperties` in the folder `constant`, including its initial radius R_b, position $\vec{x}_\mathrm{b}$, and pressure p_b. With finitely sized square computational cells, a smooth curved bubble surface is not possible. To approximate the bubble surface and to avoid instabilities, the bubble surface is smeared by setting α in each cell according to the following function:

$$\alpha = \frac{1 - \tanh\left(\frac{k_\mathrm{b}-1}{\varepsilon_\mathrm{b}}\right)}{2},\ k_\mathrm{b} = \left(\frac{\vec{x} - \vec{x}_\mathrm{b}}{R_\mathrm{b}}\right)^2 . \tag{3.14}$$

To cause further smearing, the following Laplace equation is solved:

$$\alpha' - \varepsilon_{\mathrm{b},2}\,\Delta\alpha' = \alpha\ . \tag{3.15}$$

The new field α' then replaces α.
Then, the pressure is calculated as $p = p_\mathrm{l}\,\alpha + p_\mathrm{b}\,(1 - \alpha)$. The resulting bubble is shown in figure 3.6.
An alternative way to define the initial state of the simulated fields is by using the built-in function `setFields`. The script `initBubble` was chosen because of its fewer limitations.

3.3 MultiphaseCavBubbleFoam

The version OpenFOAM-v2006 [125] features `compressibleMultiphaseInterFoam`, which is largely similar to `compressibleInterFoam`, with the important difference that it can be used to model n compressible fluids, instead of just two. Instead of outputting just one phase fraction field α, it exports one for each fluid, α_i. Additionally, the sum of all phase fraction fields is calculated as $\alpha_\mathrm{s} = \sum_i \alpha_i$, which is useful to visualise all fluids at the same time during post-processing.
By making equivalent modifications as were done to `compressibleInterFoam` to obtain `CavBubbleFoam`, `compressibleMultiphaseInterFoam` was used as a basis to create `MultiphaseCavBubbleFoam` [42], which can be used to model a single expanding and collapsing bubble in the presence of additional fluids.
The same corrections and features as explained in section 3.2 were implemented. The fluids are meant to be named "air" for the bubble contents, and "water" and "oil" for two additional fluids, regardless of whether their properties match those of air, water, and oil. In the output file `info.csv`, additionally to the bubble mass $\sum_i V_i\,\alpha_{\mathrm{air},i}\,\rho_i$, the masses of the other fluids $\sum_i V_i\,\alpha_{\mathrm{water},i}\,\rho_i$ and $\sum_i V_i\,\alpha_{\mathrm{oil},i}\,\rho_i$ are written.

3.4 fsiFoam

The FluidStructureInteraction package [126] for the version Foam-Extend-4.0 [127] includes the solver `fsiFoam`, which couples a viscous fluid to an elastic solid.
Both the fluid and solid domains are given in separate subfolders in the simulation folder, called `fluid` and `solid`, each of which contains initial and boundary conditions, physical constants, as well solver parameters and numerical schemes as discussed in section

3.2.1. The solvers for the fluid and for the solid can be chosen individually. Those choices are specified in the simulation folder under `fluid/constant/fluidProperties` and `solid/constant/solidProperties`. The FluidStructureInteraction package features for example `icoFluid`, which is a solver for a viscous, incompressible fluid.
The FluidStructureInteraction package provides a solver for a linear elastic solid called `unsTotalLagrangianSolid`. It solves the linear elasticity equation of motion (2.90). Because of the last term in equation (2.90), the components of the deformation field $\vec{D}$ are coupled. Because of this, the equation must be solved iteratively to achieve convergence towards the correct solution, until either a certain number of iterations is reached or the mismatch between successive iterations falls below a tolerance value, both of which are specified in the file `solid/constant/solidProperties`. The physical properties of the solid are given through its density ρ, elastic modulus E, and Poisson's ratio ν, all of which are given in the file `solid/constant/rheologyProperties`.
Two-way coupling is used, where viscous and normal stresses in the fluid at the fluid-structure interface are imposed as boundary conditions to the solid solver, and the position and velocity of the solid in its deformed state are imposed as boundary conditions to the fluid solver. An important distinction from `CavBubbleFoam` is that a dynamic mesh is used to conform the fluid domain to the motion of the fluid-structure interface. Other than the deformation of the solid, the fluid mesh deformation is not tied to any physical mechanism but can be chosen freely in compliance with the boundary conditions. To keep the deformation of each cell small, a Laplace equation for the fluid mesh deformation is solved, $\Delta\vec{D} = 0$, using the mesh motion solver `dynamicMotionSolverFvMesh`.
Solving each of the solvers typically results in a mismatch between the deformation $\vec{D}$ and stress $\overleftrightarrow{\sigma}$ fields on both sides of the fluid-structure interface, which is why the equations describing the fluid and the solid are solved alternatingly. Like before, both the maximum number of iterations and the tolerance value are specified in the file `fluid/constant/fsiProperties`.
Note that in Foam-Extend-4.0, the region of the mesh that is to be refined is defined in `system/cellSetDict` and applied using the command `cellSet` instead of `topoSet`.

3.5 CavBubbleFsiFoam

To attain a solver capable of modelling an expanding and collapsing bubble, code of `compressibleInterFoam` was implemented into `icoFluid`. This new fluid solver was named `CavBubbleFluid`. Additionally, the same corrections as described in section 3.2 were implemented. Since this solver was used to simulate phenomena on very small time scales, the threshold value α_{limit} is adjusted to $\alpha'_{\text{limit}} = 1 - (1 - \alpha_{\text{limit}}) \cdot \frac{h}{3\,ns}$ if the time step size h falls below 3 ns. This effectively weakens the correction to avoid the negative side effect of the bubble surface being locked in place at a computational cell border.
The solid solver `unsTotalLagrangianSolid` was lightly modified to output the minimum and maximum of each stress tensor component over time, $\overleftrightarrow{\sigma}_{\text{min}}$ and $\overleftrightarrow{\sigma}_{\text{max}}$. The modified solid solver was called `CavBubbleSolid`.
For the implementation of the code of `compressibleInterFoam`, the fluid-structure interaction solver `fsiFoam` also needed to be modified, thus creating the overarching solver `CavBubbleFsiFoam`. All of these solvers along with some example simulation cases can be found on GitHub [43].

4 Microscopic pumping of viscous liquids with single cavitation bubbles

This work has been published in [22]:

H. Reese, R. Schädel, F. Reuter, and C.-D. Ohl. "Microscopic pumping of viscous liquids with single cavitation bubbles". *Journal of Fluid Mechanics* **944**, A17 (2022)

A cavitation bubble expanding and collapsing near a rigid boundary develops a directed jet flow towards the boundary. In the case of a perforated plate, some of the jet flow passes through the plate and thus the bubble acts as a pump transporting liquid from one side of the plate to the opposite side. The transport is rather complex, it is time-dependent and varies with the geometric parameters of the bubble and the connecting channel. Therefore, we first model the transport of liquid through a perforated rigid plate for a large range of parameters and then compare some regimes with experiments using single laser-induced bubbles. The simulations are based on a volume of fluid solver in OpenFOAM and account for surface tension, compressibility, and viscosity. The resulting flux and generated velocity in the channel obtained in the simulations are discussed in dependence of the channel geometry, liquid viscosity, and stand-off distance of the bubble to the plate. In general high flow rates are achieved for long cylindrical channels that have a similar width as the jet produced by the collapsing bubble. At low stand-off distances combined with thick plates, an annular inflow creates a fast and thin jet, also called *needle jet*, which is about a magnitude faster and significantly thinner than the usually encountered microjet. In contrast, for thin plates and small stand-off distances liquid is pumped in the opposite direction via a *reverse jet*.

4.1 Introduction

After Silberrad [1] reported propeller erosion on the ships "Lusitania" and "Mauretania", Rayleigh [2] proposed cavitation as the likely cause for the damage. The model named after him describes a collapsing spherical, empty cavity. He found that such a collapse creates high pressures in the liquid that may be responsible for the damage observed on the steel propellers. Improved spherical bubble models for example by Hickling and Plesset [3] and later on Keller and Miksis [64] include the pressure of non-condensable gas inside the bubble, liquid viscosity, surface tension, and the energy loss from acoustic radiation. Boundaries that violate the spherical symmetry of the flow are not accounted for in these models. Early experimental investigations to understand the origin of erosion studied the effect of boundaries and geometries that break the spherical symmetry. For example, Shutler and Mesler [19] studied the dynamics and collapse of a non-spherical spark-generated bubble near rigid plates, Benjamin and Ellis [20] used an evacuated free fall device, and Lauterborn and Bolle [128] introduced laser-induced cavitation bubbles to increase control on location and timing of the bubble. They all observed directed liquid flows or jets that form during the shrinkage of the bubble. Blake and Gibson [5] developed a boundary element method to simulate the inviscid flow which helped to understand the mechanism of jet creation and the movement of the bubble towards the rigid boundary. Very good agreement between the experimental and the simulated bubble dynamics was found, see also Best and Kucera [6].

As we know that an infinitely extended rigid boundary induces a jet towards the boundary, one may expect that a narrow diameter through-hole embedded in the boundary may not much alter the jetting dynamics. As a result, some of the liquid volume of the jet may be accelerated through the perforated boundary. This cavitation-based liquid pump was first suggested by Khoo et al. [129] in a numerical work using the boundary integral method to simulate a bubble near a plate with a small diameter through-hole. This was followed by experiments from Lew et al. [130] and later Karri et al. [131], who used a spark-generated bubble with a radius of several millimetres demonstrating the pumping mechanism. Dijkink and Ohl [132] down-scaled the technique for microfluidic application using considerably smaller, laser-generated bubbles.
Karri et al. [133] revealed that in the presence of a gaseous domain on the opposite side of the perforated plate, the bubble dynamics result in high-speed liquid jetting into the gas. The jet fragments into a spray of many smaller droplets. Initially, they used a lithotripter to create a bubble with $R_{\max} \approx 250\,\mu\text{m}$, and later a spark discharge for a bubble with $R_{\max} \approx 6\,\text{mm}$ [134]. Further investigations of such jets and sprays followed by Gonzalez-Avila et al. [135] and Kannan et al. [136] using a spark-generated bubble very close to a plate with a hole, with $R_{\max} = 1\,\text{mm}$ and $8\,\text{mm}$, respectively.
Wang et al. [137] experimentally studied the dynamics of a spark-generated cavitation bubble with length scales of millimetres near a thin perforated plate. Numerical investigations followed by Dawoodian et al. [138] using the boundary element method to simulate a bubble in a tube near a thin plate with a hole. Continuous pumping of the liquid has been demonstrated by Cao et al. [139] with periodically created cavitation bubbles just above a channel of radius $r_c = 2.5\,\mu\text{m}$. The particular shape of the plate has an effect on the bubble and therefore on the pumping as demonstrated by Cui et al. [140], who conducted cavitation experiments with relatively large bubbles on top of a curved perforated plate. The experiments were later simulated by Moloudi et al. [141] based on the boundary element method and for certain parameters revealed a pronounced jet in the opposite direction. However, the simulations stopped once the jet pierced the bubble and the resulting fluid transport past that instant was not obtained.
While there is strong experimental support of the pumping effect of bubbles near through-holes, there is a considerable lack in numerical simulations that include the jetting dynamics through the hole and the following bubble dynamics, and that study the influence of various geometrical parameters of the hole as well as viscosity. These aspects are addressed in the present work, which also accounts for the surface tension and the compressibility of the liquid and the gas.
We start with a description of the governing flow equations and continue with the implementation in a volume of fluid (VoF) solver in section 4.3. Selected simulation results are compared to experiments. Therefore, we describe a suitable experimental setup in section 4.4 that can reveal not only the bubble dynamics but also the liquid transport. The results section starts with a detailed description of the pumping mechanism (section 4.5.1). Then, the influence of various parameters on the pumping effectiveness is revealed and discussed in section 4.5.2. We then take a closer look at two particular flow phenomena in section 4.6, namely the so-called *needle jet* and the *reverse jet* using and comparing simulations with experiments, before we discuss and summarise the results.

4.2 Governing equations

The simulation model describes two immiscible, isothermal, compressible, and viscous fluids, i.e. water and a non-condensable gas and accounts for their surface tension. Mass and heat transfer across the fluid-fluid interface are neglected. The initial process of cavitation nucleation, e.g. from a laser or a spark discharge, is ignored. Instead, we start the fluid mechanics model with a small gas bubble at a high pressure at time $t = 0$.
The fluids satisfy the continuity equation (4.1) and the law of conservation of momentum (4.2) of Newtonian fluids,

$$\frac{\partial \rho}{\partial t} + \nabla \cdot (\rho \, \vec{u}) = 0 \ , \tag{4.1}$$

$$\rho \, \frac{D\vec{u}}{Dt} = \rho \, \vec{f} - \nabla p + \mu \, (\Delta \vec{u} + \frac{1}{3} \, \nabla(\nabla \cdot \vec{u})) \ . \tag{4.2}$$

Here the physical quantities are density ρ, time t, velocity $\vec{u}$, volume acceleration $\vec{f}$ (e.g. gravity), and the dynamic viscosity μ. A liquid viscosity of $\mu = 1\,\mathrm{mPa\,s}$ and a gas viscosity of $\mu = 0.0184\,\mathrm{mPa\,s}$ is used, as well as a surface tension of $\sigma = 70\,\mathrm{mN/m}$. For both components, the Tait equation is used as an equation of state,

$$p = (p_0 + B) \left(\frac{\rho}{\rho_0} \right)^{\gamma} - B \ , \tag{4.3}$$

where the constants are $p_0 = 101325$ Pa, $B = 303.6\,\mathrm{MPa}$, $\rho_0 = 998.21\,\mathrm{kg/m^3}$, and $\gamma = 7.15$ for the liquid (water) and $p_0 = 10320$ Pa, $B = 0$, $\rho_0 = 1\,\mathrm{kg/m^3}$, and $\gamma = 1.33$ for the gas. With $B = 0$, the equation of state (4.3) describes the adiabatic change of state of an ideal gas.
The Rayleigh collapse time is the idealised time it takes for an empty cavity under the action of a constant external pressure to shrink to zero size. Lord Rayleigh solved the energy equation for an inviscid, incompressible fluid initially at rest once a portion of the liquid was instantaneously removed [2]. He obtained an equation for the bubble radius as a function of time that could be integrated to obtain the Rayleigh collapse time

$$\tau \approx 0.91468 \, R_{\max} \sqrt{\frac{\rho}{p_0}} \ . \tag{4.4}$$

This Rayleigh collapse time is about $\tau = 46\,\mu\mathrm{s}$ for typical bubbles of $R_{\max} = 0.5\,\mathrm{mm}$. The spherical bubble dynamics obtained from the VoF solver can be compared to the Keller-Miksis model [64],

$$R \, \ddot{R} \left(1 - \frac{\dot{R}}{c} \right) + \frac{3}{2} \, \dot{R}^2 \left(1 - \frac{\dot{R}}{3c} \right) + \frac{4\nu \dot{R}}{R} + \frac{2\sigma}{\rho R} + \frac{p_0 - p_{\mathrm{g}}}{\rho} \left(1 + \frac{\dot{R}}{c} \right) - \frac{R \dot{p}_{\mathrm{g}}}{\rho c} = 0 \ , \tag{4.5}$$

which is a solution to the Navier-Stokes equation and accounts for compressibility in the limit of linear acoustic waves.

4.3 Numerical implementation

4.3.1 Numerical solver

For the simulations a modified version of the VoF solver `compressibleInterFoam` from the open-source framework OpenFOAM [125] is used. It models two compressible, non-isothermal, immiscible fluids using a phase-fraction based interface capturing scheme.

The solutions are obtained in 250,000 to 370,000 computational cells, each of which is assigned its respective flow equations. The solver solves for the five fields pressure p, non-gravitational pressure $p_{\mathrm{rgh}} = p - \rho\, \vec{g} \cdot \vec{r}$, velocity $\vec{u}$, temperature T, and phase fraction α, which is a non-dimensional scalar field ranging between 0 and 1 that specifies the relative volume amount of a cell occupied by one of the fluids. In this case, $\alpha = 1$ means that a cell is fully occupied by water and $\alpha = 0$ means it is fully occupied by gas. Since gravitational effects are neglected, $\vec{g}$ is chosen to be 0, and thus $p_{\mathrm{rgh}} = p$.
The solver is derived from `CavBubbleFoam` by Zeng et al. [118], which itself was a modification of the original `compressibleInterFoam`. `CavBubbleFoam` updates the compressibility field in every time step and neglects non-isothermal effects by removing the temperature equation. This simplification has been used successfully for cavitation bubble simulations by Zeng et al. [118].
In each time step the equations for α, ρ, $\vec{u}$, and p are solved. In the following, the notation $\alpha_1 := \alpha,\ \alpha_2 := 1-\alpha$ is used. Since phase transitions are ignored, each component satisfies the continuity equation separately (4.1), i.e.,

$$\frac{\partial(\alpha_j \rho_j)}{\partial t} + \nabla \cdot (\alpha_j\, \rho_j\, \vec{\phi}) = 0 \ , \tag{4.6}$$

where $\vec{\phi}$ denotes the interpolation of $\vec{u}$ at the cell faces since $\vec{u}$ is only defined at the centre of each cell, and $j = 1, 2$ represents the two fluid components. By using the definition of the compressibility, $d\rho_j = \psi_j\, dp$, equation (4.6) yields

$$\frac{\partial \alpha_1}{\partial t} + \nabla \cdot (\alpha_1\, \vec{\phi}) + \frac{\alpha_1}{\rho_1}\, \psi_1\, \frac{Dp}{Dt} + \nabla \cdot (\alpha_1\, \alpha_2\, \vec{\phi}_{\mathrm{r}}) = 0 \ . \tag{4.7}$$

The last term on the left-hand side was added to counteract the smearing of the fluid-fluid interface due to numerical diffusion [115]. The vector $\vec{\phi}_{\mathrm{r}}$ is defined as

$$\vec{\phi}_{\mathrm{r}} = c_\alpha \sum_i \frac{|\phi_i|}{|\vec{A}_i|}\, \frac{\nabla \alpha_{1,i}}{|\nabla \alpha_{1,i}|} \ , \tag{4.8}$$

with the parameter $c_\alpha \leq 1$ and the cell face vector $\vec{A}_i$. Solving equation (4.7) yields an updated α_1 for the new time t. The partial derivatives are discretised using low-order discretisation schemes like the Euler scheme for temporal and the upwind scheme for spatial derivatives. Numerical errors of this solution may result in α_1 being slightly below 1 within the bulk of the liquid. Once such a cell is exposed to a low pressure we wrongly observe the creation of new gas regions. We overcome this problem by a correction of α_i, i.e. cells with a value of $\alpha_i > 0.9999$ are clamped to $\alpha_i = 1$. This threshold value was chosen to remove those wrongly created gas regions without significantly affecting the main bubble dynamics.
Next the Navier-Stokes equation (4.2) is solved to update the velocity field $\vec{u}$. Since gravitational effects are neglected, the volume force term disappears ($\vec{f} = 0$). The pressure field is computed iteratively, using the pressure-implicit method with splitting of operators (PISO) scheme. For that, the Navier-Stokes equation (4.2) is written as

$$M\, \vec{u} = -\nabla p \ , \tag{4.9}$$

where M is a known tensor. Now the diagonal elements of M are defined as A and another quantity $\vec{H} = (M - A)\, \vec{u}$ is defined. Then, equation (4.9) can be written as

$$\nabla(-A^{-1}\, \nabla p) = A^{-1}\, \vec{H} - \nabla \cdot \vec{u} \ . \tag{4.10}$$

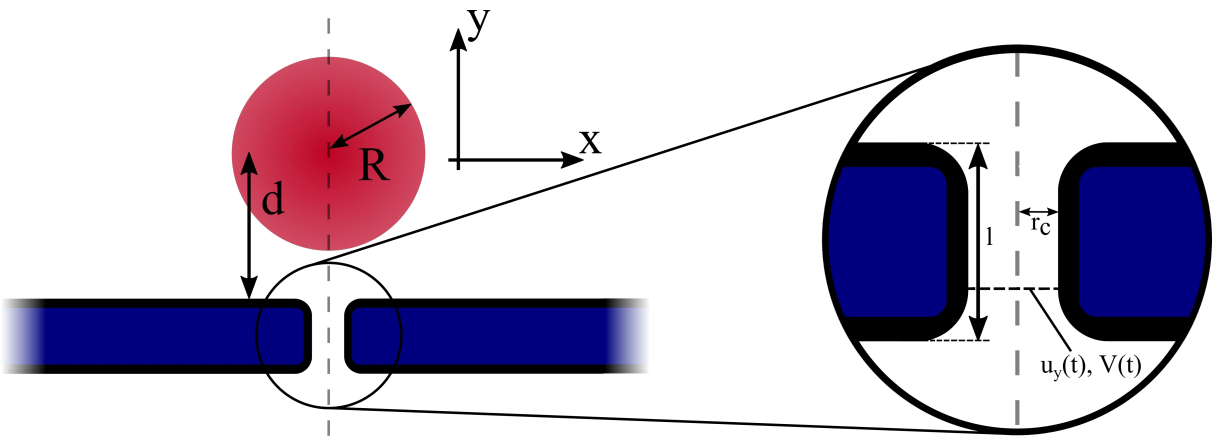

Figure 4.1: Simulation geometry (not to scale) of a single bubble in the vicinity of a plate with thickness l including bubble radius R and stand-off distance d. The plate is perforated by a channel of radius r_c.

This is solved to update the pressure field p and from there the velocity and density fields are corrected. Discretisation errors cause the bubble mass, which is calculated from $m = \sum_i^{\text{cells}} \alpha_{2,i}\,\rho_{2,i}\,V_i$, to fluctuate. To counteract this, the density is corrected as $\rho'_{2,i} = \frac{m_0}{m}\,\rho_{2,i}$ to keep the bubble mass constant, m_0 being the initial bubble mass calculated at $t = 0$.
The updated $\vec{u}$ and ρ are used to correct p, and are then corrected once again. Finally, the density field ρ is updated using $\rho = \alpha_1\,\rho_1 + \alpha_2\,\rho_2$, and the new compressibility fields ψ_1 and ψ_2 are obtained from

$$\psi_j = \frac{1}{\gamma_j(p + B_j)}\ . \tag{4.11}$$

4.3.2 Geometry

The geometry of interest is axisymmetric. It consists of two cylindrical reservoirs (each with a height of 5 mm and a radius of 5 mm) connected via a thin channel with a common axis of symmetry, as shown in figure 4.1. Both orifices of the channel are filleted (with a radius of curvature of 25 µm) to avoid numerical instabilities from sharp edges. Because of the symmetry, only half of the geometry shown in figure 4.1 is calculated in the simulation. The flow equations are solved in the x-y-plane, where the y-axis is the rotational axis of the system. This results in an effectively two-dimensional simulation, which greatly reduces the cost of computation.
Within the OpenFOAM framework, the geometry is reduced to a thin wedge that is thinnest at the y-axis and is only divided into cells along the x- and y- directions.
The geometry is discretised into a square mesh as seen in figure 4.2, which close to the location of the bubble is resolved with a cell width of 2.5 µm. Outside of this region of interest, an unstructured mesh is used, where the cell size increases with the distance from the bubble to approximately 100 µm width at the outer boundary of the geometry.

4.3.3 Initial conditions

The simulations are started with a small spherical bubble seed on the axis of symmetry with 50 µm radius. The bubble interior is assigned $\alpha = 0$ while the bubble exterior is

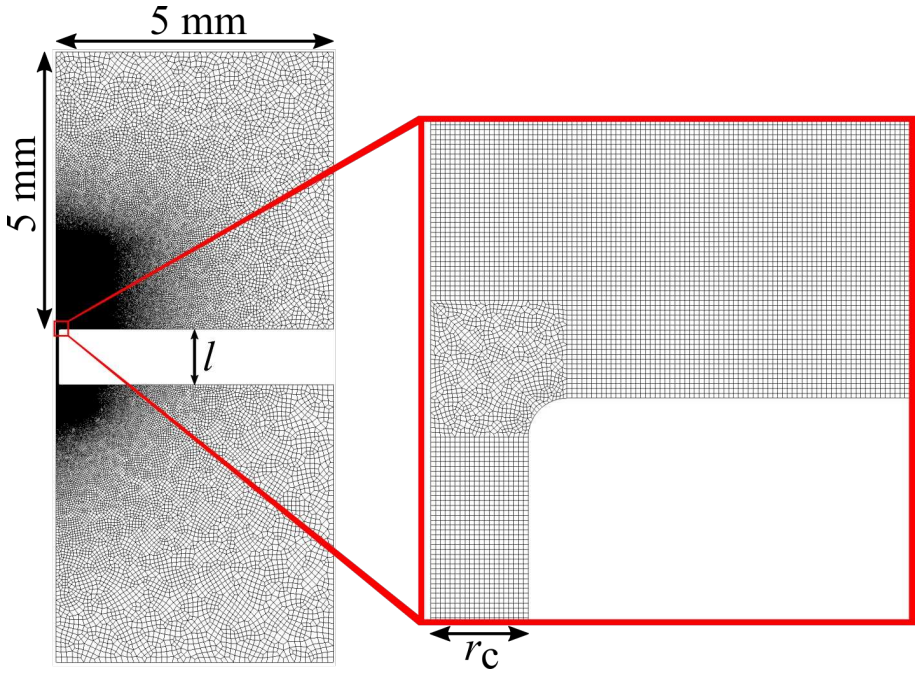

Figure 4.2: Computational mesh of the channel geometry with $r_c = 50\,\mu m$ and $l = 1\,mm$. An unstructured mesh is used far from the bubble and at the filleted channel orifices. Close to the bubble and in the channel a structured mesh is used.

assigned $\alpha = 1$. The field α is then smoothed by solving the Poisson equation,

$$\alpha' - 4 \cdot 10^{-11}\,\Delta\alpha' = \alpha\ , \tag{4.12}$$

where α' denotes the replacement of the initial field α. This smoothing procedure reduces Rayleigh-Taylor instabilities during the early stage of rapid bubble expansion. The parameter is chosen to provide minimum smoothing but a numerically stable bubble surface during the early expansion phase.
The pressure field is set as $p = \alpha\, p_0 + (1-\alpha)\, p_g$ with the atmospheric pressure p_0 and the initial gas pressure p_g. p_g is chosen such that the density of the gas is equal to the liquid density, $\rho_g = \rho_l$. Using this and the Tait equation (4.3) for the gas, a gas pressure of $p_g = 16.88$ kBar is obtained. This is based on the assumption that for a laser-generated bubble, the energy deposition by the laser pulse is much faster than the bubble expansion, so that the liquid seed vapourises almost instantaneously before the bubble seed expands significantly. Initially, the velocity field is zero in the entire fluid domain.
The simulations were carried out as parallel processes using 4 CPU cores of an AMD Ryzen Threadripper 1900X at 3.8 GHz each with 64 GB of RAM. The time needed to run a simulation is roughly proportional to the square of the number of cells computed. For this work, the time taken ranged between 21 and 51 hours to simulate 200 µs of the bubble dynamics after bubble initiation.

4.3.4 Boundary conditions

In the following, the directions x, y, and z in the simulation results are considered synonymous with right, up, and front, respectively. The leftmost boundary is imposed with the `symmetryPlane` boundary condition for all fields. Similarly, the boundary condition `wedge` is used for the front and back planes of the geometry. The fluid boundaries of

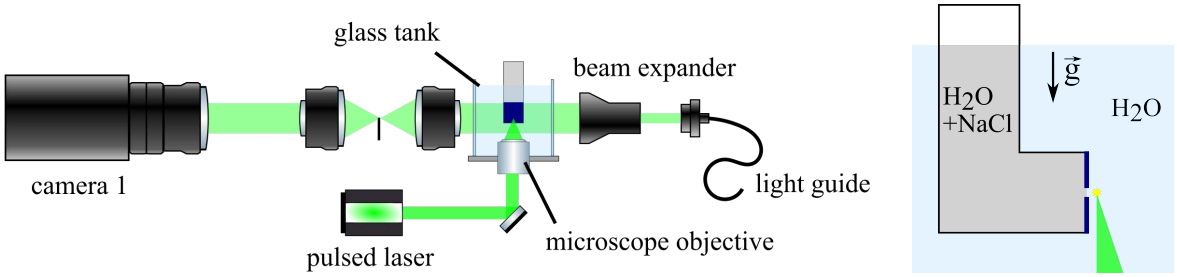

Figure 4.3: Schematic experimental setup (not to scale); left: optical path for bubble generation as well as Schlieren imaging through the glass tank; right: cuvette with a perforated plate in side view submerged in the glass tank and position of bubble generation.

the two large fluid regions located at the top, bottom, and right in figure 4.2 represent an infinitely large fluid domain, therefore their boundary conditions are $p = 101325$ Pa, $\nabla u_i = 0$, and $\nabla \alpha = 0$. The remaining boundary is the one separating the two fluid domains, which also bounds the channel that connects them. This is a rigid wall with a no-slip boundary condition, $\vec{u} = 0$ and $\nabla p = 0$. There we also impose a boundary condition of $\alpha = 1$. This can be justified to some extent by the experiments of Reuter and Kaiser [124], who found that a bubble collapsing very close to a wall in water does not touch the wall but is separated from it via a thin liquid film during its first collapse. Their experiments covered the stand-off distances $0.47 < \gamma < 1.07$, $\gamma = \frac{d}{R_{\max}}$ here denoting the dimensionless stand-off parameter with the maximum bubble radius $R_{\max}$ and the distance between the bubble centre and the wall d. In the present work, we assume this separation of the gas and the wall for the full range of γ-values studied. Whether this assumption holds true in an experimental setting may depend on the wettability and structure of the surface. If in such a setting the bubble came into contact with the wall, the contact angle would be expected to play a minor role in the bubble dynamics. Thus, we would still expect the formation of the main jet to cause the pumping effect.

4.4 Experimental setup

The experiments utilise a laser-induced bubble in front of a perforated boundary. A schematic representation of the setup is shown in figure 4.3. It consists of a glass tank with dimensions 55 mm × 55 mm × 65 mm filled with deionised water. A microscope objective (Mitutoyo 50 × Plan Apochromat Objective, 436-656 nm, 0.55 NA, 13 mm WD) is sealed water-tight and incorporated into the bottom of the tank. This objective focuses an Nd:YAG laser pulse (Litron Nano SG-100-2, $\lambda = 532$ nm, FWHM = 6 ns, pulse energy ≈ 5 mJ) into the water to seed the bubble. A smaller L-shaped cuvette that accommodates a plate with a micro-perforation is submerged into the glass tank connected to a motorised three-axis stage. The plate is made out of a flexible polymeric material used for printed circuit boards (supplier: PCBWay). It has dimensions of 16 mm × 12 mm × 170 µm. The perforation is a cylindrical drilled hole of 195 µm in diameter (measured with a light microscope). The bubble is produced axially in front of the perforation which is confirmed by a high-speed camera with a perpendicular view of the plate surface (Photron FASTCAM MINI AX200). To avoid the generation of spurious bubbles on the plate, which can happen as the laser energy is not entirely absorbed in the plasma, the laser is focused in parallel to the plate. This implies a partial blocking of the focusing cone that is dependent on the stand-off distance. To assure constant maximum bubble size over all stand-off

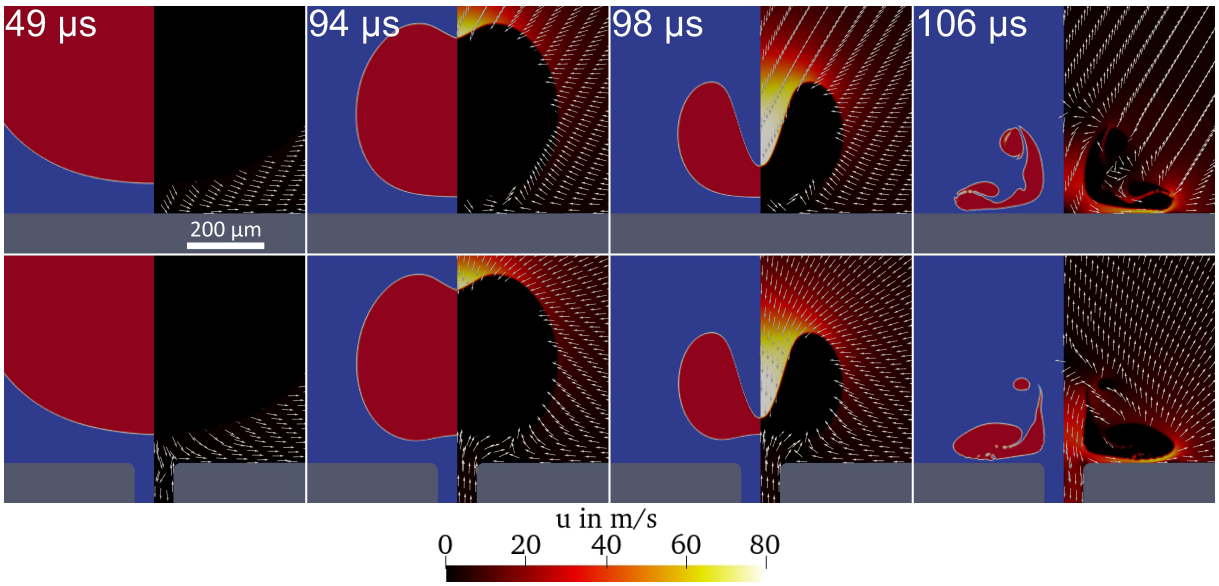

Figure 4.4: Simulations of a cavitation bubble close to a rigid boundary with stand-off parameter $\gamma = 1.05$, comparison of the flow dynamics for a boundary without (top) and with a channel below the bubble (bottom); The left side of each frame shows the bubble gas in red and water in blue, the right side shows the velocity field in the liquid.

distances, half of the laser beam is blocked at the input aperture side of the objective. To visualise the pumping effect of the bubble, the L-shaped cuvette is filled with an aqueous 3 wt% NaCl solution which results in optical Schlieren at the mixing interface. Schlieren high-speed imaging is implemented to visualise the transport of two nearly identical liquids. For that the water tank is illuminated by a collimated pulsed laser beam (Ekspla FemtoLux 3, $\lambda = 515$ nm, 1 MHz) parallel to the plate. After passing the tank, the light gets focused by an objective where the undeflected part is blocked by a knife edge and the deflected light is directed into a second high-speed camera (Shimadzu Hyper Vision HPV-X2, camera 1 in figure 4.3, operated at 500 000 frames per second, shutter opening time 1 µs, effective exposure time 0.3 ps, 7.8 µm/pixel). The imaging is also sensitive to density changes in the liquid from shock waves which are emitted during the creation and the collapse of the bubble and reflected at the boundaries.

4.5 Results

We start by demonstrating the effect of the presence of the channel in the rigid boundary on the bubble dynamics via simulations.

4.5.1 Jetting through the perforated boundary

Figure 4.4 compares the axisymmetric fluid dynamics of a bubble expanding and collapsing close to a rigid wall with an identical bubble close to a perforated wall. The bubble is seeded at a stand-off distance of 500 µm and reaches a maximum radius of around 475 µm. This gives a dimensionless stand-off distance of $\gamma = 1.05$. The cylindrical channel has a radius of 50 µm and a length of 1 mm, which is the same as the thickness of the wall separating the two fluid domains. In both cases the bubble expands and then collapses, creating a jet towards the wall. As a result, the bubble re-expands as a torus close to the wall.

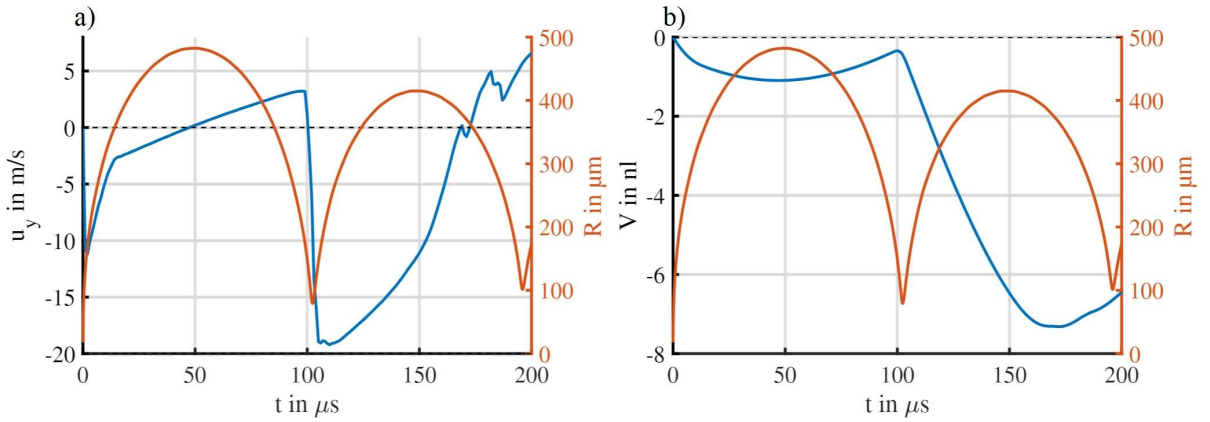

Figure 4.5: a) velocity u_y at channel exit (near the solid surface facing away from the bubble) and b) the liquid volume $V(t)$ transported through the channel, each overlaid with the bubble radius R to show the correlation between the bubble dynamics and the flow through the channel

There are small but noticeable differences between the bubble dynamics in the two geometries: In the case with the hole, during the shrinking phase a small indentation on the lower side of the bubble develops, which is not present in the continuous wall case. This feature is caused by the axial inflow from the opposing fluid domain through the channel and onto the lower bubble wall. The flow deforming the bubble is driven by the pressure difference during the shrinking phase of the bubble, i.e. the low pressure in the bubble and the atmospheric pressure far from the bubble below the boundary.
Overall, both bubbles form a jet starting from the wall distant pole of the bubble. After this jet has pierced the lower bubble wall, in the continuous wall case we find a stagnation point at the wall on the axis of symmetry. Further outside a radially spreading flow along the continuous wall is formed. In contrast, in the perforated wall case the stagnation point flow is lost and the liquid flows through the hole in the boundary. Viscous stresses oppose the flow through the boundary and some of the jet flow still feeds into the radially spreading flow along the wall. Overall, we find for these particular chosen parameters a rather small effect of the perforation on the familiar bubble shape or timing of the bubble dynamics during expansion and collapse, albeit there is a fluid transport occurring through the plate.
To quantify this pumping effect of the bubble, the liquid flow velocity u_y through the channel outlet, i.e. on the plate surface facing away from the bubble, is measured (just above the rounded edge, see figure 4.1) and averaged over the channel cross-section as $u_y = \frac{1}{\pi r_c^2} \int_0^{r_c} \alpha_1 \, \vec{u}_y(r) \cdot \vec{e}_y \cdot 2\,\pi\, r \, dr$. The result is plotted in figure 4.5 a). Here, a positive sign of u_y indicates a flow from the bottom water reservoir to the top, and a negative sign a flow in the downward direction. The red line in figure 4.5 depicts the volume equivalent bubble radius R to help the reader to link the bubble dynamics to the channel flow. Figure 4.5 a) shows that during bubble expansion, the liquid is initially accelerated downwards to about $u_y = -10\,\mathrm{m/s}$ before the velocity reduces to approximately 0 at the time of maximum bubble expansion ($t = 50\,\mu\mathrm{s}$). Then, rather symmetrically, the liquid is transported in the opposite direction and slowly accelerated during bubble shrinkage. Just prior to the collapse a rapid acceleration sets in, reverting the flow direction and accelerating it to about $u_y = -18\,\mathrm{m/s}$ at $t = 105\,\mu\mathrm{s}$. At this time the jet has developed and pushes the liquid through the channel. Examining the bubble dynamics between $t = 100\,\mu\mathrm{s}$ and

$t = 200\,\mu s$, we find a second oscillation cycle of the bubble with a reduced equivalent bubble radius. We want to remind the reader that the bubble is not spherical but has now transformed into a toroidal shape. While the fluid velocity u_y is rather symmetrical for most of the expansion and shrinkage of the first bubble oscillation, i.e. downward during bubble expansion and upward during shrinkage, we see a different feature during the second oscillation cycle. Here the velocity u_y remains negative for most of the second oscillation cycle, and only shortly before the second collapse the flow reverses. As a consequence, we can expect that a net downward flow occurs during this part of the bubble oscillation. This expectation is confirmed in figure 4.5 b). It plots the liquid volume V transported through the channel as a function of time, which is calculated as $V(t) = \pi r_c^2 \int_0^t u_y(t')\,dt'$. Again, a negative sign stands for a net liquid transport downwards through the channel. Figure 4.5 b) shows a roughly symmetrical flow during the first oscillation period as discussed above, pumping liquid downwards during bubble expansion and upwards during bubble shrinkage. The cumulative volume flow V remains negative for this entire oscillation cycle. Upon bubble collapse, the developed jet creates a strong downward flow through the channel, which lasts until the maximum expansion of the second bubble oscillation cycle and reaches up to 7 nl at 170 µs, before the flow is reversed and the net amount of pumped liquid is slightly reduced. It is instructive to compare the pumped liquid with the maximum bubble volume, which is about 500 nl, and with the volume of the channel, which is approximately 8 nl.

4.5.2 Variation of parameters

The present fluid transport problem is rich in the choice of parameters, e.g. the geometry of the channel (length l, radius r_c, shape), the stand-off distance d of the bubble and the properties of the liquid to name a few. In this section, we vary some of these parameters individually and document their effect on the pumped liquid through the channel. The flow behaviour in the channel in tandem with the evolution of the bubble radius R observed in figure 4.5 happens in a similar fashion in all the following cases studied, meaning that the first bubble collapse is accompanied by the formation of a microjet towards the perforated plate and a sudden acceleration to a high magnitude negative flow velocity u_y in the channel.

Variation of the channel length

The three channel lengths $l = 200\,\mu m$ ($= 0.42\,R_{max}$), $l = 400\,\mu m$, and $l = 1000\,\mu m$ ($= 2.11\,R_{max}$) are studied. The main difference caused by this change is the viscous flow resistance of the channel flow. As a result, for shorter channels we observe higher flow velocities u_y (see figure 4.6 a) at $t = 110\,\mu s$), yet the duration of the flow driven by the liquid jet also lasts shorter. This is because after the first collapse, the inertia of the liquid jet transports gaseous fragments of the bubble along and through the channel. Once the bubble content reaches the lower end of the channel (where the liquid flow is measured), the liquid flow rate abruptly diminishes, which happens at about $t = 110\,\mu s$ for $l = 200\,\mu m$ and $t = 120\,\mu s$ for $l = 400\,\mu m$. Also, for shorter channels a stronger backflow towards the collapsing bubble is created (around $t = 150\,\mu s$), which affects and reduces the net flow further. This is due to the second bubble collapse when the channel begins to fill with liquid from the bottom again. During the third expansion (starting at around $t = 180\,\mu s$) the liquid is pushed downwards through the channel again. For $l = 200\,\mu m$,

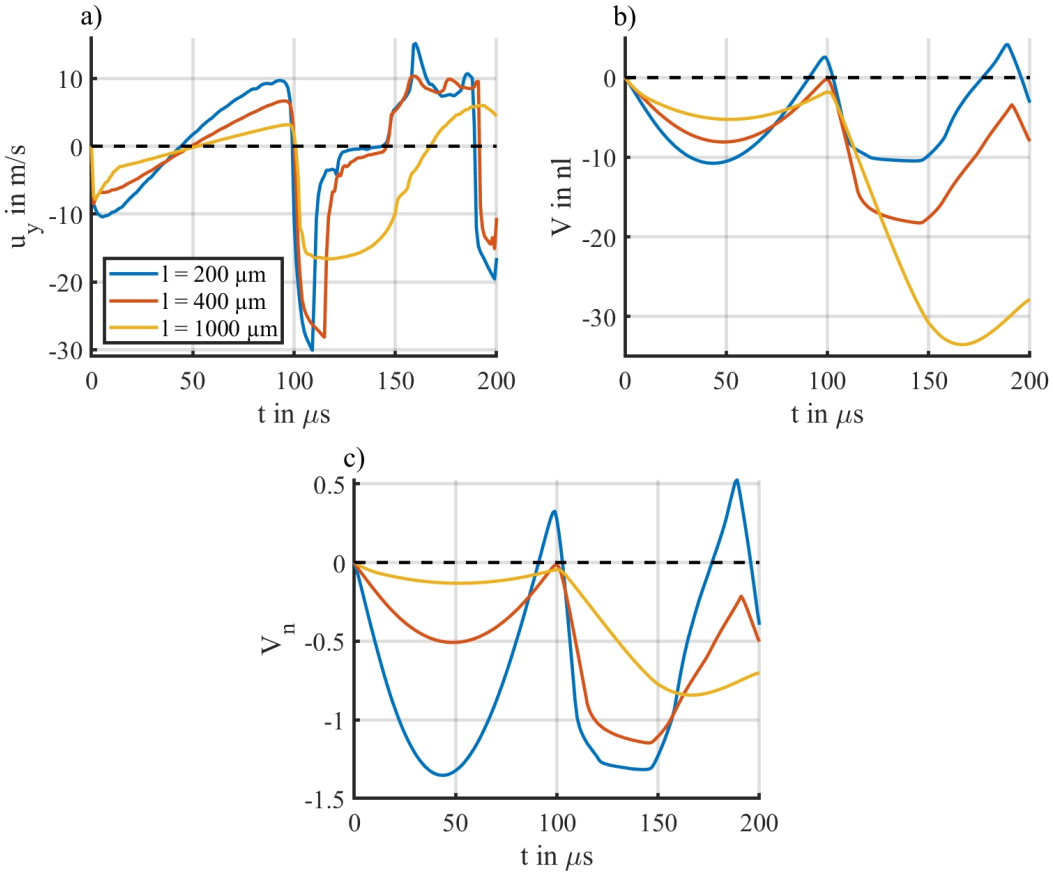

Figure 4.6: Study of the liquid transport as a function of the length of the channel l for $r_c = 112.5\,\mu m$, $d = 500\,\mu m$, $R_{max} = 475\,\mu m$; a) velocity $u_y(t)$ at channel exit, b) liquid volume $V(t)$ transported through the channel, and c) transported liquid volume normalised by the channel volume $V_n(t)$

similar amounts of liquid are being moved up and down through the channel, respectively, creating a roughly periodic pattern in the volume transport curve $V(t)$ in figure 4.6 b). The bubble dynamics for short channels are discussed in greater detail during the comparison with the experiments, see section 4.6.2. Since the transported liquid volume V increases with increasing channel length l, one may suspect that the transported volume scales with the channel volume ($\sim l$). Therefore, we plotted the transported liquid volume normalised by the channel volume, $V_n(t)$, in figure 4.6 c). This reveals that $V(t)$ does *not* scale with the channel length l and relatively smaller liquid volumes are pumped for longer channels.

Variation of the channel radius

Next the radius of the channel r_c is varied between 25 µm (or $0.05\,R_{max}$) and 200 µm (or $0.42\,R_{max}$). Figure 4.7 a) shows that for thinner channels the liquid jet causes a higher velocity u_y, yet for a shorter duration compared to the wider channels (see $100\,\mu s \leq t \leq 150\,\mu s$). Similar to section 5.2.1, the faster decay in fluid velocity can be attributed to the stronger viscous drag in the thinner channels. For wider channels, an increasingly larger part of the bubble moves into the channel after collapse. In the case of $r_c = 200\,\mu m$, the bubble collapses downwards after the second expansion, entirely entering the channel.

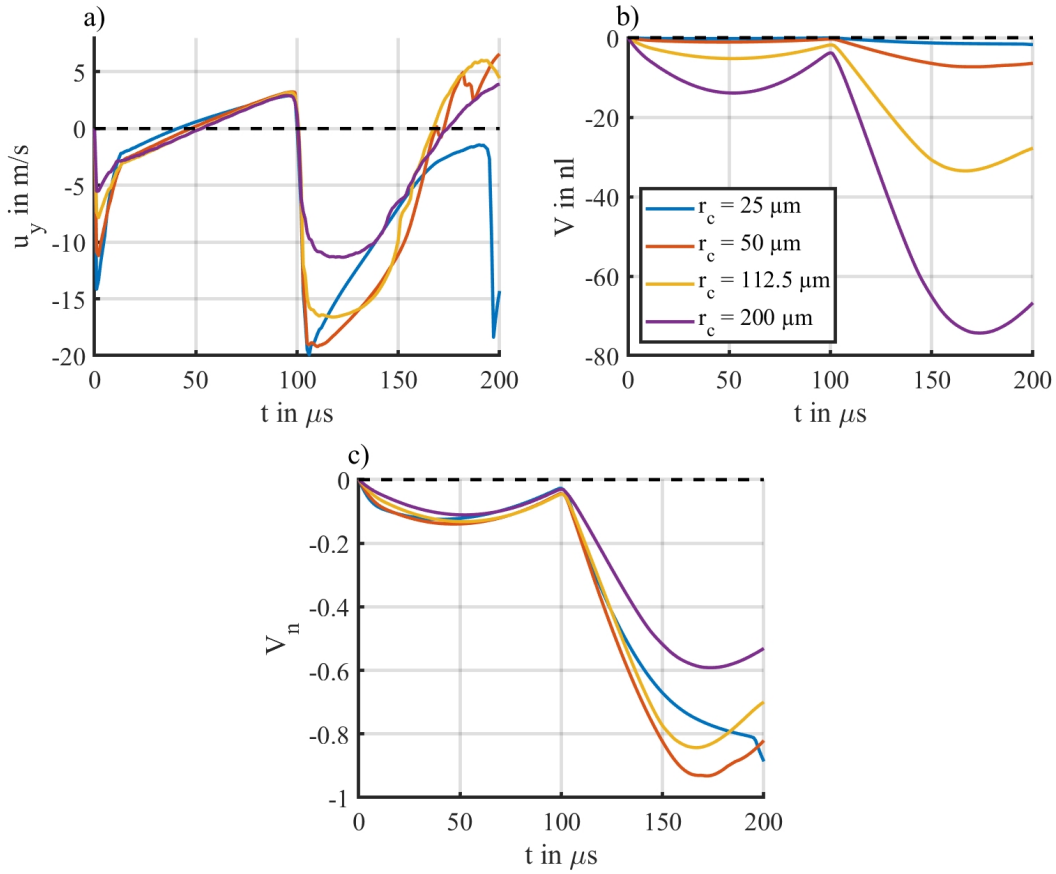

Figure 4.7: Study of the liquid transport as a function of the radius of the channel r_c for $l = 1000\,\mu\mathrm{m}$, $d = 500\,\mu\mathrm{m}$, $R_\mathrm{max} = 475\,\mu\mathrm{m}$; a) velocity $u_y(t)$ at channel exit, b) liquid volume $V(t)$ transported through the channel, and c) transported liquid volume normalised by the channel volume $V_\mathrm{n}(t)$

This stands in contrast to the previous cases, where the second bubble collapse is directed towards the axis of symmetry. The larger cross sections allow a much larger liquid flux to pass through them compared to thinner channels (see figure 4.7 b). If the flow velocity u_y is almost unaffected by the channel width, which it is at least until the bubble collapse, we expect the transported volume V to scale with the channel volume ($\sim r_\mathrm{c}^2$). This is indeed supported by figure 4.7 c), where the normalised transported liquid volume V_n during the first bubble oscillation is approximately the same for each r_c. Yet, after jetting V_n is affected by the channel radius r_c and reaches the largest magnitude value for $r_\mathrm{c} = 50\,\mu\mathrm{m}$.

Variation of the channel shape

The channel shape is varied by fixing the radius at the upper end of the channel at $r_\mathrm{c,upper} = 50\,\mu\mathrm{m}$ and changing the radius at the lower end to $r_\mathrm{c,lower} = 25\,\mu\mathrm{m}$ to obtain a narrowing channel, and $r_\mathrm{c,lower} = 100\,\mu\mathrm{m}$ for a widening channel. The ends are connected via a straight line, creating channels of a truncated cone geometry. Figure 4.8 d) schematically depicts these three channel shapes. In the narrowing channel, a higher absolute pumping velocity is reached as seen in figure 4.8 a). For the widening channel, a higher amount of fluid is transported through them (while the channel volume also increases) as

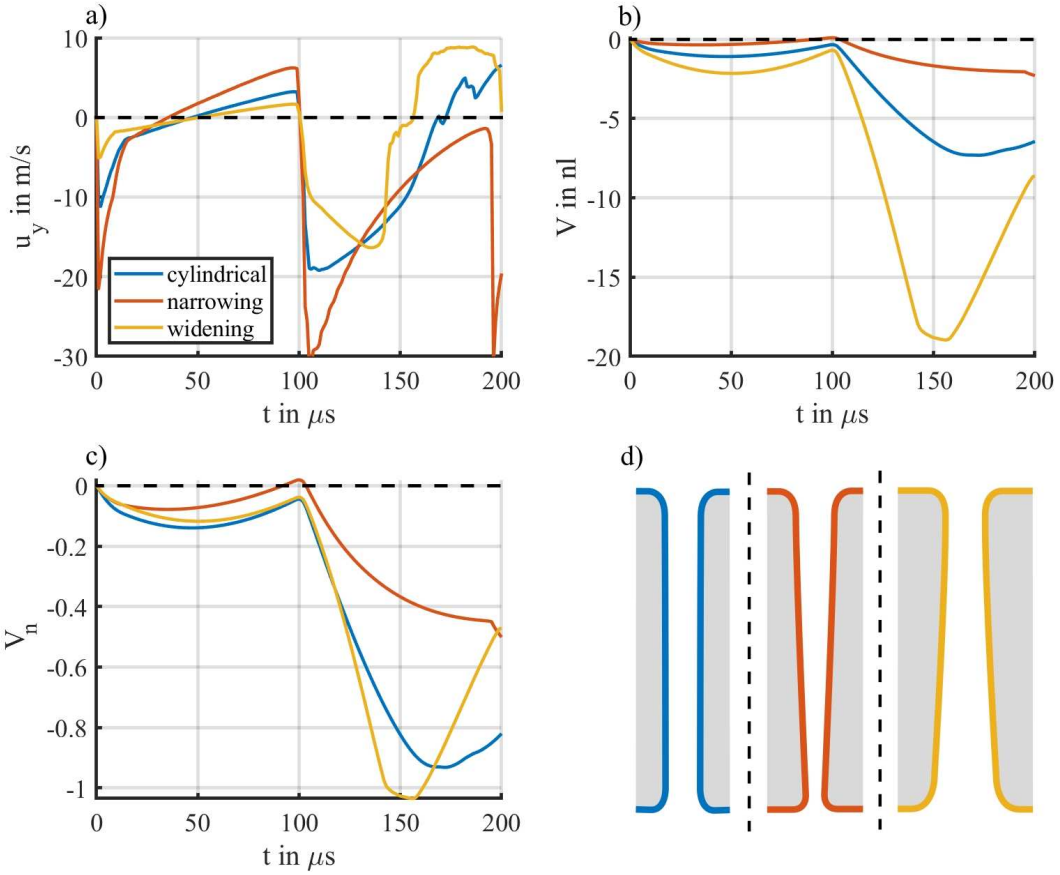

Figure 4.8: Study of the liquid transport as a function of the shape of the channel for $r_{\mathrm{c,upper}} = 50\,\mu\mathrm{m}$, $l = 1000\,\mu\mathrm{m}$, $d = 500\,\mu\mathrm{m}$, $R_{\max} = 475\,\mu\mathrm{m}$; a) velocity $u_y(t)$ at channel exit, b) liquid volume $V(t)$ transported through the channel, c) transported liquid volume normalised by the channel volume $V_{\mathrm{n}}(t)$, and d) schematic of channel shapes used

seen in figure 4.8 b), but there is also a stronger backflow that acts against the net amount of fluid pumped downwards through the channel, see figure 4.8 b) at $150\,\mu\mathrm{s} \leq t \leq 200\,\mu\mathrm{s}$. Plotting the transported liquid volume divided by the respective channel volumes, V_{n}, reveals that the cylindrical channel transports the largest absolute volume over the first $200\,\mu\mathrm{s}$ (see figure 4.8 c)).

Variation of the liquid viscosity

Next, we increase the viscosity of the liquid from that of water ($\mu = 1\,\mathrm{mPa\,s}$) by 1 and 2 orders of magnitude, respectively, while keeping the gas viscosity constant. Figure 4.9 summarises the results and reveals the expected drastic decrease of absolute pumping velocity u_y and pumped volume V, as well as a stronger damping of the flow in the channel. Interestingly, the backflow towards the bubble is strongly reduced for $\mu = 100\,\mathrm{mPa\,s}$. This can be contributed to the strong viscous damping of the microjet. Unlike in the cases with lower viscosity, the jet drags no bubble gas into the channel that would create a backflow during the collapse later. The viscous damping also causes the bubble to have a 37 % larger collapse time during its first oscillation and reach a 42 % smaller rebound volume upon its second expansion than in the case of $\mu = 1\,\mathrm{mPa\,s}$. In the appendix (section 4.8.3),

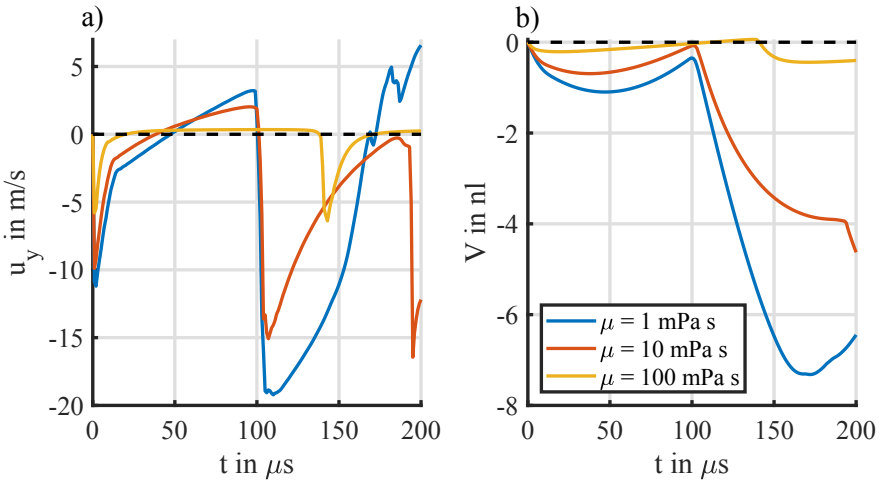

Figure 4.9: Study of the liquid transport as a function of the liquid viscosity μ for $r_c = 50\,\mu m$, $l = 1000\,\mu m$, $d = 500\,\mu m$, $R_{max} = 475\,\mu m$; a) velocity $u_y(t)$ at channel exit and b) liquid volume $V(t)$ transported through the channel

we estimate the total pumped volume as a function of the viscosity (equation (4.16)) assuming a dissipating Hagen-Poiseuille flow. From that consideration, neglecting the effect of viscosity on the jetting, the pumped volume can be considered to be proportional to r_c^4 and μ^{-1}.

Variation of the stand-off distance

Increasing the stand-off distance of the bubble seed from $d = -50\,\mu m$ ($\gamma = -0.11$) up to $d = 750\,\mu m$ ($\gamma = 1.58$) reveals a general trend that the velocity u_y and the amount of liquid pumped V decreases with the distance (see figure 4.10 a)). For the smallest distances d, considerably higher velocities of up to $u_y = -55\,m/s$ at $d = -50\,\mu m$ are achieved, yet these distances also result in a stronger backflow during the second bubble oscillation period. This can be partly attributed to the bubble expanding into the channel after jet formation, pushing liquid down through it and dragging liquid up again during the subsequent collapse. Overall, the highest pumped volume through the channel V is achieved for the smallest distances d (see figure 4.10 b)). For large distances, i.e. $d = 750\,\mu m$, a net pumped volume of nearly zero is observed just prior to the first bubble collapse. This behaviour is expected for an inviscid, spherically oscillating bubble that does not translate, i.e. one that can only be fulfilled for large stand-off distances. Interestingly, the decrease in peak velocity and pumped volume up to the second collapse is not a monotonic function of d but contains a local maximum around $d = 500\,\mu m$ ($\gamma = 1.05$, see figure 4.10 a) at $t = 105\,\mu s$ and 4.10 b) at $t = 170\,\mu s$). The bubble dynamics change significantly as a function of the stand-off distance d. As the bubble is generated closer to the boundary, it becomes more deformed from a spherical shape until it obtains an almost hemispherical shape at maximum expansion with a small protrusion reaching into the perforation in the boundary. In the case of $d = 100\,\mu m$, no pronounced jetting is visible, instead an annular flow develops in the late stage of an almost hemispherical collapse. This flow competes with the later-created microjet from above and mitigates jetting. For $d = 0$, the bubble develops a considerably thinner jet that due to its higher speed pulls along gas from the bubble into and through the channel during bubble re-expansion. This change in jetting behaviour is discussed in greater detail in the following section. Figure 4.10 c)

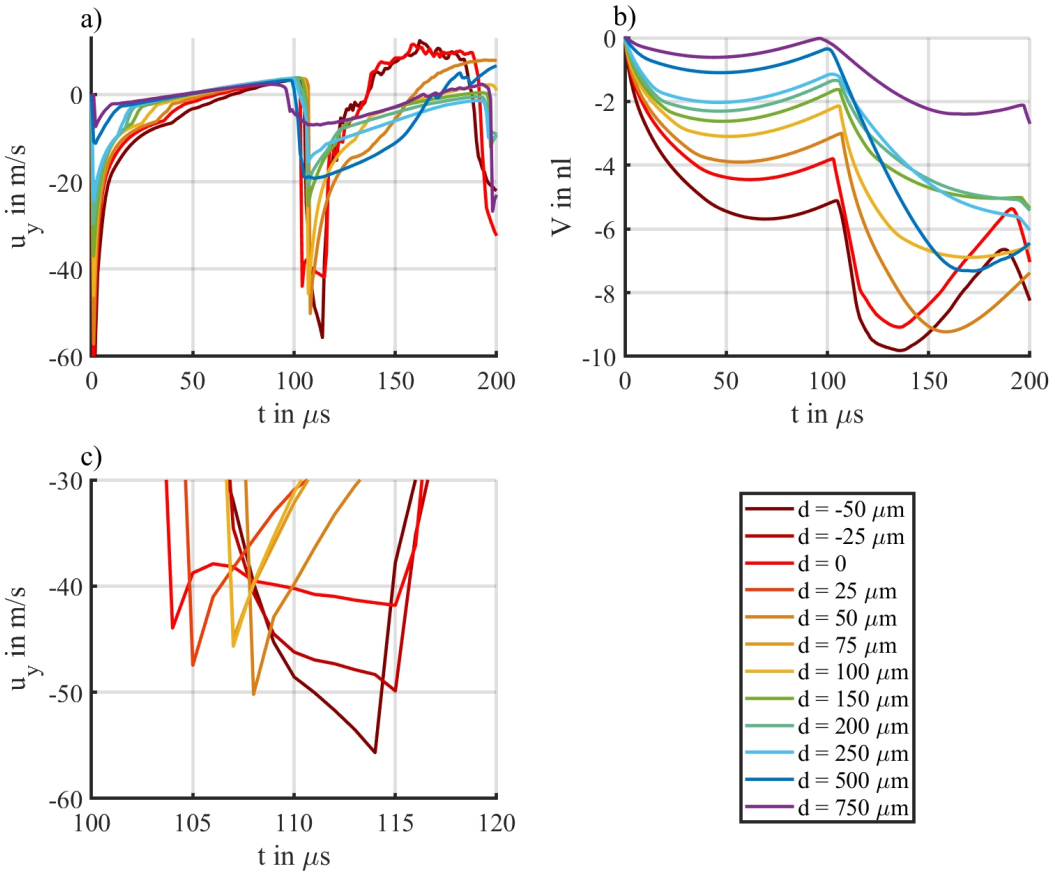

Figure 4.10: Study of the liquid transport as a function of the stand-off distance d for $r_c = 50\,\mu m$, $l = 1000\,\mu m$, $R_{max} = 475\,\mu m$; a) velocity $u_y(t)$ at channel exit, b) liquid volume $V(t)$ transported through the channel, and c) velocity $u_y(t)$ at channel exit after jetting for $d = -50 \ldots 100\,\mu m$

shows that for $d < 0$, the velocity peak is reached at a later time, which can be linked to the bubble expanding further into the channel. There, the gas phase collapses only a few microseconds after the collapse of the main bubble (see figure 4.11 at 103.0 µs).

4.6 Selected pumping regimes

After studying the pumping effect and the influence of parameters thereon in the preceding sections, we now examine the effect of the channel on the bubble dynamics for two distinct regimes in greater detail.

4.6.1 Needle jet regime: small stand-off distance and long channel

Figure 4.4 reveals that for $\gamma \approx 1$ the shape of the bubble near a plane, unperforated boundary is rather similar to the shape observed near one which is perforated with a long and slender hole ($l = 1\,mm$, $r_c = 50\,\mu m$). When the bubble is generated very close to an unperforated boundary, the jetting behaviour of the bubble transitions from the commonly known rather wide jets to a considerably thinner and faster jet, termed *fast, thin jet* [83] or *needle jet* [86] that can reach a velocity with an order of magnitude of

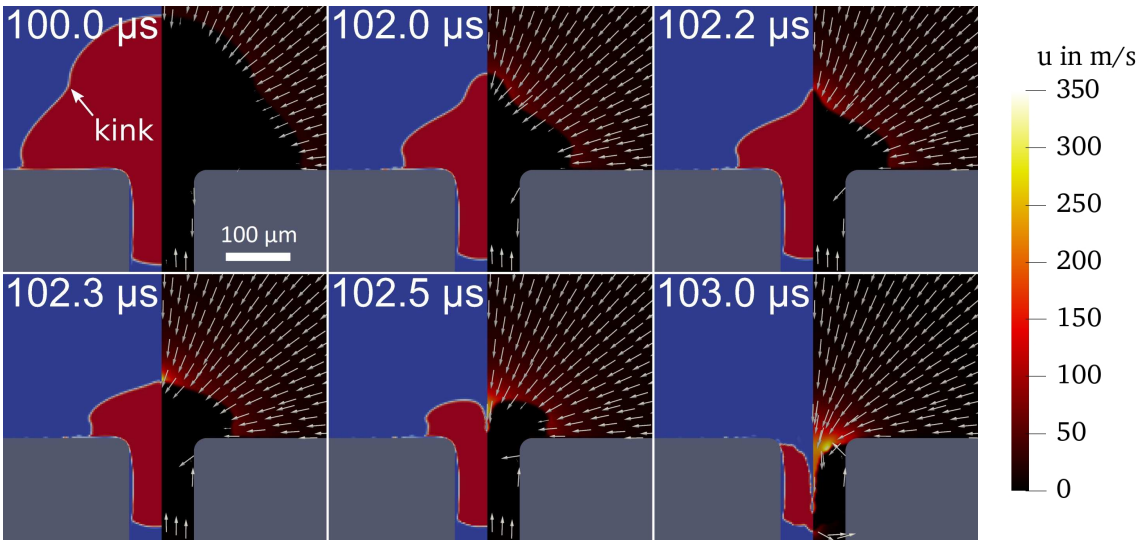

Figure 4.11: Simulation of cavitation bubble dynamics in the perforation of a rigid plate in the plane of the upper wall of the plate ($\gamma = 0$); The left side of each frame shows the bubble gas in red and water in blue, the right side shows the velocity field in the liquid.

1000 m/s as revealed in simulations and experiments. We want to address the question of whether this needle jet may also occur at a perforated boundary. With a hole in the boundary, the bubble can be initiated even closer and even within the channel, offering the possibility to probe negative stand-off distances. Figure 4.11 shows a bubble initiated on the boundary ($\gamma = 0$), where the bubble penetrates into the perforation during expansion. There, the upper part of the bubble obtains an approximately hemispherical shape and the lower takes on that of a cylinder filling the cross-section of the hole. As it starts to collapse, a circular kink forms at the upper part of the bubble ($t = 100.0\,\mu s$) As the bubble shrinks, the kink remains roughly at the same distance from the wall, yet it converges in diameter (see $t = 102.0\,\mu s$ and $t = 102.2\,\mu s$ in figure 4.11). This has been connected with a wall parallel radially convergent inflow focusing on the axis of symmetry [83]. Upon impact, this focused flow is responsible for the acceleration of liquid in the shape of a needle to high speeds along the axis of symmetry (see $t = 102.3\,\mu s$, $t = 102.5\,\mu s$, and $t = 103.0\,\mu s$ in figure 4.11). Please note that, besides the prominent downward needle-like jet flow, in the perforation also a flow upwards is created that competes against the spherically convergent main flow. The very thin downwards jet pierces the bubble with a velocity of 367 m/s, whereas the commonly known jet flow of a bubble at larger stand-off distances does not exceed about 100 m/s. It is important to note that the velocity of the fast jet is strongly dependent on the grid size as reported by Lechner et al. [83] and thus may here be underestimated. The present observation shown in figure 4.11 resembles the bubble dynamics reported by Lechner et al. [83] and confirms that a needle jet can occur in the presence of a perforated boundary, too.

The emergence of the needle jet phenomenon with decreasing γ is easily revealed by plotting the maximum of the absolute velocity of the entire liquid domain, u_j and the radius of the jet r_j in figure 4.12 a) and 4.12 b). Following the curves from a large γ-values to smaller γ in figure 4.12 a), the velocity of the liquid jet u_j decreases slowly at first from about 100 m/s and then sharply rises to values of several 100 m/s, showing the lowest value at $\gamma = 0.3$.

The radius of the jet r_j is defined as the radius of the widest column along the axis of

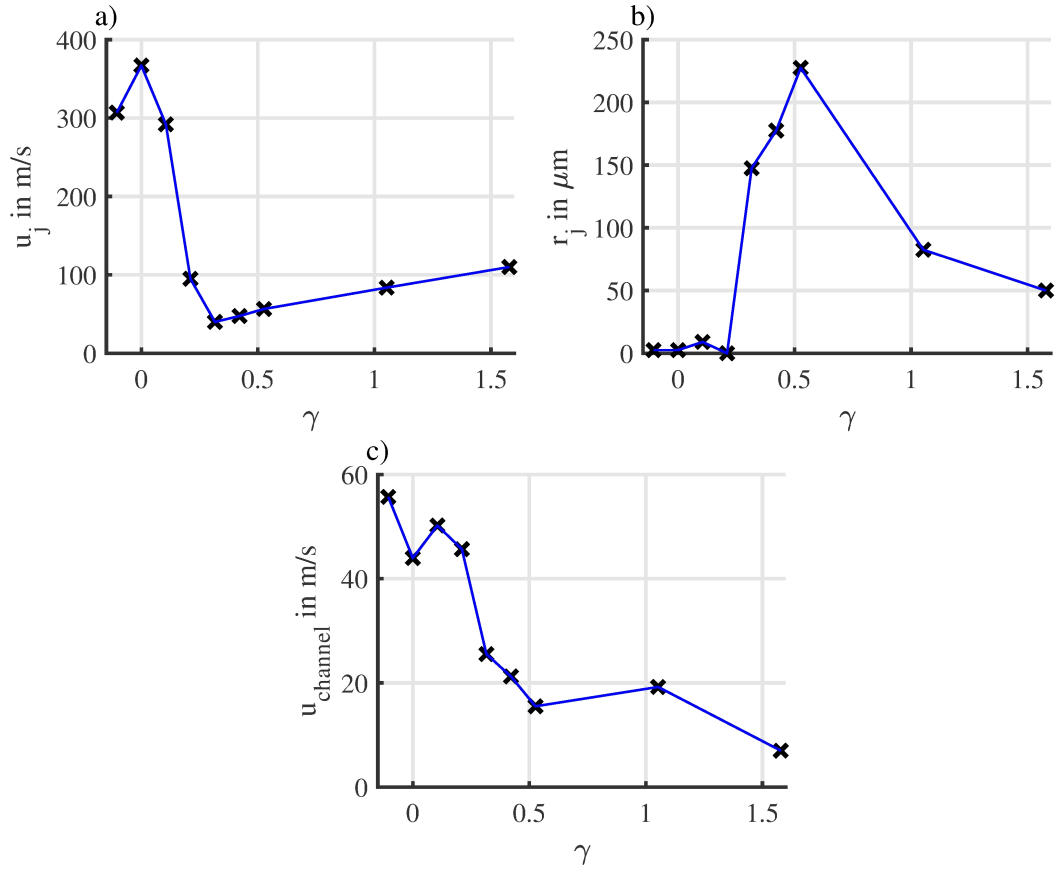

Figure 4.12: Study of the transition between jet and needle jet as a function of the normalised stand-off parameter γ; a) jet velocity $u_\mathrm{j}(\gamma)$, b) jet radius $r_\mathrm{j}(\gamma)$, c) maximum flow velocity at the channel exit $u_y(\gamma)$

symmetry that is entirely filled with liquid after the jet has pierced the bubble (see figure 4.12 b)). This jet radius r_j reveals a maximum at $\gamma = 0.5$ but sharply drops to a very low value for $\gamma \lesssim 0.2$. Here, the jet becomes so thin that it is not fully resolved in the present simulations and splits into small droplets without fully penetrating the bubble. Then, a jet radius of $r_\mathrm{j} = 0$ is plotted in figure 4.12 b).
The velocity produced at the lower end of the channel u_y (see figure 4.12 c)) shows a pronounced rise for $\gamma < 0.5$. However, it is not as abrupt as during the formation of the needle jet. Judging from these results, the needle jet occurs at $\gamma \lesssim 0.2$, while the standard jet occurs at $\gamma \gtrsim 0.5$, with a transition region between $\gamma = 0.2$ and $\gamma = 0.5$, where no needle jet occurs, but the jetting behaviour changes.

4.6.2 Reverse jet regime: small stand-off distance and short channel

Next we investigate the bubble dynamics close to a short channel ($l = 170\,\mu\mathrm{m}$). We chose this regime because in the experiments, both sides of the plate can be captured by a single camera in the case of a thin plate. A second motivation was the report of a jet directed away from the wall by Cui et al. [140] that formed only near a thin perforated plate which is also absent for unperforated walls. In this regime, we provide two comparisons between the simulated flow and the experiment in figure 4.13 with a stand-off distance of $d = 108\,\mu\mathrm{m}$ and figure 4.14 with $d = 202\,\mu\mathrm{m}$. In these figures, on the left the simulated bubble and on the right the experiment is depicted. We present not only the shape but

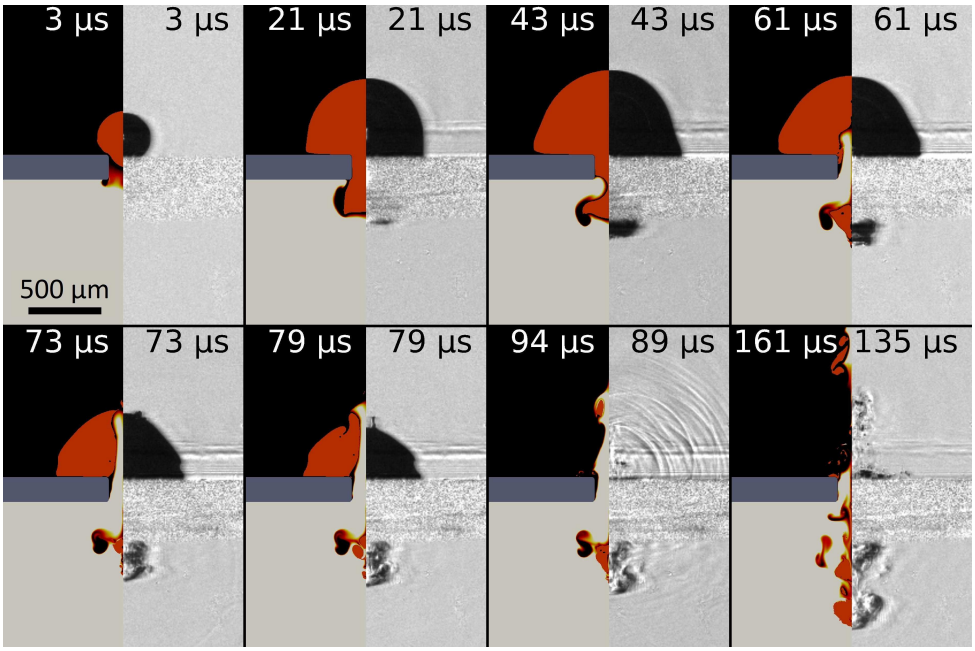

Figure 4.13: Comparison between simulation (left) and experiment (right) of a cavitation bubble of maximum radius $R_{\max} \approx 460\,\mu\text{m}$ at distance $d = 108\,\mu\text{m}$ from a perforated wall, $l = 170\,\mu\text{m}$, $r_c = 97.5\,\mu\text{m}$, bubble is shown in red, ink map of the liquid above the channel in black, liquid below the channel in white

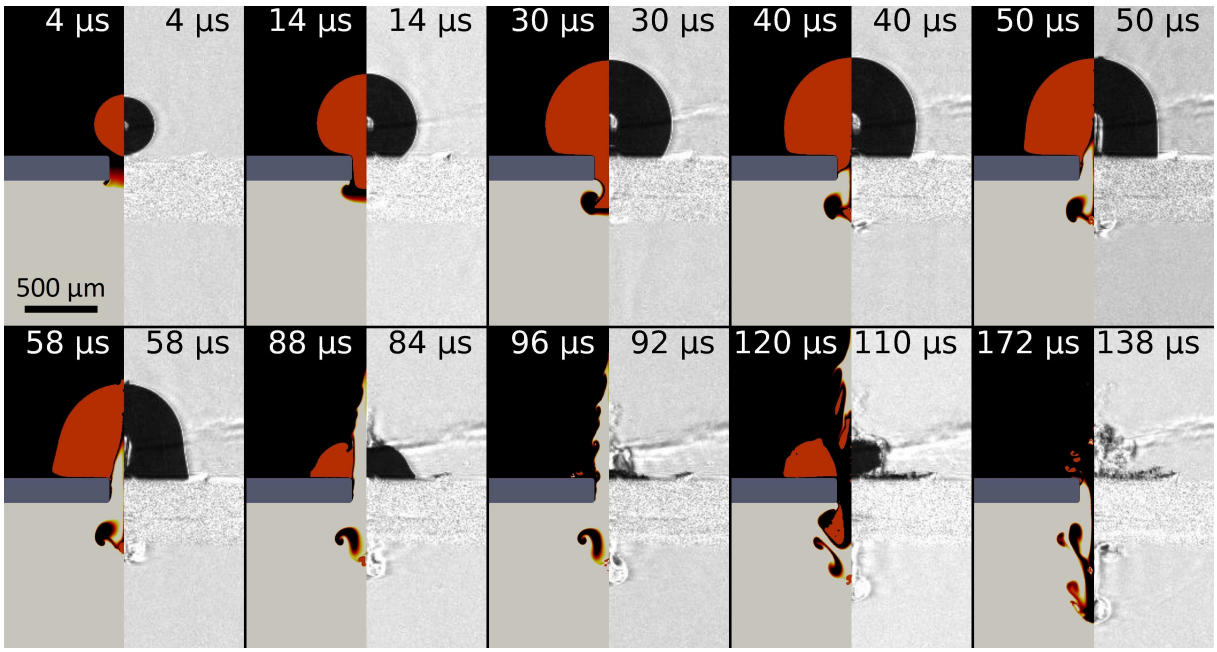

Figure 4.14: Comparison between simulation (left) and experiment (right) of a cavitation bubble of maximum radius $R_{\max} \approx 460\,\mu\text{m}$ at distance $d = 202\,\mu\text{m}$ from a perforated wall, $l = 170\,\mu\text{m}$, $r_c = 97.5\,\mu\text{m}$, bubble is shown in red, ink map of the liquid above the channel in black, liquid below the channel in bright grey.

also the transported liquid using a digital ink map in the simulations to visualise the net fluid transport from the unsteady flow field of cavitation bubbles as introduced by Reuter et al. [142]. This passive tracer field of different colours is advected with the simulated flow field. Initially, the liquid in the upper reservoir is coloured black and that in the lower with a bright grey. Additionally, the liquid in the perforation is coloured continuously from the top to the bottom from black to red to yellow to bright grey at the bottom. Adding the ink map we can not only depict the bubble shape but also the origin of liquid at a later stage during the pumping. For example, the black blob in the lower reservoir in the simulation part of figure 4.13 a) is liquid that has been pumped from the upper into the lower reservoir.

The experiment uses the higher index of refraction of the aqueous NaCl solution to visualise liquid transport via Schlieren imaging. This allows for contrasted high-speed recordings in regions of liquid entrainment. Note that due to the optical configuration, the liquid leaving the channel at the lower side can only be observed once it has propagated about 310 µm downwards into the bulk.

We start the discussion with the simulated bubble dynamics for a rather small stand-off distance of $d = 108\,\mu\text{m}$ ($\gamma = 0.23$) as shown in figure 4.13. In this regime, in the case of an unperforated boundary a needle jet is observed (see section 4.6.1) as well as when the boundary is perforated with a long channel. However, in the presence of a short channel, a different dynamics is observed: During early bubble expansion ($t = 3\,\mu\text{s}$) some of the liquid from the upper reservoir is pushed through the hole into the lower reservoir. This liquid is visible as a small black and coloured blob below the boundary. During the later expansion of the bubble ($t = 21\,\mu\text{s}$) a small part of the bubble invades through the hole into the lower reservoir. The two parts of the bubble are now exposed to different flow fields. While the upper mostly hemispherical part of the bubble continuously expands to a maximum size at $t = 43\,\mu\text{s}$, the lower part pinches off from the main bubble near the exit of the hole. The stagnation pressure from this pinch-off drives a liquid jet back through the hole into the upper part of the bubble (see $t = 61\,\mu\text{s}$ in figure 4.13). This *reverse jet* then impacts at the apex of the upper bubble and eventually injects liquid from the lower reservoir into the upper one at $t = 79\,\mu\text{s}$. A careful inspection reveals that the upper hemispherically shaped bubble develops a kink about 100 µm from the surface, starting from $t = 73\,\mu\text{s}$. The location of the kink converges towards the axis of symmetry at $t = 79\,\mu\text{s}$. Yet, the reverse jet prevents a further convergence of this annular flow towards the axis of symmetry. The main bubble collapses at $t = 94\,\mu\text{s}$, while the pinched-off bubble in the lower reservoir already collapses at around $t = 73\,\mu\text{s}$. The pinch-off ($t = 43\,\mu\text{s}$) of the bubble protruding through the plate creates a complex mixing flow below with vortices and bubble fragments transported deeper into the lower reservoir. Overall we find a good agreement between experiments and simulations. It is important to note that the bubble in the simulations collapses earlier than in the experiments. While we have no definite proof, a likely explanation is the elastic deformation of the boundary seen in the experiments and not accounted for in the simulation.

A comparison for a larger stand-off distance of $d = 202\,\mu\text{m}$ is shown in figure 4.14 ($\gamma = 0.44$). This results in a lesser invasion of the bubble into the lower reservoir during the bubble expansion as compared to figure 4.13. Consequently, a smaller part of the protuberant bubble is pinched off below the wall between $30\,\mu\text{s} < t < 40\,\mu\text{s}$. As a consequence, the reverse jet forms a thinner tip that partly breaks up into small droplets at $t = 50\,\mu\text{s}$. The vortex flow created upon pinch-off below the wall is more pronounced, which is likely due to a weaker disturbance of the flow by oscillating gas fragments as

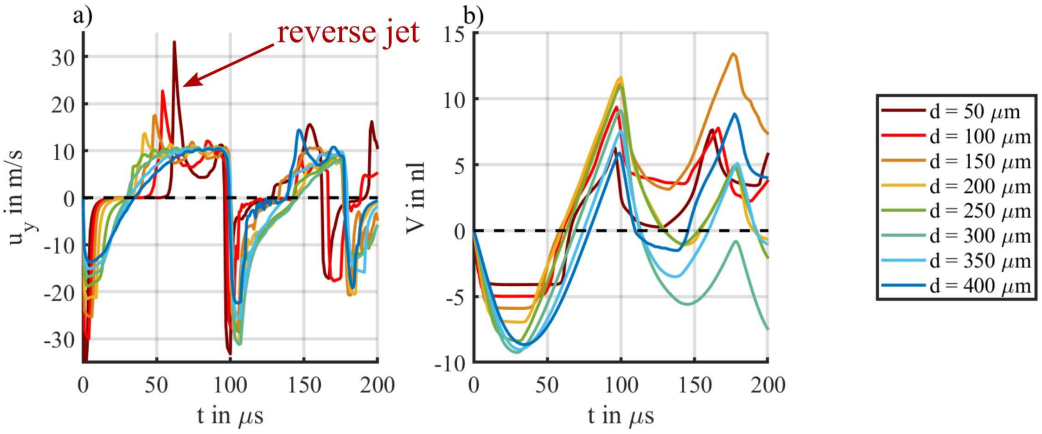

Figure 4.15: Study of the liquid transport as a function of the stand-off distance d for $r_c = 97.5\,\mu m$, $l = 170\,\mu m$, $R_{max} = 475\,\mu m$; a) velocity $u_y(t)$ at channel exit and b) liquid volume $V(t)$ transported through the channel

compared to figure 4.13.
Further simulations using the same geometry as in figures 4.13 and 4.14 reveal the dependence of the pumping behaviour on the stand-off distance d in figure 4.15. The backflow is clearly visible in the channel velocity u_y as a positive spike occurring prior to the bubble collapse at $t \approx 100\,\mu s$ in figure 4.15 a). This stronger backflow is mostly due to the rather small channel length (see also figure 4.6). The highest amount of pumped liquid can be achieved at $d = 300\,\mu m$ or $\gamma = 0.63$ (see figure 4.15 b)), which is in contrast to the γ-dependence of the amount of pumped liquid for a longer channel reported in figure 4.10.

4.7 Discussion and conclusion

The simulations and experiments in this work present the flow through a perforation in a thin rigid plate produced by a cavitation bubble collapsing in front of the perforated plate. The effect of several geometric and liquid parameters are studied and overall reveal clear trends on the transport of liquid from the bubble side to the opposite plate side, i.e. the pumping of liquid: A longer channel increases the flow resistance and as a result reduces the liquid exchange between the two fluid domains, i.e. not only the pumping of fluid but also the backflow. For longer and longer channels the flow resembles more and more that of a bubble close to an unperforated wall. Mixing of fluids rather than pumping can be achieved with shorter channels. If a part of the bubble penetrates through the perforation during bubble expansion, that part collapses earlier than the main body of the bubble, resulting in an early jetting flow from the lower fluid domain (see figure 4.6). We have termed the flow as *reverse jet* and confirmed it in experiments (see figures 4.13 and 4.14). The experiments utilise a Schlieren technique to reveal the mixing of rather similar liquids, i.e. water and an aqueous NaCl solution. While for the mixing of two liquids it may find applications, for the unidirectional pumping it should be reduced. This can be done by increasing the channel length such that the bubble does not expand beyond the lower end of the channel.
A straight cylindrical channel results in larger amounts of liquid being pumped as compared to simple sloped channels. Yet we suspect that other geometries such that of a Tesla valve [143] may reduce the backflow and increase the pumped volume. An optimisation

of the geometry is open for future studies. Even without conducting a study, an optimal value of the channel width r_c for the highest amount of pumped liquid is to be expected, since for the extreme cases of $r_c \to 0$ and $r_c \to \infty$ no liquid pumping will occur, i.e. non-perforated wall and spherical bubble collapse with absence of jetting, respectively. This has been confirmed and narrowed down in the present study. For the regular jet the jet radius r_j ranges between $0.1 \ldots 0.5\, R_{max}$ (see figure 4.12). Figure 4.7 shows that for $r_c = 50\,\mu m$ ($\approx 0.1\, R_{max}$), overall the highest flow velocities through the channel are reached and the amount of liquid pumped relative to the channel volume reaches a maximum. Thus an optimum in pumping is achieved when the channel radius is similar to the jet radius. Varying the stand-off distance d of the bubble near a long channel ($l = 1\,mm$) reveals two distinct regimes of strong pumping behaviour: one being around $\gamma = 1$, featuring the typical jet, the other at very small stand-off distances, where the *needle jet* is observed. This is very similar to the continuous rigid boundary for sufficiently small stand-off distances.

Since the occurrence of the three regimes *reverse jet*, *needle jet*, and *standard jet* (jetting without the former two particular jets) depends foremost on the stand-off distance d and the channel length l, we summarise this in the regime map in Figure 4.16. It shows the type of jet formation as a function of the normalised stand-off distance γ and the normalised channel length $l^* = \frac{l}{R_{max}}$ and is collected from simulations and experiments. The reverse jet occurs once a part of the expanding bubble reaches the lower end of the channel. A rough criterion for that to occur is $R_{max} \gtrsim d + l \;\Leftrightarrow\; l^* \lesssim 1 - \gamma$, the dashed diagonal line shows $l^* = 1 - \gamma$. Thus, as this line is approached from the standard jet regime, an increasingly stronger backflow occurs. The transition region between the standard jet and the reverse jet spans nearly the entire regime map shown in figure 4.16. Only for the case $l^* = 2.11$, $\gamma = 1.58$ (data point on the top right of figure 4.16), the bubble is seeded so far away from the boundary that we cannot detect an effect of the channel on the bubble shape, i.e. the indentation in the lower bubble wall as seen in figure 4.4 (bottom row) is not formed. The needle jet is only found for $\gamma \lesssim 0.25$ and sufficiently long channels. This region is indicated with the horizontal line in figure 4.16). For very short channels the reverse jet and not the needle jet occurs. This is caused by the fact that the reverse jet develops earlier than the main collapse and therefore prevents the annular flow focusing necessary for the needle jet formation. Thus for small l^* the reverse jet region takes over even if $\gamma \lesssim 0.25$. The simulations presented in this work are limited by the assumption of axisymmetry. This causes noticeable differences compared to the experiments once fragmentation of bubbles or droplets occurs. In the simulation, this yields torus-like structures that are unstable in reality [9]. Another important limitation is the lack of a phase transition model, which prevents an accurate prediction of the condensation of water vapour present in real cavitation bubbles. Instead, the simulated bubble contains a non-condensable gas that cushions further bubble oscillations. This affects the rebound but also the development of non-axisymmetric instabilities that grow with time. Therefore we only show the first $200\,\mu s$ of bubble dynamics, which includes the first and second bubble collapse only. However, this may have important contributions during the later bubble dynamics. The axisymmetric simulations reveal that not only the first but also successive collapses transport considerable amounts of liquid through the channel. With asymmetries and instabilities as well as energy losses due to condensation influencing the fluid dynamics in reality, we expect lesser liquid transport than predicted in the simulations.

While understanding the pumping mechanism of viscous liquids was the initial goal, the

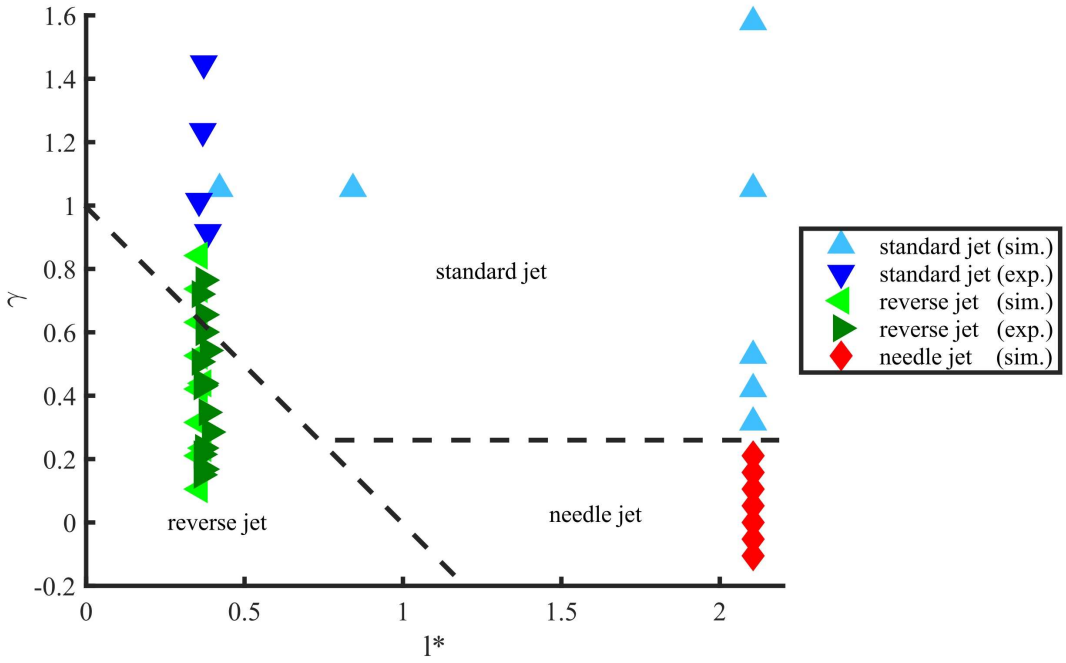

Figure 4.16: Regime map showing the parameter space of the standard jet, the reverse jet, and the needle jet in dependence of the normalised stand-off distance γ and the normalised channel length $l^* = l/R_{\max}$, the dashed lines show $\gamma = 1 - l^*$ and $\gamma = 0.25$.

work could be extended to utilise the flow below the boundary. This flow affects the strength of the bubble collapse as some of the kinetic energy is used for the transport in the micro-channels. For example, a perforated plate with through-holes that are filled with an immiscible and sufficiently viscous liquid may dissipate some of the kinetic energy and therefore reduce the energy available that is focused during the near boundary bubble collapse. This may reduce cavitation erosion as was discussed already for perforated plates containing gas [98]. Also, we speculate that emulsification of liquids in an ultrasonic bath where two liquids are separated by a perforated plate could benefit from the here-found reverse jet. Another point of interest is the jet and spray produced by the bubble if the domain on the opposite side of the perforated wall is filled with a gas instead of a liquid. Potential applications include needle-less micro-injections via a fast liquid jet in air and jet-based printing.

Acknowledgements

This work was funded by the German Research Foundation (Deutsche Forschungsgemeinschaft, DFG) under contract OH 75/4-1.
We are thankful for the discussions with Max Koch, Christiane Lechner, and Qingyun Zeng on details of the solver in OpenFOAM. Also the help from Fabian Denner is gratefully acknowledged. We thank Robert Mettin for lending some of the laser equipment.

4.8 Appendix

4.8.1 Supplementary material

Videos of the numerical and experimental results as well as the code of the numerical solver `CavBubbleFoam` and an example simulation case can be found as supplementary material to [22].

4.8.2 Verification of the simulations

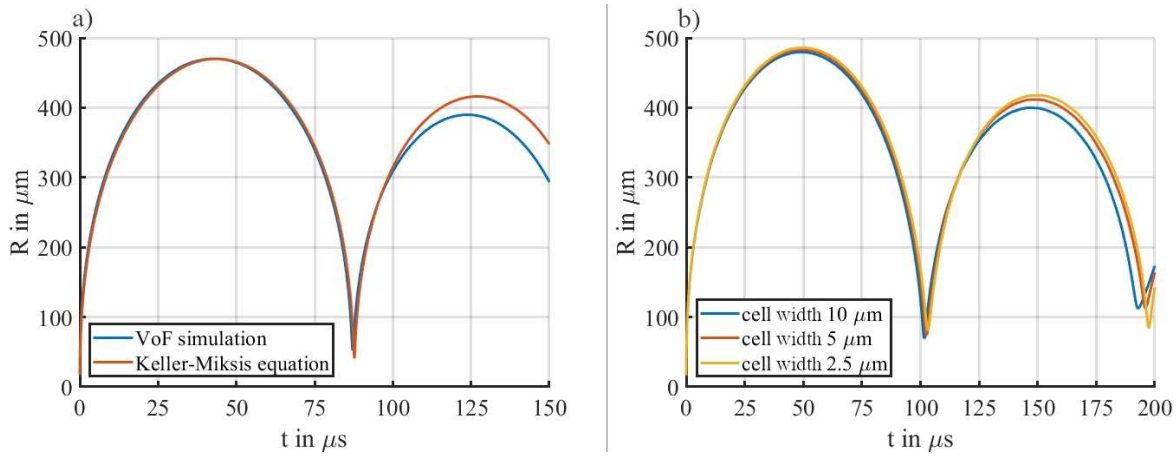

Figure 4.17: a) Comparison between a VoF simulation of a cavitation bubble far from any boundaries in a large geometry (100 mm × 50 mm) and a solution of the Keller-Miksis equation for a radially oscillating bubble with equal maximum bubble radius $R_{\max}$ and b) grid dependence study for the case of a bubble near a perforated boundary for $l = 1000\,\mu\text{m}$, $r_c = 50\,\mu\text{m}$, $d = 500\,\mu\text{m}$

Figure 4.17 a) shows a comparison between the volume of fluid simulation of a freely oscillating (unbound) bubble and the prediction of the Keller-Miksis equation with equal maximum bubble radius $R_{\max} = 470\,\mu\text{m}$. It was done for a geometry of dimensions 100 mm × 50 mm, which is tenfold larger than what was used for the rest of this work to avoid shock wave reflections at the outer boundaries of the simulation geometry. It shows excellent agreement for the first oscillation period. Since the collapse of the bubble in the VoF simulation is not perfectly spherical due to asphericities in the geometry and the mesh grid, its second oscillation period shows a weaker expansion than the Keller-Miksis equation predicts.
A mesh resolution dependence study is shown in figure 4.17 b), using the case of a bubble near a perforated plate with the same geometric parameters as in figure 4.4, bottom row. The grid resolution at the outer boundary of the geometry was kept constant, while the region including the bubble and the channel was discretised using square cells with a width of $10, 5, 2.5\,\mu\text{m}$. A cell width of $2.5\,\mu\text{m}$ was used in the rest of this work. For a better direct comparison between different cell sizes, a cylindrical bubble is seeded without interface smearing, and the seed size is kept constant at a radius of $10\,\mu\text{m}$ and a height of $20\,\mu\text{m}$. For finer meshes, the bubble reaches a slightly larger maximum radius and exhibits a sharper liquid-gas interface. The interface of the thin liquid film that forms between the bubble and the wall after the first collapse is sharper with a finer mesh.

4.8.3 Estimation of the pumped volume

Here we aim to estimate the pumped volume in dependence on the liquid viscosity μ and the channel radius r_c in general form including later times than the simulation covers, i.e. $t > 200\,\mu\mathrm{s}$ We neglect the driving force associated with the bubble dynamics. The laminar volumetric flow rate $\dot{V}$ in a cylindrical channel is given via the Hagen-Poiseuille equation [144],

$$\dot{V} = \frac{\pi r_\mathrm{c}^4 \Delta p}{8\mu l} \ . \tag{4.13}$$

The pressure drop Δp is in equilibrium with the viscous forces acting upon the fluid in the channel. Is the flow driving force taken away, viscosity decelerates the flowing liquid via $\Delta p = -\frac{F}{A} = -\frac{\rho A l \dot{u}}{A} = -\frac{\rho l \ddot{V}}{\pi r_\mathrm{c}^2}$, turning equation (4.13) into a differential equation for the flow rate $\dot{V}$,

$$\dot{V} = -\frac{r_\mathrm{c}^2 \rho}{8\mu} \ddot{V} \ . \tag{4.14}$$

Equation (4.14) is solved by

$$\dot{V}(t) = \mathrm{e}^{-\frac{8\mu}{r_\mathrm{c}^2 \rho} t} \dot{V}_0 \ . \tag{4.15}$$

Integrating equation (4.15) from $t = 0$ to $t = \infty$ gives the total pumped volume,

$$V = \frac{r_\mathrm{c}^2 \rho}{8\mu} \dot{V}_0 = \frac{\pi r_\mathrm{c}^4 \rho}{8\mu} u_0 \ . \tag{4.16}$$

5 Microemulsification from single laser-induced cavitation bubbles

This work has been published in [23]:

K. A. Raman, J. M. Rosselló, H. Reese, and C.-D. Ohl. "Microemulsification from single laser-induced cavitation bubbles". *Journal of Fluid Mechanics* **953**, A27 (2022)

This work has been continued in [145]:

K. A. Raman, J. M. Rosselló, and C.-D. Ohl. "Cavitation induced oil-in-water emulsification pathways using a single laser-induced bubble". *Applied Physics Letters* **121** (19), 194103 (2022)

We study the interaction between a laser-induced cavitation bubble and a submillimeter-sized water droplet submerged in silicone oil. High-speed imaging reveals the pathways through which droplet fragmentation occurs and three distinct regimes of bubble-droplet interaction are identified: *deformation*, *external emulsification* and *internal emulsification*. We have observed that during the bubble collapse the droplet elongates towards the bubble, which acts as a flow sink pulling on the droplet. For silicone oils with higher viscosity, the droplet jets into the cavitation bubble and forms a satellite water droplet in the continuous oil phase. In contrast, for lower-viscosity oils the droplet encapsulates the collapsing bubble as it jets inside and undergoes multiple cycles of expansion and collapse. These internal bubble collapses create tiny oil droplets inside the parent water droplet. The kinematic viscosity of the silicone oil, maximum bubble diameter, and centre-to-centre distance between the bubble and the droplet are varied. The regimes are separated in a parameter space set up by the non-dimensional distance and a cavitation Reynolds number.

5.1 Introduction

Droplet deformation and fragmentation are the fundamental building blocks of emulsification. Examples of conventional emulsification methods are the rotor-stator system and the high-pressure valve homogeniser [146, 147]. There, droplets break up into smaller droplets due to intense shear from turbulent flows in fast-rotating mechanical mixers or from high-pressure pumping through the homogenising valves. For instance, the mechanical energy imparted by the rotating rotors generates large eddies with a characteristic length corresponding to the rotor dimension. Through the energy cascade, the flow is driven into smaller and smaller scales down to the Kolmogorov length scales [148]. This cascade provides the transfer of the energy necessary to break up the macroscopic phase. Similarly, in a microfluidiser the transmission and collision of two strongly pressurised streams of emulsions with macro-sized droplets through microchannels results in much finer-sized emulsions [149–152]. Here, a combination of strong shear and cavitation in the region of collision between the two streams leads to the disintegration of the macroscopic phases. Localised intense stresses may also be generated by irradiating the liquid with ultrasound. Here, the shear is not generated by the sound field directly. Instead, small gas bubbles in the liquid are driven to large volume oscillations that generate the necessary

stresses. For example, during the collapse, mild asymmetries in the flow field are amplified. The resulting liquid jets drive shear flow [153–155]. Insights into the mechanism of how a particular technique leads to droplet deformation and fragmentation are pertinent for improving the current emulsification techniques [156].

There are several ways to realise the fragmentation of a single droplet. Droplet deformation and breakup could be triggered by either modulating the conditions in the surrounding ambient flow, such as shear flow, which in turn would interact with the droplet. In another approach, localised disturbances are introduced inside or near the droplet interface, which has been widely employed to explore the mechanism and the resulting breakup regimes. For instance, the droplet deformation and breakup in a shear flow have been investigated in great detail [157–162]. The flow-induced stress on the droplet surface leads to either a steady ellipsoidal deformation or, by overcoming interfacial forces, the droplet disintegrates into smaller droplets. The interplay between the viscosity ratio of the continuous and dispersed phases and the shear rate was found to determine the transition between the deformation and the breakup regimes [163, 164]. The two major droplet fragmentation mechanisms - *end pinching* and *capillary instability* were reported through the experimental findings by Rallison [165]. Formation and breakup mechanisms of double emulsions in extensional flows have been explored numerically [166, 167]. The uniaxial extensional flow deforms the double emulsion into a prolate spheroidal shape while the recirculating flow inside the annular region deforms the core into an oblate spheroid.

Unlike the laminar transition from deformation to breakup observed in shear flow, a complex fragmentation phenomenon is noticed when a droplet encounters a gas stream [168–170]. The intricate synergy between the aerodynamic forces and surface tension-based instabilities leads to varying droplet morphologies which are sensitive to the flow conditions and fluid properties. Aerodynamic droplet fragmentation has been categorised into five breakup modes: vibrational [171], bag breakup [172, 173], multimode breakup [174–176], sheet thinning [177, 178] and catastrophic breakup [179, 180]. In certain circumstances, instead of altering the conditions of the surrounding flow, droplet fragmentation is achieved when it undergoes a mechanical impact onto a solid surface [181–186]. In these scenarios, the rim bordering the radially expanding droplet breaks up into fragments due to Rayleigh-Taylor and Rayleigh-Plateau instabilities.

Droplet fragmentation can also be realised by introducing a localised region of high shear near the droplet surface. Acoustic emulsification is a technique in which large droplets are successively broken down into smaller scales through cavitation bubbles [153, 187–190]. When acoustic waves travel through the continuous phase with amplitudes above the cavitation threshold, cavitation bubbles are nucleated. The collapse of these bubbles results in localised high pressures and temperatures, high-speed liquid jets, the emission of shock waves, and strong localised shear fields [73, 191]. These intense hydrodynamic effects facilitate droplet breakup and the formation of stable emulsions. As such, ultrasonic cavitation has been employed as an efficient technique to deliver highly localised shear forces to small volumes for emulsification [192].

The quality of the emulsification process may be characterised by the emulsion droplet size and the energy input. Here, we want to obtain a deeper insight into the sequence of hydrodynamic events leading to emulsification. This will be achieved by studying the interaction between a cavitation bubble and a droplet in well-controlled experiments with a single bubble and a single droplet. The ability to precisely regulate the key parameters such as the location of the bubble, its maximum diameter, and the time of its inception is vital to reveal the intricate bubble-droplet dynamics. To attain such flexi-

bility and experimental precision, nanosecond pulsed lasers offer a convenient method to generate cavitation bubbles inside a liquid with good control of location and time. For instance, laser-induced bubble generation and its dynamics near a wall have been thoroughly investigated [193–195]. This flexibility in nucleating cavitation bubbles at specific locations inside a liquid has been utilised previously to investigate droplet fragmentation. Thoroddsen et al. [196] studied the evolution of a cylindrical liquid sheet and spray when a laser is focused below the free surface of a hemispherical droplet. The structure of sheet rupture was found to be similar to the crown structure observed in droplet impact scenarios. Fragmentation dynamics of acoustically levitated water droplets, when irradiated with a laser pulse, were studied by Gonzalez-Avila and Ohl [197]. They identified three distinct fragmentation scenarios: rapid atomisation, sheet formation, and coarse fragmentation. Owing to the substantially short time scales through which the laser-induced nucleation of a cavitation bubble occurs, fragmentation dynamics of droplets in free fall by laser pulses has been investigated [198–200].

While most of the works have focused on droplet deformation and breakup dynamics when a laser pulse is irradiated on or in the droplet, the present study investigates the hydrodynamic response of a droplet residing inside another liquid when a laser-induced cavitation bubble is nucleated near its interface. The mechanism of cavitation-induced emulsification has so far been explored only by very few works aiming to address the same. The breakup of millimetre-sized oil droplets in water through ultrasonic cavitation has been recently investigated [201]. They demonstrated additional intermediate steps for the formation of oil-in-water (O/W) emulsions in which water-in-oil (W/O) emulsions are formed in the bulk oil phase. These are later separated from the oil phase under the influence of ultrasonic waves and undergo breakdown into O/W emulsions. Characteristics of the liquid jet obtained during acoustic cavitation in water/gallium/air and water/silicone oil/air systems were investigated numerically by Yamamoto and Komarov [202]. They found that the maximum jet velocity depends on the initial distance between the cavitation bubble and the liquid droplet. Yamamoto et al. [203] investigated the emulsification process of a water-gallium system using ultrasound irradiation and high-speed imaging. They observed the formation of fine gallium droplets when the maximum radius of the cavitation bubble is large. The emulsification process is initiated during the collapse phase of the cavitation bubble. Further investigations through numerical simulations revealed that the fast-moving liquid jet that forms during the collapse phase of the bubble is responsible for the emulsification. The interaction of cavitation bubbles created by an electrical discharge near a water-oil interface was studied by Han et al. [204]. They investigated the interaction dynamics by initiating cavitation bubbles separately in water, oil, and at the water-oil interface. Mixing of the fluids was reported when the bubble is initiated at the water-oil interface or in the oil phase below a critical standoff parameter. In addition, the authors identified a secondary emulsification mechanism that occurred due to the formation and pinch-off of an interface jet. Experimental investigation by Orthaber et al. [205] further demonstrated these intermediate steps of O/W emulsification using laser-induced cavitation bubbles. They attributed the initial jetting of water droplets into the oil medium to primary Bjerknes forces. Later, oil droplets containing large cavitation nuclei enter the bulk water phase due to Rayleigh-Taylor instability. The present situation deviates from these two studies: both of the above-mentioned works start with a cavitation bubble near an oil-water interface visible as a curved line. In the current work, we consider a bubble and a droplet of similar sub-millimetre size. The characteristic length scales of droplet deformation are expected to be similar to that of

the collapsing bubble. Therefore, the shear forces created during bubble collapse should lead to vigorous fragmentation and deformation dynamics as it affects the entire droplet. Here we only look into the emulsification of a water-in-oil system. By varying the distance between the bubble and the droplet, the continuous phase viscosity, and the size of the cavitation bubble, distinct regimes of interaction are identified. We start with the details of the experimental setup. We then present the three regimes and subsequently elaborate on each of the regimes using fluid mechanics simulations.

5.2 Methodology

5.2.1 Experiment

Figure 5.1 depicts the central part of the experimental setup with the droplet dispenser on top and the focusing optics for the laser on the right. The central element is an acrylic cuvette with a square cross-section (1 cm width, 5 cm height) that contains silicone oil (Carl Roth GmbH, Germany) with kinematic viscosities ranging from $5\,\mathrm{mm^2/s}$ to $100\,\mathrm{mm^2/s}$. The water droplets are generated with a dispensing system (BioFluidix, Pipejet toolkit) located above the cuvette. A frequency-doubled Nd:YAG laser (Q2-1064 series, pulse duration 10 ns, wavelength 1064 nm and pulse energy between 0.1 and 1 mJ) is focused into the silicone oil using a microscope objective (*Zeiss LD Achroplan 20X*, NA = 0.4, focal distance = 10 mm). The bubble is generated to the right of the droplet. By varying the pulse energy, the maximum bubble diameter can be adjusted between 0.95 and 1.7 mm. The laser is triggered once the droplet comes into the field of view of the high-speed camera (AX-Mini 200, Photron) utilising its image trigger functionality. The camera image trigger activates when it detects the change in the image grey levels, starts recording, and triggers the laser to fire a single light pulse. The motion of the sinking droplet is sufficiently slow so that the inherent jitter of approximately 25 ms of this triggering technique does not pose a timing problem. The camera is equipped with a macro lens (*LAOWA f2.8*) with a variable magnification of up to $2\times$. It views the dynamics from the same direction as the reader in figure 5.1. The droplet from the dispensing system can be adjusted in size by varying the shape, amplitude, and duration of the current applied. Here we selected parameters to obtain a droplet with a diameter of $616 \pm 33\,\mu\mathrm{m}$. Once generated, the droplet impacts on the air-oil interface and slowly sinks into the oil due to gravity. To characterise droplet deformation caused by bubble collapse near its vicinity, we use the elongation parameter E_l. It is defined as the difference between the position of the extreme ends of the droplet along the direction of the line joining the two centres normalised by the initial droplet diameter D_d. The geometric schematic defining this parameter is shown in figure 5.1 (b).

5.2.2 CFD Simulation

Simulations were done using the open-source software OpenFOAM [125]. The pressure-based Volume of Fluid (VoF) solver `multiphaseCompressibleInterFoam` for N viscous, compressible, non-isothermal fluid components was modified to suit our purposes. Three components were used to create a numerical representation of the present problem: water, oil, and gas representing the bubble contents, i.e. the gas created during the optical breakdown in oil. The component interfaces are modelled using a phase fraction approach, meaning that each component is assigned a field called α_i, which specifies how much of a given cell is filled with that fluid. Each cell of the domain is filled completely with

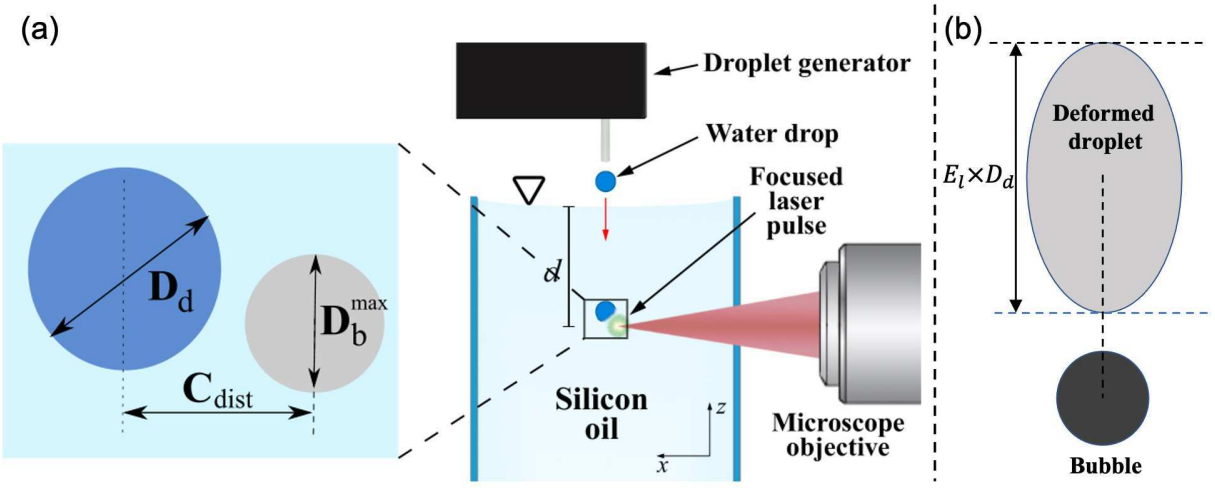

Figure 5.1: (a) Schematic diagram of the experimental setup and pertinent geometric parameters of the cavitation-induced microemulsification problem. A droplet of diameter D_d interacts with a bubble whose maximum diameter D_b^{max} is varied based on the laser energy. The centre-to-centre distance between the bubble and the droplet is denoted by C_{dist}. (b) Schematic definition of the droplet elongation length ($E_l \cdot D_d$).

	p_0 in Pa	ρ_0 in kg/m^3	γ	B in MPa
oil	101325	960	6.4	150
water	101325	998.2061	7.15	404.6
gas	10320	0.12	1.33	0

Table 5.1: Physical parameters of the different fluid components used in the numerical simulations.

fluid. This demands that the sum of all α_i is 1. To model the fluid compressibility, the Tait-equation of state was used,

$$p = (p_0 + B)\left(\frac{\rho}{\rho_0}\right)^{\gamma} - B \ . \tag{5.1}$$

For $B = 0$ the Tait-EoS gets reduced to the ideal-gas-EoS. Table 5.1 shows the parameters used for the different fluid components.

Several modifications from the base solver have been made: The temperature field is omitted for simplicity. The compressibility field $\kappa = \frac{1}{\rho}\frac{\partial \rho}{\partial p} = \frac{1}{\gamma(p+B)}$ for each fluid is calculated in every time step, instead of only once at the beginning of the simulation. This is necessary since a cavitation bubble changes its internal pressure and density over several orders of magnitude, which significantly changes the compressibility. We correct the α-field to counteract the emergence of small bubbles throughout the domain as a result of numerical errors. This is done by clamping all α values below 0.001 (above 0.999) to 0 (1). Furthermore, a correction was introduced to keep the bubble mass $m = \sum_i^{\text{cells}} \alpha_{\text{air},i}\ V_i\ \rho_{\text{air},i}$ constant, since the model does not include any phase transitions and all changes to the amount of vapour present in the bubble stem from numerical errors. Apart from the cavitation process itself, significant phase transitions do happen in the experiments, mainly the partial condensation of the bubble contents, which decreases the bubble pressure and thus reduces the bubble size over time. For this reason, once the

bubble reaches its first volume maximum, a one-time correction is applied which reduces the bubble pressure by a factor (0.35), which was chosen to fit the bubble size in the second oscillation period to the experiments. This correction accounts for the condensable gas that drives the initial expansion, yet later condenses, and leads to a smaller size for the subsequent oscillation periods.
The problem is modelled with axisymmetry. The axis of symmetry is the line that connects the centres of the bubble and the droplet. The simulation geometry is a thin slice of a cylinder with a radius of 5 mm and a height of 10 mm. The outer boundary conditions are chosen to be open, wave-transmissive boundaries to mimic a larger fluid domain. This geometry is divided into square cells with a width of 40 µm. Close to the bubble and the droplet, the mesh is refined by successively splitting the cells into 4 so that a cell width of 2.5 µm is reached. Initially, the bubble is at rest and contains a high-pressure gas of $p \approx 16$ kBar, which is chosen so that the gas density is equal to the density of the surrounding oil. This is similar to a laser-created bubble, using the assumption that the oil absorbs the energy of the laser pulse much faster than the created bubble seed expands. We smear out the bubble-oil interface to reduce Rayleigh-Taylor instabilities that would otherwise appear during early bubble expansion. In the experiments, the distribution of the energy deposited by the laser is expected to be spread around the point of focus, according to the local laser wave energy density. Thus just after the energy position, instead of a bubble with a sharp interface, we assume a gradual transition from the liquid to a supercritical fluid to a plasma, having the same effect of mitigating Rayleigh-Taylor instabilities that could form on the later bubble surface.

5.3 Results

We now discuss the events that occur when a single laser-induced bubble inside silicone oil undergoes multiple cycles of expansion and collapse next to a water droplet. We begin by presenting an overview of three distinct regimes, followed by detailed investigations of each regime.

5.3.1 Overview of the identified regimes

In the experiments the maximum diameter of the cavitation bubble ($D_\mathrm{b}^\mathrm{max}$), the centre-to-centre distance between the droplet and the laser focus (C_dist), and the viscosity of the oil is varied. From 106 experiments conducted, recorded, and analysed we can categorise three distinct regimes with typical examples presented in figure 5.2. These three regimes are the deformation of the droplet by the flow induced by the oscillating cavitation bubble (figure 5.2 (a)), the ejection of liquid from the droplet into the continuous phase (figure 5.2 (b)), and the injection of the continuous phase into the droplet as shown in figure 5.2 (c). For the latter two processes, we introduce the terms *external emulsification* and *internal emulsification*, respectively. In the *deformation* regime, a bubble collapses near the droplet without interfacial destabilisation that may result in fragmentation or injection of liquid. However, the droplet loses its spherical shape due to the flow created by multiple bubble expansions and rebounds while the bubble and the droplet remain separated by the continuous phase. After undergoing multiple shape oscillations, the droplet slowly obtains back its spherical shape, see $t = 2$ ms, the bubble however has fragmented into a number of smaller bubbles. These contain non-condensable carbon-based gases that are created during the laser-induced optical breakdown in the oil.

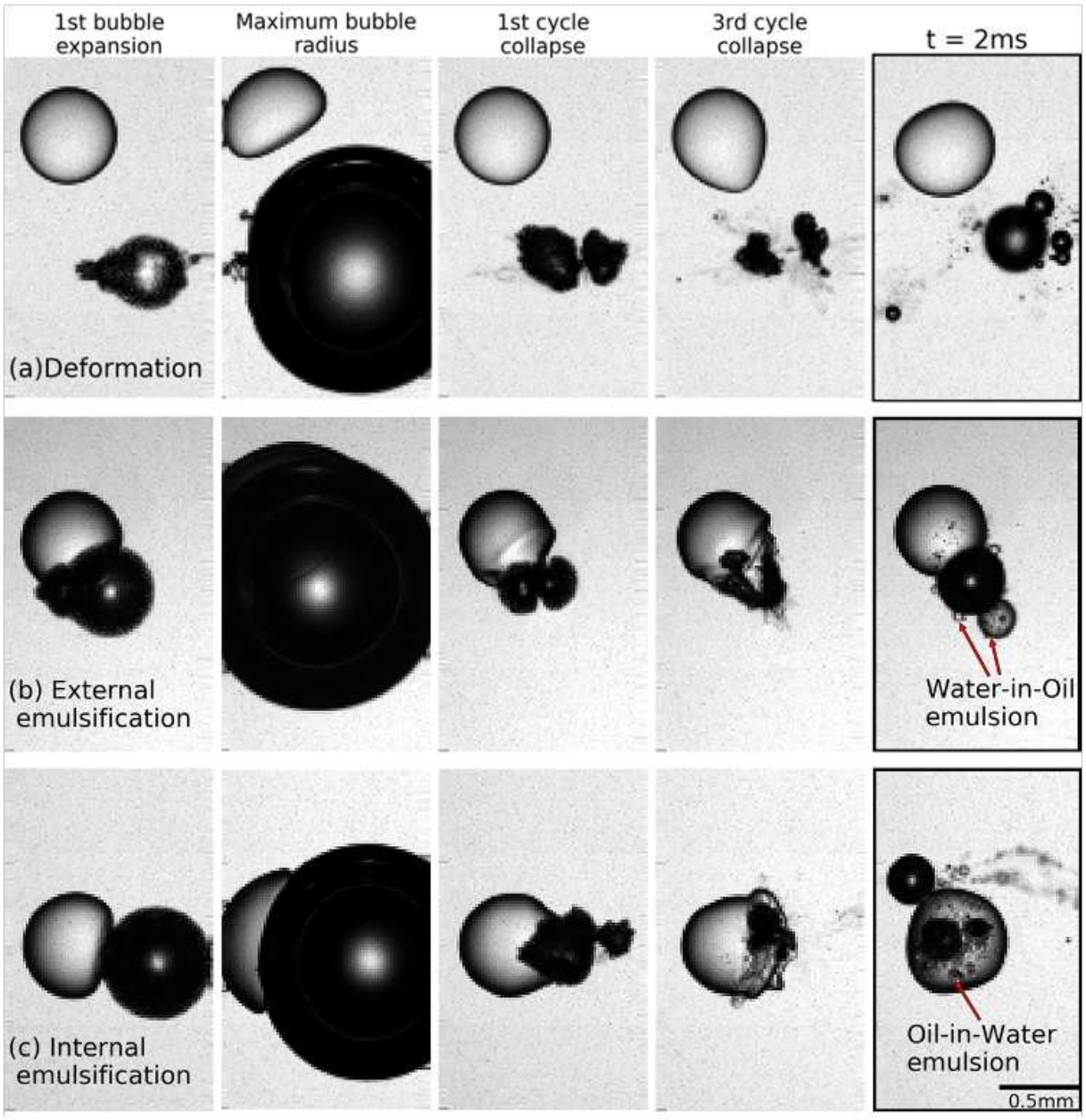

Figure 5.2: Three main regimes of interaction are identified when a laser-produced silicone oil vapour bubble collapses near a water micro-droplet interface: (a) *deformation* (b) *internal emulsification* and (c) *external emulsification*.

The events leading to the *external emulsification* regime are distinguished from the *deformation* regime by an initial physical contact between the bubble and the droplet during the first cycle of expansion, see figure 5.2 (b). As the bubble undergoes its first collapse, the part of the droplet interface which was in contact with the bubble transforms into a protruding ligament pointing outwards into the silicone oil. As time proceeds, the bubble continues to oscillate on this structure resulting in a breakup of this ligament and the formation of a satellite water droplet in the oil.
Parallel to the first cycle of *external emulsification*, during *internal emulsification* the bubble is physically in contact with the droplet as it reaches its maximum radius, see figure 5.2 (c). However, we notice that during the successive collapses and expansions the bubble penetrates into the droplet. These events lead to the formation of a thick

destabilised interfacial region as observed during the collapse in the third cycle, see figure 5.2 (c). The shearing of this interfacial region and the later expansions and collapses of the bubble result in the formation of an oil-in-water emulsion.
We will now look closer into each of these regimes.

5.3.2 Deformation regime

Even if there is no contact between the bubble and the droplet, the flow created by the bubble deforms the droplet. Selected snapshots of this bubble-droplet interaction are shown in figure 5.3 where the frame before the bubble is first seen is defined as time $t = 0$. In figure 5.3 a single bubble is created in the silicone oil with 20 mm^2/s viscosity at a

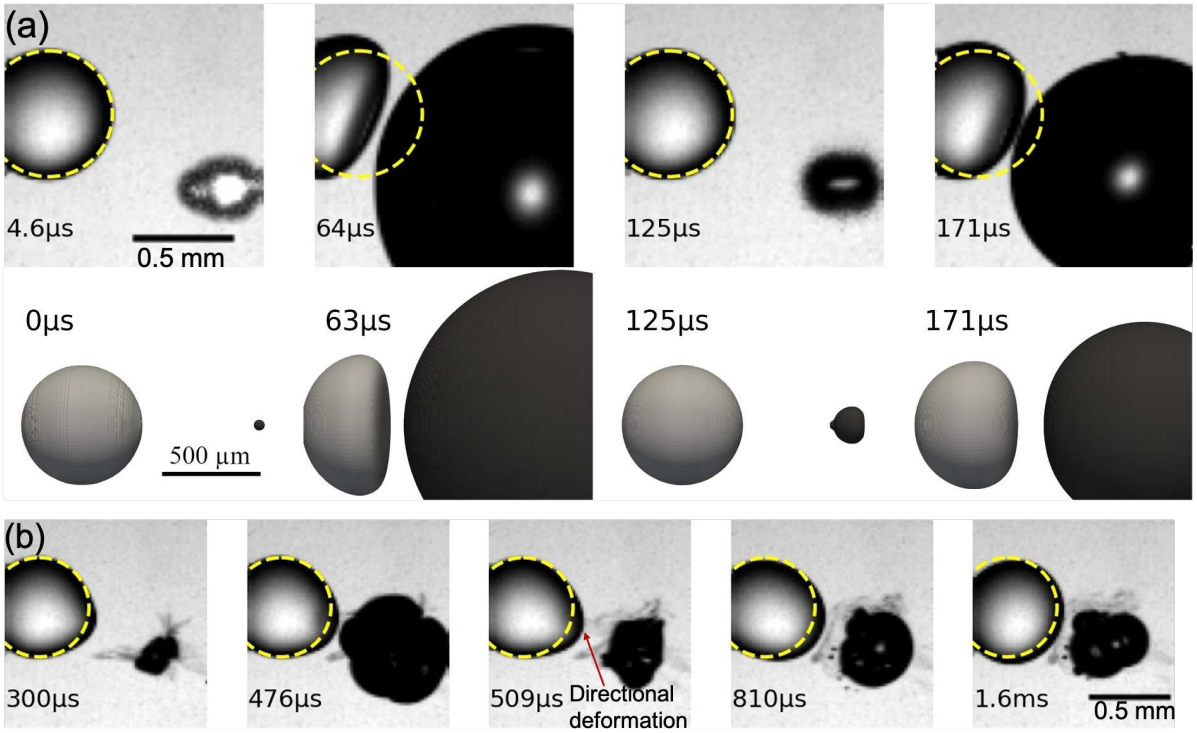

Figure 5.3: (a) Comparison between experiments and numerical simulations illustrating the evolution of the *deformation* regime. (b) Temporal evolution of the droplet interaction with the collapsing bubble at later times illustrating directional *deformation* of the droplet towards the oscillating bubble. The diameter of the droplet is 616 µm ± 33 µm and the video was recorded at 216000 frames per second. The frame before the first appearance of the bubble is defined as time $t = 0$. The maximum bubble diameter is 1583 µm which is generated in silicone oil with 20 mm^2/s viscosity. The centre-to-centre distance between the bubble and the droplet is 910 µm. The sketch of a dashed circle on all the frames represents the droplet shape before the generation of the laser bubble.

distance $C_{\text{dist}} = 0.91$ mm. During early expansion, $t = 4.6$ µs, the bubble is initially elongated due to imperfection of the laser focus, yet at $t = 63$ µm the bubble has expanded to an approximate sphere with a diameter of $D_{\text{b}} = 1.58\,\text{mm} \pm 33\,\mu\text{m}$. The bubble expansion results in a flattening of the droplet on the side facing the bubble. To visualise the extent of droplet deformation and translation, the shape of the droplet before bubble generation is superimposed on the photograph as a dashed curve. During the first bubble collapse

at $t = 125\,\mu s$ the droplet regains its spherical shape and translates back to its original location. The droplet is flattened again as the bubble undergoes a second expansion, though the deformation is considerably weaker.
A comparison of the experimental images with interfaces obtained from numerical simulations is shown in the second row of figure 5.3 (a). Note that the simulation is axisymmetric and the axis of symmetry is horizontal while in the experiments it is under some angle. Overall, a good qualitative agreement between the simulation and the experiment is obtained, especially for the first two cycles of bubble oscillation. The shape of the deformed droplet during primary and secondary expansion matches with the corresponding frames observed experimentally. Similarly, relaxation of the droplet shape to a spherical configuration is noted at $t = 125\,\mu s$ in both situations. At the time $t = 300\,\mu s$ the bubble collapses a second time, now showing clear surface instabilities, see figure 5.3 (b), and the droplet is elongated in the direction towards the bubble's centre. As time proceeds and the bubble undergoes subsequent cycles of expansion and collapse, the droplet regains its original spherical configuration. Yet the droplet has translated towards the bubble. It should be noted that the axisymmetric assumption employed in the numerical model holds well for the first two cycles of bubble expansion and collapse. During this time, as can be seen from figure 3(a), the bubble dynamics are approximately axisymmetric. However, in later cycles, the bubble shows surface instabilities and undergoes jetting along non-axial directions. It also breaks down into smaller bubbles. Therefore, for later times the scenario is no longer axisymmetric and the axisymmetric boundary condition would show deviations from the experimental results.
As the bubble expands and collapses, it acts as a flow source and sink that compresses and elongates the droplet, respectively. We compare the deformation $E_\mathrm{l}(t)$ between the experiment and the numerical simulation in figure 5.4 (a). The centre-to-centre distance and the maximum bubble diameter considered here are $C_\mathrm{dist} = 1003\,\mu m$ and $D_\mathrm{b} = 1.58\,mm \pm 33\,\mu m$, respectively. We see a continuous increase of the droplet elongation until the full expansion of the bubble and a return to a spherical shape during the first bubble collapse at $t = 125\,\mu s$. For this analysis, we used a high-speed recording at a lower magnification compared to the close-up frames shown in figure 5.3 that captures the bubble and droplet in full. Overall, the experimental droplet deformation during the primary and secondary bubble expansion shows a good agreement with the simulation.
The magnitude of the velocity field generated in the surrounding flow depends on the amplitude and the frequency of the bubble oscillation, which is governed by the value of $D_\mathrm{b}^\mathrm{max}$. Similarly, C_dist determines the extent to which the surrounding flow field incurs deviations in the droplet's sphericity. Figure 5.4 (b) illustrates the temporal evolution of $E_\mathrm{l}\,(t)$ for the first few cycles of bubble oscillation in silicone oil with $20\,mm^2/s$ viscosity. Three cases with different C_dist and $D_\mathrm{b}^\mathrm{max}$ are selected. All cases reveal an initial dip of E_l during the bubble expansion and recovery during the bubble collapse. A variation of the magnitude and damping of the oscillations of $E_\mathrm{l}\,(t)$ is clearly observed. Generally, a smaller bubble results in a faster decay of the droplet's surface oscillation and a smaller elongation during primary bubble expansion. For example, for the first case with lowest $D_\mathrm{b}^\mathrm{max}$ and relatively large C_dist of $963\,\mu m$, we observe that after the primary dip the oscillations in E_l cease quickly. In contrast, the largest amplitude in E_l is found for a combination of a large bubble and a small distance, i.e. $C_\mathrm{dist} = 771\,\mu m$ and $D_\mathrm{b}^\mathrm{max} = 1333\,\mu m$. It is to be noted that, even though the maximum bubble diameter considered in this case is lower than the third case with $D_\mathrm{b}^\mathrm{max} = 1583\,\mu m$, the maximum elongation is considerably higher than in the other two cases. The deformation also lasts longer for this case

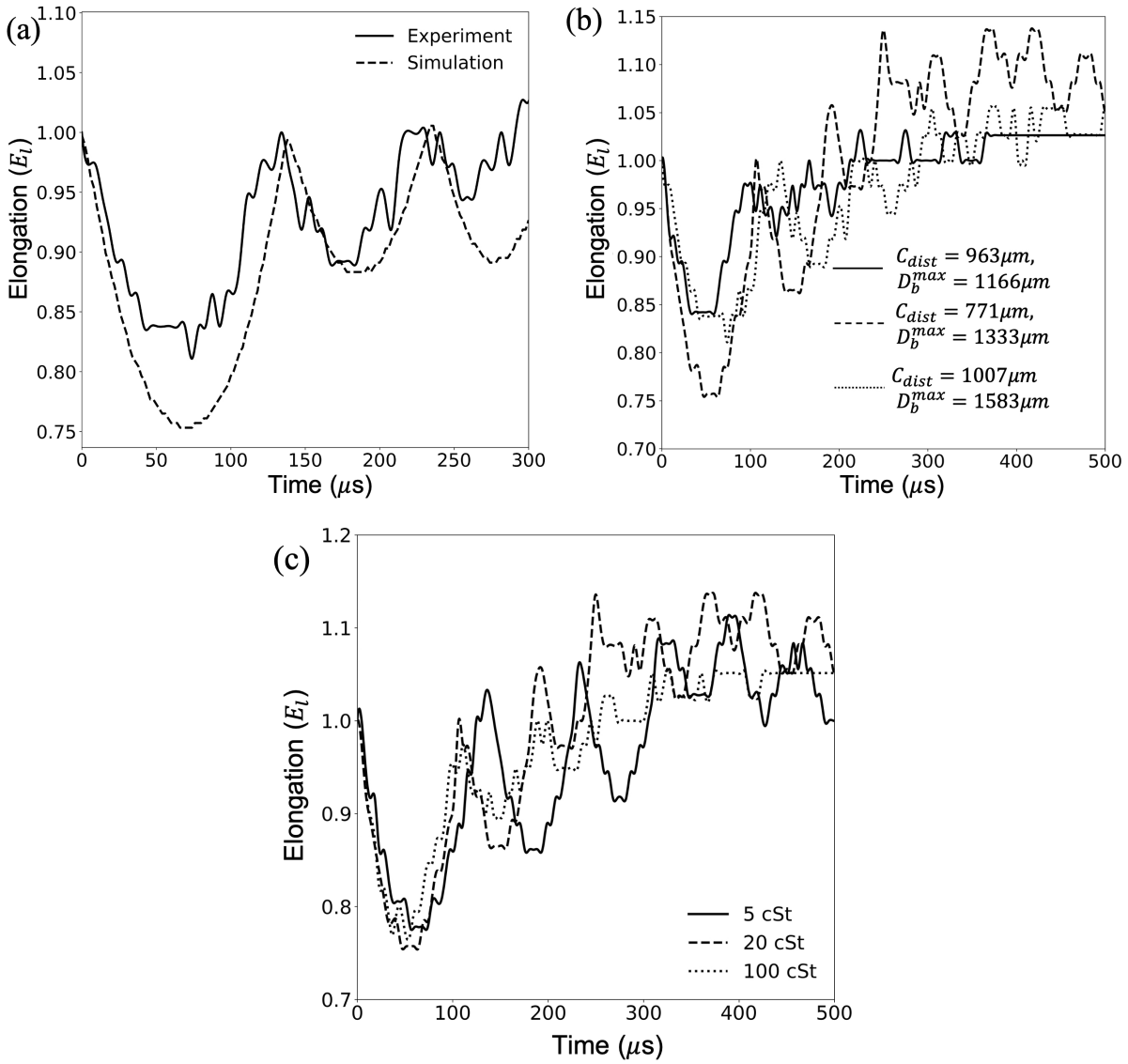

Figure 5.4: Droplet elongation parameter (E_l) along the direction of bubble collapse. (a) Comparison between the experimental and numerical temporal evolution of E_l in 20 mm^2/s silicone oil (C_dist = 1003 µm, $D_\mathrm{b}^\mathrm{max}$ = 1.58 mm) (b) Temporal evolution of E_l for three different cases of varying C_dist and $D_\mathrm{b}^\mathrm{max}$ with an oil viscosity of 20 mm^2/s (b) Effect of viscosity on the droplet elongation with the following parameters: 5 mm^2/s, C_dist = 819 µm, $D_\mathrm{b}^\mathrm{max}$ = 1.45 mm; 20 mm^2/s, C_dist = 771 µm, $D_\mathrm{b}^\mathrm{max}$ = 1.33 mm; 100 mm^2/s, C_dist = 883 µm, $D_\mathrm{b}^\mathrm{max}$ = 1.40 mm.

than for the other two cases. For the case with C_dist = 771 µm and $D_\mathrm{b}^\mathrm{max}$ = 1333 µm, we notice a consistent overshoot in the value of E_l above 1.0 after the first cycle, signifying that the droplet is being pulled and elongated towards the bubble centre.
The effect of viscosity is demonstrated in figure 5.4 (c), with roughly constant parameters C_dist and $D_\mathrm{b}^\mathrm{max}$. Both the cases with lower viscosity sustain the oscillatory behaviour in the temporal evolution of E_l. However, for the case with 100 mm^2/s, we notice stronger damping of the droplet oscillation, as expected.

5.3.3 External emulsification

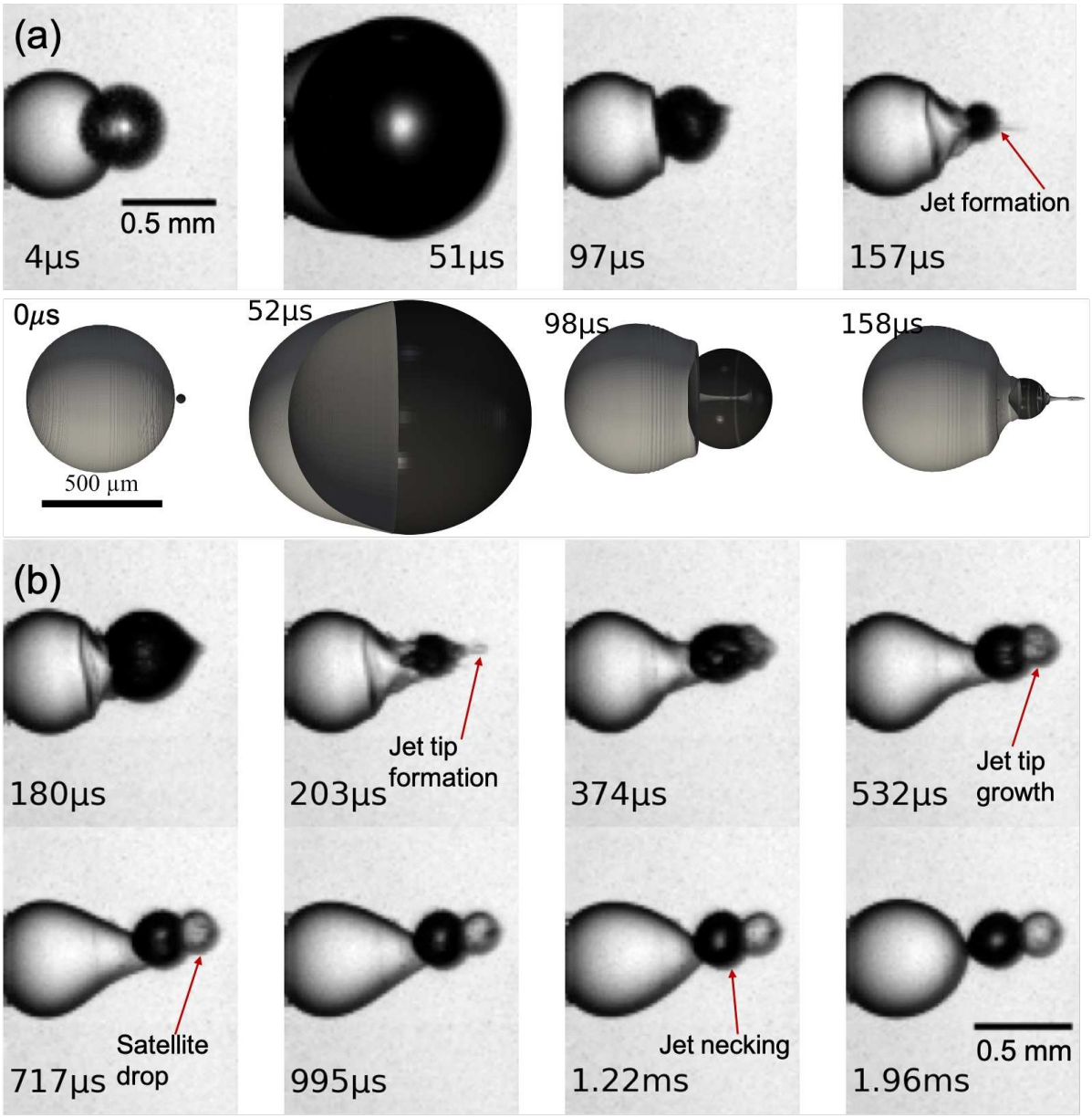

Figure 5.5: (a) Comparison of selected frames between experiments and numerical simulations illustrating the evolution of *external emulsification*. (b) The temporal evolution of the droplet interaction with the collapsing bubble at later time frames illustrates the formation of a water-in-oil emulsion. The diameter of the droplet is 616 µm. The maximum bubble diameter is 1.11 mm which is generated in silicone oil with 100 mm^2/s viscosity. The centre-to-centre distance between the bubble and the droplet is 335 µm.

In figure 5.5 (a), the bubble is generated closer to the droplet surface with a centre-to-centre distance of 335 µm. Here the viscosity of the silicone oil is rather high at 100 mm^2/s and the applied laser energy generates a bubble with a maximum diameter of 1116 µm. Similar to the initial phase in the *deformation regime*, the droplet flattens on the bubble proximate side during the first expansion. Due to the proximity of the bubble the droplet becomes crescent-shaped, see $t = 51$ µs in figure 5.5 (a) top row. An additional difference as compared to the deformation regime is that during the bubble collapse, only on the

bubble distant side the water droplet regains its spherical shape. The bubble-facing part of the droplet develops an edge as a result of the disturbed and now non-spherical converging flow field, $t = 97\,\mu s$. The frame $t = 157\,\mu s$ in figure 5.5 (a) top row shows the droplet during the second bubble collapse. Between the first and second collapse, the bubble has translated towards the right and pulled the right part of the droplet towards itself, forming a conical shape. Collapsing and translating bubbles are known to develop jets [20]. Upon close inspection, one can see a fine protrusion of the droplet pointing out of the right side of the bubble indicated with an arrow in figure 5.5 (a) top row at $t = 157\,\mu s$. This protrusion is the result of a thin water jet flow formed during the first bubble collapse. Numerical simulations of the flow allow a look into the bubble. The frames in the lower row of figure 5.5 (a) depict the surfaces of the bubble and the droplet, yet some transparency for the rendering of the bubble offers a peek inside. We already notice the formation of a jet during the first bubble collapse in frame $t = 98\,\mu s$. This jet however has not penetrated the opposite side of the bubble and therefore only becomes visible during the second collapse $t = 158\,\mu s$.

Figure 5.5 (b) shows that over the course of nearly 2 ms a satellite droplet is drawn from the main water droplet. Early on at $t = 203\,\mu s$ the bubble collapses a third time during which a thicker liquid filament becomes visible. The bubble continues to undergo subsequent oscillations, albeit at a diminishing amplitude, and from $t = 374\,\mu s$ the thick droplet filament gradually grows in size. At $t = 532\,\mu s$ the transformation of the jet tip into a satellite droplet is clearly visible. With the bubble undergoing weaker oscillations, the satellite droplet stops growing leading to the detachment of the satellite droplet from the parent drop. At $t = 717\,\mu s$ the shape of the parent droplet consists of a spherical base and a conical-shaped connecting neck which links to the satellite droplet through the oscillating bubble. Eventually, as the parent droplet relaxes to regain its spherical configuration, a pinch-off of the connecting neck occurs and the satellite droplet is detached. The result of this process is the formation of the water-in-oil emulsion shown at $t = 1.96\,ms$.

To investigate the mechanism of *external emulsification*, we show the simulated bubble's interface during the first oscillation cycle at different times in figure 5.6 (a). The direction of the bubble's radial displacement is indicated by the dashed arrow. After the nucleation of the bubble inside the oil, it expands radially and contacts the water droplet. The left part of the bubble surface displaces the oil and thereby forms a water-gas interface. During the expansion phase of the bubble, it is almost spherical. Upon close inspection, the shape of the bubble at maximum expansion is that of two half spheres with very similar radii of curvature of approximately $R_{max} = 580\,\mu m$ and their centres are separated by some small distance. A similar behaviour is also reported by Han et al. [204] who proposed an extended Rayleigh-Plesset model to study the dynamics of a bubble initiated at a water-oil interface. During the expansion phase, they observed spherical expansion of the upper half and the lower half of the bubble, respectively. During bubble shrinkage, the part of the bubble making contact with the water droplet shrinks faster than the part in contact with oil. The bubble also loses its spherical shape and becomes oval with the longer semi-axis in the radial direction, i.e. at $t = 92\,\mu s$ in figure 5.6 (a). At $t = 94\,\mu s$ an indentation in the bubble surface is observed that develops into a jet directed towards the oil phase, $t = 96\,\mu s$. At that time the bubble part in oil has not yet undergone collapse.

It is instructive to study the spherical problem of a bubble collapsing in water, in oil, and in a droplet of water surrounded by oil. While the first two problems can be solved with the well-known Rayleigh-Plesset model [34], a derivation of the equation of motion for a bubble surrounded by two liquids of different density and viscosity is provided in

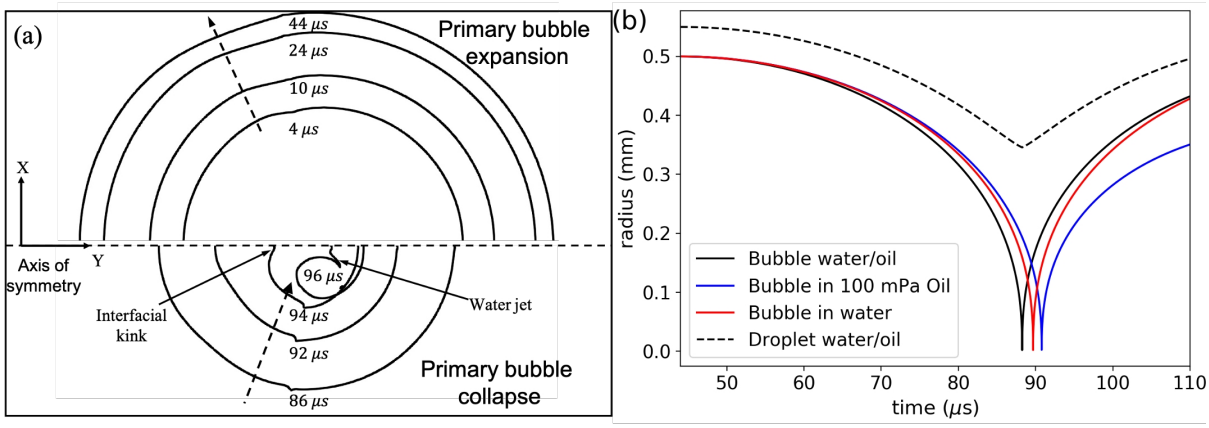

Figure 5.6: (a) Interface profile of the cavitation bubble during its primary expansion (top) and collapse phase (bottom) taken from the simulation in figure 5.5. The top part shows the bubble expansion (oil on the left and water on the right) and the lower part the primary bubble collapse. (b) Simulation of a collapsing bubble via the Rayleigh-Plesset equation (5.7) in different environments with $R_{\max}(t = 44\,\mu s) = 580\,\mu m$. The parameters are $\mu = 1\,\mathrm{mPa\,s}$ and $\rho = 1000\,\mathrm{kg/m^3}$ for water and $\mu = 100\,\mathrm{mPa\,s}$ and $\rho = 900\,\mathrm{kg/m^3}$ for oil, the initial thickness of the oil layer at time $t = 44\,\mu s$ is $40\,\mu m$.

the Appendix. This derivation follows a model by Church [68] for coated bubbles used in medical diagnostics. Ignoring viscosity, a bubble collapsing in the less dense oil would collapse faster than in water. Yet, the normal viscous stresses oppose the pressure forces and delay the collapse. Let us now compare these two cases of the collapse shown in figure 5.6 (b) where the blue curve is a bubble in oil and the red curve is a bubble in water. The initial size of $R_{\max} = 580\,\mu m$ is taken from the maximum bubble radius at time $t = 44\,\mu s$ in figure 5.6 (a). For this viscosity, the bubble collapses later in oil, i.e. the viscous stresses in oil are dominating the higher inertia of water. Yet, the bubble in the experiment is not oscillating in bulk water but is only surrounded by a layer of water in the continuous oil phase. We abstract the complex crescent shape of the water layer in the experiment with a concentric shell of oil. This situation is shown in figure 5.6 (b) as a black curve. The initial thickness of the water layer at maximum expansion is $40\,\mu m$. The bubble now experiences lower inertia than water and less viscous stresses than oil. As a result, the bubble covered with a thin layer of water collapses approximately $5\,\mu s$ earlier than the same bubble in oil and about $3\,\mu s$ earlier than in water. This faster collapse of the water-covered part of the bubble gives an initial clue why eventually a jet flow develops from the water phase towards the continuous oil phase. In reality, the water layer is not a concentric shell and it is expected that the varying thickness of the layer contributes to the jet formation, too.

Figure 5.7 depicts the bubble's and the droplet's interfaces during the primary expansion and collapse phases, the liquid velocity magnitude via a colour scale, and the direction of the velocity field with arrows. At $t = 36\,\mu s$ the bubble reaches its first maximum expansion. The magnitude of the velocity along the bubble-water interface is almost constant. From $t = 48\,\mu s$ the velocity field on the left part of the bubble, i.e. the side in contact with oil has changed direction and the bubble starts to shrink. This is in contrast to the bubble-water interface where the bubble still expands and a non-uniform velocity distribution with a stagnation point at the central region is visible. Thus the left part of the bubble is expanding slower in water than in oil. The magnitude of the velocity depends

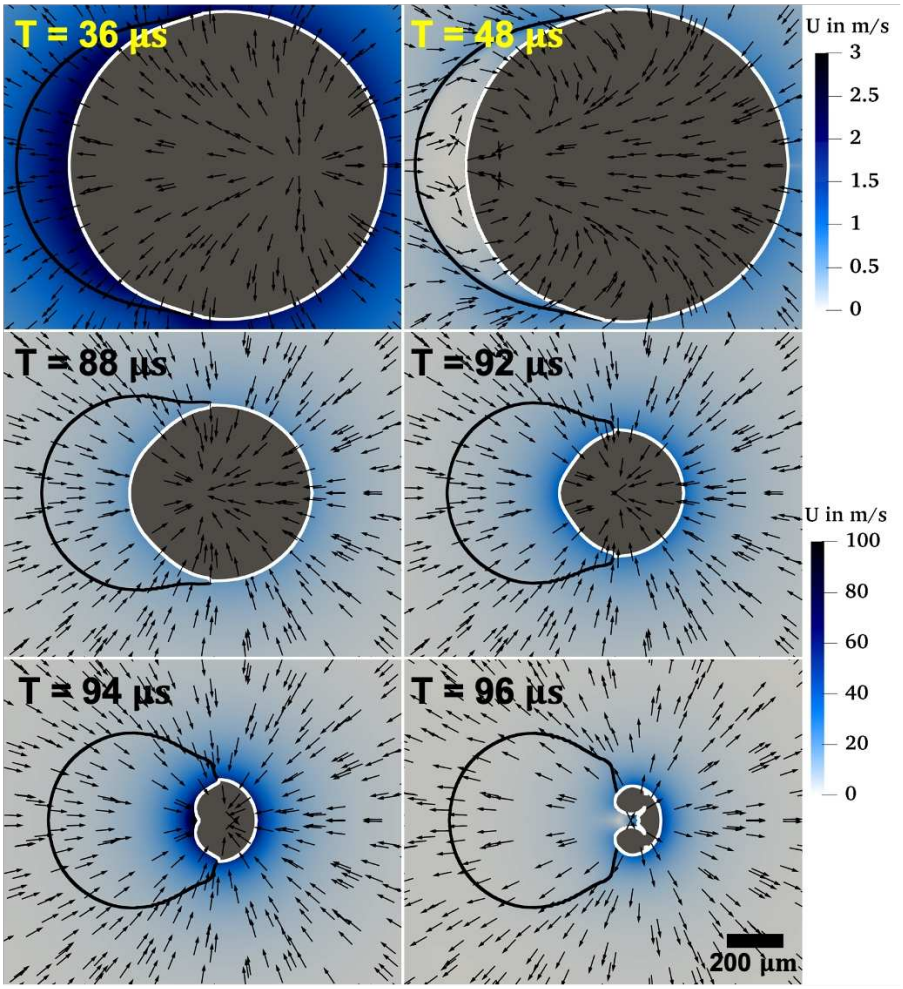

Figure 5.7: Numerically obtained interfacial profiles of the droplet and bubble showing the process of the initial jet formation. The velocity field shown in the liquid is coloured by the velocity magnitude.

on the thickness of the water layer: along the thinner regions of the droplet, the direction of the velocity vectors indicates an inward flow while the thicker central water layer is approximately stationary. This leads to the formation of an oval-shaped bubble-water interface, see $t = 88\,\mu s$ in Fig 5.7. As discussed in the solution of the Rayleigh-Plesset equation for a bubble surrounded by two liquids in figure 5.6 (b), the presence of a thin water layer leads to lower viscous stress than in bulk oil. This in turn leads to a faster bubble collapse. It is instructive to note that the thickness of the water layer covering the bubble-water interface is a significant parameter. It controls the degree to which the water layer dampens the influence of viscous stresses exerted by the surrounding $100\,mm^2/s$ silicone oil. As the bubble continues to collapse, the thickness of the water layer covering the central portion of the bubble-water interface increases. Therefore, a sharp rise in velocity magnitude is observed in the central portion of the bubble-water interface between $t = 92\,\mu s$ and $t = 94\,\mu s$. We notice the formation of an indentation into the bubble at the axis of symmetry at $t = 94\,\mu s$. At the same time, the higher viscous stresses exerted on the bubble-oil interface counteract its radially inward motion. The non-spherical bubble collapse and subsequent expansion accelerate this indentation into a jetting flow clearly visible at $t = 96\,\mu s$. As a result, the jetting flow transports some of

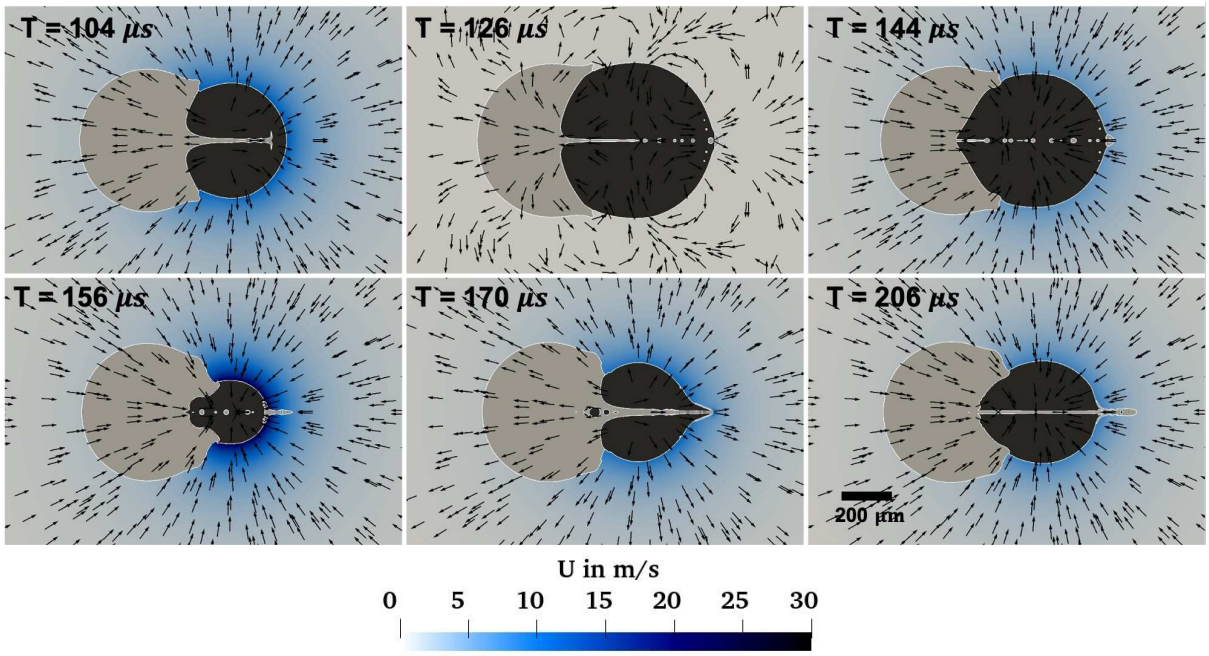

Figure 5.8: Numerically obtained temporal evolution of the interface profiles illustrating the process of the *external emulsification* mechanism. The colour map shows the magnitude of the velocity field in the oil.

the water from the droplet into the oil phase.
Figure 5.8 reveals the second stage of the emulsification process, which starts with the re-expansion of the bubble. Then the jet is stretched and remains entrained within the bubble, see $t = 104 \ldots 144\,\mu s$ in figure 5.8. During the second collapse phase, $t = 156\,\mu s$, the jet eventually penetrates the opposite bubble wall.
Simultaneously, the bubble similar to the first collapse shrinks faster on the waterside, resulting in a second jetting from the water to the oil. This flow is nicely visible during the third bubble expansion at $t = 170\,\mu s$ in figure 5.8. Here, as in the experiments, we see that the non-spherical bubble oscillation with jetting from the water droplet into the oil results in the formation of a satellite droplet. Over time the amplitude of the oscillation diminishes and the filament connecting the main droplet with the satellite droplet splits due to the Rayleigh-Plateau instability.

5.3.4 Internal emulsification

Figure 5.9 illustrates the temporal sequence of the *internal emulsification* regime. In this example, the bubble is generated in silicone oil with a viscosity of $5\,mm^2/s$. Again, the bubble ($D_b = 1283\,\mu m$) is created at a small distance of $C_{dist} = 464\,\mu m$ near a droplet of $D_d = 616\,\mu m$. Similar to the *external emulsification* regime, the bubble makes contact with the droplet during its first expansion. A deviation in the dynamics from the *external emulsification* arises at the end of the first collapse as the bubble begins to jet into the droplet. After the first collapse, $t = 102\,\mu s$, the bubble re-expands with nearly half of its surface covered by the droplet as shown at $t = 148\,\mu s$. We also notice the injection of tiny bubbles from the main bubble into the droplet. The bubble translates towards the water droplet and during its second collapse, it becomes fully encapsulated in the droplet, $t = 171\,\mu s$. A distinct feature at this time is the toroidal rim or lamella of water

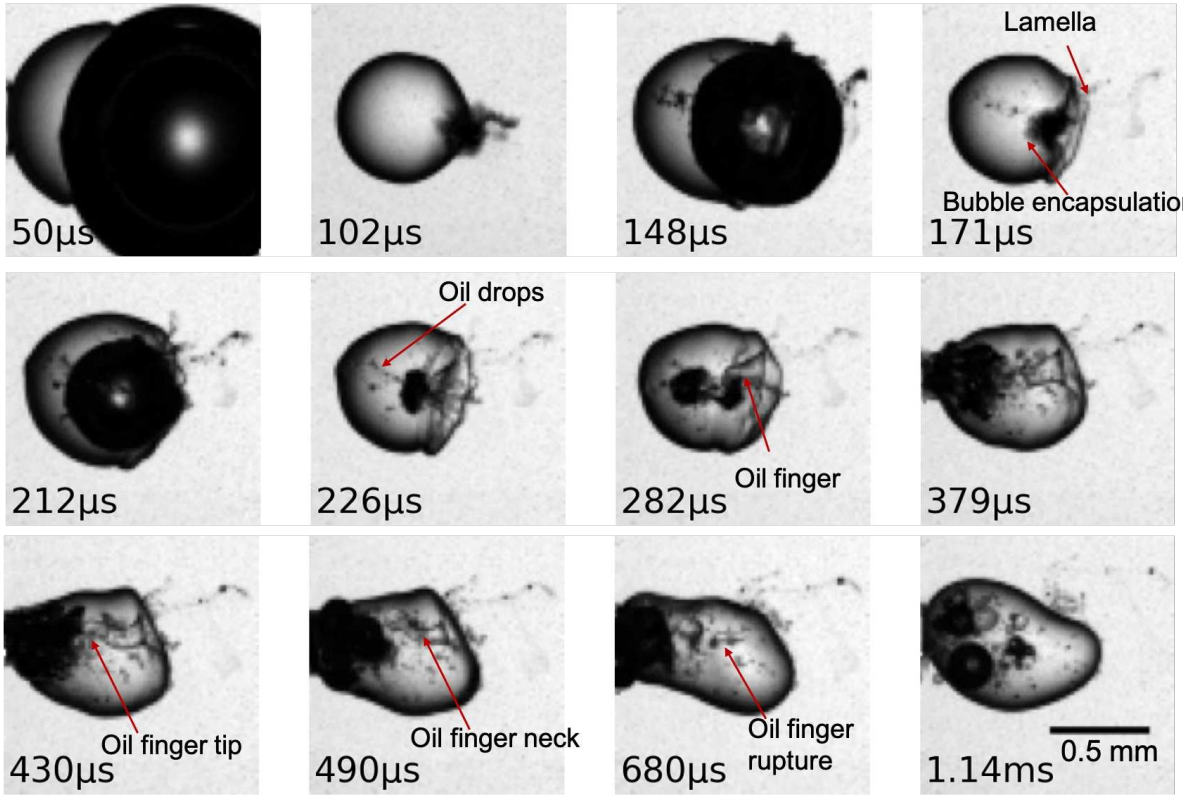

Figure 5.9: *Internal emulsification* regime with maximum bubble diameter of 1.28 mm in silicone oil with 5 mm^2/s viscosity. The centre-to-centre distance between the bubble and the droplet is 464 µm and the droplet diameter is 616 µm

on the right side of the droplet. During the re-expansion of the bubble within the droplet, we notice the entrainment of tiny oil drops into the water droplet emerging from the bubble's front at $t = 212$ µs. This is in contrast to the *external emulsification* scenario where the dispersed phase is injected into the continuous phase. During bubble collapse at $t = 226$ µs these oil droplets are stretched by the radial flow and thereby fragment into smaller droplets due to the Rayleigh-Plateau instability. Simultaneously the expansion and contraction of the lamella occur on the opposite side of the bubble. Also during bubble collapse, $t = 226$ µs, a finger-like structure of oil is injected from the lamella into the droplet, see $t = 282$ µs. That is likely caused by the translation of the bubble to the left. Over the next couple of bubble oscillations, the bubble moves further to the left and eventually leaves the droplet. The flow induced by the bubble translation stretches the oil finger. At $t = 490$ µs this structure breaks at the location indicated as *oil finger neck*, likely due to the Rayleigh-Plateau instability. As a result, two larger oil droplets are now suspended inside the water droplet, see $t = 680$ µs. Through this entire process, an oil-in-water emulsion is formed where the large droplets are due to destabilisation of the entrained column of oil, the *oil finger*, that is stretched by the translating bubble. In contrast, the fine emulsion is formed due to radial stretching from the translating bubble font. At this point, it is important to comment on the long-term fate of the engulfed gas bubbles inside the droplet during internal emulsification. The entire process of internal emulsification occurs within approximately two milliseconds. At such small time scales, we have observed that the bubbles still remain inside the droplet. However, the engulfed bubbles eventually move into the oil at later times (within a few seconds) due to buoyancy

and some get dissolved. We have not observed any entrapped bubbles inside the water droplets in the cuvette at later times.

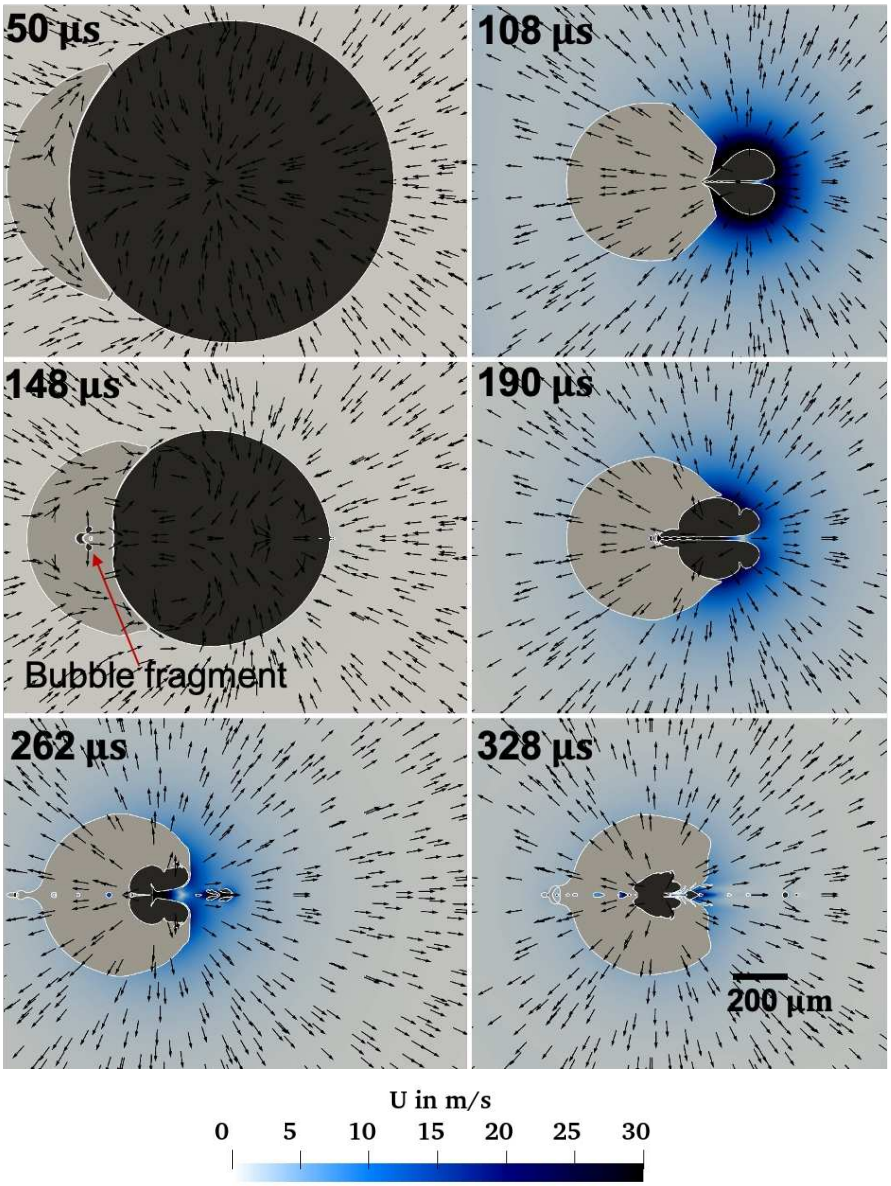

Figure 5.10: Numerically obtained temporal evolution of the interface profiles illustrating the process of the *internal emulsification* mechanism. The colour map shows the magnitude of the velocity field in the oil. The simulation parameters are chosen to correspond to the experimental case shown in figure 5.9.

To investigate the mechanism leading to the oil-in-water emulsion as compared to the previously observed water-in-oil emulsion we perform axisymmetric simulations with the experimental parameters taken from figure 5.9. The temporal evolution of the flow field and the fluid interfaces is illustrated in Figure 5.10. In the simulation, the bubble reaches its maximum expansion at $t = 50\,\mu s$ similar to the experiment. At $t = 108\,\mu s$, we observe jetting of the bubble into the droplet at the end of the first collapse. Similar jetting of the bubble into the droplet at the end of the first collapse is also noticed in figure 5.2 (c). Unlike the *external emulsification* scenario, the inertial forces exerted on the bubble dominate the viscous stresses. Therefore the bubble jets into the denser water droplet at

the end of its first collapse. The bubble proceeds to undergo a secondary expansion and attains its maximum radius in this cycle at $t = 148\,\mu s$. At this time we notice a tiny bubble fragment transported into the droplet. This matches well with the experimental observation showing the entrainment of bubble fragments just ahead of the bubble into the droplet at $t = 148\,\mu s$ in figure 5.9. Nearly complete encapsulation of the bubble inside the droplet is found at $t = 190\,\mu s$. Bubble encapsulation during the second collapse is observed in the experiments as well at $t = 171\,\mu s$. The bubble continues to jet into the droplet as it undergoes multiple cycles of expansion and collapse. This internal bubble jetting creates a pathway for the entrainment of oil inside the droplet. At $t = 328\,\mu s$, we observe entrainment of oil inside the droplet which leads to the formation of the *oil finger*. Clearly, the viscosity of the continuous medium is a critical parameter that decides between the regimes of external and internal emulsification.

5.3.5 Regimes

After examining 106 experiments, we could identify that the interaction between the cavitation bubble and the water droplet is most sensitive to the distance C_{dist} and the viscosity of the fluid. For consistency, the regime is observed during the first 2 oscillation periods of the bubble. If emulsification does not occur during these first two cycles the case is categorised as deformation. In the experiments we have varied the bubble diameter between 950 µm and 1733 µm, the distance C_{dist} between 330 µm and 1123 µm, and the viscosity between $5\,\mathrm{mm}^2/\mathrm{s}$ and $100\,\mathrm{mm}^2/\mathrm{s}$. The droplet diameter was fixed in all experiments, i.e. $D_{\mathrm{d}} = 616\,\mu m \pm 33\,\mu m$.
For small kinematic viscosities of the continuous phase, i.e. for $\nu \leq 20\,\mathrm{mm}^2/\mathrm{s}$ only deformation or internal emulsification are found. In this case, the dynamics are mostly determined by the centre-to-centre distance. An example for $\nu = 5\,\mathrm{mm}^2/\mathrm{s}$ is depicted in figure 5.11 (a). Above a value of $C_{\mathrm{dist}} \approx 650\,\mu m$ only the *deformation* regime is observed, while *internal emulsification* is dominant below this distance. This value is slightly larger than the droplet diameter, i.e. the bubble at maximum expansion forms a large contact area with the droplet. As a result, upon collapse the bubble jets into the droplet. At such a low viscosity, the inertia-dominated internal emulsification is the only emulsification regime observed.
For higher viscosities, we observe a transition from the internal to the external emulsification regime. Therefore it is instructive to look into the role of the two predominant forces acting on the cavitation bubble. Naturally, these are the inertial stress [34] given by

$$\tau_{\mathrm{in}} = \frac{3}{2}\,\rho_{\mathrm{oil}}\,\dot{R}_{\mathrm{b}}^2 \tag{5.2}$$

and the viscous stress given by

$$\tau_{\mathrm{vis}} = 4\,\nu\,\rho_{\mathrm{oil}}\,\frac{\dot{R}_{\mathrm{b}}}{R_{\mathrm{b}}}\ . \tag{5.3}$$

Let us identify the velocity $\dot{R}_{\mathrm{b}}$ with an average velocity of the bubble wall, $\left\langle \dot{R}_{\mathrm{b}} \right\rangle$, that can be obtained from the maximum bubble radius ($R_{\mathrm{b}}^{\mathrm{max}}$) and the Rayleigh collapse time ($T_c^{Rayleigh}$) [2] while ignoring viscosity,

$$T_{\mathrm{c}}^{\mathrm{Rayleigh}} = 0.91468\,R_{\mathrm{b}}^{\mathrm{max}}\sqrt{\frac{\rho_{\mathrm{oil}}}{P_{\mathrm{a}}}}\ , \tag{5.4}$$

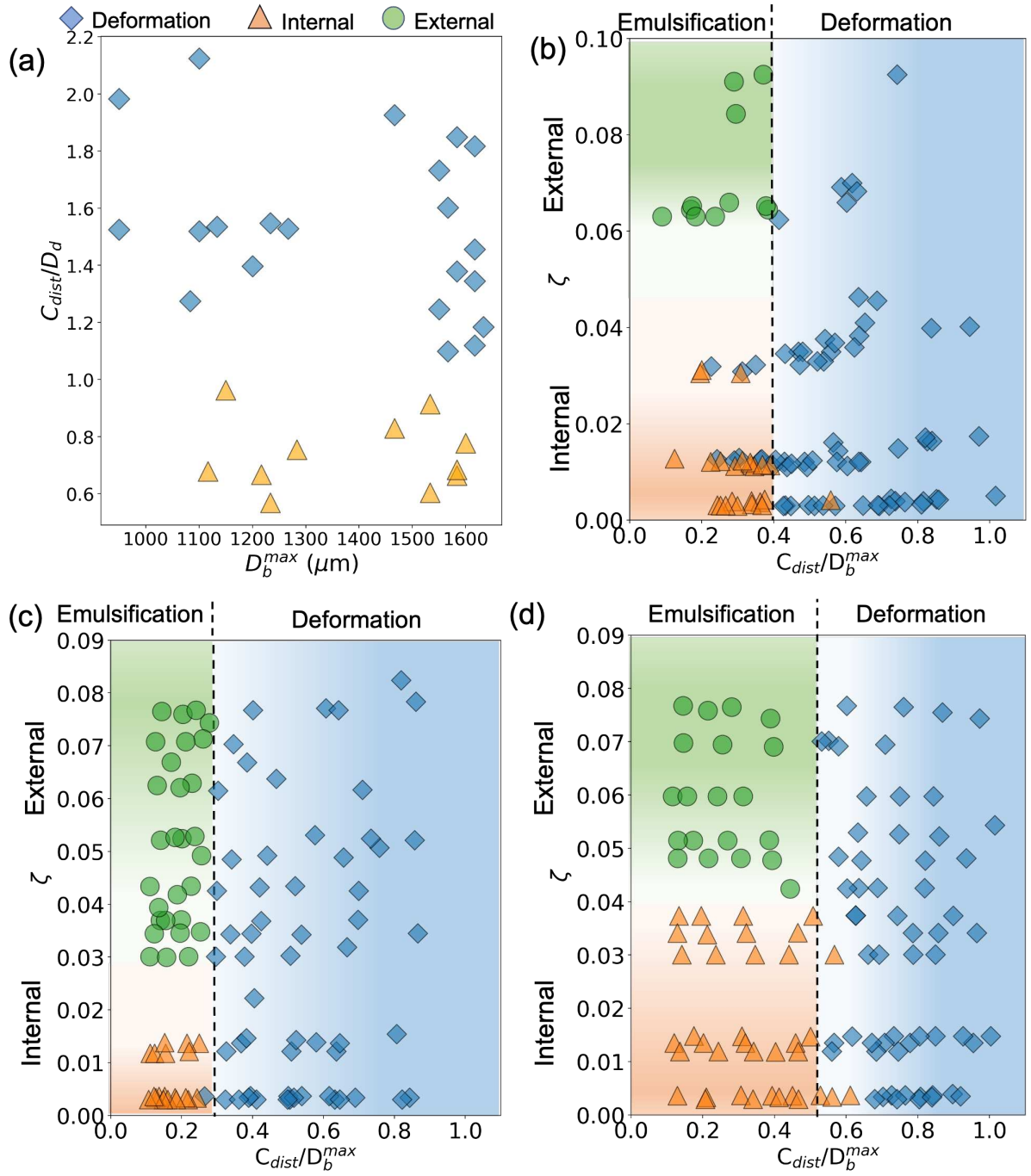

Figure 5.11: Regime map obtained between (a) centre-to-centre distance C_{dist} and maximum bubble diameter $D^{\mathrm{b}}_{\mathrm{max}}$ for silicone oil with viscosity $5\,\mathrm{mm^2/s}$ (b) ζ and $C_{\mathrm{dist}}/D^{\mathrm{max}}_{\mathrm{b}}$ at $D_{\mathrm{d}} = 616 \pm 33\,\mu\mathrm{m}$ (experiments), (c) $D_{\mathrm{d}} = 340\,\mu\mathrm{m}$ (simulations), (d) $D_{\mathrm{d}} = 980\,\mu\mathrm{m}$ (simulations) for viscosities in the range between $5\,\mathrm{mm^2/s}$ and $100\,\mathrm{mm^2/s}$. The regime map illustrates the three different regimes of micro emulsification: (i) *deformation* ($\diamond$), (ii) *internal emulsification* ($\triangle$), and (iii) *external emulsification* ($\bigcirc$).

$$\left\langle \dot{R}_{\mathrm{b}} \right\rangle = \frac{R^{\mathrm{max}}_{\mathrm{b}}}{T^{\mathrm{Rayleigh}}_{\mathrm{c}}} \approx 1.09 \sqrt{\frac{P_{\mathrm{a}}}{\rho_{\mathrm{oil}}}}\,, \tag{5.5}$$

where P_{a} is the ambient pressure taken as $10^5\,\mathrm{Pa}$. Then the ratio of the inertial to viscous

stresses is defined as

$$\zeta = \frac{\tau_{\mathrm{vis}}}{\tau_{\mathrm{in}}} \approx 4.88 \, \frac{\nu}{D_{\mathrm{b}}^{\mathrm{max}}} \sqrt{\frac{\rho_{\mathrm{oil}}}{P_{\mathrm{a}}}} \, . \tag{5.6}$$

The number ζ can be considered a *cavitation Reynolds number*. Please note that the viscosity of the droplet is ignored in this formulation.
Figure 5.11 (b) presents a parameter plot of the cavitation Reynolds number ζ as a function of the non-dimensional distance $C_{\mathrm{dist}}/D_{\mathrm{max}}^{\mathrm{b}}$ that covers all experiments between $5\,\mathrm{mm}^2/\mathrm{s}$ and $100\,\mathrm{mm}^2/\mathrm{s}$. We notice that around a value of $C_{\mathrm{dist}}/D_{\mathrm{max}}^{\mathrm{b}} \approx 0.4$ the bubble-droplet interaction is split between emulsification and deformation, i.e. for distances $C_{\mathrm{dist}}/D_{\mathrm{max}}^{\mathrm{b}} \lesssim 0.4$ emulsification is predominantly observed. Notice here the overlap between *deformation* and *internal emulsification* near the transition boundary. In order to be consistent, we have considered only the first two cycles of bubble oscillation to categorise our regimes. In certain cases, we have noticed internal emulsification after the first two cycles. However, based on our criterion to be consistent in defining ζ, we have categorised these cases as deformation. Since the first expansion of the bubble is approximately spherical, we can define ζ using its first maximum diameter $D_{\mathrm{max}}^{\mathrm{b}}$. The emulsification regime is additionally split into external and internal emulsification. This is because the direction of the jet depends on whether the forces counteracting the bubble collapse are dominated by viscosity (large ζ, jetting away from the droplet, external emulsification) or inertia (small ζ, jetting towards the droplet, internal emulsification). It should be noted that the transition boundary between internal and external emulsification lies somewhere between $\zeta = 0.03$ and 0.06. As we consider a fixed size of droplet diameter, the transition boundary is determined by the ratio of oil viscosity and maximum bubble diameter.
We now look into the role of the droplet diameter in the position of the transition boundary between the *deformation* and *emulsification* regimes. Figure 5.11 (c) and (d) illustrate the regime maps obtained from numerical simulations for $D_{\mathrm{d}} = 340\,\mu\mathrm{m}$ and $980\,\mu\mathrm{m}$, respectively. It is to be noted that $D_{\mathrm{d}} = 616 \pm 33\,\mu\mathrm{m}$ for the experimental regime map shown in figure 5.11 (b). When D_{d} is decreased to nearly half of this value in figure 5.11 (c), we notice that the transition boundary ($C_{\mathrm{dist}}/D_{\mathrm{b}}^{\mathrm{max}}$) shifts from 0.4 to 0.3. Similarly, the transition boundary is found to increase from 0.4 to 0.52 as we increase D_{d} to $980\mu\mathrm{m}$. At a given $C_{\mathrm{dist}}/D_{\mathrm{b}}^{\mathrm{max}}$, emulsification occurs if the oil-water and oil-gas interfaces come close to each other over a large area, allowing the bubble and the droplet to strongly interact such that a jet is formed. A smaller droplet inhibits this interaction and favours the *deformation* regime. However, a droplet with a larger diameter facilitates this interaction and promotes emulsification. For example, at $C_{\mathrm{dist}}/D_{\mathrm{b}}^{\mathrm{max}} = 0.4$ we observe *deformation* for $D_{\mathrm{d}} = 340\,\mu\mathrm{m}$ and emulsification for $D_{\mathrm{d}} = 980\,\mu\mathrm{m}$. Another interesting observation from figure 5.11 (c) and (d) is the influence of the droplet on the transition boundary between *internal* and *external* emulsification. For $D_{\mathrm{d}} = 340\,\mu\mathrm{m}$ this transition boundary is found for ζ between 0.015 and 0.03 at, while for $D_{\mathrm{d}} = 980\,\mu\mathrm{m}$ it is found at about $\zeta = 0.04$.

5.4 Conclusion

We have studied the interaction between water droplets in silicone oil and laser-induced cavitation bubbles that are created near the liquid-liquid interface. From the experiments we identify three distinct regimes of interaction, namely *deformation*, *external emulsification* and *internal emulsification*. The regimes are sensitive to the maximum bubble diameter $D_\mathrm{b}^\mathrm{max}$, the centre-to-centre distance between the bubble and the droplet C_dist, and the viscosity of the oil μ. We observe the *deformation* regime when the centre-to-centre distance was large. The droplet undergoes flattening and elongation as the cavitation bubble expands and collapses. As the bubble goes through successive cycles of oscillation, it acts as a flow source and sink, leading to a characteristic directional elongation of the droplet towards the bubble centre. For closer distances, the droplet is fragmented, which is primarily caused by a liquid jet formed by the collapsing bubble. The viscosity affects the direction of the jet. High viscosities lead to a jetting into the water droplet, while low viscosities to a jetting into the oil. The former leads to an oil-in-water emulsion (*internal emulsification*) and the latter to a water-in-oil emulsion (*external emulsification*). The experimental observations are nicely reproduced by simulations using a three-phase compressible volume of the fluid solver. Particularly, they verify that the decaying rebounds and collapses of the bubble contribute to a continuous transport of the two liquid phases into each other. It is further shown that the three regimes are separated in a parameter plot using the non-dimensional distance and a Reynolds number for cavitation.
The present work looked into the fundamental processes of cavitation bubble-induced emulsification of a low-viscosity droplet into a higher-viscosity liquid. While this was obtained with a laser-generated bubble with diameters in the millimetre range, emulsification based on acoustic cavitation at ultrasound frequencies uses smaller bubbles. We expect that these regimes and their boundaries also hold for ultrasound emulsification, yet this would need to be confirmed. The smaller spatial and shorter temporal scales together with lesser control of the bubble dynamics in acoustic driving add challenges to experiments. Here simulations using well-tested codes could be a way to understand emulsification from acoustic cavitation.

Funding

K.A.R. and J.M.R. acknowledge support by the Alexander von Humboldt Foundation (Germany) through the Humboldt and Georg Forster Research Fellowships. The work was supported in part by the Deutsche Forschungsgemeinschaft (DFG, German Research Foundation) under contract OH 75/4-1.

5.5 Appendix

Church [68] has modelled a spherical bubble shelled with a layer of linear elastic material that is surrounded by a viscous fluid. This model can easily be modified to describe a bubble surrounded by two layers of different viscous fluids by replacing the stresses of the elastic shell with the stresses of the viscous fluid. We start with equation (5) from Church and replace the stress of the linear elastic solid $T_{\mathrm{S},rr}$ with the viscous fluid stress of the shell of liquid 1, i.e. $T_{\mathrm{L1},rr} = 2\,\mu_1\,\partial u/\partial r$ and $\partial u/\partial r = 2\,R^2\,\dot{R}/r^3$. Integrating this expression from the bubble radius R_b to the shell radius R_d and keeping all other terms results in the model used for figure 5.6 (b),

$$R_\mathrm{b}\,\ddot{R}_\mathrm{b}\left(1+\frac{\rho_1-\rho_2}{\rho_1}\,\frac{R_\mathrm{b}}{R_\mathrm{d}}\right)+\dot{R}_\mathrm{b}^2\left(\frac{3}{2}+\frac{\rho_1-\rho_2}{\rho_1}\,\frac{4\dot{R_\mathrm{d}}^3-{R_\mathrm{b}}^3}{2{R_\mathrm{d}}^3}\,\frac{R_\mathrm{b}}{R_\mathrm{d}}\right)= \frac{1}{\rho_1}\left(p_\mathrm{g}-p_\infty-\frac{2\sigma_1}{R_\mathrm{b}}-\frac{2\sigma_2}{R_\mathrm{d}}-4\,\dot{R}_\mathrm{b}\left[\frac{\mu_1}{R_\mathrm{b}}-\frac{{R_\mathrm{b}}^2}{{R_\mathrm{d}}^3}\,(\mu_1-\mu_2)\right]\right)\,. \tag{5.7}$$

Here, the dynamic viscosity of the droplet is μ_1 and μ_2 for the continuous phase. Similarly, the density of the droplet and the continuous phase are ρ_1 and ρ_2, respectively. The surface tension between the gas phase and the droplet phase is σ_1 and the interfacial tension between the droplet and the continuous phase is σ_2. Because the liquid of the droplet is incompressible, the time-dependent droplet radius is a simple function of the bubble radius and the initial radius of the droplet,

$$R_\mathrm{d}(t)=\sqrt[3]{R_\mathrm{b}(t)^3+\left(R_\mathrm{d}(t=0)-R_\mathrm{b}(t=0)\right)^3}\,. \tag{5.8}$$

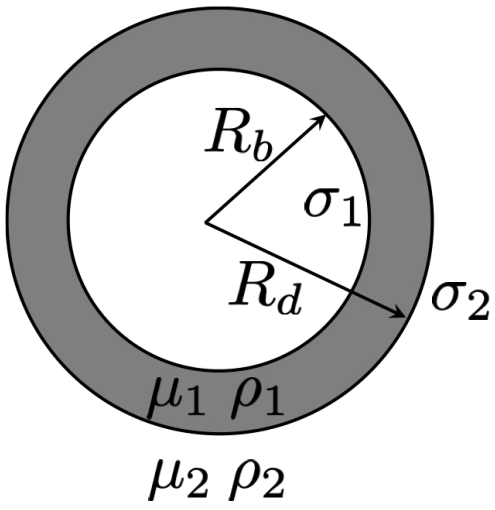

Figure 5.12: Schematic representation of an oscillating bubble inside a droplet that is suspended in a continuous phase.

6 Dynamics of pulsed laser-induced cavities on a liquid-gas interface: from a conical splash to a "bullet" jet

This work has been published in [24]:

J. M. Rosselló, H. Reese, and C.-D. Ohl. "Dynamics of pulsed laser-induced cavities on a liquid–gas interface: from a conical splash to a 'bullet' jet". *Journal of Fluid Mechanics* **939**, A35 (2022)

This work has been continued in [14]:

J. M. Rosselló and C.-D. Ohl. "Bullet jet as a tool for soft matter piercing and needle-free liquid injection". *Biomedical Optics Express* **13** (10), 5202–5211 (2022)

The inception of a cavitation bubble in a liquid by focusing a short and intense laser pulse near its free surface develops not only an upwards-directed jet but a second jet of opposite direction into the bulk liquid. When the laser is focused a few microns below the surface, the rapid deposition of energy produces a splash, whose later sealing gives origin to two particularly elongated opposing jets. Interestingly, the evolution of the downward jet flowing into the liquid pool has many similarities to that observed in free water entry experiments, e.g. the creation of a slender and stable cavity in the liquid. The downward jet can reach speeds of up to 40 m/s and travels distances of more than 15 times the maximum radius of the laser-induced cavity before losing momentum. The longer lifetime of this so-called "bullet" jet as compared to conventional cavitation-based jets, the alignment of the jet perpendicular to the free surface, and the possibility to scale the phenomenon open up potential applications when generated on small droplets or in shallow liquids. In this work, the underlying mechanisms behind the formation of the bullet jets are initially investigated by performing a set of experiments designed to address specific questions about the phenomenon under study. Those were followed by numerical simulations used to give a quantitative and detailed explanation of the experimental observations.

6.1 Introduction

The behaviour of air bubbles bursting into the atmosphere on a liquid-free surface has kept the attention of researchers for decades, especially due to the fast and long liquid jets they produce [206–209]. This natural phenomenon gave an explanation to the formation of sea mist, which plays an important role in the physical and chemical processes occurring on the ocean surface [210]. Thin liquid sheets that atomise into a mist may also be induced from oscillating vapour bubbles near a free surface. These cavitation bubbles can be created by an electrical discharge [211, 212], or by the dielectric rupture of the liquid provoked by a high-power focused laser pulse [88, 97, 213–217]. Those studies discuss the dynamics of cavities produced at different distances below the liquid level, and also the formation of an upward liquid jet rising from the surface after the cavity collapse [5, 211, 218–220]. In most of the existing literature on this topic, the behaviour of both the submerged cavity and the subsequent upwards-directed jet was classified using a single

parameter, the stand-off distance $\gamma = h/R_{\max}$, defined as the ratio between the depth where the bubble is initially produced h (see figure 6.1 (a)) and the maximum radius achieved by the bubble during the initial expansion phase $R_{\max}$ [88]. The latter definition carries with it some ambiguity issues related to the fact that, as the bubble gets closer to the liquid boundary, its deviation from a spherical shape becomes more pronounced, and thus the dilemma on how to measure $R_{\max}$ sets in. In addition to the uncertainty introduced by the bubble deformation, the cavity centre might displace during expansion. These issues do not allow a direct comparison between results performed by different authors, considering that in many existing studies the specific method used for measuring $R_{\max}$ is not even mentioned. Lauterborn et al. [117] proposed an alternative normalised stand-off distance D^* given by

$$D^* = \frac{h}{R_{\max,\text{unbound}}} \ , \tag{6.1}$$

where $R_{\max,\text{unbound}}$ is the maximum radius of a bubble produced under fixed initial conditions, for instance by using a defined laser pulse to generate a cavity far away from the surface, i.e. in an unbounded liquid. This definition is useful for comparing cases of bubbles close to any kind of boundary (e.g. a solid or an elastic boundary, bubbles growing next to a crevice or non-planar objects, etc.), but in particular for cases where the gas cavity does not preserve its initial mass, like for example when the cavity is not perfectly sealed. Further details about this discussion can be found in the appendix, section 6.5.1.
The fluid mechanics following the impact of rigid objects is catalogued in literature as the water entry problem. Duclaux et al. [221] and Aristoff and Bush [222] studied the water entry of small hydrophobic spheres into a liquid pool. Generally, the impact leads to a splash above the water-air interface and the formation of a deep and slender cavity in the liquid. A similar splash curtain was observed by Bergmann et al. [223] after a flat disk was suddenly submerged in water. For sufficiently high impact speeds or high Weber numbers the splash curtain closes from its top and seals the cavity from the ambient air. Similarly, for impact velocities above 3 m/s in water, Mansoor et al. [224] noticed that the cavity produced in the liquid by the passage of the object was partially filled with a fine spray during the closure of the splash. Recently, Eshraghi et al. [225] performed detailed measurements of the splash curtain closure dynamics and compared those with an analytical model.
In this work we study the cavity and plume dynamics generated by a nanosecond laser pulse focused close to a free surface, in particular, the case of a bubble initially produced just below the liquid interface (i.e. a few tens of microns below the surface). Similar to the fluid mechanics created by an object impacting on a free surface [226], laser focusing gives origin to an explosive expansion of a cavity front into the liquid and a recoil-induced material expulsion (or splash) into the air [196, 227, 228]. While typical impact velocities of objects result in cavity front velocities of tens of meters per second, and splashes rising in the opposite direction with similar velocities, laser-induced splashes are considerably faster. For instance, in a case of a laser pulse focused on the surface of water with a radiant exposure of 5 J/cm^2, the induced plasma originates a gas cavity in (and below) the liquid interface which expands at 590 m/s, and also producing a splash that rises up with an average velocity of 150 m/s, as reported by Apitz and Vogel [228].
Here we present a phenomenon which combines the two physical mechanisms described above, namely the splash dynamics and the formation of a jet from the collapse of a transient cavity created just below a standing liquid surface. This finite-length liquid jet

is formed after the closure of a splash canopy, which takes the shape of an inverted cup usually referred to as a water "bell" [229]. While one would expect a splash moving away from the surface, the initially outward splash changes direction and moves towards the liquid bulk, resulting in a jet that penetrates into the water from the top. The dynamics of a liquid splash produced by localised explosions (or even impacting objects) have already received considerable attention. Nevertheless, the formation of such a downward jet has not been fully addressed yet. The resulting shape of the elongated gas cavity linked to this kind of jet resembles a bullet entering a liquid (see Bodily et al. [230] and Kiyama et al. [226]) and we have therefore termed this regime the "bullet jet regime".
In general, jets developed from the collapse of a bubble are defined by their boundary conditions, for instance by the stand-off parameter and characteristics of the surrounding surfaces (e.g. geometry, hardness or elasticity) [84, 88, 98, 102, 231]. In contrast to the bubble jets discussed in the current literature, the "bullet" jets presented in this work are remarkably less sensitive to the presence of neighbouring surfaces, which makes them an interesting case of study. Some unique aspects are: the relatively long distances that the liquid stream can reach, and also the amount of fluid transported in the liquid jet. Furthermore, this kind of jet could be of use in diverse applications like bubble cleaning [80], or a drug delivery system that automatically directs the drug to a specific location repeatably, like micro-vaccination or drug delivery platforms [12, 13, 232].

6.2 Experimental method

In this study, we nucleate a bubble with an IR laser pulse (*Quantum Light Instruments Q2*, wavelength 1064 nm, energy of (850 ± 10) µJ, 4 ns of duration) focused with a microscope objective (*Zeiss LD Achroplan 20×*, NA = 0.4) at a distance h below the free surface of water. The liquid was contained in an optical glass cuvette shaped like a rectangular prism with sides of 1 cm and a height of 5 cm (see figure 6.1 (a)). The dimensions of the plasma spot created by the laser pulse were measured using a combination of optical filters to avoid the glowing effect and pixel saturation in the video frames, obtaining a repeatable elliptical spot with a length of (92 ± 2) µm in the incident direction of the laser beam and (60 ± 2) µm in the direction perpendicular to the beam. That plasma produced spherical bubbles with a maximum radius of (585 ± 5) µm when focused far away from the liquid surface (i.e. some millimetres). The position of the plasma spot geometrical centre fluctuated within an interval of 15 µm in the direction of incidence of the beam.
The water level in the cuvette was continuously monitored and h could be adjusted with micrometric precision by modifying the relative distance between the liquid surface and the laser focusing position. When the bubble was produced a few tens of microns below the liquid surface, an accurate measurement of the plasma spot depth h was not always possible, mostly due to the distortion of the image produced by the reflection (and diffraction) of rays on the inner side of the interface, and also caused by an imperfect camera alignment. Therefore, we determined h with a pixel size precision from the distance between the shock wave emitted during the bubble generation and its reflection on the liquid surface (see appendix, section 6.5.1). When the latter was not possible, for example when the frame rate used was not fast enough to visualise the shock waves, h was estimated from the geometrical centre of the plasma/initial bubble, although this alternative method was less accurate.
High-speed video recordings of the surface liquid splash produced after the laser dielectric

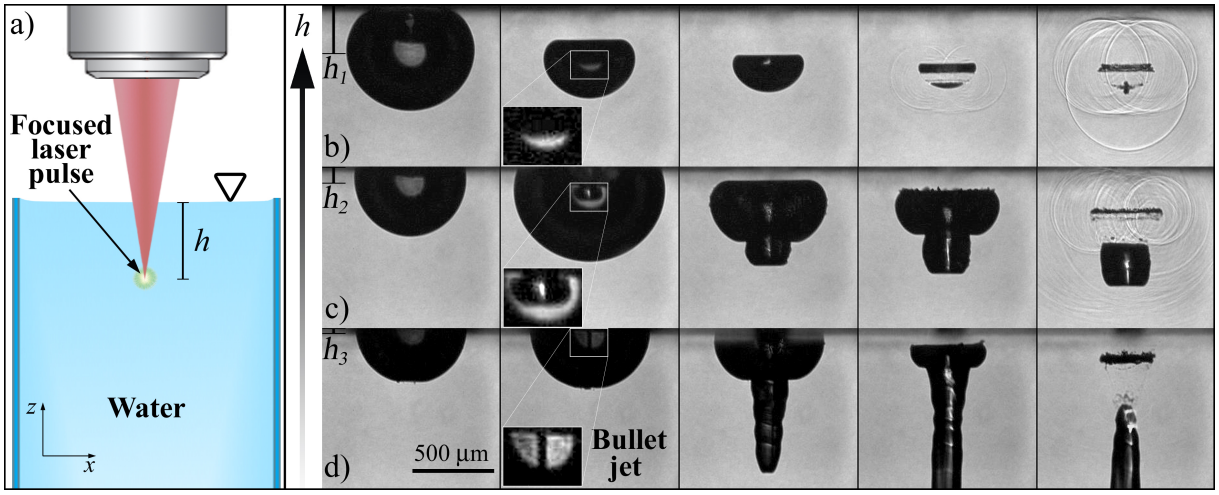

Figure 6.1: Experimental setup and bubble jet shape evolution for measurements with different depths of the focused laser pulse. (a) A bubble is created in the bulk of a static liquid by focusing an IR laser pulse at a depth h below the surface. The error in the inception depth was 10 µm. (b) Jetting bubble at $h_1 = 580$ µm. The times of the frames are 60, 70.6, 73.8, 75.2 and 75.6 µs. (c) Jet formation at $h_2 = 194$ µm. The times of the frames are 10, 51, 66, 69 and 74 µs. (d) The "bullet" jet is produced at a depth $h_3 = 86$ µm. The times of the frames are 15, 26, 38, 49 and 53 µs. See online supplementary movies 1-3.

rupture and also of the resultant bubble dynamics were taken with a *Shimadzu XPV-X2* camera. The optical magnification was performed with a 5 × long-distance microscope objective (*Edmund Optics*) in combination with a macro lens (*LAOWA f2.8*) with a variable magnification of up to 2 ×. As the focal plane differs for objects above and below the liquid-free surface. For instance, the liquid curtain composing the splash and the details of the submerged gas cavity, a second high-speed camera (*Photron AX-Mini 200*) was used in some of the experiments. In those cases, the two cameras were set to obtain simultaneous video recordings of the same event, duplicating the magnified image by means of a 30:70 plate beamsplitter. As a measure to optimise the image quality, each one of the cameras was set to have a defined focus (and zoom level) in a region occupied just by one of the two media, the air or the liquid. Interestingly, this technique also allowed us to record distinct aspects of the phenomenon with different characteristic speeds, using two temporal resolutions and video lengths.
The light sources in the shadowgraphs were either given by a pulsed femtosecond laser (*Ekspla FemtoLux 3*, $\lambda = 515$ nm;) emitting ultra-short pulses (230 fs) at a frequency of 5 MHz, or a continuous white LED lamp *SMETec* with 9000 lm. While the pulsed laser illumination was ideal to capture the ultra-fast dynamics of the shock waves and the liquid splash, the LED lamp was intense enough to visualise the internal structure of the jets using diffused back illumination.

6.3 Experimental results

It is well established in the literature that the dynamics of both the induced bubble and the subsequent jet (occurring after the cavity collapse), are strongly dependent on the nucleation distance h [88, 211, 212, 220]. Figure 6.1 depicts the resulting dynamics for laser-induced cavities produced at three decreasing distances (i.e. $h_1 > h_2 > h_3$). For the

larger distance, here $h_1 = 580 \pm 10\,\mu m$ (i.e. $D_1^* \simeq 1$), a concavity (with a curvature similar to the radius of the bubble) is observed on the bubble side closer to the liquid surface during the collapse. At the minimum bubble volume, the concave side of the bubble hits the opposite bubble wall along a contact line similar to a ring, and a complex sequence of multiple shock waves is emitted (see last frame in figure 6.1 (b)). When the nucleation distance h is reduced to $h_2 = 194 \pm 10\,\mu m$ ($D_2^* = 0.33$) as in figure 6.1 (c), a broad jet is visible within the bubble about 50 µs after its generation (see inset). This jet penetrates the bubble along the direction normal to the liquid surface and impacts the lower side of the bubble, folding the whole cavity into a *tubular* shape. If the distance h is progressively reduced, this is if the laser-induced bubble is produced even closer to the liquid surface, the thickness of the jet piercing the gas cavity is also gradually reduced. A limit case is obtained when the laser is focused $\sim 100\,\mu m$ below the surface (here at $h_3 = 86 \pm 10\,\mu m$; $D_3^* = 0.15$) as shown in figure 6.1 (d). In the figure inset, a thin downward jet is clearly visible. This liquid jet penetrates the lower bubble wall with a speed of around 40 m/s and forms an elongated lower cavity. This cavity remains considerably more stable than in the cases with depths h_1 and h_2, and it also does not undergo a violent collapse.
Both the dynamics of the bubbles and the jets of cases similar to the ones shown in figure 6.1 (b) and (c) have already been extensively discussed in the literature, e.g. [5, 88, 97, 211, 219], therefore we will not discuss those cases in detail and will focus on the bullet jets instead, i.e. the one in figure 6.1 (d). In what follows we will refer to the cases with $h \gtrsim h_3$ as "standard jets".
Now let us study the underlying mechanisms behind the bullet jet formation. figure 6.2 (a) presents an image sequence taken at 72 kfps showing the complete jet dynamics, i.e. both the splash above the liquid surface and the temporal evolution of the submerged cavity. Those pictures reveal that the main difference between the bullet jet case (i.e. when the laser is focused very close to the liquid surface) and the standard cases described in figure 6.1 (b) and figure 6.1 (c) is caused by a shortly opened splash that is explosively ejecting the vapour produced from the laser plasma into the atmosphere (see appendix, section 6.5.2). The images also suggest that the thin downward jet observed in the bullet jet case of figure 6.1 (d) is the result of the closure of a canopy formed during that initial splash. The canopy first takes the shape of a water bell and then collapses towards the liquid pool pushing the origin of the thin jet downwards. As the thin jet pierces the bottom of the cavity, the gas surrounding the central laminar jet is driven downwards, shaping a continuously growing cavity in the direction of the jet.
The later dynamics of this elongated cavity are depicted in figure 6.2 (b). The bottom end of the cavity in the time series is connected with a solid blue line that has an initial slope of 35 m/s and progressively slows down to a speed of 10 m/s. As discussed below in section 6.3.5, the gas phase of the standard jets collapses shortly after the liquid jet passes through the submerged cavity, which results in a violent fragmentation of the gas phase and the "extinction" of the jet. When compared with the standard jets, the elongated cavity found in the bullet jets is remarkably stable. As an example, the jet/cavity in figure 6.2 (b) penetrates more than 3 mm deep before losing momentum, which is about 15 times the maximum radius of the laser-induced cavity.

6.3.1 Details of the bullet jet formation

A closer inspection of the liquid splash behaviour above the surface reveals the precise way in which the canopy is sealed to form a water bell, and also how little liquid droplets are sprayed back into the cavity, as shown in figure 6.3 (a) (i.e. in the frames between 8

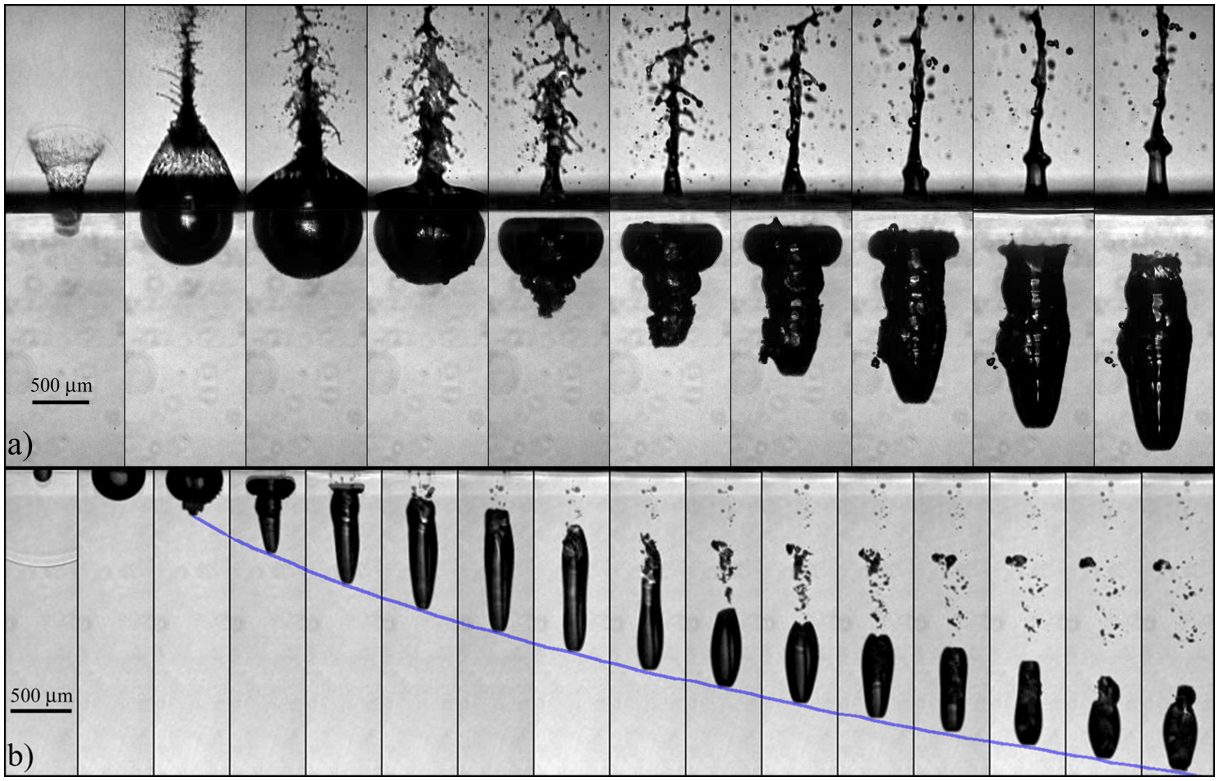

Figure 6.2: Overview of the resulting "bullet" jet dynamics. (a) The image sequence was composed by combining two different high-speed videos taken simultaneously with two cameras at 72 kfps. One of the cameras was set to focus on the splash above the water level, while the remaining one was set to focus on the submerged cavity. Here, $D^* = 0.15$. (b) Long-term bullet jet dynamics ($D^* = 0.08$.). The time between frames is 10 µs. The solid blue line indicates the jet tip position extracted from the complete video. The liquid jet pierces the wall of the cavity with a speed of 35 ± 2 m/s. After ~ 130 µs, the jet slows down and dissolves at a depth of ~ 3 mm. See online supplementary movies 4.

and 26 µs). These images confirm that the origin of the "bullet" jets resides in the detail of the superficial splash dynamics.

The key moments of the jet's temporal evolution are summarised in figure 6.3 (b). Initially, the laser shot produces a fine liquid spray upwards immediately followed by a conically shaped splash curtain with a mean wall thickness of 20 ± 5 µm (obtained from an inspection of the experimental images). As the hemispherical cavity below starts growing, the pressure of the gas in its interior is rapidly lowered. This pressure difference (Δp) between the outside and the inside of the cone acts as the main driver of the splash, also influenced by the surface tension (σ). Thus, the angle formed by the splash wall and the water surface (θ) is increased and the cone closes from the top forming a water bell (e.g. first row in figure 6.3 (a)). Right before cavity sealing, a fine mist is sucked into the bell due to Δp along the symmetry axis (Thoroddsen et al. [196]) at $r = 0$. Those liquid particles are followed by the formation of a thin liquid jet directed downwards, together with the vertical collapse of the water bell. As the water bell gets almost flattened the thin jet pokes the wall of the laser-induced cavity and flows smoothly into the liquid pool dragging the gas around the cavity centre with it, and also driving the gas into the elongated part of the cavity by reshaping it with the jet tip.

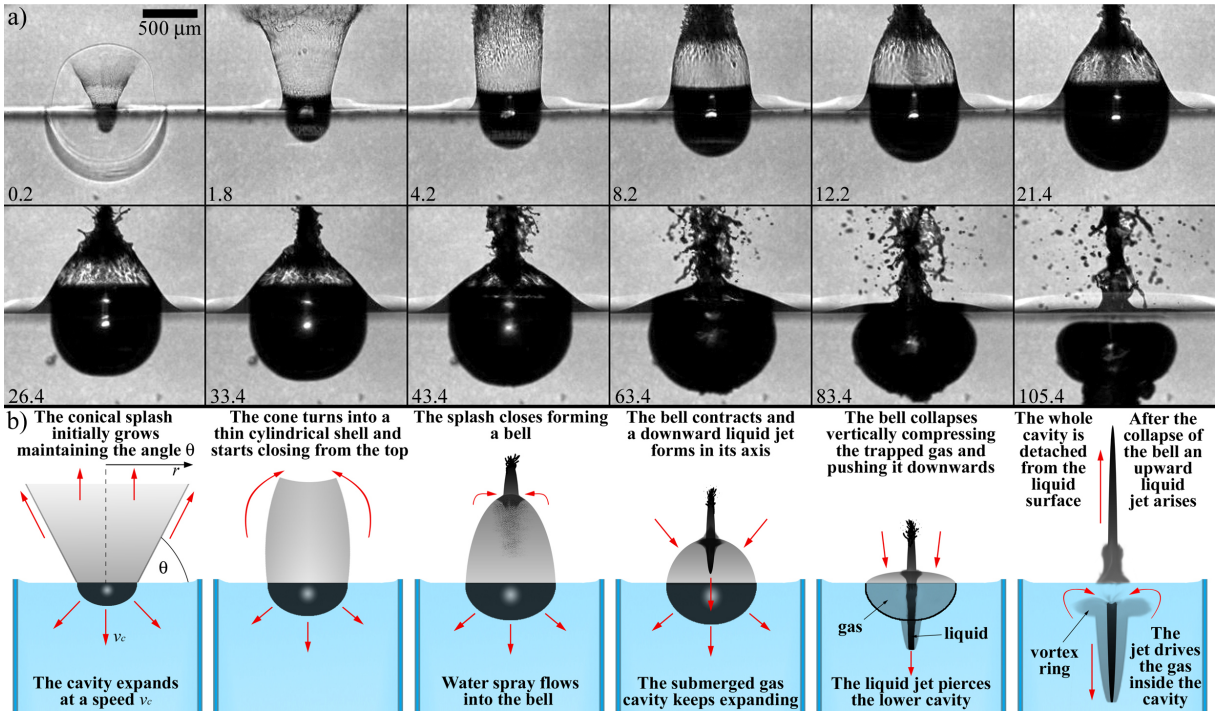

Figure 6.3: Details of the bullet jet formation process. (a) High-speed video frame sequence composed from two equivalent measurements taken with 5 Mfps and 1 Mfps. Here, $D^* = 0.14$. The numbers indicate the time in µs after the focused laser shot. Full video available in online supplementary movie 5. (b) Key moments in the bullet jet formation. The red arrows represent the motion of the liquid.

6.3.2 Modelling the splash dynamics

The shape and closure of the splash can be modelled as an axisymmetric water bell following the analysis of Clanet [229] and Aristoff and Bush [222]. This formulation is derived from the Bernoulli equations for a flow in a stationary film. It takes into account the Laplace pressure from the local curvature of the film and an additional pressure difference Δp across the sheet. The equations in non-dimensional form are

$$\frac{d\phi}{ds'} = \frac{\alpha r' - \cos\phi}{\mathrm{We}_s - r'} , \tag{6.2}$$

$$\frac{dr'}{ds'} = \sin\phi , \tag{6.3}$$

where ϕ is the angle of the splash to the vertical (i.e. $\pi/2 - \theta$ in figure 6.3 (b)), $r' = r/R_c$ is the non-dimensional distance of the splash from the symmetry axis, s' is the arc length along the central line of the sheet, $\alpha = \frac{\Delta p\, R_c}{2\,\sigma}$ the pressure coefficient and $\mathrm{We}_s = \rho\, v_s^2\, \delta_0/(2\,\sigma)$ the Weber number of the sheet. The pressure difference between inside and outside the cavity is $\Delta p = p_0 - p_c$ (i.e. the difference between the ambient pressure p_0 and the pressure inside the conical cavity p_c), v_s is the speed of the splash, and the average cavity radius at the surface level and sheet thickness is R_c and δ_0, respectively. The closure of the splash may be caused by surface tension and/or the pressure difference between the outside and the inside of the splash curtain Δp. Here we model the pressure reduction with the expansion of the gas contained in the hemispherically shaped cavity below the splash. The dynamics of the gas within the splash is simplified to that

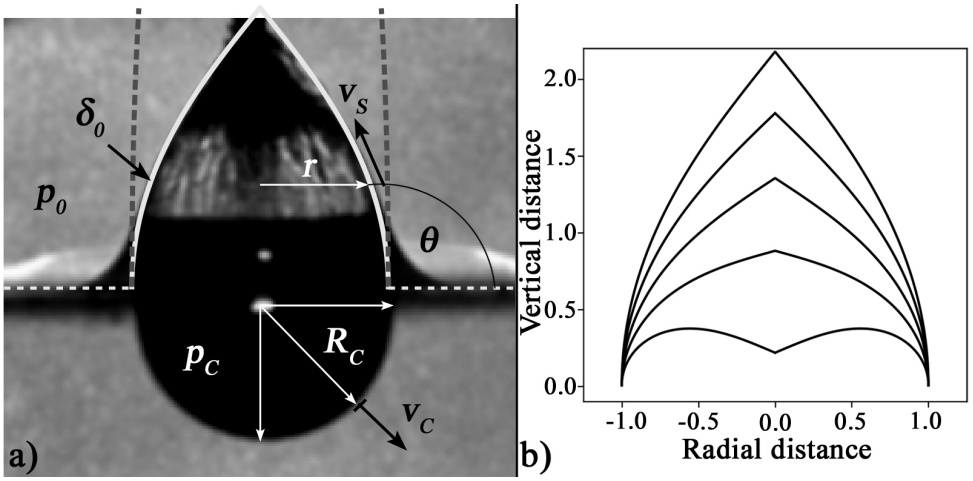

Figure 6.4: (a) Comparison of the experimental splash of figure 6.3 (a) at time $t = 20\,\mu s$ with the water bell model. The solid line accounts for a pressure drop from the piston-like expanding submerged cavity and the dashed line is the result in absence of this pressure difference. (b) Development of the splash shape once it is closed and its velocity reduces. The splash velocities and Weber numbers of the sheet from top to bottom are $v_s = 20, 17, 14, 11, 8\,m/s$ and $We_s = 55.6, 40.1, 27.2, 16.8, 8.9$ respectively. The radial and vertical scale are non-dimensionalised with the cavity radius R_c.

resulting from the motion of a flat cylindrical piston moving downwards with velocity v_c, i.e. the velocity of the cavity bottom. This leads to a reduced pressure region between the modelled cylindrical cavity and the far field static pressure $p_0 = 1\,bar$. From gas dynamics [233], the pressure at a planar piston surface p_c is

$$p_c = p_0 \left(1 - \frac{\gamma - 1}{2} \frac{v_c}{c_0}\right)^{2\gamma/(\gamma-1)} , \tag{6.4}$$

where γ is the ratio of specific heats and $c_0 = \sqrt{\gamma \mathcal{R} T_0}$ is the speed of sound at temperature T_0. Now we insert this pressure term into the water bell model [222]. First let us investigate the shape of the splash around the time of closure, i.e. $t \approx 20\,\mu s$. Then the velocity of the cavity wall has reduced to a measured $v_c = 40\,m/s$ and the splash velocity is approximately $v_s = 20\,m/s$, which can be determined by following the upward motion of the wrinkles of the liquid curtain (see figure 6.3 (a)). The initial conditions for the equations (6.2) and (6.2) are given by the radius of the cavity and an initial angle of 0° to the normal. Additionally, we estimated the mean thickness of the splash in $\delta_0 = 20 \pm 5\,\mu m$ and use as the coefficient of surface tension $\sigma = 0.07\,N/m$. The remaining parameters going into the model are $\gamma = 1.4$ and the liquid density $\rho = 1000\,kg/m^3$. The Weber number of the sheet at $t \approx 20\,\mu s$ is $We_s \approx 55$. Applying these values to the water bell model we obtain a shape that closely resembles the sheet in the experiment, see figure 6.4. In contrast, when the pressure difference Δp is ignored, the simulations predict a nearly straight upward splash, as represented with dashed grey lines in figure 6.4 (a). There, a potential closure of the splash would be only driven by surface tension, as investigated by Aristoff and Bush [222].

In the experiment we find that once the splash closes, the opening angle of the approximate cone-shaped splash increases and eventually a downward jet forms at the apex. Using the splash model, these dynamics can be reproduced. For this, we assume that once the splash has closed, the volume of the bubble remains approximately constant, i.e. while

the hemispherically shaped lower part increases in volume, the volume of the conical region enclosed by the splash decreases. This assumption was verified with the CFD simulations presented in figure 6.6 of section 6.3.4. As a result, the bubble pressure also remains constant. Yet, as the radial expansion of the cavity is decelerating, the upwards velocity is slowing down too. In figure 6.4 (b) the shapes of the splash with the same parameters as in figure 6.4 (a) are plotted for splash velocities ranging from $v_s(t_0) = 20\,\mathrm{m/s}$ to $v_s(t > t_0) = 8\,\mathrm{m/s}$. Remarkably, the deceleration of v_s transforms the shape of the closed splash from convex to concave, meaning that at later times, i.e for the lower values of the splash velocity, the liquid in the splash will be focused downwards. This may explain how the "bullet" jet is injected and focused centrally into the cavity.

6.3.3 Numerical simulations of the jet dynamics using OpenFOAM

The water bell formation model implemented in the previous section provides an analytic interpretation of the cavity closure and also gives a rough explanation of the origin of the water jet that produces the bullet jets. Although that simple model covers the very basics, it is insufficient to address the details of such a complex phenomenon. Accordingly, those details were studied by implementing numerical Volume of Fluid (VoF) simulations carried out using OpenFOAM [125]. Specifically, a modified version of the numerical solver `multiphaseCompressibleInterFoam` suitable to simulate N compressible, viscous, and non-isothermal fluids was used. For the sake of simplicity, temperature non-homogeneities are neglected in this work. The solver uses phase fractions to model interfaces between components by assigning a scalar field α_j to each component. α_j specifies the relative amount of each component in the respective cell, meaning that it assumes values ranging between 0 and 1, and $\sum_j \alpha_j = 1$.
The present problem features 3 fluid components: a liquid domain (water), a gaseous domain (air), and the bubble contents, which are treated as a non-condensable gas for the lack of an implemented phase transition model. The properties of the gas inside the bubble are considered to be the same as in the gaseous domain, but computed as a separate component, to enable precise control over the amount of gas present in the bubble in its early expansion phase. The surface tension between these two gaseous components is kept at 0, making them physically the same type of gas; the distinction between them is purely computational. The surface tension between the liquid and the respective gaseous components is $0.07\,\mathrm{N/m}$.
The compressibility is accounted for by the Tait equation of state

$$p = (p_0 + B)\left(\frac{\rho}{\rho_0}\right)^{\gamma} - B \ , \tag{6.5}$$

with the values $p_0 = 101325\,\mathrm{Pa}$, $\rho_0 = 998.2061\,\mathrm{kg/m^3}$, $\gamma = 7.15$, $B = 303.6\,\mathrm{MPa}$ for water and $p_0 = 10320\,\mathrm{Pa}$, $\rho_0 = 0.12\,\mathrm{kg/m^3}$, $\gamma = 1.33$, $B = 0$ for the gas domains (i.e. atmospheric and inside the bubble), turning the equation of state into the ideal gas equation.
To counteract numerical errors that change the amount of gas within the bubble during its initial expansion, the mass of the bubble gas is kept constant by applying the correction $\rho \rightarrow \frac{m_0}{m}\rho$ at every time step, ρ being the density field of the gas component used to produce the bubble and the mass of this gas being calculated as $m = \sum_i^{\mathrm{cells}} \alpha_{j,i}\,\rho_{j,i}\,V_i$. To account for condensation, 70 % of the bubble mass is removed when the cavity reaches its first maximum volume. For a closed bubble this gives a good approximation for the first and second bubble oscillation cycles. If the cavity opens, the gas/vapour initially inside

the bubble is almost completely replaced by the atmospheric gas, meaning that the applied condensation correction is likely less accurate than for a closed bubble. Even so, the same correction is applied in all cases for the sake of consistency, but it has a negligible effect on the open cavity case. Another correction is imposed onto the α_j fields to counteract tiny bubbles and droplets forming amidst the bulk of the fluid due to numerical errors by setting values of $\alpha_j < 0.001$ and $\alpha_j > 0.999$ to $\alpha_j = 0$ and $\alpha_j = 1$, respectively.
The computed domain describes a straight cylinder of length $l = 15\,\text{mm}$ and radius $r = 5\,\text{mm}$, which is filled to a height of 10 mm with water, the rest being filled with the gaseous component. Due to the axisymmetric nature of the present problem, the geometry is represented by a radial slice of the cylinder described above, creating an effectively two-dimensional simulation. Compared to the size of the bubble, the outer boundaries are far away and equipped with open, wave transmissive boundary conditions, representing an infinitely extended fluid domain.
The bubble is created along the axis of symmetry at a variable height and initial radius. The initial pressure is chosen to satisfy the condition $\rho_{\text{bubble}} = \rho_{\text{liquid}}$ to resemble a plasma spot produced by a short laser pulse that has not had time to significantly expand yet, which with the fluid properties results in an initial pressure of $p \approx 16.8\,\text{kBar}$. The initially spherical shape of the bubble tends to be perturbed by Rayleigh-Taylor instabilities, which are avoided by smearing the initial bubble interface. The energy of the bubble and thus its maximum radius can be modified by varying the initial bubble radius or pressure. In the experiments, this can be done by adjusting the energy of the laser pulse that produces the cavity.

6.3.4 Analysis of the bullet jets formation through numerical VOF simulations

The OpenFOAM simulations were set up to match the experimental conditions and then compare the dynamics of both simulated and experimental jets. Figure 6.5 presents an image sequence detailing the simulated bubble dynamics for a prototypical case with $D^* = 0.155$. In general, the agreement between the simulation and the experiments (e.g. the ones in figure 6.2 and figure 6.3) is excellent. While the model is not able to reproduce the dynamics of the fine mist ejected after the plasma rapid expansion [234], the overall dynamics of the splash and the characteristic features of the bullet jets were captured by the model, as displayed in figure 6.5 (a). Some of these features are: the closure of the splash/liquid curtain; the development of the elongated bubble with a central liquid jet that occurs after the piercing of the submerged cavity; and the shape of the upward jet produced after the water bell collapses towards the surface. The last frame of the sequence in figure 6.5 (a) is represented using a volume of fluid tracking technique to demonstrate that the liquid "injected" into the liquid pool by the bullet jet is coming exclusively from the surface. This interesting feature can be relevant for certain applications as discussed in section 6.3.8.
Figure 6.5 (b) present a qualitative comparison between the simulated results and an experimental case with similar parameters (i.e. D^* and R_{cm}). The evolution of both the experimental and the simulated submerged cavities is similar until the jet pierces the submerged cavity wall. After that, the times of the experimental and simulated matching frames in figure 6.5 (b) have an increasing shift. The simulated jet advances into the pool faster, differing from the experiment in 10 % at the beginning and ending the image sequence with a speed difference of roughly 25 %. This can be explained by the difference in the thickness and shape found on the simulated and experimental downward jets. A flat

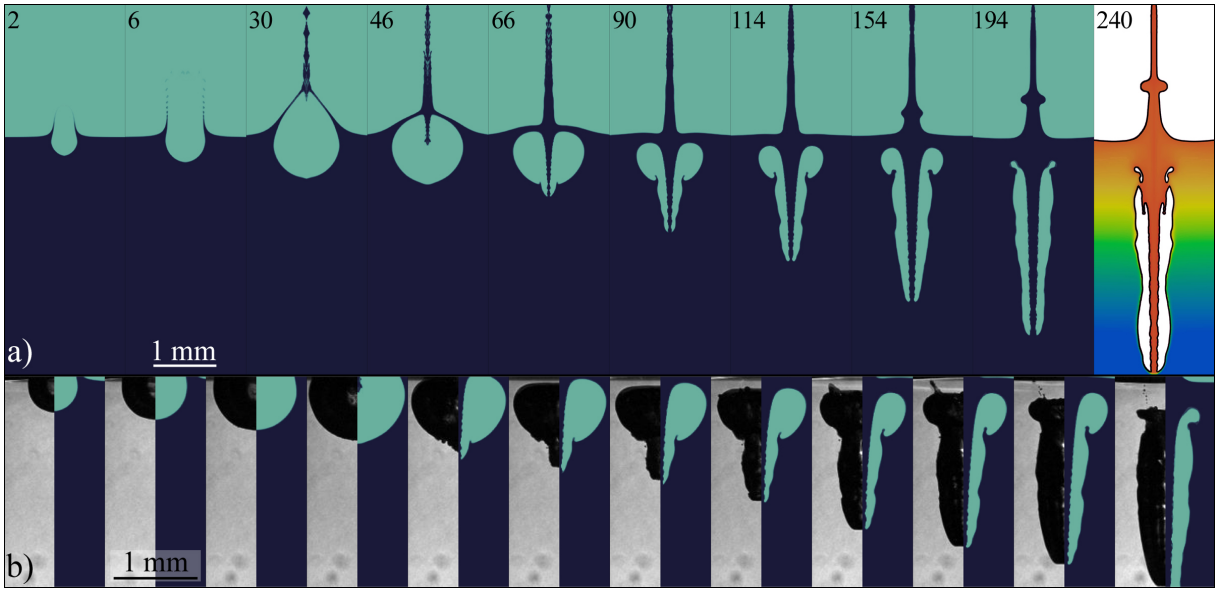

Figure 6.5: OpenFOAM simulation of the development of a bullet jet for a prototypical bubble with $D^* = 0.155$. a) Temporal evolution of the gas and liquid phases. The last frame is represented using a fluid volume tracing technique where the liquid has initially different colour at different depths (i.e. a Lagrangian ink map). The numbers indicate the time in µs. b) Comparison between the simulated results and an experimental case with similar parameters (i.e. D^* and R_c). After the jet pierces the submerged cavity wall the simulated jet advances faster (about 25 %) than the experimental. Then, the matched frames in the sequence have an increasing temporal shift.

tip has a bigger drag coefficient than one, for example, with a sharp conical or spherical tip [230], and will also lose more energy during the cavity piercing. The jet tip is mostly defined by the specific way that the liquid converges to the centre of the water bell during the splash closure. As seen in figure 6.2 (a) and figure 6.3, the initial part of the sealing of the water curtain might not be perfectly symmetric in some cases. Then, the jet tip might be thicker than in the numerical simulations and non-symmetrical at the moment when it pierces the bubble. Once the jet penetrates into the liquid pool it self-stabilises and a smooth front is observed in both the experiments and the simulations.
In the same way we did for the analytical model of section 6.3.2, the OpenFOAM model was used to study the effect of surface tension (σ) and gravity on the development of the bullet jets. This confirmed that σ has a small impact on the water bell dynamics but plays an important role in stabilising the shape of the elongated gas cavity (i.e. preventing fragmentation) once it is flowing into the pool. Gravity has a small impact on the bullet jet in the range of bubble sizes comprehended in this study (as shown in section 6.3.7), but according to the simulations its influence grows with increasing bubble size.
The numerical simulations also gave an insight into critical aspects involved in the jet formation that were not visible in the experimental trials, like the pressure, velocity and vorticity fields around the cavity. Those are depicted in figure 6.6 for both gas and liquid phases. In figure 6.6 (a) it is possible to see how the water vapour produced by the laser plasma (here modelled as a compressed gas) is explosively vented into the atmosphere, but as the submerged cavity grows rapidly, the pressure inside it suffers a dramatic drop and atmospheric air is driven into the cavity, replacing the water vapour originally in it. By the time the liquid curtain is sealed (here at ~ 28 µs), a stagnation point is developed

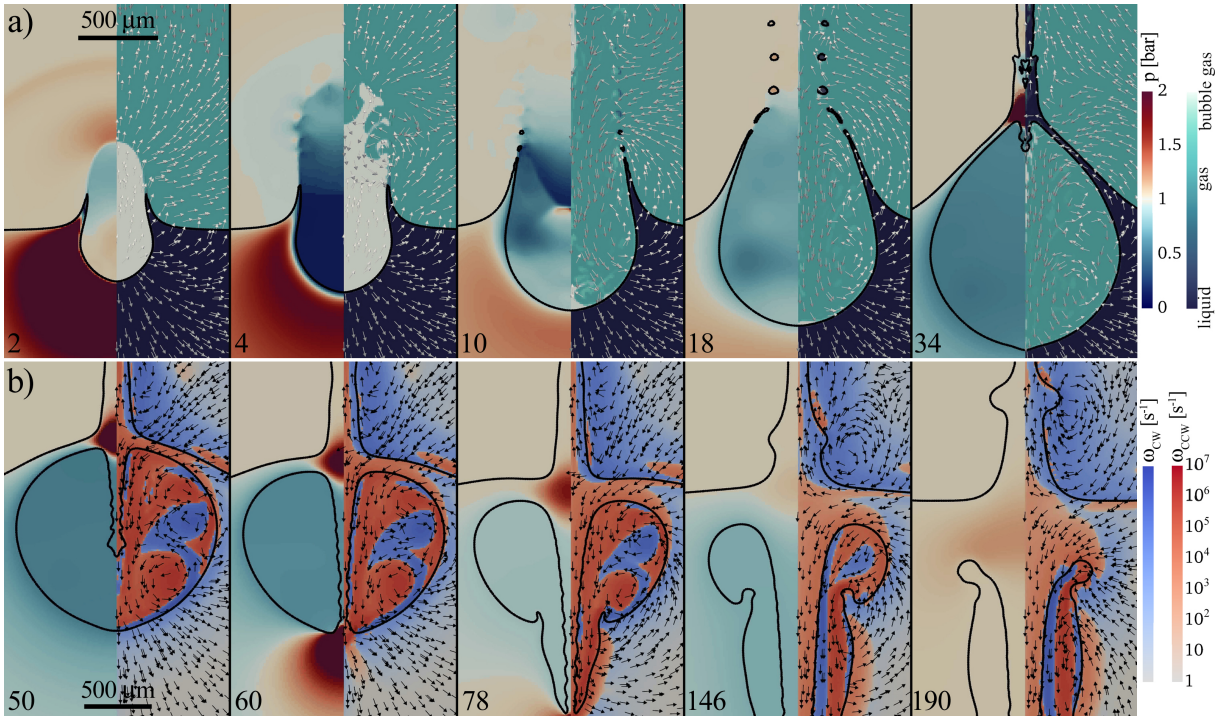

Figure 6.6: Details of the physical mechanisms involved in the bullet jet formation. The numerical simulations represent the pressure and vorticity fields of both phases (gas and liquid) along with the flow streamlines. The numbers indicate the time in µs. The frames composing the image sequence were divided into two halves. The half on the left always shows pressure amplitude. The right side shows the gas exchange between the original bubble and the atmosphere in subplot (a), and the vorticity field in subplot (b). See online supplementary movie 6.

at its axis, where the radial and downward motion of the liquid splash converges. As shown in the last column of figure 6.6 (a), the higher pressure at the stagnation point gives origin to the downward liquid jet which causes the bullet jets. At this instant, the submerged part of the cavity is still expanding, maintaining the pressure inside the trapped gas below the atmospheric pressure, and at the same time provoking the collapse of the water bell. The CFD simulations make clear how the evolution of the stagnation point and the water bell is directly linked to the expansion of the submerged cavity. It is important to remark that the previous mechanism of generation of the downward jet is not exclusive of the open splash case associated with the bullet jets. This means that once the canopy is closed and the water bell is formed, the downward jet observed on both vented and closed cavities originates in a similar way (i.e. from a stagnation point). That has been observed also in standard jetting bubbles [5, 97, 212, 218–220], like the case described in figure 6.1 (c) and also shown in figure 6.12 (e) included in the appendix, section 6.5.2.

The cavity evolution after the jet impingement can be followed from the image sequence of figure 6.6 (b). The thin downward jet, driven by the stagnation pressure on its base, grows through the gas pocket and pierces the lower side of the cavity without losing its shape. When the jet impacts the bottom of the cavity, there is a transfer of impulse (via added mass) which removes part of the jet momentum and imparts a velocity to the cavity bottom. In the bullet jet case, the transfer of momentum is clearly lesser than for standard jets, where it is common to observe shock waves emitted when the piercing

occurs. From that moment on, the liquid column starts driving the surrounding gas as it grows into the pool. This happens mainly because the jet tip pushes a section of the cavity wall downwards turning it into an increasingly elongated shape, but also due to the drag produced by the liquid flow along the cavity axis. This, along with the action of the stagnation point on the neighbouring liquid, promotes the apparition of a vortex ring on the upper part, i.e. where the cavity folds acquiring a toroidal shape. According to the numerical simulation, there are regions with strong vorticity both inside the gas phase cavity and also close to the interface. The transport of liquid from the surface to deeper regions ceases when the water bell completes its collapse (at around $\sim 100\,\mu s$). At that moment the stagnation point in the jet's base disappears. As a consequence of that collapse, the upward jet becomes significantly thicker and the elongated cavity flows downwards along with the bullet jet.
As discussed in the previous section, the model accounts for the condensation inside the elongated cavity by removing 70 % of the bubble mass when the cavity reaches its maximum volume. In the bullet jet case, the gas created by the breakdown (modelled as non-condensable air) is expelled and replaced by ambient gas. Considering that the cavity never collapses, and thus the pressure never reaches a value far off the atmospheric (as shown in figure 6.6 (b)), then the gas condensation has almost no effect on the bullet jet dynamics.
In summary, these simulations confirm that the main driver of the bullet jets is the closure of the water splash, which in turn is provoked by a sudden pressure drop due to the expansion of the submerged part of the laser-induced cavity.

6.3.5 Critical stand-off distance for the formation of a bullet jet

One still unanswered question regarding the bullet jets deals with the existence of a critical stand-off distance D^* for which this particular type of jet occurs. However, to shed some light on that question we first need to precisely define what is a bullet jet and what is a standard jet. For making such a classification of the jet's behaviour we will use four reference cases, namely the three cases introduced in figure 6.1 plus a case where no jet is observed. As the change in the rather complex evolution of the jets with D^* takes place gradually, we will also identify the intervals where the transition from one regime to another happens. Figure 6.7 presents a parametric plot including 126 individual measurements classified according to the following criteria:

- *Case of figure 6.1 (b):* This kind of standard jet occurs when $0.7 \lesssim D^* \lesssim 4$. The liquid intruding the bubble does not always pierce the bubble. Fragmentation of the cavity is observed at collapse.

- *Transition between cases of figure 6.1 (b) and figure 6.1 (c):* For $D^* \sim 0.7$ the situation is similar to the one in figure 6.1 (b), but this time a thick cylindrical jet pierces the bubble and splits it into two toroidal halves. The two parts get atomised after collapse.

- *Case of figure 6.1 (c):* Observed at $0.25 \lesssim D^* \lesssim 0.7$. As the piercing jet becomes thinner it produces a cylindrical cavity after piercing the bubble. Typically, the jet reaches a depth similar to the bubble radius before the gas phase collapses and breaks.

- *Transition between the case of figure 6.1 (c) and the bullet jet case:* Around $D^* \sim 0.25$, the piercing liquid jet is thin enough to pass through the hemispherical cavity

and fold it into the elongated shape typically found in the bullet jets. However, the cavity tip detaches from its upper part before the folding is complete. Even when the jet tip reaches depths higher than 3 times R_{cm}, the structure breaks and dissolves.

- *Bullet jet case:* The bullet jets were observed for stand-off distances ranging between $0.075 \lesssim D^* \lesssim 0.25$. The folding produced by the central jet happens in a smooth way (see figure 6.6). The displacement of a section of the cavity drives the gas into its elongated part. The jet tail can detach like in the transition case or not, the difference between both is that the bullet jet can travel longer distances maintaining the structure of the elongated cavity.

- *No jet case:* Here, the laser is focused on the very surface of the water (i.e. $D^* \lesssim 0.07$) and the liquid above the plasma spot is not sufficient to produce a water curtain splash. Then, only an open cavity is observed (without a later jetting).

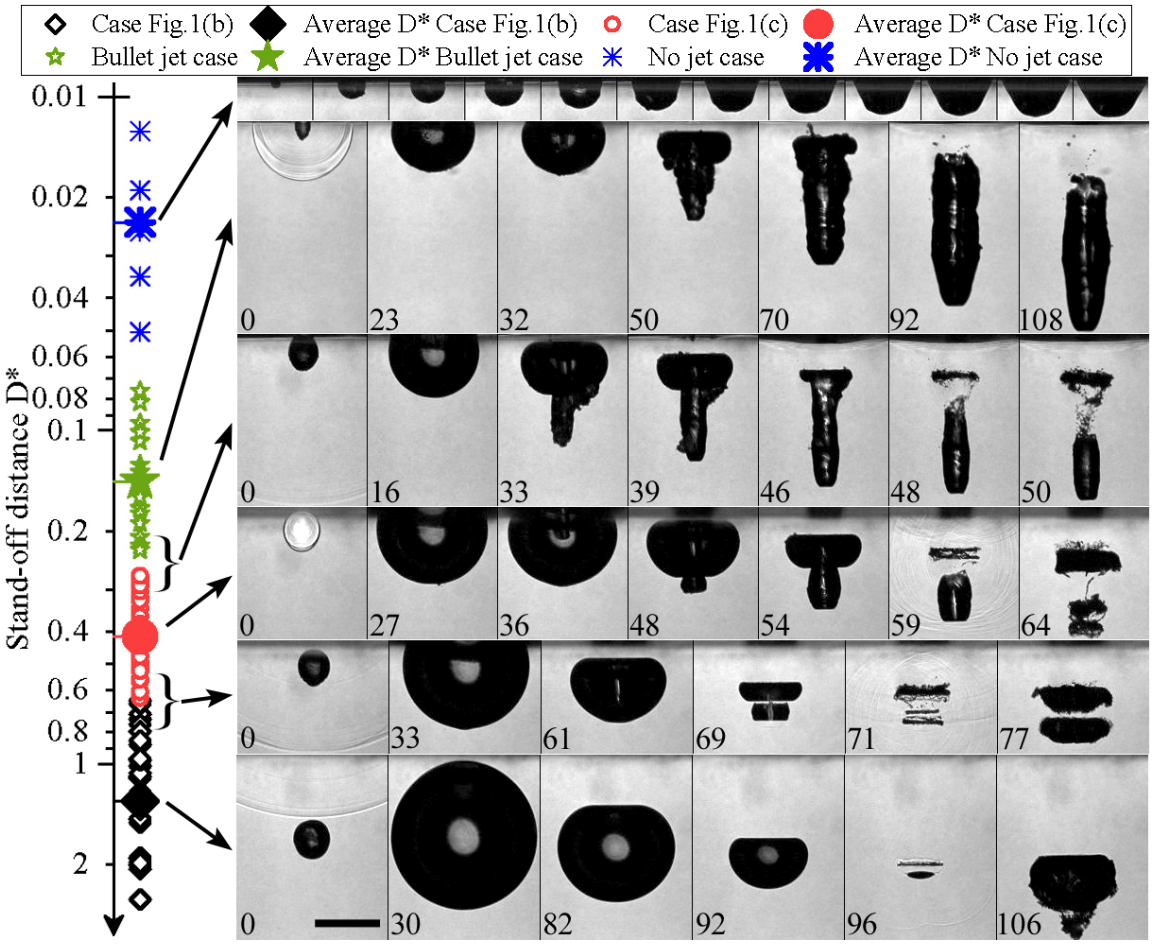

Figure 6.7: Bubble jet behaviour as a function of the stand-off distance D^*. The parametric plot includes 126 individual measurements (high-speed videos) classified as one of the cases described in figure 6.1. The image sequences exemplify each subgroup. Those measurements have the same D^* as the mean value of the subgroup they represent. The piercing of the jets presents a sustained change for cases with $D^* \lesssim 3$. The bullet jets were only observed in a narrow band ($0.08 \lesssim D^* \lesssim 0.22$). The numbers indicate time in µs. The inter-frame time in the upper row is 10 µs. The length of the scale bar is 500 µm.

The classification performed in figure 6.7 makes clear that the difference between the bullet jets and the standard jets is not only given by the reduced diameter of the liquid jet. On top of that, there are at least four distinctive aspects observed exclusively in the bullet jet case: 1- The splash is always open to the atmosphere (see appendix, section 6.5.2); 2- The gas cavity does not collapse but it folds into an elongated cavity; 3- due to 2 the gas cavity shape is significantly more stable (it hardly fragments) and; 4- The liquid jet reaches distances of several times the maximum radius of the initial cavity.
The differences in the shape stability observed for the distinct cavity types can be understood by analysing the maximum pressure reached within the gas phase in each case, estimated from the numerical simulations. In the case corresponding to figure 6.1 (b), the full collapse of the cavity occurs 1 µs after the jet touches the opposite wall (see figure 6.7), reaching a gas pressure of around 23 bar. For the case in figure 6.1 (c), the collapse is completed approximately 15 µs after the jet pierces the cavity wall, reaching a lower pressure of around 5.5 bar. In the case of the bullet jets, the maximum pressure reached during the whole lifetime of the jet is barely above the atmospheric (i.e. 1.2 bar), explaining why the cavity remains as a single piece in most of the cases.
The values for D^* shown in figure 6.7 are strictly valid for $h > 50\,\mu m$ (i.e. $D^* \lesssim 0.085$). For smaller depths (blue dots) the portion of the laser plasma spot that is actually submerged changes, and then there is a loss of accuracy. As shown in the appendix, section 6.5.2, the cavities start to be open to the atmosphere at $h \lesssim 175\,\mu m$. This value is in agreement with the VoF simulations.

6.3.6 Shape factor of the bullet jets

The bullet jet formation dynamics are only dependent on the interplay of the inertially driven ejection of liquid and the pressure-driven closure of the splash curtain. Therefore, we expect that this type of jet can be produced for a broad range of cavity sizes. To test that idea, we produced splashes/cavities of different sizes by adjusting the energy of the laser pulses. In order to observe a bullet jet in each case, the distance where the laser light was focused had to be corrected. Here, we defined R_{cm} as the mean radius of the submerged hemispherical cavity just before the downwards jet crosses the water-free surface level. Figure 6.8 shows a comparison of the shape of cavities with radii in the range of $150\,\mu m \leq R_{cm} \leq 600\,\mu m$. The upper row of figure 6.8 shows the submerged cavities at $R_c = R_{cm}$. The images in the lower row present the same cavities in a later moment when the bullet jet is fully developed, i.e. when the transition from a toroidal to a "cylindrical" cavity is complete.
To study the jet's shape we have defined two dimensionless quantities: a shape factor given by l_{bj}/w_{bj} and a "volume reciprocity" factor $V|_{R_{cm}}/V_{bj}$. Here, l_{bj} and w_{bj} represent the length and the equivalent diameter of a cylinder computed from the area of the elongated cavity in the recordings. $V|_{R_{cm}}$ and V_{bj} are the volume of the hemispherical cavity at $R_c = R_{cm}$ and the equivalent bullet jet cylindrical volume (i.e. gas plus liquid) computed from l_{bj} and w_{bj}, respectively. Interestingly, both factors remain approximately constant in the measurements included in figure 6.8, being $l_{bj}/w_{bj} = 3.5 \pm 0.1$ and $V|_{R_{cm}}/V|_{l_{bj}} = 0.78 \pm 0.03$. Similarly, we have found a proportionality constant of ~ 3.5 between l_{bj} and R_{cm}, then the diameter w_{bj} of the bullet jets is similar to R_{cm} (at least in the studied range). These values may not hold for much bigger bubbles, where the gravity and the buoyancy forces acting on the splash and the elongated cavity might play an important role in the jet dynamics.
Regarding the jet tip velocity, we found a clear correlation between the speed at full

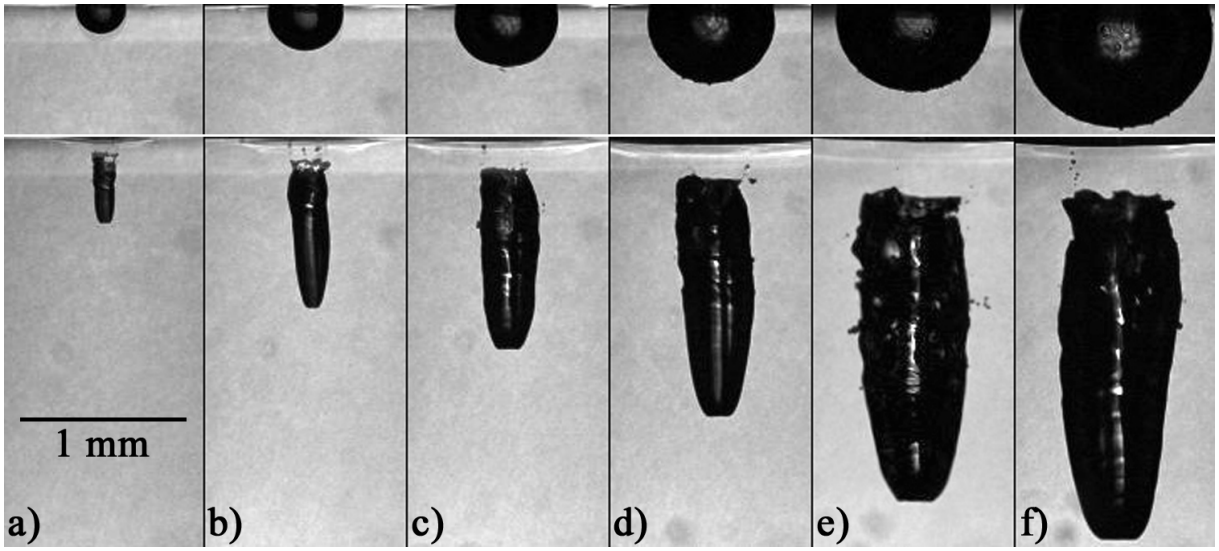

Figure 6.8: Bullet jet shape factor. (upper row) It shows the submerged cavity just before the liquid jet crosses the surface level. (lower row) These images present the same cavities at the moment when the bullet jet is fully developed. (a) $R_{\mathrm{cm}} = 149\,\mu\mathrm{m}$. (b) $R_{\mathrm{cm}} = 229\,\mu\mathrm{m}$. (c) $R_{\mathrm{cm}} = 316\,\mu\mathrm{m}$. (d) $R_{\mathrm{cm}} = 393\,\mu\mathrm{m}$. (e) $R_{\mathrm{cm}} = 564\,\mu\mathrm{m}$. (f) $R_{\mathrm{cm}} = 592\,\mu\mathrm{m}$. See online supplementary movie 7.

development of the jets and the average area of the cavity (which is proportional to the jet tip section). As a rule of thumb, we observed that thinner bullet jets move faster than thick ones. This is consistent with the simulated results for bubbles/cavities of different sizes (producing jets of different thicknesses). For the measurements included in figure 6.8, the jet tip speed decays roughly by 40 % when comparing the smallest bubbles with the bigger ones. The discrepancy in the speed of the jet tip exists also before the jet pierces the lower part of the cavity but in a lesser proportion. This suggests that the energy loss responsible for the tip deceleration is mostly due to the impact of the jet on the wall and the posterior drag acting on the cavity front. In the long term, the higher speeds of the smaller jets would lead to increased drag forces which make them lose their momentum much faster as well. However, an extensive statistical study, supported by a theoretical analysis, would be required to establish a robust correlation between the main parameters involved in the jet's translational dynamics.

6.3.7 Surface curvature effect

Due to the "local" nature of the phenomenon, the bullet jets can occur in a wide range of curvatures of the liquid surface (i.e. as long as the cavity size is lower than the curvature radius of the surface). Figure 6.9 presents a measurement of a bullet jet produced on the top of a water meniscus sitting on a 3.6 mm glass capillary illuminated by a white LED lamp. This configuration allows us to visualise the jet's internal structure with remarkable clarity, although the proportions of the cavity might look distorted in the region close to the capillary surface due to its curvature [85]. The video corresponding to figure 6.9 makes evident how the initially rough surface, observed when the liquid jet tip emerges from the cavity lower wall, disappears as the jet penetrates further in the liquid. Both the gas and liquid phase turn into a smooth and stable front probably due to the stretching of their surfaces. The initial roughness is caused by the entrance of liquid drops (from the top)

which happens during the downward jet formation. This feature is not well reproduced by the numerical simulations.
When a slender object enters a liquid, the shape of the gas envelope around it is defined by its tip [230]. Interestingly, the tip of the bullet jet resembles the one of a flat cylinder and therefore displaces the water accordingly. Additionally, figure 6.9 depicts the characteristic shape of the upward jet arising from the cavity's initial location, which occurs shortly before the jet's tail detachment from the liquid surface. The shape of the upward jet is clearly related to the spherical form observed in the downward jet tail (see the first frame of the lower row in figure 6.9). More details about the bullet jets induced within a drop are discussed below in figure 6.10.
Another interesting feature of "bullet" jets is that they always point in the direction normal to the canopy at the moment of closure. Due to the fine focusing of the laser pulse achieved in our experiment, the resultant plasma is confined to a small region (i.e. with a size of tens of micrometres). As a consequence, the canopy/water bell axis points normally to the liquid surface in the spot the laser cavity is produced. Panels (b) and (c) of figure 6.9 show some examples of the latter. In figure 6.9 (b) three "bullet" jets were produced by focusing the laser at different locations along the surface of the water meniscus. The image is a superimposition of these three experiments which demonstrates that for a hemispherical droplet, they point towards the geometrical centre. The same behaviour was observed in a case where the laser was focused on the lower side of a pendant drop, as shown in figure 6.9 (c). This last example gives an account of the weak effect of gravity on the dynamics of these millimetric cavities.

6.3.8 Jet impact on a solid surface and potential applications

As discussed in the previous sections, the bullet jet's evolution is mostly defined by the "local" dynamics of the splash, instead of the boundary conditions outside of the region where the laser cavitation takes place (for instance a neighbouring solid wall). This, combined with the particularly long distances that the jet can reach ($\sim$ 12 times R_{cm}) and the total length of the liquid stream ($\sim$ 3 times R_{cm}), make the bullet jets potentially useful for certain applications, specifically, applications dealing with the cleaning of millimetric surfaces [80], membrane poration [98] or even micro-vaccination or drug delivery platforms [12, 13, 232]. The bullet jet could be particularly useful in systems with limited access, for example one which can only be accessed by optical means.
This feature is analysed in figure 6.10 (a). There, the bullet jet is induced at the top of a drop placed on a rigid surface covered by paraffin tape (hydrophobic). The temporal evolution of the jet speed in this case is very similar to the one observed in figure 6.9 until the jet tip hits the rigid wall, meaning that the jet is not aware of the wall's presence during its formation. Once the jet impacts the target (i.e. the rigid bottom), it can produce a highly localised elevated pressure for a few microseconds. Taking into account the optical distortion produced by the drop curvature on the displacement of the jet, the water column hits the surface with a speed of $\sim 11\,\mathrm{m/s}$ in the example of figure 6.10 (a). At this speed, the target surface experiences a quick transient overpressure (i.e. the *water-hammer effect*) followed by a milder pressure given by the stagnation pressure [235]. A representation of the liquid jet flow on the solid boundary is given in figure 6.10 (b). It is worth mentioning that the impact speeds observed during these trials should be high enough to produce the piercing of a soft material or biological tissue, as discussed in Cu et al. [12], Oyarte Gálvez et al. [13], and Robles et al. [232].

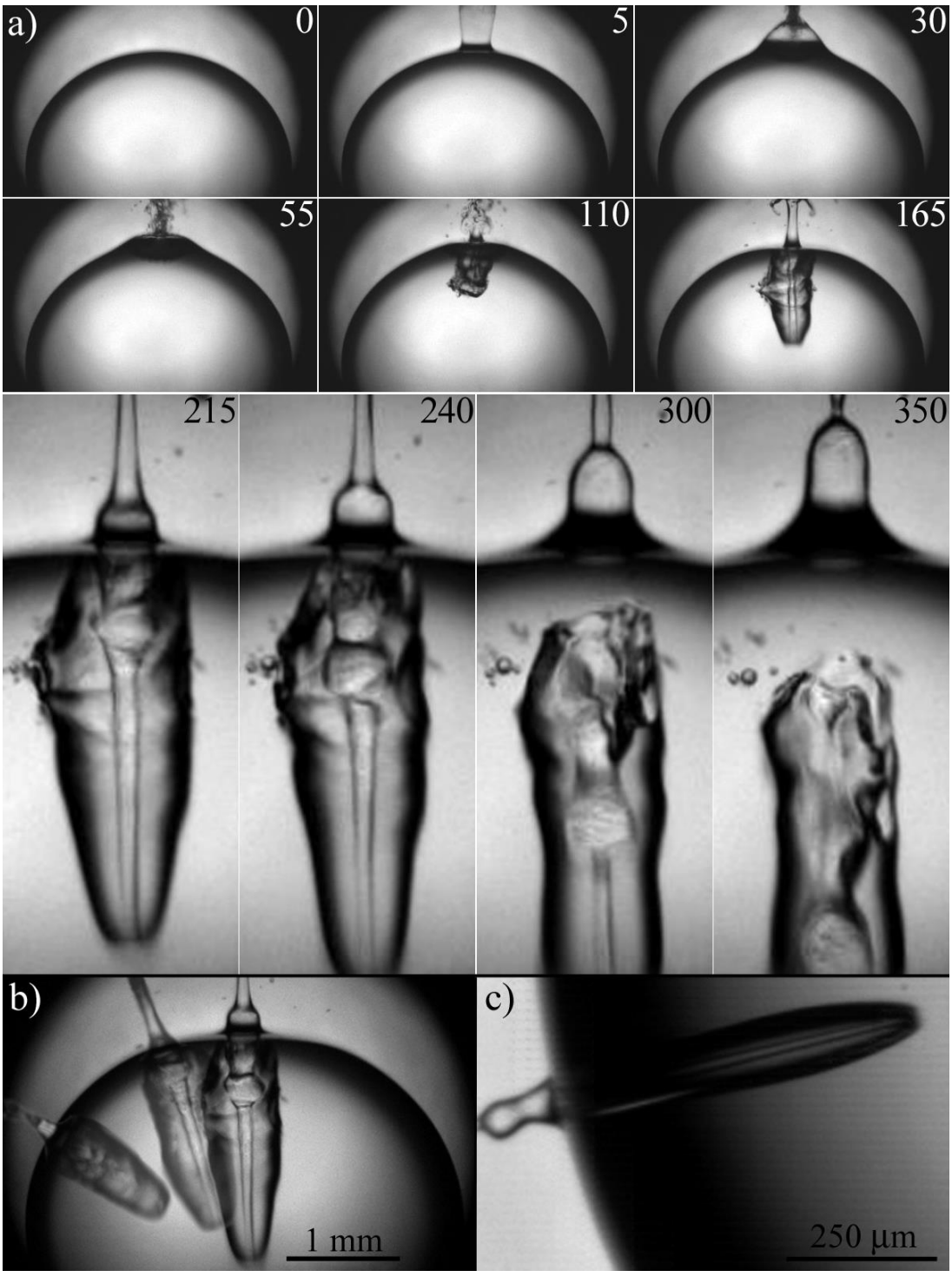

Figure 6.9: Bullet jet internal structure. The jet was produced on the curved surface of a water meniscus sitting on the top of a (filled) glass capillary. The image sequence reveals the details of the liquid jet inside the elongated cavity. (a) The width of the six upper frames is 4.6 mm. The zoomed images have a width of 1.15 mm. In addition to the clear view of the jet interior, the formation of an upward jet arising from the splash location is shown. The numbers indicate time in µs. See online supplementary movie 8. (b) Controllability of the jet direction. (c) Bullet jet on the side of a pendant drop of ~ 2 mm.

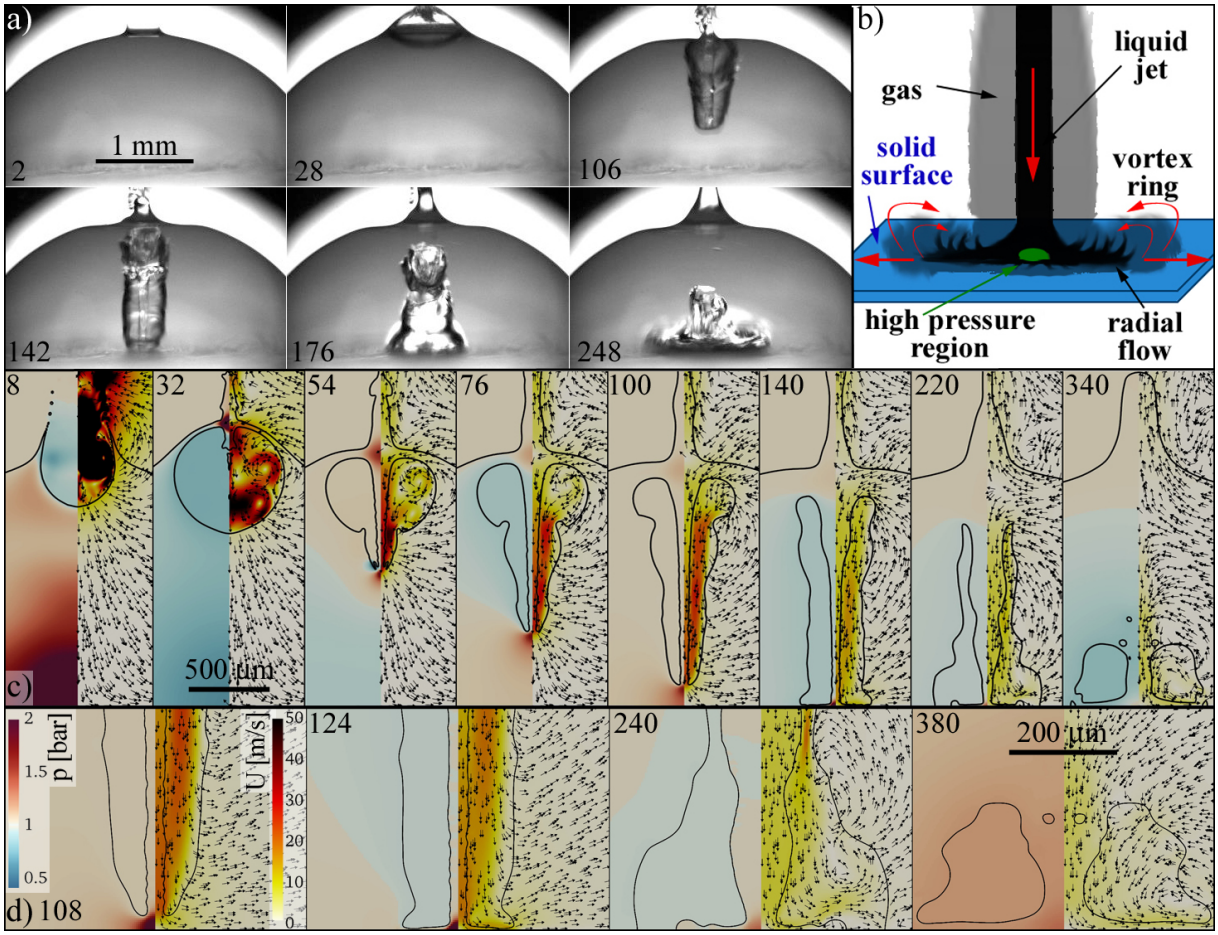

Figure 6.10: "Bullet" jet impacting a rigid surface. The numbers in the frames represent the times (after the laser shot) in µs. (a) The water drop had a height of 1.4 mm and it was sitting on paraffin tape fixed on a glass plate. (b) Illustration of the jet flow on the target surface. (c) Simulation corresponding to the case in (a). The frames were split to show the pressure (left) and velocity (right) fields. (d) Detailed view of the pressure/flow around the region of impact of the jet. The jet hits the wall with U$\sim 23\,m/s$ and reaches a stagnation pressure of ~ 3.4 bar. Full videos available in online supplementary movies 9 and 10.

The simulated dynamics of a bullet jet produced at the top of a drop is depicted in figure 6.10 (c). The bullet jet's internal structure noticed in the simulations are in excellent agreement with the experimental observations presented in figure 6.9. The numerical results also confirm how the jet "ignores" the presence of the solid boundary downstream until it gets very close to it, as observed in figure 6.10 (a). Once again, we found some disagreement between the speed measured from the experimental jet and the one computed for the drop in figure 6.10. In this measurement, the thickness of the jet front is visible in the images. The jet cross section in the experiment of figure 6.10 (a) was around 51 µm, and just half in the simulated jet.
From an applied point of view, the impact speed of a bullet jet is much slower than the one found in typical bubble jets used in particle removal [80, 117]. The same goes for the overpressure they produce on a surface. In spite of that, the bullet jets exhibit an extended flow duration (between 100 µs and 250 µs) compared with the $\sim$ 5-10 µs usually observed in regular jets. This relative increment in the shear flow can be relevant for

surface contamination removal. While the initial water hammer pressure can effectively detach particles from the surface, the extended flow coming afterwards would drive the particles away and prevent them to fall on the same spot. A detailed view of this process is shown in figure 6.10 (d). After impact the liquid jet spreads over the surface presenting some hydraulic jumps (e.g. at 240 µs). By the end of the sequence (i.e. at $\sim$ 380 µs) a laminar flow is established close to the stagnation point and a vortex ring flow is formed at its vicinity.

6.4 Conclusion

We have reported on a laser-induced liquid jetting phenomenon that is caused by the closing of a splash sheet. This particular type of cavity is open to the atmosphere and does not collapse inertially, as observed in previous reports on cavitation bubbles near a free surface. Instead, a submerged gas volume is pierced by a liquid jet. Both the gas and the liquid jet travel away from the free surface as a unit and considerably deeper into the pool than typically observed in jetting bubbles.
The closure of the liquid curtain that leads to the formation of a water bell was first explained using a simple model in section 6.3.2. Those simulations revealed that the sealing and later collapse of the water splash is provoked by a pressure difference between the cavity interior and the atmosphere. Furthermore, they showed how the surface tension has an almost negligible influence on the splash dynamics. These conclusions were confirmed by the OpenFOAM simulations presented in section 6.3.3. The highly detailed numerical simulations allowed us to further understand the physical mechanisms behind the bullet jet formation.
In spite of the model's failure to account for the fine "mist" initially expelled from the ablated liquid surface (and later observed during the water curtain closure), the formation and later dynamics of the bullet jets were in good agreement with the experiments. One aspect to improve on the simulations would be to reproduce the asymmetric splash observed in the initial phase of water bell sealing by implementing a full 3D simulation scheme. As the radial inflow is initially not perfectly symmetric, the experimental downward jets are slightly thicker than the ones computed by the model. The latter has a significant impact on the later evolution of the jet, in particular after it pierces the submerged cavity and flows into the liquid pool. The simulations also explained the origin of the two liquid jets emerging from a stagnation point at the top of the water bell immediately after the closure of the canopy. While the upward jet grows away from the liquid surface, the downward jet impinges on the submerged cavity and gives origin to the toroidal bubble that evolves into the elongated gas cavity surrounding the bullet jet. That particular liquid flow induces a vortex ring on both the gas and liquid phases on the upper part of the cavity. The simulations proved that the bullet jet is solely a consequence of the water bell's inertial collapse, and not a vorticity-driven jet.
The specific conditions necessary for the generation of this kind of jet were found through a parametric study, finding bullet jets only in a range of the normalised stand-off distance D^* comprehended between 0.075 and 0.25. Additionally, the parametric analysis has shown in detail the transformation happening in the bubble evolution when D^* is gradually reduced, also confirming a variation in the downward jet thickness as the main changing factor.
We found within a small range of cavity sizes an invariability of the bullet jet's shape and expect that this holds for bubbles of larger volumes, too. While bigger cavities would

be difficult to achieve with lasers, electric breakdowns through sparks or even explosive charges at a proper shallow depth below the free surface may be used to explore this further. Since gravity would start playing a relevant role for bubbles with a diameter of the order of a meter, the bullet jets might occur in a different range of stand-off distances or even have a slightly changed shape factor. Related to the jet size, we also observed a clear difference in the jet speeds of bubbles with distinct thicknesses. While jets produced by small splashes are much faster at the instant of the jet formation, the increased drag forces make them lose their momentum much faster as well.
The bullet jets have many interesting properties like: 1- the possibility to control their direction independently of the boundary conditions close to the inception point (e.g. objects or rigid walls); 2- the relatively "long" distances that the liquid jets can travel; and 3- the sustained flow that they can deliver to a specific region of a surface accessible only by optical means. The combination of these features could be relevant for targeted cleaning through micro-jet applications, and also for the development of a micro-injection system.

Acknowledgements

J.M.R acknowledges support from the Alexander von Humboldt Foundation (Germany) through the Georg Forster Research Fellowship. The work was supported in part by the Deutsche Forschungsgemeinschaft (DFG, German Research Foundation) under contract OH 75/4-1. The authors thank Robert Mettin for providing helpful discussion on this topic. The authors would also like to thank the reviewers for their detailed remarks and constructive criticism, which have significantly contributed to improve this manuscript.

6.5 Appendix

6.5.1 Variation of the maximum cavity radius $R_{\mathbf{cm}}$ as a function of the depth h.

As discussed in section 6.1, the presence of a boundary of any kind greatly affects the shape taken by the laser-induced bubble during expansion. Due to the lack of sphericity of the gas cavity, the maximum radius reached by a bubble produced with identical initial conditions might change with the distance to the boundary (h). For the case of bubbles in the vicinity of a free surface, the situation is more dramatic, since the bubble not only is deformed, but also a part of its gas content is ejected into the atmosphere. In general, the maximum radius achieved by the submerged cavity matches the definition of R_{cm} given in section 6.3.2. The strong dependence of R_{cm} on h makes the adimensional parameter $\gamma_{\mathrm{so}} = h/R_{\mathrm{cm}}$ behave non-linearly in shallow water or even might take multiple values in extreme cases, e.g. if $R_{\mathrm{cm}}(h)$ changes much faster than h.
The measurement of the depth h is another factor that might introduce uncertainties in the definition of a stand-off distance. The distance h is usually measured from the centre of the laser plasma captured through high-speed photography. However, a precise determination of the plasma centre might be difficult for some experimental conditions due to spurious reflection (and diffraction) of the plasma light on the surrounding media, combined with the long exposure times of typical cameras (at least 1 µs). Additionally, h has a strong dependence on how well-defined the air-water interface is in the video frames, which in turn depends on the alignment of the liquid surface and the camera, the precise liquid level and the illumination characteristics. In order to overcome those issues, we have measured h from the reflection of the shock wave produced by the plasma, as shown in

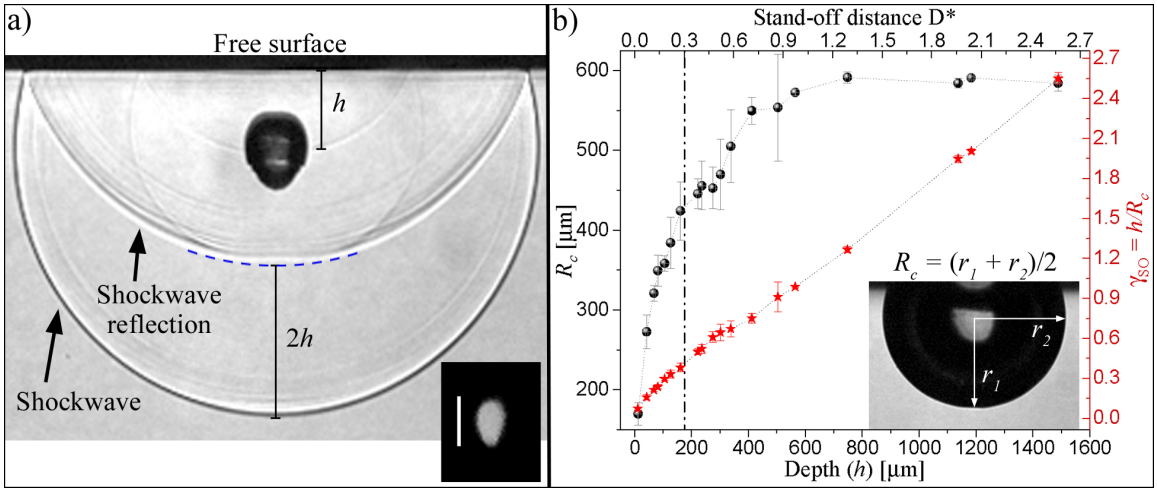

Figure 6.11: Characterisation of the cavities for different depths h. a) Measurement of h using the shock wave reflection on the liquid surface. The inset shows an example of the laser plasma spot next to a scale bar with 100 µm. b) Relationship between the average maximum radius of the submerged cavities (R_{cm}), the stand-off distance D^*, and the adimensional parameter $\gamma_{so} = h/R_{cm}$, for different depths (h). The curves summarise 126 individual measurements. The vertical dashed line indicates the minimum depth producing a close cavity.

Figure 6.11 (a). The early interaction of the reflected shock wave with the bubble seems to have a negligible effect on the bubble expansion dynamics, especially when compared with the effect of the boundary displacement on the liquid surface. In any case, every aspect affecting the bubble dynamics should be understood as a consequence of changing the bubble inception distance, and then those are considered in the system characterisation approach using D^*. In the inset of figure 6.11 (a), the laser plasma spot was photographed using a combination of optical filters, setting the lowest exposure time available in the camera (200 ns) and adjusting the camera trigger to stop the image acquisition just before the vapour starts to expand.
Figure 6.11 (b) presents a measurement of the dependence of the average R_{cm} as a function of h. There, the non-linear relationship between R_{cm} and h becomes evident. For depths below 800 µm (i.e. $D^* \sim 1.4$) the cavity radius (measured as depicted in the figure inset) matches the unbounded bubble radius. For depths between 175 µm and 800 µm the cavity remains closed, but as part of the gas expands above the water level (see appendix, section 6.5.2), the maximum radius is significantly reduced. When the cavity is generated above $h = 175$ µm the cavity starts to be open to the atmosphere, and then R_{cm} gets smaller at an accelerated pace when the laser is focused closer to the surface. For $h < 50$ µm the size of the plasma starts playing a major role, considering that part of the laser light might be focused outside the water, producing smaller amounts of vapour and thus smaller cavities. Figure 6.11 (b) also presents a comparison between D^* and γ_{so}. These two adimensional parameters are quite similar for $h > 700$ µm ($D^* \sim 1.2$), but for lower values of h the values of the parameters are progressively different. For depths $h \lesssim 300$ µm the value of D^* is around two thirds of the one of γ_{so} computed at the same h, and half when $h \lesssim 100$ µm.

6.5.2 Splash dynamics for different depths h.

As discussed in section 6.3.5, one of the conditions for the formation of a bullet jet is that the cavity is produced close enough to the surface to have a splash open to the atmosphere. Figure 6.12 presents high-speed video recordings of the splash produced by the laser on a water meniscus at different depths. The meniscus was produced by overfilling a 3.6 mm glass capillary with the liquid. The slight curvature of the water surface has no effect on the type of splash produced. The images show how the evolution of the splashes changes significantly with h. Those can be related to the dynamics of the submerged cavities presented in figure 6.7. The transition from a closed to an open cavity can be seen in figure 6.12 (d). Interestingly, the water "dome" of the gas pocket becomes unstable during expansion and several small liquid filaments grow from it, as previously shown by Thoroddsen et al. [196]. In all cases, the collapse of the cavities above the liquid surface, for instance the water bell, gives origin to an upward jet (not shown in figure 6.12) at around 120 µs [220]. For the sake of completeness, we included an image sequence of this later vertical jet in figure 6.13. These measurements are the same ones presented in figure 6.12, taken using a second camera (in simultaneous) set with a lower temporal resolution and an extended temporal window. The images show how the shape of the upward jet also depends significantly on the inception depth of the cavity, as reported by Chen et al. [214], Li et al. [211], and Bempedelis et al. [217].

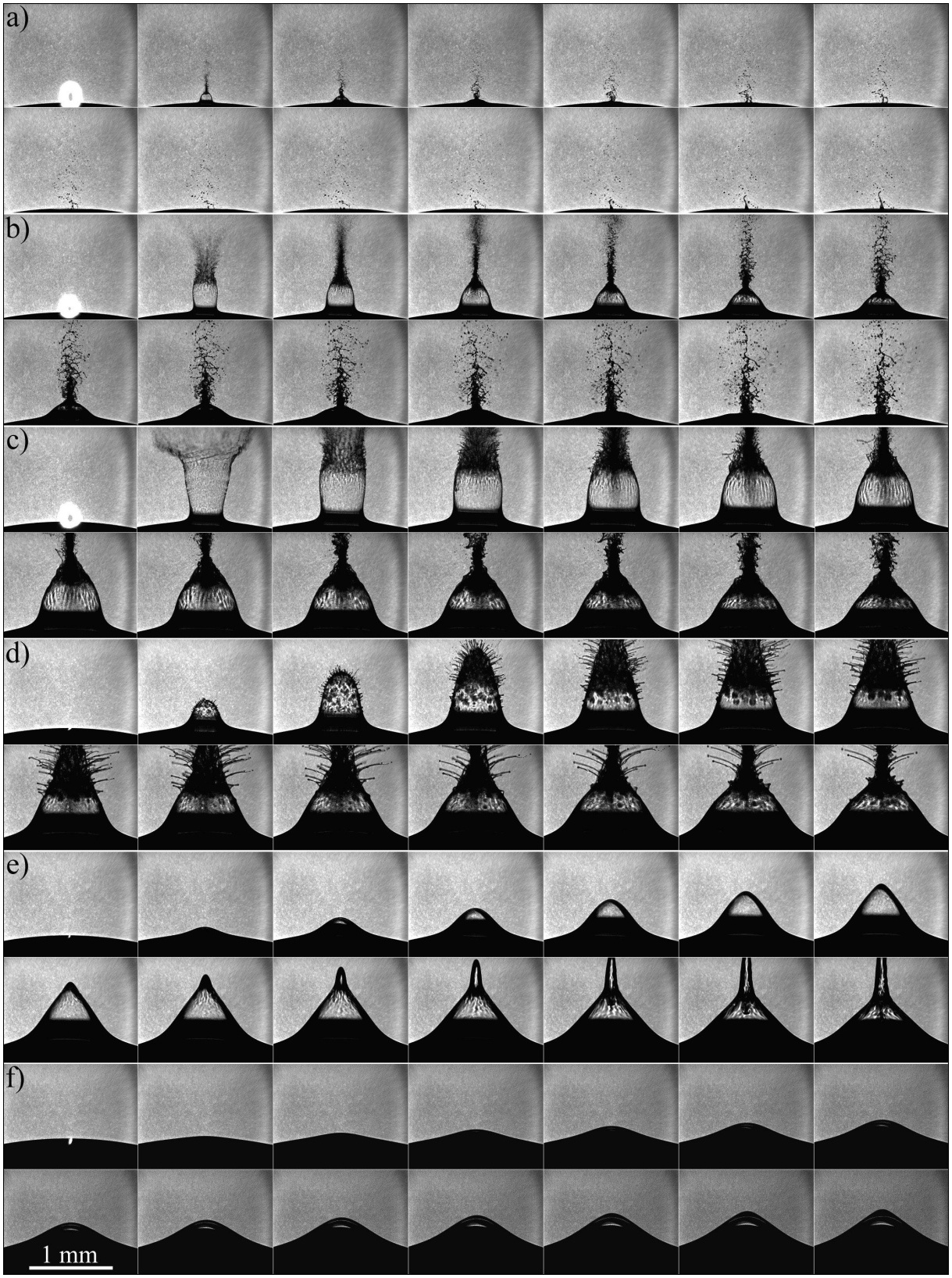

Figure 6.12: Splashes produced on the top of a water meniscus by a laser-focused at different depths h. a) $h \simeq 0\,\mu m$. b) $h \simeq 45\,\mu m$. c) $h \simeq 91\,\mu m$. d) $h \simeq 156\,\mu m$. e) $h \simeq 221\,\mu m$. f) $h \simeq 327\,\mu m$. The gas cavity is open to the atmosphere for depths lower than $\sim 175\,\mu m$. The time between frames is $1.8\,\mu s$ ($25\,\mu s$ of total duration).

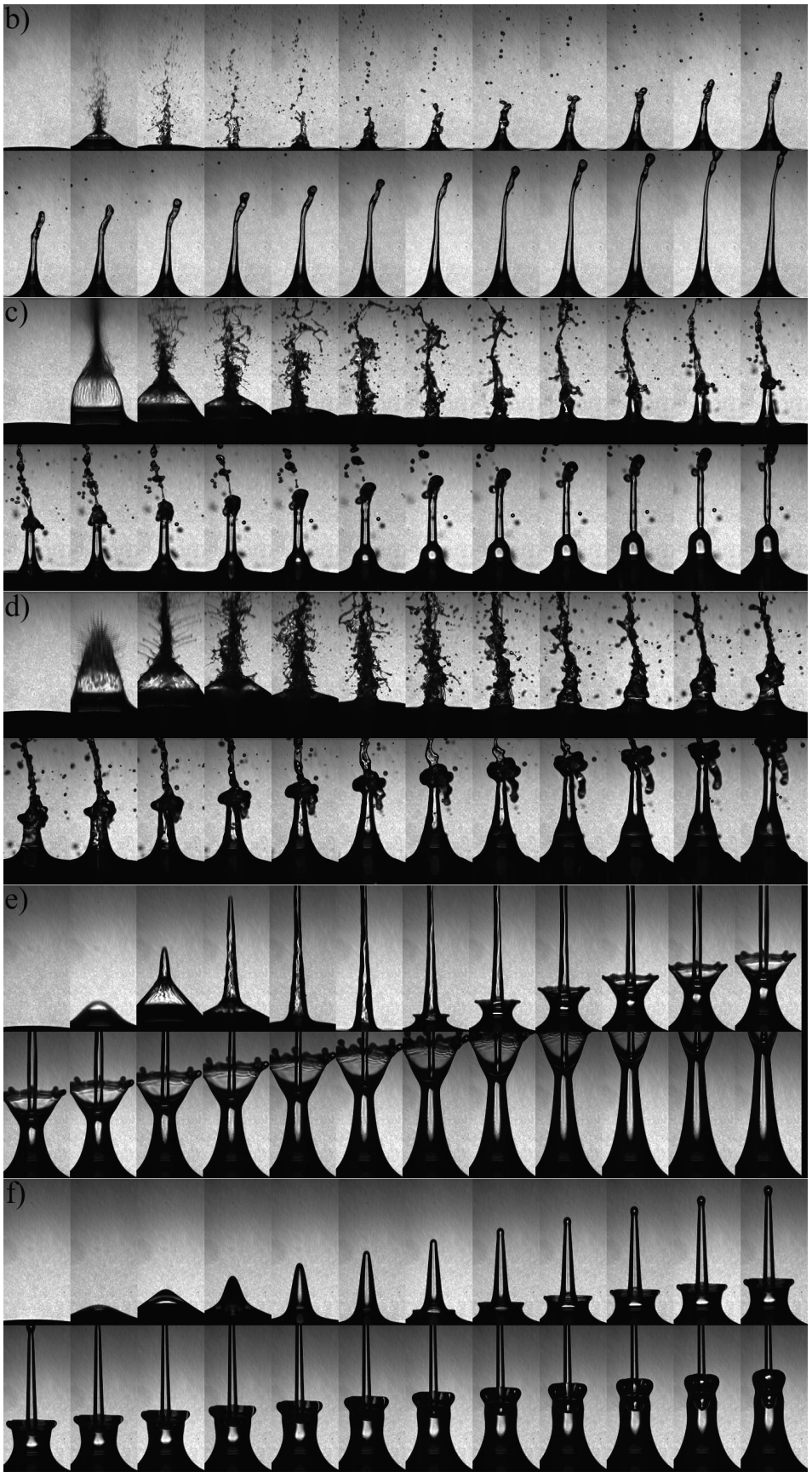

Figure 6.13: Long term visualisation of the splashes presented in figure 6.12. The depth (and labels) are the same as figure 6.12. Here, the videos were recorded at 72 kfps (333 µs of duration). The frame height was 1.91 mm.

7 Bubble nucleation and jetting inside a millimetric droplet

This work has been published in [25]:

J. M. Rosselló, H. Reese, K. A. Raman, and C.-D. Ohl. "Bubble nucleation and jetting inside a millimetric droplet". *Journal of Fluid Mechanics* **968**, A19 (2023)

In this work, we present experiments and simulations on the nucleation and successive dynamics of laser-induced bubbles inside liquid droplets in free-fall motion, i.e. a case where the bubbles are subjected to the influence of a free boundary in all directions. Within this spherical millimetric droplet, we have investigated the nucleation of secondary bubbles induced by the rarefaction wave that is produced when the shock wave emitted by the laser-induced plasma reflects at the drop surface. Interestingly, three-dimensional clusters of cavitation bubbles are observed. Their shape is compared with the negative pressure distribution computed with a computational fluid dynamics model and allows us to estimate a cavitation threshold value. In particular, we observed that the focusing of the waves in the vicinity of the free surface can give rise to explosive cavitation events that end up in fast liquid ejections. High-speed recordings of the drop/bubble dynamics are complemented by the velocity and pressure fields simulated for the same initial conditions. The effect of the proximity of a curved free surface on the jetting dynamics of the bubbles was qualitatively assessed by classifying the cavitation events using a non-dimensional stand-off parameter $\mathfrak{F}$ that depends on the drop size, the bubble maximum radius and the relative position of the bubble inside the drop. Additionally, we studied the role of the drop's curvature by implementing a structural similarity algorithm to compare cases with bubbles produced near a flat surface to the bubbles inside the drop. Interestingly, this quantitative comparison method indicated the existence of equivalent stand-off distances at which bubbles influenced by different boundaries behave in a very similar way. The oscillation of the laser-induced bubbles promotes the onset of Rayleigh-Taylor and Rayleigh-Plateau instabilities, observed on the drop's surface. This phenomenon was studied by varying the ratio of the maximum radii of the bubble and the drop. The specific mechanisms leading to the destabilisation of the droplet surface were identified.

7.1 Introduction

Phase explosion in confined liquid volumes has recently gained interest because of its connection with thriving research areas like x-ray liquid crystallography [236], x-ray holography [237, 238], extreme UV light, and plasma generation [239]. A better understanding of the interaction of high-power lasers with small liquid particles is also relevant in laser-based atmospheric monitoring techniques [240, 241] or in optical atomisation techniques that can be applied to the production of airborne transported micro-drops used as drug carriers [242]. At the heart of all of these research fields is the injection of high-power photons into a small liquid sample, the initiation of phase transition from liquid to vapour, the rapid pressure fluctuations, and the successive complex fluid mechanics driven by this impulsive energy input. In this study, we want to shed light on the fundamental flows that can be induced in liquid samples once this phase transition has been initiated. In

particular, we focus on the fluid dynamics within a spherically confined liquid sample after the violent phase explosion of the vapour bubble induced by a high-power laser pulse. We explore the non-spherical dynamics of vapour bubbles within a liquid droplet, i.e. surrounded by free boundaries only. Bubble dynamics in droplets have so far mostly been studied from the perspective of destabilisation of the liquid-gas interface of the droplet [118, 196, 197, 243–247]. Here, we explore the bubble dynamics within the droplet [248].
Pulsed lasers can be focused into optically transparent media to induce explosive bubble nucleation by dielectric breakdown. This process is accompanied by the emission of an acoustic shock wave with an amplitude on the order of GigaPascals depending on the pulse energy, duration, and wavelength. For instance, the initial amplitude of the shock wave (i.e. at the edge of the plasma rim) in water can be in the range from 2.4 GPa to 11.8 GPa for a 6 ns laser pulse with an energy between 1 mJ to 10 mJ and a wavelength of 1064 nm focused with a numerical aperture (NA) of 22° [249, 250]. Recently, the initial shock wave amplitude produced by similar nanosecond laser pulses of 24 mJ (NA = 10°) was measured with a novel x-ray probing technique, obtaining peak values of around 20 GPa [237].
When a laser-induced cavity is produced in a confined space with free boundaries, like a droplet, most of the sound wave energy reflects back from the interface with an inverted phase, meaning that the original shock wave is transformed into a rarefaction wave. If the negative pressure amplitude of the reflected wave is below the cavitation threshold of the liquid, a trail of bubbles is nucleated after the wave passage. This effect is commonly observed upon wave reflection on the free boundary of a flat surface [251], nearby bubbles [252], a liquid column [253] or, as we already mentioned, a drop [197, 248, 254–258]. Laser cavitation in some of these configurations was lately applied in studies involving x-ray holography or x-ray diffraction to investigate the propagation of shock waves in liquids [238, 259, 260]. The use of very small amounts of liquid prevents the X-rays from being fully absorbed by the sample, thus improving the contrast of the X-ray images. This technique is suitable to study the properties of opaque liquids without optical aberrations, it is less sensitive to distortions produced by wavy surfaces and also allows retrieving information about the liquid density changes produced by the passage of the pressure waves [237, 261], which represents an advantage over traditional optical imaging.
Another interesting aspect of the nucleation of bubbles in the proximity of a boundary resides in their jetting dynamics. Laser-induced bubbles produced under different boundary conditions have been widely studied, both experimentally and numerically. Perhaps the case that got the most attention is the one of a bubble collapsing in the proximity of a boundary of large extent, e.g. a solid boundary [4, 116, 128, 193, 262–265], an elastic boundary [14, 101], or a free surface [24, 97, 211, 217]. In real-world conditions, the boundary is of finite extent and the cavity may be spuriously affected by more than a single boundary (for instance, the walls of a container or the liquid-free surface), exerting a considerable influence on the direction of the jetting [89, 266].
The jet dynamics are frequently characterised by a stand-off parameter [88, 117, 193] computed as the ratio of the distance between the bubble nucleation position and the boundary (d) and the maximum radius attained by the bubble after its creation ($R_{\max}$). If the cavity collapse occurs next to boundaries other than a plane, for instance, irregular or curved surfaces [74, 194, 267–269] like pillars [94, 270], fibres [95], corners [18, 271], crevices [272, 273], perforated plates [22, 135], or spheres [274–277], the anisotropy does not have one predominant direction and thus the use of a single stand-off parameter (e.g. $d/R_{\max}$) is no longer sufficient to fully characterise the system. The same situation arises

in cases where the bubbles are produced in a constricted space, for example in narrow channels [90, 91, 278], between two surfaces [231, 279], in a liquid column [280], or inside a drop [118, 196, 197, 247, 248].
The dynamics of jetting bubbles inside drops or curved free surfaces have not been extensively explored. Recently, we have reported experimental and numerical results on the formation of a jetting bubble in the proximity of a curved free boundary, given by the hemispherical top of a water column or a drop sitting on a solid plate [24]. As a natural extension of that work, we now present a study on the jet formation during the collapse of laser-induced bubbles inside a falling drop. This is a particularly interesting case as the bubble is surrounded entirely by a free boundary. From an experimental point, the intrinsic curvature of the liquid surface offers a very clear view of the bubble's interior.
The rapid acceleration induced by the bubble oscillations in the proximity of a free boundary also gives rise to surface instabilities, in particular Rayleigh-Taylor instabilities (RTI) [281–284]. This situation is more pronounced when the oscillating bubble wall gets close to the free surface, as commonly occurs in reduced volumes like a drop [118, 200]. The Rayleigh-Taylor instability produces corrugated patterns on the liquid surface that can grow and promote the onset of other instabilities like the Rayleigh-Plateau instability. Furthermore, the multiple pits and ripples produced by the RTI on the liquid surface can interact with the acoustic emissions of the oscillating bubble to generate a fluid focusing which results in a thin outgoing liquid jet [285, 286].
This article is organised into different sections focusing on one of the above-discussed aspects, i.e. the shock wave dynamics and the nucleation of secondary cavitation bubbles, the jetting dynamics of the collapsing laser-induced bubbles, and the formation of instabilities on the drop surface as a consequence of the bubble oscillation.

7.2 Experimental method

The experimental method used to achieve controlled laser bubble inception inside a millimetric drop is depicted in figure 7.1 (a). Individual drops were released from the tip of a blunt metallic needle with an internal diameter of 330 µm (and an external diameter of 600 µm) by the action of an electronic syringe pump *KD Scientific - Legato SPLG110*. This device pushed a fixed volume of $\sim$ 12 µl of deionised water through the needle, producing single drops with a radius of (1.42 ± 0.01) mm. After a drop was released it travelled a distance of $h = 30$ cm in free-fall motion. Just before it impacted a glass plate a pulsed laser was focused into the droplet to nucleate the cavitation bubble.
The pulse energy of the laser (Nd:YAG *Q2-1064* series, pulse duration 4 ns, wavelength 1064 nm) could be varied between 1.9 mJ and 20.3 mJ and was focused with a microscope objective (*Zeiss LD Achroplan* 20×, NA = 0.4) see bottom of figure 7.1 (a). In the experiments, a standard microscope slide was placed on top of the laser focusing objective in order to prevent wetting of its outer lens, which would provoke a significant distortion of the laser beam. Accordingly, the protective glass was meticulously cleaned after each drop impact.
The fall distance h was sufficient for the surface tension to stabilise the liquid into an approximately spherical shape, reaching a velocity of (1.7 ± 0.1) m/s upon laser arrival. At the same time, the variation of the lateral position of the drop centre relative to the laser focus was typically below 200 µm, which aids experimental repeatability. The vertical position where the bubble is created within the droplet is controlled with some precision by synchronising the laser pulse with the passage of the drop through a light gate. This

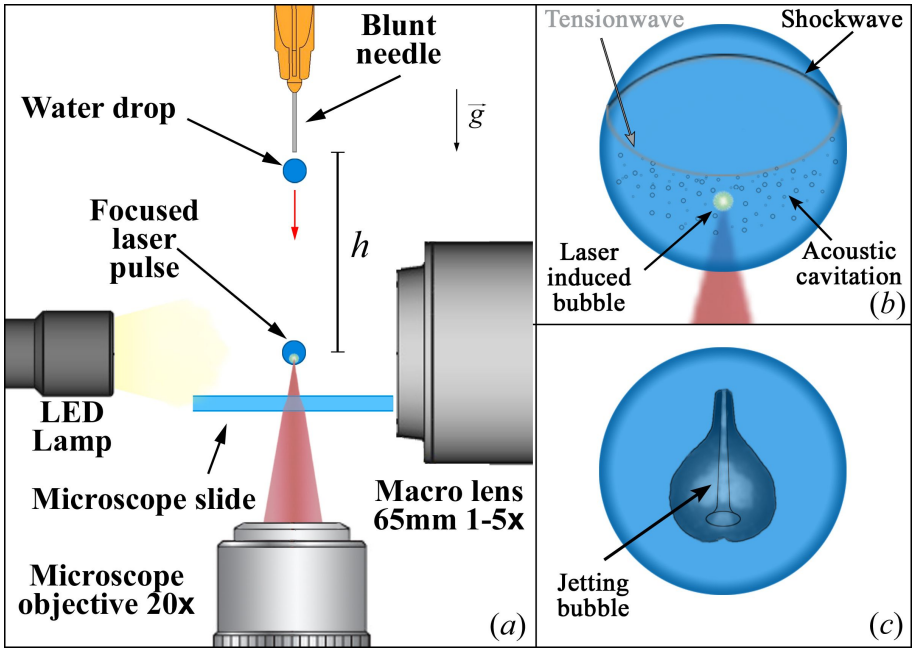

Figure 7.1: Description of the experimental setup. (a) A water drop with a volume of $\sim$ 12 µl is detached from a cylindrical blunt needle (stainless steel, 600 µm of external diameter) by gravitational forces. When the drop reaches a velocity of (1.7 ± 0.1) m/s a cavitation bubble is produced inside it by a laser pulse with a duration of 4 ns and a typical energy of (2.4 ± 0.1) mJ. (b) Once reflected from the drop surface, the shock waves emitted from the laser-induced bubble nucleate tiny bubbles inside the liquid drop. (c) The bubble undergoes an asymmetric collapse with jetting, whose shape depends on the position of the bubble inside the drop.

consists of a red laser diode paired with a photo-diode that triggers a digital delay generator *Quantum 9520* which then fires the laser after a specified time.
The dynamics of the cavitation bubble within the droplet and the resulting surface instabilities were captured in high-speed videos using a *Shimadzu XPV-X2* camera equipped with a photography macro lens *Canon MP-E 65 mm f/2.8 1-5×*. A diffused back illumination from a continuous white LED lamp *SMETec* (9000 lm) in combination with the curved nature of the drops allowed us to obtain clear images of the droplet interior. Furthermore, the curvature of the liquid refracted the light in a way that reveals the internal structures of the jetting bubbles, knowing that it distorts the apparent position and shape [85]. For direct comparison of the experimental and the numerical results, an *in-house* script was applied to the simulated results to compensate for such image distortions [287]. This correction (based on Snell's law) was also used to obtain the "real" nucleation position of the laser bubble.
Due to the limited number of recorded frames, the framing rate of the high-speed videos had to be adjusted to capture the important features of the phenomena under study. For instance, to visualise the shock wave propagation and the resulting nucleation of bubbles from the reflected rarefaction wave, see figure 7.1 (b)) required a frame rate of 5 Mfps (i.e. the maximum achievable by the camera), while the temporal evolution of the jets (depicted in figure 7.1 (c)) and the instabilities of the drop surface are captured already at 200 kfps or 500 kfps, respectively.

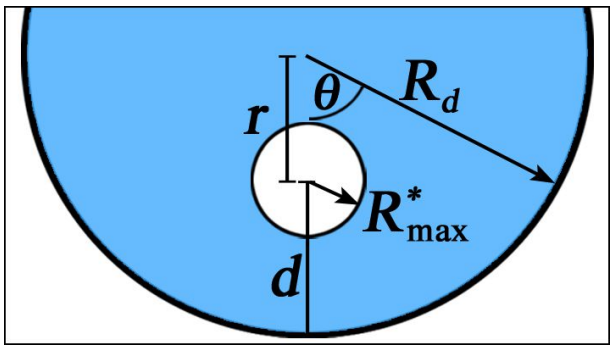

Figure 7.2: Schematic of the drop interior with relevant dimensional parameters.

7.2.1 Definition of a stand-off parameter for a curved boundary ϓ

In order to consider the curvature of the drop's surface in the characterisation of the jet dynamics, we defined a non-dimensional coefficient ϓ that combines two non-dimensional numbers, each one representing a relevant dimension of the problem. First, we use the stand-off distance D^* [117] as the ratio of the bubble "seeding" position (d) and the maximum radius achieved by the bubble when produced at the centre of the spherical drop ($R^*_{\max}$). The second non-dimensional distance χ is given by the ratio of the drop radius (R_d) and the distance of the bubble from the drop centre (r). To summarise,

$$D^* = \frac{d}{R^*_{\max}} \,, \tag{7.1}$$

$$\chi = \frac{R_d}{r} = \frac{R_d}{R_d - d} \,, \tag{7.2}$$

$$ϓ = \chi\, D^* = \frac{R_d}{(R_d - d)}\,\frac{d}{R^*_{\max}} \,. \tag{7.3}$$

A schematic representation of the aforementioned parameters is presented in figure 7.2. Here, $R^*_{\max}$ is tightly related to the energy of the laser pulse [117] and, as we explain later in section 7.4.3, it also varies slightly with the drop size as $R_d \to \infty$. For the purpose of having reproducible results, the use of ϓ should be limited to values of $R^*_{\max}$ for which the bubble is contained inside the drop volume (i.e. $0 \leq R^*_{\max} < R_d$) and the drop shape is not significantly distorted by surface instabilities [118]. Additionally, the symmetry of the drop/bubble configuration implies that $d \leq R_d$.
In principle, the parameter ϓ behaves similarly as the traditional stand-off distance (e.g. $d/R_{\max}$), however, the addition of χ as a weighting factor represents a measure of the influence of the boundaries all around the bubble, and not only its closest point. This means that the regions of the free surface in directions other than $\theta = 0°$ could also be relevant to the bubble dynamics as the separation from the bubble and the boundary in those angular directions gets smaller, i.e. when the radius R_d is decreased and the bubble is located at a reduced d. Alternatively, ϓ could be understood as a measure of the anisotropy, with high anisotropy at the liquid boundary ($d \to 0$) and perfect isotropy at the bubble centre, $d = R_d$.
The tight relation between the traditional stand-off distance and ϓ is also evidenced by the following considerations and limiting cases:

- ϓ rises monotonically with d for a fixed laser pulse energy (or $R^*_{\max}$).

- In the limit $R_d \to \infty$ the traditional stand-off distance is recovered.
- If the bubble is near the drop wall, $d \to 0$, then $\text{ϒ} \to 0$.
- If the bubble is near the drop centre, $d \to R_d$, then $r = 0$, $\text{ϒ} \to \infty$, and we recover the traditional unbounded case, in which the bubble collapses spherically due to symmetry.

It is important to note that ϒ can take the same value for different combinations of d, $R^*_{\max}$, and R_d. Therefore, two identical values of ϒ computed from two different values of D^* and χ do not necessarily result in identical bubble dynamics. A comparison between cases could be made by fixing the value of one or two of the parameters. For example, the effect of the surface curvature R_d on the bubble dynamics can be evaluated by maintaining D^*, or the influence of the "seeding" depth d can be studied by fixing the drop size R_d and the energy of the laser pulse. In this way, the parameter preserves the same functionality as the traditional stand-off parameter [117] but now includes the surface curvature dimension.

7.3 Numerical method

Volume-of-Fluid simulations were carried out in *OpenFOAM-v2006* [125] using a modification of the solver *compressibleMultiphaseInterFoam*. This modified version is called *MultiphaseCavBubbleFoam* and was already implemented in previous works to study the formation of the "bullet jet" [24] and micro-emulsification [23]. In those works, similar simulations of a single expanding and collapsing bubble in the vicinity of a liquid-gas and a liquid-liquid interface were performed, respectively. Since the solver is explained in detail there, we will only give the information that is specific to the present case of a bubble created in a free-falling liquid drop.

Considering the approximate rotational symmetry of the experimental configuration, we carried out the simulations as quasi-two-dimensional. The computational domain represents a slice of a cylindrical domain with a height of 3 mm and a radius of 3 mm, which is filled with a gas representing the surrounding air at ambient pressure. The domain is divided into a square mesh of cells with a width of 40 µm, which is then further refined to a cell width of 10 µm in the region occupied by the liquid drop. The boundaries of the domain in the radial and axial directions are open, wave transmissive boundaries.

A slightly prolate ellipsoidal liquid drop representing a falling water drop is initiated in the centre of the cylinder with an axial radius of 1440 µm and a radial radius of 1400 µm. We neglect the relative motion of the drop through the air and thus take the drop and the air to be initially at rest. This is because the speed of the falling drop and the effects of drag are negligible when compared with the speeds developed by the bubble wall and the jets. We also neglect any subsequent gravitational acceleration, since its effect is negligible on the time scales considered. Inside the drop, a bubble is seeded on the symmetry axis with an initial over-pressure of 1.69 GPa and an initial radius of 25.7 µm. The initial pressure was chosen such that the initial bubble gas density equals the density of the surrounding liquid, in accordance with equation (7.4). This is based on the assumption that the laser energy deposition occurs on a much smaller time scale than the expansion of the bubble. The initial bubble radius R_0 is chosen to match the maximum expansion $R^*_{\max}$ in the experiment.

The bubble contents are modelled with the same properties as the gas surrounding the

	B in MPa	ρ_0 in kg/m^3	p_0 in Pa	γ	μ in mPa s
liquid	303.6	998.2061	101325	7.15	1
gases	0	0.12	10320	1.33	0.013

Table 7.1: Tait equation of state parameters and dynamic viscosities μ of the simulated fluid components. Both gaseous components are treated as the same type of gas.

liquid droplet but are calculated as a separate component. This allows us to apply a mass correction to the gas in the bubble only that accounts for the mass loss due to condensation during the bubble's first oscillation cycle. This is done as a one-time correction at the time of maximum bubble expansion, at which the bubble gas density is reduced by 70 %. More details can be found in our previous work [24]. The surface tension between the liquid and the gases is 70 mN/m, and that between the gases is 0. The Tait equation of state is used for all components,

$$p = (p_0 + B)\left(\frac{\rho}{\rho_0}\right)^{\gamma} - B \ , \tag{7.4}$$

with the parameters given in table 7.1. Here, γ is the adiabatic exponent.
The output of the numerical data was done in intervals of 10 ns to capture shock wave propagation dynamics, and every 1 µs for the bubble and jetting dynamics.

7.4 Results and discussion

The inception of a laser-induced bubble inside a liquid drop gives rise to a rich and complex chain of events. We start with an overview of the fluid dynamics that are observed following the creation of the cavitation bubble by the dielectric rupture of the liquid, as shown in figure 7.3. Here, the bubble is nucleated off-centre and close to the upper interface of the droplet. The fluid dynamics can be divided into three stages, which are discussed in detail in the later sections. For now, we provide a brief description of these 3 stages: (1) The bubble is nucleated into a rapidly expanding vapour cavity that launches during its deceleration a shock wave into the droplet, not visible in figure 7.3. Upon reflection at the acoustic soft liquid-gas interface, the rarefaction wave propagates through the drop leaving behind a trail of cavitation bubbles in certain regions where the wave convergence produces sufficient tension to induce local acoustic cavitation, $2\,\mu s \leq t \leq 6\,\mu s$ in figure 7.3. Depending on the location of the laser bubble the rarefaction wave may focus in a reduced volume close to the interface, creating secondary cavitation and provoking the ejection of a single jet at the opposite side of the laser bubble nucleation site (e.g. $t > 6\,\mu s$ in figure 7.3). (2) In the second stage, the laser-induced bubble undergoes an asymmetrical collapse from its maximum size. Here, the anisotropy of the boundary conditions results in the formation of a jet, which starts as an indentation on one side of the cavity and grows to pierce the bubble at the opposite extreme. In cases where the laser cavity is created near the drop surface, we also observe the destabilisation of the liquid surface by a Rayleigh-Taylor instability. (3) In the third and last stage, the bubble re-expands after jetting, adopting a liquid-gas structure that depends mostly on the stand-off distance (i.e. $\mathfrak{F}$). On its second collapse, the cavity fragments and later disperses due to the complex flow created by its first collapse.
In the following, the reported values of $\mathfrak{F}$ are computed for a surface curvature of 1.42 mm, which corresponds to the mean radius of the drops produced in this work.

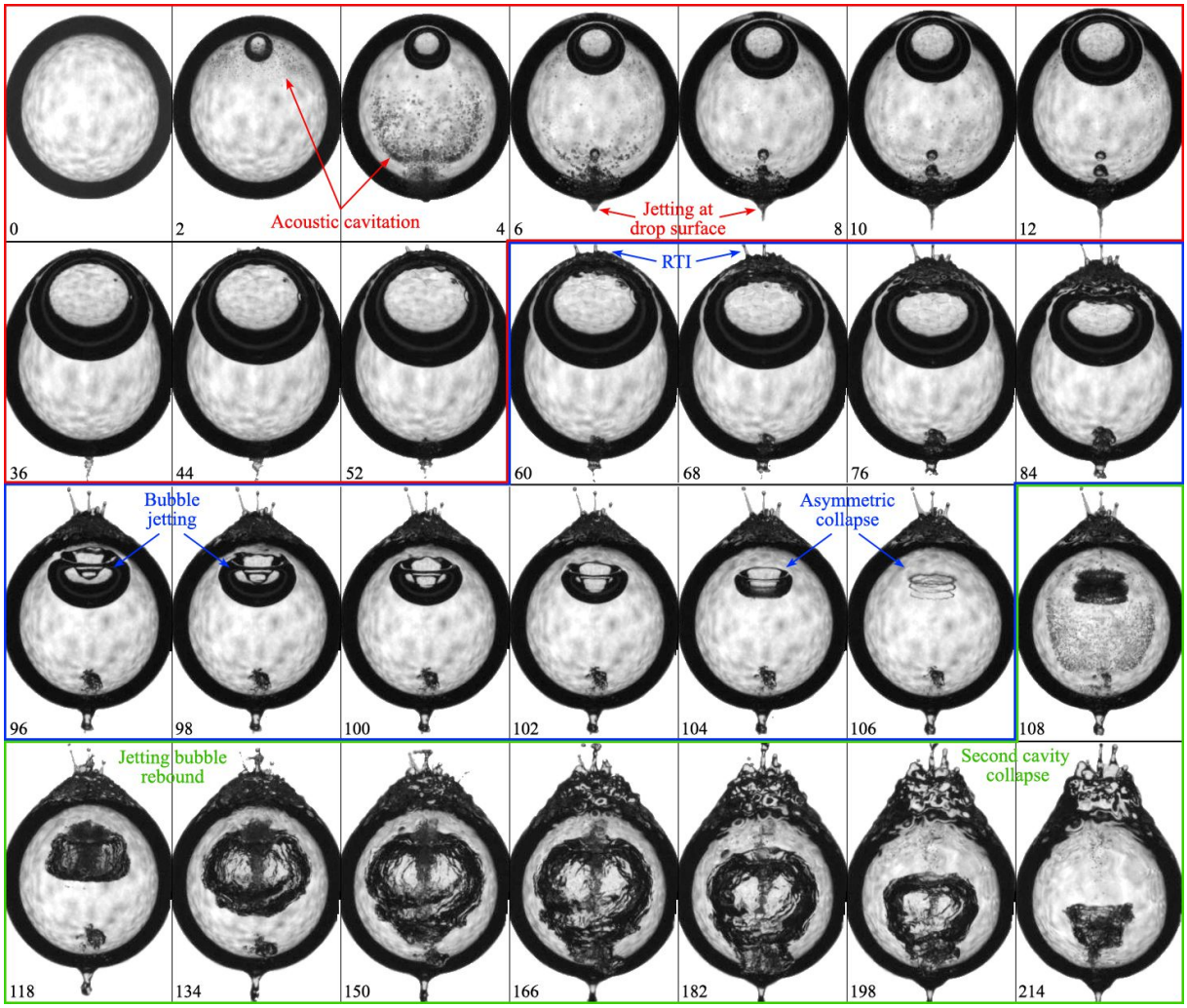

Figure 7.3: Stages of the events developing inside the drop. The numbers indicate the time in µs after the laser shot. In the first stage, spanning from $t = 0$ µs to $t = 52$ µs(framed in red), a rarefaction wave (i.e. the reflection of the shock wave) produces a trail of cavitation bubbles. For low values of $\mathfrak{H}$ a liquid jet is ejected from the extreme of the drop opposite to the bubble inception. In the second stage, defined between $t = 60$ µs and $t = 106$ µs(framed in blue), the bubble collapses after reaching its maximum size and a jet forms. In some cases, a Rayleigh-Taylor instability (RTI) is observed near the bubble. The third stage (framed in green) runs from $t = 108$ µs until the end of the video at $t = 214$ µs. Here, the bubble re-expands after jetting and adopts a characteristic shape during its second collapse that depends mostly on $\mathfrak{H}$. The width of each frame is 2.70 mm.

7.4.1 Acoustic cavitation nucleation

The specific shape of the cavitation bubble clusters produced by the passage of the rarefaction wave is highly dependent on $\mathfrak{H}$. This is because the negative pressure focuses differently when the original shock wave is emitted from a different location. As the acoustic nucleation only occurs below a certain pressure threshold, the resulting bubble clouds can assume complex three-dimensional structures. Figure 7.4 presents experimental results showing the temporal evolution of bubble clouds generated for different values of $\mathfrak{H}$. In this study, the bubble "seeding" position was varied by changing the delay between the drop release and the laser shot, thus shifting the laser focus position along the vertical

symmetry axis of the drop.
As aforementioned, the shock waves emitted from the laser focal spot will reflect from the free boundary of the drop as a rarefaction wave. Due to the nearly spherical shape of the drop, the reflected acoustic waves will focus in a region located at a similar distance from its centre r (where the laser bubble was created) but on the opposite side of the drop. In the case where the shock wave originates near the surface (i.e. $\mathfrak{F} \lesssim 1$), the resulting pressure distribution is characterized by a negative pressure zone moving close to the liquid surface which produces a spherical shell of tiny cavitation bubbles, as displayed in the panels (a) to (c) (and also (i) to (j)) of figure 7.4. This phenomenon occurs when the sound reflects multiple times on the drop walls and travels circumferentially near the liquid surface without a significant loss of intensity, which is usually referred to as the "whispering gallery effect" [288]. As the rarefaction waves focus at a similar depth where the shock wave was emitted, it produces explosive cavitation events close to the free boundary and on the drop's vertical axis. The rapid expansion of those larger cavitation bubbles gives rise to the liquid jets shown in the first row of figure 7.3. A more detailed explanation of the formation and dynamics of this particular type of jet will be published elsewhere.
As the laser focusing depth d is increased, the negative pressure is distributed in larger regions, but still, the nucleation of bubbles predominantly occurs on the side opposite to the laser focus. Additionally, the bubble clusters turn from having the structure of a shell (see panels (g), (h), and (i) of figure 7.4) into a volumetric cavitation cloud when the laser bubble is generated near the drop centre, as shown in the panels (e) and (f) of figure 7.4. This transition can be explained by analysing the pressure distribution dynamics with the numerical simulations [197, 252, 289]. Figure 7.5 demonstrates the clear correlation between the evolution of the acoustic pressure profile and the nucleation of secondary cavitation bubbles. Furthermore, this correlation can be used to determine the cavitation pressure threshold of the liquid by comparing the shape and the location of the negative pressure front with the shape of the bubble cloud within the drop. Such a comparison was only possible after applying a numerical algorithm to the simulated results to compensate for the image distortions induced by the drop curvature. The last frames in panels (a) and (b) of figure 7.5 display an overlap of both the experimental video frames and the simulated pressure profiles. From the measurements, we found a consistent cavitation threshold of approximately 4.5 MPa. Considering that we did not filter the water sample we assume that the cavitation is most likely heterogeneous.
The acoustic cavitation thresholds reported for water in the literature vary strongly, depending on the measurement method, water purity, gas saturation, and water temperature. Atchley et al. [290] used distilled, deionised, and filtered (0.2 µm) tap water irradiated by pulsed ultrasound and found thresholds between 0.5 and 2.0 MPa, depending on the pulse duration and frequency. Sembian et al. [253] subjected a water column to a single shock wave and found a cavitation threshold between 0.42 and 2.33 MPa. Biasiori-Poulanges and Schmidmayer [258] compared numerical simulations and experiments of a liquid drop subjected to a planar shock wave and found a threshold between 0.37 and 2.4 MPa. A similar shock front can be found when a droplet impacts on a solid surface at a high speed (e.g. higher than 100 m/s) as studied by Kondo and Ando [254], Wu et al. [256], and Wu et al. [257]. Assuming homogeneous nucleation, Ando et al. [289] and later Quinto-Su and Ando [252] found a cavitation threshold of 60 MPa and 20 MPa, respectively, comparing experiments and simulations of a reflected shock wave at a free boundary. Therefore, the threshold value obtained in this work falls around the middle

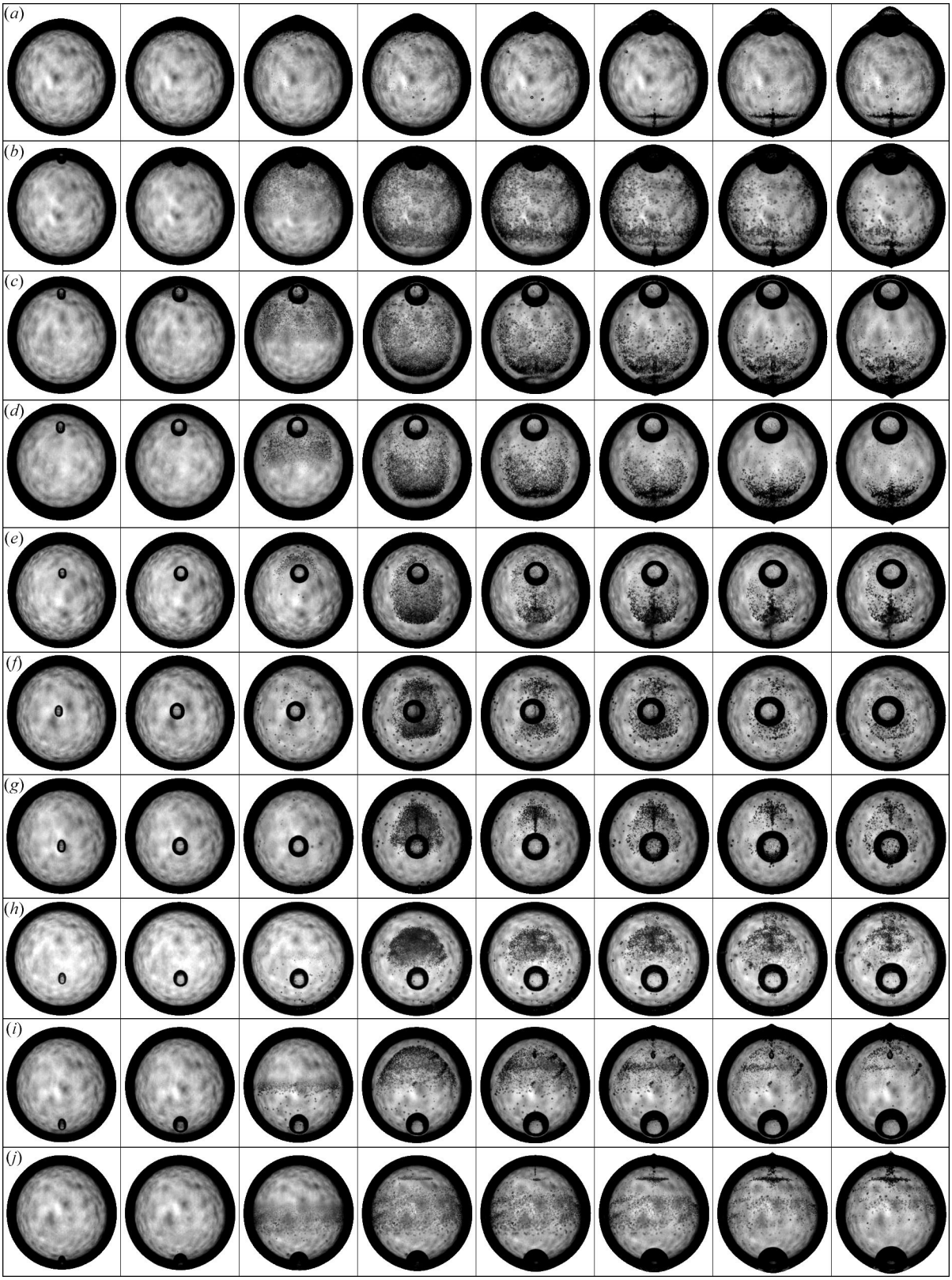

Figure 7.4: Acoustic cavitation inside a water droplet. The distribution of bubbles in the liquid changes significantly with the position of the laser-induced bubble. The frame width is 3.15 mm. The time between consecutive frames is 600 ns. (a) $\Upsilon = 0.65$. (b) $\Upsilon = 1.1$. (c) $\Upsilon = 1.7$. (d) $\Upsilon = 2.5$. (e) $\Upsilon = 7.5$. (f) $\Upsilon = 68$. (g) $\Upsilon = 13$. (h) $\Upsilon = 5.4$. (i) $\Upsilon = 1.8$. (j) $\Upsilon = 0.9$. Full videos of panels (b), (d) and (f) are available in the online supplementary movies 1-3.

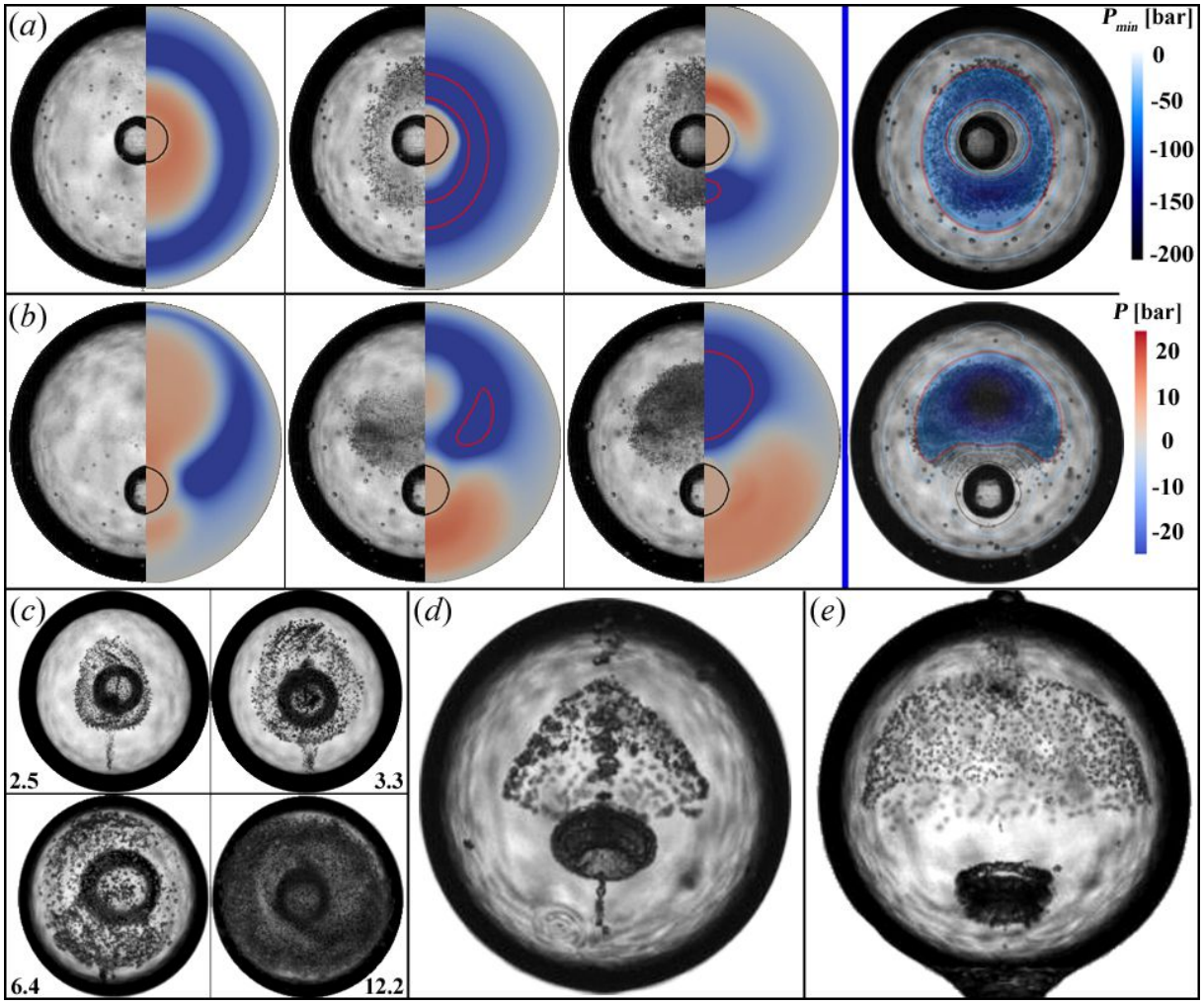

Figure 7.5: Acoustic cavitation bubble clouds for laser-induced bubbles at different relative positions in the drop. The frames compare the advance of the shock/tension waves within the drop with the observed nucleation sites. The average drop diameter is (2.84 ± 0.05) mm in all cases. The last frame of each series presents an overlay of the frames and the cumulative minimum pressure after the first reflection of the shock wave at the free boundary. The red line indicates the isobar of -4.5 MPa, i.e. the approximate nucleation threshold pressure. (a) Here, the bubble is slightly off-centre (i.e. $d \simeq R_d$). (b) $\Upsilon = 5.4$. (c) Change in the cluster dimensions with increasing laser pulse energy (indicated in mJ). (d) and (e) present evidence of the formation of complex hollow three-dimensional bubble structures. Here, Υ is 3.5 and 1.45, respectively.

of the spectrum of values measured by other authors. Figure 7.5 (c) evidences a growth in the secondary bubble cluster with increasing energy of the laser pulse, demonstrating the resulting shift in the location of the cavitation threshold isobar for higher amplitudes of the initial shock wave. It is relevant to point out that VoF simulations are notorious for numerical diffusion which causes the shock wave to smear out over time. Because of this, the simulations may underestimate the pressures reached in the experiments. Please note that the VoF model does not account for phase transitions and the subsequent interaction of nucleated cavitation bubbles with the finite amplitude waves. A model for high-frequency waves interacting with small cavitation clouds that may be applicable was recently developed by Maeda and Colonius [291]. Finally, panels (d) and (e) of fig-

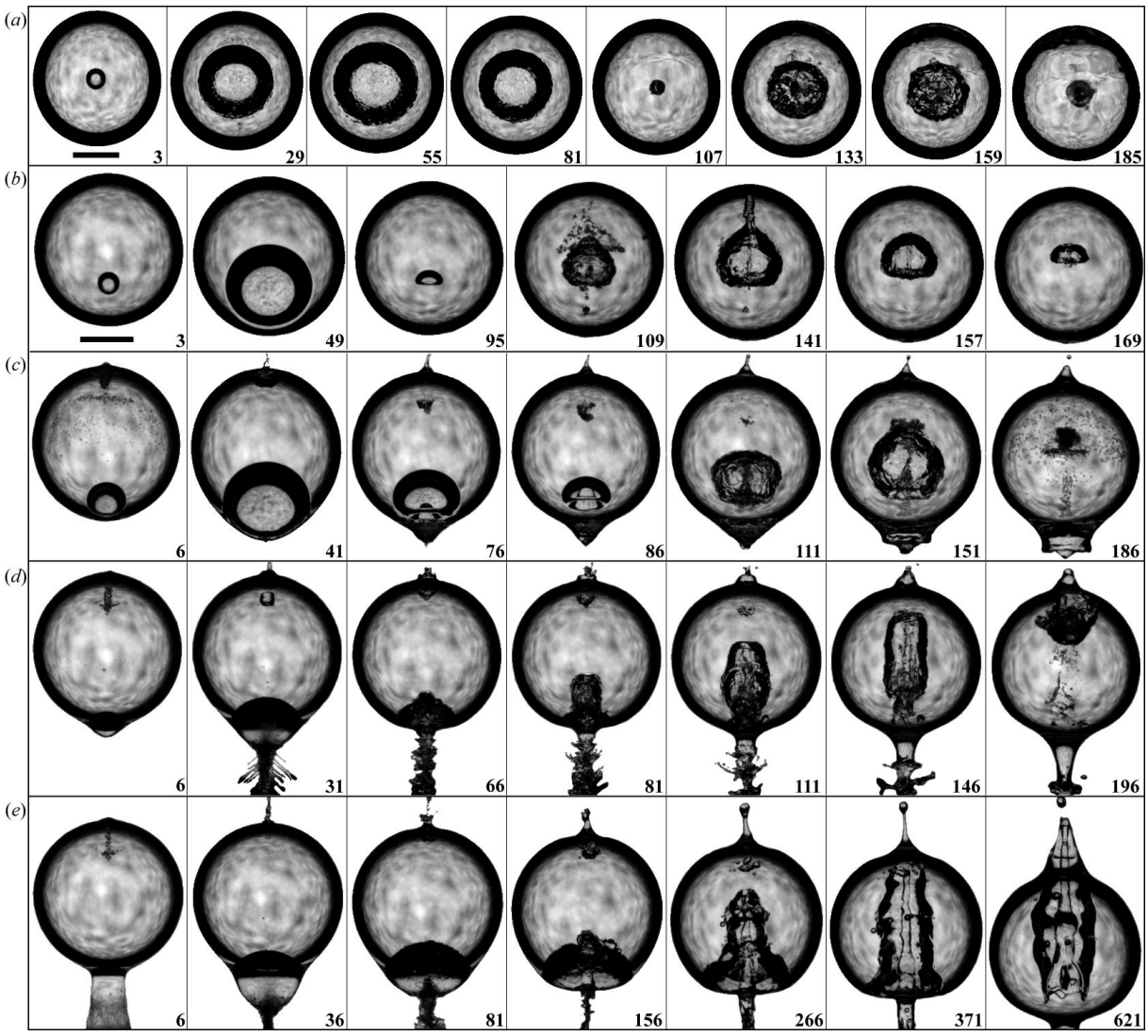

Figure 7.6: Bubble jetting is produced by a laser-induced bubble generated at different relative positions inside the drop. The numbers indicate the time in µs. The length of the scale bars is 1 mm. (a) Spherical oscillation case, $\Upsilon = 203$. (b) Weak jet case, $\Upsilon = 3.9$. (c) Standard jet case, $\Upsilon = 1.5$. (d) $\Upsilon = 0.44$. (e) Bullet jet case, $\Upsilon = 0.22$. Full videos are available in the online supplementary movies 4-8.

ure 7.5 exemplify some of the hollow three-dimensional bubble structures observed in the experiments.

7.4.2 Bubble jetting

In the second stage presented in figure 7.3 the laser-induced bubble reaches its maximum radius and then collapses. At this point, it becomes clear that a non-uniform distance between the bubble and the free surface produces an asymmetric collapse, which culminates in a liquid jet. In this section, we explore the effect of varying the parameter Υ (as performed in section 7.4.1), but this time we lay focus on the development of the jets, as shown in figure 7.6.

The experiments reveal that, as the position of the laser focus is varied between the centre and the surface of the drop, the characteristics of the jetting change smoothly: For large

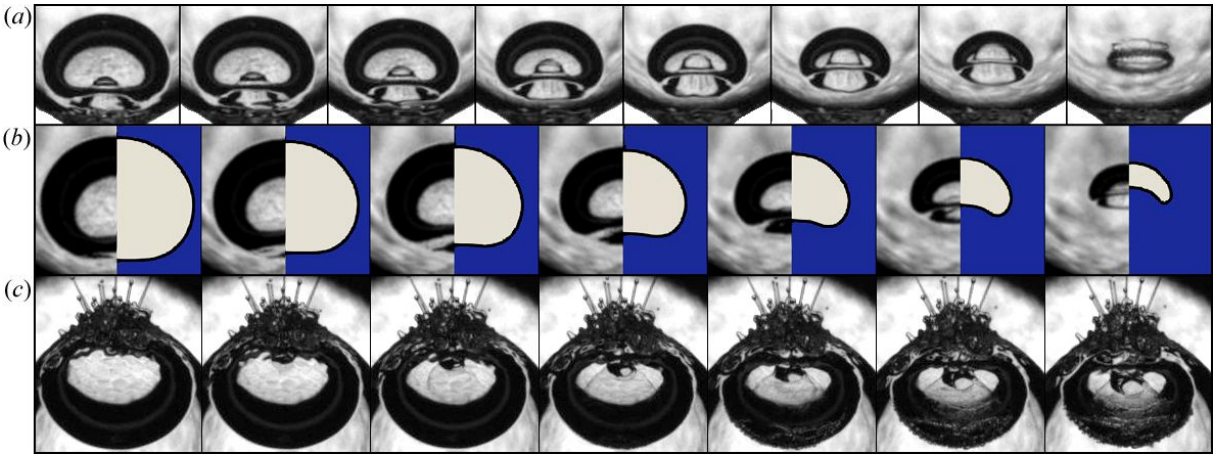

Figure 7.7: Detailed view of the interior of a jetting bubble. The time between frames is 2 µs. (a) Jet formation for $\Upsilon = 1.6$. The frame width is 1.46 mm. (b) Comparison between experimental data and a simulation performed for $\Upsilon = 2.9$. The frame width is 1.38 mm. (c) Spray produced by air entering the gas cavity (in which the pressure is lower than the atmospheric pressure) while the jet is formed. The frame width is 2.11 mm.

values of Υ, a spherical rebound of the bubble without any jetting is observed. The values of $\Upsilon \gtrsim 3.5$ are accompanied by the formation of a very thin liquid jet crossing through the centre of a weakly deformed bubble. In this "weak jet" case, the tip of the jet separates from the main cavity when it starts to collapse during its second oscillation cycle (see figure 7.6 (b)). For $1.2 \lesssim \Upsilon \lesssim 3.5$, as in panel (c) of figure 7.6, the "whispering gallery" effect becomes relevant, causing the inception of larger acoustic bubbles on the side opposite to the laser cavity and the ejection of liquid driven by their expansion. The deformation of the bubble in its rebound phase is significantly stronger than in panel (b) of figure 7.6. As the laser is focused closer to the drop's surface, i.e. $0.3 \lesssim \Upsilon \lesssim 1.2$, the expansion of the bubble provokes the onset of a Rayleigh-Taylor instability. This can be seen in figure 7.6 (d) by the formation of several "spikes" growing from the thin liquid film trapped between the cavity and the surrounding air. At the same time, the bubble collapse (from $t = 66$ µs) results in an elongated cavity, similarly as in the "bullet jet" case [24]. This behaviour is more pronounced for even smaller stand-off distances, as presented in figure 7.6 (e). The dynamics of this particular jet are described in detail in Ref. [24] and correspond to the case where the laser cavity is generated almost directly on the surface of the drop (i.e. $0.01 \lesssim \Upsilon \lesssim 0.3$). Here, atmospheric gas is trapped after the closure of a conical ventilated splash and later dragged into the liquid by the liquid jet that grows from a stagnation point located on the top of a "water bell" (at the bottom of the frame at $t = 36$ µs). As a result, an elongated gas cavity is shaped and driven across the drop.

The combined effects of the curved shape of the drop in addition to the diffuse illumination lead to images of the interior of the gas cavity with remarkable clarity. A few examples of this are presented in figure 7.7.

Panels (a) and (b) of figure 7.7, reveal the temporal evolution of the liquid indentation into the bubble, as well as the toroidal shape acquired by the gas upon its collapse. Moreover, figure 7.7 (b) demonstrates the accuracy of the numerical simulations to reproduce the jetting process. In panel (c) we see how a perforation of the thin liquid sheet between the cavity and the atmosphere resulted in a spray of aerosol droplets ejected into the

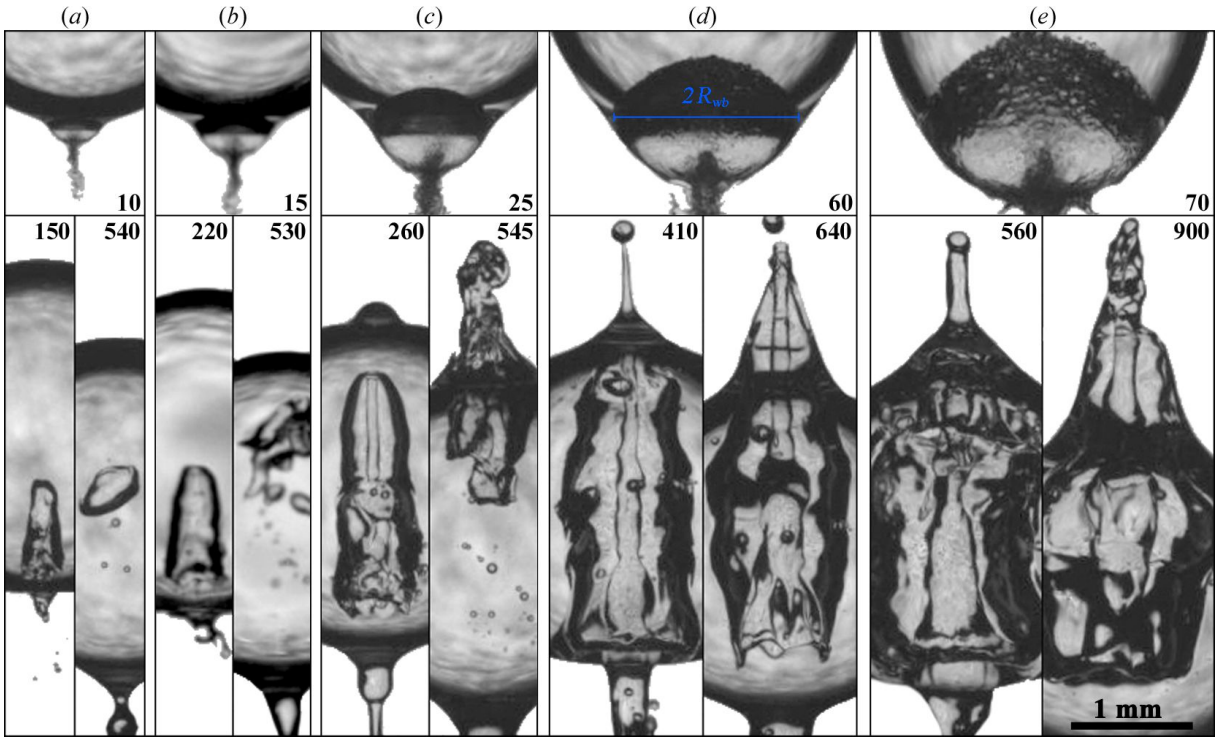

Figure 7.8: Scalability of the bullet jet in a millimetric droplet. The measurements, organised in columns, show bullet jets formed from different splash sizes. In each column, the upper frame shows the time at which the water bell closes. In the lower frame, composed of two vertical stripes, the time at which the bullet jet is fully developed is shown on the left, and a frame illustrating the position of the jet tip at an advanced time indicated in µs is shown on the right. (a) $R_{wb}/R_d = 0.16$. (b) $R_{wb}/R_d = 0.27$. (c) $R_{wb}/R_d = 0.37$. (d) $R_{wb}/R_d = 0.56$. (e) $R_{wb}/R_d = 0.74$.

cavity during jetting. This event can be explained by the lower pressure inside the bubble compared to the atmospheric pressure and the disruption of the liquid on the upper side of the drop caused by the RTI. The spray front spreads into the cavity and collides with the lower wall of the bubble, disrupting the smoothness of the interface.

The bullet jet case of figure 7.6 (e) distinguishes itself from the other cases by its unique features, i.e. its enhanced shape stability during its formation from an open splash, but also by the near robustness against the surrounding fluid and geometry. Bullet jets have been observed in shallow waters [14] and near flexible or rigid materials, without these conditions affecting their dynamics. Furthermore, in a previous work [24], we demonstrated that the bullet jet is scalable and independent of the orientation of the surface with respect to gravity. In figure 7.8, we expand the list of remarkable robustness by showing it to exist of various sizes even within a highly curved and finite volume. Here, the bullet jet size was characterised by the ratio between the radius of the water bell at its base (R_{wb}) measured right after its formation and the initial drop radius R_d (i.e. R_{wb}/R_d).

The images depict that the penetration depth of both the gas and the liquid conforming to the bullet jet is proportional to the initial splash size. For instance, in figure 7.8 (a) the jet loses its momentum and stops around the middle of the drop, but it crosses the drop for the larger splashes shown in the panels (c) to (e). Remarkably, in the latter case the bullet jet occupies almost the entire drop while still preserving its characteristic features.

The physics behind the evolution of the bubble jetting cases classified in figure 7.6 can be further explained with the aid of numerical simulations, as presented in figure 7.9.

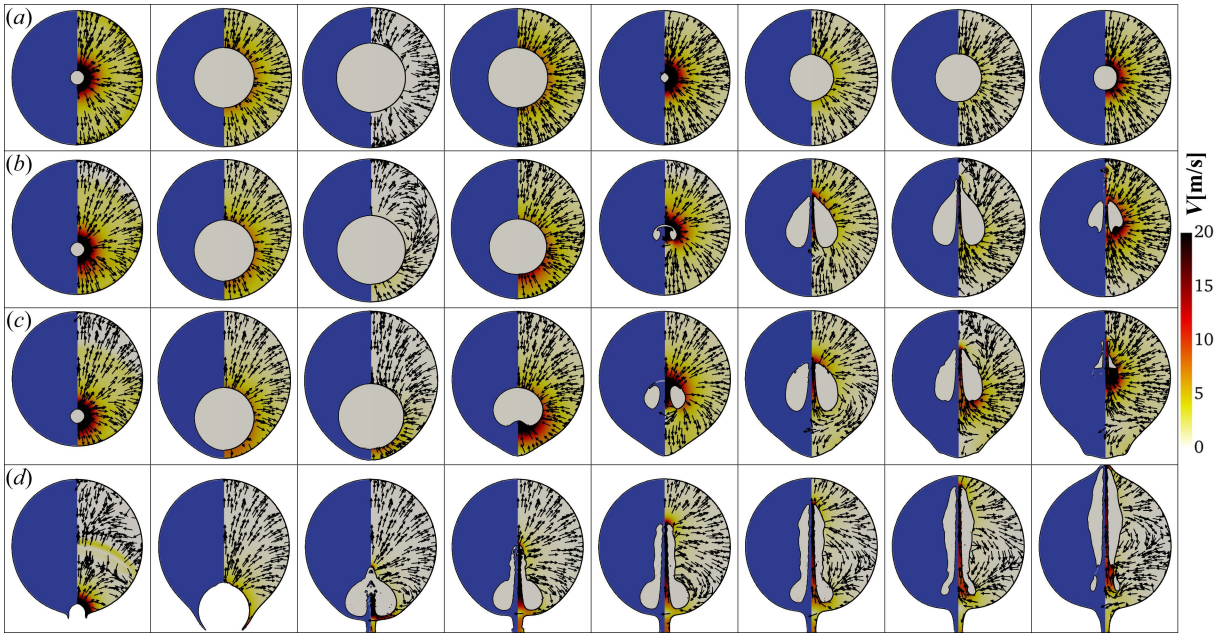

Figure 7.9: Numerical simulations of the temporal evolution of jets produced inside the drop for different Υ. The simulated drop has a height of 2.88 mm and a width of 2.8 mm as measured in the experiments. The plot shows the gas and liquid phases along with the velocity field. The time between frames is 26 µs for (a)-(c) and 30 µs for (d) starting at $t = 1$ µs in the first frame. (a) Spherical oscillation case, $\Upsilon \to \infty$. (b) Weak jet case, $\Upsilon = 3.896$. (c) Standard jet case, $\Upsilon = 1.518$. (d) Bullet jet case, $\Upsilon = 0.028$.

Figure 7.9 (a) depicts a purely radial oscillation of both the gas and liquid, found when the bubble is placed in the centre of the drop (i.e. $\Upsilon \to \infty$). The simulations shown in panels (b) and (c) of figure 7.9 were computed using the same Υ measured from the experimental cases displayed in the corresponding panels of figure 7.6. In general, the agreement between the simulations and the experiments is excellent, even though small variations in the size of the experimental and simulated bubbles show some differences in the specific timing of their oscillation cycle. The resemblance can be seen in some of the morphological features that characterise the dynamics of each type of jet at different stages, like the width of the indentation formed during bubble piercing, the shape of the cavity after the first rebound, and the way in which the second collapse evolves in each case. More details on noteworthy features are provided below in figure 7.10.
In panels (a) to (c) of figure 7.9 the bubble is initiated with a much larger pressure than the atmospheric gas outside the drop. This pressure difference, which is constant in all directions, accelerates the liquid between the two gas domains. Since this force is proportional to the pressure gradient, the liquid gets accelerated more strongly between the bubble and the nearest part of the drop surface (where the liquid is thinner), causing the drop to bulge out in that location. Within the first few microseconds of the explosive bubble expansion, the pressure within the bubble decreases rapidly and reaches values much smaller than the atmospheric pressure. Thus, the pressure gradient changes its direction and now accelerates the liquid towards the bubble, which first slows down the cavity's expansion and afterwards causes its collapse. In the same way as in the expansion phase, the thinnest part of the liquid experiences the strongest acceleration, which ultimately

leads to a liquid jet indenting the bubble from the nearest part of the drop surface.
The case presented in figure 7.9 (d) differs greatly from the previous cases by the fact that now the bubble is close enough to the drop surface to generate an open cavity, allowing the ejection of the initially pressurised gas inside it into the atmosphere, and later the flow of gas into the expanded cavity before the splash closes again. Once the cavity is closed, it remains with an approximate atmospheric pressure, which prevents it from undergoing a strong collapse as it occurs in the previously discussed cases (a) to (c). The radial sealing of the splash forms an axial jet directed toward the centre of the drop, which pierces the bubble and drags its content through the drop. More details on the mechanisms behind the bullet jet formation can be found in Ref. [24].
As a consequence of the conservation of momentum, the collapse of the gas cavity gives origin to a stagnation point, from which the liquid flows both inside the pierced bubble and away from it in opposite directions. In particular, the stagnation point is not stationary but moves along the axis of symmetry, following a different trajectory in each case. In the case of figure 7.9 (b) the stagnation point shifts towards the surface as the bubble moves deeper into the drop. For the case in figure 7.9 (c) the stagnation point does not reach the surface and its movement is less pronounced. In the bullet jet case, shown in figure 7.9 (d), the stagnation point forms on the apex of the water bell (i.e. the splash after its closure). It then trails the bell's collapse and remains very close to the drop surface afterward, moving slightly towards the drop centre while the bullet jet moves across the drop.

Cavity dynamics on its second collapse

After the jetting, the subsequent re-expansions and collapses of the cavities are characterised by the bubble's and the drop's distorted shapes and even more complicated flow fields. A good example of this can be found in the second collapse of the bubbles analysed in figure 7.10, which shows a significant dependence on $\mathfrak{Y}$.
Figure 7.10 compares the shape taken by the bubble for two cases with $\mathfrak{Y} = 3.9$ (panels (a) and (b)) and $\mathfrak{Y} = 1.9$ (panels (c) and (d)). Interestingly, the flattened side of the "teardrop" shape acquired by the cavity after the re-expansion develops a curved indentation during its second collapse. The numerical simulations make clear that such an indentation is created by the flow produced by an uneven pressure gradient on the cavity surface. The shape of this ring-shaped indentation visibly changes with $\mathfrak{Y}$. For example, the case presented in figure 7.10 (c) displays an annular bubble necking with the detachment of two gaseous rings as the cavity shrinks. These concentric rings have two different diameters and are arranged in two distinct planes, as highlighted in figure 7.10 (d).

Influence of R_d on the jet dynamics: Behavioural similarity vs. structural similarity

The bubble dynamics observed in the falling drop case have many similarities with what is typically seen in bubbles collapsing near a planar rigid surface [117] or a planar free surface [24, 88]. Moreover, the analysis of the values of the stand-off parameter D^* reveals that each type of jet (qualitatively classified according to figure 7 in Ref. [24]) occurs in a comparable range of values of D^*. One example of the latter can be found in figure 7.11. The parallel found between cases with dissimilar curvature of the liquid surface suggests that, contrarily to the reported observations for bubbles collapsing near concave solid surfaces [269], R_d does not have a dominant role in the particular jetting regime adopted

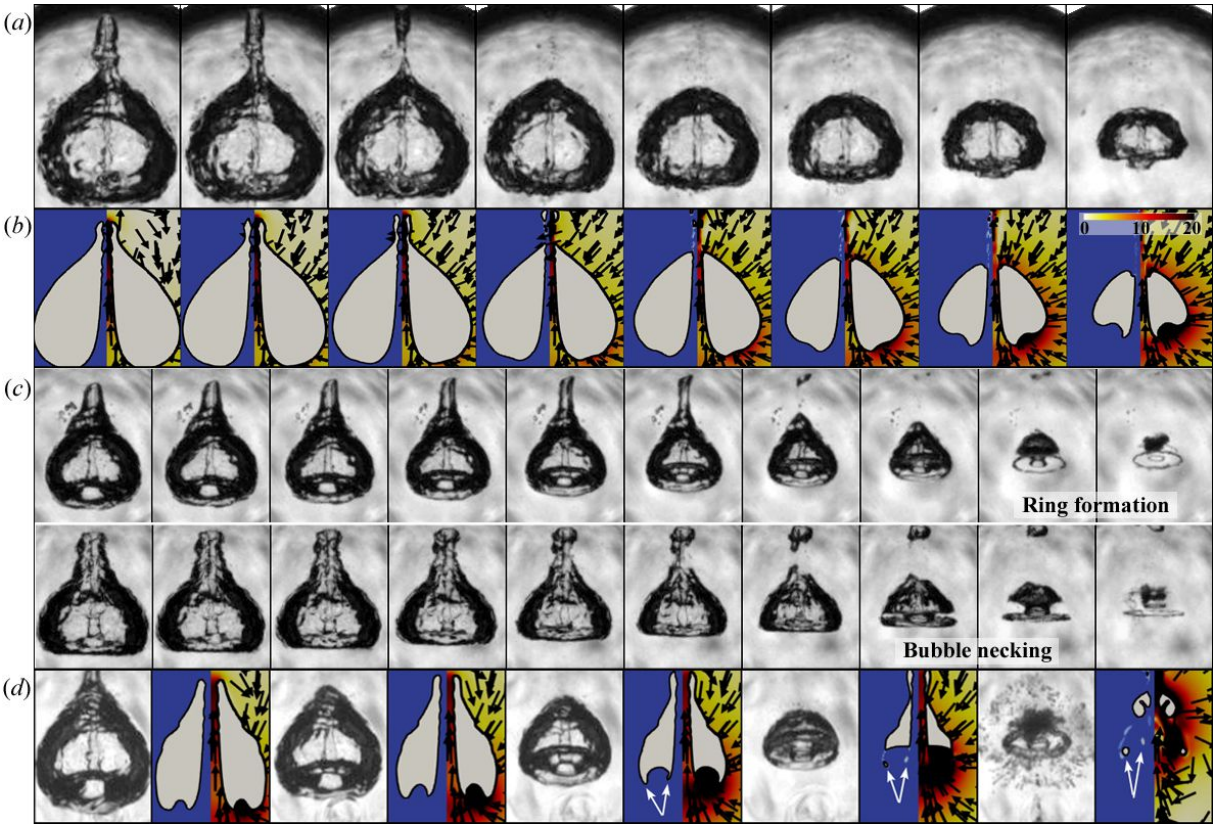

Figure 7.10: Detailed collapse dynamics of the gas cavity immediately after the jetting of the laser bubble. Experimental (a) and simulated (b) view of the "weak" jet obtained when $\Upsilon = 3.9$. The images were taken at 200 kfps. (c) Ring formation after the necking of the cavity typically observed on cases with $\Upsilon \approx 1.9$. The images were taken at 500 kfps. (d) Direct comparison between experiment and simulation, revealing the precise flow pattern leading to the ring detachment (indicated by the white arrows). The time between frames is 2.5 µs. The colour scale in the simulations corresponds to the one in figure 7.9.

by the cavities when the bubbles are located near the free boundary. This statement was confirmed by the numerical simulations depicted in figure 7.12. There, the dynamics of identical bubbles expanding and collapsing near the surface of the drop, or the flat free surface of an ideally infinite pool, are compared for three stand-off distances D^*.
The simulations show that the correspondence between the flat and the curved surface cases is gradually lost when the bubble is placed further away from the drop surface. The deviation between the two cases is already visible in figure 7.11 (c) and (d). There, the jet dynamics are matched only when D^* takes a higher value for the flat free surface measurement. The simulations indicate that this discrepancy starts at around $D^* = 1.2$ (shown in figure 7.12 (c)) and keeps growing for higher values. We can portrait these changes as being enclosed between two extreme scenarios: (1) the bubble is produced right on the liquid surface, generating a bullet jet, which is not affected by the characteristics of the boundaries and thus is independent on R_d. As the cavity is placed closer to the drop centre the surface curvature becomes increasingly relevant to the jet dynamics. This is consistent with our definition of Υ, since D^* and Υ take similar values for lower values of d, and grow apart as the cavity is placed deeper in the drop. (2) When the bubble is almost at the drop centre (i.e. $\Upsilon \to \infty$) there is no jetting for the curved case. However, in the flat surface case the jetting still occurs for comparable values of D^* (e.g., $D^* \sim 2$),

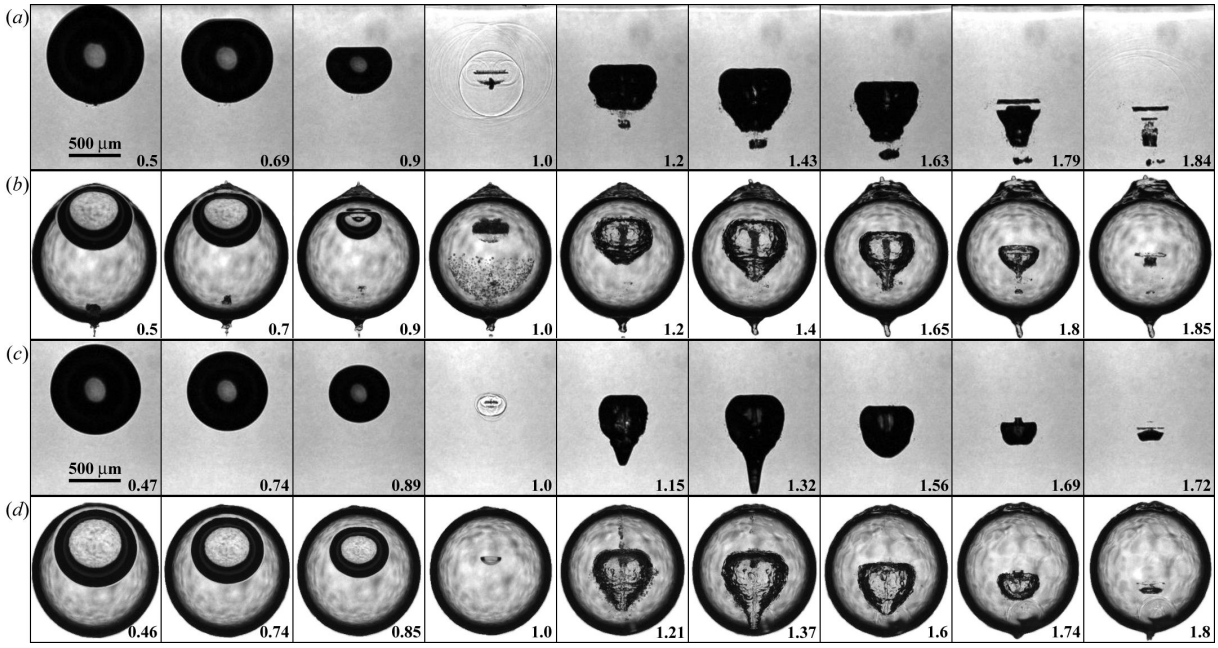

Figure 7.11: Comparison of cases with similar bubble dynamics and a different curvature of the free surface R_d. The panels (a) and (c) show cases where the cavity is produced near a flat free surface. The cases in (b) and (d) show similar bubbles generated inside a drop with a mean radius of 1.42 mm. Here, the numbers represent the time normalised with the time of collapse of the cavities from each case. (a) Here, $D^* = 0.85$. (b) $D^* = 0.88$. (c) $D^* = 1.6$. (d) $D^* = 1.37$.

demonstrating how the curvature weighting factor χ becomes increasingly relevant.
It is important to stress that if the bubble is placed near the drop boundary, for instance at $D^* \lesssim 1.4$, the discrepancies found in the jetting dynamics of a bubble in the "semi-infinite" liquid pool when compared with the droplet case are mainly provoked by the surface curvature, and not by the dissimilar extension of the liquid below the gas cavity. This particular point is corroborated in the appendix (section 7.6) by means of complementary measurements and numerical simulations of jetting bubbles in the proximity of a hemispherical tip of a cylindrical water column.
So far, we have classified and compared the characteristics of the jetting regimes produced at different D^* qualitatively, i.e. based on their general morphological features as presented in previous works [24, 88]. In the following, we will refer to this as *behavioural similarity*. An alternative and more precise way of analysing the spatial correlation between the dynamics of two different jets can be achieved by contrasting the pixel distribution on the video frames to find common features between images. This quantitative comparison method is usually referred as *structural similarity* analysis and can be implemented using different image scanning algorithms [292]. Here, we use the *complex wavelet structural similarity index* (CW-SSIM) [293] to evaluate the correlation between the temporal evolution of two different jetting cavities. The CW-SSIM approach has some advantages over direct pixel to pixel comparison methods (e.g. intensity-based) or the simpler versions of the structural similarity index (e.g. SSIM). For instance, it accounts (up to some point) for both intensity variations and non-structural geometric distortions like object translation, scaling and rotation [292]. The CW-SSIM index can take values ranging from zero (if there is no correlation at all) to one (when the images are identical).
In figure 7.13, we contrast the dynamics of two bubbles initially located at a distance D^*

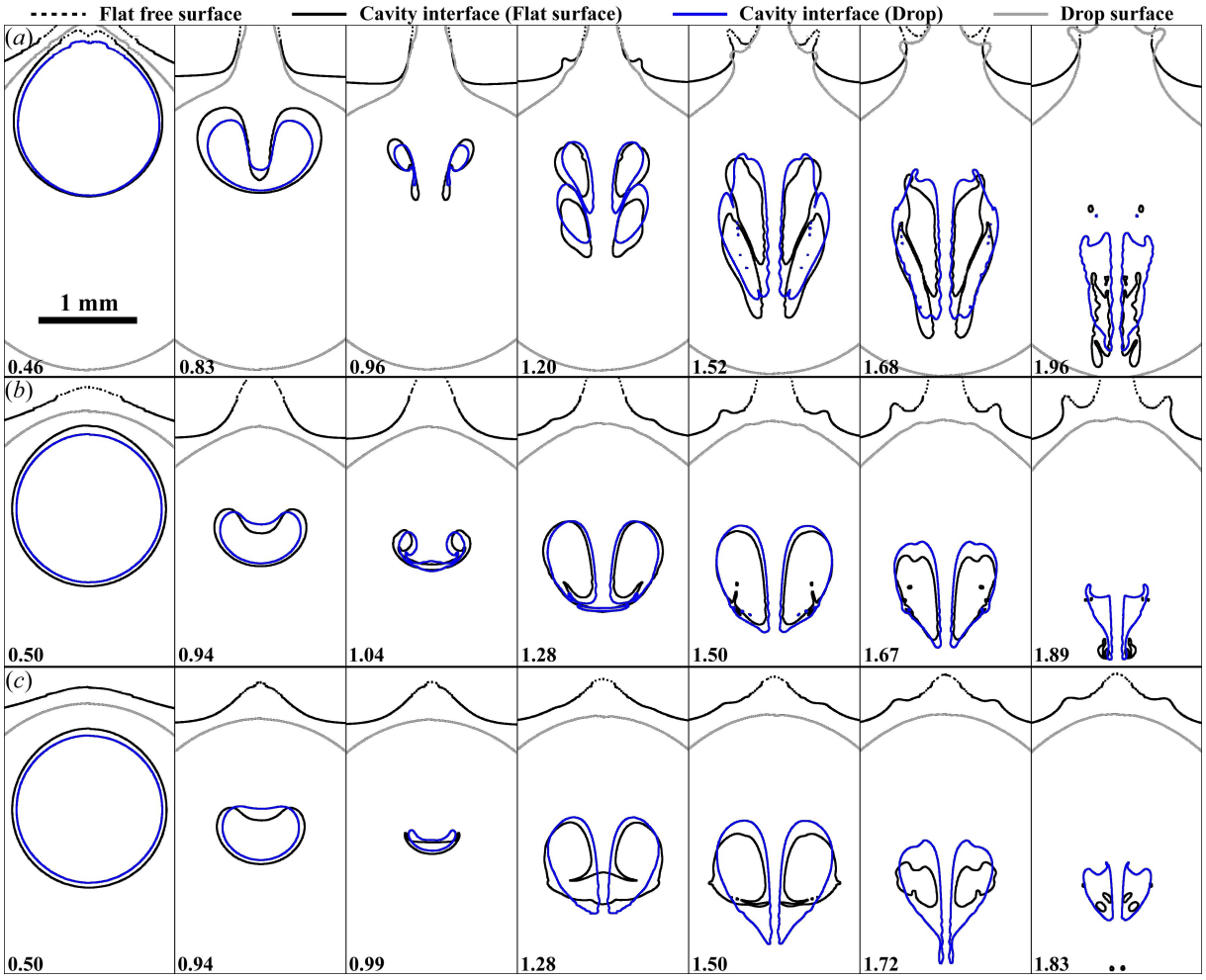

Figure 7.12: Jetting dynamics of identical bubbles produced near a flat surface or the curved surface of a droplet ($R_d = 1.42\,\mu m$). The non-dimensional time, indicated by the numbers, was normalised with the collapse time of each bubble. (a) Here, $D^* = 0.61$. (b) $D^* = 1.02$. (c) $D^* = 1.23$.

from a flat or a curved surface as already done in figure 7.12, but this time using the CW-SSIM index to evaluate their similarity. The non-dimensional time (t^*) was computed using the collapse time of the bubbles for each case. Figure 7.13 presents plots of the temporal evolution of the similarity index next to a series of selected frames at $t^* = 0.3; 0.6; 0.9; 1.05; 1.2; 1.35; 1.5; 1.7$; and 1.9, which illustrate and compare the shape of the cavities in the flat boundary case (grey background on the left side) and the drop case.

The results expose the differences between the behavioural similarity and the structural similarity approaches, i.e. two bubbles can have the same jetting regime but still have dissimilar structures. This is observed in bubbles at lower stand-off distances like the case with $D^* = 0.47$ in figure 7.13. The discrepancy can be explained by the higher degree of fragmentation of the bubble after jetting, acquiring an elongated shape in regimes with a ventilated cavity, or where the liquid layer between the gas in the bubble and the atmosphere is affected by the RTI. In particular, the cases producing an open cavity (i.e. $D^* \lesssim 0.35$) were not suitable for the structural similarity analysis. Here, the fluctuations of the splashing dynamics observed in the numerical simulations and the impossibility to define a collapse time due to the non-collapsing nature of those cavities (see figure 7.6 (d)

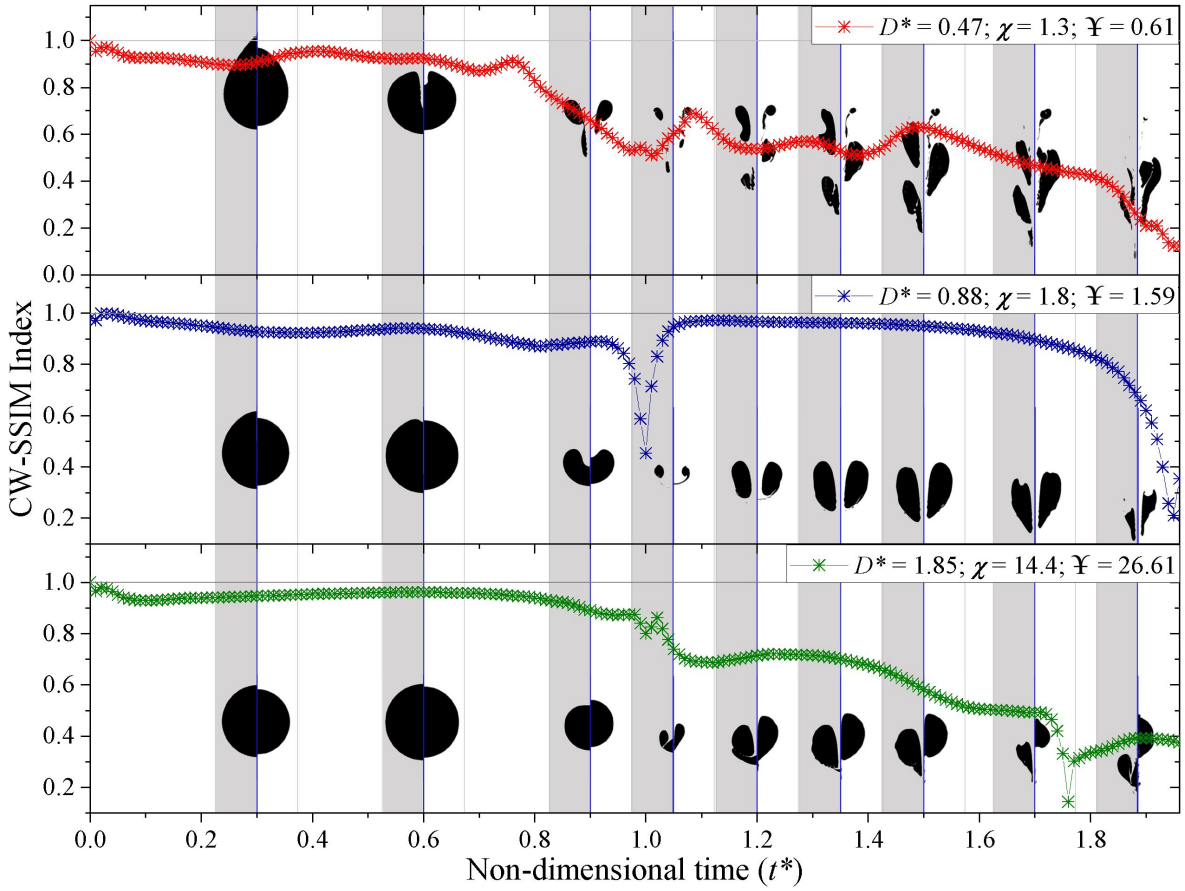

Figure 7.13: Structural similarity of the dynamics of jetting bubbles produced near a flat surface or the drop boundary at an identical stand-off distance. Here, the temporal evolution of the CW-SSIM index is presented for three examples corresponding to cases with $D^* = 0.47$, $D^* = 0.88$, and $D^* = 1.85$. The insets show a comparison of the images of both simulated bubbles. The frames are centered at specific non-dimensional times (blue vertical lines), displaying a half frame corresponding to the flat surface case (grey background on the left) and a half frame taken from the drop case with the same D^*.

and (e)) prevented us to perform a reliable assessment of the CW-SSIM index.
As the laser bubble is produced deeper into the liquid, both structural and behavioural approaches lead to the same conclusions (previously discussed in figure 7.12). The similarity found in the development of bubbles near surfaces with or without curvature is excellent for some stand-off distances, e.g. around the middle point located between the liquid surface and the drop centre. One example of this is shown in the central panel of figure 7.13 corresponding to $D^* = 0.88$. As we already mentioned, near the centre of the drop (i.e., $D^* \simeq 2$) the difference in the anisotropy in both cases produces dissimilar bubble oscillations (see the lower panel of figure 7.13).
A more general overview of those three scenarios is presented in figure 7.14, where the mean value of the CW-SSIM index is plotted along with D^* and Υ. Considering that all the bubbles have a very similar initial expansion phase, only the times corresponding to the first collapse and the complete second oscillation cycle were computed in the mean value of CW-SSIM. After the second collapse, the bubble is heavily fragmented and there is no longer a recognisable structure. Figure 7.14 confirms that the structural similarity is rather poor for bubbles near the surface (i.e. $0 \lesssim D^* \lesssim 0.7$). Around $D^* = 0.9$,

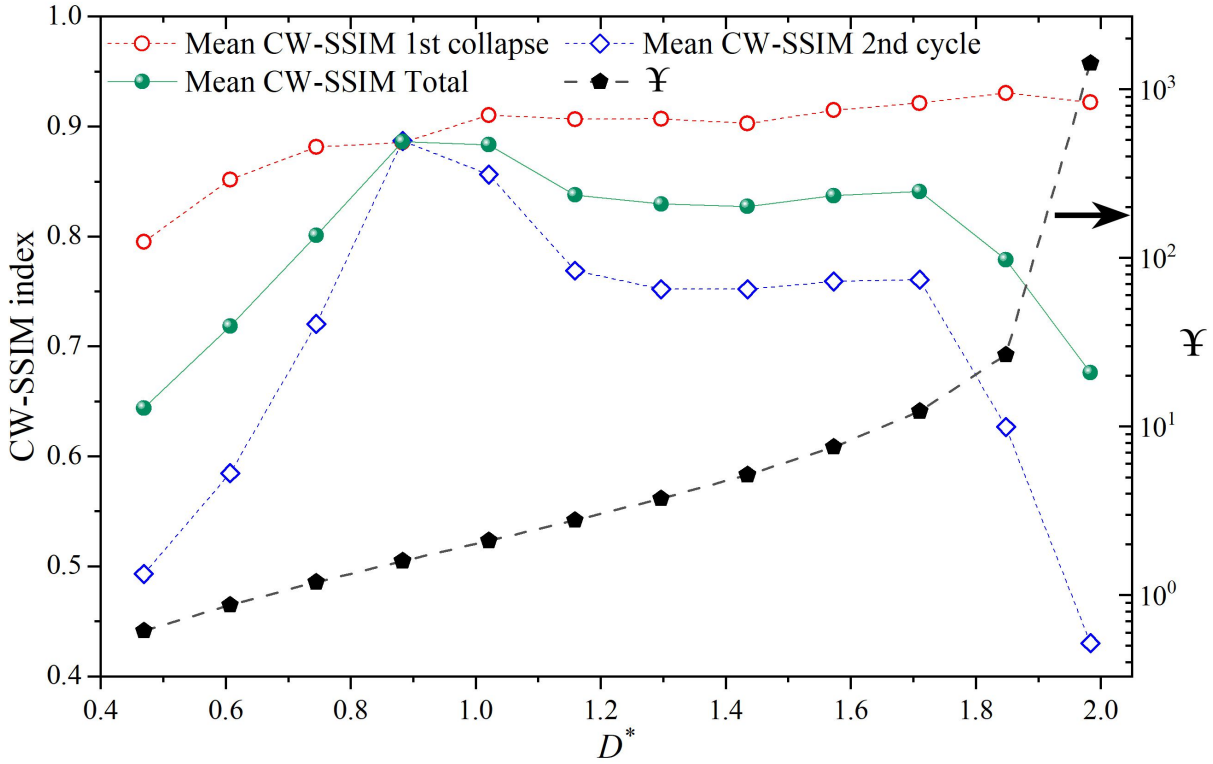

Figure 7.14: Structural similarity between cases with bubbles seeded at different stand-off distances from a flat free surface or inside the drop. The curve shows the mean value of the "total" CW-SSIM index (green) computed as the average of the mean indices observes in the first bubble collapse (red) and in its second oscillation cycle (blue). The sudden increase in ϒ (black markers) as we seed the bubble close to the drop centre is linked to a decay in the similarity between the cavities.

the similarity index reaches a peak where the match is excellent. A good agreement is sustained over a range of D^* values between approximately 0.7 and 1.7, meaning that even when the features of the cavities are not identical they have a similar distribution of the gas phase (and the same jetting regime). For $D^* \gtrsim 1.7$, the similarity index suffers an abrupt fall and the value of ϒ diverges as the bubble seeding position gets closer to the drop centre. This is consistent with the definition of ϒ, which relates its magnitude to the influence of the drop curvature in the bubble dynamics.

The experimental results displayed in figure 7.11 suggest that there is a correspondence between the dynamics of a bubble seeded with a given D^*_{flat} in the flat surface case and the temporal evolution of a bubble with D^*_{drop} inside the droplet. We explore this apparent "equivalence" between values of D^*_{flat} and D^*_{drop} in figure 7.15 and figure 7.16. Since the result of the CW-SSIM analysis is affected by a significant translation of the objects being compared, the initial positions of the bubbles were matched by performing a vertical shift on the drop case simulations. Figure 7.15 shows evidence of the mentioned correspondence by presenting two examples, one with $D^*_{\text{flat}} = 1.02$ and $D^*_{\text{drop}} = 0.95$, and a second one where the bubble is closer to the drop centre, i.e., $D^*_{\text{flat}} = 2.40$ and $D^*_{\text{drop}} = 1.68$.

These two examples in figure 7.15 prove that there are pairs of D^* values where the similarity between the dynamics of bubbles produced near two surfaces with uneven curvature is remarkable, at least during the whole period comprised in the first two oscillation cycles. This correlation analysis was performed for an extended range of values of D^* to

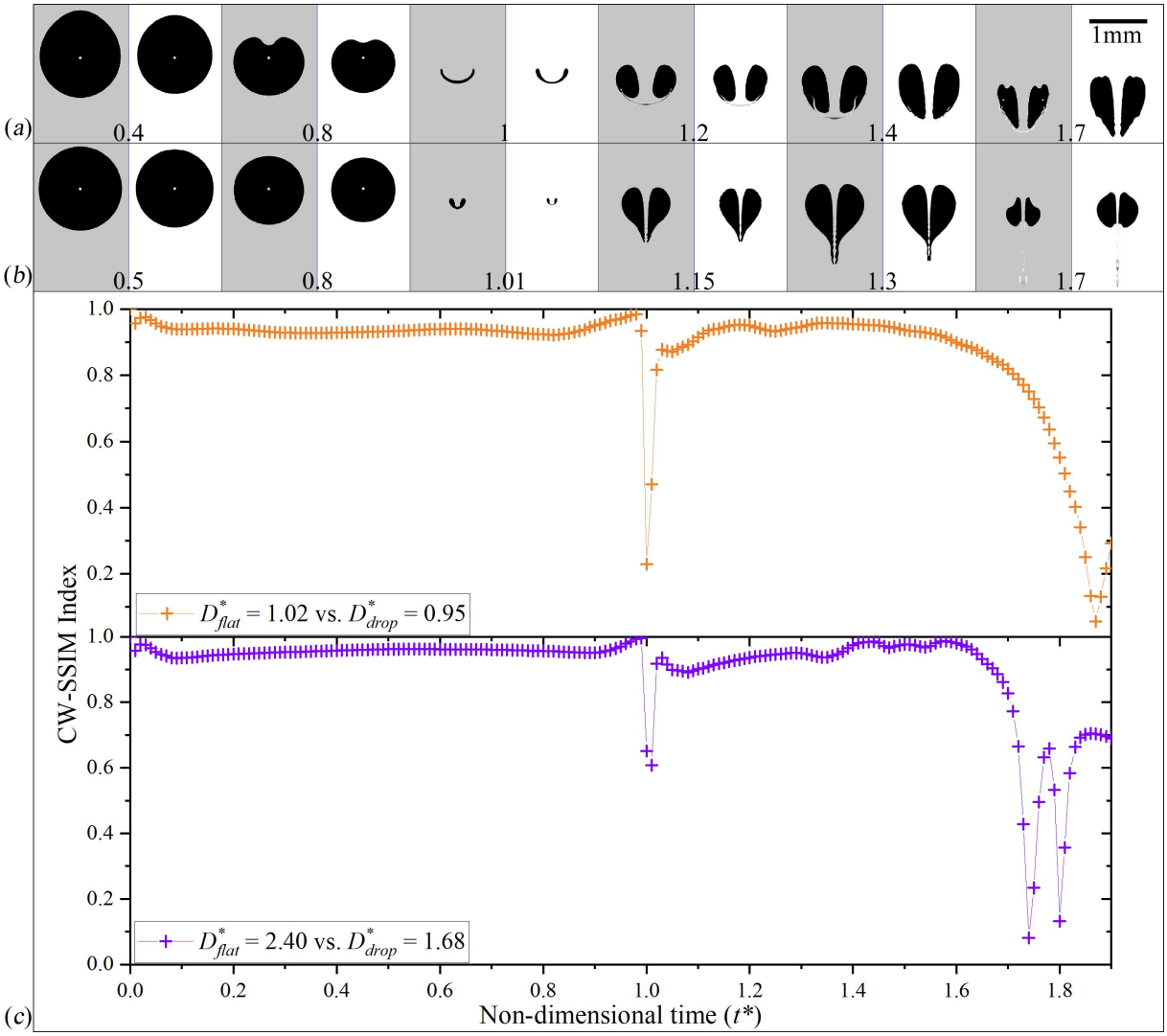

Figure 7.15: Similarity study of the jetting dynamics of bubbles near a flat surface (grey background) or a drop (white background) with a different D^*. The initial position of the bubbles was matched by performing a vertical shift on the drop case simulations. For each value of D^*_{flat} there is one value of D^*_{drop} with similar dynamics, i.e. producing the maximum CW-SSIM index when a simulation of a given D^*_{flat} is compared against simulations with every possible value of D^*_{drop}. The numbers indicate non-dimensional time t^*. (a) For $D^*_{\text{flat}} = 1.02$ the maximum average CW-SSIM index was achieved with $D^*_{drop} = 0.95$. (b) The best match for $D^*_{\text{flat}} = 2.40$ was $D^*_{\text{drop}} = 1.68$. (c) Temporal evolution of the CW-SSIM index for the cases on panels (a) and (b).

find that for each value of D^*_{drop}, there is one value of D^*_{flat} with similar dynamics, i.e. which maximises the CW-SSIM index when a simulation made with that particular D^*_{flat} is compared against simulations with every possible value of D^*_{drop}. As shown in figure 7.16, the dependence of the equivalent stand-off distance starts as a linear function in the proximity of the surface and grows rapidly as the bubble is placed deeper in the liquid. Interestingly, the linear fit performed on smaller values of D^*, which meet the conditions for the CW-SSIM analysis, projects a ratio between equivalent D^*_{drop} and D^*_{flat} near 1 when the seeding position approaches the surface. Now, bearing in mind the definition of $\mathfrak{F} = \chi D^*$, the previous observation is consistent with the limiting case at the surface

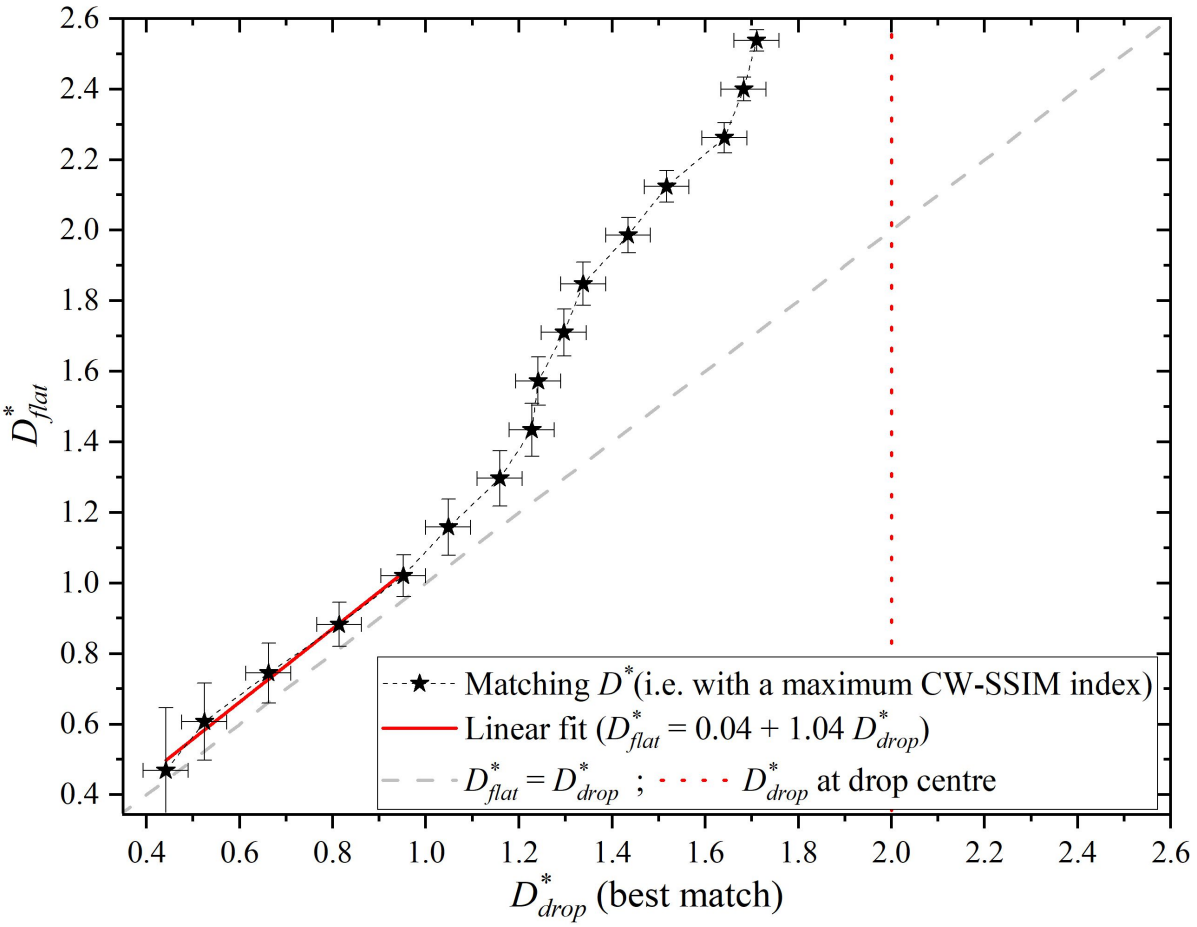

Figure 7.16: Best match between the dynamics of bubbles in the flat boundary and the drop cases for different stand-off distances, i.e. D^*_{flat} and D^*_{drop}. For each value of D^*_{flat}, the best match was obtained by finding the corresponding value of D^*_{drop} that maximises the mean CW-SSIM index. As indicated by the parameters of the linear fit, the best match is found at similar values of D^* at the lower depths, but they become increasingly different as $d \to R_d$, where the bubble is seeded at the drop centre (indicated with a vertical dotted line). The dashed grey line was added as a visual reference. The vertical error bars represent the deviation of CW-SSIM from the perfect similarity case (i.e. CW-SSIM = 1)

where $\chi \to 1$, meaning that the curvature does not play a significant role for the bubble jetting dynamics. At the other extreme, i.e. as $d \to R_d$, $\aleph$ diverges, indicating a strong influence of the drop geometry on the bubble evolution. At this point, it is important to stress that in this context, "equivalence" does not mean that the dynamics are identical, but their structure is "as similar as it could be" for the matching of D^*_{flat} and D^*_{drop}. The same clarification applies to bubbles with the same $\aleph$, which is a multivalued function as explained in section 7.2.1.

7.4.3 Radial bubble oscillations

In the previous section, we studied features found in the dynamics of an axisymmetric jetting bubble. Let us now have a closer look at the only case with spherical symmetry, i.e. where the laser cavity is placed in the centre of the drop ($\aleph \to \infty$). In this scenario, the

bubble undergoes several spherical oscillations with a decaying amplitude, as commonly observed in laser bubbles created in unbounded liquids [294]. Figure 7.17 (a) presents a comparison between an experiment and simulated data computed using the VoF solver, finding an excellent agreement. Like for the previously simulated results, here we applied the correction script that accounts for the distortion induced by the drop curvature.

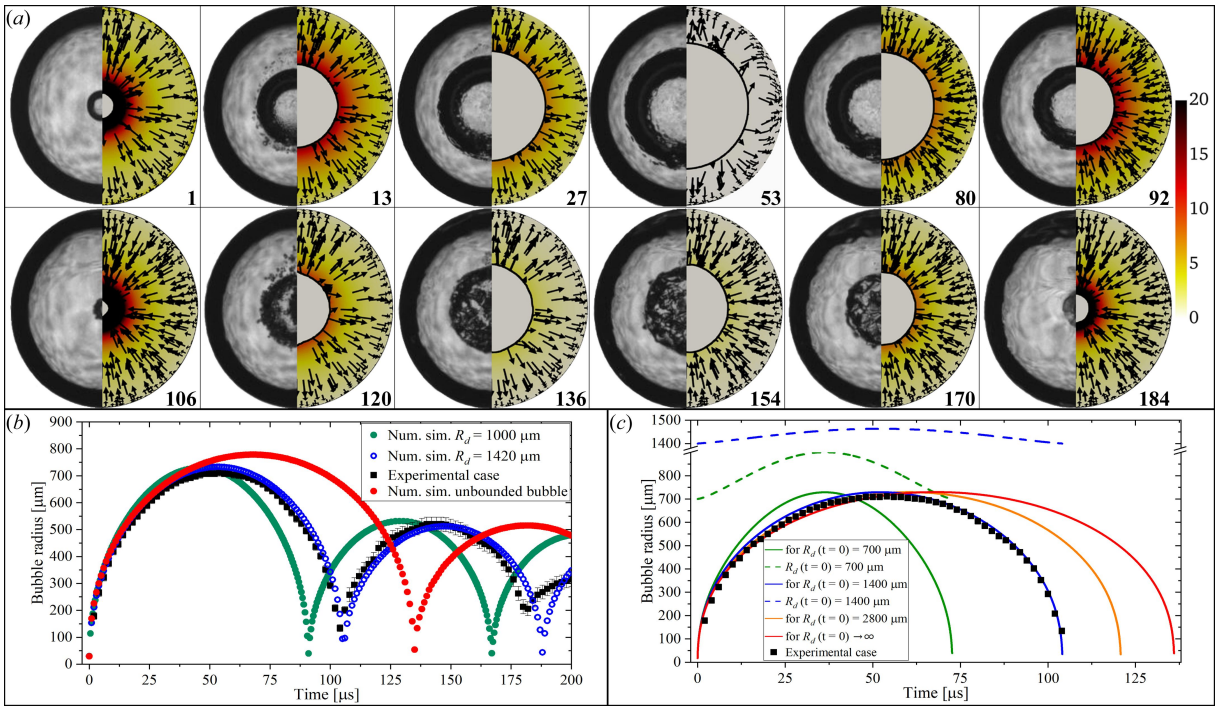

Figure 7.17: Direct comparison between the experiment and a numerical simulation for a case where the laser bubble is placed at the centre of the drop. (a) The median diameter of the drop is 1.42 mm. The simulated images showing the velocity field have been remapped to account for the distortion provoked by the curvature of the drop. The numbers indicate time in µs and the colour scale is given in m/s. (b) Radial dynamics of the experimental and simulated bubbles. The experimental radius was obtained by fitting a circle on the bubble. The radius in the simulations was estimated using the gas volume (i.e. the spherical equivalent radius). The results were compared with the unbounded case to find that the bubbles inside the drop have a shorter expansion/collapse cycle. (c) Bubble dynamics are obtained with a modified Rayleigh-Plesset model for different drop sizes. The radii of the larger drops remain almost unaltered during the bubble oscillation.

Figure 7.17 (b) depicts the temporal evolution of the bubble radius $R(t)$ for the examples in panel (a). In addition, it presents $R(t)$ calculated for a case of a drop of an ideally infinite size, which corresponds to the case of an unbounded liquid domain. The initial conditions in the VoF model were chosen to match the experimental $R^*_{\max}$, and then the other cases were simulated maintaining the same parameters while changing the drop size. Notably, the bubble computed with CFD reaches a slightly larger maximum radius as the liquid layer thickness is increased to infinity (i.e. an unbounded bubble case) and thus also has a larger collapse time. This might be due to the effect produced by the consecutive (and alternating) tension and pressure waves interacting with the bubble during its expansion (see figure 7.17 (a)).
To shed some light on this matter, we use a spherical bubble model based on a modified Rayleigh-Plesset model (RP) [118, 248] that accounts for the finite droplet size, viscosity

of the liquid and interfacial tension. It is worth noting that in those previous works the millimetre sized droplet was sitting on the top of a blunt needle or deformed into an ellipsoidal shape by a strong levitating acoustic field. This lead to a non-spherical boundary conditions that affect the bubble dynamics. In the present analysis, the droplet is nearly perfectly spherical, thus matching with the purely spherical RP model within a droplet. The results, presented in figure 7.17 (c), show that the bubble grows up to almost the same size independently of the drop size. For the same initial conditions set in the VoF model ($p_g(t = 0) = 1.69\,\mathrm{GPa}$ and $R_b(t = 0) = 17.3\,\mu\mathrm{m}$) the work is almost completely done against the surrounding pressure ($p_\infty = 1\,\mathrm{bar}$) while surface energy and viscous dissipation is negligible. Yet, for smaller droplet volumes, the inertia is reduced and therefore the expansion time to maximum bubble radius and the almost symmetrical collapse reduce, too.
For the particular initial conditions, both models agree on the elongation of the oscillation cycle, however they predict dissimilar results on the maximum radius reached by the bubbles. The simple Rayleigh-Plesset model is used to give a comparison to the VoF simulations and to evaluate the impact of the shock wave (and its reflections) on the bubble dynamics. From figure 7.17 (c) we can infer that the maximum expansion of the bubble is nearly independent of the droplet size, while in the VoF simulations it is not. The VoF model accounts for the reflected wave, thus the discrepancy suggests that upon the acoustic soft reflection of the shock wave momentum is imparted on the droplet interface. The importance of reflected waves on cavitation nucleation in confined liquid samples was recently also found for an acoustic hard reflection where the bubble expansion was lowered [295]. A more comprehensive formulation for the bubble dynamics than the RP model which incorporates both the bubble-shockwave interaction and compressibility effects can be found in Zhang et al. [70].

7.4.4 Drop surface instabilities

In the previous sections, the formation of radial liquid jets growing from the drop surface in the shape of "spikes" was mentioned. As explained above, this phenomenon stems from an initial perturbation of the liquid interface and the posterior ejection of liquid produced by the Rayleigh-Taylor instability. This kind of instability occurs when the rapid expansion or the collapse of the bubble wall accelerates a thin liquid layer trapped between the cavity and the atmospheric gas, producing a pattern of ripples on the drop surface that grow further in the consecutive bubble oscillations. A clear example of the events leading to the onset of this kind of instability in this particular experiment is shown in figure 7.18 (a). There, the acoustic emissions from the laser dielectric breakdown nucleate a cloud of bubbles within the drop. As the cavity expands, all these smaller bubbles are incorporated (by coalescence) into the main bubble, producing a series of dimples on the bubble surface, visible at $t = 50\,\mu\mathrm{s}$ of figure 7.18 (a). These dimples may contribute to the later destabilisation of the drop surface, which is highly dependent on the ratio R^*_{max}/R_d. Additionally, R^*_{max}/R_d determines the liquid layer thickness and its acceleration by the bubble/drop dynamics. The ripples in the drop surface become noticeable just after the first bubble collapse (i.e. $t = 130\,\mu\mathrm{s}$) and grow significantly during the bubble re-expansion, as shown at $t = 190\,\mu\mathrm{s}$. However, the most dramatic events take place after the second bubble collapse (i.e. at $t = 230\,\mu\mathrm{s}$). There, the ripples grow into liquid "spikes" which lead to the detachment of small droplets due to the action of the Rayleigh-Plateau instability, as shown in figure 7.18 (b). At the same time, the second bubble collapse releases a strong shock wave in the radial direction. This shock

wave interacts with the array of meniscus-shaped pits on the liquid surface to produce fast radial jets (see the frame at $t = 420\,\mu s$). The later sequence is clearly captured in the frames of figure 7.18 (c). It is important to note that this complex phenomenon not only depends on the shock wave strength but also requires certain conditions to be met [285, 286], like a minimum depth and curvature of the pits, which may explain the absence of "spikes" during the first bubble collapse.

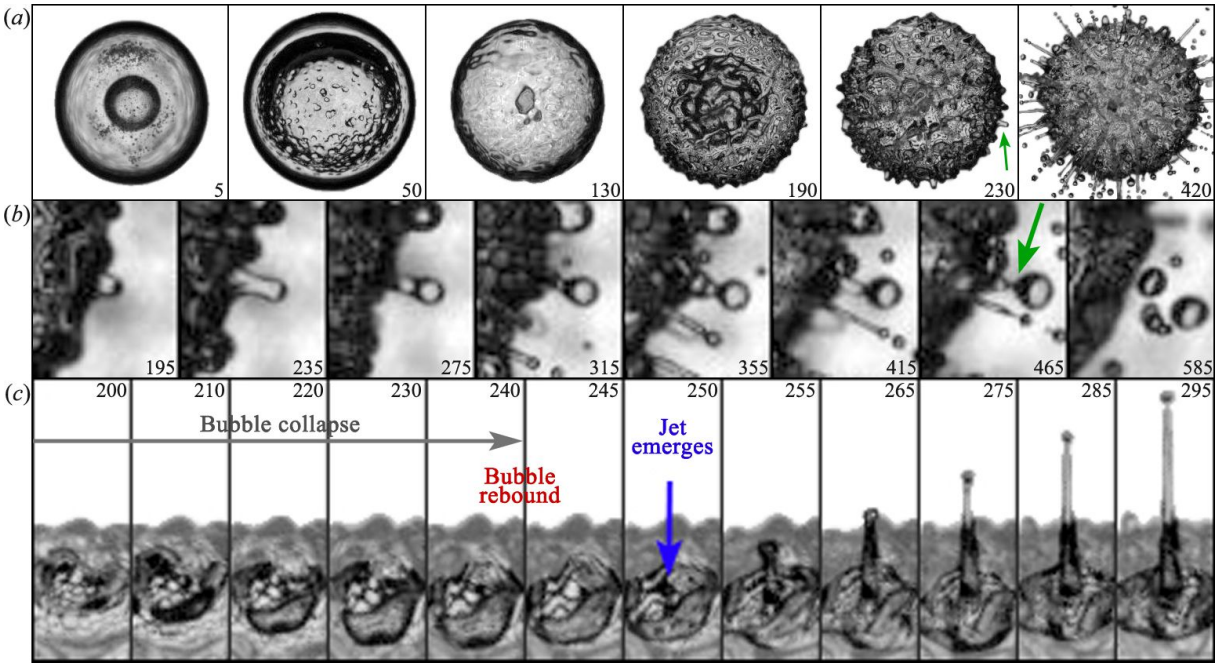

Figure 7.18: Drop surface destabilisation mechanisms. The mean drop radius is 1.42 mm and the numbers represent time in µs. (a) As the main bubble expands, the secondary, acoustic cavitation bubbles produce small dimples on the gas cavity surface (e.g. at 50 µs). Those may promote the formation of a series of ripples during the bubble collapse (at 130 µs). As the bubble re-expands, the Rayleigh-Taylor instability causes the growth of liquid "spikes" that later lead to the detachment of small drops due to the Rayleigh-Plateau instability, as indicated with a green arrow in panel (b). There, the frame width is 570 µm. At the same time, the second collapse of the bubble enhances the surface irregularities and pits that appear in the areas between the ripples. The shock wave emitted during the second collapse gives origin to fast liquid jets ejected from the centre of the pits, as highlighted with a blue arrow in panel (c). The frame width in this sequence is 490 µm. The full video is available in the online supplementary movie 9.

To further analyse the onset of these instabilities, we varied the energy of the laser pulse, hence producing bubbles with various sizes and thus with distinct ratios R^*_{max}/R_d. The results are presented in figure 7.19. Even when the extreme image distortion produced near the drop interface prevent us to obtain an accurate value of the bubble radius, these measurements make evident that the amplitude of the ripples increases with increasing R^*_{max} and with each consecutive bubble oscillation.
In figure 7.19 (a) the expansion of the bubble is not sufficient to visibly disturb the drop's spherical surface. In the case shown in figure 7.19 (b) the bubble's first collapse does not break up the drop surface, however, a mild wave pattern is observed on the surface after the bubble re-expansion (at $t = 420\,\mu s$). In spite of the presence of these low amplitude ripples, no radial jets are ejected from the drop upon the second bubble collapse. When the ratio

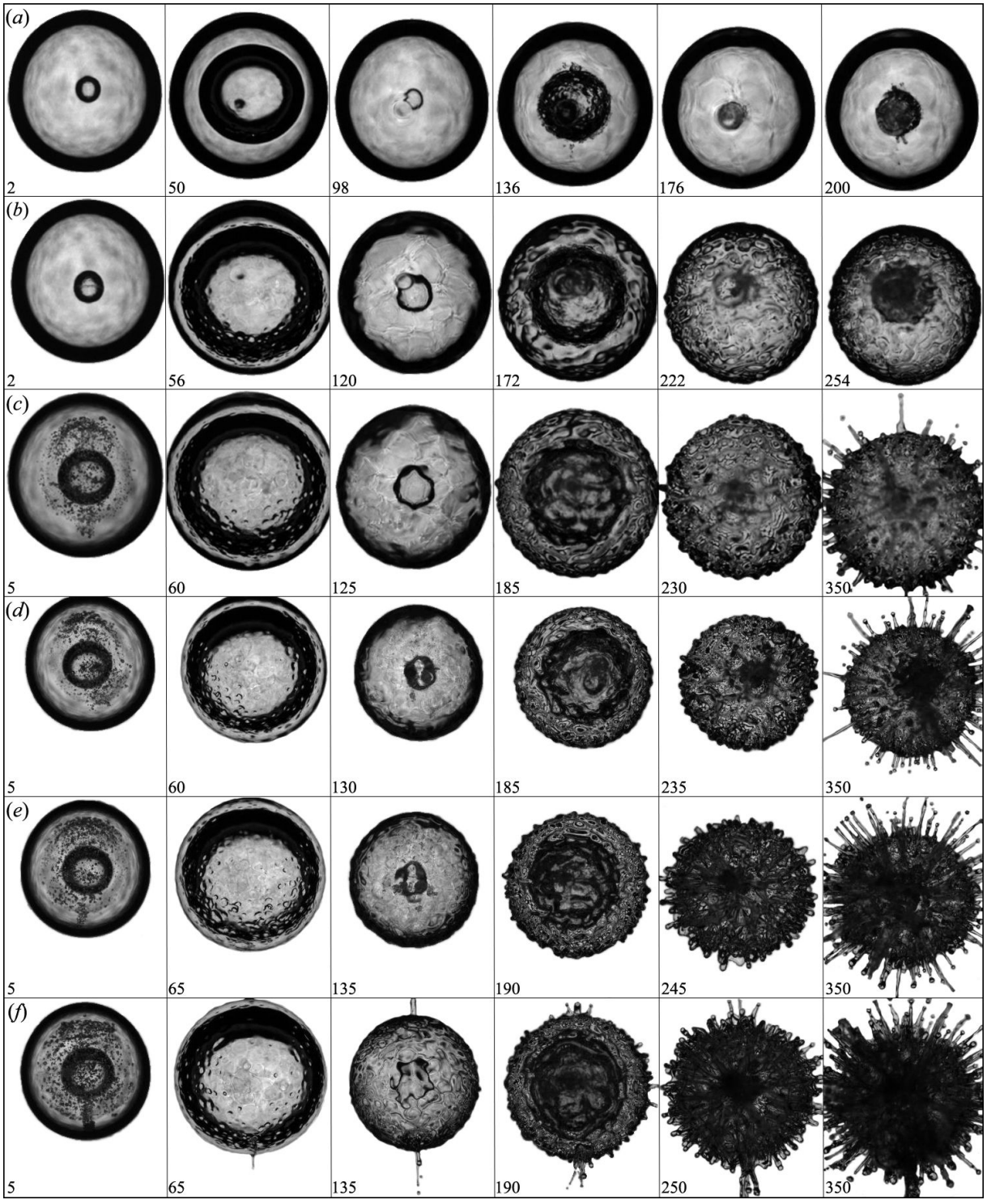

Figure 7.19: Onset of the drop surface instabilities for bubbles produced with different laser pulse energies. The mean drop radius is 1.42 mm and the numbers represent time in µs. (a) Here, the energy of the laser pulse is $L = 1.9\,\mathrm{mJ}$. (b) $L = 3.1\,\mathrm{mJ}$. (c) $L = 3.9\,\mathrm{mJ}$. For this energy, the RTI affects the drop surface enough to produce liquid ejection after the second bubble collapse. (d) $L = 4.6\,\mathrm{mJ}$. (e) $L = 5.2\,\mathrm{mJ}$. (f) $L = 6.4\,\mathrm{mJ}$. Note that the panels (d)-(f) are shown in wider frames than the panels (a)-(c) to show the larger "spikes". A full video of panel (f) is available in the online supplementary movie 10.

R^*_{max}/R_d is further increased, as shown in figure 7.19 (c), we find very similar dynamics of the bubble/drop system, but now the valleys between the ripples (and the acoustic pressure wave) are deep enough to trigger the radial jetting. This confirms the existence of threshold conditions for the "spikes" to be formed. In the remaining cases presented in panels (d) to (f) of figure 7.19, the general dynamics of the bubble/drop system are very similar to the previous cases, although as the laser pulse energy is increased the instabilities become perceivable at an earlier time. For example, in figure 7.19 (f) liquid "spikes" are already formed after the first bubble collapse [118].

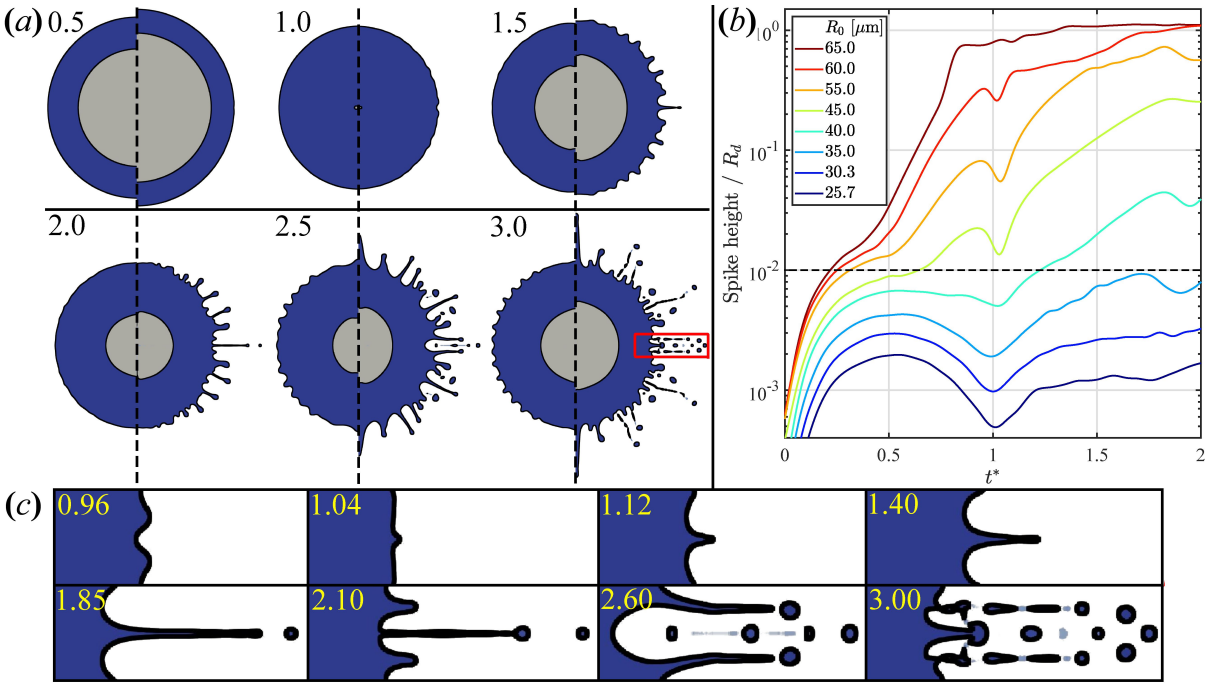

Figure 7.20: Numerical simulations of the instabilities development at the surface of the drop. (a) Selected frames for a case with $R_0 = 35$ µm (left) and $R_0 = 45$ µm (right). The non-dimensional time t^* is shown on the top-left of each frame. (b) Temporal evolution of the Rayleigh-Taylor instability (RTI) spike height for various R_0. An *ad hoc* threshold for the instability onset is indicated by a dashed line at 1 % of R_d. (c) Selected frames of a zoomed view of the drop surface for $R_0 = 45$ µm (frame window indicated by a red square in (b)), showing the RTI and the Rayleigh-Plateau instability.

Figure 7.20 shows VoF simulations of the Rayleigh-Taylor instability found on the drop surface. From figure 7.20 (a) it is clear that the instability is grown by the volumetric oscillation of the bubble, while the shock waves emitted from the bubble upon its creation (and later at its collapse) accelerates the ripples on the drop surface and form the thin "spikes". This kind of simulation was previously performed by Zeng et al. [118] for an ellipsoidal droplet with the RTI manifesting only in a reduced region of the surface located on the drop poles. In the present work, we study a nearly spherically symmetric case where the spikes have no preferred origin, i.e. they escape the droplet isotropically.
The instability was quantified by defining the spike height as half of the difference between the maximum and minimum radial deviations from the initial drop shape, which was then normalised with the average drop radius, $R_d = 1420$ µm. In figure 7.20 (b), it is evident that the instability is formed immediately after bubble creation, as it grows during the bubble's initial expansion. It starts shrinking at $R_0 \leq 40$ µm during its first collapse and

grows again upon its rebound.
For $R_0 = 25.7$ µm, the normalised spike height stays below 0.2 %, meaning that the instability does not further develop in the first bubble oscillation cycles. As the initial radius R_0 is increased in steps of 5 µm, the spike height approximately doubles. Thus, the spike height is exponentially related to the bubble size, i.e. spike height$/R_d \sim e^{R_0 \cdot \text{const.}}$. Considering that the instability increases continuously with increasing laser energy, a threshold for the onset of the instability can only be chosen arbitrarily. Here, we choose an *ad hoc* threshold value as the normalised spike height of 1 % of R_d, around which the spike height does not shrink during most of the bubble's first collapse.
Similarly to the observed in the experiments, the simulations of figure 7.20 (b) show how the spikes are ejected earlier in time as the maximum radius reached by the bubble is increased. For $R_0 = 35$ µm, the spikes nearly cross the threshold (indicated in the plot with a dashed line) in the second oscillation cycle, while for $R_0 = 40$ µm, the threshold is crossed shortly after the first collapse, and for $R_0 \geq 45$ µm it is already exceeded during the first oscillation cycle. Figure 7.20 (a) compares the instability for a case below ($R_0 = 35$ µm) and above ($R_0 = 45$ µm) the established threshold, showing a strong increase in the spike size as well as the ejection of droplets for a larger bubble. This droplet separation from the spikes, highlighted in the bottom row of figure 7.20 (c), was previously discussed in figure 7.18 (b) as an example of the effect of the Rayleigh-Plateau instability. An upper limit of the spike height is reached at $\approx 1\, R_d$ for $R_0 = 65$ µm, where the outer spikes reach about twice the drop size, while the inner spikes breach the liquid layer that separates the bubble from the outside air. Because of this, the bubble interior is partially filled with atmospheric gas and the cavity ceases to oscillate. At this point, the drop can not be longer defined as such, as shown in the experiments of figure 7.19 (f) where the liquid mass becomes an intricate collection of spikes and a significant portion of it is ejected away as smaller droplets.

7.5 Conclusion

In this manuscript, we presented some of the complex fluid dynamics occurring once a vapour bubble expands within a water droplet. Specifically, we analysed the appearance of acoustic secondary cavitation, and the formation of liquid jets in the proximity of highly curved free surfaces, and finally, we provided detailed experimental and simulated images of the onset and the development of shape instabilities on the surface of the drop.
The first part of the research highlights that acoustic waves emitted from the micro-explosion nucleate complex secondary cavitation clouds. Further, the study corroborates the existing relation between the evolution of the negative pressure profile and the shape of the bubble clusters inside the drop. A cavitation threshold pressure of around -4.5 MPa was estimated by performing a direct comparison between the experiments and the simulations. The numerical model does not account for the bubble nucleation induced by the rarefaction waves. The implementation of this experimental technique to other liquids, particularly in cases where large samples are not available, might contribute to achieving a deeper understanding of the nucleation of bubbles by sound waves. The present experimental setup may be modified to create a bubble within a superheated droplet to reveal in a well-defined system the coupling of fluid dynamics with thermodynamics, and also study how the liquid temperature affects the later fragmentation dynamics [296].
The secondary bubbles cluster and several types of jets, both caused by the generation of laser bubbles at different positions inside the droplet, were classified using a stand-off

parameter $\mathfrak{Y}$. The use of a single quantity to characterise the system simplifies the direct comparison between cases. The optical lens effect linked to the spherical shape of the drops allowed us to obtain images of the bubble jet's interior with a remarkable level of detail.

The numerical simulations were crucial to explain the complex flow fields generating these jets, as well as to explain the shape acquired by the gas cavities during their second collapse phase, including many interesting features like the annular bubble necking and the detachment of multiple vapour rings.

The effect of the liquid surface curvature on the bubble jetting has been analysed, by comparing the evolution of a bubble inside a droplet and in a semi-infinite pool, using two complementary points of view. First, a qualitative assessment (here called *behavioural similarity*) indicates that the jetting regime differs rather little when the cavity is seeded nearby the free boundary. In this part of the study, we have shown that for the droplet case, the non-dimensional distance D^* is the most determining quantity, while the curvature of the liquid does not have a dominant role in the evolution of the jetting cavities. This conclusion is based on the analysis of numerical simulations where only the parameter R_d was modified, and also by comparing the current results with the previously reported for a flat surface.

A second type of analysis, which uses the CW-SSIM index to evaluate the *structural similarity* of the cavities, was applied to the same numerical data to perform this time a quantitative comparison of the jetting near a flat and a curved surface. Here, we found that for bubbles in the vicinity of the liquid surface (i.e. $0 \lesssim D^* \lesssim 0.7$) the structural similarity is rather poor, mostly due to the higher degree of fragmentation of the gas phase developed in regimes with a ventilated cavity, or where the liquid surface is affected by the RTI.

Both similarity criteria indicate the existence of a seeding depth around $D^* \sim 1$ where the bubbles in the flat and curved cases resemble each other the most. In addition, as the bubble seeding position is set further away from the surface, the jetting regimes are progressively dissimilar, in particular when the laser cavity is generated nearby the drop centre. The sudden drop in the CW-SSIM index found in this situation matches an equally abrupt rise in the value of $\mathfrak{Y}$ starting around $\mathfrak{Y} = 10$.

The CW-SSIM analysis confirmed that for each stand-off distance in the flat boundary case (i.e. D^*_{flat}), there is another value of D^* (i.e. D^*_{drop}) where the bubble dynamics of both cases resemble each other the most. The relation between D^*_{flat} and D^*_{drop} supports the definition and the functionality described for $\mathfrak{Y}$. This kind of similarity study could be used to span a more comprehensive parameter space with D^*_{flat} and $\mathfrak{Y}$ computed with different curvature radii, and thus achieve a more general picture of the group of parameter values having "equivalent" jetting dynamics. Moreover, the jet matching would greatly benefit from the implementation of more complex comparison methods or the use of machine learning techniques that consider both the behavioural and the structural criteria.

The spherical bubble oscillations observed in the experiments where the laser was focused on the geometrical centre of the droplet were analysed using two different numerical models. Both models were in excellent agreement with the measured temporal bubble radius evolution. More importantly, both models predict a reduction in the expansion/collapse time when the drop size is decreased. Of course, this study is valid as long as the liquid layer around the bubble is not thin enough to promote the onset of the RTI, as it happens in cases with a low R_d/R^*_{max} ratio.

The radial oscillations of a central bubble were also used to study the onset of shape in-

stabilities at the gas-liquid interfaces, given by the Rayleigh-Taylor and Rayleigh-Plateau instabilities. The destabilisation mechanism of each instability and its effect on the droplet surface was illustrated by detailed high-speed images. Here, we have demonstrated how the radial acceleration imposed by the bubble oscillation triggers the RTI, which in turn induces a pattern of superficial ripples on the drop. Those acquire a concave shape during the bubble collapse and give rise to liquid filaments due to the transfer of the momentum from the bubble shock wave emissions to the curved pits formed on the gas-liquid interface. The ejected filaments later break up by the action of the RPI causing the detachment of smaller droplets and thus the atomisation of the drop.
The phase change from liquid to vapour within droplets is observed in a wide variety of applications, such as in flash boiling atomisation [297], in spray-flame synthesis [298], spray cooling [299], extreme ultraviolet light generation [300], and laser-induced breakdown spectroscopy of liquids [301] to name a few. They all have in common that through a complex non-spherical symmetric process a liquid is fragmented through a micro-explosion within. While Rayleigh-Taylor instabilities determine the growth of ripples on the surface of the droplet, the non-spherical bubble dynamics that lead to jetting out of the droplet affect the resulting size distribution of liquid particles, too. The high degree of control achieved in the current experiments opens up the possibility of studying RTI of more complex interfaces, e.g. the effect of particles covering the surface, surfactants, or complex fluids. Those experiments could be supported by complementary numerical simulations to optimise the workflow in the laboratory.

Funding

J.M.R and K.A.R. acknowledge support from the Alexander von Humboldt Foundation (Germany) through the Georg Forster and Humboldt Research Fellowships. This project has received funding from the European Union's Horizon research and innovation programme under the Marie Skłodowska-Curie grant agreement No. 101064097, as well as the Deutsche Forschungsgemeinschaft (DFG, German Research Foundation) under contract OH75/4-1 and INST 272/280-1. The authors would also like to thank the anonymous reviewers for their constructive criticism and suggestions that helped to improve this work.

Declaration of interests

The authors report no conflict of interest.

Author contributions

Juan Manuel Rosselló: Conceptualisation, Data curation, Formal Analysis, Funding acquisition, Investigation, Methodology, Software, Visualisation and Writing – original draft, Writing – review & editing. **Hendrik Reese**: Conceptualisation, Data curation, Formal Analysis, Software, Visualisation and Writing – review & editing. **K. Ashoke Raman**: Conceptualisation, Funding acquisition and Investigation. **Claus-Dieter Ohl**: Conceptualisation, Formal Analysis, Funding acquisition, Resources and Writing – review & editing.

7.6 Appendix: Bubble jetting in a liquid pool with a curved free surface

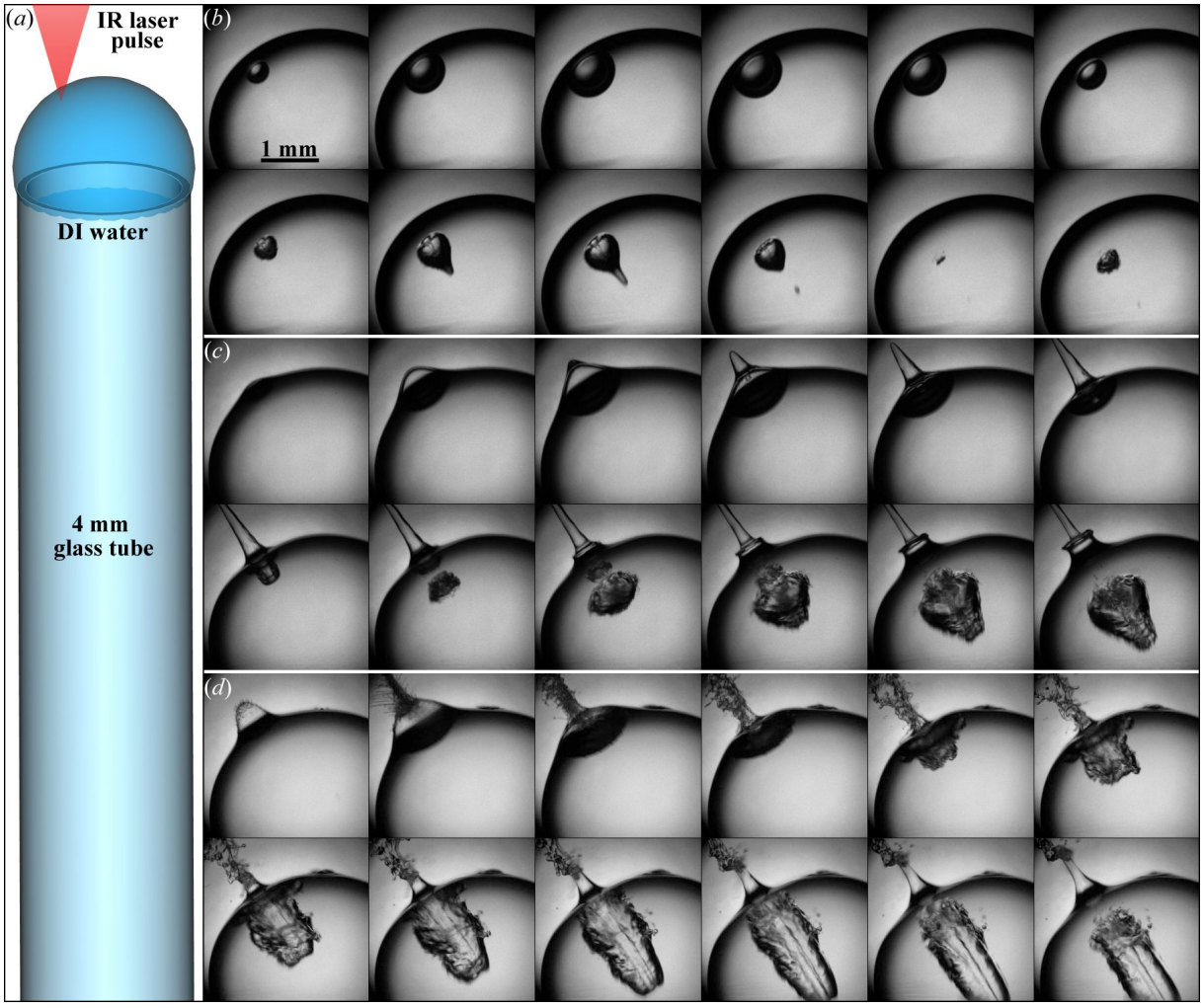

Figure 7.21: Bubble jetting on a curved surface. (a) A cylindrical tube with an external diameter of 3.6 mm, an internal diameter of 2.7 mm and a length of 4 cm was overfilled with DI water to produce the curved top. Infra-red laser pulses were focused from the top at different depths and slightly away from the cylinder axis. (b) $\Upsilon = 1.9$ ($D^* = 1.3$). (c) $\Upsilon = 0.7$ ($D^* = 0.6$). (d) $\Upsilon = 0.4$ ($D^* = 0.3$). The time between frames is 10 µs for (b) and (c) and 20 µs in case (d).

In section 7.4.2, the role of the curvature of the free surface was analysed by comparing the bubble jetting observed near a flat surface to the jetting dynamics of bubbles within the falling droplet. There, both the experimental and numerical results indicate that the effect of the curvature on the bubble jetting regime is almost negligible for low values of D^*, but the specific shape acquired by the cavity during and after the jetting is no longer similar as D^* takes values larger than 1.2, as shown by the structural similarity analysis. However, the curvature of the surface is not the only difference between these two cases, since in one case the liquid is confined (i.e. the droplet), and in the other the bubble is produced on top of an ideally "semi-infinite" liquid column (which has a length of 5 cm in the experiments and was numerically infinite in the simulations). An intermediate step between those two experimental scenarios is given by the configuration

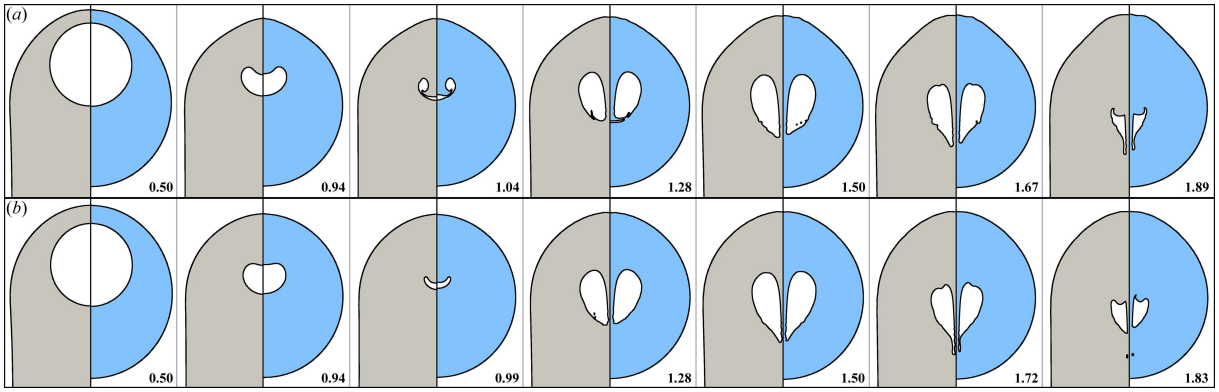

Figure 7.22: Comparison of the bubble jetting on the curved top of a long liquid column (left half) and in a drop of equal radius (right half). The numbers represent the time normalised with the time of collapse of the cavities from each case. (a) $D^* = 1.02$. (b) $D^* = 1.23$. The dynamics of the bubbles are almost identical.

described in figure 7.21 (a). Here, the bubbles are also produced close to the free surface of a liquid pool, but in this case the top of the liquid column presents a curved surface with the shape of a dome. Panels (b), (c) and (d) of figure 7.21 show three examples of jetting bubbles generated at different depths d. The bubbles were located away from the symmetry axis to make evident that the jets always point in the direction normal to the surface. As discussed in section 7.4.2, we observed a similar behaviour of the jetting dynamics for both curved surfaces at comparable values of the stand-off parameter. The example shown in panel (b) of figure 7.21 corresponds to the case (c) of figure 7.12, while the jet dynamics of the case (c) of figure 7.21 matches the one of figure 7.12 (a).
Figure 7.22 compares the jetting of bubbles in the drop case with the jetting of bubbles in a configuration as the one shown in figure 7.21 (a). The results present almost identical bubble dynamics even in the case with $D^* = 1.23$, meaning that the differences observed between the case with the flat surface and the drop case are indeed caused by the effect of the surface curvature and not by the difference in the boundary conditions below the bubble or in the liquid volume. As previously discussed for the flat surface case, the similarity found in the cases displayed in figure 7.22 will be eventually lost as the laser bubble is produced closer to the drop centre.

8 Cavitation bubble induced wall shear stress on an elastic boundary

This work has been published in [26]:

H. Reese, S.-W. Ohl, and C.-D. Ohl. "Cavitation bubble induced wall shear stress on an elastic boundary". *Physics of Fluids* **35** (7), 076122 (2023). ISSN: 1070-6631

A cavitation bubble imposes shear stresses onto a nearby structure during its expansion and collapse. Experimentally we probe the tangential stresses on an elastic surface by measuring the displacement of embedded particles and the deformation of an elastic structure. Corresponding numerical simulations are done using a fluid-structure interaction Volume-of-Fluid solver in OpenFOAM, where a linear elastic solid is coupled to two viscous, immiscible and compressible fluids. We find good agreement in terms of bubble dynamics and displacement motions. During the initial bubble expansion and its first collapse, the experiment agrees with the simulation that the strain of the elastic sheet at a distance of $1.25\,R_{\max}$ from the stagnation point centre is larger than at $0.51\,R_{\max}$. The maximum lateral strain occurs at a non-dimensionalised bubble stand-off distance of $\gamma \approx 1.1$. The highest calculated wall shear stress is 250 kPa (for position $y = 0$). However, the largest overall shear stress of 1.9 MPa is found within the elastic sheet at $y = 24\,\mu\text{m}$ that corresponds to a maximum displacement of $D_x = 44.5\,\mu\text{m}$. Thus fracture may start from within the elastic material rather than from the surface. To further examine the fluid-structure interaction, we construct a simple axisymmetrical elastic ring and analyse its deformation. In this case, we find strong deformations during the bubble collapse but also during the bubble's initial expansion.

8.1 Introduction

Cavitation bubbles expanding and collapsing near solid boundaries first caught the attention of the scientific community when they were found to be responsible for damages to fast-rotating ship propellers. Lord Rayleigh modelled the spherical cavitation bubble dynamics, enabling the calculation of the radius of an oscillating bubble as a function of time [2]. However, the damage on the (steel or copper) propellers is not in fact due to spherically collapsing bubbles but a result of non-spherical flow and shock wave emission in close proximity to the boundary [20, 82, 302, 303]. Besides the shock wave emission, jet impact and its successive radially spreading flow outwards on the surface, results in strong wall shear stresses [8, 304–306]. Apart from experimental observations using high-speed photography, cavitation bubble interaction with rigid boundaries has been modelled with various numerical methods. The most popular ones are perhaps the Boundary Element or Integral Method where only the boundaries of the domains are discretised, i.e. the bubble surface and the solid (rigid) boundary [5, 307–309]. Other numerical methods have also been used, such as the Free-Lagrange method [310], the Arbitrary Eulerian-Lagrangian method [311, 312], the Level-Set method [77, 313] and the Lattice-Boltzmann method [314].

When the solid boundary is sufficiently elastic, the cavitation bubble may collapse differently. Brujan et al. [101] studied experimentally how a laser-generated cavitation bubble expands and collapses near a transparent polyacrylamide (PAA) gel with 80 % water con-

centration (elastic modulus $E = 0.25\,\mathrm{MPa}$). As the bubble expands, it pushes the elastic boundary away. During its collapse phase, the elastic boundary moves towards the bubble. At certain stand-off distances, a radial in-flow of the liquid causes the bubble to split into two and the resulting bubbles collapse with opposing jets away from the point of splitting. The bubble behaviour near two boundaries of different stiffnesses was compared directly by Ma et al. [102]. Bubble dynamics with more pronounced boundary movement were reported by Turangan et al. [315] where an elastic membrane was used instead. However, when the elastic layer is attached to a rigid plate, the bubble dynamics depend on both the elastic modulus and the thickness of the elastic layer [316–318]. The numerical modelling of the elastic layer was done either using the Boundary Element Method where the layer was modelled as a linear elastic fluid [319, 320], or it was calculated using the Finite Element Method for an elastic solid and coupled to the fluid domain [318, 321]. When the elastic layer attached to the solid wall is very thin, the bubble expands and collapses in a similar manner to one which is near a rigid boundary, i.e. the formation of a high-speed jet is observed. Damages and erosion on the thin layer have been documented [322, 323]. The impact of the jet from a collapsing bubble creates high stresses on the material surface (with or without an elastic layer). This phenomenon is being utilised for many applications, such as ultrasonic cleaning [80, 324], lithotripsy for kidney stones [306, 325, 326] and sonoporation of cells [327, 328]. It is known that the jetting of the bubble is correlated to the cleaned area generated in acoustic surface cleaning [9, 329]. The transient cleaning mechanisms, however, are not fully resolved. Yet the current understanding is important to the aforementioned wall shear stresses. This wall shear stress was first measured directly by Dijkink & Ohl [132] using a constant temperature anemometer. A maximum stress of more than 3 kPa was recorded. Maisonhaute et al. [79] reported higher estimates for the shear stress of 25-50 bar (2.5 to 5.0 MPa). More recently, Reuter and Mettin [329] confirmed the initial measurement by employing electrochemical techniques. Clearly, the measurements are limited in bandwidth and average over some areas, thus they would not be able to resolve the amplitude of high-frequency and small-scale stresses. Indeed these are found in numerical simulations based on the Volume-of-Fluid (VoF) method. Zeng et al. [118] modelled the wall shear stresses as a function of the bubble's stand-off distance and the liquid viscosity. They found that the peak stresses are more than one order of magnitude higher (between 50 and 100 kPa) than those measured in the earlier experiments. The authors attributed this discrepancy to the experimental limitations of the sensor used. The shear stress may even be enhanced when the bubble is constrained in a narrow gap [330].

The main aim of the present work is to evaluate the shear stress a collapsing and jetting cavitation bubble induces on solid boundaries. We chose a direct method to quantify the shear stress through the elastic response using experimental high-speed imaging techniques and compare the response with simulations using a Volume-of-Fluid (VoF) solver coupled to an elastic solid. The work starts by describing the numerical and experimental techniques. After that, we show the results of the lateral displacement of a thin elastic sheet covering a rigid boundary as a bubble expands and collapses on top of it. We compare the experimental observations and the simulation results in terms of bubble dynamics and local displacement of the sheet surface. Then we show the results of an elastic ring structure and its deformation. Specifically, we study the deformations of a corner of the ring in the vertical and horizontal directions. The resulting stresses in both the ring and the sheet are then presented and discussed.

8.2 Numerical Model

The VoF (Volume-of-Fluid) simulations are carried out in OpenFOAM using the version Foam-Extend-4.0 [127]. Coupled liquid and solid solvers are provided by the FluidStructureInteraction [126] package. The solver `fsiFoam` was modified to simulate a single expanding and collapsing bubble near a deformable structure. We named the new solver `CavBubbleFsiFoam`. This solver has already been shown to accurately describe the propagation of waves in the liquid and a solid plate emitted by a bubble nucleated at high pressure (see Pfeiffer et al. [27], Gutiérrez-Hernández et al. [29], Gutiérrez-Hernández et al. [30]).

8.2.1 Governing equations

The solid is governed by the linear elastic equation of motion,

$$\frac{\partial^2 \rho D}{\partial t^2} - \nabla \cdot \left[G\nabla \circ D + G(\nabla \circ D)^{\mathrm{T}} + \lambda \mathrm{tr}(\nabla \cdot D)\overset{\leftrightarrow}{1} \right] = 0 \ , \tag{8.1}$$

where D denotes the deformation, $\overset{\leftrightarrow}{1}$ the unity matrix, $\cdot$ a scalar product, $\circ$ a tensor product and λ, G the Lamé parameters given by

$$\lambda = \frac{\nu}{1-2\nu}\frac{1}{1+\nu}E, \ G = \frac{1}{2}\frac{1}{1+\nu}E \ . \tag{8.2}$$

The fields in the solid are given in material coordinates. The equation of motion is solved by the solver `unsTotalLagrangianSolid`.
To represent PDMS or SLA resin, which are used in the experiments, a solid density of $\rho = 1000\,\mathrm{kg/m^3}$ and a Poisson's ratio of $\nu = 0.4$ is used. To avoid numerical instabilities, a very high Young's modulus of $E = 1000\,\mathrm{GPa}$ is used, along with the assumption that the achieved deformation in the experiments is sufficiently small, such that its effect on the fluid domain can be neglected, effectively resulting in a one-way coupling between the fluid and the elastic solid. Furthermore, the assumption of linear elasticity allows us to calculate the corresponding deformation at a lower Young's modulus $E_{\mathrm{experiment}}$ by simply multiplying it by the ratio $E_{\mathrm{simulation}}/E_{\mathrm{experiment}}$. This was done to improve the convergence of the solver. This decision is discussed further in the results section.
A compressible Newtonian fluid is governed by the law of conservation of momentum,

$$\rho\frac{D\vec{u}}{Dt} = \rho\vec{f} - \nabla p + \mu(\Delta\vec{u} + \frac{1}{3}\nabla(\nabla \cdot \vec{u})) \ , \tag{8.3}$$

the continuity equation,

$$\frac{\partial \rho}{\partial t} + \nabla \cdot (\rho\vec{u}) = 0 \tag{8.4}$$

and an equation of state, for which the Tait equation of state was chosen:

$$p = (p_0 + B)\left(\frac{\rho}{\rho_0}\right)^{\gamma} - B \ , \tag{8.5}$$

The provided solver `icoFluid` only models one fluid. For this reason, it was replaced by our solver `CavBubbleFluid`, which models two immiscible compressible fluids. The Tait parameters for these fluids are chosen to be $p_0 = 101325\,\mathrm{Pa}$, $\rho_0 = 998.2061\,\mathrm{kg/m^3}$, $\gamma = 7.15$, $B = 303.6\,\mathrm{MPa}$ to represent water and $p_0 = 10320\,\mathrm{Pa}$, $\rho_0 = 0.12\,\mathrm{kg/m^3}$, $\gamma =$

1.33, $B = 0$ to represent the bubble contents, which are treated as a non-condensible gas. With $B = 0$, equation (8.5) corresponds to an ideal gas equation of state. Temperature variations are not taken into account, and thus all state changes are modelled as adiabatic. The fluid-fluid interface is modelled with a phase fraction field α, which for each cell gives the fraction to which it is filled by water, while the rest is filled by the gaseous component. As opposed to other multi-phase solvers like `compressibleInterFoam`, further corrections are applied to mitigate numerical inaccuracies. The compressibility is calculated in every time step, which is necessary because the gas density and thus also its compressibility varies significantly during the bubble dynamics.
The model does not include any phase transitions, and thus the total amount of gas contained in the domain should stay constant. Despite this, the total amount of gas present in the simulated domain varies over time due to numerical errors. To counteract this, the bubble's mass, calculated as $m = \sum_i^{\text{cells}} \alpha_{2,i}\, \rho_{2,i}\, V_i$, is kept constant via the correction $\rho'_{2,i} = \frac{m_0}{m}\, \rho_{2,i}$. This stands in contrast to a real bubble, which is partly filled with water vapour that condenses over the course of the expansion and collapse. To account for this condensation, a one-time correction reduces the pressure and thus the total gas content by 70 % at the time of maximum bubble expansion. This has been shown to give an accurate bubble behaviour during its first collapse and rebound [24]. New gaseous regions may be created in the liquid bulk when α falls slightly below 1 due to numerical errors, which can then expand if the local pressure is low. To correct this, cells with values above a limit value $\alpha > \alpha_l$ are set to $\alpha = 1$. For large time steps, this value is chosen to be $\alpha_l = 0.998$. For smaller time steps ($dt < 3\,\text{ns}$) this limit becomes less strict as $\alpha_l = 1 - 0.002 \cdot dt/3\,\text{ns}$, because it would otherwise prevent existing slow-moving liquid-gas interfaces to cross cell borders.
The fluid domain interacts with the solid structure via interfacial forces $\vec{F} S_i = \overleftrightarrow{\sigma} \cdot \vec{n}_i$ on the fluid-structure interface and by conforming to the deformation D and velocity $\dot{D}$ of the boundary. Here, S_i are cell faces with normal vectors $\vec{n}_i$ at the fluid-structure interface, and $\overleftrightarrow{\sigma} = -p\overleftrightarrow{1} + \mu\left[\nabla \circ \vec{u} + (\nabla \circ \vec{u})^{\mathrm{T}}\right]$ is the stress tensor in the fluid. While the deformation of the solid is calculated via a physics-based equation, the deformation of the conforming fluid mesh is not tied to the motion of the fluid and can thus be chosen arbitrarily. The mesh motion of the fluid domain is done by interpolation of the displacement at the corresponding boundary conditions for the fluid-structure interface and the boundaries of the simulation domain.

8.2.2 Geometry and initial conditions

In the configuration of interest, the bubble is created in a cylindrical, effectively infinite fluid domain that sits on top of a solid boundary. The boundary is connected to a deformable elastic sheet, or, to model a bubble near a more complex structure, an elastic ring. This is placed at the bottom of the fluid tank on the (in this case rigid) boundary. All cases are axisymmetric such that the problem becomes effectively two-dimensional and the equations only need to be solved in the axial and radial directions. The solution in the angular direction is trivially given by the symmetry condition.
Figure 8.1 shows the geometry used for a bubble near an elastic solid sheet and a bubble near an elastic ring structure. It is bound by symmetric boundary conditions on the left, front and back surfaces. The upper and right boundaries represent a continuation of the fluid domain and the solid sheet. Here, `waveTransmissive` boundary conditions are applied for the fluid velocity, which corresponds to an advection equation, $\frac{\partial u_{\mathrm{f}}}{\partial t} +$

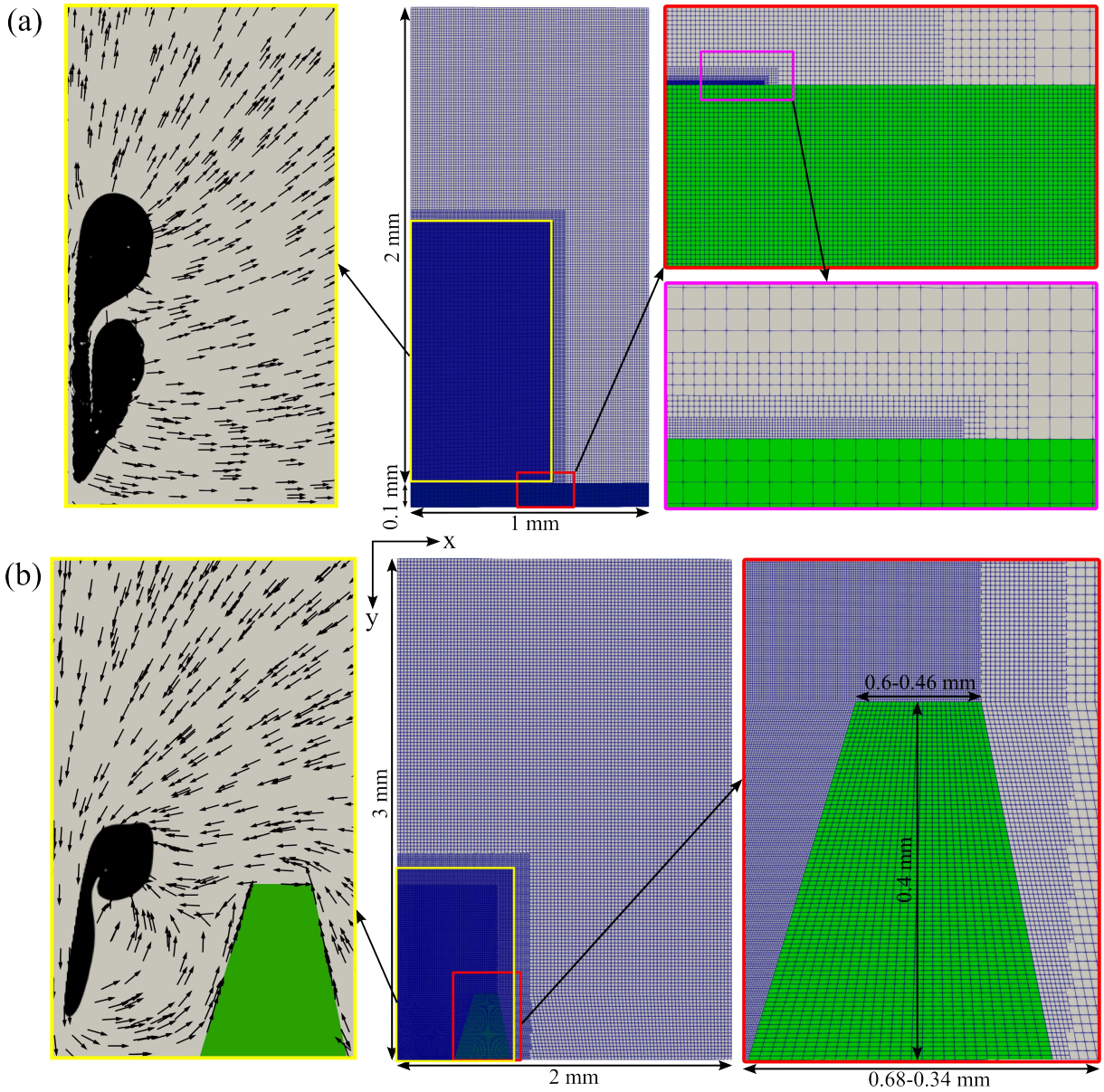

Figure 8.1: Geometries and computational meshes used along with an example of a simulated jetting bubble. The solid domain is given in green, the fluid domain is in light grey and the bubble in black. The fluid mesh is refined in the region occupied by the bubble. (a) Case of an elastic sheet. The mesh is further refined at the wall to resolve the boundary layer flow. (b) Case of an elastic ring.

$(\vec{u} \cdot \vec{n} + c)\,(\nabla \cdot \vec{n})\,u_\mathrm{f} = 0$, with the unit normal vector at the boundary cell face $\vec{n}$, the interpolated normal velocity at the boundary cell face $u_\mathrm{f} = \vec{u} \cdot \vec{n}|_\mathrm{f}$ and the speed of sound $c = \sqrt{\frac{\gamma}{\psi}}$, as calculated from the adiabatic exponent γ and the compressibility ψ. The `zeroGradient` boundary condition is used for α. The solid deformation is fixed to 0 at its lower boundary. At the fluid-structure interface, a `noSlip` boundary condition is applied for the fluid velocity. Here, α is kept equal to 1 to prevent the bubble from making contact with the solid wall, which is consistent with [124]. The deformation of the mesh is allowed to `slip` along the outer boundaries such that the shape of the full domain is preserved. In the axial and radial directions, the domain is divided into computational cells arranged on a square grid. The cell width is chosen to be 10 µm in the fluid domain and 2.5 µm in

the solid domain. In the fluid, the mesh is refined two times from a cell width of 10 µm to 2.5 µm in the region later occupied by the bubble. In the case of an elastic sheet, it is refined a further three times to 0.3125 µm below the bubble to resolve the boundary layer at the fluid-structure interface. Note that in the zoomed-out top image, the blue mesh lines are drawn very close together, such that the solid domain does not appear green.
A bubble seed is initiated on the axis of symmetry with an initial pressure of $p_\mathrm{b} = 16.9\,\mathrm{kbar}$ and an initial radius of 19.3 µm. Elsewhere an atmospheric pressure of $p_0 = 101325\,\mathrm{Pa}$ is applied. The bubble seed is initiated with a smeared interface in the form of

$$\alpha = 1 - \frac{1}{2}\left(1 - \tanh\left(\frac{10}{3}\left(\left(\frac{\vec{x}_i - \vec{x}_0}{R_0}\right)^2 - 1\right)\right)\right), \tag{8.6}$$

where $\vec{x}_i$ are the cell coordinates, $\vec{x}_0$, the bubble center and R_0 the initial bubble radius. This is helpful to avoid Rayleigh-Taylor instabilities during the early expansion phase.

8.3 Experimental method

The top view of the experimental setup for the elastic sheet and ring experiment is presented in figure 8.2. The cavitation bubble is generated in water in the glass cuvette with a focused pulsed laser (Quantum Light Instruments, Q2-E10-1064-SHG1). This is a Class IV Nd:YAG laser where the pump diode current (LD1) is set to 105 V, and the generator crystal temperature (SH) is set to 43 °C. The focusing of the laser is done using a 5× microscopic lens. The bubble interacts with a rigid custom-made acrylic cap. A 60 µm thick PDMS sheet with embedded particles (particle diameter = 15 µm) is coated onto an acrylic cuvette cap (see section 8.3.1). The particles' movement is captured with a 10× microscopic lens attached to a high-speed camera C1 (Shimadzu Inc., HPV-X2). The magnification is necessary to provide sufficient resolution for the particle-tracking. The framing rate is 1 million frames per second. The light is provided by a LED illuminator (SMETech, SugarCube (Light source 1)). At the same time, the corresponding bubble dynamics are captured using another high-speed camera C2 (Photron, Mini AX100) with an LED light source (SMETech, LED P-40 (Light source 2)). This is needed because of the high magnification for the particle resulting in C1 capturing only part of the bubble. Since camera C2 is placed in line with the laser source, a notch filter is used to block out the laser light, and a piece of the microscope glass slide is used to reflect some of the LED light into the camera. This camera is recording with a framing rate of 160,000 frames per second. The two cameras are synchronised using a delay generator (Berkeley Nucleonics, BNC Model 525).
A similar setup is used for the elastic ring experiment (figure 8.2). Instead of the acrylic cap coated with a PDMS layer, a stereolithography (SLA) 3D printed cuvette cap (see section 8.3.2) in similar dimensions with a ring structure attached is used. Also, a smaller magnification is used in this set of experiments. A 5× macro lens (Canon Inc, E 65 mm) is used together with the high-speed camera C1.

8.3.1 Preparation of PDMS layer with micro-particles

Polydimethylsiloxane (PDMS) sheet preparation is a multi-step procedure. First, a small number of fluorescent micro-particles with a diameter of 15 µm (Thermo Scientific, FluoroMax) are added to the curing agent. The curing agent with micro-particles is then vortexed with a laboratory shaker (Heidolph Instruments, REAX 2000) for 1 minute in order

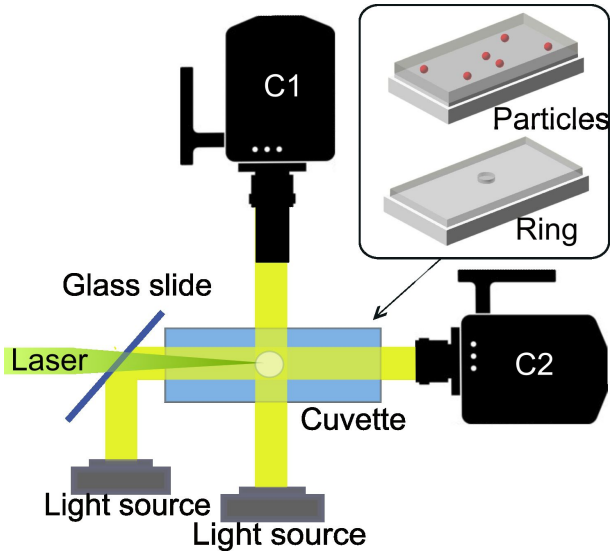

Figure 8.2: Top view of the experimental setup (not to scale). Glass cuvettes of dimensions $22.5 \times 12.5 \times 45\,\text{mm}$ with custom-made caps (with embedded particles on an elastic sheet or a printed ring) are filled with water. A bubble is created in the cuvette by a focused laser beam. A high-speed camera C1 with a magnifying lens is used to record particles or ring movement while the high-speed camera C2 is used to capture the bubble dynamics simultaneously. Each camera is illuminated by an LED light source.

for the particles to be evenly distributed in the liquid. The next step in the preparation is the mixing of the elastomer and the curing agent in a ratio of 10:1 by weight. The mixture is stirred and then placed in a vacuum desiccator for approximately 5 minutes so that residual air in the mixture is removed.
The PDMS mixture with micro-particles is then spin-coated onto the bottom side of the cuvette cap. The cap is custom-made of acrylic and fits the cuvette top. It is fixed to the spin-coater with double-sided tape and is spun at 300 rotations per second for approximately 10 seconds. The spin-coater is homemade out of a repurposed old hard drive disk. The last step of the PDMS preparation involves thermal curing. The coated cap is placed in a laboratory oven (UniEquip, Vacuum OvenVos-90A) at 100 °C for 2 hours.
The elastic modulus of a block of PDMS sample depends on the preparation procedure and its elastomer to curing agent ratio. With thermal curing, the elastic modulus E, is typically around 560 kPa [331]. However, the sheet we used in the experiment is very thin. It has a height of only 60 µm. Liu et al. [332] confirmed that their bulk sample of PDMS with 10:1 elastomer to curing agent ratio has indeed a measured elastic modulus $E = 500\,\text{kPa}$. However, when the thickness of their PDMS sheet is reduced to 60 µm, they found that E has increased to 1.4 MPa. Therefore, we use the value $E = 1.4\,\text{MPa}$ for our experimental elastic sheet data analysis and in comparison with simulation results.

8.3.2 Stereolithography 3D printed cuvette cap

A transparent elastic cuvette cap with the bottom dimensions $19.0 \times 9.2 \times 1.5\,\text{mm}^3$ that fits into the top of the cuvette is printed using a stereolithography 3D printer (Formlabs, Form 3+). The top part of the cap is slightly bigger ($22.0 \times 12.0 \times 1.5\,\text{mm}^3$) to allow it to sit on the cuvette. A ring of 450 µm radius is placed at the centre of the bottom surface

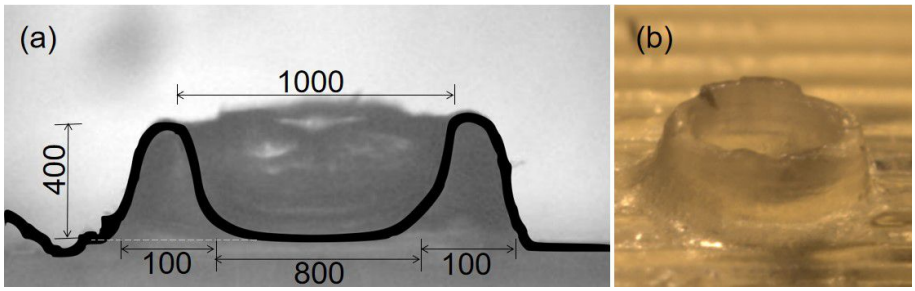

Figure 8.3: SLA 3D printed ring structure on the cuvette cap. (a) Outline and dimensions (in µm) of a cross-section of the printed ring. (b) A magnified photograph of the printed ring. The ridges on the surface are from printing defects common in 3D printing. They are however small (less than 50 µm in height) and therefore do not affect the bubble dynamics or the ring deformation.

of the cap. These rings have a wall thickness of approximately 100 µm and a wall height of about 400 µm (see figure 8.3 (a)). The 3D design is made using OpenSCAD and is then ported to the specialised software of the printer (Formlabs, Pre Form) for printing. The elastic resin (Formlabs, Elastic 50A) is used. Domingo-Roca et al. [333] measured the elastic modulus of the printed samples using the same elastic resin. They used both the standard tensile testing and a new measurement technique they proposed with laser Doppler vibrometer. They reported an elastic modulus of $E = 1.132 \pm 0.039$ MPa from the tensile testing, and a slightly higher value of $E = 2.05 \pm 0.21$ MPa from their new method. We took the value $E = 1.2$ MPa for our experimental data analysis and in comparison with numerical simulation.
The 3D-printed cap is transparent and elastic. The ring structure, however, is printed at the resolution limit of the 3D printer for that particular resin and turns out to have a slightly slanted wall and a top rim that is not very smooth (figure 8.3 (b)). Also, there are visible lines (ridges) on the surface of the cap (outside of the ring). These are all artefacts and imperfections from the printing process. However, these ridges are much lower in height than the ring wall. In fact, their height is measured to be less than 50 µm. Therefore we assume that they do not interfere with the bubble dynamics and the ring wall movement as studied in this experiment.

8.4 Results

8.4.1 Bubble near elastic layer

Figure 8.4 (multimedia available online) shows the expansion and collapse of a laser-generated cavitation bubble near an elastic layer of 60 µm thickness, with experimental photographs on the left and VoF-simulation cross-section frames on the right. The elastic layer is coated on a cuvette cap and therefore the actual video is flipped upside down for comparison with the simulations. There is no scientific concern as gravity does not play a significant part in the bubble dynamics in these time scales. The first frame shows the circled particles that are tracked, particle 1 and particle 2. They are located to the left of the bubble centre at a horizontal distance of $s_x = 710$ µm and $s_x = 290$ µm, respectively. The bubble is created at time $t = 0$ µs at a stand-off distance of $d = 875$ µm (not shown as it is outside the observation frame). Within the first microsecond after its creation, it sends

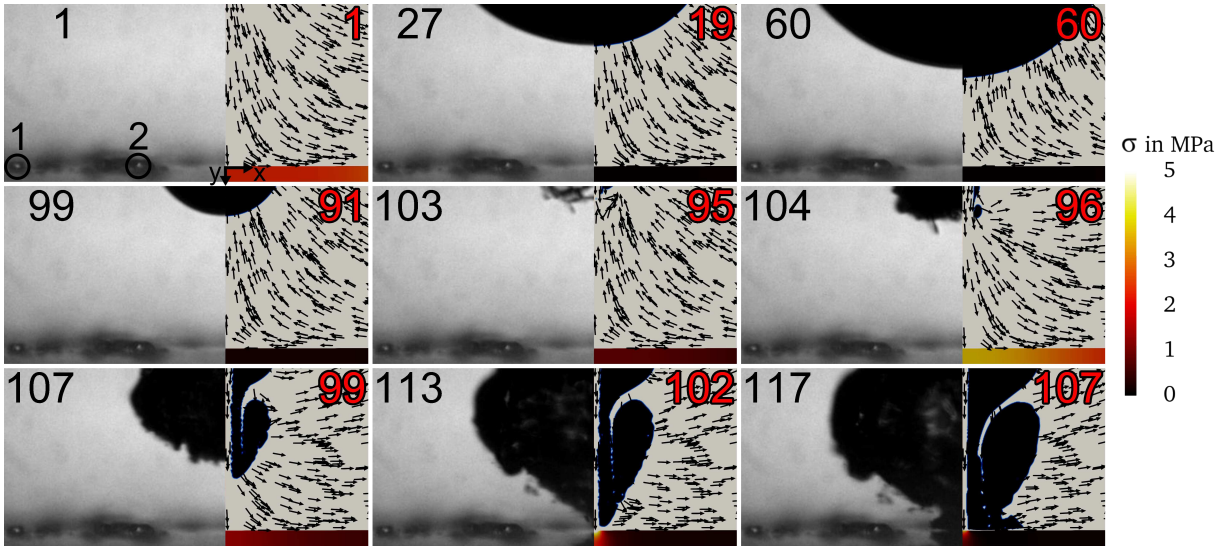

Figure 8.4: Expansion and collapse of a cavitation bubble near an elastic layer. Layer thickness $s = 60\,\mu\text{m}$, $R_{\max} = 569\,\mu\text{m}$ at around $t = 60\,\mu\text{s}$, stand-off $\gamma = 1.5$. The left side of each frame shows experimental photographs, with particles 1 and 2 (in black circles) at $s_x = 710$ and $290\,\mu\text{m}$, respectively. The x- and y-axes are indicated. The framing rate is 1 million frames per second (Mfps). The time in microseconds is given in each frame. The frame height is $625\,\mu\text{m}$. The right side of each frame shows the numerical simulations with the bubble in black, the liquid in bright grey and the flow field with arrows. The absolute solid stress is indicated with the colour scale on the right (multimedia available online).

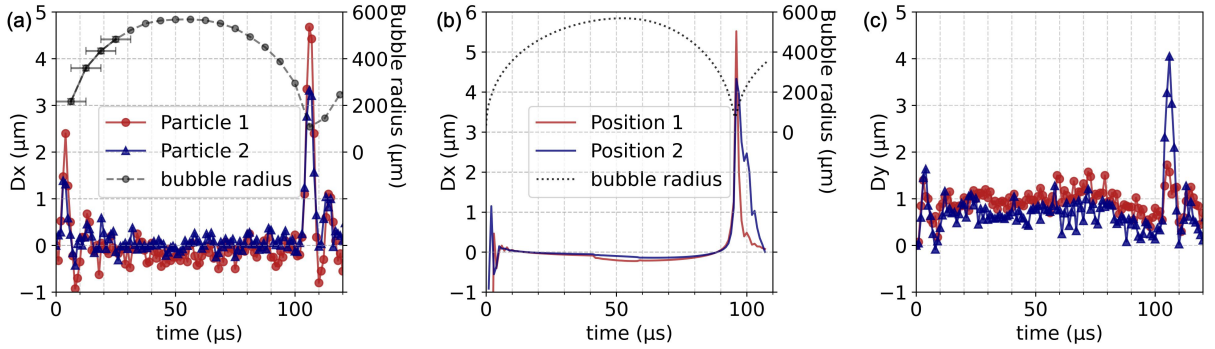

Figure 8.5: Comparison of horizontal displacement D_x between (a) experimental observation and (b) simulation result for $R_{\max} = 569\,\mu\text{m}$, sheet thickness $s = 60\,\mu\text{m}$, $E = 1.4\,\text{MPa}$ (1000 GPa in simulation, corrected by a factor of $10^6/1.4$). Both show slight lateral sheet movement during bubble initiation. When the bubble collapses, both experimental particle 1 and position 1 in simulation (at $710\,\mu\text{m}$ from bubble centre) show a peak D_x of $4.68\,\mu\text{m}$ and $5.52\,\mu\text{m}$, respectively. The nearer particle 2 and position 2 (at $290\,\mu\text{m}$) record lower D_x of $3.32\,\mu\text{m}$ and $4.33\,\mu\text{m}$, respectively. (c) Experimental vertical displacement D_y displays similar peaks at bubble expansion and collapse. However, particle 2 which is closer to the stagnation point, records a higher D_y of $4.05\,\mu\text{m}$ compared to that of particle 1 ($1.72\,\mu\text{m}$). The simulated D_y is not included because the model precludes the validity of the sheet's vertical movement. Also plotted on the secondary y-axis is (a) the bubble radius in time and (b) the volume equivalent bubble radius over time.

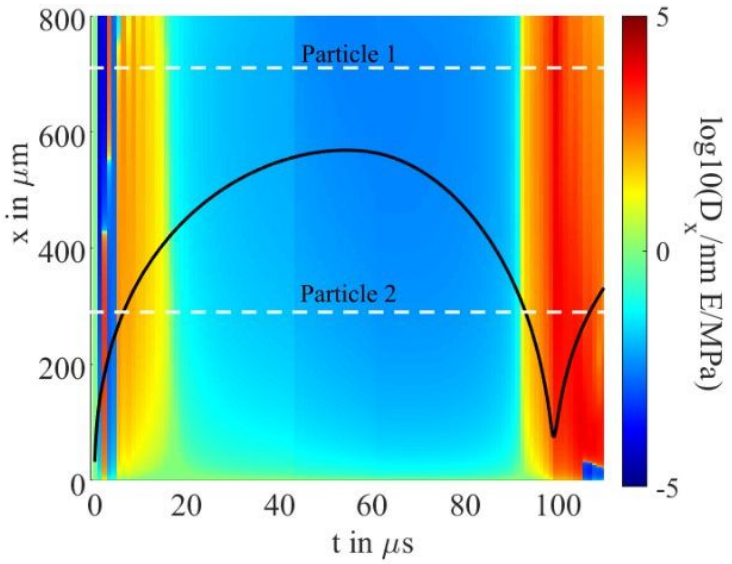

Figure 8.6: Streak plot of the deformation D_x of the wall as a function of the radial position r and time t in logarithmic scale, where for negative deformation values the logarithm was taken as $-\log_{10}(-D_x/\text{nm}\ E/\text{MPa})$. $R_{\max} = 535\,\mu\text{m}$, $s = 100\,\mu\text{m}$, $d = 500\,\mu\text{m}$, $E = 1000\,\text{GPa}$. The plot includes the volume equivalent bubble radius over time as a black curve and the positions of position 1 and position 2 as the upper and lower white dashed line, respectively.

out a shock wave that impacts the elastic wall and sets the liquid in motion away from the bubble. Large stresses are observed in the simulated solid, $\sigma = 2.27\,\text{MPa}$ at $x = 0$, $y = 0$. The stress magnitude is calculated from the stress tensor as $\sigma = \sqrt{\sum_{i,j} \sigma_{ij}^2}$. The bubble then expands and reaches its maximum size of $R_{\max} = 569\,\mu\text{m}$ at around $t = 60\,\mu\text{m}$, which is measured in the radial direction parallel to the elastic wall. Thus the non-dimensionalised stand-off distance is $\gamma = d/R_{\max} \approx 1.5$. Then the bubble starts to collapse while moving towards the solid wall and reaches its minimum size at around $t = 103\,\mu\text{s}$ ($t = 95\,\mu\text{s}$ in the simulation). This collapse creates another shock wave similar to the one emitted at $t = 0$, causing even larger stresses than before in the solid, $\sigma = 3.71\,\text{MPa}$ at $t = 96\,\mu\text{s}$. The bubble re-expands but has no longer a spherical, but a toroidal shape, as can be seen in the last three simulated frames in figure 8.4. This behaviour is not clearly visible in the high-speed photography images, but toroidal bubble formation is widely known for such a bubble collapsing near a solid boundary [21, 142, 334]. A liquid jet towards the solid surface has now developed and pulls the bubble along with it. The bubble reaches the wall at $t = 113\,\mu\text{s}$ ($t = 102\,\mu\text{s}$ in the simulation), after which the liquid jet impinges on the surface, causing a large localised water-hammer pressure which dominates the stress, $\sigma = 6.13\,\text{MPa}$. It then turns into a shear flow directed radially outwards, achieving a maximum wall shear stress of 159.5 kPa near the axis of symmetry ($x = 25\,\mu\text{m}$) at $t = 103\,\mu\text{s}$.

The movement of the particles is tracked using the software TRACKMATE, which is part of the freeware Fiji (also known as ImageJ) [335]. The horizontal movement D_x of the particles to the left of the frame (away from the bubble centre) is plotted in figure 8.5 (a), the vertical movement D_y in figure 8.5 (c). There is an initial horizontal movement of around 2.4 µm for particle 1 (around 1.4 µm for particle 2). The vertical movement is

smaller, about 1.4 µm for particle 1 and 1.6 µm for particle 2. This happens during the initial expansion of the bubble. During the first oscillation cycle of the bubble, the particles remain close to $D_x = 0$ and $D_y = 1\,\mu\text{m}$. The vertical displacement can perhaps be explained by the acrylic cap bending or displacing by this value over a large area in this time period. There are again strong particle movements when the bubble reaches its minimum volume at around 103 µs. A horizontal displacement of 4.7 µm for particle 1 (around 3.3 µm for particle 2) as well as a vertical displacement of 1.7 µm (around 4.1 µm for particle 2) is observed. Thus the deformation of particle 1, which is further from the bubble, is larger than that of particle 2 in the horizontal direction, but smaller in the vertical direction. This makes sense because due to the symmetrical configuration, a stagnation point must form below the bubble, where after its collapse the pressure is highest. Since this pressure causes vertical displacement, a particle closer to the stagnation point will be displaced further than one far away from it. At the same time, the horizontal displacement on the axis of symmetry must be zero. The shear force caused by the collapsing bubble must have a maximum at some horizontal distance from the stagnation point, and thus a particle near the stagnation point will be displaced less than one near this region of maximum shear.
The simulation is done using a much stiffer elastic solid of $E = 1000\,\text{GPa}$, and thus the deformation achieved is much smaller than that observed in the experiment. Nevertheless, a comparison with the experiment can be made under the assumptions of linear elasticity (where $D \propto E^{-1}$) and negligible effect of the sheet deformation on the bubble behaviour, by multiplying the calculated deformation by $E_{\text{simulation}}/E_{\text{experiment}}$, the resulting horizontal deformation D_x is shown in figure 8.5 (b). A reasonable agreement with figure 8.5 (a) is achieved for both positions corresponding to the particles 1 and 2, showing smaller deformation peaks just after bubble creation and, after some time of small displacement from the initial positions, larger peaks, where the displacement of position 1 is larger than that of position 2.
The deformation of the fluid-structure interface as a whole is visualised in figure 8.6 using streak plots, where the deformation over a line from $x = 0$, $y = 0$ to $x = 800\,\mu\text{m}$, $y = 0$ is plotted on the vertical axis over time t on the horizontal axis, for the horizontal deformation D_x. A logarithmic scale is used for better visualisation of the deformation between the large deformation peaks, where positive values on the colour bar correspond to positive deformation values and vice versa. For the deformation direction (x axis), the reader is referred to frame 1 of figure 8.4. The peaks just after bubble creation and bubble collapse are prominently seen. Some oscillations of the surface are also observed during the bubble's initial expansion. On the axis of symmetry, the horizontal deformation must be zero. Therefore there is a transition to small D_x in green near $x = 0$.
When the bubble starts to re-expand, features spreading radially outwards corresponding to the bubble expansion are observed.

Maximum displacements

The maximum displacement of the particles after the first collapse of the bubble is shown in figure 8.7 for various experimental and simulated cases. The parameters governing the displacement of the particles in the experiments are the stand-off distance between the bubble centre and the top of the elastic sheet (γ) and the horizontal distance between the particle and the bubble centre (s_x). Both γ and s_x are normalised by the maximum bubble radius (R_{max}) in the bubble's first oscillation period in order to ease the compar-

ison between experiments with slightly different maximum bubble radii. The maximum bubble radius ranges between 486 µm and 690 µm for the 36 cases presented.
As shown in figure 8.7, for γ between 1.34 and 1.79, the bubble collapses before jetting towards the elastic sheet and collapsing for a second time on the sheet. These dynamics have been shown previously in figure 8.4. Considering only the first collapse, the increasing maximum displacement ($D_{x,\max}$) with decreasing γ is clearly observed. Large maximum displacements are measured for bubbles with γ close to 1.1. At this stand-off distance, the bubble jets towards the surface as it collapses. The jet blocks the view of the particles, making tracking extremely challenging. However, for the two cases where the particles could be seen and tracked, the maximum displacements are as large as 13.4 µm ($\gamma = 1.07$, $s_x = 0.49$) and 11.0 µm ($\gamma = 1.09$, $s_x = 0.83$).
For cases with stand-offs $\gamma \leq 1.0$, the bubbles are not spherical at their maximum expansion. Typically, the bottom bubble surface is flattened due to the nearby boundary. For $\gamma \approx 0.5$, the bubble is approximately hemispherical at its maximum size. Only particles with a large distance from the bubble, $s_x \geq 0.89$, are not blocked in view and therefore could be tracked. Large maximum horizontal displacements, $9.6 \leq D_{x,\max} \leq 12.1$, are recorded for these cases. The proximity of the collapsing bubble induces a strong jet and water hammer pressure on the boundary [119, 336].
At a high stand-off distance of $\gamma \geq 2.2$, the maximum displacements of particles as the bubble collapses are all below 2.0 µm and they are not shown in figure 8.7. This low value of displacement is due to the fact that at this stand-off, the bubble has collapsed far from the boundary. The jet that has penetrated the bubble during the collapse, would proceed to move towards the boundary. However, most of the jet's energy has been dissipated by the time it reaches and impacts the boundary.
Simulation results for the horizontal stand-offs $s_x = 0.2$ and $s_x = 1.1$ are also plotted. Using the assumption of linear elasticity, the deformation values were corrected to match the parameters in the experiments. Since the sheet thickness is $s = 100$ µm in the simulations and $s = 60$ µm in the experiments, the deformation is corrected by a factor of 0.6. Similarly, since the elastic modulus in the simulations is $E = 1000$ GPa, the deformation was multiplied by a factor of $10^6/1.4$ to reach the value for $E = 1.4$ MPa. The simulated results are in the same order of magnitude and show a similar trend as the experimental values, and thus are in reasonable agreement. The field data was sampled in time intervals of 1 µs, though the maximum deformation may be reached in between those sample points. In some cases, the maximum deformation may occur closer to one of the sample points than in other cases. This explains the non-smooth variations between neighbouring data points in figure 8.7.

Correlation of stress and deformation

Figure 8.8 (a) shows the maximum pressure, maximum wall shear stress (τ_x) and overall maximum shear stress (σ_{xy}) in the elastic sheet for the different stand-off distances, γ. The largest pressure calculated is found at $\gamma = 1.17$, where $p = 12.2$ MPa. For τ_x and σ_{xy}, the maximum values are recorded for $\gamma = 1.12$, where $\tau_x = 250$ kPa and $\sigma_{xy} = 1.9$ MPa. In fact, the pressure is also near its maximum at this stand-off with $p = 12.0$ MPa. For $\gamma \approx 1.1$, the bubble is roughly spherical at its maximum size with its bottom surface close to, but not touching the elastic sheet. Collapsing from this position allows for an efficient transfer of the kinetic energy of the jet onto the boundary. For larger γ, some of the energy is dissipated into the liquid when the jet pierces through the collapsing bubble

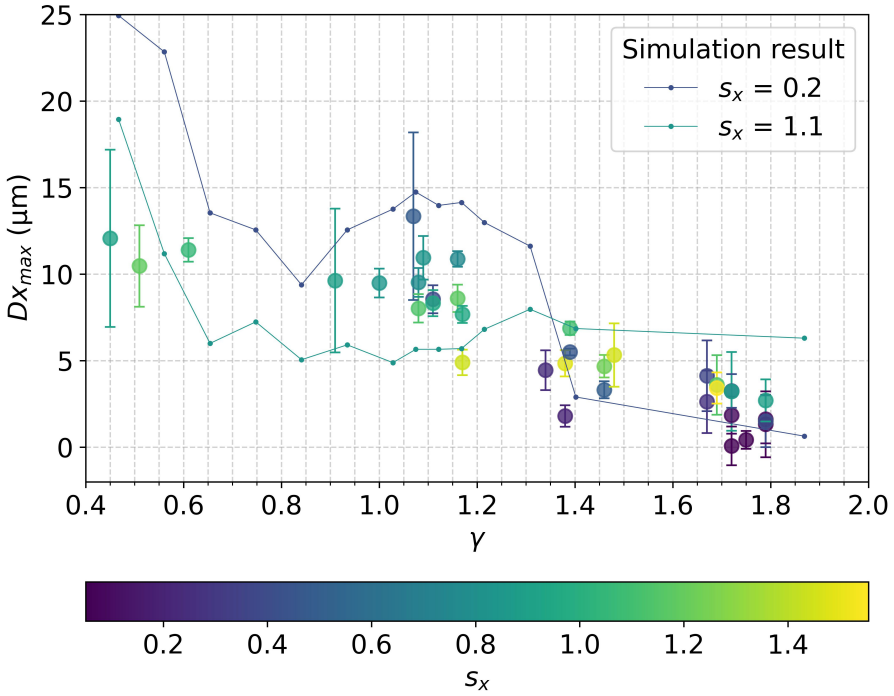

Figure 8.7: Maximum horizontal displacements ($D_{x,\max}$) of the particles from their initial positions. The bubbles are initiated at different stand-off distances, γ. In the experiments, the particles are initially located in the elastic sheet with a horizontal distance s_x from the bubble centre (see colour bar). The displacement is highest at the non-dimensionalised stand-off, $\gamma = 1.07$. The displacement tends towards zero at large stand-offs. The maximum horizontal deformations from the simulation at two different normalised horizontal distances $s_x = 0.2$ and $s_x = 1.1$ are also plotted, for $R_{\max} = 535\,\mu\text{m}$, sheet thickness $s = 100\,\mu\text{m}$ (corrected by a factor of 0.6), $E = 1000\,\text{GPa}$ (corrected by a factor of $10^6/1.4$).

.

to reach the elastic sheet. On the other hand, for $\gamma < 1.1$, the bottom part of the bubble is deformed. For $\gamma \approx 0.5$, the bubble at its maximum size is approximately hemispherical and its vertical size is decreased. The resulting jet gets formed over a smaller distance than the jets created for larger γ and thus reaches a lower velocity. The largest stresses are achieved for $\gamma \approx 1.1$, since a high-velocity jet is created from the almost spherical bubble, which pierces through the lower bubble boundary, leaving no time for the jet energy to be dissipated.

Figure 8.8 (b) shows the observable deformation values for correlation with inner and surface stresses caused by the bubble on the elastic solid wall, allowing for an estimation of the stresses induced in the experiments. It is worth noting that the maximum shear stress within the solid sheet is an order of magnitude larger than the maximum wall shear stress. We suggest that this may be responsible for ruptures or crack formation and thus could contribute to damage. A similar observation has been reported in Chahine and Hsiao [337] (figure 11) where the maximum stress they found in their aluminium sheet is 0.2 mm below the surface of the sheet due to plastic deformation.

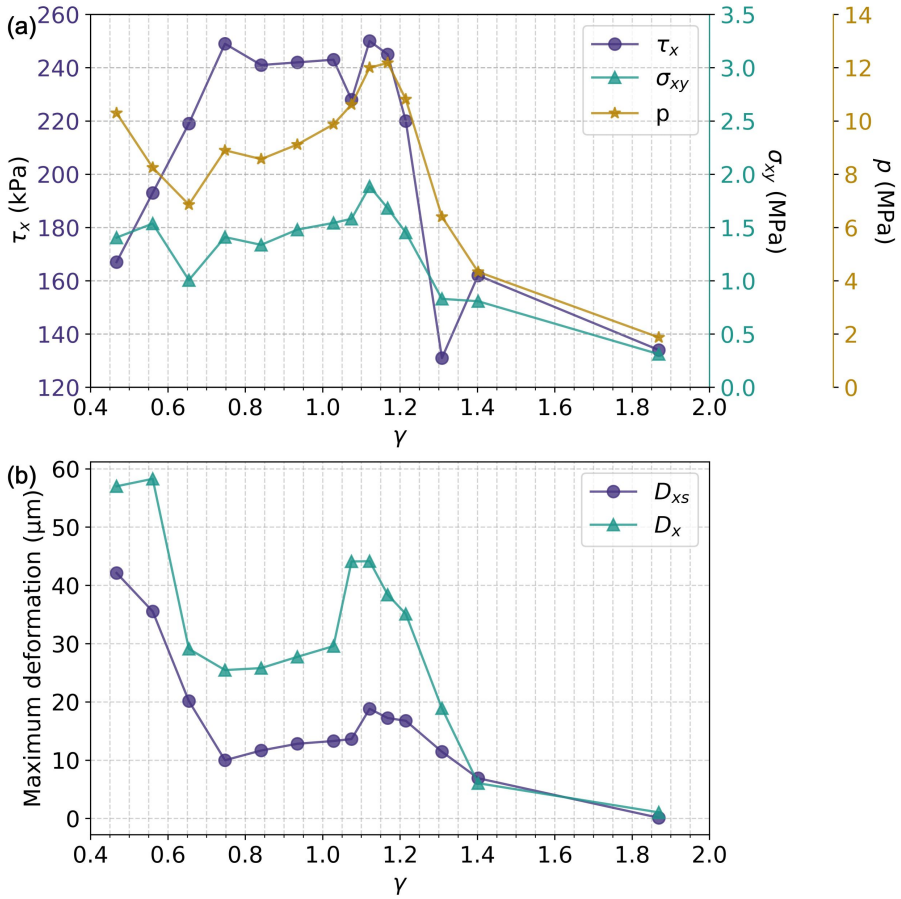

Figure 8.8: Dependence of numerical quantities on normalised stand-off γ of the bubble from the elastic layer. (a) Maximum pressure p at $\vec{x} = 0$, maximum wall shear stress τ_x, overall maximum shear stress σ_{xy}. The latter two quantities have been multiplied by a numerical factor for better visibility. (b) Maximum horizontal deformation at the surface D_{xs}, overall maximum horizontal deformation D_x for $R_{\max} = 535\,\mu\text{m}$, $s = 100\,\mu\text{m}$ (corrected by a factor of 0.6), $E = 1000\,\text{GPa}$ (corrected by a factor of $10^6/1.4$).

8.4.2 Bubble near elastic ring structure

Apart from understanding the wall shear stress on an elastic boundary, we would like also to extend the study to include stresses on structures due to a cavitation bubble collapse. One of the simplest and axisymmetrical structures is a ring. Therefore we studied the bubble dynamics near an elastic ring structure with two high-speed cameras as depicted in section 8.3. The cavitation bubble collapses with a jet directed toward the centre of the ring. The presence of the ring influences the bubble dynamics, especially if the bubble is created close to the ring. We vary the size of the ring and the bubble stand-off distance from the ring center (the top of the plate that the ring is attached to). There is also a slight variation in the maximum bubble radii. They are, however, all around 500 µm.
Figure 8.9 (a) (multimedia available online) shows the expansion and collapse of a cavitation bubble with a non-dimensionalised stand-off distance of about $\gamma = 1$, i.e. the bubble is created about one maximum bubble radius away from the bottom surface of the ring centre. Upon expansion, part of the bubble is inside the ring. A fringe forms on the bubble surface near the ring rim (frames $t = 50, 70, 88\,\mu\text{s}$). Nevertheless, in the bubble

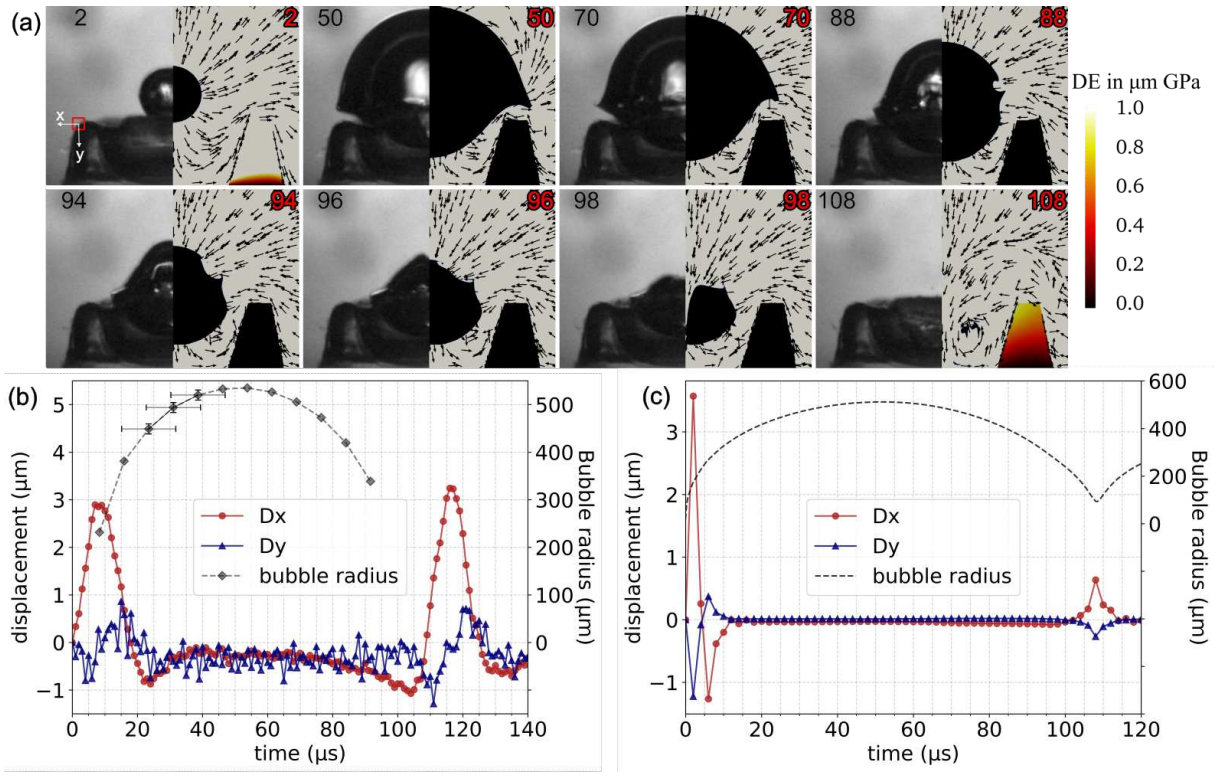

Figure 8.9: (a) Selected frames of a cavitation bubble collapse near a ring of 550 µm in radius. The framing rate is 1 Mfps. The bubble is created about $d = 555$ µm from the wall. It reaches its maximum radius of $R_{\max} = 564$ µm at $t = 50$ µs after its creation. The timing in µs is given in each frame. The frame height is 1.35 mm. (b) Experimental horizontal (D_x) and vertical (D_y) displacement of the ring corner (red square) is plotted together with the bubble dynamics. The error bars for the bubble radius are plotted only for 3 points but they apply to all radii. Maximum displacements are seen during the bubble's initial expansion and after its first collapse (around $t = 105$ µs). (c) D_x and D_y were obtained from the simulation. $E = 1000$ GPa (corrected by a factor of $10^6/1.2$). Bubble radius over time is superposed (multimedia available online).

collapse phase, a jet develops on the top of the bubble and moves towards the bottom of the ring centre.

The ring is deformed and the ring wall moves accordingly as the bubble oscillates. We track the movement of the upper outer corner of the ring. The tracking is done using a Python code developed by the authors. The basic algorithm is as follows:

The region of interest tracked is shown as a red square in figure 8.9 (a), frame $t = 2$. The consecutive frames are cross-correlated. The location of the maximum of the displacements is obtained. To measure sub-pixel displacement, a Gaussian curve in x- and y-directions is fitted to 11 points centred upon the maximum. The x- and y-position of the maximum of this Gaussian curve is reported as displacement in the horizontal and vertical directions with sub-pixel accuracy, respectively.

Figure 8.9 (b) shows the tracked movement of the upper outer left corner of the ring in figure 8.9 (a). The corner moves strongly during the initial bubble expansion and again after its first collapse (around 105 µs). The small distance between the bubble and ring results in a larger horizontal movement outwards (in the x-direction) of about 2.90 µm as the bubble expands. During bubble collapse, before the formation of the jet ($t = 96$ µs and

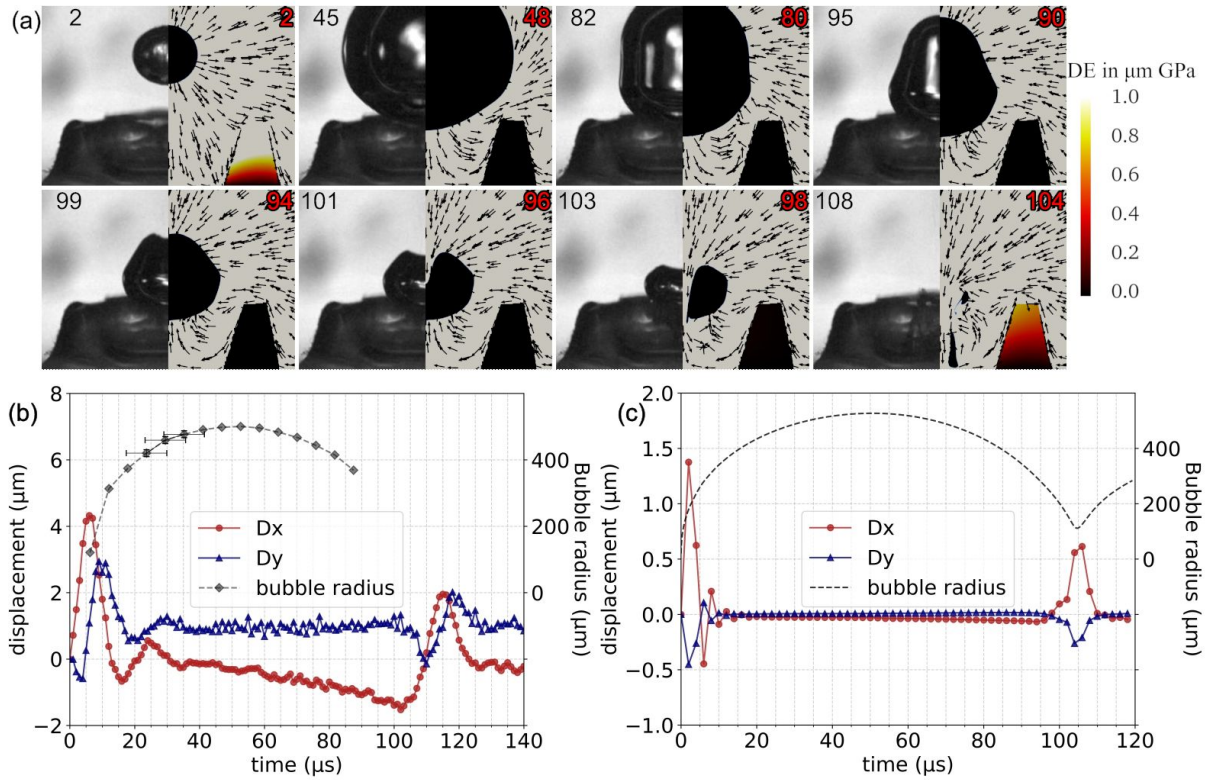

Figure 8.10: (a) Selected frames of a cavitation bubble expansion and collapse near a ring of 550 µm in radius. The framing rate is 1 Mfps and timing in µs is given in each frame. The bubble is created about $d = 810$ µm from the wall at the bottom centre of the ring. It reaches its maximum radius of $R_{\max} = 535$ µm at $t = 50$ µs after its creation. The frame height is 1.35 mm. (b) Experimental horizontal (D_x) and vertical (D_y) displacement of the ring corner is plotted together with the bubble dynamics. The error bars for the bubble radius are plotted only for 2 points but they apply to all radii. Maximum displacement is seen during the bubble's initial expansion and slightly less so during its collapse. (c) D_x and D_y were obtained from the simulation. $E = 1000$ GPa (corrected by a factor of $10^6/1.2$). Bubble radius over time is superposed (multimedia available online).

$t = 98$ µs in figure 8.9 (a)), most of the bubble has moved into the ring. During this period, the ring corner is slowly pulled inwards in the x-direction by about 1.5 µm. After the minimum bubble size, the ring corner is pushed outwards. The maximum lateral displacement reached is $D_x = 3.24$ µm. the corner is also moved slightly downwards to $D_y = 0.71$ µm. The configuration of the experiment is axisymmetrical. The upper outer right corner of the ring structure shows displacements in x and y directions of similar magnitude. Therefore the tracked movement is not shown here.

Figure 8.9 (c) shows the deformation obtained by the simulations. Again prominent peaks after bubble creation and after bubble collapse are visible. While the first peaks stemming from the bubble creation are of the same order as the deformation observed in the experiments, the peaks that occur after bubble collapse are smaller by about a factor of 4. The strongest shear stresses by far are observed at the inner bottom corner of the ring, reaching 17.04 MPa at $t = 2$ µs and 3.52 MPa at $t = 108$ µs. These strong stresses may lead to failure and damage in some materials.

The movement of the ring's corner of the case shown in figure 8.10 (multimedia available online) can be compared to the previously shown case in figure 8.9. Both cases have the

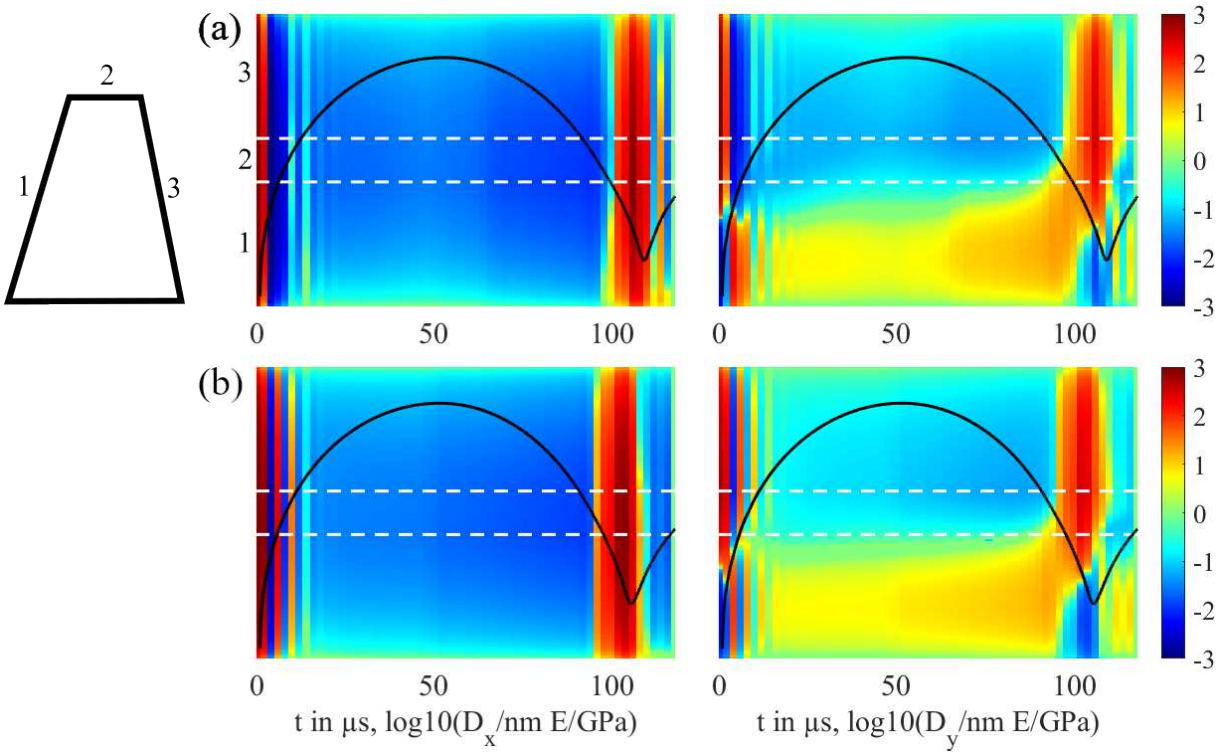

Figure 8.11: Streak plot of the deformation D_x and D_y of the ring surface as a function of time t in logarithmic scale, where for negative deformation values the logarithm was taken as $-\log_{10}(-D/\text{nm}\ E/\text{GPa})$. The deformation of the three fluid-structure interfaces of the ring structure is plotted, as indicated by the numbers 1, 2 and 3 in the sketch on the left. The ring corners are indicated by white dashed lines. $R_{\max} = 535\,\mu\text{m}$, $E = 1000\,\text{GPa}$. The plots include the volume equivalent bubble radius over time as a black curve, the axis ranging from 0 to 600 µm. (a) $d = 550\,\mu\text{m}$ (b) $d = 800\,\mu\text{m}$.

same ring size. The main difference between them is the stand-off distance of the bubble. In figure 8.10 $\gamma = 1.5$, while in the previous case $\gamma = 1$.
In general, similar dynamics are observed. The bubble expands spherically and reaches its maximum size of $R_{\max} = 535\,\mu\text{m}$ at $t = 50\,\mu\text{s}$. During the bubble's initial expansion ($t = 0$ to $t = 15\,\mu\text{s}$), we observe a strong movement at the ring wall corner. As seen in figure 8.10 (b), the corner moves about 4.3 µm in the positive x-direction and 2.9 µm in the positive y-direction. This represents a sudden high pressure on the ring, causing its corner to move downwards vertically and outwards horizontally. After that, the bubble expands to its maximum size and starts to collapse ($40\,\mu\text{s} < t < 100\,\mu\text{s}$), and the corner remains on average at about $y = 0.96$. In the x-direction, however, the corner moves inwards towards the bubble and reaches $x = -1.52\,\mu\text{m}$ just before the bubble collapses. During the bubble's collapse ($t = 100\,\mu\text{s}$ to $t = 110\,\mu\text{s}$), the corner is slightly pulled towards the bubble in the y direction. However, when the bubble reaches its minimum size at around $t = 115\,\mu\text{s}$, the corner is pressed outwards strongly in the x direction (more than 3 µm, x increases from its minimum of $-1.52\,\mu\text{m}$ to $1.95\,\mu\text{m}$). It is also pressed slightly downwards in the y-direction.
As shown in figure 8.10 (c), again a qualitative agreement between the experimental and the numerical deformation is seen. Though again, the positive peaks observed in the simulations are significantly smaller. The ring being pulled inwards due to the bubble collapsing is also observed, but the effect is weaker than in the experiment. Again,

at the inner bottom corner, the strongest shear stresses are achieved with 6.21 MPa at $t = 2\,\mu s$ and 3.68 MPa at $t = 106\,\mu s$.
The deformation D_x and D_y of the simulated ring cases shown in figure 8.9 and figure 8.10 are illustrated using streak plots in figure 8.11 (a) and (b), respectively. The y-axes of the plots follow the fluid-structure interface, starting from the inner bottom corner of the ring and going over the inner top corner and the outer top corner to the outer bottom corner. The two top corners of the ring are indicated by white lines. The large deformations after bubble creation and after bubble collapse are prominently seen over the entire ring surface. Since the ring structure is fixed at the bottom and the top of the ring moves horizontally, a bend in the structure is to be expected. For instance, when the ring is deformed inwards (outwards), it is bent counter-clockwise (clockwise). This behaviour can be observed in the plots for the vertical deformation D_y on the right side of figure 8.11. During the bubble shrinking phase, the ring is pulled inwards and thus the outer surface of the ring is stretched and deformed upwards (negative y-direction), while the inner surface of the ring is compressed and deformed downwards (positive y-direction). The signs of these deformations flip after the bubble collapse when the ring is pushed outwards. Now, the outer surface is being compressed and the inner surface is being stretched, which is reflected accordingly in the vertical deformation D_y.

8.5 Conclusion

In this paper, we presented experimental and numerical simulation studies attempting to understand the shear stresses on elastic material during the expansion and collapse of a single cavitation bubble. The fluid-structure interaction simulation is done by coupling a finite-volume solver for two compressible, viscous fluids with a solver for a linearly elastic solid. Refinement on the boundary layer is carefully done to ensure sufficient resolution to resolve the wall shear stress. We compare the experimental tracked movement of particles on the surface of an elastic layer with the displacement of the elastic material from simulations at the same positions. Reasonable agreements between experimental and simulated results lend confidence to the wall shear stresses calculated. From our summary of maximum lateral displacements of particles due to a collapsing bubble at different stand-off distances (γ), a maximum wall shear stress of 250 kPa is found for $\gamma \approx 1.1$. Wall shear stress values this large have not been reported before. Recently, Zeng et al. [119] reported a wall shear stress of 100 kPa for a collapsing bubble at $\gamma = 1$. Denner et al. [338] reported a peak wall shear stress of 68.3 kPa for a bubble at $\gamma = 0.4$. This discrepancy by a factor of about 2.5 may be caused by an overestimation of the stresses in this work, an underestimation of the cited works, or a combination of both. The resulting stresses are highly sensitive to the details of the bubble and jetting dynamics. Nonetheless, we argue that in this work the boundary layer is sufficiently refined, since a further refinement yields similar stresses within a 10 % difference. Simulations with and without fluid-structure interaction coupling also yield similar results with variations of less than 5 %.
We also studied the interaction of a cavitation bubble with an elastic ring structure. The vertical and lateral displacement of the ring corner is measured with high-speed photography and compared with the numerical simulation. Both agree that the lateral displacement is larger than the vertical displacement during the bubble's initial expansion and its first collapse. The complex interaction between the bubble and elastic structure may shed some light on the mechanism of bubble cleaning on complex surfaces. We

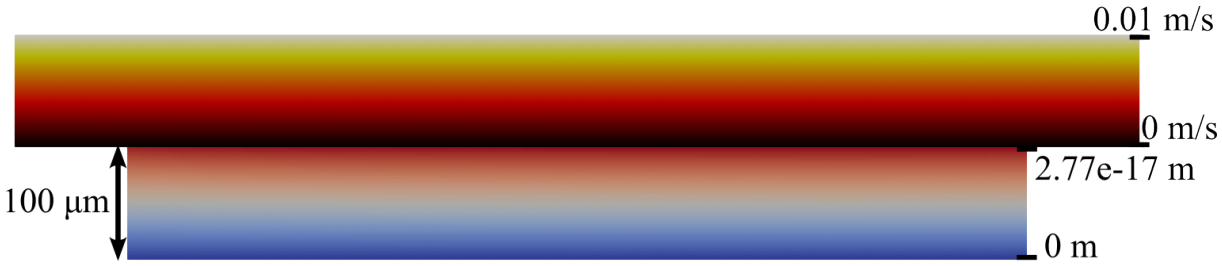

Figure 8.12: Developed shear flow near an elastic solid. Velocity is 0.01 m/s over 100 µm, $E = 1000\,\mathrm{GPa}$, $\tau_x = 1000\,\mathrm{Pa}$, $D_x = 2.77 \cdot 10^{-17}\,\mathrm{m}$ (calculated: $2.8 \cdot 10^{-17}\,\mathrm{m}$). The error can be attributed to the boundary conditions.

express a note of caution as to the scope of validity for the linear elastic model that we have utilised. At high strain rates, other non-linear or plastic behaviour may become important. Also, because of the high elastic modulus used in the simulation, information about wave propagation in the elastic solid is lost, since only quasi-static deformation can be scaled linearly with the elastic modulus. Nevertheless, we believe that our model is valid for the small displacement regime that we have presented. Lastly, we conclude that our method of correlating the observed elastic material displacement with the calculated wall shear stress is potentially useful for the generalisation of wall shear stress measurements for different materials. An automated system using a high-speed camera and simulation software, similar to commercialised Particle Image Velocimetry (PIV), could be developed.

8.6 Acknowledgments

H.R. and S.W.O. contributed equally to this work. The present work was supported by the Deutsche Forschungsgemeinschaft (DFG, German Research Foundation) under contract OH75/4-1. We thank Qingyun Zeng and Fabian Denner for helpful discussions on the solver.

8.7 Appendix

8.7.1 Validation of the solver

A simple shear flow case over a thin elastic sheet of thickness $d = 100\,\mu\mathrm{m}$ is employed to check the validity of the solver to model linear elastic shear deformation. Above the elastic solid, the horizontal flow velocity is chosen to be 0.01 m/s at a distance of 100 µm. This relatively small velocity is chosen to achieve a Reynolds number of $Re = 1$, to ensure a laminar flow. With a viscosity of 1 mPa s and an elastic modulus of $E = 1000\,\mathrm{GPa}$, the wall shear stress is $\tau_x = 1000\,\mathrm{Pa}$ and the surface deformation is $D_x = 2.77 \cdot 10^{-17}\,\mathrm{m}$, which is in agreement with the theoretical value of $D_x = 2.8 \cdot 10^{-17}\,\mathrm{m}$. The small discrepancy can be attributed to the computational domain not being infinitely extended and the deformation being restricted at the outer solid boundaries.

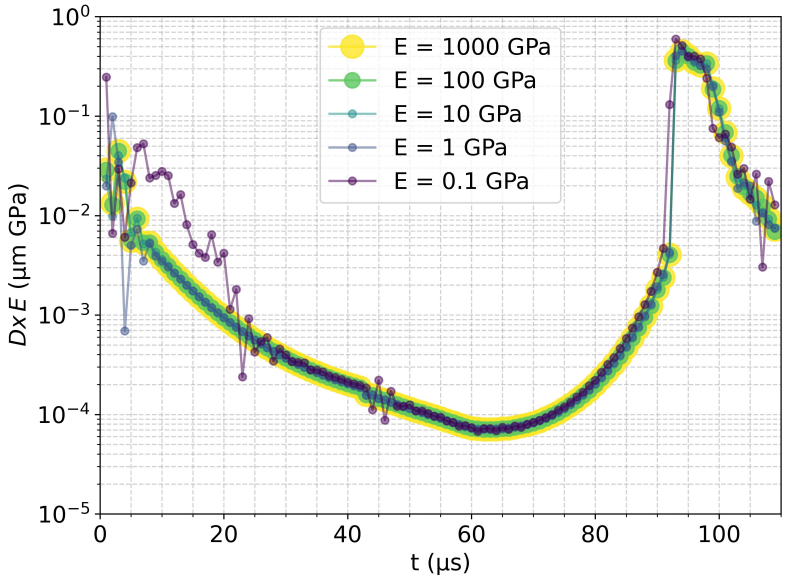

Figure 8.13: Deformation D multiplied by E at $\vec{x} = 0$ for a bubble expanding and collapsing near an elastic layer at different Young's moduli E. $R_{\max} = 535\,\mu\text{m}$, stand-off $d = 500\,\mu\text{m}$, layer thickness $s = 100\,\mu\text{m}$.

8.7.2 Elasticity dependence

Figure 8.13 shows that the deformation over time is approximately proportional to $1/E$ in the range of $1\,\text{GPa} \leq E \leq 1000\,\text{GPa}$. $E = 1\,\text{GPa}$ shows some and $E = 0.1\,\text{GPa}$ shows much stronger oscillations, especially in the early stage (during bubble expansion). But most importantly, the peak after jet creation is very similar across a large range of values of E. Thus the effect of the fluid-structure interface deformation on the bubble dynamics is negligible and simulations with a high elasticity modulus can be used to represent cases with a softer material, for which the deformation found simply needs to be scaled up by a factor of $E_{\text{simulation}}/E_{\text{experiment}}$.

8.7.3 Counter-jet for a bubble near a smaller ring

In the next case, a smaller ring with a radius of 250 µm, about half that of the previous rings, is used. Figure 8.14 (a) (multimedia available online) shows the bubble dynamics for a non-dimensionalised stand-off distance of about $\gamma = 0.9$. Similar to the previous cases in which a larger ring is used, as the bubble expands, part of the bubble moves into the ring structure. During bubble collapse, however, an upwards-directed liquid jet is seen in the frames corresponding to $t = 27$, 50 and 72 µs. It is especially visible at the bubble's maximum size at $t = 50\,\mu\text{s}$ (see figure 8.14, red arrow). This *counter-jet* is very reproducible, but it only occurs for $\gamma \approx 1$, and only for this smaller ring, not for the larger rings. We postulate that the counter-jet is caused by a large stagnation pressure forming in the centre of the ring, which is confined by the elastic ring, the cap wall and the bubble gas. This causes this liquid jet to form and enter the bubble before its collapse. A remnant of this counter-jet is seen in frame $t = 97\,\mu\text{s}$ (figure 8.14) when the bubble has collapsed.

The formation mechanism of this jet is elucidated by the corresponding finite-volume simulation shown in figure 8.14 (b). The simulation reveals that the liquid confined between

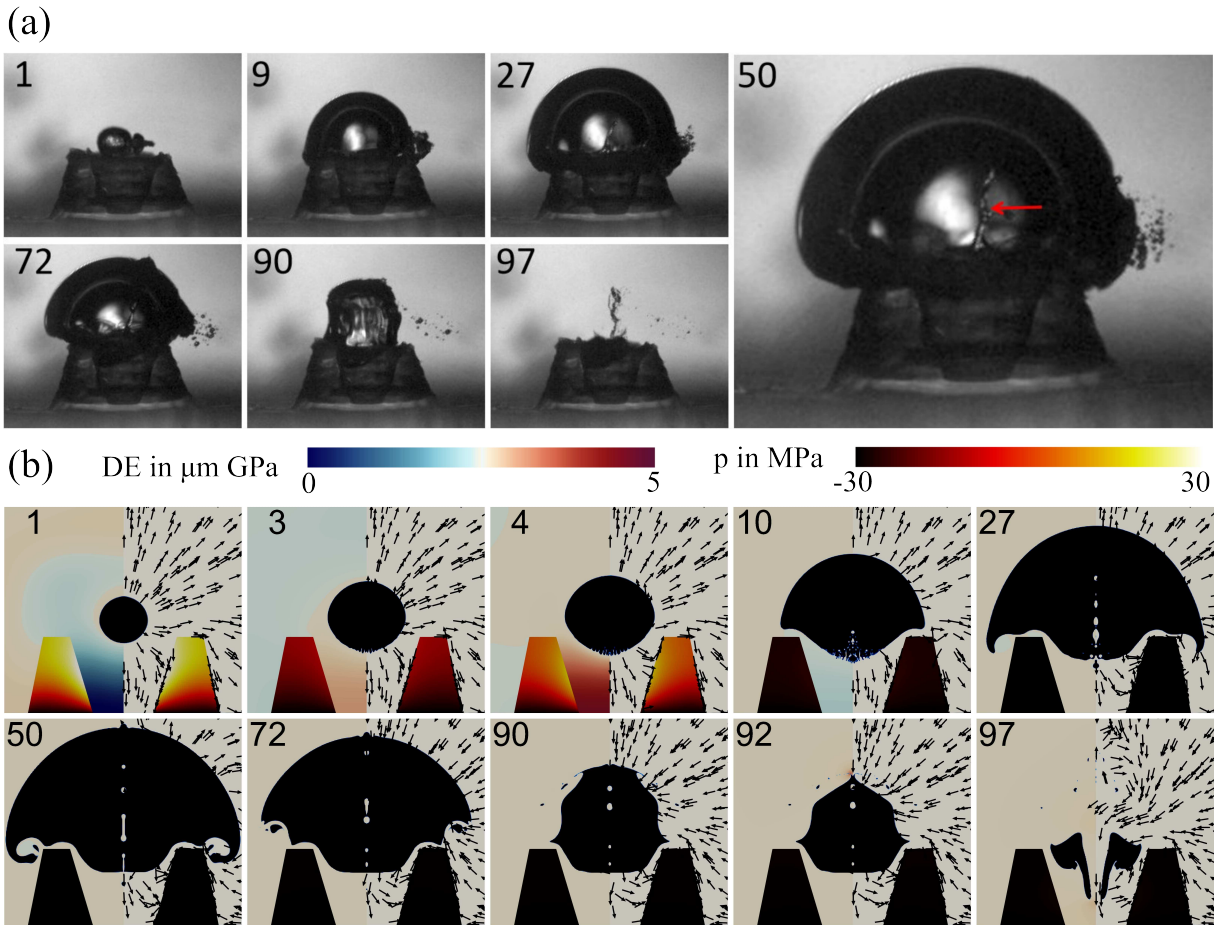

Figure 8.14: (a) Selected frames of a cavitation bubble created near a ring of 250 µm in radius. The framing rate is 1 Mfps. The bubble is created about $d = 475\,\mu m$ from the wall. It reaches its maximum radius of $R_{max} = 551\,\mu m$ at $t = 50\,\mu s$ after its creation. A counter-jet formed inside the bubble is clearly seen (indicated by a red arrow). After this, the bubble collapses with the counter jet piercing through the bubble top. The time in µs is given in each frame. The frame width of the first frame is 1.62 mm. (b) Simulated frames of a bubble near a ring of 160 µm inner radius and 500 µm outer radius and a stand-off distance of $d = 475\,\mu m$. Multiple jets are ejected from the lower bubble wall and coalesce to form the counter-jet (multimedia available online).

the bubble wall, the elastic ring, and the solid substrate prevents a strong dissipation of the shock wave initially emitted by the laser-induced cavitation bubble. This shock wave is thus successively reflected back and forth between the bubble and the solid boundaries, its phase being inverted at every reflection on the free boundary. Note that the phase of the wave flips about two times per microsecond. The resulting alternating high and low pressure in the confined liquid combined with the motion of the bubble wall gives rise to the formation of a Rayleigh-Taylor instability on the lower bubble wall, eventually leading to small liquid jets being ejected into the bubble. This phenomenon has been reported to lead to the break-up of droplets [339, 340]. These jets then coalesce and form a single upwards-directed jet moving through the bubble at a velocity of about 20 m/s. The bubble then collapses, with a kink moving upwards from the outer part of the bubble wrapped over the ring structure and meeting the axis of symmetry, causing the formation of a needle jet [83] with a velocity of 217 m/s.

9 Thermally assisted heterogeneous cavitation through gas supersaturation

This work has been published in [27]:

P. Pfeiffer, J. Eisener, H. Reese, M. Li, X. Ma, C. Sun, and C.-D. Ohl. "Thermally Assisted Heterogeneous Cavitation through Gas Supersaturation". *Physical Review Letters* **128**, 194501 (19 2022)

This work has been continued in [60]:

P. Pfeiffer, M. Shahrooz, M. Tortora, C. M. Casciola, R. Holman, R. Salomir, S. Meloni, and C.-D. Ohl. "Heterogeneous cavitation from atomically smooth liquid–liquid interfaces". *Nature Physics* **18** (12), 1431–1435 (2022)

We demonstrate that besides gaseous pockets also a gas supersaturated spot on a substrate can be a nucleus for cavitation. The supersaturation is achieved by either a formerly dissolved bubble or by heating locally the surface below the boiling temperature. The experiments are conducted in a thin film of water; one side of the water film is in contact with a gold-coated substrate that is heated by a continuous laser through plasmonic heating. For the nucleation of a bubble, the pressure at the heated spot is reduced by a transient rarefaction wave. The experimental findings suggest that the local gas supersaturation is responsible to nucleate cavitation and thus connects the phase transitions of cavitation and boiling. Additionally, the pressure waves in the liquid gap are studied numerically.

9.1 Introduction

The ubiquitous formation of gas bubbles in liquids is still challenging our understanding of the origin of bubble nucleation. The ratio between gas concentration in the liquid and its saturation concentration dictates if bubbles in a liquid grow or shrink by diffusion. Concerning the origin of bubbles, Jones et al. [341] explain the heterogeneous nucleation of bubbles from surfaces at low supersaturation levels of gas with preexisting nucleus (type III nucleation), while in the absence of a nucleus high levels of gas supersaturation are necessary for nucleation (type II nucleation). Supersaturation can be obtained, e. g. through heating the liquid. Gas bubbles may be expanded by a transient reduction of pressure. When the pressure reduction is sufficiently fast that gas does not diffuse into the bubble, a mostly empty cavity is formed that upon pressure recovery will acceleratingly shrink and collapse [20, 342]. In a widely accepted and tested model, preexisting gas nuclei in non-oversaturated liquids require a hydrophobic pore [343–346]. The Laplace pressure then leads to a stable gas pocket even in a gas under-saturated liquid. Yet, once a sufficiently strong tension is applied, the gas pockets explosively expand into cavitation bubbles. In real liquids, surfaces of the container and impurities from contaminant particles can provide these stabilising hydrophobic crevices [347, 348].
In the present Letter, we test experimentally if locally and temporally modulated gas supersaturation is a nucleus for cavitation bubble formation. Typically, transient pressure reduction is obtained with focused acoustic waves. They can easily reach several tens of

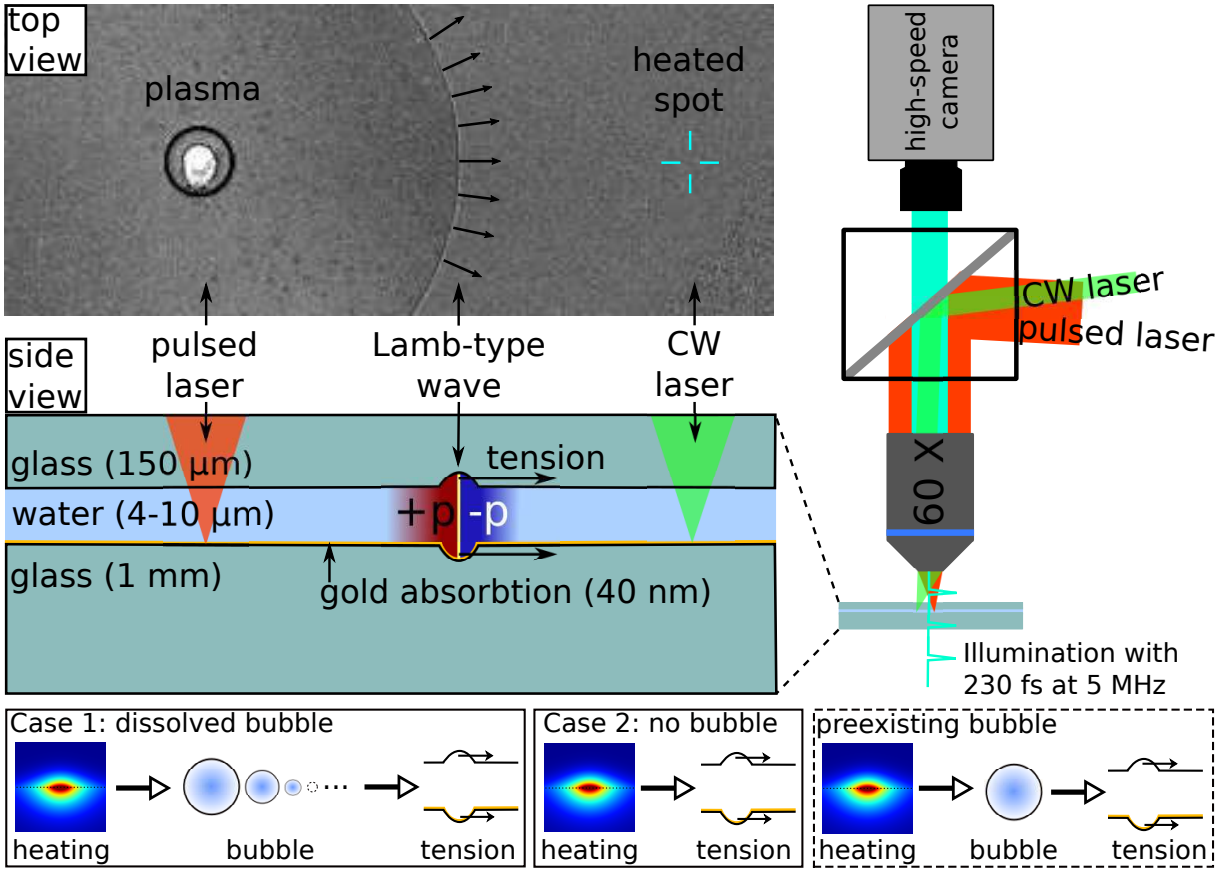

Figure 9.1: Experimental setup for cavitation inception by a focused pulsed laser in a water-filled gap. The latter consists of a gold-coated microscope slide and a cover slip. Between both glass plates, a 4-10 µm thick water layer is sandwiched. The pulsed laser is focused onto the gold layer, creating a plasma and transverse Lamb-type wave. As it pushes the glass plates apart, the pressure in its wake is positive ($+p$) and in its front negative ($-p$), nucleating secondary cavitation bubbles. The visual wave is caused by the second spatial derivative of the pressure gradients. A second laser (CW) used for local heating is focused into the gap at a slightly different position compared to the pulsed laser. The setup allows a simultaneous generation of cavitation bubbles and observation with a high-speed camera. Illumination is provided from the opposite side with a femtosecond laser. Two different cases are studied to act as a cavitation nucleus: 1) a vapour bubble, created by localised boiling with sufficient time to dissolve, and 2) a locally heated spot during the passage of a rarefaction wave. For comparison a preexisting vapour bubble is studied as well [27].

Mega-pascals of negative pressure [57, 349]. Here, we use a rarefaction wave propagating within a liquid sample sandwiched between two glass slides. The wave is a transverse Lamb-type wave (tension or rarefaction wave), which first reduces the pressure in the liquid, thereby nucleating cavitation bubbles while the trailing pressure wave may collapse the bubbles afterwards [7]. The wave is launched from a dielectric breakdown spot created with a focused nanosecond laser pulse. The pressure amplitude in the gap is determined from numerical simulations.

Using sufficiently fast imaging modality we can observe if a nucleus was present by detecting a bubble expanding larger than the optical resolution limit. The geometry and technique offer a view of the details of the nucleation events microscopically and at a very

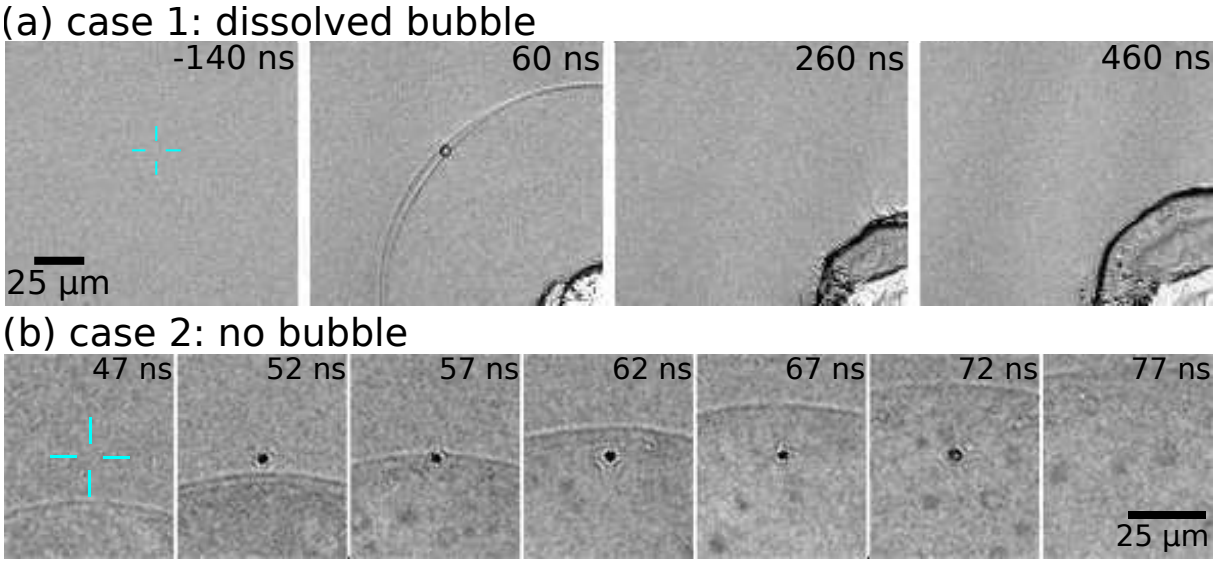

Figure 9.2: Nucleation of a bubble by a rarefaction wave in a $\approx 4\,\mu m$ thick gap. The lower right shows part of the primary cavitation bubble. (a) A vapour bubble is created and has dissolved at $t = -4\,ms$ at the blue cross. Upon the passage of the tension wave, a cavitation bubble is nucleated ($t = 60\,ns$) at the location where the vapour bubble dissolved. $t = 0$ corresponds to the time when the laser pulse reaches the glass slide. (b) A spot is heated (blue cross) below the boiling temperature. The heated spot acts as a cavitation nucleus once the rarefaction wave passes.

high temporal resolution due to the high repeatability of the experiments.
Local supersaturation is achieved as follows: nucleating a vapour bubble through heating and letting it dissolve or heating the surface below the boiling temperature. Both methods are probed with a rarefaction wave (figure 9.1). The case of a preexisting bubble is shown in the supplementary material of [27].

9.2 Experimental setup

Figure 9.1 shows the experimental setup. The liquid gap is formed by placing a droplet of water (10 µl) between a microscope slide (*Paul Marienfeld GmbH & Co. KG*, Germany) and a coverslip (*Menzel Gläser* #1, Germany). The side of the microscope slide facing the water is coated with a 40 nm thick gold layer [27] for laser heating through plasmonic absorbance [350]. The gap is clamped and stabilised against evaporation by adding a water reservoir around the edge of the coverslip. The thickness of the gap is controlled either with a spacer (6 µm thick tin film; Sn98Sb2, *Eppstein FOILS*, Germany) resulting in a gap thickness of 10 µm or in the absence of any spacer, where a film thickness of about 4 µm is achieved. The gap thickness is measured with a confocal fluorescence microscope. Shock and rarefaction waves are created from the focus of a nanosecond Q-switched laser, forming a plasma and a rapidly expanding vapour bubble. The latter emits a shock wave in the liquid, which is *preceded* by a Lamb wave [7]. Transient waves and phase transitions of the liquid are observed via high-speed video recording (HPV-X2, Shimadzu, Kyoto, Japan at 5×10^6 frames/s). A laser line filter (FL514.5-3, Thorlabs) protects the camera from the pulsed laser light but lets the illumination light pass. The focusing of the lasers and the observation is done through the same Olympus LUCPlan FLN 60x/0.7 microscope objective at a spatial resolution of 1.2 µm per pixel. Each frame of the high-

speed camera is exposed with a single light pulse from a femtosecond laser (FemtoLux 3 SH, EKSPLA, Vilnius, Lithuania, pulse duration 213 fs at a maximum repetition rate of 5 MHz, wavelength $\lambda = 515\,\mathrm{nm}$). The short exposure enables us to visualise the waves travelling in the solid and in the liquid without motion blurring.
Localised heating and boiling of the liquid is done by focusing a continuous-wave (CW) laser (frequency-doubled Nd:YAG DPSS laser, $\lambda = 532\,\mathrm{nm}$) for an adjustable time onto the gold layer. The light path of the CW laser is slightly tilted with respect to the pulsed laser, such that both lasers are focused at an adjustable distance from each other.
The output of the CW laser is controlled by a delay generator (Quantum Composers, 9520 series) and measured with a photodiode (APD430A2/M, Thorlabs). We measure about 30 % of the light absorbed in the gold, which corresponds to a power of 25 mW.

9.3 Numerical model

Numerical finite-volume simulations are carried out to understand the pressure modulation in the liquid gap using a modified strongly coupled fluid-structure-interaction solver [27] (base solver `fsiFoam`, see [126]) for the OpenFOAM framework [127]. The modified version we call `CavBubbleFsiFoam` couples a linear elastic solid representing glass (Young's modulus $E = 67\,\mathrm{GPa}$, density $\rho = 2500\,\mathrm{kg\,m^{-3}}$, Poisson's ratio $\nu = 0.21$) to a multi-phase Volume of Fluid (VoF) solver of two compressible, immiscible, isothermal, viscous fluids using a phase fraction approach for interface modelling. The two fluids represent Tait-compressible water and a non-condensible adiabatic gas representing the bubble contents. The axisymmetric simulation sample consists of two glass plates of thicknesses 150 µm and 1 mm, respectively, sandwiching a water layer of 4 µm [27] or 10 µm thickness, modelled as a slice of a cylinder.
A cylindrical gas bubble with the height of the gap and an initial radius of 11 µm (4 µm gap) or 12.5 µm (10 µm gap) is seeded at an initial pressure of 100 MPa. This value was chosen to fit the expansion velocity of the bubble in the simulations to that of the experiments.

9.4 Results

Figure 9.2 depicts two representative examples of the interaction of a rarefaction wave with the heated region. (1) A vapour bubble is formed (blue cross). After stopping the heating, the bubble quickly dissolves and is already optically undetectable after 200 ns [27]. 4 ms later the rarefaction wave passes over the dissolution spot and nucleates a single cavitation bubble at precisely the location where the vapour bubble dissolved (figure 9.2 (a)). (2) The liquid is heated (blue cross in figure 9.2 (b)) but prior to the nucleation of a vapour bubble the rarefaction wave is applied, nucleating a cavitation bubble at the heated spot. Here, bubble nucleation was only observed if the spot is still heated when the rarefaction wave passes. The heating is done for 4 µs, starting 3 µs prior to the high-speed recording and continues for 1 µs (with decreasing power) when the rarefaction wave passes. Immediately *before* the rarefaction wave passes, a cavitation bubble is nucleated at the heated spot (figure 9.2 (b) at $t = 57\,\mathrm{ns}$). For this experiment, stroboscopic illumination at different delays ($\Delta t = 2.5\,\mathrm{ns}$ between runs; every second frame shown) instead of a continuous high-speed recording is conducted. The rarefaction wave (not visible in figure 9.2 (b)) precedes the shock wave, which explains the nucleation of the cavitation bubble ahead of the visible wave, which travels at a speed of $1450 \pm 250\,\mathrm{m/s}$. The lifetime of the cavitation bubbles is approximately $27 \pm 3\,\mathrm{ns}$.

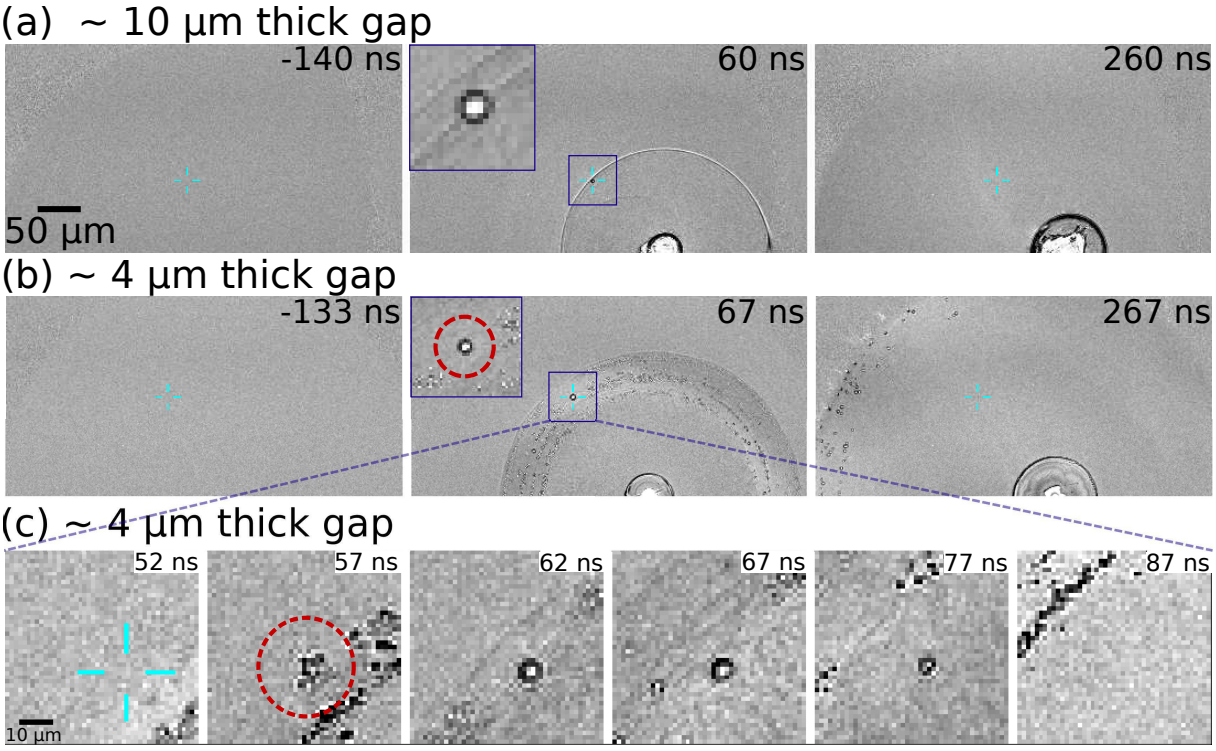

Figure 9.3: Nucleation of a cavitation bubble from a dissolved bubble by a rarefaction wave (a) in a $\sim$ 10 µm gap, (b-c) in a $\sim$ 4 µm gap. A CW laser is focused for 20 - 40 µs at the position with the blue cross. It is switched off 1 ms before the high-speed recording has started. (c) Detail image of (b) with higher temporal resolution. The red circles (diameter: 25 µm) mark the region which is void of random cavitation.

In case (1) a vapour bubble is created and dissolved at least 1 ms *prior* to the passage of the rarefaction wave. A single bubble is nucleated once the rarefaction wave passes in the 10 µm gap (figure 9.3 (a)). Interestingly, when reducing the gap height (figure 9.3 (b)) besides the controlled nucleation of a bubble at the location of dissolution more and seemingly randomly distributed cavitation occurs. These bubbles are considerably smaller than the one nucleated at the position of the blue cross and are located in an annular ring of about 60 µm width. The region around the induced cavitation bubble is void of random cavitation, see inset (red ring) in figure 9.3 (b) at $t = 67$ ns.
The suppression of uncontrolled cavitation from the central induced nucleus is now resolved in time steps of 5 ns (figure 9.3 (c)). At $t = 57$ ns secondary uncontrolled cavitation occurs in the lower right area of the frame which is part of the annular ring shown above. Besides multiple cavitation, bubbles at the dissolution spot appear. At $t = 62$ ns these bubbles coalesce and expand to a considerably larger size than the naturally occurring cavitation bubbles. Interestingly, a region of about 25 µm (red ring) is cleared from any cavitation bubbles. A reason may be the emission of a pressure wave of the explosively expanding cavitation bubbles [351]. Yet, the speed at which this suppression wave travels (2500 m/s) is too fast to travel in the liquid. A possible explanation could be a surface wave on the glass that is radiating into the liquid.
Figure 9.4 (a) shows a numerical snapshot of the 10 µm gap. A Lamb wave is emitted from the main cavity boundary, travelling with a speed of 1200 m/s in the thin and 1400 m/s in the thick gap, respectively. Figure 9.4 (b) shows a zoomed view of (a). The deformation from the initial configuration is multiplied by a factor of 200 to visualise the deformation

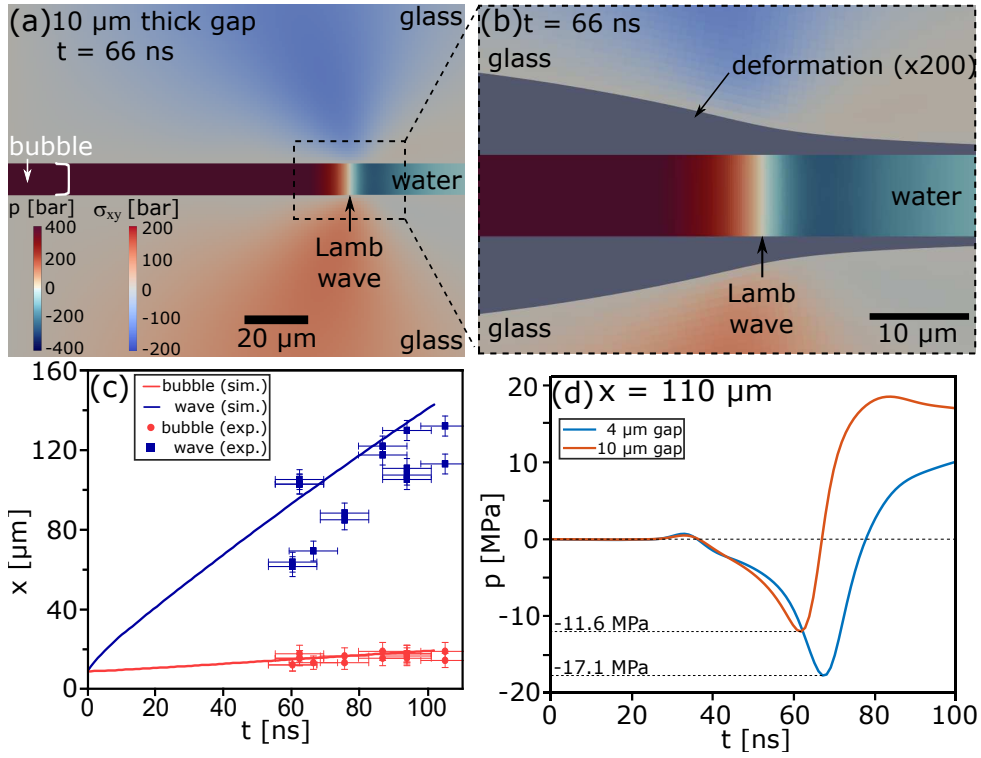

Figure 9.4: Numerical simulations (a) in the 10 µm gap [27]. The bubble boundary is indicated with a white line. σ_{xy} is component of the stress tensor, i. e. the shear stress corresponding to a shear wave with vertical deflection (y-direction) and horizontal propagation direction (x-direction). (b) shows a magnified view where the amplitude of deformation is multiplied by a factor of 200. (c) Position of bubble boundary (radius) and the Lamb wave over time with experimental values. (d) Pressure over time at a distance of 110 µm from the bubble centre. The duration of the tension wave is estimated from the time between minimum and maximum pressure, which are ≈ 41 ns in the thin gap and 29 ns in the thick gap.

of the glass. In (c) the positions of the bubble boundary and the wave is shown (solid lines). Experimental values are added for comparison. The pressure wave at a distance of 110 µm from the bubble centre (as in the experiments) is shown in figure 9.4 (d). In the 4 µm gap the tension in front of the Lamb wave is −17.1 MPa and in the thicker gap −11.6 MPa, followed by a region of high pressure [27].

As random cavitation occurs in the thin gap, the cavitation threshold is reached. The value here although in a different geometry is not far from the value found by Caupin & Herbert [57] of ≈ 25 MPa for water. Yet, we also want to note that higher values were found for shock wave reflections [289]. In contrast, randomly occurring cavitation cannot be observed in the thicker gap, meaning the maximum tension is lower than in the thin gap. Only at the heated spot cavitation occurs, showing that the cavitation threshold has been locally reduced.

9.5 Discussion

A simple 2D axisymmetric simulation of the heat introduced by the CW laser is carried out using a finite element solver for the heat equation in Comsol. A region with a radius of 40 µm and height of 40 µm is simulated in which the upper half contains water and the

lower half is glass. Both materials are separated by a 40 nm thick gold layer (cf. inset in figure 9.5). The plasmonic heating of the gold layer is modelled with a heat source (radius 1 µm) located at the origin. The heat input is time-dependent. We model the measured intensity of the laser by first increasing the power of the heater linearly from zero to $P_{cw} = 25\,\mathrm{mW}$ within 5 µs, then it remains at maximum for 5 µs before it is suddenly switched off. The resulting temperature distribution is shown in figure 9.5.
By neglecting phase changes, the model overestimates the temperature increase considerably once boiling sets in. Yet the gross features fit nicely with the observed phenomena. In particular, we obtain the minimum duration to reach the boiling temperature and how long it takes to cool down back to ambient temperature. After a few microseconds of heating, the boiling point is already exceeded and after switching off the heating, it only takes a few tens of microseconds to distribute the heat. Increasing the size of the heated area [27], heating slows down but the size is only marginally affected. This suggests that after about 1 ms the temperature of the liquid has equilibrated. Heat and gas diffusion are governed by the same diffusion equation, yet the diffusion constant of heat in water is about 100 times higher than that of dissolved gas. This suggests that it is not the higher temperature where the bubble has dissolved but a local gas supersaturation that nucleates the cavitation bubble.

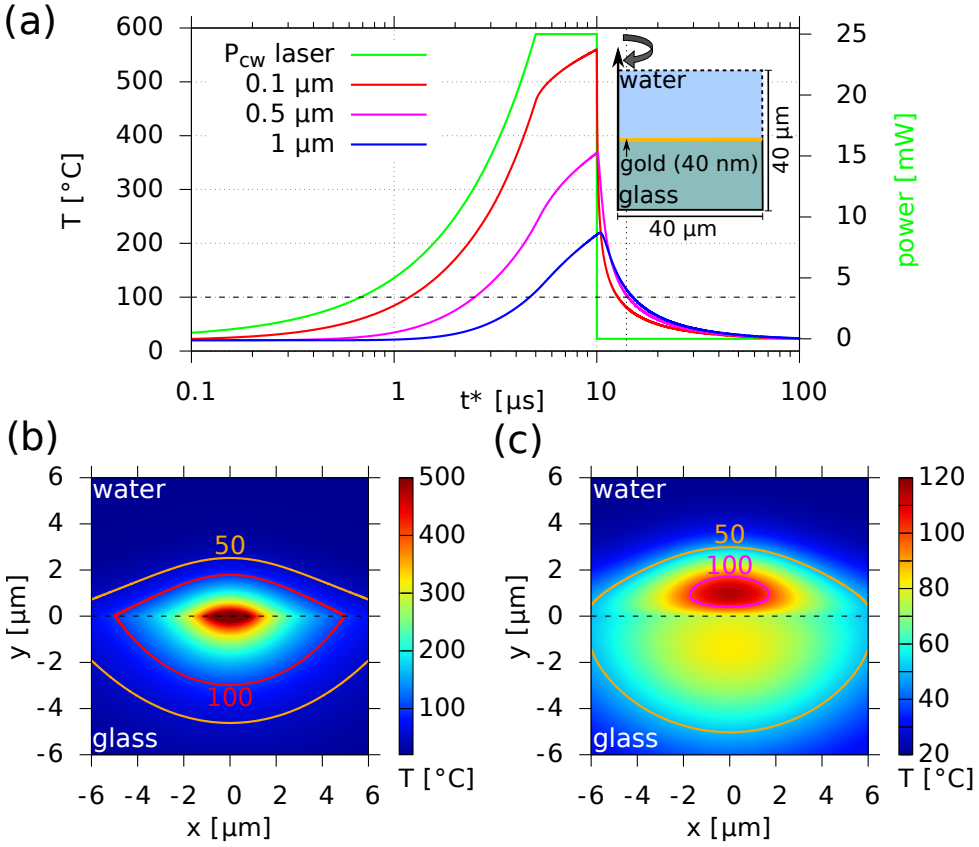

Figure 9.5: (a) Temperature in the water on the axis of rotation above the centre of the heated spot at a height of 0.1 µm (red), 0.5 µm (magenta) and 1 µm (blue) above the gold layer. The green line shows the assumed heating power. The inset represents the simulation setup. (b) Temperature at the end of heating ($t^* = 10\,\mu\mathrm{s}$) and (c) 4 µs after the heating has stopped. The dashed line in (b) and (c) represents the position of the gold layer, water is simulated above and glass below. The orange and red lines represent the temperature isoclines of 50 and 100 °C, respectively.

Initially the bubble generated with the CW laser consists mainly of vapour. The condensation time t_{cond} of this bubble can be calculated as follows [352]:

$$t_{\mathrm{cond}} = \frac{\pi R_0^2}{4\,Ja\,D_l}\ , \tag{9.1}$$

where Ja is the Jakob number, and D_l the liquid thermal diffusivity. For a typical vapour bubble in the experiments, an initial radius of $R_0 = 2\,\mu\mathrm{m}$ is assumed, which gives a Jakob number of 71.4 and D_l is $1.4{\times}10^{-7}\,\mathrm{m}^2/\mathrm{s}$. This results in a condensation time of 300 ns, a value compatible with the observed dissolution times of 200 ns [27]. Yet the bubble may also contain gas as the liquid in the vicinity of the vapour bubble is heated and therefore over-saturated with gas [211]. This may lead to a diffusion of gas into the bubble and the realistic condensation times are longer than the one calculated above. Thus, for a time interval $\geq 1\,\mathrm{ms}$ between vapour bubble condensation and tension wave, it is reasonable to assume that no vapour bubble remains to act as a cavitation nucleus. Consequently, a possible explanation for the bubble nucleation is a local over-saturation of gas in the liquid, which acts as a cavitation nucleus. It has been shown by molecular dynamics simulations that over-saturation of gas in water can reduce the hydrogen bonds between the water molecules [59]. Additionally, the surface tension is reduced by the surface activity of gas molecules, which can lower the threshold of cavitation inception, as well [353].

9.6 Conclusion

We created cavitation nuclei by locally heating a gold substrate and tested their activity by applying a rarefaction wave. Two techniques were demonstrated: First, a boiling vapour bubble was created, which was allowed to dissolve. Yet the location of bubble dissolution remained an active cavitation nucleus for a duration of up to 4 ms. Second, the substrate was heated below the boiling temperature. Again, the heated spot became a cavitation nucleus once the rarefaction wave passed over it. The possibility of a nanobubble formation prior to the phase explosion cannot be entirely ruled out here. It is an interesting line of research for future work. Both techniques may be explained by a local increase in the concentration of dissolved gas molecules. This simple technique facilitates the connection of boiling and cavitation nucleation. It opens the possibility to apply experimental techniques to understand molecular adsorbed gases on surfaces, for example through surface-enhanced Raman [354] or high-resolution atomic force microscopy [355].
We are grateful to A. Dempewolf and O. August for the gold coating and SEM images. We thank A. Eremin for the confocal thickness measurements of the liquid gap. This work was financially supported by the European Social Fund (No. ZS/2019/10/103050) as part of the initiative “Sachsen-Anhalt WISSENSCHAFT Spitzenforschung/Synergien”, and the Deutsche Forschungsgemeinschaft (Programs No. OH 75/3-1, OH 75/4-1 and PF 951/3-1) and the National Natural Science Foundation of China (NSFC, No. 11861131005).

10 Controlled inertial nano-cavitation above 100 MHz

This work has been published in [28]:

U. J. Gutiérrez-Hernández, H. Reese, C.-D. Ohl, and P. A. Quinto-Su. "Controlled inertial nano-cavitation above 100 MHz". *Journal of Fluid Mechanics* **972**, A16 (2023)

The maximum size and lifetime of an acoustically nucleated cavitation bubble is inversely proportional to the driving frequency and has achieved a limit of about 10 MHz. Smaller cavitation bubbles that are critical to microscopic applications require shorter lifetimes which correspond to higher oscillation frequencies. Here we demonstrate that acoustic cavitation in the 100 MHz range and beyond can be achieved through wave propagation in a solid rather than in a liquid. The cavitation bubble is nucleated at a nano-sized fracture on a glass substrate and its expansion is driven by a leaky Rayleigh wave, while the inertial collapse is induced by a trailing shock wave. As both waves travel at different velocities, the time interval between these two events is a function of the distance to the source. In this way, we experimentally demonstrate control of the lifetime of the bubbles in a range between 6 and 80 ns, corresponding to oscillation frequencies between 13 and 166 MHz. Our results agree with finite volume fluid-structure interaction simulations.

10.1 Introduction

Acoustic cavitation refers to bubble generation in a liquid using acoustic waves. These bubbles have been used in various fields, e.g. medical research for drug delivery [356], cell and cell organelle surgery [357, 358], semiconductor cleaning [81, 359], and nanochemistry [360]. In the case of microscopic and submicroscopic applications, controlling the size of the bubbles is important [361, 362]. In general, the maximum size of a cavitation bubble is proportional to its lifetime (or oscillation time) [2], so that smaller bubbles require shorter oscillation times and thus higher driving frequencies.

In particular, inertial acoustic cavitation (i.e. an explosive bubble expansion due to the tension exceeding the cavitation nucleation threshold followed by the bubble's collapse) at high frequencies is difficult to achieve for two reasons. Firstly, since the time available for a bubble to expand to a significant size is inversely proportional to the driving frequency, the driving forces expanding the bubble must be larger for higher frequencies [363]. Secondly, the acoustic waves become strongly attenuated at high frequencies [364], thereby making it difficult to reach the amplitude required to drive the bubble expansion. This is why controlled acoustic cavitation has not exceeded MHz frequencies [365], with bubble lifetimes of a few microseconds, while bubbles nucleated in a substrate have longer lifetimes exceeding tens of microseconds [346, 366–368].

Cavitation has also been produced via surface acoustic waves (SAWs, [7]), also known as Rayleigh waves, which propagate along the surface of an elastic material [47]. Their amplitude decays exponentially with the distance from the surface (depth) and most of the energy carried by the wave is concentrated in just one wavelength below the surface. So far, the highest frequency attained for cavitation bubbles is around 30-40 MHz (lifetimes of 27 ± 3 ns, [27]); it required a combination of localised heating and a Lamb wave propagating in a very thin liquid gap. In the work of Rosselló and Ohl [54, 55], the on-demand production of bulk nanobubbles through the passage of an intense laser pulse

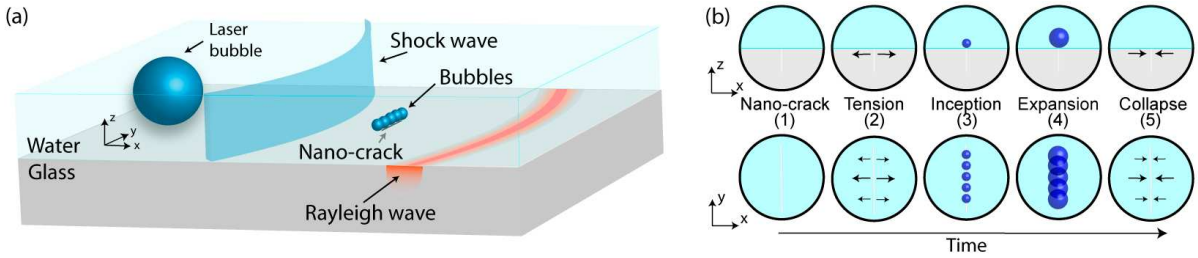

Figure 10.1: Inertial cavitation process. (a) A schematic of the sample is shown. The Rayleigh and shock waves are drawn. The Rayleigh wave travels faster in the elastic solid than the shock wave in the liquid and thus arrives first at the position of the nano-crack. (b) Close-up at the nano-crack position: (1) unperturbed nano-crack, (2) tension induced by the Rayleigh wave, (3) cavitation inception due to the tensile pressure, (4) bubble expansion due to ongoing tensile pressure, (5) bubble collapse induced by the arrival of the shock wave.

in water was demonstrated. Transient bubbles appear within the region exposed to light once a rarefaction wave passes through, attaining temporal and spatial control of the bulk nanobubble nucleation.
In this work we have achieved controlled inertial nanobubble cavitation with continuously adjustable lifetimes in the range between 6 ns and 80 ns (oscillation frequencies in the range between 13 MHz and 166 MHz), nucleated at a nano-sized fracture on a glass substrate. Control is attained with a transient rarefaction wave, induced by the passage of a leaky Rayleigh wave on the glass surface. The tensile pressure explosively expands the nanobubbles which are later collapsed by the trailing shock wave in the liquid. Both pressure excitations are generated by a single laser pulse
The process of the nanobubble nucleation and collapse is illustrated in figure 10.1 (a), where a laser pulse is focused in the vicinity of the nano-crack generating a cavitation bubble and a Rayleigh wave in the substrate followed by a slower shock wave in the liquid. Figure 10.1 (b) depicts the sequence of events (1-5) close to the nucleation site (1). The second frame represents the time of arrival of the Rayleigh wave on the solid surface, leading to a tension state (2) in the liquid (positive stress in the glass that "opens" the crack). The induced tension is strong enough to nucleate nanobubbles at the nano-crack, the uneven structure of which acts as a cavitation nucleation site (3). The enduring negative pressure state in the liquid, induced by the passage of the SAW, keeps expanding the nucleated nanobubbles (4) until the shock wave induces the collapse of the bubbles (5). The experiments are complemented with Finite Volume (FV) simulations, showing an excellent agreement.

10.2 Methods

10.2.1 Experimental setup

The experimental setup is based on our previous work [369] where a laser pulse (6 ns, $\lambda = 532$ nm, SOLO PIV NewWave Research) is focused at the bottom of a thin liquid gap. The liquid (Epson printer ink, T6643 Magenta) is bounded by two borosilicate glass substrates, a microscope slide of 1 mm thickness and a coverslip at the bottom of 160 µm thickness. The mechanical properties of the substrates are provided by the manufacturer (Fisherbrand, `https://www.fishersci.es`): elastic modulus $E = 63$ GPa,

Poisson ratio $\nu = 0.2$ and density $\rho = 2230\,\mathrm{kg/m^3}$. The height of the liquid is determined by spacers ($\approx 80\,\mu\mathrm{m}$). The sample is mounted on a motorised x-y stage. The laser beam is focused on a single spot above the lower substrate with a radius of $12\,\mu\mathrm{m}$ and an energy of $(200 \pm 4)\,\mu\mathrm{J}$. The linear absorption of the focused laser pulse causes the liquid to vaporise and shock waves are emitted due to the sudden local increase of pressure [370]. In the work of Quinto-Su et al. [121] it has been shown that, for laser-induced microbubbles similar to those presented here, the rise in temperature is rather small with only a few Kelvin and quickly decays.
Since the laser is focused near the lower substrate, the sudden expansion of the bubble transfers energy to it almost instantaneously. This induces elastic deformation, transmitted as a bulk wave and a surface acoustic wave (SAW), also known as a Rayleigh wave. In its propagation over the solid surface, the SAW also causes pressure changes in the liquid, inducing tensile pressures near the solid surface, i.e., the passage of the Rayleigh wave on the fluid-structure interface induces a rarefaction in the former.
We use a nano-crack in the glass at a lateral distance d from the position at which the laser bubble is generated, oriented orthogonally to the distance vector $\vec{d}$. The nano-crack is generated by convergent shock waves [29, 30], and has a width of less than 100 nm. The distance d between the laser bubble and the nano-crack is controlled using the motorised stage.
The events are imaged with a CCD camera (Sensicam QE, PCO) and illuminated stroboscopically by a 6 ns laser pulse ($\lambda = 690\,\mathrm{nm}$, Orion, NewWave Research) at different delay times. Streak images are taken with a streak camera (SC-10, Optronis) and a 1 µs laser pulse ($\lambda = 637\,\mathrm{nm}$, L637G1 Thorlabs). Both red light sources are transmitted through a dichroic mirror of an inverted microscope.

10.2.2 Numerical model

Finite volume (FV) simulations are carried out using the FluidStructureInteraction (FSI) package [126] of the CFD software OpenFOAM [127]. The numerical solver `CavBubbleFsiFoam` is employed, which can model two compressible, immiscible fluids coupled with a deformable linear elastic solid. It has been used in previous works to model Rayleigh and shock waves in a thin liquid domain between two glass plates, obtaining good agreement with experimental observations [27, 29]. The borosilicate glass with Young's modulus $E = 63\,\mathrm{GPa}$, density $\rho = 2230\,\mathrm{kg/m^3}$, and Poisson's ratio $\nu = 0.2$ is modelled as a linear elastic solid, and solved for by the solver `unsTotalLagrangianSolid`. The linear elastic equation of motion is

$$\frac{\partial^2 \rho \vec{D}}{\partial t^2} - \nabla \cdot \left[G\,\nabla \vec{D} + G\,(\nabla \vec{D})^{\mathrm{T}} + \lambda\,\mathrm{tr}(\nabla \vec{D})\,\mathbb{1} \right] = 0\ , \tag{10.1}$$

where $\vec{D}$ is the deformation, given in the solid's internal coordinates, $\mathbb{1}$ the unity matrix and

$$\lambda = \frac{\nu}{1-2\nu}\,\frac{1}{1+\nu}\,E,\ G = \frac{1}{2}\,\frac{1}{1+\nu}\,E \tag{10.2}$$

the Lamé parameters.
The Newtonian fluids are modelled by the law of conservation of momentum,

$$\rho\,\frac{D\vec{u}}{Dt} = \rho\,\vec{f} - \nabla p + \mu\,(\Delta \vec{u} + \frac{1}{3}\,\nabla(\nabla \cdot \vec{u}))\ , \tag{10.3}$$

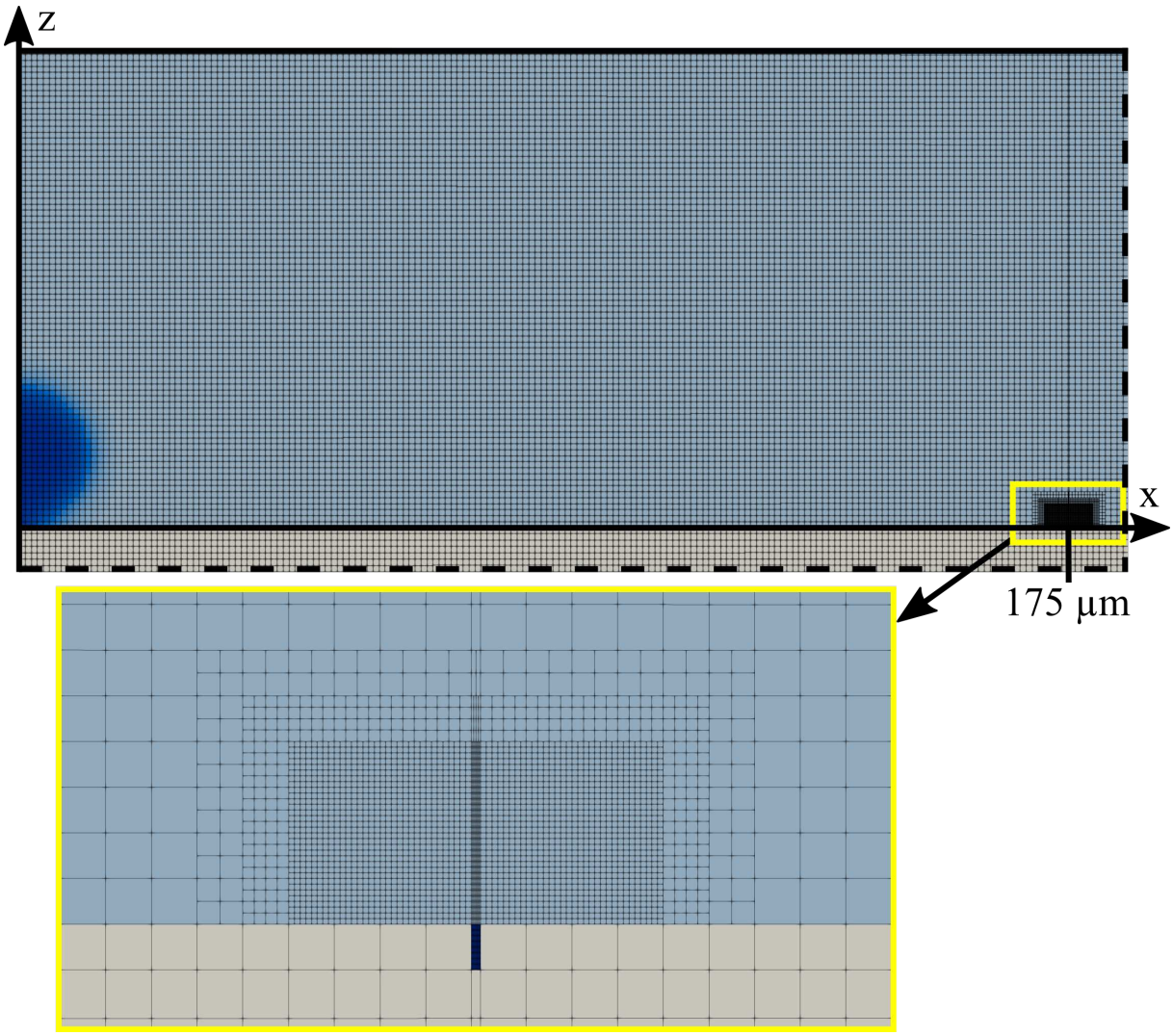

Figure 10.2: Computational mesh used for one of the axisymmetric FV simulations. The liquid is shown in light blue, the gas in dark blue, and the solid in light grey. A cylindrical fluid domain with a height of 80 µm and a radius of 1 mm sits on top of a solid domain with a height of 160 µm (not fully shown), which in turn sits on a gas-filled domain with a height of 80 µm (not shown). A cylindrical ring-shaped gas-filled defect is defined at $x = 175\,\mu\text{m}$ with a depth of 1 µm and width of 200 nm. The mesh is refined near the defect. A bubble is initiated on the axis of symmetry (z) with a radius of 12 µm.

as well as the continuity equation,

$$\frac{\partial \rho}{\partial t} + \nabla \cdot (\rho\, \vec{u}) = 0 \ . \tag{10.4}$$

Gravitational effects are neglected.
The fluids represent a bubble filled with a non-condensable gas in water satisfying the Tait equation of state,

$$p = (p_0 + B) \left(\frac{\rho}{\rho_0}\right)^{\gamma} - B \ , \tag{10.5}$$

with the values $p_0 = 101325\,\text{Pa}$, $\rho_0 = 998.2061\,\text{kg/m}^3$, $\gamma = 7.15$, $B = 303.6\,\text{MPa}$ for water and $p_0 = 10320\,\text{Pa}$, $\rho_0 = 0.12\,\text{kg/m}^3$, $\gamma = 1.33$, $B = 0$ for the gas (which turns the equation of state into the ideal adiabatic gas equation). p_0, ρ_0 is a known pair of values

for the pressure and the density of a fluid. For water, γ and B are empirical parameters describing its low compressibility. For an ideal adiabatic gas with $B = 0$, γ becomes the adiabatic exponent. All changes of state are thus treated as adiabatic, and heat transfer is neglected.
The interface is captured using a phase fraction field α with interface compression to counteract numerical diffusion. Phase transitions and mass transfer between the fluid components are not modelled. Due to numerical inaccuracies, the mass of each fluid component is not exactly conserved, which is why in every time step the bubble mass is corrected to stay constant over time.
The fluid-structure interaction is modelled using two-way coupling, where the elastic solid is acted upon by the fluids via surface forces $\vec{F}\, S_i = \overset{\leftrightarrow}{\sigma} \cdot \vec{n}_i$ that are given by the stress tensor in the fluid, $\overset{\leftrightarrow}{\sigma} = -p\, \mathbb{1} + \mu \left[\nabla \circ \vec{u} + (\nabla \circ \vec{u})^{\mathrm{T}}\right]$. The solid acts on the fluid-structure interface by imposing its deformation $\vec{D}$ and velocity $\dot{\vec{D}}$ onto the boundary of the fluid domain. The solid and fluid equations of motion are solved alternatingly, either until a residual value characterising the discrepancy between the solid and fluid domains falls below a tolerance value, or for at most 100 iterations.
The numerical schemes used, such as the first-order upwind scheme, are at least of the order of accuracy 1.
The simulated geometry, as in the experiment, describes a thin sheet of water (80 µm height) between a rigid upper boundary and an elastic glass sheet (160 µm height). A defect in the shape of a cylindrical ring with a height of 1 µm and a radial thickness of 200 nm is inserted at the surface of the glass sheet. Since phase changes and thus cavitation processes are not modelled, it is filled with a gas that represents either trapped gas or a cavity created by the opening of the nano-crack in the experiment and acts as a cavitation bubble nucleus. As in the experiment, a gas-filled domain of 80 µm height is added on the opposite side of the glass plate, allowing it to move away from or towards the water-filled domain. The outer boundaries as well as the bottom of the gas-filled domain below the solid plate are modelled as open, wave transmissive boundaries. Because the geometry is chosen to be axisymmetric, it becomes an effectively two-dimensional problem and only a thin wedge of a cylinder with a radius of 1 mm has to be modelled.
On the axis of symmetry of the domain a spherical bubble with a radius of 12 µm and a pressure of 1.69 GPa is initiated. The initial condition for the pressure is consistent with previous works [29, 369, 371]. It is based on the assumption that the energy deposition by the laser pulse happens on a much smaller time scale than the expansion of the created bubble, and it is thus assumed that its initial density is equal to the density of the surrounding liquid. The initial radius is chosen such that the shock wave position over time closely matches that observed in the experiments. Since the shock wave velocity depends on its amplitude (the wave is faster in a denser medium), this is an indirect validation of the pressure amplitudes obtained in the simulations. Its vertical position is chosen to be equal to its radius such that the lower end of the bubble touches the glass plate. To smoothen the surface of the bubble seed it is smeared by applying the equation $\alpha' - 4 \cdot 10^{-11} \Delta\alpha' = \alpha$ to the phase fraction field α. The geometry is discretised into cells with a width of 10 µm in the gaseous domain below the glass plate and 1 µm in most of the solid and the liquid domains. Near the crack, it is refined to a width of 125 nm. Since the crack is thinner than the 1 µm mesh before refinement, the cells above and below it are 5 times thinner than the surrounding cells.

10.2.3 Modified Rayleigh-Plesset equation

To describe the dynamics of a spherical bubble including the compressibility of the liquid, we consider the modified Rayleigh-Plesset equation [62, 372],

$$\rho\left(R\,\ddot{R}+\frac{3}{2}\,\dot{R}^2\right)=p_{\mathrm{g}}(t)-p_0-P(t)-4\,\mu\,\frac{\dot{R}}{R}-\frac{2S}{R}+\frac{R}{c}\,\frac{\mathrm{d}p_{\mathrm{g}}}{\mathrm{d}t}\ , \tag{10.6}$$

where $R = R(t)$ is the radius of the bubble, $\dot{R} = \frac{dR}{dt}$, p_{g} is the gas pressure inside the bubble, p_0 (101325 MPa) is the pressure in the liquid far away from the bubble, $S = 72.8\,\mathrm{mN/m}$ is the liquid surface tension, $\mu = 1\,\mathrm{mPa\,s}$ is the dynamic viscosity of water, $P(t)$ is the driving pressure at the location of the bubble, and $c = 1500\,\mathrm{m/s}$ is the speed of sound in the liquid. Considering the process as adiabatic, we use the Van-der-Waals equation of state to describe the gas pressure inside the bubble,

$$p_{\mathrm{g}}(t)=\left(P_0+\frac{2S}{R_i}\right)\left(\frac{R_i^3-h^3}{R^3(t)-h^3}\right)^{\gamma}\ , \tag{10.7}$$

where R_{i} is the initial radius, $\gamma = 4/3$ is the adiabatic index of water vapour and $h = R_{\mathrm{i}}/8.86$ is the characteristic Van-der-Waals hard-core radius of the gas inside the bubble [373]. The external pressure $P(t)$ is obtained from the FV simulation without a defect in the glass and without any bubble besides the wave source in the centre of the domain. We extract the pressure from the fluid just above the solid as a function of time $P(t)$ at different distances d. Then, $P(t)$ for a given d is used in the modified Rayleigh-Plesset equation as the external driving pressure. The initial conditions are $\dot{R}(0) = 0$, and $R(0) = R_{\mathrm{i}}$. Although this modified Rayleigh-Plesset model models a spherical bubble and does not consider complex interactions such as bubble-bubble interaction or proximity to solid surfaces, it is sufficient to understand and explain the cavitation process in this work.

10.3 Results and discussion

10.3.1 Bubble formation and collapse

The left side of figure 10.3 shows a direct comparison between the strobe photographs taken in the experiment and simulation frames with a nano-crack placed at a lateral distance $d = 175\,\mu\mathrm{m}$ from the center of the laser bubble.
The top half of each frame shows strobe photographs (x-y plane) of the events produced by the generation of the laser bubble at the sample. The strobe photographs are cropped (x-y plane, $x > 0$) to have a better comparison with the simulation. The thick dark semicircle on the left in the strobe photographs is the expanding laser-induced cavitation bubble, while the thinner dark curve propagating to the right is the shock wave. The bottom half of each frame shows FV simulation results of the same time as the photograph in a cross-section of the x-z plane, where z is the axis of symmetry and is located on the left border of the frame. The glass boundary is initially at $z = 0$, at half the height of the frame. The upper half of the simulated frame contains the liquid, where we observe the initial bubble and the shock wave ($\approx 1800\,\mathrm{m/s}$). In the solid at the bottom half of the simulated frame, we can observe surface waves. In the first frame (50 ns), only the bulk wave ($\approx 5100\,\mathrm{m/s}$, not shown) has reached the fracture position. In the frame at 65 ns the Rayleigh wave ($\approx 3150\,\mathrm{m/s}$) has passed (on the solid surface) and the tension region trailing behind it (in the liquid) causes the formation of nano-sized cavitation bubbles

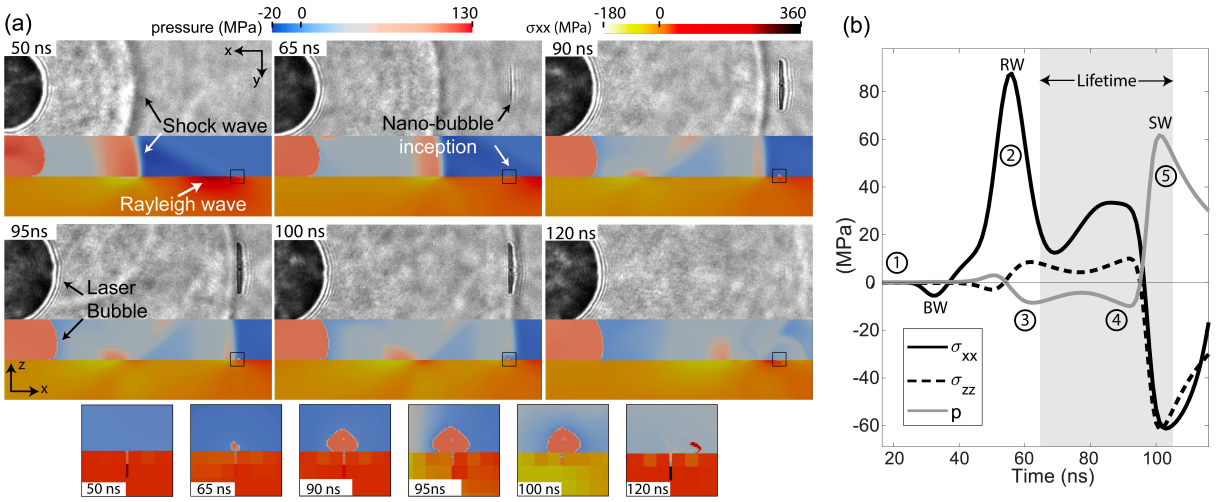

Figure 10.3: (a) Wave dynamics and nanobubble nucleation. The first row shows strobe photographs (x-y plane), while the second shows frames extracted from a FV simulation (x-z plane, z is the axis of symmetry). The size of each strobe photograph is 200 µm × 70 µm. The simulation frames show the fluid in the top and the glass in the bottom half. The size of each simulation frame is 200 µm × 60 µm. The zoomed square frames (7 µm × 7 µm) on the bottom show a section of each frame centred at the fracture position in the simulation. Colour bars represent pressure (left) and σ_{xx} (right), both in MPa. In the fluid, negative values indicate tensile pressure. In the solid, the positive and negative values of the σ_{xx} stress component mean tensile and compressive stress, respectively.
(b) Simulated σ_{xx} and σ_{zz} stress components and pressure at the fluid-structure interface ($z = 0$) for a fracture at $d = 175$ µm. The arrival of the different waves is labelled at their respective peaks: Bulk wave (BW), Rayleigh wave (RW) and shock wave (SW). The shaded region represents the time period in which the bubbles are visualised (strobe experiment). The stages drawn in figure 10.1 are indicated here as circled numbers.

at the nano-crack. In the simulation, the tension causes the gas in the surface defect to begin to expand. In the next frames, the nanobubbles continue to expand until the shock wave passes through the position and collapses the bubbles, as we can see in the frames for 100 ns and 120 ns. We find an excellent agreement between the FV simulations and the experiments. On the bottom, we show close-ups of the black squares drawn in the simulation frames. There we can see in detail the behaviour of the gas in the cavity that emulates the nano-crack in the experiment. The Rayleigh waves that propagate on the solid are not visible in the experiment, likely because the deformation and density variations are so small that the change in the index of refraction is too small to overcome the noise of the image.

The calculated σ_{xx} (continuous black line) and σ_{zz} (dotted black line) stress components in the solid surface, and pressure in the liquid (continuous grey line) are extracted from the FV simulation and plotted in figure 10.3 (b) for a case in which the laser pulse is focused at a distance of $d = 175$ µm from the nano-crack. There, the steps (1)-(5) of figure 10.1 are labelled. In the fluid, negative values indicate tensile pressure. In the solid, positive values of the stress components means tensile stress, while negative values indicate compressive stress.

Initially, the nanocrack position ($d = 175$ µm) is undisturbed (1). Then, the bulk wave (BW) in the solid, which is the fastest wave excitation, arrives at 33 ns and is detected

as a small negative (compressive) peak of the σ_{xx} stress component (−5.44 MPa). It is followed by the Rayleigh wave (RW) on the surface of the solid which creates a large positive (tensile) peak of the σ_{xx} stress component, starting at 37 ns and reaching its maximum (87.5 MPa) at 56 ns (2). Meanwhile, the pressure in the liquid and the σ_{zz} stress component in the solid surface mirror each other. The σ_{zz} stress component has a small negative (compressive) peak (−3 MPa) at 50 ns followed by a positive (tensile) stress region which remains a few tens of nanoseconds, ending at 95 ns. On the other hand, in the liquid, the pressure has a small positive (compressive) peak (3 MPa), followed by a negative (tensile) pressure region. Two local minima are observed: −8.5 MPa at 62 ns (3) and −9.94 MPa at 92 ns. The pressure remains negative until the arrival of the shock wave (SW) in the liquid (5). This wave induces a pressure peak in the liquid of 61.6 MPa at 101 ns. In the solid surface, the shock wave induces strong compressive stresses, both in the σ_{xx} and σ_{zz} stress components, −61.24 MPa at 103 ns and −61 MPa at 101 ns, respectively. The videos in the supplementary material, extracted from the simulations, show the expansion and collapse of the nanobubbles at the fracture position for distances d = 30, 40, 50, 75, 125, 175 and 235 µm. A simulation is performed for each position of the fracture.

10.3.2 Control of the bubble lifetime

The time delay between the arrival of the Rayleigh wave and the shock wave is approximately proportional to their travelling time and the difference between their velocities. Hence, by adjusting the lateral distance d between the laser focus and the nano-crack, we can control the lifetime of the nanobubbles. To observe these extremely fast cavitation events in a single shot we use a streak camera, which sweeps a one-dimensional image along a slit. The streak camera outputs a two-dimensional image (see figure 10.4 (a)), where the vertical dimension is the slit and the horizontal dimension is time. The shock wave is seen as a shadow that propagates at a speed of 1800 m/s (SW, slope of the dashed red line). The laser-induced cavitation bubble is centred on the horizontal dashed white line and appears dark. The dashed blue line is the predicted position of the Rayleigh wave (RW, 3150 m/s) which is not captured. The bulk wave (BW) travelling at a speed of 5100 m/s is also not captured. In comparison with the wave propagation dynamics, the expansion of the laser-induced bubble is relatively slow (200 m/s). A few nanoseconds after the Rayleigh wave reaches the position of the nano-crack (d = 175 µm), one or multiple bubbles are nucleated and expand for several tens of nanoseconds until the shock wave arrives, which induces their collapse. The lifetime of the nanobubbles is the horizontal dimension denoted as LF. The section of the lifetime after the shock wave has passed is denoted as the collapse time t_{col}.
Figure 10.4 (b) shows the superposition of 21 streak images, each with a different distance d between the nano-crack and the laser-induced bubble. We observe that the lifetime increases monotonically with d. In particular, we highlight 4 distances d_1 = 75 µm, d_2 = 125 µm, d_3 = 225 µm and d_4 = 235 µm, at which we also performed experiments with stroboscopic illumination in order to image the nanobubbles in the x-y plane. Selected frames at different time delays are shown in figure 10.4 (c).
In figure 10.5, the measured lifetime is plotted as a function of the lateral distance d between the laser focus and the nano-crack. The black square symbols are the measurements from the streak camera for 21 distances. The error bars represent the standard deviation over 40 repetitions. The streak images are analysed considering the light intensity at each position in order to differentiate the bubble from the background.

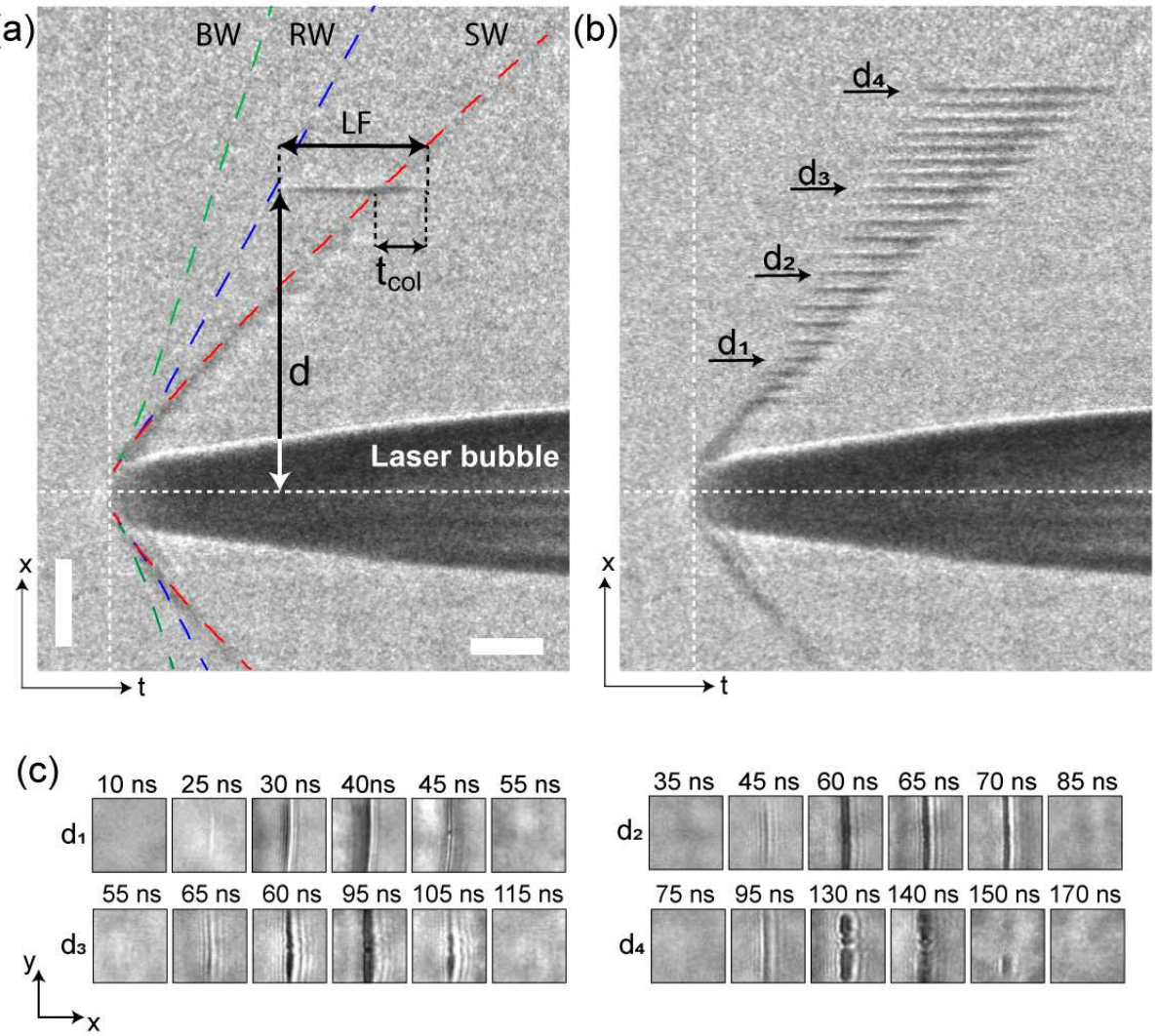

Figure 10.4: Control of the bubble lifetime. (a) Streak image for $d = 175\,\mu m$. The vertical scale bar height (spatial) is $50\,\mu m$, and the horizontal scale bar width (time) is 25 ns. The red, blue and green lines represent the shock, Rayleigh and bulk waves extracted from the simulations, respectively. (b) Superposition of the streak images for different positions d. (c) Strobe images of the nano-crack and cavitation bubbles for four distances: $d_1 = 75\,\mu m$, $d_2 = 125\,\mu m$, $d_3 = 175\,\mu m$ and $d_4 = 235\,\mu m$. The size of each strobe photograph is $30\,\mu m \times 30\,\mu m$ (x-y plane)

The largest distance at which we observed a bubble is $d = 235\,\mu m$, with a lifetime of (71 ± 6) ns. A decrease in the lifetime is observed as d gets smaller. The smallest distance at which a bubble is observed is $d = 50\,\mu m$. For this distance, we measured a lifetime of (9 ± 3) ns. A further decrease of d is expected to result in even smaller lifetimes, but because of the large values of the stress components, a modification in the fracture on the glass surface was observed, so the conditions were modified in each shot.
To get a better understanding of the nanobubble dynamics, we use the modified Rayleigh-Plesset equation [62, 372] that describes the bubble dynamics $R(t)$ and considers the effects of the compressibility of the liquid (equation (10.6)).
The external pressure $P(t)$ is obtained from the FV simulation without a defect in the glass. In this way, we extract the pressure in the liquid just above the solid surface as

a function of time $P(t)$ at different distances d. The equation is solved with R_i in the range of 10-1000 nm. In order to make an estimation of a realistic initial bubble radius R_i, we consider the spatial resolution which yields 600 nm/px. Hence, we do not resolve the initial stages of bubble expansion, but we can still detect the change in the transmitted light intensity as the bubbles expand.

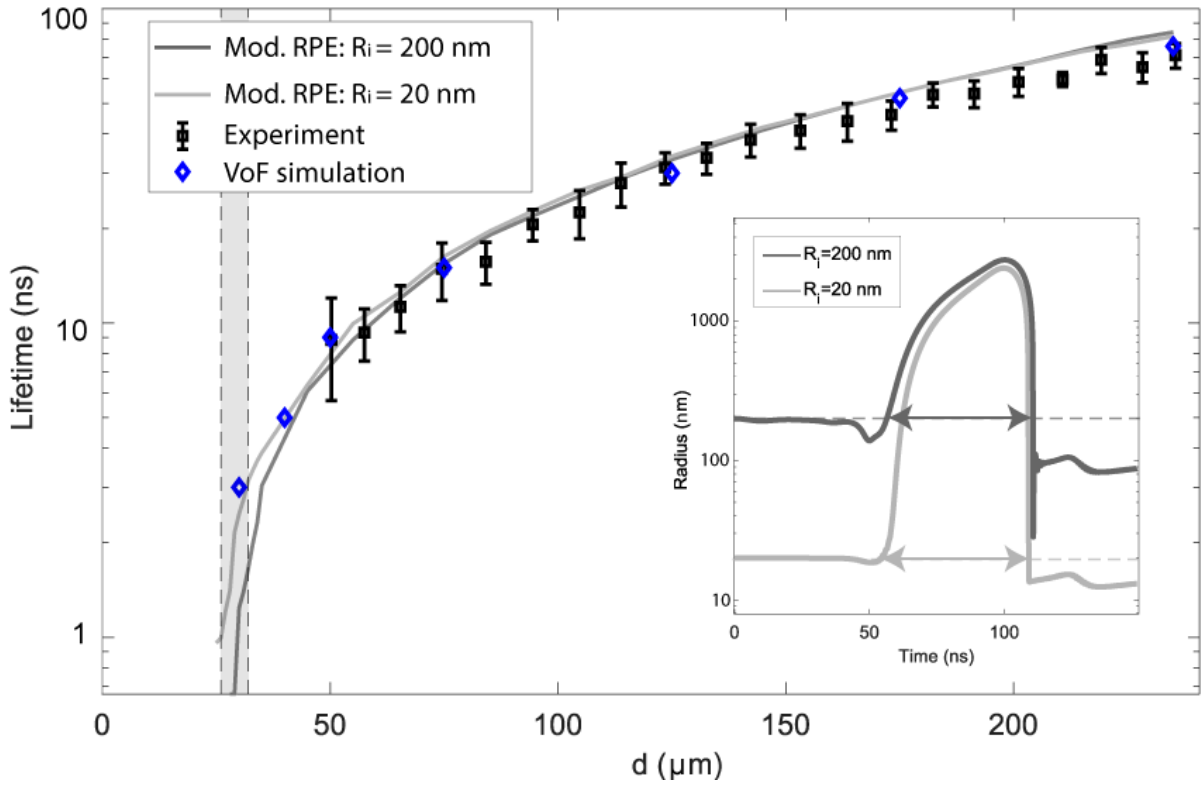

Figure 10.5: Bubble lifetime as a function of d. The black symbols represent the lifetime measured from the streak experiments for 21 distances. The error bars represent the standard deviation over 40 repetitions. The blue symbols indicate the lifetime extracted from the FV simulations. The continuous lines represent the lifetime extracted from the solution of the modified Rayleigh-Plesset equation using two different initial radii: 200 nm (grey) and 20 nm (light grey). The vertical dotted line at 26 µm indicates the smallest distance d at which there is no bubble expansion in the modified Rayleigh-Plesset equation, while the dotted vertical line at 32 µm indicates the smallest distance d at which the bubble surpasses 10 times its initial radius. Inset: Rayleigh-Plesset equation solution. Radius as a function of time for $R_i = 20$ nm and $R_i = 200$ nm (shown as horizontal dotted lines) at $d = 175$ µm. The arrows denote the bubble's lifetime. The external pressure as a function of time is extracted from the FV simulation (figure 10.3 (b))

.

Since the initial bubble is invisible, we can assume that $R_i < 300$ nm. Furthermore, we find that a bubble with $R_i = 10$ nm ceases to expand for larger distances ($d > 175$ µm), since there the magnitude of the negative pressure does not reach Blake's threshold. This is explained in detail in the section 10.3.2. Hence, we consider R_i in the range between 20 and 200 nm. In this range, the maximum bubble radius and bubble lifetime are fairly insensitive to R_i.

The results for the calculated lifetimes as a function of d are plotted in figure 10.5 as continuous lines. The inset is a plot of the nanobubble dynamics $R(t)$ for $R_i = 20$ nm

(light gray) and $R_\mathrm{i} = 200\,\mathrm{nm}$ (grey) at $d = 175\,\mu\mathrm{m}$. For each case, the arrow denotes the bubble's lifetime. Since the bubble first experiences a small compression due to the moderate over-pressure in the liquid, the measurement starts once the bubble exceeds its initial size, and ends once it is again smaller than the initial radius. Figure 10.5 also shows two vertical lines. The line at 26 µm indicates the smallest distance at which there is no bubble expansion, while the line at 32 µm indicates the smallest distance at which the bubble with $R_\mathrm{i} = 20\,\mathrm{nm}$ surpasses 10 times its initial radius.
The lifetimes extracted from the FV simulation are plotted as blue diamonds, which show a similar trend as the measurements, including the absence of bubbles for $d \leq 26\,\mu\mathrm{m}$. At those distances, the pressure in the liquid does not reach negative values due to the lack of separation between the Rayleigh wave and the shock wave. Hence, for such a small d the nanobubbles do not expand regardless of their initial size. For $d = 30\,\mu\mathrm{m}$, the lifetime obtained from the simulation is only 3 ns.
The results obtained from the experimental observations, the FV simulations and the modified Rayleigh-Plesset equation are in excellent agreement for smaller d, with the modified Rayleigh-Plesset equation slightly overestimating the lifetimes for larger d.

Initial radius

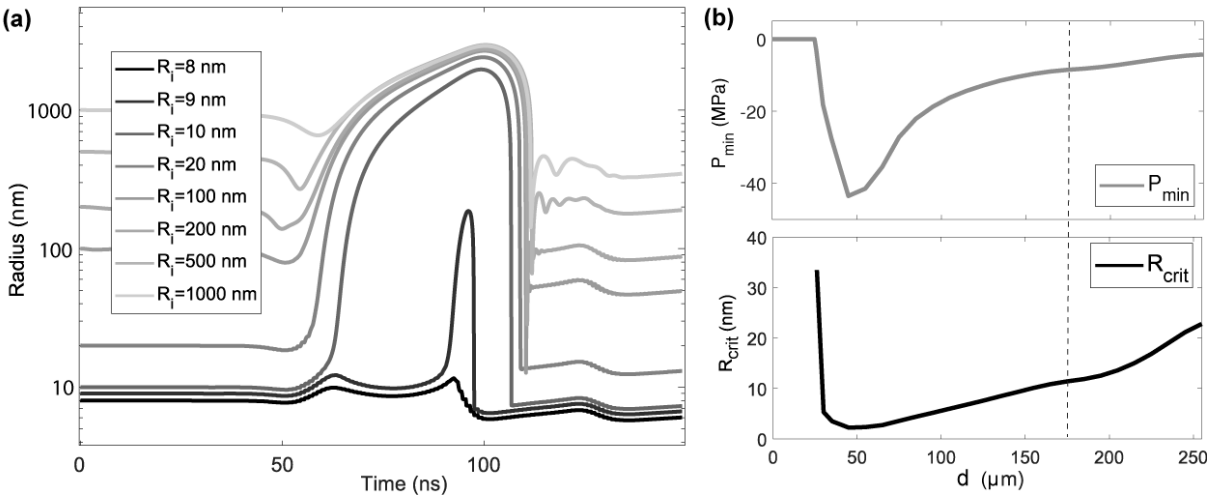

Figure 10.6: Solutions of the modified Rayleigh-Plesset equation with different initial radii R_i. (a) The external pressure used is for a bubble placed at the distance $d = 175\,\mu\mathrm{m}$ from the origin. $R_\mathrm{i} = 8\,\mathrm{nm}$ is the first radius at which a strong bubble expansion is seen ($R_\mathrm{max} = 0.17\,\mu\mathrm{m}$). We observe an approach to a maximum radius ($R_\mathrm{max} \approx 3\,\mu\mathrm{m}$) for bigger R_i. (b) Above, the extracted minimum pressure P_min as a function of the distance from the origin d is plotted. We observe the first negative pressure at $d = 26\,\mu\mathrm{m}$, an absolute minimum at 46 µm, and an approach to zero as d gets bigger. Below, the graph shows the critical radius (R_C) obtained with equation (10.8), with the P_min values from the upper graph. The dotted line indicates $d = 175\,\mu\mathrm{m}$, where R_C is close to 10 nm for a pressure of $-8.5\,\mathrm{MPa}$.

The radius evolution predicted by the modified Rayleigh-Plesset equation (10.6) for $d = 175\,\mu m$ and several initial radii R_i is plotted in logarithmic scale figure 10.6 (a). The driving pressure used is shown in figure 10.3 (b). For $R_i = 8\,nm$ we observe a significant expansion of the bubble at about $t = 90\,ns$. Nevertheless, the maximum radius reached is below 200 nm. For smaller initial radii R_i, the expansion is even smaller. For R_i in the range from 10 nm and 1 µm the dynamics, lifetimes and maximum radii are similar. The expansion starts at $\approx 57\,ns$ and the maximum radius is attained at $\approx 100\,ns$. Hence, the experimentally observable dynamics are only weakly sensitive to the initial condition of the simulated bubble. For $R_i = 10\,nm$ the maximum radius is 2.14 µm at 99 ns, i.e. an expansion of 214 times its initial size. For $R_i = 200\,nm$ the maximum radius is 2.74 µm, at 100 ns, i.e. ∼14 times larger. This expansion factor becomes smaller for larger initial radii. The maximum bubble expansion R_{max} seemingly approaches an upper limit of around 3 µm. For $R_i > 200\,nm$ we observe weak volume oscillations after the collapse.

Blake's limit

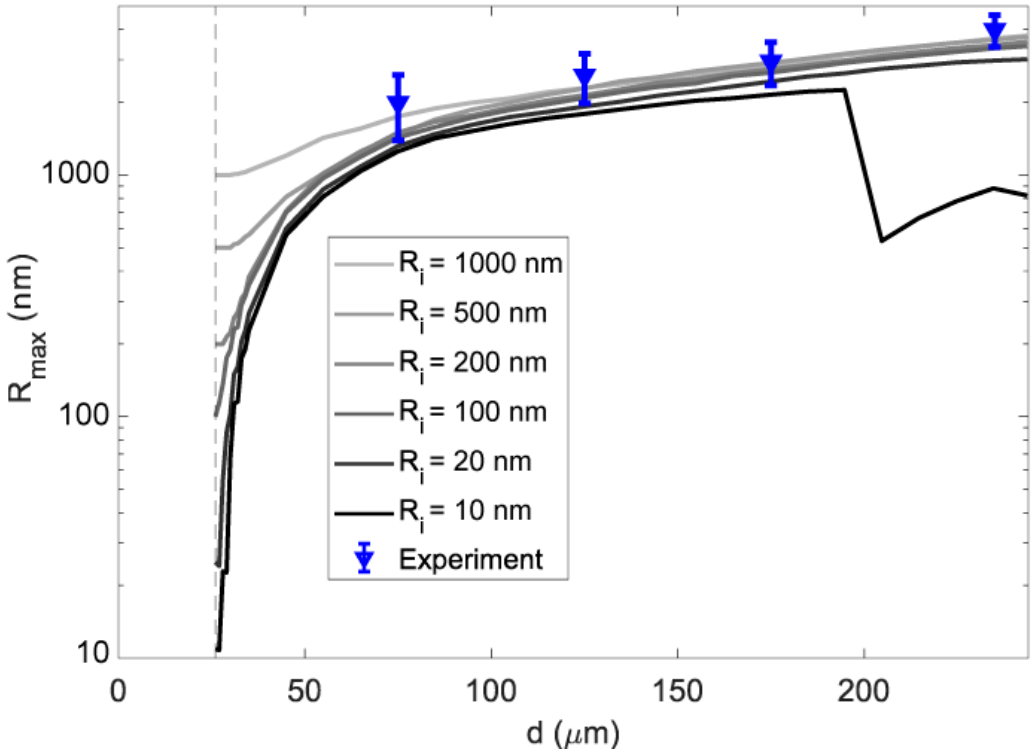

Figure 10.7: Maximum radius as a function of the distance d. The solid lines are the maximum radius plotted at each position, obtained from the solutions of the modified Rayleigh-Plesset equation. Each curve with different initial conditions for R_i. The vertical dotted line at 26 µm indicates the smallest distance at which we observe bubble expansion, independently of the initial radius. At $d = 25\,\mu m$ no negative pressure occurs. The blue symbols represent the maximum radius measured from the strobe experiments for the distances $d = 75$, 125, 225 and 235 µm

If a bubble's surface tension force exceeds the external tension acting at its surface plus its internal gas pressure, it does not expand. The critical bubble size R_C below which the bubble does not expand is given by Blake's limit [34],

$$P_{min} = p_v - \frac{4S}{3R_C} , \tag{10.8}$$

where P_{min} is the smallest external pressure (strongest tension) and p_v the vapour pressure. The upper graph in figure 10.6 (b) shows the minimum pressure extracted from the FV simulation without a defect as a function of the distance d from the wave source. The bottom graph shows the critical radius R_C obtained with equation (10.8) using the values for P_{min} from the upper graph. We observe the first negative pressure at $d = 26\,\mu m$, with a corresponding critical radius of about $R_C = 34\,nm$. The strongest tension ($P_{min} = -43\,MPa$) is found at $d = 46\,\mu m$. Here, the critical radius is only $R_C = 3\,nm$. As is expected, after the absolute minimum, the tension decays and the critical radius increases with increasing d. The dotted line indicates the distance $d = 175\,\mu m$ used for figure 10.6, where $R_C = 12\,nm$ for a pressure of $P_{min} = -8.5\,MPa$. This threshold agrees with the limit of $R_i = 10\,nm$ obtained from the modified Rayleigh-Plesset equation. The last distance for which bubbles are observed is $d_4 = 235\,\mu m$, where the maximum tensile pressure is $-5.12\,MPa$ and the corresponding critical radius has a value of 19 nm. It is important to point out that the impurities in the liquid sample could cause the cavitation threshold to be different from that of pure water.

Figure 10.7 shows the maximum bubble radius as a function of the distance d obtained from the solution of the modified Rayleigh-Plesset equation, with different initial radii R_i. For $R_i = 10\,nm$ at $d = 195\,\mu m$, the maximum expansion R_{max} is significantly smaller compared to that for larger R_i. This is explained by Blake's limit. The minimum pressure at this distance is $-7.74\,MPa$ and the critical radius is 12.5 nm. Although an expansion is observed, it does not exceed 600 nm. The vertical dotted line at 26 µm indicates the distance at which no tensile pressure occurs.

10.4 Conclusion

We demonstrate a novel approach to nucleate cavitation bubbles on a surface at a precise location on previously deposited nanometer-sized inhomogeneities. The expansion is driven by a leaky Rayleigh wave that propagates on the surface of the glass, while the inertial collapse is induced by a trailing shock wave that propagates in the liquid. Both waves are generated by a single laser pulse. We show experimentally that the bubble lifetimes can be controlled by varying the distance of wave propagation. For the largest distance studied, the measured lifetime is (71 ± 6) ns, while for the smallest distance, the measured lifetime is (9 ± 3) ns.
We find a good agreement between the experimental results and those obtained from the finite volume simulations and the modified Rayleigh-Plesset equation. Although the latter is a rather simple model valid only for a single spherical bubble, in which neither bubble-bubble interaction nor its interaction with a nearby solid wall is considered, it shows an excellent agreement with the experimental and finite volume simulation results in terms of the bubble lifetimes and allows us to make a complete description of the expansion and collapse of the bubbles at various distances d from the wave source.
This new regime of ultra-high frequency inertial cavitation scales the well-known energy-focusing capability of cavitation bubbles from the micrometre world to the nanoworld, still maintaining perfect and repeatable control over their dynamics in time and space.
In future works, by varying the geometry, we could explore even shorter bubble lifetimes. In a previous study, using a ring geometry for the laser-induced bubble and the emitted waves [29], we show a time delay of only 7 ns between the convergence of a Rayleigh wave on the surface and a shock wave in the liquid. Therefore, we expect to study bubbles with lifetimes below 10 ns. The present work opens up novel perspectives in frameworks such as the detection of nano-fractures in surfaces using the expansion of nano-cavitation.

Acknowledgements

We thank Cristian Mojica-Casique for technical support and José Rangel for machining optomechanical components.

Author contributions

U. J. G.-H. and H.R. contributed equally to this work.

Funding

This work is partially funded by DGAPA UNAM PAPIIT grant IN107222; CTIC-LANMAC; CONACYT LN-299057; and the DFG (German Research Association) under contracts OH 75/4-1 and OH 75/3-1.

11 Bullseye focusing of cylindrical waves at a liquid-solid interface

This work has been published in [29]:

U. J. Gutiérrez-Hernández, H. Reese, C.-D. Ohl, and P. A. Quinto-Su. "Bullseye focusing of cylindrical waves at a liquid–solid interface". *Physics of Fluids* **34** (11), 112013 (2022). ISSN: 1070-6631

Two pairs of converging and superimposing shock and Rayleigh waves are generated on a glass substrate by focusing laser pulses on two concentric rings in a bullseye configuration (67 µm and 96 µm radii). We study experimentally the threshold for substrate damage as a function of the number of repetitions and the delay (0-20 ns). The bullseye focusing experiments are compared to a single focusing ring. Additionally, fluid-structure interaction simulations using a volume of fluid framework are utilised to estimate the stresses. The lowest number of repetitions to attain surface damage is found for constructive superposition of the Rayleigh waves, i.e., here for a delay of 10 ns. The observed damage is consistent with the simulations where the largest positive stresses ($\sim$ 5.6 GPa) are achieved for bullseye focusing with $\Delta t = 10$ ns followed by $\Delta t = 20$ ns which corresponds to simultaneous shock wave focusing. In all these cases, the positive stresses are followed (a few nanoseconds later) by negative stresses that can reach ~ -6.4 GPa.

11.1 Introduction

Inertial confinement fusion is a prominent example where convergent shock waves cause extreme states of matter [17, 374, 375]. The shock waves may be launched by a laser-generated plasma from an absorbing spherical shell [376]. The group of K. Nelson [377] demonstrated that a tabletop version of shock wave focusing is able to reach pressures of up to 30 GPa near the focus point. There, a cylindrical shock wave in water at a glass-water interface was driven by laser-induced vaporisation of the liquid along an annular ring. After focusing, the outgoing wave creates a large reduction of pressure that is sufficient to nucleate cavitation bubbles at the focal region [61]. This strong loading of the substrate from gigapascals of positive pressure to many megapascals of negative pressure causes material fatigue. The strength of the initial shock waves was enhanced by replacing the initially used carbon nanoparticles in the liquid that act as a linear absorber with a thin layer of gold as a plasmonic absorber [371]. As a result, not only longitudinal shock waves in the liquid but also radially converging surface waves are launched into the substrate. In absence of a liquid film, [378] obtained that the axial displacement of the substrate at the point of focus reaches up to one micrometre within less than 5 ns. Simulations reveal that at a threshold of tensile stresses of around 6 GPa cracks are formed in their particular glass substrate. These extreme conditions can be utilised to explore the response of matter to these high pressures, e.g. the transformation of pyrolytic graphite [379] or the pressure threshold response of plastic explosives [380].
Using the same ring excitation geometry, Klokov et al. [381] studied experimentally the propagation of converging SAW on a silicon surface with (001) and (111) orientations. They found that the acoustic energy can be concentrated into a circle with dimensions $\sim$ 5-7 µm. In another study [382], a non-destructive method for characterisation of alu-

minium grain size was developed using the convergent waves of the ring-shaped geometry. Other techniques have been achieved for focusing acoustic waves, e.g., through an optical approach, high-amplitude focused ultrasound has been achieved: a light-absorbing coating is formed on concave lenses and used as an opto-acoustic source [383]. It also has been shown that the waveform and the focus of acoustic waves can be arbitrarily modified through 3D printing [384]. Recently, focused Rayleigh waves generated with an electromagnetic transducer were used for characterisation of surface defects [385]. Zhao et al. report focusing of Rayleigh waves using gradient-index phononic crystals using a non-contact technique.

Glass is one of the most common materials, because of the wide range of applications. Nevertheless, its dynamic properties are not fully understood at the nano-scale. During the last decade, researchers elucidated important results about the physical properties of silicate glasses [387–390]. Particularly, it is important to understand the dynamics and the induced phenomena by shock waves in glassy materials. Xie et al. [389] investigated the structural change and permanent densification of silica glass under shock compression using atomistic simulations. Zhang et al. [391] utilised an electric discharge to excite surface waves and show that damage on the fluid-glass interface may originate from flaws, which are then grown through Rayleigh waves. Here, a single point of excitation, also called a monopole source, was used. Amplification using monopole sources can be obtained through time-delay focusing. The basic idea stemmed from a Fresnel lens and was implemented with two sets of successively launched pairs of shock waves as demonstrated by [369].

Here we extend that idea, replacing the two pairs of point sources with two concentric ring excitations to superposition the longitudinal waves in the liquid with the surface waves on the solid to amplify stresses in the solid substrate. Therefore, we investigate the damage to the substrate as a function of the delay between their launch and compare the effect of these double excitations with that of the individual sources.

11.2 Experimental setup

The experimental setup is derived from our previous work for transient focusing of excitation pairs [369]. However, this time the two laser pulses are shaped into concentric rings with a spatial light modulator (SLM, Hamamatsu, X10468-01).

Figure 11.1 (a) depicts a cross-section (x-z plane) of the thin liquid sample that is bounded by two glass substrates. The top is a microscope slide (1 mm thick) and the bottom substrate is a thin cover slip (160 µm thick). Both substrates are made of borosilicate with density $\rho = 2230\,\mathrm{kg/m^3}$, Poisson ratio $\nu = 0.2$ and elastic modulus $E = 63\,\mathrm{GPa}$ [392]. The height of the liquid sample is approximately 80 µm and it is determined by spacers.

The independent beams (Nd:YAG, SOLO PIV 6 ns, $\lambda = 532\,\mathrm{nm}$) are focused at the bottom of the container and are absorbed by the liquid (Epson printer ink, T6643 Magenta, viscosity and density are similar to water). The absorption of the focused laser pulses leads to stress confinement [370, 393]. This generates cavitation bubbles with the shape of the laser pulses and shock waves are emitted because of the sudden local rise of pressure [369]. The shock wave hits the solid and transfers energy to it in the form of deformation, which then becomes a bulk wave (BW) and a surface acoustic wave (SAW), or Rayleigh wave (RW), in the solid [391]. Both the BW and RW, also induce pressure changes in the liquid.

The two laser pulses are shaped into concentric rings with an axicon phase (corresponding

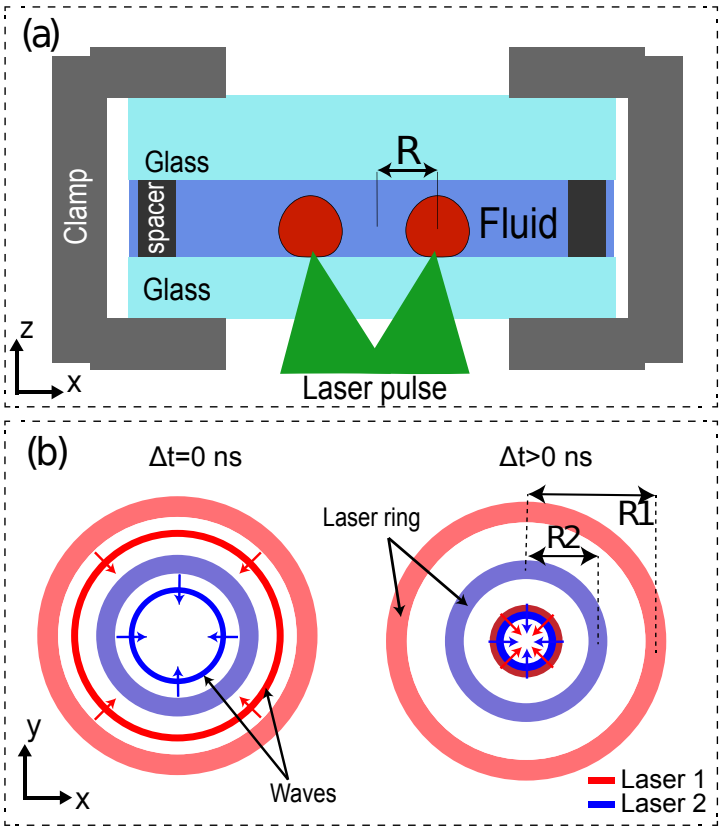

Figure 11.1: (a) cross-section (x-z plane) of a single ring emitter. Detail of laser pulse focusing on the liquid bounded between a microscope slide and a thin cover slip. (b) Examples of (left) the two emitters launched at the same time ($\Delta t = 0$), and (right) $\Delta t > 0$ ns resulting in simultaneous wave focusing at the centre.

to a conical lens) and with the radii $R_1 = 96\,\mu$m and $R_2 = 67\,\mu$m. The outer ring is fired at $t = 0$ and the inner ring at time $t = \Delta t \geq 0$.

Figure 11.1 (b) shows the emission from the excitations represented by the thin lines (blue for inner and red for outer), while the position of the laser beams is represented by thicker shaded lines. An example for simultaneous ($\Delta t = 0$) arrival of the laser pulses is on the left, while the right depicts a case with $\Delta t > 0$ where the emitted waves are about to converge simultaneously at the centre. In the drawing, the emitted waves can represent either shock waves in the liquid or Rayleigh waves in the solid.

The energy per ring is set to $(360 \pm 7)\,\mu$J. Since the two independent laser pulses have differences in their transverse profiles, with the width of the inner ring $\sim 12\,\mu$m and that of the outer $\sim 8\,\mu$m, they have a similar fluence ($\sim 7\,\mathrm{J/cm^2}$).

The dynamics of the events are captured stroboscopically using a third Nd:YAG laser, (Orion, New Wave, 6 ns, 532 nm converted to 690 nm with a dye cell) and imaged with a CCD (Sensicam QE). The red probe light is transmitted through the microscope condenser to illuminate the sample, and Schlieren photography is used to image the shock waves. The Rayleigh waves are not visible, likely because the deformation and change in density are so small that the created variation in brightness via a change in the index of refraction is smaller than the noise of the image. Thus the presented information on the Rayleigh wave propagation has been obtained through the simulations alone.

All instruments are synchronised with a programmable delay generator (Berkeley Nucleonics 575-8C).

11.3 Numerical model

The FluidStructureInteraction (FSI) package [126] of the CFD software OpenFOAM [127] provides the finite volume solver `fsiFoam`, which strongly couples an elastic solid and an incompressible viscous fluid. It was modified to model a laser-generated cavitation bubble expanding close to a linear elastic boundary. We call the new solver `CavBubbleFsiFoam`. It has been used to accurately model the propagation of Rayleigh waves caused by a cavitation bubble in a thin liquid-filled gap between two glass plates, showing good agreement with the experiments [27]. Similar solvers in OpenFOAM have been used to model an expanding and collapsing cavitation bubble in an infinitely extended liquid and have been verified against experiments [115] and against other bubble models like the Rayleigh collapse and the Rayleigh-Plesset equation [117]. They have further been used to model an oscillating bubble near a rigid wall [78, 119], near a rigid perforated plate [22], between two rigid walls [394] and near a free boundary [24]. For each of these works the numerical results show good agreement with experiments. The acoustic pressure radiated by such a bubble has been verified by Gonzalez-Avila et al. [265] who uses a similar volume of fluid approach. In this work, the solver is additionally validated by a close match of the shock wave propagation with the experimental observation.

11.3.1 Solid Solver

The solid is modelled as a linear elastic material representing borosilicate glass with Young's modulus $E = 63\,\mathrm{GPa}$, density $\rho = 2230\,\mathrm{kg/m^3}$, and Poisson's ratio $\nu = 0.2$. The solver `unsTotalLagrangianSolid` solves the equation of motion for a linear elastic solid,

$$\frac{\partial^2 \rho \vec{D}}{\partial t^2} - \nabla \cdot \left[G \nabla \vec{D} + G(\nabla \vec{D})^{\mathrm{T}} + \lambda \,\mathrm{tr}(\nabla \vec{D})\, \mathbb{1} \right] = 0 \;, \tag{11.1}$$

with the deformation field $\vec{D}$, the unity matrix $\mathbb{1}$ and the Lamé parameters

$$\lambda = \frac{\nu}{1-2\nu}\,\frac{1}{1+\nu}\,E,\;\; G = \frac{1}{2}\,\frac{1}{1+\nu}\,E \;. \tag{11.2}$$

All coordinates, at which values for deformations and stresses of the solid are given, correspond to the internal coordinates of the deformed solid.

11.3.2 Fluid Solver

Since the base fluid solver `icoFluid` is not suited to model an expanding bubble, a new fluid solver we call `CavBubbleFluid` was made to suit our purposes. It uses code from the solver `compressibleInterFoam` which can model two compressible, viscous, non-isothermal, immiscible fluids. It uses a phase fraction field α to model the fluid-fluid interface (for more details see [115]). The fluids of interest are water and a non-condensable ideal gas describing the bubble contents. As thermal processes exceed the scope of this study, the temperature equation is omitted and all changes of state are treated as adiabatic, using the assumption that the presented dynamics are faster than any significant heat exchanges. Due to numerical errors, the phase fraction can fall slightly below $\alpha = 1$ in the bulk of the liquid. A correction is applied which replaces the cell values of $\alpha > 0.99$ with $\alpha = 1$ and of $\alpha < 0.01$ with $\alpha = 0$, thus removing the wrongly created gas from the liquid bulk. The governing equations for the fluids are the law of conservation

	τ (N/m)	μ (mPa s)	p_0 (Pa)	ρ_0 (kg/m^3)	γ	B (MPa)
liquid	0.07	1	101325	998.2061	7.15	303.6
gas		0.013	10320	1.33	0.12	0

Table 11.1: Simulation fluid parameters, including surface tension τ, dynamic viscosity μ and parameters of the Tait equation of state .

of momentum of Newtonian fluids,

$$\rho \frac{D\vec{u}}{Dt} = -\nabla p + \mu \left(\Delta \vec{u} + \frac{1}{3} \nabla(\nabla \cdot \vec{u})\right) , \tag{11.3}$$

and the continuity equation,

$$\frac{\partial \rho}{\partial t} + \nabla \cdot (\rho \, \vec{u}) = 0 , \tag{11.4}$$

with the velocity $\vec{u}$, density ρ, and pressure fields p as well as the dynamic viscosity μ. The compressible behaviour of the fluids is modelled via the Tait equation of state,

$$p = (p_0 + B) \left(\frac{\rho}{\rho_0}\right)^{\gamma} - B . \tag{11.5}$$

The surface tension τ, the dynamic viscosities μ and the coefficients of the Tait equation of state p_0, ρ_0, γ, B are given in table 11.1. With $B = 0$, the gas is modelled as an ideal adiabatic gas where γ is the adiabatic exponent. For water, equation (11.5) shows the relationship between its density and pressure without a temperature dependence.
Since the fluid-structure interface moves, the fluid mesh must be deformed to conform to the boundary conditions. The dynamic mesh motion is done by solving a Laplace equation for the mesh deformation field, with the condition that the mesh boundary must coincide with the specified rigid boundaries and the deformed fluid-structure interface.

11.3.3 Fluid-Structure Interaction

The fluid exerts surface forces $\vec{F}\, S_i = \overleftrightarrow{\sigma} \cdot \vec{n}_i$ onto the fluid-structure interface via the stress tensor $\overleftrightarrow{\sigma} = -p\, \mathbb{1} + \mu \left[\nabla \circ \vec{u} + (\nabla \circ \vec{u})^{\mathrm{T}}\right]$. In turn, the deformation $\vec{D}$ and velocity $\dot{\vec{D}}$ of the solid boundary get imposed onto the fluid at the fluid-structure interface. The FSI solver uses strong coupling, meaning that in each time step, the fluid solver and solid solver get solved alternatingly until a maximum number of iterations (100) is reached or the residual between the interfaces of the fluid domain and the solid domain falls below a tolerance value. The maximum number of iterations is included for cases in which the solver converges to some accuracy above our tolerance value but not further, perhaps oscillating between multiple states. Even so, this only happens occasionally and the accuracy of the solver is sufficient for our purposes.
The stress tensor in the linear elastic solid is given by $\sigma = G\,(\nabla \vec{D} + (\nabla \vec{D})^{\mathrm{T}}) + \lambda \,\mathrm{tr}(\nabla \vec{D})\, \mathbb{1}$. We analyse the horizontal stress σ_{xx} (equal to the radial stress due to axisymmetry), the axial stress σ_{zz} and the shear stress σ_{xz}.

11.3.4 Geometry and initial conditions

The simulated geometry describes a thin sheet of water (80 µm height) between a rigid boundary at the top and a linear elastic glass sheet (160 µm height) at the bottom. As in the experiment, a gaseous domain is put on the opposite side of the glass plate

(80 µm height), allowing it to move away from or towards the water-filled domain. Because of the rotationally symmetric nature of the experimental setup, the simulated geometry can be chosen to be axisymmetric. It thus becomes an effectively two-dimensional problem, and only a thin wedge of a cylinder of radius 1 mm has to be modelled. The geometry is divided up in the horizontal and axial directions into a square mesh of computational cells with a width of 1 µm.
The ring bubbles are initiated at a major radius of 67 µm and a minor radius of 12 µm for the inner ring, and a major radius of 96 µm and a minor radius of 8 µm for the outer ring. The initial major and minor radii of the torus bubbles was chosen such that the shock wave position over time closely matches that observed in the experiments. Their centre is chosen to be at $x = 0$ µm and the height to be equal to the minor radius so that the lower end of each ring touches the glass plate. To smoothen the surface of the bubble seed it is smeared via $\alpha' - 4 \cdot 10^{-11} \Delta\alpha' = \alpha$. The initial pressure is 1.69 GPa, which is consistent with previous works [369, 371].
This pressure is chosen such that the initial gas density is equal to the liquid density, implying that the laser energy absorption happens much faster than the bubble expansion. `symmetryPlane` boundary conditions are applied to the front and back of the wedge, and to the inner side representing the axis of symmetry. The outer boundary of the fluid domain acts as an outlet and is imposed with `waveTransmissive` boundary conditions. The fluid domains are bound by either rigid or deformable solid boundaries at the top and bottom, which are treated with a `zeroGradient` boundary condition for the pressure and a `noSlip` boundary condition for the velocity, which means that the relative motion between the fluid at the boundary and the boundary itself it kept at 0. For the mesh deformation, a `slip` boundary condition is applied to the perimeter of the wedge geometry, whereas the deformation of the fluid-structure interface is calculated within the solver.

11.4 Experimental results

In this section, we present the experimental results including the measured dynamics of the shock waves compared with the simulations. We also show photographs of the substrate damage and the statistics for repeated experiments.

11.4.1 Shock wave dynamics

Selected results for the inner and outer ring laser excitation are shown in figure 11.2 (a) and (b), respectively.

The respective top rows of figure 11.2 (a) and (b) show strobe photographs (x-y plane) of the events caused by the generation of the laser ring excitation at the sample, while the bottom rows show the simulation results (x-z plane) for the same time. Notice that the strobe photographs are cropped (x-y plane, $y > 0$) to have a better comparison with the simulation.
The thick dark ring in the strobe photographs is the expanding cavitation bubble, while the thinner ring that propagates towards the centre is the converging shock wave. The bottom rows of figure 11.2 (a) and (b) show the corresponding simulated events for the inner (figure 11.2 (a)) and outer ring (figure 11.2 (b)). The simulations show a cross-section of the x-z plane. The glass boundary is at $z = 0$, at half height of the frame. The upper half of the simulated frames contains the liquid, where we observe the bubble ring and the shock wave. In the solid, we can observe the surface waves propagating at a higher speed than the shock waves in the fluid.

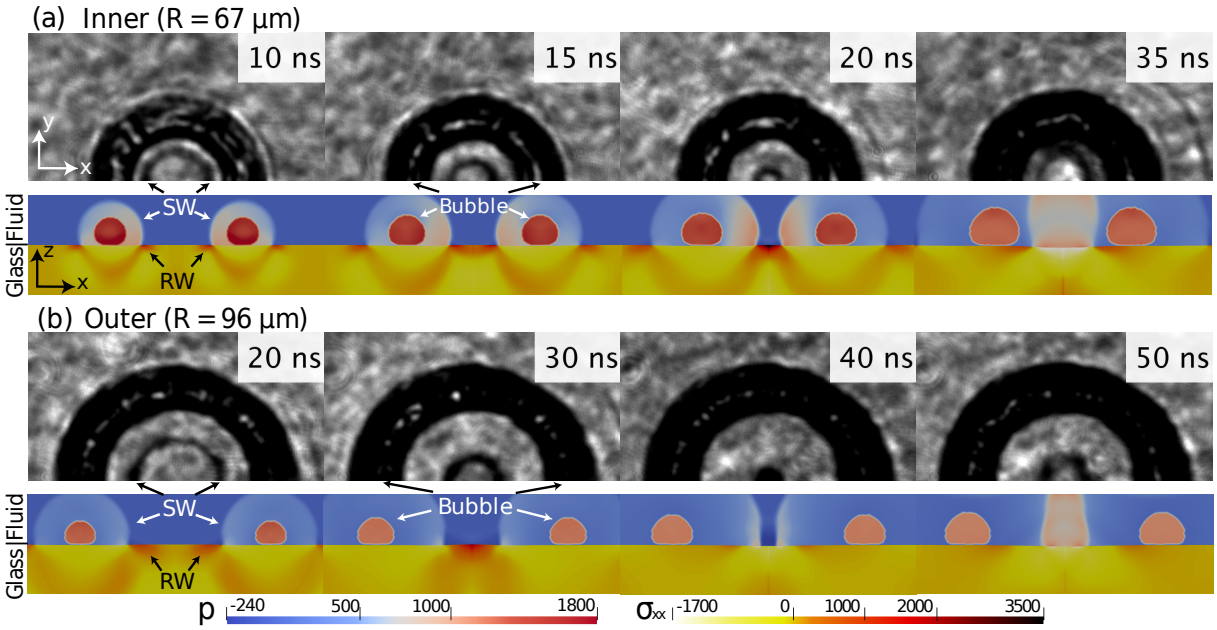

Figure 11.2: Shock wave dynamics of the two rings. The first row shows the strobe photographs (x-y plane), while the second shows the frames extracted from the simulation (x-z plane). The size of each strobe photograph is 150 µm × 300 µm (x-y plane). In the results of the simulation, above is the fluid and below the glass. The size of each simulation frame is 100 µm × 300 µm (x-z plane). Colour bars represent pressure (left) and σ_{xx} (right), both in MPa. (a) Inner ring. (b) Outer ring.

The Rayleigh wave is marked by arrows in the first frame of figure 11.2. The position of the Rayleigh waves was extracted by finding the maximum value of the horizontal stress, σ_{xx}, until the moment where the waves converge at the centre, where it is no longer possible to track the wave once it passes through itself at the centre due to interaction with the stresses induced by the incoming shock waves. On the other hand, tracking the shock wave after it passes through itself at the centre can be done as in the liquid the induced pressure due to the surface waves is very small.

The position of the shock and Rayleigh waves over time is plotted in figure 11.3. The waves emitted from the inner ring are drawn with black symbols and lines, and the outer ones in grey colour. The continuous lines show the positions of the simulated shock waves over time, while the dashed lines represent the dynamics of the Rayleigh waves on the surface of the substrate extracted from the simulation.

In the simulation, the inner Rayleigh and shock waves arrive at the origin at 19 and 24 ns and the outer ones at 29 and 42 ns, respectively. Assuming no interactions between inner and outer excitations, the difference in time between the Rayleigh waves is 10 ns, while for the shock waves the time difference is 18 ns.

Figure 11.3 shows that there is a reasonable agreement between the numerical simulations and the experimental results for the positions of the shock waves (speed ~ 1800 m/s), while the initial speeds of the Rayleigh waves are ~ 3000 m/s for the inner and ~ 3100 m/s for the outer ring, which agree with the expected value of $v_{\mathrm{RW}} = \sqrt{E/(2\,\rho\,(1-\nu)}\,(0.862 + 1.14\nu)/(1+\nu) = 3116$ m/s [395].

Furthermore, in the simulation we also identified other surface waves like the bulk wave (BW) that propagates at ~ 5350 m/s which is in reasonable agreement with the expected speed of 5602 m/s. In this work, we do not consider the induced stresses by the BW

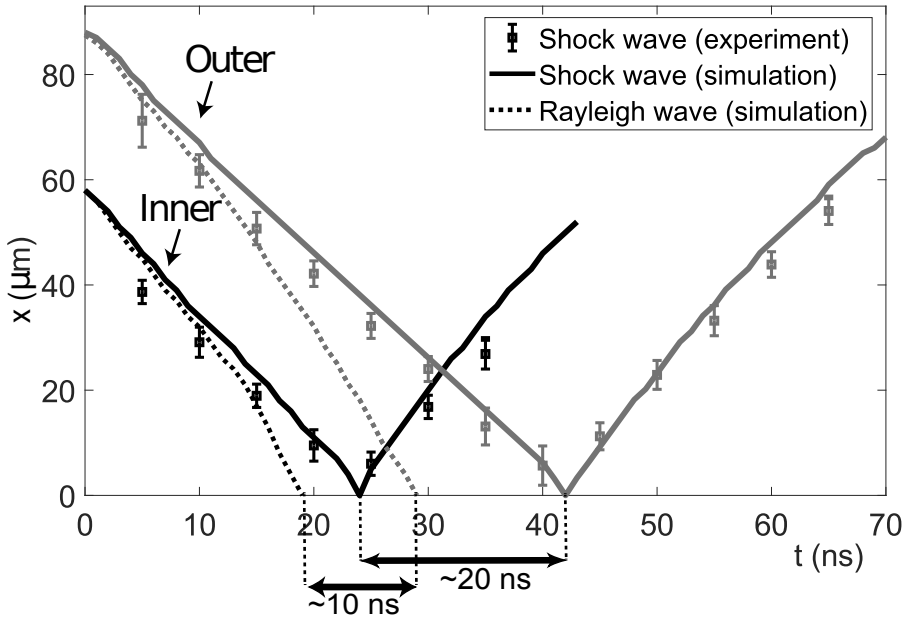

Figure 11.3: Shock and Rayleigh wave dynamics. The symbols show the measurements of the shock wave. The continuous lines represent the position of the shock waves extracted from the simulations ($p_{\max}$ in the fluid). The dotted line represents the position of the Rayleigh wave from the simulation ($\sigma_{xx,\max}$ in the glass). Gray for the outer, black for the inner.

because these are a factor ~ 30 smaller than those of the Rayleigh waves. Also, the pressures that are induced in the liquid by the waves in the solid are much smaller than those induced by the convergence of the shock waves. The bulk wave (BW) generates negative stresses (compression) in the solid, inducing positive pressures in the liquid that are between 45-49 times smaller than the pressures reached during shock wave convergence. The Rayleigh wave propagates by generating positive stresses (tension) inducing negative pressures in the liquid that are ~ 17 times smaller than those induced by the shock waves.

11.4.2 Substrate damage

The experiments are done for the cases of individual rings (inner/outer) and the bullseye configuration with a time delay between both rings $\Delta t = 0$, 10 and 20 ns where the outer ring is fired first at $t = 0$ and the inner ring at time $t = \Delta t$. For each case, the experiments are performed repeatedly at a rate of 0.5 Hz in pairs where the first shot fires the excitations and then one second later a photograph is acquired in bright-field to analyse the damage after the bubbles have disappeared.
Typical examples of the progression of damage at one position for repeated figure 11.4 (a). The different rows represent the five cases, and show the respective developments of the damage in terms of the number of repetitions (labelled in the bottom right corner of each image).
We observe that for the outer ring (first row), damage is visible after ~ 240 repetitions, while in the case of the inner ring (second row), the number of repetitions to observe damage is lower at about 50.
It is worth noting that in the case of the outer ring, a blurred circle starts to emerge in the

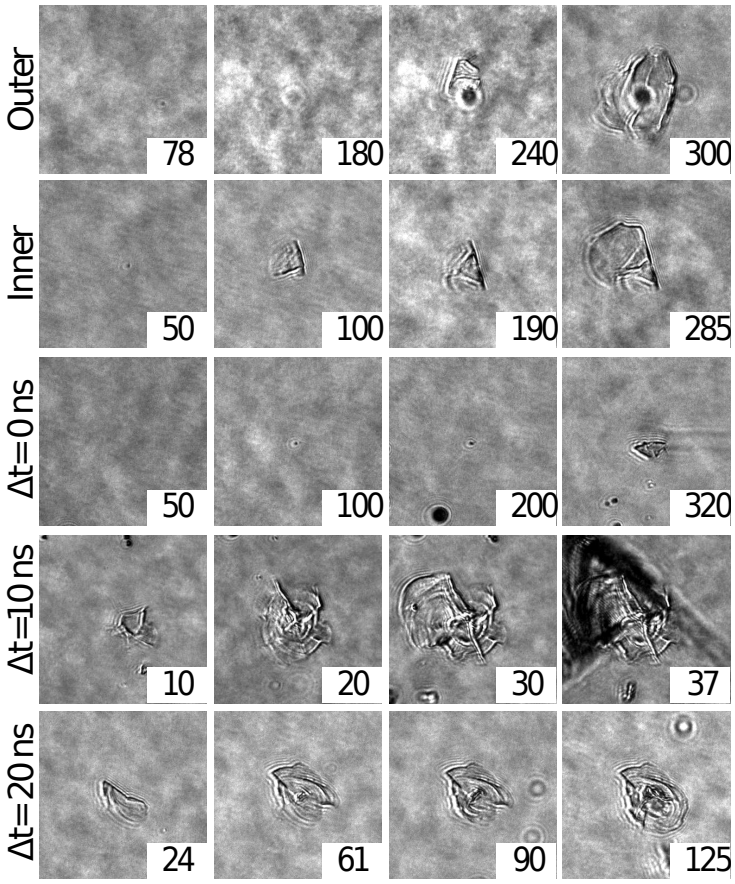

Figure 11.4: Damage as a function of the number of repetitions. The first row is with only the outer ring. Second row with only the inner ring. Third row: simultaneous firing of both rings. Fourth row: Time delay of 10 ns (superposition of inner and outer Rayleigh waves at the centre). Last row: Time delay of 20 ns (superposition of inner and outer shock waves at the centre). Each individual frame has a width of 150 µm.

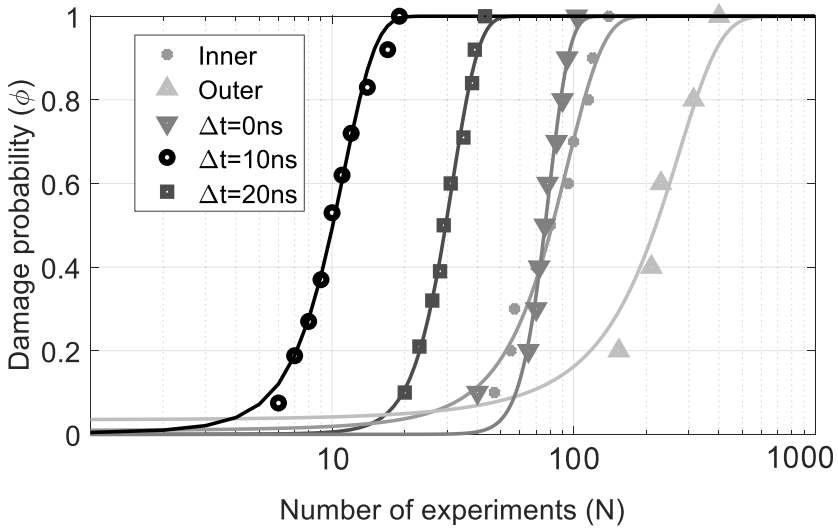

Figure 11.5: Probability of glass damage as a function of the number of repetitions for the five different conditions: outer ring, inner ring, and two rings with time delays of 0, 10 and 20 ns. The continuous lines are fitted to the cumulative distribution functions of the standard normal distribution.

	Inner	Outer	$\Delta t = 0\,\text{ns}$	$\Delta t = 10\,\text{ns}$	$\Delta t = 20\,\text{ns}$
a	81.54	219.27	76.23	10.16	29.55
b	34.51	120.88	14.46	3.24	7.72

Table 11.2: Fitting parameters for a Gaussian distribution of the number of repetitions at which damage occurs, for the five cases studied. Mean value (a) and standard deviation (b).

second frame (after ~ 180 repetitions), which was identified as damage to the upper glass substrate. This indicates that high pressures are achieved that can induce high enough stresses to damage the upper solid boundary. We only observe that kind of damage (upper substrate) for the individual outer ring.
Surprisingly, in the case of the two rings appearing simultaneously (third row), the damage is smaller than that produced by the individual inner ring for a similar number of repetitions. The case of $\Delta t = 10\,\text{ns}$ (fourth row) is the one that shows the strongest damage to the substrate with a smaller number of repetitions. This is followed by the delay of $\Delta t = 20\,\text{ns}$, in the fifth row.
To measure the probability of damage as a function of the number of repeated excitations we start the experiment in an undamaged region of the substrate, then the excitations are fired N times, where N varies between 20 (for $\Delta t = 10\,\text{ns}$) and 400 (individual outer ring) depending on the configuration (individual or bullseye) which changes the rate at which the substrate is damaged. Then, the substrate is displaced to expose an undamaged area to another N excitations. The process is repeated n times so that $n \cdot N = 2000$, with n between 5 and 100 (smallest for the outer ring, largest for $\Delta t = 10\,\text{ns}$). The probability for observing damage is $\phi(N) = \sum_{i=1}^{n} p_i(N)/n$, with $p_i(N) = 1$ when damage is observed (at the N-th shot) and $p_i(N) = 0$ with no visible damage at the N excitation. Note that the experiments are independent for each condition, which is why we have to adjust the number of repetitions N at a single position and the number of sampled positions n in order to have enough points for $\phi(N)$.
Figure 11.5 shows the probability of observing damage (ϕ) in the glass as a function of repetitions (N) for the five different cases (individual outer and inner and both with $\Delta t = 0$, 10, and 20 ns). The symbols represent the experimental data and the continuous lines are fitted cumulative distribution functions of the standard normal distribution for each case,

$$\phi_{\text{fit}} = \frac{1}{2}\left(1 + \text{erf}\Big(\frac{N-a}{b\sqrt{2}}\Big)\right) , \tag{11.6}$$

where a is the mean, b the standard deviation and erf is the error function. Table 11.2 contains a and b for all cases. We find the smallest mean value (10.16) for the case $\Delta t = 10\,\text{ns}$, while the largest is for the individual outer ring (219.27). The values are similar for the individual inner ring (81.54) and for $\Delta t = 0$ (76.23). However, the observed damage after some repetitions, subsequent to the first damage, is larger for the inner ring.

11.5 Numerical results and discussion

In this section, we show the numerical results including the deformation of the solid, the calculated stresses for the individual rings and for the bullseye configuration and discuss the results considering the experimental observations.

11.5.1 Details of the solid deformation

Snapshots from the simulation of the individual inner ring are shown in figure 11.6 (a), where pressures and stresses are plotted in the x-z plane for the inner ring.

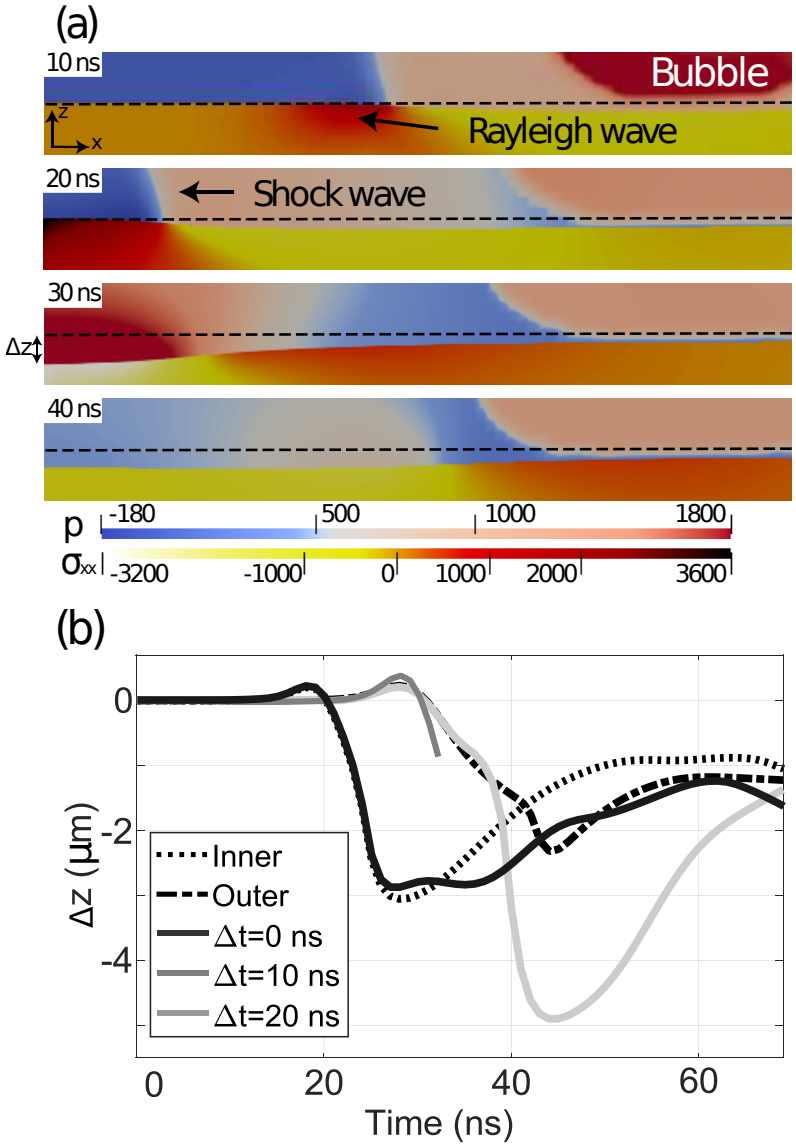

Figure 11.6: Solid deformation. (a) Frames extracted from the simulation for the inner ring. The dashed line represents the original position of the solid boundary ($z = 0$). The height of the frames is 10 µm and the width is 75 µm. The horizontal coordinate goes from $x = 0$ to $x = 75$ µm. The colour bars represent pressure (upper) and σ_{xx} (lower) both in MPa. (b) Deformation in the axial dimension (Δz of the solid at the centre ($z = 0$, $x = 0$) for all focusing conditions.

Figure 11.6 (b) shows the deformation in the axial dimension $\Delta z = z - z_0$ of the solid surface at the centre ($x = 0$, $z = z_0 = 0$) for all focusing configurations. We observe that a lesser deformation is reached for the outer ring, with a minimum value of about -2.3 µm. The inner ring results in Δz reaching ~ -3 µm and the result for $\Delta t = 0$ is similar up to 27 ns but Δz does not reach -3 µm. The largest Δz is close to -5 µm for $\Delta t = 20$ ns. The case for $\Delta t = 10$ ns does not converge past 33 ns. However, we observe that it reaches the largest positive Δz. It is also worth noting that in all cases due to

σ	Minimum			Maximum		
	value (GPa)	pos. (µm)	t (ns)	value (GPa)	pos. (µm)	t (ns)
Inner						
xx	-4.97	(0,0)	26	3.67	(0,0)	19
zz	-5.65	(0,-3)	25	0.88	(0,-7)	20
xz	-1.13	(11,-8)	20	1.31	(6,-6)	26
Outer						
xx	-3.86	(0,0)	43	2.14	(0,0)	29
zz	-4.46	(0,-3)	43	0.61	(0,-10)	30
xz	-0.60	(17,-19)	20	0.91	(5,-5)	44

Table 11.3: Maximum and minimum stress values (σ_{xx}, σ_{zz}, σ_{xz}), their position (x,z) and time of occurrence t for the individual inner and outer ring.

the excess pressure in the liquid, the glass plate keeps being pushed downwards over the course of the simulation. Unsurprisingly, this only occurs in places the shock wave has already passed over. For example, in the case of the inner ring (black dotted line in figure 11.6 (b)) $\Delta z = -3\,\mu\text{m}$ at 29 ns due to the focusing of the shock wave, but later the substrate does not return to its original position ($\Delta z = 0$) but reaches $\Delta z \sim -1\,\mu\text{m}$. At later times $t \sim 85$ ns (not shown in the plot) there is another negative peak due to the rebound of the shock wave. After that, the glass is still pushed downwards in its entirety due to the enduring overpressure. At $t = 150$ ns the displacement has reached $-3.39\,\mu\text{m}$.

11.5.2 Individual rings

The calculated pressures and stresses at the centre of the rings ($x = 0$) on the fluid-structure interface in the case of individual rings are plotted in figure 11.7.
In the plots, the grey continuous line shows the pressure in the liquid at the fluid-structure interface at the origin ($x = z = 0$). The peak of the pressure curve indicates the shock wave converging at the axis of symmetry. However, prior to shock wave convergence, there is a slight increase in the pressure due to the previous passage of the bulk wave and a subsequent slight decrease to negative values due to the Rayleigh wave. The stresses σ_{xx}, σ_{zz} and σ_{xz} at the same point of the solid are represented by the continuous black, dotted grey and black dashed lines, respectively. The arrows point out the peaks created by the convergence of the different waves. Notice that σ_{xz} is multiplied by a factor of 10, as the amplitudes are much smaller.
We observe that in the case of σ_{xx} (continuous black line), at first there is a slight decrease to negative values due to the bulk wave convergence which induces (negative) stresses much smaller (in magnitude) than those of the Rayleigh wave, the inner ring bulk wave reaches $\sigma_{xx} = -0.16$ GPa at $t = 11$ ns, and the one from the outer ring $\sigma_{xx} = -0.12$ GPa at 17 ns.
The stress reaches a significant positive peak (tension) when the Rayleigh waves converge, followed by a negative peak (compression). A similar trend is observed with σ_{zz}, where the initial increase is moderate and the drop to negative values is similar to σ_{xx}. The case for the shear stress, σ_{xz}, has a similar trend to the pressure, which initially shows a small increase followed by a more significant decrease to negative values and an increase as the shock wave arrives at the centre.

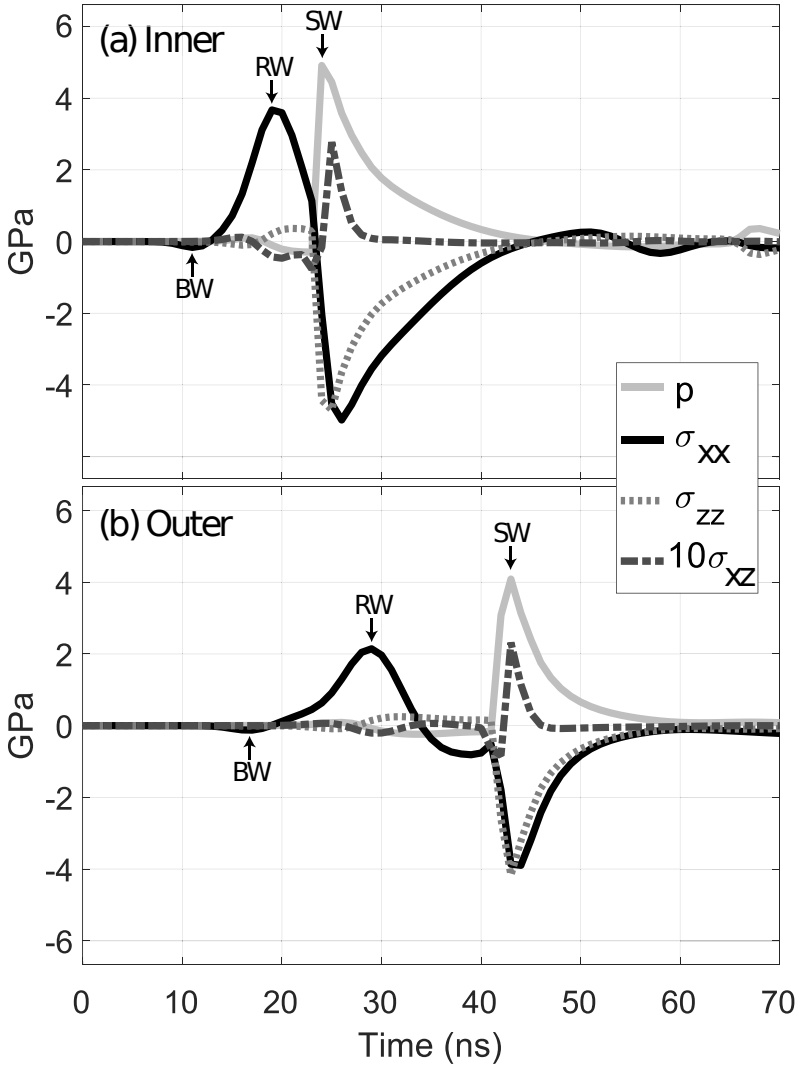

Figure 11.7: Calculated pressures and stresses at the centre of the rings ($x = 0$) at the solid/liquid interface ($z = 0$). The arrows indicate the peaks associated with the arrival of the bulk wave (BW), Rayleigh wave (RW) and shock wave (SW). (a) Inner ring. (b) Outer ring.

In the case of the inner ring, the Rayleigh wave induces positive stress (tension) on the glass, with a maximum of σ_{xx}= 3.67 GPa at $t = 19$ ns. At $t = 26$ ns, as the shock wave reaches the centre with a positive pressure peak of about 5 GPa, it induces a negative peak of σ_{xx}= −4.97 GPa. The corresponding minimum in σ_{zz}= −5.65 GPa is reached one nanosecond earlier, at $t = 25$ ns.
The stresses induced by the outer ring reach a maximum of σ_{xx}= 2.14 GPa at $t = 29$ ns. The positive pressure peak of around 4 GPa, at $t = 42$ ns induces negative peaks of σ_{xx}= −3.86 GPa and σ_{zz}= −4.46 GPa. These stresses have the smallest amplitudes (considering all five studied cases), which could explain the large number of repetitions required to start observing damage ($a = 219$ repetitions, mean value of the cumulative distribution function).

11.5.3 Bullseye configuration

Figure 11.8 shows the corresponding results for $\Delta t = 0$, 10 and 20 ns. The first column (a) contains the plot of pressures in the liquid and stresses at the solid surface at $x = z = 0$ as a function of time.
First, we analyse the case of $\Delta t = 0$ ns (figure 11.8 (a)). As in figure 11.7, the pressure in the liquid is plotted with a grey continuous line. We observe a similar trend to that of the individual inner ring (figure 11.7 (a)). The stresses σ_{xx}, σ_{zz} and σ_{xz} are represented by a black continuous, grey dotted and black dashed line, respectively.

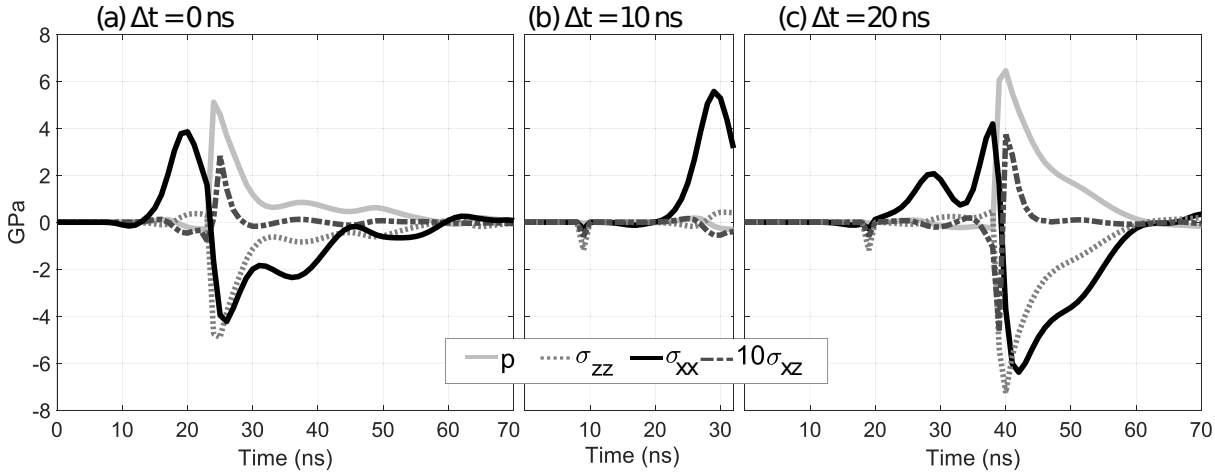

Figure 11.8: Calculated pressures and stresses at the centre of the rings ($x = 0$) at the solid/liquid interface ($z = 0$). (a) $\Delta t = 0$. (b) $\Delta t = 10$ ns. (c) $\Delta t = 20$ ns.

σ	minimum			maximum		
	value (GPa)	pos. (µm)	t (ns)	value (GPa)	pos. (µm)	t (ns)
Δt = 0 ns						
xx	-4.22	(0,0)	26	3.84	(0,0)	20
zz	-5.90	(0,-3)	25	0.88	(0,-9)	19
xz	-1.10	(11,-7)	20	1.30	(5,-5)	26
Δt = 10 ns						
xx				5.56	(0,0)	30
zz				1.30	(0,-9)	29
xz						
Δt = 20 ns						
xx	-6.38	(0,0)	42	4.18	(0,0)	38
zz	-8.46	(0,-3)	40	0.81	(0,-5)	37
xz	-1.50	(6,-5)	38	1.92	(7,-8)	42

Table 11.4: Maximum and minimum stress (σ_{xx}, σ_{zz}, σ_{xz}) values at a given position (x, z) and time for $\Delta t = 0$, 10 and 20 ns.

In the case of σ_{xx} we observe a large increase when the inner Rayleigh waves arrive at the origin at $t = 19$ ns with a peak of 3.84 GPa, followed by a rapid transition to a negative peak with a gradual relaxation and several smaller negative peaks. The first negative peak in σ_{xx} is due to the arrival of the inner bulk wave, this is followed by a positive

maximum when the inner Rayleigh wave converges, then a negative minimum is reached with the convergence of the inner shock wave, followed by other negative peaks due to the arrival of the outer Rayleigh and shock waves. σ_{zz} shows a smaller first positive peak than σ_{xx}, followed by a large drop to negative values, with small subsequent variations during relaxation.

We note that for $\Delta t = 0$ the minimum has a value of $-4.43\,\mathrm{GPa}$, while for the individual inner ring it reaches $-4.98\,\mathrm{GPa}$. That might explain the less destructive effect of $\Delta t = 0$ compared with the individual rings once the substrate is damaged (figure 11.4).

The case of $\Delta t = 10\,\mathrm{ns}$ shows the largest peak in σ_{xx} among all cases ($5.56\,\mathrm{GPa}$) as the Rayleigh waves from both sources converge in the centre at the same time (figure 11.8 (b)), then the code seizes to converge shortly after the pressure becomes negative (with a larger amplitude than for the individual rings). We suspect that this case should achieve the strongest negative stresses because with this delay time we observe the maximum amount of damage (figure 11.4) in the experiments. To avoid the numerical model collapse, we explored adjusting different parameters including finer meshes, smaller time steps and others. However, in all cases, the simulation does not converge for delay times Δt between 8 and 16 ns. This might be explained by a sudden decrease of the stresses (if it follows the trends for the other delay times), preventing convergence of the elasticity equation. The experimental results for $\Delta t = 10\,\mathrm{ns}$ (figure 11.4) show that only after 10 repetitions, there is significant glass damage. After 37 repetitions, the damage is extensive and reaches the opposite side of the glass coverslip (height of 160 µm).

The case of $\Delta t = 20\,\mathrm{ns}$ (figure 11.8 (c)) corresponds to simultaneous convergence of the shock waves, so the increase in pressure in the liquid appears at a later time as expected, with a larger amplitude. σ_{xx} has two main positive peaks: one at $t = 29\,\mathrm{ns}$ due to the arrival of the outer Rayleigh wave and another at $t = 38\,\mathrm{ns}$ induced by the inner Rayleigh wave. Then, as the pressure in the liquid increases to $6.44\,\mathrm{GPa}$, σ_{xx} shows a rapid decrease from $4.38\,\mathrm{GPa}$ at $t = 38\,\mathrm{ns}$ to $-6.38\,\mathrm{GPa}$ at $t = 42\,\mathrm{ns}$, staying negative for about 20 ns. The case of σ_{zz} again shows a moderate increase, followed by a decrease to a negative peak of $-7.26\,\mathrm{GPa}$. The plot or σ_{xz} (dotted black line) shows an abrupt change from negative to positive values, from $-0.46\,\mathrm{GPa}$ at $t = 39\,\mathrm{ns}$ to $0.37\,\mathrm{GPa}$ at $t = 40\,\mathrm{ns}$.

In another study [371], using a gold-coated glass substrate, the authors mentioned that it was possible that the observed glass delamination is caused by the rapid changes in σ. σ_{zz} achieves the largest negative values, but σ_{xx} undergoes the largest changes in amplitude (positive/negative) as it reaches large positive values and swings to large negative values. Those results are consistent with our simulations and the experimental results. Another important observation is that while the maximum/minimum values of σ_{xx} are reached at $x = z = 0$, the largest amplitudes for σ_{zz} are reached at $x = 0$ inside the glass at heights z between $-3\,\mu\mathrm{m}$ and $-10\,\mu\mathrm{m}$. In the case of σ_{xz}, the maximum/minimum values are reached inside the glass as well, at heights ranging from $-5\,\mu\mathrm{m}$ to $-19\,\mu\mathrm{m}$, and at horizontal positions x between $17\,\mu\mathrm{m}$ and $5\,\mu\mathrm{m}$. The tables 11.3 and 11.4 list the positions and times at which the maximum and minimum stresses are reached for each case.

Out of the delay times (8-16 ns) for which the code does not converge, the maximum positive amplitude ($5.81\,\mathrm{GPa}$) is reached for $\Delta t = 13\,\mathrm{ns}$.

11.6 Conclusion

Two cylindrical shock and Rayleigh waves launched at different radii from a common centre, when superpositioned constructively, significantly increase the magnitude of stresses as compared to a single focused wave. We have termed this focusing strategy of two cylindrical waves "bullseye focusing".
In the experiments, the initial radius of the two cylindrical waves was kept constant, yet the delay between their launches was varied. Here, bullseye focusing works best for a delay of $\Delta t = 10\,\mathrm{ns}$, where the largest damage to the substrate is obtained, also with the lowest number of runs. The simulations reveal for this delay the highest tension on the substrate due to the focused Rayleigh waves. Here the simulations did not converge, yet the highest compressive stresses were found for a delay of $\Delta t = 20\,\mathrm{ns}$. Utilising a more advanced model for the glass may allow us to overcome the convergence problem. Then we expect the highest compressive stresses in the simulations also for the delay of $\Delta t = 10\,\mathrm{ns}$. Interestingly, for a delay of $\Delta t = 0$ the same number of runs as for a single inner ring is necessary to cause damage. Still, the superposition of the two waves has an effect: the area of the central damage. There the damaged area is considerably smaller than in the case of a single inner ring. We explain this observation with a partial destructive interference of the two Rayleigh waves. In all simulated cases, we observe abrupt changes in the sign of the stress components σ_{xx} and σ_{zz}. The biggest positive peak is caused by the arrival of the Rayleigh waves at the centre (tension) while the following negative peak that is caused by the arrival of the shock wave (compression). In the case of σ_{xz}, the trend is reversed; the first peak due to Rayleigh waves convergence compresses the substrate, while the second, generated by the convergence of the shock wave, is applying a tension. These peaks last for a few nanoseconds and drop from positive to negative within a few nanoseconds. The induced stresses range between $5.56\,\mathrm{GPa}$ and $-6.38\,\mathrm{GPa}$.
The concept of bullseye focusing as presented here is not limited to two rings. It can be extended to more rings to potentially achieve even larger stresses at their common focus. For example, adding a third pulsed laser and illuminating a separate region of the spatially multiplexed digital hologram would give rise to a third converging wave with arbitrary timing. The finding that the size of the damage can be controlled, too, could be another advantage of the present focusing scheme. Here we envision using the setup to explore the possibility to control the damage size to the substrate with the idea to create a bullseye cutter for glass.
The simulations of the fluid-structure interaction can be improved, too, e.g., through a more realistic model for the structural deformation that accounts for non-linearities and plastic deformation and by implementing more accurate numerical schemes to improve convergence.
Overall, we have demonstrated a comparatively simple method to generate stresses in solids that can easily overcome the yield strength of many materials. Enhancing the amplification of the stresses and utilisation for cutting of brittle materials are two straightforward extensions of the bullseye focusing technique.

Acknowledgments

Thanks to Jose Rangel for machining components and to Cristian Mojica-Casique for programming and Arduino-controlled flip mount. This work is partially funded by DGAPA UNAM PAPIIT grant IN107222; CTIC-LANMAC; CONACYT LN-299057; and the DFG (German Research Association) under contract OH 75/4-1.

12 Nano-cracks and glass carving from non-symmetrically converging shocks

This work has been published in [30]:

U. J. Gutiérrez-Hernández, H. Reese, F. Reuter, C.-D. Ohl, and P. A. Quinto-Su. "Nano-Cracks and Glass Carving from Non-Symmetrically Converging Shocks". *Advanced Physics Research* **2** (10), 2300030 (2023). eprint: `https://onlinelibrary.wiley.com/doi/pdf/10.1002/apxr.202300030`

We present a method to carve into a glass submerged in water with laser-induced surface and shock waves. We start with an elliptic wave source that launches an elliptically converging Rayleigh and shock wave. At the wave focus a single microscopic crack with controlled location and orientation is induced that has a length of a few micrometres and a width of about one hundred nanometers. Through successive surface waves, this crack may be extended along a specific direction which can be controlled by adjusting the distance, shape, and orientation of the laser focus. Here, either point-like or elliptical laser foci are generated using a spatial light modulator. Furthermore, When the crack is guided along a closed circular path using a point-like laser focus, a conchoidal hole may be carved through the glass slide demonstrated with a 160 µm thick cover slip. We model the shock waves in the fluid and the elastic waves in the glass in 3 dimensions with a finite volume framework that accounts for fluid-structure interaction. The resulting pressures and stresses for both the elliptical and point-like Rayleigh and shock wave sources are reported.

12.1 Introduction

To break glass along a line, one typically creates a small crack with a glass cutter and then applies a force on the sample for the crack to propagate and split the glass apart. While this method is simple and straightforward, an understanding of what exactly happens on the microscopic scale is far from complete. There contradicting views on the nature of fracture propagation in glasses exist. For example, Guin and Wiederhorn [396] found using atomic force microscopy that the crack propagates in silicate glasses without forming a cavity at its tip suggesting a completely brittle fracture. While Célarié et al. [397] report on the nanoscale ductility in crack propagation thus fracture propagates similarly to that in metal, recently, Shen et al. [398] revealed that crack propagation in various glasses is dominated by self-organised nucleation, growth, and coalescence of nano-cavities resulting in nano-patterns on the crack's surface, arguing that these cavities confirm the presence of nano-scale ductility of brittle glasses.

There are different methods to generate cracks and modify the properties of glass. Some require direct contact like the case of indenters and others are contactless and rely on lasers or/and acoustic waves. For example, diamond-tipped indenters can generate the formation of cracks at micro- and nano-scale by pressing the surface with controlled forces [399–403]. Nano-scratching is another technique based on indentation, but the tip that presses the surface moves laterally, generating microscopic channels on the material surface [404]. Recently, abrasive nanoparticles driven by ultrasonic vibration [405, 406] have been used to study the hardness of materials and also for micro-machining.

Among the optical methods for micro structuring, the application of ultrashort laser pulses (femtoseconds) direct writing technology stands out. It has been widely used for the microfabrication of optical devices. The quality of the structures generally depends on the optical characteristics of both the experimental setup and the sample. The three main types of nano-scale modifications to materials: melting, high-density cavity, and nano-grating, are based on the energy of the laser pulse used [407].
Shock waves have also been used to damage materials including glass. Zhang et al. [391] studied the generation and propagation of leaky Rayleigh waves induced by a spherical shock wave at a water-glass interface. Symmetric convergent laser-induced shocks and acoustic waves have induced fracture in glass [371], where a picosecond laser pulse shaped into a ring is absorbed by a gold coating deposited on the glass surface. The induced stresses resulted in the removal of a small fragment of the gold film ($\sim$ 15 µm) at the centre of the ring. Other studies with the same system [378] investigated glass failure at the nanosecond scale, generating craters with a depth of about 4-5 µm and a diameter of 10-20 µm. Their simulations estimated a tensile stress threshold of at least 6 GPa for borosilicate glass.
Other experiments with shocks and acoustic waves have used time-delayed excitations [369], including converging ring sources [29] where shock waves were induced in the liquid and Rayleigh waves in the solid. It was shown that the greatest damage induced on the surface was generated with the time delay corresponding to constructive superposition from the simultaneous focusing of Rayleigh waves.
In the present manuscript, we propose a novel non-contact method to nano-structure borosilicate glass in a controlled way. A shaped laser pulse focuses into the liquid close to the glass substrate; unlike direct laser writing methods, the laser energy is not deposited within the substrate. A nano-sized crack is induced via the convergence of laser-induced elliptical shock and surface waves. The direction of the cracks is along the minor axis of the ellipse with a width on the order of 100 nanometers, which allows control via the orientation of the elliptically-shaped laser pulse. The optical detection of the nano-sized crack relies on the observation of the induced cavitation when it is exposed to the acoustic waves. We also demonstrate the controlled propagation of those cracks drawing different geometric shapes with sizes of tens of microns. Repeated exposure to the shocks and surface waves can carve the glass, drilling out a piece of the substrate.

12.2 Methods

12.2.1 Experimental setup

The experimental setup is based on previous works [29, 369] and is shown as a schematic in figure 12.1 A. The laser pulse (Orion, New Wave, 6 ns) is shaped into an elliptical ring using a spatial light modulator (SLM, Hamamatsu, X10468-01). The sizes of the major (104 µm) and minor (78 µm) axes in the focal plane are controlled through the hologram displayed on the SLM screen, which can be easily modified in real-time to change the shape of the laser pulse.
The liquid (ink, EPSON T6643, Magenta) with a similar density and viscosity as water, is bounded by a microscope slide of 1 mm thickness at the top and a microscope slide of 160 µm thickness at the bottom. The properties of the glass are provided by the manufacturer: $\rho = 2230\,\mathrm{kg/m^3}$, $\nu = 0.2$ and $E = 63\,\mathrm{GPa}$ (Fisherbrand, `www.fishersci.com`). The thickness of the liquid layer is about 80 µm, set by a spacer (double-sided tape) placed between both glass substrates. As the top glass substrate is far from where the laser pulse

is focused, it is not shown in figure 12.1 A.
The shaped pulse is focused at the bottom of a liquid container by a microscope objective (Olympus, 10×, NA 0.4). Due to the low intensity of the pulse within the glass, the laser pulse by itself does not damage the substrate. Instead, it is linearly absorbed by the dyed liquid, forming an elliptic ring bubble. Consequently, a shock wave front with the shape of the elliptical torus bubble is emitted. The outer front propagates outwards from the bubble and diverges, thus decaying in amplitude over time. The inner front propagates inwards from the elliptical bubble, leading to energy focusing near the centre of the ellipse. In figure 12.1 A, the laser bubble in water is shown in blue, while the convergence of the inner shock wave front is shown in shades of red. Since the laser-induced bubble is formed at the bottom of the liquid, the bubble expansion loads this surface almost instantaneously, resulting in an energy transfer that deforms the surface and generates the Rayleigh wave.
The energy of the elliptically-shaped laser beam is set to $(202 \pm 7)\,\mu J$, measured between the SLM and the dichroic mirror of the inverted microscope. This energy is used to induce crack formation.
Later, to circularly propagate the induced crack, the hologram displayed on the SLM screen is modified to induce the formation of a single spherical bubble of 12 µm radius, which leads to the formation of a shock wave in the liquid and a Rayleigh wave on the solid surface. The energy of the laser pulse is set to $(300 \pm 8\,\mu J)$.
To capture the fast dynamics of the events, we use stroboscopic photography. For illumination, we use a second laser pulse with a wavelength of 532 nm that is converted to 690 nm using a dye cell. The pulse illuminates the sample, and propagates through the dichroic mirror of the microscope, after which the light reaches a CCD camera (Sensicam QE).
The fracture topology is measured via areal confocal microscopy (Mahr nanofocus μ surf custom P). As the measurement principle makes use of the light reflected at the sample surface, reflectivity is increased by sputtering the glass samples with a thin gold layer (thickness approximately 40 nm). A difficulty encountered with the fracture topologies here is that planar surfaces may easily overexpose the camera sensor while curved surfaces are underexposed as they reflect light out of the microscope's objective aperture. This has been solved by performing measurements of the same region four times with increasing light intensity. The data was combined by choosing at each pixel position the darkest measurement run that still yielded a reliable result which has been performed with a Matlab script.

12.2.2 Numerical model

For the numerical simulations, a finite volume solver of two compressible, viscous fluids is coupled to a solver for a linear elastic solid. One of the fluids represents water and the other is the gas within the bubble, which represents the bubble created by the laser in the experiments. All changes of state are treated as adiabatic, assuming that the presented dynamics are faster than any significant heat exchanges. Indeed, for nanosecond laser-induced microbubbles similar to those generated in the experiments of the present investigation, Quinto-Su et al. [121] has shown that the rise in temperature is only a few Kelvin. The elastic solid represents the microscope slide made of glass that neighbours the created bubble. The solver `CavBubbleFsiFoam` is a modified version of `fsiFoam`, which is found in the fluid-structure interaction package [126] in the OpenFOAM version foam-extend-4.0 [127]. Details on the solver method can be found in [27, 29], where we

	τ (N/m)	μ(mPa s)	p_0 (Pa)	ρ_0 (kg/m^3)	γ	B (MPa)
liquid	0.07	1.00	101325	998.2061	7.15	303.6
gas		0.013	10320	1.33	0.12	0
		E (GPa)	ν	ρ (kg/m^3)		
solid		63	0.20	2230		

Table 12.1: Simulation fluid and solid parameters, including surface tension τ, dynamic viscosity μ and parameters of the Tait equation of state, as well as the elastic modulus E, Poisson's ratio ν and density ρ.

have used it to simulate similar configurations.
The parameters characterising the properties of the two fluids involved and of the elastic solid, as well as the initial conditions are given in table 12.1. The fluid domain containing the liquid and the bubble has a thickness of 80 µm and is sandwiched between a rigid boundary and the elastic solid plate, which has a thickness of 160 µm. On the opposite side of the plate, another gas-filled fluid domain with a thickness of 80 µm is placed which is bounded by an open boundary, allowing the plate to move freely with respect to the liquid-filled fluid domain. The outer boundaries far from the region of interest are open boundaries, representing an infinitely extended domain.
Two simulation cases with different initial bubble shapes are presented, where we take advantage of their respective symmetries. In the first case, the seeded bubble is an elliptical torus, as seen in figure 12.1, and thus has two symmetry planes, the x-z and y-z planes. Thus, only a quarter of the full domain is simulated. The computational mesh is initiated as a cubic grid with a grid parameter of 20 µm. In the liquid-filled domain near the bubble, the cells are successively split into 8 cells of halved grid parameter for 4 iterations to reach a grid parameter of 1.25 µm. The initial conditions are chosen to match the experimentally observed shock wave dynamics. The initial length of the major semi-axis is 52 µm, while that of the minor semi-axis is 39 µm. The ellipse width is 5 µm, which is close to the diffraction limit of the microscope objective that is used in the experiment. The centre of the bubble is placed 2.5 µm above the elastic solid wall, such that they are in contact.
In the second case, a small spherical bubble is seeded on the (vertical) z-axis, in which case the configuration is axisymmetric. Thus, a quasi-two-dimensional simulation can be employed, and the governing equations only need to be solved in the x-z plane. For the computational mesh, a square grid with a grid parameter of 1 µm is used. The initial bubble radius is chosen to be 12 µm and its centre is placed 12 µm above the solid wall such that they again are in contact. In both cases, the initial bubble pressure is chosen to be 1.69 GPa, such that the initial gas density is equal to the liquid density, implying that the laser energy absorption happens much faster than the bubble expansion, as it was done in [29, 369, 371]. This resembles the very fast energy deposition from the nanosecond laser pulse used in the experiment. Our solver is additionally validated by a close match of the shock wave propagation with the experimental observation. The initial sizes of the bubbles (radius, and/or minor axis and major axis, depending on the case) were chosen such that the shock wave position over time closely matches that observed in the experiments.

12.3 Results and discussion

12.3.1 Nano-crack generation

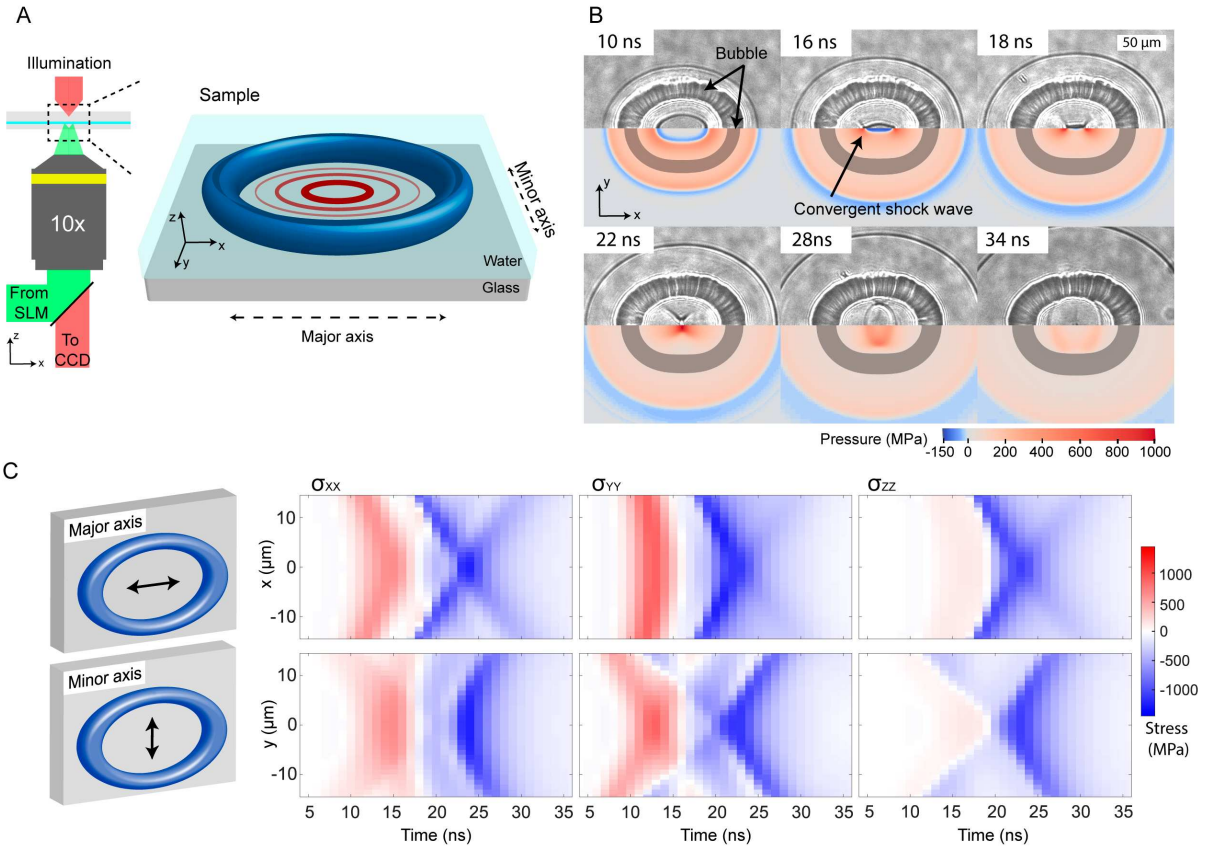

Figure 12.1: **A** Schematic of the experimental setup. The laser bubble in water is shown in blue, while the propagation of the wavefront is shown in shades of red. **B** Dynamics of the elliptical bubble. The top of each frame is a strobe photograph, while the bottom is extracted from a finite volume method simulation. The size of the individual frames is 200 µm × 200 µm. **C** Stresses on the surface of the solid ($z = 0$) close to the centre to which the waves converge. In the top row for a line on the major axis ($x = -15$ µm to $x = 15$ µm), in the bottom row for a line on the minor axis ($y = -15$ µm to $y = 15$ µm).

Figure 12.1 B depicts the dynamics of the elliptical bubble and its shock wave emission in top view. At the top of each frame, strobe photographs are shown, while at the bottom, frames extracted from the simulation are presented. Both the simulated and the experimental frames are cropped along $y = 0$ for ease of comparison. The frames from the simulation are extracted from a slice in the x-y plane at $z = 2.5$ µm. The bubble appears grey. The size of the bubble and the locations of the pressure wavefront show a good agreement between simulations and experiments.
In the first two frames, corresponding to 10 ns and 16 ns, we find an expanding laser-induced bubble that has emitted a shock wave front with the shape of the bubble (elliptical torus), propagating with a velocity close to 1900 m/s. The convergent shock wave front is indicated with an arrow.
The negative pressures (induced by the Rayleigh wave) reach the centre first ($t \approx 16$ ns). Thus, at $t = 18$ ns they are already diverging, while the positive pressures are still converging towards the centre. The top and bottom fronts (y-axis) of the inner shock wave

front reach the centre first, before the side fronts (x-axis). At 18 ns, we observe two large pressures along the major axis ($p = 1050\,\text{MPa}$ at $x = \pm 8\,\mu\text{m}$, $y = 0$). Later, at 22 ns, the highest pressure overall is reached when the two high-pressure regions converge at the centre creating an elongated focus ($p = 1090\,\text{MPa}$, at $x = 0$ and along a line of 10 µm on the minor axis). In the next frames, 28 ns and 34 ns, the inner shock wave front has passed through the centre and is now diverging. As a result of the superposition of converging and diverging waves and the higher positive pressure amplitudes, negative pressures are diminished for later times. Due to the convergence of the waves, in the time interval shown in figure 12.1 B (10-34 ns), the maximum values of pressure in the liquid and stresses in the solid are reached.

Figure 12.1 C depicts the evolution of the stresses σ_{xx} (left), σ_{yy} (centre) and σ_{zz} (right) on a line on the surface of the solid along the major axis (above), and along the minor axis (below). The vertical and horizontal axes are the spatial and temporal coordinates, respectively. The spatial coordinate ranges from $-15\,\mu\text{m}$ to $15\,\mu\text{m}$, while the temporal coordinate ranges from 5 ns to 35 ns. A region of positive stress (i.e. tensile stress) is observed, followed by a region of negative stress (i.e. compressive stress). Although similar, the stresses on the two axes show several differences.

The positive stress is induced by the Rayleigh wave, which propagates with a velocity of about 3200 m/s. For σ_{xx}, the maximum value is 650 MPa, reached at 15 ns. It is approximately constant along 4 µm on the major axis and along 2 µm on the minor axis. For σ_{yy}, the maximum value is 875 MPa, reached at 13 ns. It is approximately constant along 10 µm on the major axis and along 2 µm on the minor axis. For σ_{zz}, the maximum value is 132 MPa, reached at 17 ns. It is approximately constant along 6 µm on both axes.

The negative stress is induced by the shock wave, which propagates slower than the Rayleigh wave, with a velocity of about 1900 m/s. The minimum value of σ_{xx} is -1230 MPa, reached at 24 ns. For σ_{yy}, the minimum value is -1120 MPa, reached at 23 ns. For σ_{zz}, the minimum value is -1077 MPa, reached at 23 ns. Similar maximum values are reached along 10 µm on the minor axis and only along 2 µm on the major axis.

In absolute value, the maximum compressive stress (-1230 MPa for σ_{xx}) is 1.4 times larger than the maximum tensile stress (875 MPa for σ_{yy}). The values for this ratio (|max. tensile stress/max. compressive stress|) are 1.89, 1.28 and 8.16, for each component, σ_{xx}, σ_{yy} and σ_{zz}, respectively.

The strongest compressive stress for σ_{xx}, σ_{yy} and σ_{zz} is reached along a line on the surface in the direction of the minor axis, $-5\,\mu\text{m} < y < 5\,\mu\text{m}$. These minima for the stresses in the solid are reached only one and two nanoseconds after the greatest pressure in the liquid is reached, due to the convergence of the shock wave. The videos in the supplementary material show the dynamics of the bubble and the shock wave fronts for almost 100 ns, both for the simulation and for the experiment. The dynamics in the x-y plane are shown for the pressure p ($z = 2.5\,\mu\text{m}$), as well as the stress components σ_{xx}, σ_{yy} and σ_{zz} separately ($z = 0$). Additionally, a 3d view is given showing the pressure in the fluid, along with each of these stress components separately.

The waves induced by the elliptical laser torus bubble create lines on the surface with almost constant values of tensile and compressive stresses. In comparison, for a circular ring bubble (rotational symmetry case), the convergence of a Rayleigh wave and a shock wave induces stresses with maximum and minimum values at the centre of convergence, which rapidly decays in the radial direction [29].

Figure 12.2 A depicts how a nano-crack is generated through a sequence of successive experimental runs of the elliptical laser focus shown in figure 12.1. After wave focusing, a

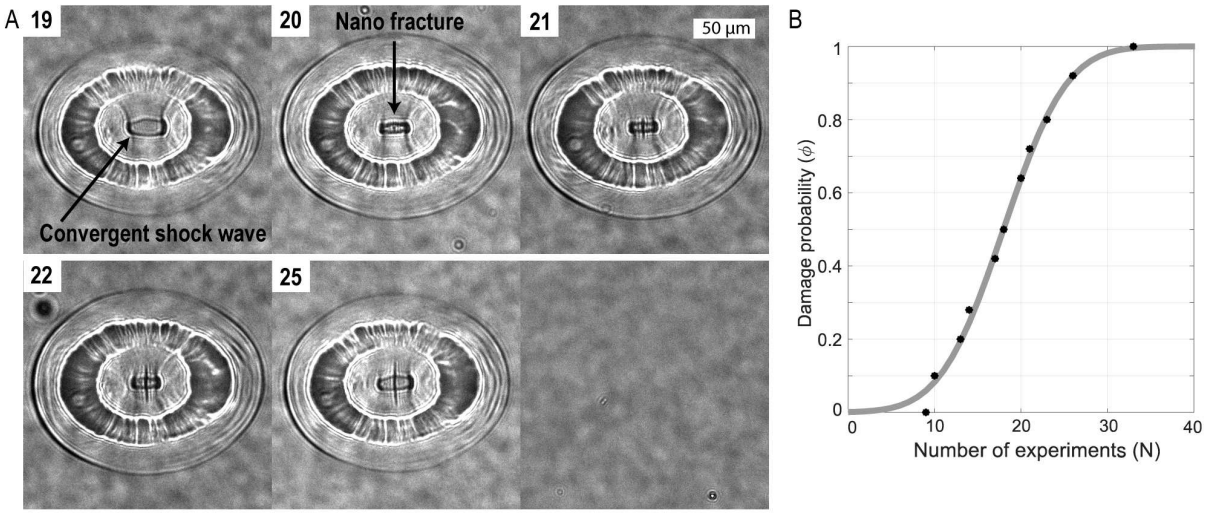

Figure 12.2: **A** Sequence of experimental runs leading to the formation of a nano-crack. The number indicates the number N of experimental runs performed in the same position. Here, after 20 experimental runs, the crack becomes visible through the expansion of small bubbles formed on the crack. In the successive runs, i.e. from $N = 21$ to $N = 25$, the nano-crack grows vertically. The photographs are taken at 15 ns after the laser bubble generation. The last frame corresponds to the same position without the elliptical laser-induced bubble after 25 runs. Although present, the nano-crack is not visible. The size of the individual frames is 200 µm × 200 µm. **B** Probability of glass damage ϕ as a function of the number of repetitions N. The continuous line is a fit to the cumulative distribution function of the normal distribution. The expectation value is $E(N) = 17.92$ and the standard deviation is $s = 5.73$.

rarefaction wave induces tension in the liquid that is strong enough to nucleate cavitation at the position of the crack. Thus the crack becomes visible by the presence of small bubbles which is accomplished by recording the images at 15 ns, after the time of Rayleigh wave focusing.

After 19 repetitions, no damage to the glass is observed. After the 20^{th} run, a small bubble at the centre becomes visible. In the subsequent runs, a vertical line of small bubbles expands, indicating that the crack has now grown vertically. As the propagating shock wave is of high-pressure amplitude as it reaches the centre, it collapses the nucleated bubbles, limiting the lifetime of the bubbles to the interval between the high stresses induced by the Rayleigh wave and the high pressure induced by the convergent shock wave. For the present experiments, this duration is less than 10 ns! The direction of the nano-crack, along the ellipse's minor axis, is explained by the strong and approximately constant compression in σ_{xx}, σ_{yy}, and σ_{zz} over 10 µm along the minor axis mentioned above (figure 12.1 C).

To determine the probability of crack generation ϕ as a function of the number of repeated shots N, the experiment is repeated $n = 50$ times, each time in a new region of the glass. Each time, the number of shots after which the damage is first observed is noted as N_i. The probability for observing the crack after N shots is then $\phi(N) = \sum_{i=1}^{n} p_i(N)/n$, with $p_i(N) = 1$ if the crack is observed at the N-th shot, i.e. if $N \geq N_i$, and $p_i(N) = 0$ otherwise. $\phi(N)$ is plotted in figure 12.2 B. The symbols represent the experimental data and the continuous line is a fit to a cumulative distribution function of a normal distribution. The expectation value is $E(N) = 17.92$ and the standard deviation is

$s = 5.73$.
Continuing the experiments for many more runs after the initial crack is formed results in cracks in other directions and eventually the ejection of small glass fragments.

12.3.2 Controlled crack patterns

Figure 12.3 A shows the process of creating a 150 µm long vertical crack. A first nano-crack is created in the centre of the elliptical laser-induced bubble. Then a motorised stage moves the glass downwards by about 5 µm and a second bubble is created. This is repeated 30 times. The movement can be seen by following the movement of marks on the glass, see the blue and red dashed circles in figure 12.3 A. While multiple shots ($E(N) = 17.92$, mean of the cumulative distribution function) are needed to initiate the first crack, each successive shot of the laser propagates the crack further.

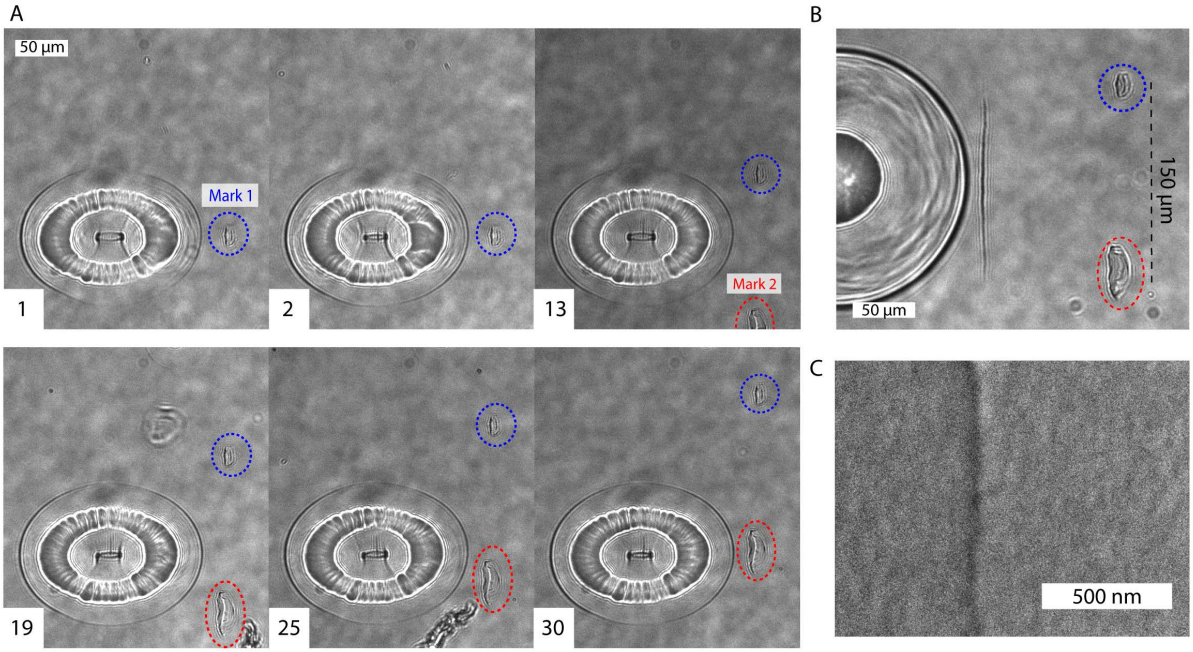

Figure 12.3: **A** Generation of a vertical nano-crack of 150 µm length. In each frame, the vertical nano-crack is observed in the centre of the elliptical laser bubble. The sample is moved upwards in steps of 5 µm using a motorised stage. On the right, two marks in the glass with a distance of 150 µm are labelled. The nano-crack grows downwards. In the bottom row, a second fixed mark in the glass is labelled. **B** visualisation of the finished 150 µm long crack using a smaller circular laser pulse shape. The emitted Rayleigh wave causes tension in the liquid, inducing cavitation bubbles, which make the path of the crack visible. **C** SEM photograph of the crack (SEI, 5 kV, x50000).

To visualise the crack, we change the hologram to create a smaller circular bubble that launches a radially outgoing Rayleigh wave. The stresses of this wave nucleate small bubbles all over the line, see figure 12.3 B. The photograph is recorded 50 ns after the generation of the laser-induced bubble. While the shock wave in the liquid visible as a dark circle in the image has not reached the crack, the Rayleigh wave already has reached the crack and expanded the bubbles.
The resulting crack is further characterised using SEM, see figure 12.3 C. Here, the non-conductive glass surface has been coated with ~ 10 nm thick gold layer. The SEM image

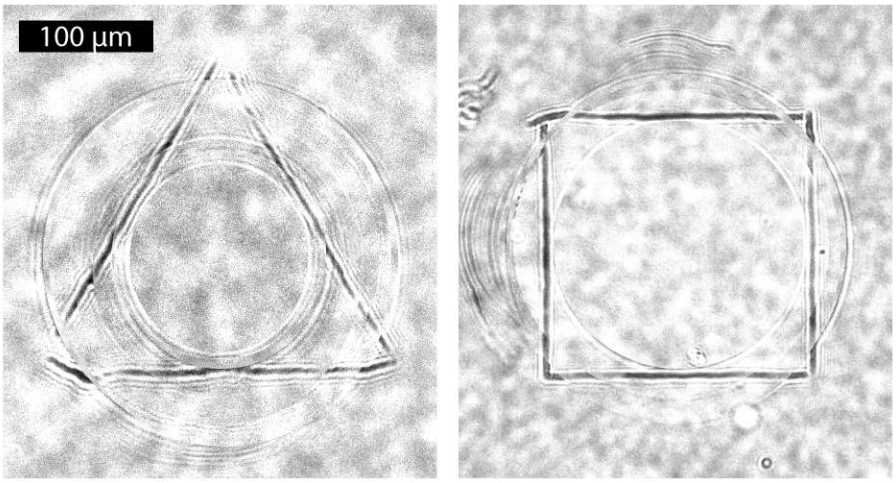

Figure 12.4: Nano-cracks on the sides of a triangle (left) and a square (right). The laser is focused in the centre of each shape, the emitted Rayleigh wave inducing bubbles on the cracks which make them visible. The images are the superposition of several photographs.

reveals a width of the crack of less than 100 nm.
The orientation of the crack can be changed by displaying different digital holograms on the SLM during the experiments. Together with the ability to translate the glass sample with the motorised stage, linear cracks can be arranged into patterns. This feature is demonstrated in figure 12.4. There, we have oriented cracks along the sides of a square and an equilateral triangle.
To visualise the crack patterns within the means of the experimental setup, we again changed the hologram to create a smaller circular bubble and varied the timing of the image recording. Figure 12.4 is the overlay of several photographs taken with different delay times (15-85 ns) to fully observe the bubbles induced on the crack positions on the created pattern. Since the bubbles formed on the crack reach their maximum size shortly before the shock wave reaches that position, the photos are circularly cropped close to the position of the shock wave.
By increasing the laser energy (with constant ellipse size) the number of shots needed to induce a crack is reduced, and eventually a single shot would be required. However, we did not use higher energies because it prevented good control when expanding the crack. Once the damage was induced with higher energy, extending it detached small shards of glass ($\sim 3\,\mu$m, i.e. visible) along the crack.

12.3.3 Carving

Zhang et al. [391] showed that concentric circle-like patterns can be created on a glass surface from pre-existing flaws via shock wave impact generated with a Nano-Pulse Lithotripsy (NPL) probe. They observe and study circumferential crack propagation induced by the symmetric radial stress.
In this section, we study the circular propagation of the crack induced by the described elliptical configuration. Once the crack in the centre of the ellipse is observed, the shots with that configuration are stopped.
The hologram displayed on the SLM screen is modified to induce a single spherical bubble at the bottom of the liquid. The crack is placed at a distance d from the position where the laser-induced bubble is created, as shown in figure 12.5 A. The laser pulse, with an

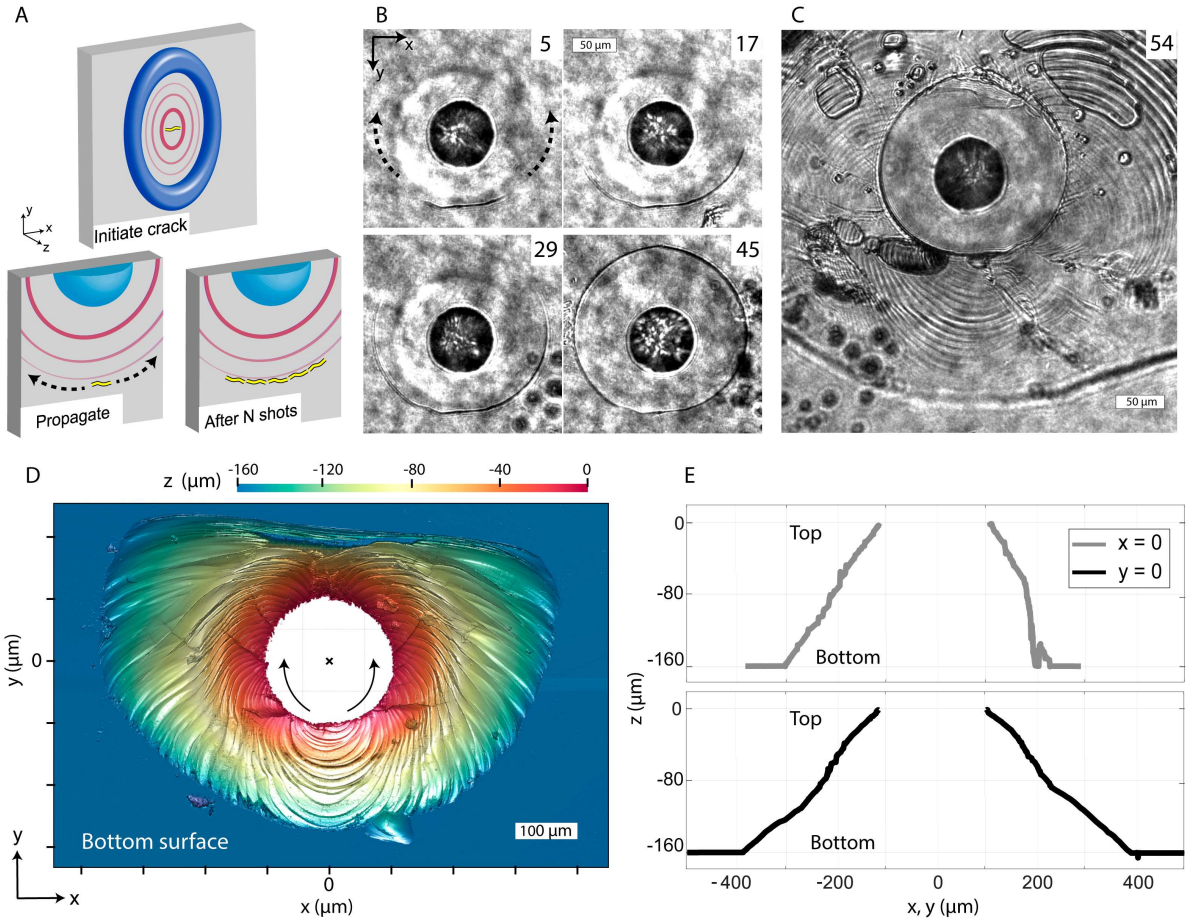

Figure 12.5: Carving process. **A** Above, the elliptical configuration to induce a crack on the solid surface. Below, the geometry used to circumferentially propagate the crack. The laser bubble in water is shown in blue, while the propagation of the wavefront is shown in shades of red. **B** Circumferential crack propagation progression. The number of shots is indicated in each frame on the top left. After 45 shots, the circle-like crack is fully closed. **C** Conchoidal structure before its detachment. The small conchoidal marks are enclosed by the propagated crack and a blurry line (bottom) on the opposite side of the glass. **D** Topography of the conchoidal structure (seen from the bottom). **E** Profiles of the conchoidal structure, along $x = 0$ (top) and along $y = 0$ (bottom).

energy of (300 ± 8) µJ, induces a spherical bubble and the emission of a shock wave. Almost instantaneously, the bubble expansion loads the surface which results in an energy transfer that deforms the glass surface and causes the formation of a surface acoustic wave (Rayleigh wave). This is represented schematically in figure 12.5 A, where the red shaded circular lines represent either the shock wave or the Rayleigh wave emitted by the bubble. As in the previous case, those waves allow us to observe the crack through small bubbles nucleated on it.

Figure 12.5 B shows the progression of the circularly propagating crack, each photograph is labelled with the corresponding experimental run number. The dark circle in the centre is the laser bubble, while the blurred dark line is the emitted shock wave. The Rayleigh wave is not visible in the photographs. To observe the small bubbles on the crack, the photographs are taken at a delay of 35 ns after the generation of the laser bubble, only the last one (45 runs) is taken with a delay of 45 ns, where the approximately circular

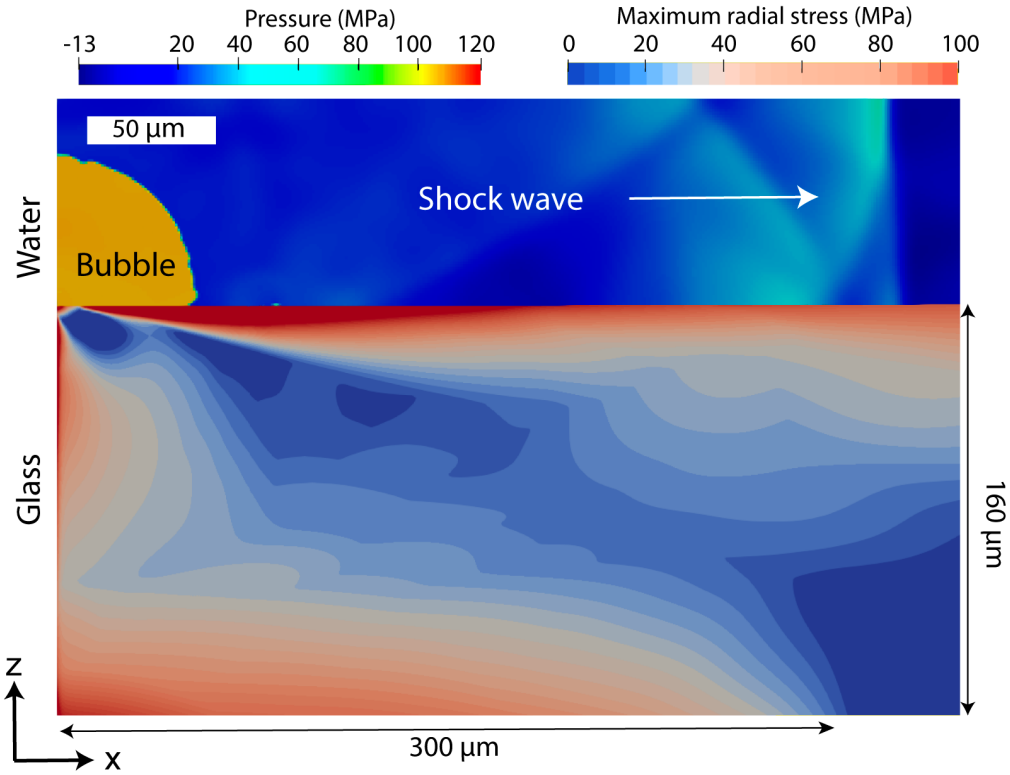

Figure 12.6: Maximum radial stresses on the glass over the full simulated time (200 ns).

damage has closed completely.
Figure 12.5 C shows the damage created after 54 experimental runs performed in the same position. The full frame is not large enough to observe the entire fracture. In the subsequent 55^{th} run, a piece of glass is completely detached, remarkably in one piece.
The detachment can be seen by the blurred thick line on the bottom and the several curved conchoidal marks. The fracture is further analysed via the surface topology presented in figure 12.5 C, measured using areal confocal profilometry. It shows the glass now from the bottom with the depth colour-coded with $z = 0$ being the top and $z = -160\,\mu\text{m}$ the bottom of the plate. Around the circular through hole of about 100 µm (white), a larger region of spallation is present. In figure 12.5 E a profile through the structure is shown, along $x = 0$ (top), and along $y = 0$ (bottom).
The fracture reaches a depth of $z = -50\,\mu\text{m}$ near the perimeter of the circular hole, measured at a radial distance of about 75 µm from the perimeter of the circle, or 175 µm measured from the centre of the circle ($x = y = 0$). This depth is reached with an approximate rotational symmetry. From $z = -50\,\mu\text{m}$ to the bottom side of the glass ($z = -160\,\mu\text{m}$), the propagation of the damage is not axisymmetric but shows only an approximate planar symmetry with respect to the y-z plane. The lateral outer edge of the damage is at $x \approx \pm 380\,\mu\text{m}$, the top is at $y \approx 215\,\mu\text{m}$, and the bottom is at $y \approx -250\,\mu\text{m}$.
The conchoidal marks appear as half circles in the area where the first surface crack is placed. These marks grow to form a shape similar to the ends of a cardioid that closes in the zone where the circular crack has closed on the surface.
In figure 12.6 we show a cross-section (x-z plane) of an axisymmetric finite volume simulation of a circular bubble. The liquid in which the bubble is induced and the shock wave is emitted is shown on the top. The elastic plate where the Rayleigh wave is transmitted is shown on the bottom. In the solid, the maximum radial stress over the full simulation

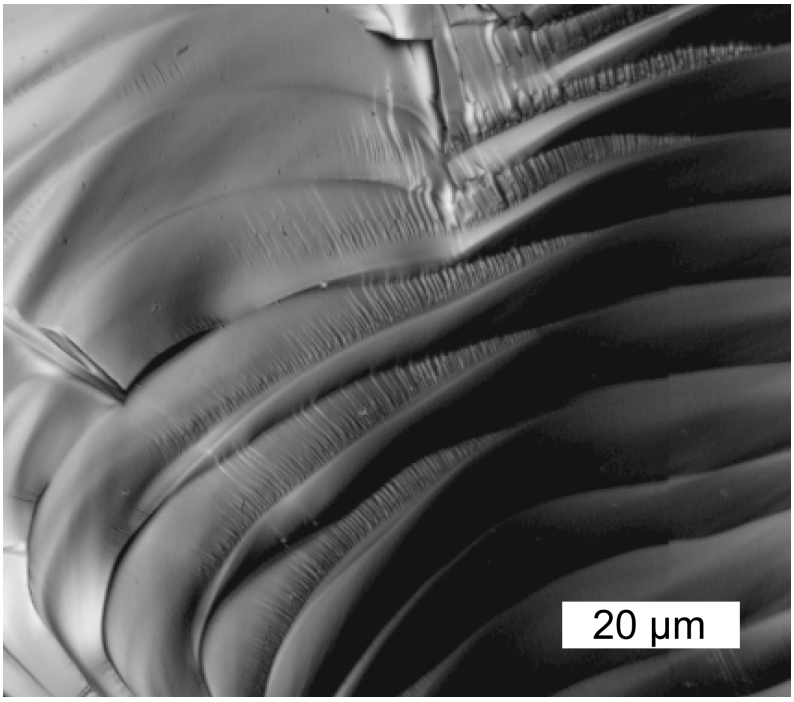

Figure 12.7: Close-up of conchoidal marks in the glass. Hackle lines can be seen perpendicularly to the conchoidal marks.

time (200 ns) is shown. As expected, the highest stresses are reached on the surface of the glass. Nevertheless, at the bottom of the glass, a region in which large radial stresses are reached extends laterally for about 300 µm. That region reaches a height of about 50 µm. The simulation and the corresponding maximum stress distribution may explain the conchoidal fracture of figure 12.5 D. The radial stress σ_{xx} creates the complex fracture, but the vertical stress σ_{zz} eventually causes its detachment. Even so, in the experiment the situation is more complex. As the damage grows, the distribution of maximum stress changes with each shot.

We identify the curvilinear marks as shell-like or conchoidal marks [408]. The conchoidal marks are typical in isotropic rocks such as obsidian and limestone. As is explained by Li and Moelle [409], an individual conchoidal mark is a ridge delineated by a change of fracture orientation. If the conchoidal marks are periodically repeated, the result is a conchoidal structure. McJunkins and Thornton [408] has described how the characteristic lines between the conchoidal marks represent the locations of maximum tensile stress.

In figure 12.7, a close-up of the marks on the glass is observed using confocal microscopy. We identify hackle marks [410] intersecting conchoidal marks perpendicularly. The hackle marks are parallel to the crack propagation.

We also study the experimental case without an initial crack. There, only a circular laser bubble is created in the liquid sample close to the glass surface. Using the same laser energy as for the case presented in figure 12.5, the conchoidal structure is observed, but the crater has just half of the size compared to the previous case. The number of shots necessary to detach the conchoidal structure is significantly larger if there is no initial crack, with 156 shots compared to the previous 55.

12.4 Conclusion

We have developed a simple tool for micro- and nano-structuring on glass in a controlled way using shaped laser-induced shocks and surface waves. In contrast to existing direct-writing methods, energy is not deposited directly into the glass. The laser pulse focuses into the liquid, close to the solid surface, which leads to the formation of shock waves in the liquid and Rayleigh waves in the glass. The results are compared with finite volume simulations with reasonable agreement.

A directed nano-crack with a width of less than 100 nm can be created by focusing a pulsed, elliptically-shaped laser beam. The nano-crack is created by repeated loading ($\sim$ 18 events) in the direction of the minor axis of the ellipse. The crack can be propagated by displacing the sample and changing the rotation angle of the laser ellipse which is digitally controlled in real-time with the SLM. In this way, arbitrary shapes can be engraved on the glass surface (e.g. triangle, square). The presented method, as it is not dependent on ablation, produces much fewer unwanted material fragments, in comparison with other methods for micro- and nano-structuring. Also, as the technique relies on "cutting" along a surface rather than gradually removing material, larger volumes should be easier to carve. In future studies, this technique, together with others of fine measurement, could help to determine the nature of the propagation of damage in this type of material (brittle or ductile).

Since the width of the crack is too small to observe with optical microscopy, we utilise the nucleation of secondary cavitation bubbles in the crack, thereby indicating its location.

Focusing the laser into a point near a crack generates diverging shocks and surface waves with a circular shape, propagating the crack around the focused spot and eventually closing a loop. This also generates several conchoidal marks in the glass, leading to the formation of a conchoidal structure. Hackle marks, perpendicular to the conchoidal marks, are also observed. The crater size is determined by the initial distance between the nano-crack and the laser-induced bubble. The biggest crater radius observed with the energy used in this manuscript was about 115 µm. The smallest radius, of about 50 µm, was observed in a case in which no previous crack was induced.

To fully explain the conchoidal structure, a simulation would require considering the repeated loading and changes in the glass structure. However, the calculated maximum radial stresses on the glass (figure 12.6) help understand the structure of the crater.

In future work, we could use objective lenses with shorter focal lengths to reduce the length and width of the shaped laser pulse, which might yield even better control of the crack. Another possible future experiment could involve trying to observe the crack-generating mechanism, but that will require combining our asymmetrical acoustic wave excitation with other techniques. This non-contact method of crack generation and propagation may be used for micro-structuring delicate surfaces. It would be interesting to expand it from amorphous to crystalline materials where currently microcracks are induced through thermal ablation [411].

Acknowledgements

We thank Cristian Mojica-Casique for technical support, José Rangel for machining optomechanical components, and Artemisa Mazón-Martinez and Víctor Hugo Meza-Laguna for making the SEM analysis possible. This work is partially funded by DGAPA UNAM PAPIIT grant IN107222; CTIC-LANMAC; CONACYT LN-299057; and the DFG (German Research Foundation) under contracts OH 75/4-1 and OH 75/3-1.

13 Discussion and conclusion

The results and their reliability are to be critically assessed.
A popular choice to visualise numerical data is through rainbow-like colour schemes, especially the colour scheme "jet". These offer visually pleasing colour transitions but have the disadvantage that some colours stand out over others, such that in images relatively sharp lines are created, where actually a continuous transition occurs. Such lines are thus misleading and have no physical meaning. An example of this is shown in figure 13.1, where the colour schemes "grayscale" and "jet" are compared using the velocity field $u = |\vec{u}|$ of an expanding bubble. The comparison reveals that only one of the lines visible on the right half of the image has a physical meaning.
"Grayscale" is a specifically good choice, as it only consists of a gradual transition from one colour to another. A colour scheme commonly used in the present work is "cool to warm", which is a gradual transition between the three colours blue, white, and red. This commonly causes an apparent white line to occur at the midpoint of the chosen colour scale. In the case of the phase fraction field α ranging from 0 to 1, this line occurring at $\alpha = 0.5$ has the physical meaning of the fluid-fluid interface. If it is used to visualise a stress field (e.g. p, σ_{ij}, $|\overleftrightarrow{\sigma}|$), and its range is chosen to equally include negative and positive values, the white line denotes the absence of stress.
Another commonly used colour scheme is "black body radiation", which offers an especially smooth transition between its colours. Some lines as described above can occur, but they are much weaker than the ones encountered with the colour scheme "jet". In some cases, the colour scale range is chosen to be smaller than the range of values encountered in the image, with the aim of being able to more clearly see transitions in that smaller value range. In such a case, all cells exceeding those values are shown in the same colour, which is equivalent to overexposure in photography. If this only affects few cells, this might be a good trade-off. This has to be judged for each case individually.
The deviations of the results from reality, i.e. their error, essentially have two origins. On one side stand any errors of the underlying physical model used to describe the problem, including any assumptions, omissions, and approximations that have led to the equations used for the simulations. On the other side stand all numerical errors including discretisation errors and rounding errors.
Regarding the former, the Navier-Stokes equations are a widely accepted model for the flow behaviour of Newtonian fluids. It uses the continuum hypothesis. The system described should thus be large enough to fulfil it. Since the size of a water molecule is of the order of 10^{-10} m and the cell width typically used in the present work is of the order of 10^{-6} m, the continuum hypothesis should be a very good approximation.
Furthermore, heat conduction was neglected in the finite volume simulations. This is based on the assumption that any temperature variations occur on such short time scales that the variation of the bubble's energy over time due to heat conduction is negligible. This assumption may not be fulfilled in all cases, though it is a widely used and accepted simplification of the model.
A very important simplification for the numerical implementation is the axisymmetry of most of the systems considered in the present work since this greatly reduces the computational cost of the simulations. This symmetry is never exactly fulfilled in the experiments and presents an unstable special case, especially during the bubble's collapse. The shape of the bubble commonly deviates from approximate symmetries of the considered sys-

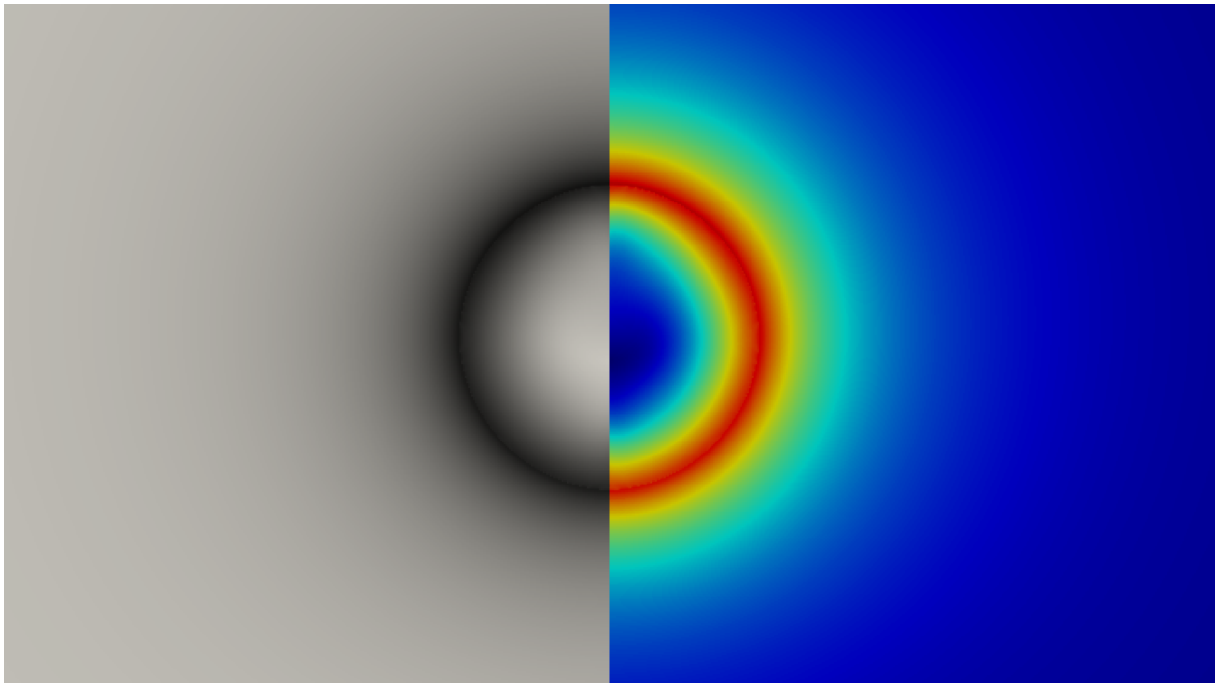

Figure 13.1: Example of the difference between colour schemes. Shown is the velocity magnitude u for an expanding bubble. Left: colour scheme "grayscale", ranging from white ($u = 0$) to black ($u = 50\,\frac{\mathrm{m}}{\mathrm{s}}$). Right: colour scheme "jet", ranging from blue ($u = 0$) to red ($u = 50\,\frac{\mathrm{m}}{\mathrm{s}}$).

tem due to Rayleigh-Taylor instabilities [11]. In reality, small, unavoidable deviations of the system from spherical or even rotational symmetry cause the bubble to disperse into smaller bubble fragments, that then oscillate separately as a bubble cloud, while in axisymmetric simulations these can only be approximated by toroidal bubble rings. This is a limitation of such simulations and must be taken into account during the discussion of each case considered. In the present work, simulations were used to gain insight into phenomena that even in the experiments maintain an approximate axisymmetry on the time scales considered, namely the interaction between a bubble and various boundaries and the thereby induced jet formation, as well as the propagation of waves emitted by the bubble. It was not an aim of the simulations to model the bubble's dispersion into a bubble cloud.

The other important source of inaccuracies is numerical errors. Rounding errors stemming from the limited information content of a number in a computer are especially important when two similar numbers are subtracted from one another, since the resulting, much smaller number carries the absolute error of the previous numbers, resulting in a large relative error. The optimisation of the implemented code through the developers of simulation software programs partly consists of avoiding such operations. But even in optimised code, the error of each numerical operation is generally finite, such that it may eventually accumulate into a large error.

Further errors stem from the discretisations of the differentiations in the flow equations considered, as well as the discretisation of time into time steps and space into computational cells. This error depends on the chosen discretisation scheme, the time step size, and the cell size, respectively. This is especially relevant when the considered field quantities vary strongly on the scale of the cell size.

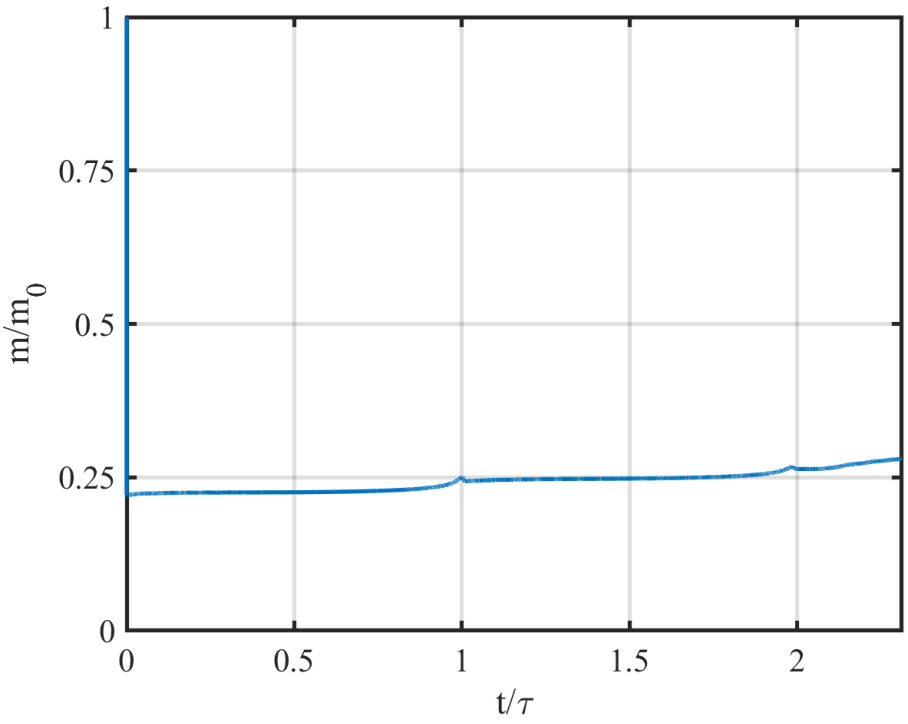

Figure 13.2: Bubble mass variation due to numerical errors. m_0 is the initial bubble mass. τ is the bubble oscillation period. m decreases by 68 % in the first time step, and subsequently increases by 25 % over the course of the simulation.

Whether a computational mesh is sufficiently resolved is often tested by carrying out a mesh refinement study, in which the simulation of interest is carried out at various mesh resolutions. If for increasing refinement the results of the simulation converge to a specific solution, all the meshes that yielded a result that is close to that solution are deemed to be sufficiently fine. For the reason given above, this is not always the case. If the results of the simulations do not converge, further arguments for their validity are to be provided, such as a sufficiently accurate match with the experimental observations without much artificial tweaking of the simulation parameters. This has been done for the results presented in the present work.
On a solid wall, the no-slip boundary condition is applied, i.e., the velocity of the fluid relative to the boundary is taken to vanish. Thus, between a flow and the boundary a boundary layer forms, in which the flow velocity relative to the boundary decays to zero. This boundary layer must be sufficiently resolved to accurately model the flow and specifically the stresses onto the boundary. A sufficient resolution means that over at least two cells, the flow velocity $\vec{u}$ decays approximately linearly to zero.
The temporal resolution of the data output of the simulations is limited by the storage space available on the workstation. Near a maximum (minimum) of a rapidly varying value, such as the flow velocity of a liquid jet, the value obtained may be underestimated (overestimated), as the sample times likely do not coincide exactly with the time of the peak.
The numerical diffusion of the phase fraction field α is counteracted by an additional term in equation (3.8), with the aim of keeping the interface between the immiscible fluids sharp. Nonetheless, the highest achievable sharpness of the interface depends on the mesh resolution, i.e. the cell size, which is why the interface still exhibits some thickness

despite the applied correction. For bubbles with sizes of the order of the cell size, this leads to a large error in their representation and their behaviour. Thus, the simulations can only accurately describe bubbles or droplets that are much larger than the cell size. This is the case for the main bubble in the simulations considered in the present work, as it is initiated at its smallest size and the cell size is chosen accordingly to resolve it in this initial state. Nevertheless, small bubbles or droplets that have been pinched off the main bubble or the liquid bulk are not accurately described.
The nucleation of secondary cavitation bubbles is possible in reality if the pressure in the liquid locally falls below its vapour pressure. However, this phenomenon is not modelled in the solvers used throughout the present work. Still, secondary small bubbles can appear in the simulations, which can be attributed to numerical instabilities in the calculation of the phase fraction field α according to equation (3.8). This is due to α being underestimated in the presence of strong pressure variations due to the term containing $\frac{Dp}{Dt}$ in equation (3.8). These specifically occur near shock waves or near solid boundaries. This behaviour corresponds to similar situations in which cavitation occurs in reality, such that this error may in some cases even increase the accuracy of the model. Nonetheless, since this effect occurs due to numerical errors and not on physical equations describing reality, it is highly dependent on the settings of the solver and is thus to be avoided.
Figure 13.2 shows the mass m of a simulated bubble as a function of time. In reality, the mass of a bubble generally changes due to condensation of its contents or due to evaporation or boiling of the surrounding liquid, which occurs especially near the bubble surface. Since the underlying model describing the bubble does not include any mass transfer between the fluids considered, the observed variations in the bubble mass are caused by numerical errors. In the simulation considered in figure 13.2, in the first time step m decreases by 68 %. Since the accurate description of this early expansion of the bubble is not of interest in the present work, this initial large error may be ignored. Over the course of the simulation, m mostly increases, except for short time periods after its collapse, reaching a total mass increase of about 25 %. To counteract this, the bubble mass is kept constant by implementing a mass correction in the solver. To account for the condensation process over the bubble's first oscillation cycle, a one-time correction of the bubble mass is applied at the time of its maximum expansion, as explained in section 3.2. These corrections contribute to an improved accuracy of the simulations.

OpenFOAM is a powerful tool for computational fluid dynamics. Its simulations show a remarkable match with experimental observations of single expanding and collapsing cavitation bubbles near various boundaries, as well as the dynamics of waves emitted by them. Furthermore, its open-source status and common availability make OpenFOAM attractive for academia, as it opens the possibility to reliably reproduce the results presented by other researchers. Over the course of the present work, three separate solvers have been developed for different classes of problems and used to gain insight into the underlying physics of several microscopic, dynamic processes, including micro-pumping through a perforated plate using a jetting bubble, special jets including the "needle jet" and the "bullet jet", micro-emulsification as it likely occurs near sonotrodes, cavitation nucleation on a localised gas-supersaturated spot in a liquid and on surface defects on a solid, and the formation of stresses and microscopic damage in an elastic solid due to elastic waves and pressure waves induced by a nearby laser-induced cavitation bubble. Specifically, the developed fluid-structure interaction solver `CavBubbleFsiFoam` is useful to model a laser-induced bubble near an elastic solid, and the stresses and waves induced therein.
Of course, as is always the case in research, the present thesis does not nearly exhaust the work that is worthwhile to be done in the field. Some specifically interesting ideas are listed in the following.
The solver `MultiphaseCavBubbleFoam` could be modified to model multiple expanding and collapsing bubbles and study their interaction. The option to model more than two fluids allows for the application of mass corrections to each bubble individually.
The simulated bubble could be driven by an external sound field or pressure wave, which could bring the model closer to bubbles oscillating in ultrasound fields, as they do in some applications.
The solvers `MultiphaseCavBubbleFoam` and `CavBubbleFsiFoam` could be combined to create a solver for a bubble in presence of another fluid *and* an elastic solid, though since both solvers are made in different versions of OpenFOAM, this may prove to be very difficult to do.
Unfortunately, due to numerical instabilities, the fluid-structure interaction solver is limited to relatively stiff elastic materials. An improved solver could use the finite element method to model the elastic solid, which may improve the stability of the computation, though such a solver is not currently available in OpenFOAM, and thus might have to be created from scratch.
If a large computational power and a lot of storage space are available, or if only few simulations are needed, the bubble could be computed at a higher cell resolution, the feasibility of which is to be evaluated for each case individually. Similarly, other configurations might require full three-dimensional simulations, as was done for the elliptical bubble in chapter 12, which is computationally expensive and thus can not be done for a large number of simulations. To alleviate some of this computational cost, an adaptive mesh refinement method could be implemented.
The effect of particles on the bubble could be modelled if the implementation of the Lagrangian particles is modified to support a two-way coupling between the particles and the fluid.
Specifically interesting additions to the model could be to account for heat conduction, phase transitions, i.e. condensation, evaporation, boiling, and specifically a cavitation model such as the Schnerr-Sauer model [412].

References

[1] D. Silberrad. "Propeller erosion". *Engineering* **33**, 33–35 (1912).

[2] L. Rayleigh. "VIII. On the pressure developed in a liquid during the collapse of a spherical cavity". *The London, Edinburgh, and Dublin Philosophical Magazine and Journal of Science* **34** (200), 94–98 (1917).

[3] R. Hickling and M. S. Plesset. "The collapse of a spherical cavity in a compressible liquid". *Office of Naval Research, Department of the Navy: Division of Engineering and Applied Sciences* (85) (1963).

[4] M. S. Plesset and R. B. Chapman. "Collapse of an initially spherical Vapor Cavity in the Neighborhood of a solid Boundary". *Journal of Fluid Mechanics* **47** (2), 283–290 (1971).

[5] J. R. Blake and D. Gibson. "Cavitation bubbles near boundaries". *Annual Review of Fluid Mechanics* **19** (1), 99–123 (1987).

[6] J. P. Best and A. Kucera. "A numerical investigation of non-spherical rebounding bubbles". *Journal of Fluid Mechanics* **245**, 137–154 (1992).

[7] J. Rapet, P. A. Quinto-Su, and C.-D. Ohl. "Cavitation Inception from Transverse Waves in a Thin Liquid Gap". *Physical Review Applied* **14**, 024041 (2 2020).

[8] W. Lauterborn and C.-D. Ohl. "Cavitation bubble dynamics". *Ultrasonics sonochemistry* **4** (2), 65–75 (1997).

[9] F. Reuter and R. Mettin. "Mechanisms of single bubble cleaning". *Ultrasonics Sonochemistry* **29**, 550–562 (2016).

[10] E. Stride and C. Coussios. "Cavitation and contrast: the use of bubbles in ultrasound imaging and therapy". *Proceedings of the Institution of Mechanical Engineers, Part H: Journal of Engineering in Medicine* **224** (2), 171–191 (2010).

[11] C. E. Brennen. "Cavitation in medicine". *Interface focus* **5** (5), 20150022 (2015).

[12] K. Cu, R. Bansal, S. Mitragotri, and D. Fernandez Rivas. "Delivery Strategies for Skin: Comparison of Nanoliter Jets, Needles and Topical Solutions". *Annals of Biomedical Engineering* **48** (7), 2028–2039 (2020).

[13] L. Oyarte Gálvez et al. "Microfluidics control the ballistic energy of thermocavitation liquid jets for needle-free injections". *Journal of Applied Physics* **127** (10) (2020).

[14] J. M. Rosselló and C.-D. Ohl. "Bullet jet as a tool for soft matter piercing and needle-free liquid injection". *Biomedical Optics Express* **13** (10), 5202–5211 (2022).

[15] C. Yao et al. "Ultrasonic emulsification: basic characteristics, cavitation, mechanism, devices and application". *Frontiers of Chemical Science and Engineering*, 1–24 (2022).

[16] K. S. Suslick. "Sonochemistry". *Science* **247** (4949), 1439–1445 (1990).

[17] R. Betti and O. A. Hurricane. "Inertial-Confinement fusion with lasers". *Nature Physics* **12** (5), 445–448 (2016).

[18] H. Zhang, R. Betti, R. Yan, and H. Aluie. "Nonlinear bubble competition of the multimode ablative Rayleigh–Taylor instability and applications to inertial confinement fusion". *Physics of Plasmas* **27** (12) (2020). 122701.

[19] N. D. Shutler and R. B. Mesler. "A photographic study of the dynamics and damage capabilities of bubbles collapsing near solid boundaries". *Journal of Fluids Engineering* **87** (2), 511–517 (1965).

[20] T. B. Benjamin and A. T. Ellis. "The collapse of cavitation bubbles and the pressure thereby produced against solid boundaries". *Philosophical Transactions of the Royal Society of London. Series A* **260** (1110), 221–240 (1966).

[21] A. Vogel, W. Lauterborn, and R. Timm. "Optical and acoustic investigations of the dynamics of laser-produced cavitation bubbles near a solid boundary". *Journal of Fluid Mechanics* **206**, 299–338 (1989).

[22] H. Reese, R. Schädel, F. Reuter, and C.-D. Ohl. "Microscopic pumping of viscous liquids with single cavitation bubbles". *Journal of Fluid Mechanics* **944**, A17 (2022).

[23] K. A. Raman, J. M. Rosselló, H. Reese, and C.-D. Ohl. "Microemulsification from single laser-induced cavitation bubbles". *Journal of Fluid Mechanics* **953**, A27 (2022).

[24] J. M. Rosselló, H. Reese, and C.-D. Ohl. "Dynamics of pulsed laser-induced cavities on a liquid–gas interface: from a conical splash to a 'bullet' jet". *Journal of Fluid Mechanics* **939**, A35 (2022).

[25] J. M. Rosselló, H. Reese, K. A. Raman, and C.-D. Ohl. "Bubble nucleation and jetting inside a millimetric droplet". *Journal of Fluid Mechanics* **968**, A19 (2023).

[26] H. Reese, S.-W. Ohl, and C.-D. Ohl. "Cavitation bubble induced wall shear stress on an elastic boundary". *Physics of Fluids* **35** (7), 076122 (2023).

[27] P. Pfeiffer et al. "Thermally Assisted Heterogeneous Cavitation through Gas Supersaturation". *Physical Review Letters* **128**, 194501 (19 2022).

[28] U. J. Gutiérrez-Hernández, H. Reese, C.-D. Ohl, and P. A. Quinto-Su. "Controlled inertial nano-cavitation above 100 MHz". *Journal of Fluid Mechanics* **972**, A16 (2023).

[29] U. J. Gutiérrez-Hernández, H. Reese, C.-D. Ohl, and P. A. Quinto-Su. "Bullseye focusing of cylindrical waves at a liquid–solid interface". *Physics of Fluids* **34** (11), 112013 (2022).

[30] U. J. Gutiérrez-Hernández et al. "Nano-Cracks and Glass Carving from Non-Symmetrically Converging Shocks". *Advanced Physics Research* **2** (10), 2300030 (2023).

[31] G. K. Batchelor. *An Introduction to Fluid Dynamics*. Cambridge Mathematical Library. Cambridge University Press, 2000. ISBN: 978-0-51-180095-5.

[32] L. D. Landau et al. *Theory of elasticity: Volume 7*. Elsevier, 1986. ISBN: 978-1-29-953600-5.

[33] C. F. Delale. *Bubble dynamics and shock waves*. Vol. 8. Springer Science & Business Media, 2012. ISBN: 978-3-642-34297-4.

[34] C. E. Brennen. *Cavitation and bubble dynamics*. Cambridge university press, 2014. ISBN: 978-1-10-733876-0.

[35] P. Koukouvinis and M. Gavaises. "Cavitation and Bubble Dynamics". Academic Press, 2021. ISBN: 978-0-12-823388-7.

[36] W. Lauterborn and T. Kurz. "Physics of bubble oscillations". *Reports on progress in physics* **73** (10), 106501 (2010).

[37] M. Darwish and F. Moukalled. *The finite volume method in computational fluid dynamics: an advanced introduction with OpenFOAM® and Matlab®*. Springer, 2016. ISBN: 978-3-319-16874-6.

[38] J. Höpken and K. G. Mooney. *The OpenFOAM® Technology Primer*. OpenCFD Ltd, 2020. ISBN: 978-3-00-046757-8.

[39] G. Tryggvason, R. Scardovelli, and S. Zaleski. "Direct Numerical Simulations of Gas–Liquid Multiphase Flows". *Cambridge University Press* (2011).

[40] H. Jasak. "Error analysis and estimation for the finite volume method with applications to fluid flows." *Imperial College London (University of London)* (1996).

[41] H. Reese. "CavBubbleFoam". *GitHub* (2023).

[42] H. Reese. "MultiphaseCavBubbleFoam". *GitHub* (2023).

[43] H. Reese. "CavBubbleFsiFoam". *GitHub* (2023).

[44] J. E. Lennard and I. Jones. "On the determination of molecular fields.—I. From the variation of the viscosity of a gas with temperature". *Proceedings of the Royal Society of London. Series A, Containing Papers of a Mathematical and Physical Character* **106** (738), 441–462 (1924).

[45] R. Brown. "XXVII. A brief account of microscopical observations made in the months of June, July and August 1827, on the particles contained in the pollen of plants; and on the general existence of active molecules in organic and inorganic bodies". *The Philosophical Magazine* **4** (21), 161–173 (1828).

[46] Y.-H. Li. "Equation of state of water and sea water". *Journal of Geophysical Research (1896-1977)* **72** (10), 2665–2678 (1967).

[47] L. Rayleigh. "On Waves Propagated along the Plane Surface of an Elastic Solid". *Proceedings of The London Mathematical Society*, 4–11 (1886).

[48] H. Lamb. "On waves in an elastic plate". *Proceedings of the Royal Society of London. Series A, Containing Papers of a Mathematical and Physical Character* **93** (648), 114–128 (1917).

[49] A. Shima, K. Takayama, Y. Tomita, and N. Ohsawa. "Mechanism of impact pressure generation from spark-generated bubble collapse near a wall". *Aiaa Journal* **21** (1), 55–59 (1983).

[50] A. Philipp and W. Lauterborn. "Cavitation erosion by single laser-produced bubbles". *Journal of Fluid Mechanics* **361**, 75–116 (1998).

[51] D. Horvat et al. "Laser-induced shock-wave-expanded nanobubbles in spherical geometry". *Ultrasonics Sonochemistry* **89**, 106160 (2022).

[52] V. Agrež, J. Mur, J. Petelin, and R. Petkovšek. "Near threshold nucleation and growth of cavitation bubbles generated with a picosecond laser". *Ultrasonics Sonochemistry* **92**, 106243 (2023).

[53] X. Li et al. "Plasmonic Bubble Nucleation and Growth in Water: Effect of Dissolved Air". *The Journal of Physical Chemistry C* **123** (38), 23586–23593 (2019). PMID: 31583035.

[54] J. M. Rosselló and C.-D. Ohl. "On-Demand Bulk Nanobubble Generation through Pulsed Laser Illumination". *Physical Review Letters* **127**, 044502 (4 2021).

[55] J. M. Rosselló and C.-D. Ohl. "Clean production and characterization of nanobubbles using laser energy deposition". *Ultrasonics Sonochemistry* **94**, 106321 (2023).

[56] Q. Wang. "Non-spherical bubble dynamics of underwater explosions in a compressible fluid". *Physics of Fluids* **25** (7), 072104 (2013).

[57] F. Caupin and E. Herbert. "Cavitation in water: a review". *Comptes Rendus Physique* **7** (9), 1000–1017 (2006).

[58] J. C. Fisher. "The Fracture of Liquids". *Journal of Applied Physics* **19** (11), 1062–1067 (1948).

[59] Y. Zhou, B. Li, Y. Gu, and M. Chen. "A molecular dynamics simulation study on the cavitation inception of water with dissolved gases". *Molecular Physics* **117** (14), 1894–1902 (2019).

[60] P. Pfeiffer et al. "Heterogeneous cavitation from atomically smooth liquid–liquid interfaces". *Nature Physics* **18** (12), 1431–1435 (2022).

[61] D. Veysset et al. "Single-bubble and multibubble cavitation in water triggered by laser-driven focusing shock waves". *Physical Review E* **97** (5), 1–8 (2018).

[62] M. P. Brenner, S. Hilgenfeldt, and D. Lohse. "Single-bubble sonoluminescence". *Reviews of modern physics* **74** (2), 425 (2002).

[63] M. S. Plesset. "The Dynamics of Cavitation Bubbles". *Journal of Applied Mechanics* **16** (3), 277–282 (2021).

[64] J. B. Keller and M. Miksis. "Bubble oscillations of large amplitude". *The Journal of the Acoustical Society of America* **68** (2), 628–633 (1980).

[65] P. S. Epstein and M. S. Plesset. "On the Stability of Gas Bubbles in Liquid-Gas Solutions". *Journal of Chemical Physics* **18** (11), 1505–1509 (1950).

[66] F. R. Gilmore. "The growth or collapse of a spherical bubble in a viscous compressible liquid". *Office of Naval Research* (1952).

[67] F. Denner. "The Gilmore-NASG model to predict single-bubble cavitation in compressible liquids". *Ultrasonics Sonochemistry* **70**, 105307 (2021).

[68] C. C. Church. "The effects of an elastic solid surface layer on the radial pulsations of gas bubbles". *The Journal of the Acoustical Society of America* **97** (3), 1510–1521 (1995).

[69] O. Vincent and P. Marmottant. "On the statics and dynamics of fully confined bubbles". *Journal of Fluid Mechanics* **827**, 194–224 (2017).

[70] A.-M. Zhang et al. "A unified theory for bubble dynamics". *Physics of Fluids* **35** (3), 033323 (2023).

[71] A.-M. Zhang, P. Cui, J. Cui, and Q. X. Wang. "Experimental study on bubble dynamics subject to buoyancy". *Journal of Fluid Mechanics* **776**, 137–160 (2015).

[72] M. Tinguely. "The effect of pressure gradient on the collapse of cavitation bubbles in normal and reduced gravity". *École Polytechnique Fédérale de Lausanne* (2013).

[73] J. M. Rosselló et al. "Acoustically induced bubble jets". *Physics of Fluids* **30** (12), 122004 (2018).

[74] J. R. Blake, D. M. Leppinen, and Q. Wang. “Cavitation and bubble dynamics: the Kelvin impulse and its applications”. *Interface focus* **5** (5), 20150017 (2015).

[75] L. A. Crum. “Bjerknes forces on bubbles in a stationary sound field”. *The Journal of the Acoustical Society of America* **57** (6), 1363–1370 (1975).

[76] G. T. Bokman et al. “High-speed x-ray phase-contrast imaging of single cavitation bubbles near a solid boundary”. *Physics of Fluids* **35** (1), 013322 (2023).

[77] A. Bußmann et al. “Investigation of cavitation bubble dynamics near a solid wall by high-resolution numerical simulation”. *Physics of Fluids* **35** (1), 016115 (2023).

[78] F. Reuter, Q. Zeng, and C.-D. Ohl. “The Rayleigh prolongation factor at small bubble to wall stand-off distances”. *Journal of Fluid Mechanics* **944** (2022).

[79] E. Maisonhaute, C. Prado, P. C. White, and R. G. Compton. “Surface acoustic cavitation understood via nanosecond electrochemistry. Part III: shear stress in ultrasonic cleaning”. *Ultrasonics Sonochemistry* **9** (6), 297–303 (2002).

[80] C. D. Ohl et al. “Surface cleaning from laser-induced cavitation bubbles”. *Applied Physics Letters* **89** (7), 074102 (2006).

[81] N. S. M. Yusof et al. “Physical and chemical effects of acoustic cavitation in selected ultrasonic cleaning applications”. *Ultrasonics Sonochemistry* **29**, 568–576 (2016).

[82] F. Reuter, C. Deiter, and C.-D. Ohl. “Cavitation erosion by shockwave self-focusing of a single bubble”. *Ultrasonics Sonochemistry* **90**, 106131 (2022).

[83] C. Lechner, W. Lauterborn, M. Koch, and R. Mettin. “Fast, thin jets from bubbles expanding and collapsing in extreme vicinity to a solid boundary: A numerical study”. *Physical Review Fluids* **4**, 021601 (2 2019).

[84] C. Lechner, W. Lauterborn, M. Koch, and R. Mettin. “Jet formation from bubbles near a solid boundary in a compressible liquid: Numerical study of distance dependence”. *Physical Review Fluids* **5** (9), 1–36 (2020).

[85] M. Koch et al. “Theory-assisted optical ray tracing to extract cavitation-bubble shapes from experiment”. *Experiments in Fluids* **62** (3), 60 (2021).

[86] F. Reuter and C.-D. Ohl. “Supersonic needle-jet generation with single cavitation bubbles”. *Applied Physics Letters* **118** (13), 134103 (2021).

[87] W. White, S. A. Beig, and E. Johnsen. “Pressure fields produced by single-bubble collapse near a corner”. *Physical Review Fluids* **8**, 023601 (2 2023).

[88] O. Supponen et al. “Scaling laws for jets of single cavitation bubbles”. *Journal of Fluid Mechanics* **802** (2016), 263–293 (2016).

[89] E. D. Andrews and I. R. Peters. “Modeling bubble collapse anisotropy in complex geometries”. *Physical Review Fluids* **7**, 123601 (12 2022).

[90] S. R. Gonzalez-Avila, E. Klaseboer, B. C. Khoo, and C.-D. Ohl. “Cavitation bubble dynamics in a liquid gap of variable height”. *Journal of Fluid Mechanics* **682**, 241–260 (2011).

[91] E.-A. Brujan et al. “Jetting and migration of a laser-induced cavitation bubble in a rectangular channel”. *Journal of Fluid Mechanics* **948**, A6 (2022).

[92] H. J. Sagar and O. El Moctar. “Dynamics of a cavitation bubble between oblique plates”. *Physics of Fluids* **35** (1), 013324 (2023).

[93] A. Sieber, D. Preso, and M. Farhat. "Dynamics of cavitation bubbles near granular boundaries". *Journal of Fluid Mechanics* **947**, A39 (2022).

[94] M. Koch et al. "Dynamics of a Laser-Induced Bubble above the Flat Top of a Solid Cylinder-Mushroom-Shaped Bubbles and the Fast Jet". *Fluids* **7** (1) (2022).

[95] J. Mur et al. "Microbubble collapse near a fiber: Broken symmetry conditions and a planar jet formation". *Physics of Fluids* **35** (2), 023305 (2023).

[96] O. Supponen, D. Obreschkow, P. Kobel, and M. Farhat. "Detailed jet dynamics in a collapsing bubble". Vol. 656. 1. IOP Publishing. 2015, p. 012038.

[97] P. Koukouvinis, M. Gavaises, O. Supponen, and M. Farhat. "Simulation of bubble expansion and collapse in the vicinity of a free surface". *Physics of Fluids* **28** (5) (2016).

[98] S. R. Gonzalez-Avila et al. "Mitigating cavitation erosion using biomimetic gas-entrapping microtextured surfaces (GEMS)". *Science Advances* **6** (13), eaax6192 (2020).

[99] Y. Sun et al. "Cavitation bubble collapse in a vicinity of a rigid wall with a gas entrapping hole". *Physics of Fluids* **34** (7), 073314 (2022).

[100] E.-A. Brujan, K. Nahen, P. Schmidt, and A. Vogel. "Dynamics of laser-induced cavitation bubbles near an elastic boundary". *Journal of Fluid Mechanics* **433**, 251–281 (2001).

[101] E.-A. Brujan, K. Nahen, P. Schmidt, and A. Vogel. "Dynamics of laser-induced cavitation bubbles near elastic boundaries: influence of the elastic modulus". *Journal of Fluid Mechanics* **433**, 283–314 (2001).

[102] X. Ma et al. "Comparisons of spark-charge bubble dynamics near the elastic and rigid boundaries". *Ultrasonics Sonochemistry* **43** (May), 80–90 (2018).

[103] A. B. Sieber, D. B. Preso, and M. Farhat. "Cavitation bubble dynamics and microjet atomization near tissue-mimicking materials". *Physics of Fluids* **35** (2), 027101 (2023).

[104] Y.-L. Liu, A.-M. Zhang, Z.-L. Tian, and S.-P. Wang. "Dynamical behavior of an oscillating bubble initially between two liquids". *Physics of Fluids* **31** (9), 092111 (2019).

[105] B. Biller, N. Hoppe, S. Adami, and N. A. Adams. "Jetting mechanisms in bubble-pair interactions". *Physics of Fluids* **34** (7) (2022). 076111.

[106] "COMSOL Multiphysics". *Comsol Multiphysics GmbH* (2022).

[107] "Ansys Fluent". *Ansys, Inc.* (2023).

[108] J.-P. Françoise, G. L. Naber, and S. T. Tsou. *Encyclopedia of mathematical physics*. Vol. 2. Elsevier Amsterdam, 2006. ISBN: 978-0-12-512666-3.

[109] O. C. Zienkiewicz, R. L. Taylor, and P. Nithiarasu. *The finite element method for fluid dynamics*. Butterworth-Heinemann, 2013. ISBN: 978-1-85617-635-4.

[110] "ParaView". *Kitware, Inc.* (2020).

[111] "MATLAB Release 2020a". *The MathWorks Inc.* (2020).

[112] "ImageJ". *National Institutes of Health* (2020).

[113] "InkScape". *GNU General Public License* (2020).

[114] "GIMP". *GNU General Public License* (2020).

[115] M. Koch et al. "Numerical modeling of laser generated cavitation bubbles with the finite volume and volume of fluid method, using OpenFOAM". *Computers & Fluids* **126**, 71–90 (2016).

[116] C. Lechner, M. Koch, W. Lauterborn, and R. Mettin. "Pressure and tension waves from bubble collapse near a solid boundary: A numerical approach". *The Journal of the Acoustical Society of America* **142** (6), 3649–3659 (2017).

[117] W. Lauterborn, C. Lechner, M. Koch, and R. Mettin. "Bubble models and real bubbles: Rayleigh and energy-deposit cases in a Tait-compressible liquid". *IMA Journal of Applied Mathematics* **83** (4), 556–589 (2018).

[118] Q. Zeng et al. "Wall shear stress from jetting cavitation bubbles". *Journal of Fluid Mechanics* **846**, 341–355 (2018).

[119] Q. Zeng, H. An, and C.-D. Ohl. "Wall shear stress from jetting cavitation bubbles: influence of the stand-off distance and liquid viscosity". *Journal of Fluid Mechanics* **932**, A14 (2022).

[120] G. Wang et al. "Numerical study on formation of a splash sheet induced by an oscillating bubble in extreme vicinity to a water surface". *Journal of Hydrodynamics*, 1–11 (2023).

[121] P. A. Quinto-Su, M. Suzuki, and C. D. Ohl. "Fast temperature measurement following single laser-induced cavitation inside a microfluidic gap". *Scientific Reports* **4**, 1–6 (2014).

[122] OpenCFD Ltd. "OpenFOAM 4.0". *ESI Group* (2016).

[123] C. Geuzaine and J.-F. Remacle. "Gmsh". *GNU General Public License* (2009).

[124] F. Reuter and S. A. Kaiser. "High-speed film-thickness measurements between a collapsing cavitation bubble and a solid surface with total internal reflection shadowmetry". *Physics of Fluids* **31** (9), 097108 (2019).

[125] OpenCFD Ltd. "OpenFOAM-v2006". *ESI Group* (2021).

[126] OpenCFD Ltd. "FluidStructureInteraction". *ESI Group* (2016).

[127] OpenCFD Ltd. "Foam-Extend-4.0". *ESI Group* (2016).

[128] W. Lauterborn and H. Bolle. "Experimental investigations of cavitation-bubble collapse in the neighbourhood of a solid boundary". *Journal of Fluid Mechanics* **72** (2), 391–399 (1975).

[129] B. C. Khoo, E. Klaseboer, and K. C. Hung. "A collapsing bubble-induced micropump using the jetting effect". *Sensors and Actuators, A* **118** (1), 1352–1361 (2005).

[130] K. S. F. Lew, E. Klaseboer, and B. C. Khoo. "A collapsing bubble-induced micropump: An experimental study". *Sensors and Actuators, A* **133** (1), 161–172 (2007).

[131] B. Karri et al. "Jets and sprays arising from a spark-induced oscillating bubble near a plate with a hole". *Physical Review E: Statistical Physics, Plasmas, Fluids* **86** (3), 036309 (2012).

[132] R. Dijkink and C. D. Ohl. "Laser-induced cavitation based micropump". *Lab on a Chip* **8**, 1676–1681 (2008).

[133] B. Karri et al. “Collapsing bubble induced pumping in a viscous fluid”. *Sensors and Actuators, A* **169** (1), 151–163 (2011).

[134] B. Karri et al. “High-speed jetting and spray formation from bubble collapse”. *Physical Review E: Statistical Physics, Plasmas, Fluids* **85** (1), 015303 (2012).

[135] S. R. Gonzalez-Avila, C. Song, and C. D. Ohl. “Fast transient microjets induced by hemispherical cavitation bubbles”. *Journal of Fluid Mechanics* **767**, 31–52 (2015).

[136] Y. S. Kannan, S. Balusamy, and B. Karri. “Laser diagnostics for characterization of sprays formed by a collapsing non-equilibrium bubble”. *Journal of Physics: Conference Series* **656** (1), 012114 (2015).

[137] S. P. Wang, A. M. Zhang, Y. L. Liu, and C. Wu. “Experimental research on bubble dynamics near circular hole of plate”. *Wuli Xuebao/Acta Physica Sinica* **62** (6), 064703 (2013).

[138] M. Dawoodian, A. Dadvand, and A. Nematollahi. “Simulation of bubble dynamics near a plate with an aperture in a vertical cylinder using a combined boundary element-finite difference method”. *Engineering Analysis with Boundary Elements* **59**, 187–197 (2015).

[139] K. Cao, Y. Liu, and S. Qu. “Quantitative microfluidic delivery based on an optical breakdown-driven micro-pump for the fabrication of fiber functional devices”. *Optics Express* **25** (20), 23690–23698 (2017).

[140] P. Cui, A. M. Zhang, S. P. Wang, and Q. X. Wang. “Experimental investigation of bubble dynamics near the bilge with a circular opening”. *Applied Ocean Research* **41**, 65–75 (2013).

[141] G. Moloudi, A. Dadvand, M. Dawoodian, and N. Saleki-Haselghoubi. “Oscillation of a transient bubble near an aperture made in a convex rigid plate”. *Engineering Analysis with Boundary Elements* **103**, 51–65 (2019).

[142] F. Reuter, S. R. Gonzalez-Avila, R. Mettin, and C.-D. Ohl. “Flow fields and vortex dynamics of bubbles collapsing near a solid boundary”. *Physical Review Fluids* **2**, 064202 (6 2017).

[143] F. K. Forster et al. “Design, fabrication and testing of fixed-valve micro-pumps”. *FED - American Society of Mechanical Engineers*. Vol. 234. 1995, pp. 39–44.

[144] J. Pfitzner. “Poiseuille and his law”. *Anaesthesia* **31** (2), 273–275 (1976).

[145] K. A. Raman, J. M. Rosselló, and C.-D. Ohl. “Cavitation induced oil-in-water emulsification pathways using a single laser-induced bubble”. *Applied Physics Letters* **121** (19), 194103 (2022).

[146] N. Vankova et al. “Emulsification in turbulent flow: 1. Mean and maximum drop diameters in inertial and viscous regimes”. *Journal of Colloid and Interface Science* **312** (2), 363–380 (2007).

[147] Z. Ren et al. “Oil-in-water emulsions prepared using high-pressure homogenisation with Dioscorea opposita mucilage and food-grade polysaccharides: guar gum, xanthan gum, and pectin”. *Lebensmittel-Wissenschaft & Technologie* **162**, 113468 (2022).

[148] A. N. Kolmogorov. “The local structure of turbulence in incompressible viscous fluid for very large Reynolds numbers”. *Proceedings of the USSR Academy of Sciences* **30**, 301–305 (1941).

[149] S. Schultz, G. Wagner, K. Urban, and J. Ulrich. "High-Pressure Homogenization as a Process for Emulsion Formation". *Chemical Engineering & Technology* **27** (4), 361–368 (2004).

[150] A. Evangelio, F. Campo-Cortés, and J. M. Gordillo. "Simple and double microemulsions via the capillary breakup of highly stretched liquid jets". *Journal of Fluid Mechanics* **804**, 550–577 (2016).

[151] N. Wang et al. "Modelling double emulsion formation in planar flow-focusing microchannels". *Journal of Fluid Mechanics* **895**, A22 (2020).

[152] Y. Ji, J. Bellettre, A. Montillet, and P. Massoli. "Fast oil-in-water emulsification in microchannel using head-on impinging configuration: Effect of swirl motion". *International Journal of Multiphase Flow* **131**, 103402 (2020).

[153] J. P. Canselier, H. Delmas, A. M. Wilhelm, and B. Abismail. "Ultrasound Emulsification—An Overview". *Journal of Dispersion Science and Technology* **23** (1-3), 333–349 (2002).

[154] L. Perrin, S. Desobry-Banon, G. Gillet, and S. Desobry. "Review of High-Frequency Ultrasounds Emulsification Methods and Oil/Water Interfacial Organization in Absence of any Kind of Stabilizer". *Foods* **11** (15), 2194 (2022).

[155] A. A. T. Hijo, R. E. Guinosa, and E. K. Silva. "Ultrasound emulsification energy strategies impact the encapsulation efficiency of essential oils in colloidal systems". *Journal of Molecular Liquids* **358**, 119179 (2022).

[156] L. Zhou et al. "Comparison of oil-in-water emulsions prepared by ultrasound, high-pressure homogenization and high-speed homogenization". *Ultrasonics Sonochemistry* **82**, 105885 (2022).

[157] B. J. Bentley and L. G. Leal. "An experimental investigation of drop deformation and breakup in steady, two-dimensional linear flows". *Journal of Fluid Mechanics* **167**, 241–283 (1986).

[158] H. A. Stone, B. J. Bentley, and L. Leal. "An experimental study of transient effects in the breakup of viscous drops". *Journal of Fluid Mechanics* **173**, 131–158 (1986).

[159] Y. Y. Renardy and V. Cristini. "Scalings for fragments produced from drop breakup in shear flow with inertia". *Physics of Fluids* **13** (8), 2161–2164 (2001).

[160] V. Cristini et al. "Drop breakup and fragment size distribution in shear flow". *Journal of Rheology* **47** (5), 1283–1298 (2003).

[161] X. Liu et al. "Formation of droplets of shear-thinning non-Newtonian fluids in a step-emulsification microdevice". *AIChE Journal* **68** (1), e17395 (2022).

[162] H. Liu et al. "Modelling a surfactant-covered droplet on a solid surface in three-dimensional shear flow". *Journal of Fluid Mechanics* **897** (2020).

[163] G. I. Taylor. "The formation of emulsions in definable fields of flow". *Proceedings of the Royal Society of London. Series A, containing papers of a mathematical and physical character* **146** (858), 501–523 (1934).

[164] N. Singh and V. Narsimhan. "Numerical investigation of the effect of surface viscosity on droplet breakup and relaxation under axisymmetric extensional flow". *Journal of Fluid Mechanics* **946** (2022).

[165] J. M. Rallison. "The deformation of small viscous drops and bubbles in shear flows". *Annual Review of Fluid Mechanics* **16** (1), 45–66 (1984).

[166] H. A. Stone and L. G. Leal. "Breakup of concentric double emulsion droplets in linear flows". *Journal of Fluid Mechanics* **211**, 123–156 (1990).

[167] S. Kim and S. Dabiri. "Transient dynamics of eccentric double emulsion droplets in a simple shear flow". *Physical Review Fluids* **2** (10), 104305 (2017).

[168] D. R. Guildenbecher, C. López-Rivera, and P. E. Sojka. "Secondary atomization". *Experiments in Fluids* **46** (3), 371–402 (2009).

[169] S. Sharma, N. K. Chandra, S. Basu, and A. Kumar. "Advances in droplet aero-breakup". *The European Physical Journal Special Topics*, 1–15 (2022).

[170] T. Kamiya et al. "Study on characteristics of fragment size distribution generated via droplet breakup by high-speed gas flow". *Physics of Fluids* **34** (1), 012118 (2022).

[171] A. A. Shraiber, A. M. Podvysotsky, and V. V. Dubrovsky. "Deformation and breakup of drops by aerodynamic forces". *Atomization and Sprays* **6** (6) (1996).

[172] M. Jalaal and K. Mehravaran. "Fragmentation of falling liquid droplets in bag breakup mode". *International Journal of Multiphase Flow* **47**, 115–132 (2012).

[173] V. Kulkarni and P. E. Sojka. "Bag breakup of low viscosity drops in the presence of a continuous air jet". *Physics of Fluids* **26** (7), 072103 (2014).

[174] H. Hirahara and M. Kawahashi. "Experimental investigation of viscous effects upon a breakup of droplets in high-speed air flow". *Experiments in Fluids* **13** (6), 423–428 (1992).

[175] L. P. Hsiang and G. M. Faeth. "Drop deformation and breakup due to shock wave and steady disturbances". *International Journal of Multiphase Flow* **21** (4), 545–560 (1995).

[176] X. K. Cao et al. "A new breakup regime of liquid drops identified in a continuous and uniform air jet flow". *Physics of Fluids* **19** (5), 057103 (2007).

[177] Z. Liu and R. D. Reitz. "An analysis of the distortion and breakup mechanisms of high speed liquid drops". *International journal of multiphase flow* **23** (4), 631–650 (1997).

[178] J. Han and G. Tryggvason. "Secondary breakup of axisymmetric liquid drops. II. Impulsive acceleration". *Physics of fluids* **13** (6), 1554–1565 (2001).

[179] D. D. Joseph, J. Belanger, and G. S. Beavers. "Breakup of a liquid drop suddenly exposed to a high-speed airstream". *International Journal of Multiphase Flow* **25** (6-7), 1263–1303 (1999).

[180] T. G. Theofanous and G. J. Li. "On the physics of aerobreakup". *Physics of fluids* **20** (5), 052103 (2008).

[181] A. L. Yarin. "Drop impact dynamics: splashing, spreading, receding, bouncing..." *Annual Review of Fluid Mechanics* **38**, 159–192 (2006).

[182] E. Villermaux and B. Bossa. "Drop fragmentation on impact". *Journal of Fluid Mechanics* **668**, 412–435 (2011).

[183] C. Josserand and S. T. Thoroddsen. "Drop impact on a solid surface". *Annual Review of Fluid Mechanics* **48** (1), 365–391 (2016).

[184] Y. Wang and L. Bourouiba. "Unsteady sheet fragmentation: droplet sizes and speeds". *Journal of Fluid Mechanics* **848**, 946–967 (2018).

[185] P. García-Geijo, E. Quintero, G. Riboux, and J. Gordillo. "Spreading and splashing of drops impacting rough substrates". *Journal of Fluid Mechanics* **917** (2021).

[186] D. Soto et al. "Droplet fragmentation using a mesh". *Physical review fluids* **3** (8), 083602 (2018).

[187] M. K. Li and H. S. Fogler. "Acoustic emulsification. Part 1. The instability of the oil-water interface to form the initial droplets". *Journal of Fluid Mechanics* **88** (3), 499–511 (1978).

[188] M. K. Li and H. S. Fogler. "Acoustic emulsification. Part 2. Breakup of the large primary oil droplets in a water medium". *Journal of Fluid Mechanics* **88** (3), 513–528 (1978).

[189] M. Kaci et al. "Emulsification by high frequency ultrasound using piezoelectric transducer: Formation and stability of emulsifier free emulsion". *Ultrasonics Sonochemistry* **21** (3), 1010–1017 (2014).

[190] S. Zhao et al. "Liquid–liquid two-phase flow in ultrasonic microreactors: Cavitation, emulsification, and mass transfer enhancement". *AIChE Journal* **64** (4), 1412–1423 (2018).

[191] A. Taha et al. "Ultrasonic emulsification: An overview on the preparation of different emulsifiers-stabilized emulsions". *Trends in Food Science & Technology* (2020).

[192] W. Li, T. S. H. Leong, M. A. Kumar, and G. J. O. Martin. "A study of the effectiveness and energy efficiency of ultrasonic emulsification". *Physical Chemistry Chemical Physics* **20** (1), 86–96 (2018).

[193] O. Lindau and W. Lauterborn. "Cinematographic observation of the collapse and rebound of a laser-produced cavitation bubble near a wall". *Journal of Fluid Mechanics* **479**, 327–348 (2003).

[194] Y. Tomita, P. Robinson, R. Tong, and J. Blake. "Growth and collapse of cavitation bubbles near a curved rigid boundary". *Journal of Fluid Mechanics* **466**, 259–283 (2002).

[195] R. Dijkink and C.-D. Ohl. "Measurement of cavitation induced wall shear stress". *Applied Physics Letters* **93** (25), 254107 (2008).

[196] S. T. Thoroddsen, K. Takehara, T. G. Etoh, and C. Ohl. "Spray and microjets produced by focusing a laser pulse into a hemispherical drop". *Physics of Fluids* **21** (11), 112101 (2009).

[197] S. R. Gonzalez-Avila and C.-D. Ohl. "Fragmentation of acoustically levitating droplets by laser-induced cavitation bubbles". *Journal of Fluid Mechanics* **805**, 551–576 (2016).

[198] S. Y. Grigoryev et al. "Expansion and fragmentation of a liquid-metal droplet by a short laser pulse". *Physical Review Applied* **10** (6), 064009 (2018).

[199] H. Gelderblom et al. "Drop deformation by laser-pulse impact". *Journal of Fluid Mechanics* **794**, 676–699 (2016).

[200] A. L. Klein et al. "Drop fragmentation by laser-pulse impact". *Journal of Fluid Mechanics* **893** (2020).

[201] T. S. Perdih, M. Zupanc, and M. Dular. "Revision of the mechanisms behind oil-water (O/W) emulsion preparation by ultrasound and cavitation". *Ultrasonics sonochemistry* **51**, 298–304 (2019).

[202] T. Yamamoto and S. V. Komarov. "Liquid jet directionality and droplet behavior during emulsification of two liquids due to acoustic cavitation". *Ultrasonics Sonochemistry* **62**, 104874 (2020).

[203] T. Yamamoto, R. Matsutaka, and S. V. Komarov. "High-speed imaging of ultrasonic emulsification using a water-gallium system". *Ultrasonics Sonochemistry* **71**, 105387 (2021).

[204] R. Han, A. Zhang, S. Tan, and S. Li. "Interaction of cavitation bubbles with the interface of two immiscible fluids on multiple time scales". *Journal of Fluid Mechanics* **932** (2022).

[205] U. Orthaber, J. Zevnik, M. Dular, et al. "Cavitation bubble collapse in a vicinity of a liquid-liquid interface–Basic research into emulsification process". *Ultrasonics sonochemistry* **68**, 105224 (2020).

[206] J. M. Boulton-Stone and J. R. Blake. "Gas bubbles bursting at a free surface". *Journal of Fluid Mechanics* **254**, 437–466 (1993).

[207] D. E. Spiel. "On the births of jet drops from bubbles bursting on water surfaces". *Journal of Geophysical Research* **100** (C3), 4995 (1995).

[208] S. Krishnan, E. J. Hopfinger, and B. A. Puthenveettil. "On the scaling of jetting from bubble collapse at a liquid surface". *Journal of Fluid Mechanics* **822**, 791–812 (2017).

[209] L. Deike et al. "Dynamics of jets produced by bursting bubbles". *Physical Review Fluids* **3** (1), 013603 (2018).

[210] J. Wu. "Evidence of Sea Spray Produced by Bursting Bubbles". *Science* **212** (4492), 324–326 (1981).

[211] T. Li et al. "Bubble interactions and bursting behaviors near a free surface". *Physics of Fluids* **31** (4), 042104 (2019).

[212] T. H. Phan, V. T. Nguyen, and W. G. Park. "Numerical study on strong nonlinear interactions between spark-generated underwater explosion bubbles and a free surface". *International Journal of Heat and Mass Transfer* **163** (October), 120506 (2020).

[213] P. Gregorčič, R. Petkovšek, and J. Možina. "Investigation of a cavitation bubble between a rigid boundary and a free surface". *Journal of Applied Physics* **102** (9), 094904 (2007).

[214] R. C. C. Chen et al. "Exploration of water jet generated by Q-switched laser induced water breakdown with different depths beneath a flat free surface". *Optics Express* **21** (1), 445–453 (2013).

[215] A. Patrascioiu et al. "Laser-generated liquid microjets: correlation between bubble dynamics and liquid ejection". *Microfluidics and Nanofluidics* **16** (1-2), 55–63 (2014).

[216] M. Jalaal et al. "Destructive mechanisms in laser induced forward transfer". *Applied Physics Letters* **114** (21), 213703 (2019).

[217] N. Bempedelis, J. Zhou, M. Andersson, and Y. Ventikos. "Numerical and experimental investigation into the dynamics of a bubble-free-surface system". *Physical Review Fluids* **6** (1), 013606 (2021).

[218] P. B. Robinson et al. "Interaction of cavitation bubbles with a free surface". *Journal of Applied Physics* **89** (12), 8225–8237 (2001).

[219] A. Pearson, E. Cox, J. Blake, and S. Otto. "Bubble interactions near a free surface". *Engineering Analysis with Boundary Elements* **28** (4), 295–313 (2004).

[220] Y. Saade, M. Jalaal, A. Prosperetti, and D. Lohse. "Crown formation from a cavitating bubble close to a free surface". *Journal of Fluid Mechanics* **926**, A5 (2021).

[221] V. Duclaux et al. "Dynamics of transient cavities". *Journal of Fluid Mechanics* **591**, 1–19 (2007).

[222] J. M. Aristoff and J. W. M. Bush. "Water entry of small hydrophobic spheres". *Journal of Fluid Mechanics* **619**, 45–78 (2009).

[223] R. Bergmann et al. "Giant Bubble Pinch-Off". *Physical Review Letters* **96** (15), 154505 (2006).

[224] M. M. Mansoor, J. O. Marston, I. U. Vakarelski, and S. T. Thoroddsen. "Water entry without surface seal: extended cavity formation". *Journal of Fluid Mechanics* **743**, 295–326 (2014).

[225] J. Eshraghi, S. Jung, and P. P. Vlachos. "To seal or not to seal: The closure dynamics of a splash curtain". *Physical Review Fluids* **5** (10), 104001 (2020).

[226] A. Kiyama et al. "Gelatine cavity dynamics of high-speed sphere impact". *Journal of Fluid Mechanics* **880**, 707–722 (2019).

[227] A. Vogel and V. Venugopalan. "Mechanisms of Pulsed Laser Ablation of Biological Tissues". *Chemical Reviews* **103** (2), 577–644 (2003).

[228] I. Apitz and A. Vogel. "Material ejection in nanosecond Er:YAG laser ablation of water, liver, and skin". *Applied Physics A* **81** (2), 329–338 (2005).

[229] C. Clanet. "Waterbells and Liquid Sheets". *Annual Review of Fluid Mechanics* **39** (1), 469–496 (2007).

[230] K. G. Bodily, S. J. Carlson, and T. T. Truscott. "The water entry of slender axisymmetric bodies". *Physics of Fluids* **26** (7), 072108 (2014).

[231] S. Li, A. M. Zhang, R. Han, and Y. Q. Liu. "Experimental and numerical study on bubble-sphere interaction near a rigid wall". *Physics of Fluids* **29** (9), 092102 (2017).

[232] V. Robles et al. "Soft material perforation via double-bubble laser-induced cavitation microjets". *Physics of Fluids* **32** (4), 042005 (2020).

[233] Y. Zel'dovich and Y. Raizer. *Physics of Shock Waves and High-Temperature Hydrodynamic Phenomena*. Dover Books on Physics. Dover Publications, 2002. ISBN: 978-0-48-642002-8.

[234] G. Nykteri et al. "A $\Sigma - \Upsilon$ two-fluid model with dynamic local topology detection: Application to high-speed droplet impact". *Journal of Computational Physics* **408**, 109225 (2020).

[235] F. Huang, S. Li, Y. Zhao, and Y. Liu. "A numerical study on the transient impulsive pressure of a water jet impacting nonplanar solid surfaces". *Journal of Mechanical Science and Technology* **32** (9), 4209–4221 (2018).

[236] M. L. Grünbein et al. "Effect of X-ray free-electron laser-induced shockwaves on haemoglobin microcrystals delivered in a liquid jet". *Nature Communications* **12** (1), 1672 (2021).

[237] M. Vassholz et al. "Pump-probe X-ray holographic imaging of laser-induced cavitation bubbles with femtosecond FEL pulses". *Nature Communications* **12** (1), 3468 (2021).

[238] J. Hagemann et al. "Single-pulse phase-contrast imaging at free-electron lasers in the hard X-ray regime". *Journal of Synchrotron Radiation* **28** (1), 52–63 (2021).

[239] C. Favre et al. "White-Light Nanosource with Directional Emission". *Physical Review Letters* **89** (3), 035002 (2002).

[240] P. Rohwetter et al. "Laser-induced water condensation in air". *Nature Photonics* **4** (7), 451–456 (2010).

[241] L. Mei and M. Brydegaard. "Atmospheric aerosol monitoring by an elastic Scheimpflug lidar system". *Optics Express* **23** (24), A1613–A1628 (2015).

[242] H. Lee et al. "A laser-driven optical atomizer: photothermal generation and transport of zeptoliter-droplets along a carbon nanotube deposited hollow optical fiber". *Nanoscale* **14**, 5138–5146 (13 2022).

[243] P. I. Singh and C. J. Knight. "Pulsed Laser-Induced Shattering of Water Drops". *AIAA Journal* **18** (1), 96–100 (1980).

[244] D. R. Alexander and J. G. Armstrong. "Explosive vaporization of aerosol drops under irradiation by a CO_2 laser beam". *Applied Optics* **26** (3), 533 (1987).

[245] J. H. Eickmans, W. F. Hsieh, and R. K. Chang. "Laser-induced explosion of H_2O droplets: spatially resolved spectra". *Optics Letters* **12** (1), 22 (1987).

[246] A. Lindinger et al. "Time-resolved explosion dynamics of H_2O droplets induced by femtosecond laser pulses". *Applied Optics* **43** (27), 5263 (2004).

[247] J. O. Marston and S. T. Thoroddsen. "Laser-induced micro-jetting from armored droplets". *Experiments in Fluids* **56** (7), 140 (2015).

[248] D. Obreschkow et al. "Cavitation Bubble Dynamics inside Liquid Drops in Microgravity". *Physical Review Letters* **97** (9), 094502 (2006).

[249] A. Vogel, S. Busch, and U. Parlitz. "Shock wave emission and cavitation bubble generation by picosecond and nanosecond optical breakdown in water". *The Journal of the Acoustical Society of America* **100** (1), 148–165 (1996).

[250] J. Noack and A. Vogel. "Single-shot spatially resolved characterization of laser-induced shock waves in water". *Applied Optics* **37** (19), 4092–4099 (1998).

[251] L. Heijnen, P. A. Quinto-Su, X. Zhao, and C. D. Ohl. "Cavitation within a droplet". *Physics of Fluids* **21** (9), 091102 (2009).

[252] P. A. Quinto-Su and K. Ando. "Nucleating bubble clouds with a pair of laser-induced shocks and bubbles". *Journal of Fluid Mechanics* **733**, R3 (2013).

[253] S. Sembian, M. Liverts, N. Tillmark, and N. Apazidis. "Plane shock wave interaction with a cylindrical water column". *Physics of Fluids* **28** (5), 056102 (2016).

[254] T. Kondo and K. Ando. "One-way-coupling simulation of cavitation accompanied by high-speed droplet impact". *Physics of Fluids* **28** (3), 033303 (2016).

[255] N. Kyriazis, P. Koukouvinis, and M. Gavaises. "Modelling cavitation during drop impact on solid surfaces". *Advances in Colloid and Interface Science* **260**, 46–64 (2018).

[256] W. Wu, G. Xiang, and B. Wang. "On high-speed impingement of cylindrical droplets upon solid wall considering cavitation effects". *Journal of Fluid Mechanics* **857**, 851–877 (2018).

[257] W. Wu, Q. Liu, and B. Wang. "Curved surface effect on high-speed droplet impingement". *Journal of Fluid Mechanics* **909** (11402298), A7 (2021).

[258] L. Biasiori-Poulanges and K. Schmidmayer. "A phenomenological analysis of droplet shock-induced cavitation using a multiphase modeling approach". *Physics of Fluids* **35** (1), 013312 (2023).

[259] C. A. Stan et al. "Liquid explosions induced by X-ray laser pulses". *Nature Physics* **12** (10), 966–971 (2016).

[260] D. Ursescu et al. "Generation of shock trains in free liquid jets with a nanosecond green laser". *Physical Review Fluids* **5** (12), 123402 (2020).

[261] M. Vassholz et al. "Structural dynamics of water in a supersonic shockwave". *Physics of Fluids* **35** (1), 016126 (2023).

[262] J. R. Blake, G. S. Keen, R. P. Tong, and M. Wilson. "Acoustic cavitation: the fluid dynamics of non–spherical bubbles". *Philosophical Transactions of the Royal Society of London. Series A: Mathematical, Physical and Engineering Sciences* **357** (1751), 251–267 (1999). Ed. by J. R. Blake.

[263] E. A. Brujan, G. S. Keen, A. Vogel, and J. R. Blake. "The final stage of the collapse of a cavitation bubble close to a rigid boundary". *Physics of Fluids* **14** (1), 85–92 (2002).

[264] Y. X. Yang, Q. X. Wang, and T. S. Keat. "Dynamic features of a laser-induced cavitation bubble near a solid boundary". *Ultrasonics Sonochemistry* **20** (4), 1098–1103 (2013).

[265] S. R. Gonzalez-Avila, F. Denner, and C.-D. Ohl. "The acoustic pressure generated by the cavitation bubble expansion and collapse near a rigid wall". *Physics of Fluids* **33** (3), 032118 (2021).

[266] A. Kiyama, T. Shimazaki, J. M. Gordillo, and Y. Tagawa. "Direction of the microjet produced by the collapse of a cavitation bubble located in a corner of a wall and a free surface". *Physical Review Fluids* **6**, 083601 (8 2021).

[267] S. Wu, Z. Zuo, Z. Ren, and S. Liu. "Dynamics of a Laser-induced Bubble Near a Convex Free Surface". *Proceedings of the 10th International Symposium on Cavitation (CAV2018)*. Ed. by J. Katz. ASME Press, 2018. ISBN: 9780791861851.

[268] S. M. Li, A. M. Zhang, Q. X. Wang, and S. Zhang. "The jet characteristics of bubbles near mixed boundaries". *Physics of Fluids* **31** (10), 107105 (2019).

[269] A. A. Aganin, L. A. Kosolapova, and V. G. Malakhov. "Bubble dynamics near a locally curved region of a plane rigid wall". *Physics of Fluids* **34** (9), 097105 (2022).

[270] E. Kadivar, T. Phan, W. Park, and O. el Moctar. "Dynamics of a single cavitation bubble near a cylindrical rod". *Physics of Fluids* **33** (11), 113315 (2021).

[271] M. Mahmud, W. R. Smith, and A. D. Walmsley. "Numerical investigation of bubble dynamics at a corner". *Physics of Fluids* **32** (5), 053306 (2020).

[272] T. Trummler et al. "Near-surface dynamics of a gas bubble collapsing above a crevice". *Journal of Fluid Mechanics* **899**, A16 (2020).

[273] E. D. Andrews, D. Fernández Rivas, and I. R. Peters. "Cavity collapse near slot geometries". *Journal of Fluid Mechanics* **901**, A29 (2020).

[274] Y. Zhang et al. "Experimental investigations of interactions between a laser-induced cavitation bubble and a spherical particle". *Experimental Thermal and Fluid Science* **98**, 645–661 (2018).

[275] S. Li, A. Zhang, R. Han, and Q. Ma. "3D full coupling model for strong interaction between a pulsating bubble and a movable sphere". *Journal of Computational Physics* **392**, 713–731 (2019).

[276] J. Zevnik and M. Dular. "Cavitation bubble interaction with a rigid spherical particle on a microscale". *Ultrasonics Sonochemistry* **69** (April), 105252 (2020).

[277] Z. Ren, Z. Zuo, S. Wu, and S. Liu. "Particulate Projectiles Driven by Cavitation Bubbles". *Physical Review Letters* **128**, 044501 (4 2022).

[278] S. P. Wang et al. "Acoustic bubble dynamics in a microvessel surrounded by elastic material". *Physics of Fluids* **30** (1), 012104 (2018).

[279] N. N. Liu, W. B. Wu, A. M. Zhang, and Y. L. Liu. "Experimental and numerical investigation on bubble dynamics near a free surface and a circular opening of plate". *Physics of Fluids* **29** (10), 107102 (2017).

[280] E. Robert et al. "Cavitation bubble behavior inside a liquid jet". *Physics of Fluids* **19** (6), 067106 (2007).

[281] G. I. Taylor. "The formation of a blast wave by a very intense explosion I. Theoretical discussion". *Proceedings of the Royal Society of London. Series A. Mathematical and Physical Sciences* **201** (1065), 159–174 (1950).

[282] J. B. Keller and I. Kolodner. "Instability of Liquid Surfaces and the Formation of Drops". *Journal of Applied Physics* **25** (7), 918–921 (1954).

[283] Y. Zhou. "Rayleigh–Taylor and Richtmyer–Meshkov instability induced flow, turbulence, and mixing. I". *Physics Reports* **720-722**, 1–136 (2017).

[284] Y. Zhou. "Rayleigh–Taylor and Richtmyer–Meshkov instability induced flow, turbulence, and mixing. II". *Physics Reports* **723-725**, 1–160 (2017).

[285] Y. Tagawa et al. "Highly Focused Supersonic Microjets". *Phys. Rev. X* **2**, 031002 (3 2012).

[286] I. R. Peters et al. "Highly focused supersonic microjets: numerical simulations". *Journal of Fluid Mechanics* **719**, 587–605 (2013).

[287] F. J. W. A. Martins, C. C. da Silva, C. Lessig, and K. Zähringer. "Ray-Tracing Based Image Correction of Optical Distortion for PIV Measurements in Packed Beds". *Journal of Advanced Optics and Photonics* **1** (2), 71–94 (2018).

[288] C. V. Raman and G. A. Sutherland. "On the Whispering-Gallery phenomenon". *Proceedings of the Royal Society of London. Series A, Containing Papers of a Mathematical and Physical Character* **100**, 424–428 (705 1922).

[289] K. Ando, A.-Q. Liu, and C.-D. Ohl. "Homogeneous Nucleation in Water in Microfluidic Channels". *Physical Review Letters* **109**, 044501 (4 2012).

[290] A. Atchley et al. "Thresholds for cavitation produced in water by pulsed ultrasound". *Ultrasonics* **26** (5), 280–285 (1988).

[291] K. Maeda and T. Colonius. "Bubble cloud dynamics in an ultrasound field". *Journal of Fluid Mechanics* **862**, 1105–1134 (2019).

[292] M. P. Sampat et al. "Complex Wavelet Structural Similarity: A New Image Similarity Index". *IEEE Transactions on Image Processing* **18** (11), 2385–2401 (2009).

[293] W. Zhou and E. Simoncelli. "Translation insensitive image similarity in complex wavelet domain". *Proceedings. (ICASSP '05). IEEE International Conference on Acoustics, Speech, and Signal Processing, 2005.* Vol. 2. 2005.

[294] X. X. Liang et al. "Comprehensive analysis of spherical bubble oscillations and shock wave emission in laser-induced cavitation". *Journal of Fluid Mechanics* **940**, 1–56 (2022).

[295] H. Bao et al. "Impact-Driven Cavitation Bubble Dynamics". *Experiments in Fluids* **64**, 27 (2023).

[296] T. Bar-Kohany and M. Levy. "State of the art review of flash-boiling atomization". *Atomization and Sprays* **26** (12), 1259–1305 (2016).

[297] D. Loureiro et al. "Droplet size distributions in cryogenic flash atomization". *International Journal of Multiphase Flow* **142**, 103705 (2021).

[298] N. Jüngst, G. J. Smallwood, and S. A. Kaiser. "Visualization and image analysis of droplet puffing and micro-explosion in spray-flame synthesis of iron oxide nanoparticles". *Experiments in Fluids* **63**, 60 (3 2022).

[299] T. Tran et al. "Drop Impact on Superheated Surfaces". *Physical Review Letters* **108**, 036101 (3 2012).

[300] O. O. Versolato. "Physics of laser-driven tin plasma sources of EUV radiation for nanolithography". *Plasma Sources Science and Technology* **28** (8), 083001 (2019).

[301] V. Lazic and S. Jovićević. "Laser induced breakdown spectroscopy inside liquids: Processes and analytical aspects". *Spectrochimica Acta Part B: Atomic Spectroscopy* **101**, 288–311 (2014).

[302] N. Bourne and J. Field. "A high-speed photographic study of cavitation damage". *Journal of Applied Physics* **78** (7), 4423–4427 (1995).

[303] E.-A. Brujan and Y. Matsumoto. "Collapse of micrometer-sized cavitation bubbles near a rigid boundary". *Microfluidics and Nanofluidics* **13**, 957–966 (2012).

[304] J. Blake, B. Taib, and G. Doherty. "Transient cavities near boundaries. Part 1. Rigid boundary". *Journal of Fluid Mechanics* **170**, 479–497 (1986).

[305] E.-A. Brujan and A. Vogel. "Stress wave emission and cavitation bubble dynamics by nanosecond optical breakdown in a tissue phantom". *Journal of Fluid Mechanics* **558**, 281–308 (2006).

[306] S.-W. Ohl, E. Klaseboer, and B. C. Khoo. "Bubbles with shock waves and ultrasound: a review". *Interface focus* **5** (5), 20150019 (2015).

[307] E. Klaseboer et al. "Experimental and numerical investigation of the dynamics of an underwater explosion bubble near a resilient/rigid structure". *Journal of Fluid Mechanics* **537**, 387–413 (2005).

[308] A. Zhang and Y.-L. Liu. "Improved three-dimensional bubble dynamics model based on boundary element method". *Journal of Computational Physics* **294**, 208–223 (2015).

[309] G. L. Chahine, A. Kapahi, J.-K. Choi, and C.-T. Hsiao. "Modeling of surface cleaning by cavitation bubble dynamics and collapse". *Ultrasonics sonochemistry* **29**, 528–549 (2016).

[310] C. Turangan, A. Jamaluddin, G. Ball, and T. Leighton. "Free-Lagrange simulations of the expansion and jetting collapse of air bubbles in water". *Journal of Fluid Mechanics* **598**, 1–25 (2008).

[311] J. Ma, C.-T. Hsiao, and G. L. Chahine. "Euler–Lagrange simulations of bubble cloud dynamics near a wall". *Journal of Fluids Engineering* **137** (4) (2015).

[312] R. E. Tipton, D. J. Steinberg, and Y. Tomita. "Bubble expension and collapse near a rigid wall". *JSME international journal. Ser. 2, Fluids engineering, heat transfer, power, combustion, thermophysical properties* **35** (1), 67–75 (1992).

[313] J. Huang and H. Zhang. "Level set method for numerical simulation of a cavitation bubble, its growth, collapse and rebound near a rigid wall". *Acta Mechanica Sinica* **23** (6), 645–653 (2007).

[314] M.-l. Shan et al. "Investigation of cavitation bubble collapse near rigid boundary by lattice Boltzmann method". *Journal of Hydrodynamics* **28** (3), 442–450 (2016).

[315] C. Turangan, G. Ong, E. Klaseboer, and B. C. Khoo. "Experimental and numerical study of transient bubble-elastic membrane interaction". *Journal of applied physics* **100** (5), 054910 (2006).

[316] A. Shima, Y. Tomita, D. Gibson, and J. Blake. "The growth and collapse of cavitation bubbles near composite surfaces". *Journal of Fluid Mechanics* **203**, 199–214 (1989).

[317] Y. Tomita and T. Kodama. "Interaction of laser-induced cavitation bubbles with composite surfaces". *Journal of applied physics* **94** (5), 2809–2816 (2003).

[318] S. Gong, S. Ohl, E. Klaseboer, and B. Khoo. "Interaction of a spark-generated bubble with a two-layered composite beam". *Journal of Fluids and Structures* **76**, 336–348 (2018).

[319] E. Klaseboer and B. Khoo. "An oscillating bubble near an elastic material". *Journal of applied physics* **96** (10), 5808–5818 (2004).

[320] S. W. Fong et al. "Numerical analysis of a gas bubble near bio-materials in an ultrasound field". *Ultrasound in medicine & biology* **32** (6), 925–942 (2006).

[321] J. Duncan, C. Milligan, and S. Zhang. "On the interaction between a bubble and a submerged compliant structure". *Journal of Sound and Vibration* **197** (1), 17–44 (1996).

[322] G. Curtiss, D. Leppinen, Q. Wang, and J. Blake. "Ultrasonic cavitation near a tissue layer". *Journal of Fluid Mechanics* **730**, 245–272 (2013).

[323] R. Dijkink et al. "Controlled cavitation–cell interaction: trans-membrane transport and viability studies". *Physics in Medicine & Biology* **53** (2), 375 (2007).

[324] W. Lauterborn and R. Mettin. "Acoustic cavitation: bubble dynamics in high-power ultrasonic fields". *Power Ultrasonics*. Elsevier, 2015, pp. 37–78. ISBN: 978-1-78242-028-6.

[325] L. A. Crum. "Cavitation microjets as a contributory mechanism for renal calculi disintegration in ESWL". *The Journal of urology* **140** (6), 1587–1590 (1988).

[326] S. Zhu, F. H. Cocks, G. M. Preminger, and P. Zhong. "The role of stress waves and cavitation in stone comminution in shock wave lithotripsy". *Ultrasound in medicine & biology* **28** (5), 661–671 (2002).

[327] C.-D. Ohl et al. "Sonoporation from jetting cavitation bubbles". *Biophysical journal* **91** (11), 4285–4295 (2006).

[328] F. Yuan, C. Yang, and P. Zhong. "Cell membrane deformation and bioeffects produced by tandem bubble-induced jetting flow". *Proceedings of the National Academy of Sciences* **112** (51), E7039–E7047 (2015).

[329] F. Reuter and R. Mettin. "Electrochemical wall shear rate microscopy of collapsing bubbles". *Physical Review Fluids* **3**, 063601 (6 2018).

[330] S. R. Gonzalez-Avila, A. C. van Blokland, Q. Zeng, and C.-D. Ohl. "Jetting and shear stress enhancement from cavitation bubbles collapsing in a narrow gap". *Journal of Fluid Mechanics* **884**, A23 (2020).

[331] I. Teixeira et al. "Polydimethylsiloxane mechanical properties: A systematic review". *AIMS Mater. Sci* **8**, 952–973 (2021).

[332] M. Liu et al. "Thickness-dependent mechanical properties of polydimethylsiloxane membranes". *Journal of micromechanics and microengineering* **19** (3), 035028 (2009).

[333] R. Domingo-Roca et al. "Non-destructive analysis of the mechanical properties of 3D-printed materials". *Journal of Nondestructive Evaluation* **41** (1), 22 (2022).

[334] D. Abbondanza, M. Gallo, and C. M. Casciola. "Cavitation over solid surfaces: microbubble collapse, shock waves, and elastic response". *Meccanica*, 1–11 (2022).

[335] J.-Y. Tinevez et al. "TrackMate: An open and extensible platform for single-particle tracking". *Methods* **115**, 80–90 (2017).

[336] T. Trummler, S. J. Schmidt, and N. A. Adams. "Effect of stand-off distance and spatial resolution on the pressure impact of near-wall vapor bubble collapses". *International Journal of Multiphase Flow* **141**, 103618 (2021).

[337] G. L. Chahine and C.-T. Hsiao. "Modelling cavitation erosion using fluid–material interaction simulations". *Interface focus* **5** (5), 20150016 (2015).

[338] F. Denner et al. "Predicting laser-induced cavitation near a solid substrate". *Proceedings in Applied Mathematics and Mechanics* **20** (1), e202000007 (2021).

[339] Q. Zeng, S. R. Gonzalez-Avila, S. T. Voorde, and C.-D. Ohl. "Jetting of viscous droplets from cavitation-induced Rayleigh–Taylor instability". *Journal of Fluid Mechanics* **846**, 916–943 (2018).

[340] J. M. Rosselló, H. Reese, K. A. Raman, and C.-D. Ohl. "Bubble nucleation and jetting inside a millimetric droplet". *arXiv* (2023).

[341] S. F. Jones, G. M. Evans, and K. P. Galvin. "Bubble nucleation from gas cavities — a review". *Advances in Colloid and Interface Science* **80** (1), 27–50 (1999).

[342] L. van Wijngaarden. "Mechanics of collapsing cavitation bubbles". *Ultrasonics Sonochemistry* **29**, 524–527 (2016).

[343] A. A. Atchley and A. Prosperetti. "The crevice model of bubble nucleation". *Journal of the Acoustical Society of America* **86** (3), 1065–1084 (1989).

[344] H. B. Marschall, K. A. Mørch, A. P. Keller, and M. Kjeldsen. "Cavitation inception by almost spherical solid particles in water". *Physics of Fluids* **15** (2), 545–553 (2003).

[345] M. Arora, C.-D. Ohl, and K. A. Mørch. "Cavitation Inception on Microparticles: A Self-Propelled Particle Accelerator". *Physical Review Letters* **92**, 174501 (17 2004).

[346] B. M. Borkent, S. Gekle, A. Prosperetti, and D. Lohse. "Nucleation threshold and deactivation mechanisms of nanoscopic cavitation nuclei". *Physics of Fluids* **21** (10), 102003 (2009).

[347] J. W. Holl. "Nuclei and Cavitation". *Journal of Basic Engineering* **92** (4), 681–688 (1970).

[348] L. A. Crum. "Tensile strength of water". *Nature* **278**, 148–149 (1979).

[349] M. E. M. Azouzi, C. Ramboz, J.-F. Lenain, and F. Caupin. "A coherent picture of water at extreme negative pressure". *Nature Physics* **9**, 38–41 (2013).

[350] G. Baffou, J. Polleux, H. Rigneault, and S. Monneret. "Super-Heating and Micro-Bubble Generation around Plasmonic Nanoparticles under cw Illumination". *Journal of Physical Chemistry C* **118** (9), 4890–4898 (2014).

[351] M. Ida, T. Naoe, and M. Futakawa. "Direct observation and theoretical study of cavitation bubbles in liquid mercury". *Physical Review E* **75**, 046304 (4 2007).

[352] A. Prosperetti. "Vapor Bubbles". *Annual Review of Fluid Mechanics* **49** (1), 221–248 (2017).

[353] S. D. Lubetkin. "Why Is It Much Easier To Nucleate Gas Bubbles than Theory Predicts?" *Langmuir* **19** (7), 2575–2587 (2003).

[354] V. Shvalya et al. "Surface-enhanced Raman spectroscopy for chemical and biological sensing using nanoplasmonics: The relevance of interparticle spacing and surface morphology". *Applied Physics Reviews* **7** (3), 031307 (2020).

[355] K. Iwata et al. "Chemical structure imaging of a single molecule by atomic force microscopy at room temperature". *Nature Communications* **6**, 1–7 (1 2015).

[356] E. Stride and C. Coussios. "Nucleation, mapping and control of cavitation for drug delivery". *Nature Reviews Physics* **1** (8), 495–509 (2019).

[357] H. Chen et al. "Blood Vessel Deformations on Microsecond Time Scales by Ultrasonic Cavitation". *Physical Review Letters* **106**, 034301 (3 2011).

[358] P. Prentice et al. "Membrane disruption by optically controlled microbubble cavitation". *Nature Physics* **1** (2), 107–110 (2005).

[359] T. Yamashita and K. Ando. "Low-intensity ultrasound induced cavitation and streaming in oxygen-supersaturated water: Role of cavitation bubbles as physical cleaning agents". *Ultrasonics Sonochemistry* **52**, 268–279 (2019).

[360] A. Sesis et al. "Influence of acoustic cavitation on the controlled ultrasonic dispersion of carbon nanotubes". *The Journal of Physical Chemistry B* **117** (48), 15141–15150 (2013).

[361] S. Xu et al. "Dependence of pulsed focused ultrasound induced thrombolysis on duty cycle and cavitation bubble size distribution". *Ultrasonics Sonochemistry* **22**, 160–166 (2015).

[362] Y. Fu et al. "Size-dependent inertial cavitation of soft materials". *Journal of the Mechanics and Physics of Solids* **137**, 103859 (2020).

[363] A. Brotchie, F. Grieser, and M. Ashokkumar. "Effect of Power and Frequency on Bubble-Size Distributions in Acoustic Cavitation". *Physical Review Letters* **102**, 084302 (8 2009).

[364] E. M. Strohm and M. C. Kolios. "Sound velocity and attenuation measurements of perfluorocarbon liquids using photoacoustic methods". *2011 IEEE International Ultrasonics Symposium*, 2368–2371 (2011).

[365] C. T. Wilson et al. "Comparative study of the dynamics of laser and acoustically generated bubbles in viscoelastic media". *Physical Review E* **99**, 043103 (2019).

[366] N. Bremond, M. Arora, C.-D. Ohl, and D. Lohse. "Cavitation on surfaces". *Journal of Physics: Condensed Matter* **17** (45), S3603–S3608 (2005).

[367] N. Bremond, M. Arora, C.-D. Ohl, and D. Lohse. "Controlled Multibubble Surface Cavitation". *Physical Review Letters* **96**, 224501 (22 2006).

[368] L. Y. Yeo and J. R. Friend. "Ultrafast microfluidics using surface acoustic waves". *Biomicrofluidics* **3** (1) (2009).

[369] U. Gutiérrez-Hernández, F. De Colle, P. A. Quinto-Su, and C.-D. Ohl. "Transient time-delay focusing of shock waves in thin liquids". *Journal of Fluid Mechanics* **910** (A27) (2021).

[370] L. M. Lyamshev. "Optoacoustic sources of sound". *Soviet Physics Uspekhi* **24** (12), 977–995 (1981).

[371] D. Veysset et al. "Acoustical breakdown of materials by focusing of laser-generated Rayleigh surface waves". *Applied Physics Letters* **111** (3) (2017).

[372] B. P. Barber et al. "Defining the unknowns of sonoluminescence". *Physics Reports* **281** (2), 65–143 (1997).

[373] R. Toegel, B. Gompf, R. Pecha, and D. Lohse. "Does Water Vapor Prevent Upscaling Sonoluminescence?" *Physical Review Letters* **85**, 3165–3168 (15 2000).

[374] K. Niu. "Shock waves in gas and plasma". *Laser and Particle Beams* **14** (2), 125–132 (1996).

[375] T. R. Boehly et al. "Velocity and timing of multiple spherically converging shock waves in liquid deuterium". *Physical Review Letters* **106** (19), 1–4 (2011).

[376] D. W. Larson. "NIF laser line-replaceable units (LRUs)". *Optical Engineering at the Lawrence Livermore National Laboratory II: The National Ignition Facility* **5341**, 127–136 (2004). Ed. by M. A. Lane and C. R. Wuest.

[377] T. Pezeril et al. "Direct Visualization of Laser-Driven Focusing Shock Waves". *Physical Review Letters* **106**, 214503 (21 2011).

[378] D. Veysset et al. "Glass fracture by focusing of laser-generated nanosecond surface acoustic waves". *Scripta Materialia* **158**, 42–45 (2019).

[379] D. Veysset et al. "Laser-induced versus shock wave induced transformation of highly ordered pyrolytic graphite". *Applied Physics Letters* **106** (16) (2015).

[380] L. E. Dresselhaus-Cooper et al. "Pressure-Thresholded Response in Cylindrically Shocked Cyclotrimethylene Trinitramine (RDX)". *The Journal of Physical Chemistry A* **124** (17), 3301–3313 (2020). PMID: 32009390.

[381] A. Y. Klokov, V. S. Krivobok, A. I. Sharkov, and N. Y. Frolov. "Optical Excitation of Converging Surface Acoustic Waves in the Gigahertz Range on Silicon". *Sensors* **22** (3), 870 (2022).

[382] R. Xue et al. "Nondestructive characterization of aluminum grain size using a ring-shaped laser ultrasonic method". *AIP Advances* **12** (4), 045114 (2022).

[383] H. W. Baac et al. "Carbon-nanotube optoacoustic lens for focused ultrasound generation and high-precision targeted therapy". *Scientific Reports* **2**, 1–8 (2012).

[384] W. Chan, T. Hies, and C.-D. Ohl. "Laser-generated focused ultrasound for arbitrary waveforms". *Applied Physics Letters* **109** (17), 174102 (2016).

[385] C. Thring, Y. Fan, and R. Edwards. "Focused Rayleigh wave EMAT for characterisation of surface-breaking defects". *NDT & E International* **81**, 20–27 (2016).

[386] J. Zhao et al. "Focusing of Rayleigh waves with gradient-index phononic crystals". *Applied Physics Letters* **108** (22), 221905 (2016).

[387] S. C. Chowdhury, E. A. Wise, R. Ganesh, and J. W. Gillespie. "Effects of surface crack on the mechanical properties of Silica: A molecular dynamics simulation study". *Engineering Fracture Mechanics* **207**, 99–108 (2019).

[388] P. Renganathan, T. S. Duffy, and Y. M. Gupta. "Hugoniot states and optical response of soda lime glass shock compressed to 120 GPa". *Journal of Applied Physics* **127** (20), 205901 (2020).

[389] Y. F. Xie et al. "Mechanical and microstructural response of densified silica glass under uniaxial compression: Atomistic simulations". *Chinese Physics B* **29** (10) (2020).

[390] W. Liu, S. Yuan, and X. Guo. "Atomic understanding of the densification removal mechanism during chemical mechanical polishing of fused glass". *Applied Surface Science* **591**, 153166 (2022).

[391] Y. Zhang, C. Yang, H. Qiang, and P. Zhong. "Nanosecond shock wave-induced surface acoustic waves and dynamic fracture at fluid-solid boundaries". *Physical Review Research* **1** (3), 33068 (2019).

[392] Fisherbrand. "Focus on Glassware & Plasticware". *Focus on Glasssware & Pasticware*, 12 (2016).

[393] B. Wu, C. Frez, and G. J. Diebold. "Photoacoustic transients produced by laser generated, ultrahigh thermal gradients". *Applied Physics Letters* **103** (12) (2013).

[394] Q. Zeng, S. R. Gonzalez-Avila, and C.-D. Ohl. "Splitting and jetting of cavitation bubbles in thin gaps". *Journal of Fluid Mechanics* **896** (2020).

[395] J. Achenbach. "Chapter 5 - Plane Harmonic Waves in Elastic Half-Spaces". *North-Holland Series in Applied Mathematics and Mechanics* **16**, 165–201 (1973).

[396] J. P. Guin and S. M. Wiederhorn. "Fracture of silicate glasses: Ductile or brittle?" *Physical Review Letters* **92** (21), 21–24 (2004).

[397] F. Célarié et al. "Glass Breaks like Metal, but at the Nanometer Scale". *Physical Review Letters* **90** (7), 4 (2003).

[398] L. Q. Shen et al. "Observation of cavitation governing fracture in glasses". *Science Advances* **7** (14), 1–8 (2021).

[399] S. Vincent, B. Murty, M. Kramer, and J. Bhatt. "Micro and nano indentation studies on Zr60Cu10Al15Ni15 bulk metallic glass". *Materials & Design* **65**, 98–103 (2015).

[400] S. Yoshida et al. "Direct observation of indentation deformation and cracking of silicate glasses". *Journal of Materials Research* **30** (15), 2291–2299 (2015).

[401] L. Gu et al. "Direct in situ observation of metallic glass deformation by real-time nano-scale indentation". *Scientific Reports* **5**, 1–5 (2015).

[402] Y. Shi, A. Neubrand, and D. Koch. "Characterization of Hardness and Stiffness of Ceramic Matrix Composites through Instrumented Indentation Test". *Advanced Engineering Materials* **21** (5), 1800806 (2019).

[403] J. Qiu et al. "Indentation Strain Rate Sensitivity of CoCrFeNiAl0.3 High-Entropy Alloy". *Advanced Engineering Materials* **21** (2), 1800744 (2018).

[404] X. Wang et al. "A review on the mechanical properties for thin film and block structure characterised by using nanoscratch test". *Nanotechnology Reviews* **8** (1), 628–644 (2019).

[405] X. Ding and M. Rahman. "A study of the performance of cutting polycrystalline Al 6061 T6 with single crystalline diamond micro-tools". *Precision Engineering* **36** (4), 593–603 (2012).

[406] S. James and M. Sundaram. "A Molecular Dynamics Simulation Study of Material Removal Mechanisms in Vibration Assisted Nano Impact-Machining by Loose Abrasives". *Journal of Manufacturing Science and Engineering* **139** (8) (2017). 081014.

[407] J. Zhao et al. "Review of femtosecond laser direct writing fiber-optic structures based on refractive index modification and their applications". *Optics & Laser Technology* **146**, 107473 (2022).

[408] S. P. McJunkins and J. I. Thornton. "Glass fracture analysis. A review". *Forensic Science* **2** (C), 1–27 (1973).

[409] G. Li and K. H. Moelle. "A SEM study of conchoidal structures on fracture surfaces of sandstones". *Tectonophysics* **216** (3-4), 255–272 (1992).

[410] V. Fréchette. *Failure Analysis of Brittle Materials*. 28. Advances in Ceramics, 1990. ISBN: 978-0-944-90430-5.

[411] D. Lewke et al. "Thermal laser separation – a novel dicing technology fulfilling the demands of volume manufacturing of 4H-SiC devices". *Materials Science Forum* **821-823**, 528–532 (2015).

[412] G. H. Schnerr and J. Sauer. “Physical and numerical modeling of unsteady cavitation dynamics”. *Fourth international conference on multiphase flow* **1** (2001).

Declaration of honour

I hereby declare that I prepared this thesis without the impermissible help of third parties and that none other than the aids indicated have been used; all sources of information are clearly marked, including my own publications.

In particular, I have not consciously:

- fabricated data or rejected undesirable results,
- misused statistical methods with the aim of drawing other conclusions than those warranted by the available data,
- plagiarised external data or publications,
- presented the results of other researchers in a distorted way.

I am aware that violations of copyright may lead to injunction and damage claims by the author and also to prosecution by law enforcement authorities. I hereby agree that the thesis may be electronically reviewed with the aim of identifying plagiarism.

This work has not yet been submitted as a doctoral thesis in the same or a similar form in Germany, nor in any other country. It has not yet been published as a whole.

Magdeburg, 22.08.2023

Hendrik Reese